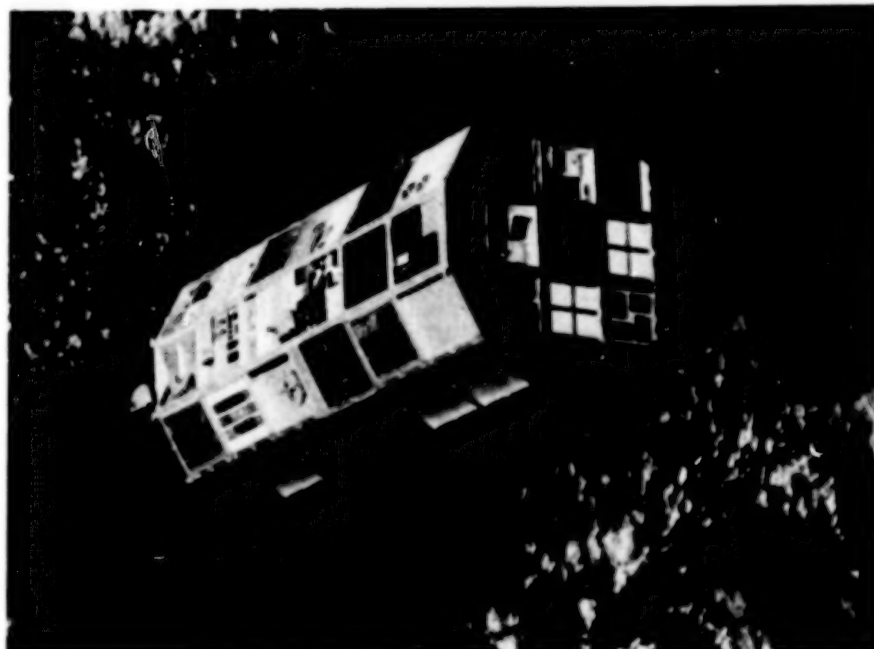


0830 - H-10
327
AUG 19 1989

NASI.55;3035/pt.1
NASA Conference Publication 3035
Part 1

NASA/SDIO Space Environmental Effects on Materials Workshop



*Proceedings of a workshop held at
NASA Langley Research Center
Hampton, Virginia
June 28-July 1, 1988*

NASA

19/12

COMPLETED

NASA/SDIO Space Environmental Effects on Materials Workshop

Compiled by
Louis A. Teichman and Bland A. Stein
NASA Langley Research Center
Hampton, Virginia

Proceedings of a workshop jointly
sponsored by the National Aeronautics
and Space Administration and the
Strategic Defense Initiative
Organization, and held at
NASA Langley Research Center
Hampton, Virginia
June 28-July 1, 1988



National Aeronautics and
Space Administration
Office of Management
Scientific and Technical
Information Division

1989

BLANK PAGE

PREFACE

Until now, most satellites have been launched with limited life expectancies (at most 3-5 years) and the materials used and the operating orbits selected for "long-term" flights have evolved from many successful shorter duration flights. During the 1990's, the Strategic Defense Initiative Organization (SDIO) plans to launch various platforms and satellites, and NASA plans to deploy Space Station Freedom and other large space structures. All of these spacecraft are expected to remain in space for 10 to 30 years at altitudes varying from low Earth orbit to geosynchronous orbit. The materials community is concerned that these systems will be vulnerable to environmentally induced degradation that will result in reduced performance. The environments of major concern are particulate radiation, atomic oxygen, micrometeoroids and debris, contamination, spacecraft charging, and solar radiation (ultraviolet (UV) and thermal cycling).

Although many spacecraft have performed successfully for relatively short periods of time, the effects of these environments, both individually and synergistically, on long-term materials performance is virtually unknown, and terrestrial facilities and tests are unable to resolve the uncertainties. In late 1987 opportunities for piggy-back or getaway special experiments or even a dedicated spaceflight seemed possible. Immediately, questions of which experiments to conduct and in what order of priority arose.

The primary objective of this workshop was to identify and prioritize candidate spaceflight experiments; that is, which materials experiments must be conducted in space to achieve maximum assurance that SDIO and NASA space assets will survive and perform for 10-30 years.

A secondary objective was to provide concise but authoritative tutorials describing each environmental factor. These tutorials would present current knowledge on topics such as each factor's applicable orbital ranges, its variations with time, how it interacts with various materials, and the subsequent consequences to materials or system performance. In addition, assessments of the sources of this knowledge (derived from true space exposure data or from modeling and laboratory simulations), the availability and authenticity of terrestrial test facilities, and the current understanding of interactions (synergisms) between these environmental effects would be offered.

The workshop was cosponsored by SDIO and NASA. It was organized by Charles F. Bersch of the Institute for Defense Analyses; Thomas W. Crooker of the Office of Aeronautics and Space Technology, NASA Headquarters; and Bland A. Stein of NASA Langley Research Center. The papers are published in the order in which they were presented at the Workshop; Section I contains an opening overview session on Environments and Materials Effects, followed by more detailed sessions on past spacecraft experience, and each of the environmental factors mentioned above. Each session was organized by its chairman, who also led the subsequent working group session for his environmental factor and prepared the presentations reproduced in Section II.

Administrative arrangements for the Workshop, as well as the collection of papers for and preparation of these Proceedings, was accomplished under the supervision of Dr. Louis A. Teichman at NASA Langley.

The efforts of the Executive Planning Committee and the Workshop Co-Chairmen are hereby acknowledged. They provided the perspective necessary to define the objectives and to organize a multidisciplinary Space Environmental Effects Workshop. They also planned the technical content of the tutorial presentations and the interactions of the groups representing the individual environmental disciplines. As a result, the objectives of the meeting regarding overall conclusions and recommendations were successfully reached by the collective efforts of all the Workshop participants.

The Executive Planning Committee consisted of

Charles F. Bersch	Institute for Defense Analysis
Herbert A. Cohen	W. J. Schafer Associates
Burton G. Cour-Palais	NASA Marshall Space Flight Center
Thomas W. Crooker	NASA Headquarters
Raymond L. Gause	NASA Marshall Space Flight Center
William Hong	Institute for Defense Analysis
Lubert J. Leger	NASA Johnson Space Center
Ranty H. Liang	Jet Propulsion Laboratory
Carolyn K. Purvis	NASA Lewis Research Center
Fred Smidt	Naval Research Laboratories
Bland A. Stein	NASA Langley Research Center
Louis A. Teichman	NASA Langley Research Center
Jack J. Triolo	NASA Goddard Space Flight Center
James. T. Visentine	NASA Johnson Space Center

The Workshop Co-Chairmen were Charles Bersch, Tom Crooker, and Bland Stein.

The excellence of the meeting facilities at the NASA Langley Activities Center and the continued cooperation of the staff, under the supervision of Ms. Patricia Gates, contributed significantly to the success of the Workshop. Arrangements were coordinated for the Executive Planning Committee by Dr. Louis Teichman.

Mr. Charles F. Bersch provided the primary impetus to the concept and basic goals of this Space Environmental Effects on Materials Workshop. The space environmental effects community owes him a debt of gratitude for his efforts.

CONTENTS

PREFACE	iii
---------------	-----

PART I

SECTION I - THE TUTORIALS

SESSION 1: Overview: Environments and Materials Effects

Chairman: B. Stein - NASA Langley Research Center

Overview of Environmental Factors	5
C. K. Purvis - NASA Lewis Research Center	
Structural Materials for Space Applications	25
Darrel R. Tenney - NASA Langley Research Center	
Radiation Effects in Spacecraft Electronics	53
James P. Raymond - Mission Research Corporation	
Environmental Effects on Spacecraft Materials	75
J. W. Haffner - Rockwell International	
Surface Treatment Using Metal Foil Liner	87
Ray Garvey - Oak Ridge National Laboratory	
The Long Duration Exposure Facility Material Experiments	101
William H. Kinard and James L. Jones, Jr. - NASA Langley Research Center	

SESSION 2: SPACECRAFT EXPERIENCE

Chairman: J. Triolo - NASA Goddard Space Flight Center

Some Examples of the Degradation of Properties of Materials in Space	109
Frederick E. Betz and Joseph A. Hauser - Naval Research Laboratory	
Trends in Environmentally Induced Spacecraft Anomalies	123
Daniel C. Wilkinson - National Oceanic and Atmospheric Administration	
Returned Solar Max Hardware Degradation Study Results	133
Jack J. Triolo and Gilbert W. Ousley - Goddard Space Flight Center	
EnviroNet: Space Environment for Strategic Defense Initiative Experiments	161
Michael Lauriente - NASA Goddard Space Flight Center	

†Paper not available at time of publication.

SESSION 3: ATOMIC OXYGEN

Chairmen: L. Leger and J. Visentine
NASA Lyndon B. Johnson Space Center

Environmental Definition of the Earth's Neutral Atmosphere	179
James T. Visentine - NASA Lyndon B. Johnson Space Center	
Atomic Oxygen Effects on Materials	197
Bruce A. Banks and Sharon Rutledge - NASA Lewis Research Center	
Joyce A. Brady - Sverdrup Technology, Inc.	
James E. Merrow - Ohio University	
Atomic Oxygen Effects Applications to Spacecraft	↑
Ann Whitaker - NASA George C. Marshall Space Flight Center	
Atomic Oxygen Effects on Spacecraft Materials - The State of the Art of Our Knowledge	241
Steven L. Koontz - NASA Lyndon B. Johnson Space Center	

SESSION 4: MICROMETEORIDS AND DEBRIS

Chairman: Andrew Potter - NASA Lyndon B. Johnson Space Center

The Long-Term Effects of the Micrometeoroid and Orbital Debris Environments on Materials Used in Space	257
Burton G. Cour-Palais - NASA Lyndon B. Johnson Space Center	
Orbital Debris Environment and Data Requirements	281
Donald J. Kessler - NASA Lyndon B. Johnson Space Center	
Microparticle Impacts in Space - Results From Solar MAX Satellite and Shuttle Witness Plate Inspections	301
David S. McKay - NASA Lyndon B. Johnson Space Center	

SESSION 5: CONTAMINATION

Chairman: C. Maag - Jet Propulsion Laboratory

S/C Contamination Environments Overview	↑
L. Bareiss - Martin Marietta Corporation	
Spacecraft Contamination Experience	331
E. N. Borson - The Aerospace Corporation	
Effects of the Contamination Environment on Surfaces and Materials	353
Carl R. Maag - Jet Propulsion Laboratory	

PART II*

SESSION 6: TRAPPED RADIATION

Chairmen: W. K. Stuckey and A. L. Vampola
The Aerospace Corporation

The Space Particle Environment	367
A. L. Vampola - The Aerospace Corporation	
Effects of Space Radiation on Electronic Microcircuits	383
W. A. Kolasinski - The Aerospace Corporation	
The Radiation Belt Mission on CRRES	†
D. Hardy - Air Force Geophysics Laboratory	

SESSION 7: SOLAR RADIATION

Chairman: Wayne S. Slemp - NASA Langley Research Center

Space Vehicle Thermal Testing: Principles, Practices, and Effectiveness	395
Donald F. Gluck - The Aerospace Corporation	
Ultraviolet Radiation Effects	425
Wayne S. Slemp - NASA Langley Research Center	
Effects of Thermal Cycling on Composite Materials for Space Structures	447
Stephen S. Tompkins - NASA Langley Research Center	

SESSION 8: SPACECRAFT CHARGING

Chairman: N. John Stevens - TRW

Dielectrics for Long Term Space Exposure and Spacecraft Charging - A Briefing	473
A. R. Frederickson - Air Force Geophysics Laboratory	
An Overview of Charging Environments	495
S. B. Gabriel and H. B. Garrett - Jet Propulsion Laboratory	
Surface Phenomena in Plasma Environments	511
C. K. Purvis and D. C. Ferguson - NASA Lewis Research Center	
Influence of Charging Environments on Spacecraft Materials and System Performance	535
N. John Stevens - TRW Space and Technology Group	

SECTION II-A

WORKING GROUP ORAL PRESENTATIONS	543
---	------------

*Part II presented under separate cover.

Atomic Oxygen	545
Micrometeoroids and Debris	553
Contamination	559
Trapped Radiation	565
Appendix: Trapped Particle Flux Models at NSSDC/WDC-A-R&S	569
D. Bilitza, D. M. Sawyer, J. H. King	
Solar Radiation	573
Spacecraft Charging	577

SECTION II-B

WORKING GROUP WRITTEN PRESENTATIONS	585
Atomic Oxygen	587
Meteoroid/Orbital Debris Effects on Materials	589
Contamination	↑
Trapped Radiation Effects	597
Solar Radiation	607
Spacecraft Charging	609

SECTION II-C

Conclusions and Recommendations to NASA and SDIO	621
As summarized by William Hong - Institute for Defense Analysis	

SECTION I

THE TUTORIALS

BLANK PAGE

SESSION 1: OVERVIEW: ENVIRONMENTS AND MATERIALS EFFECTS

Chairman: B. Stein
NASA Langley Research Center

BLANK PAGE

OVERVIEW OF ENVIRONMENTAL FACTORS*

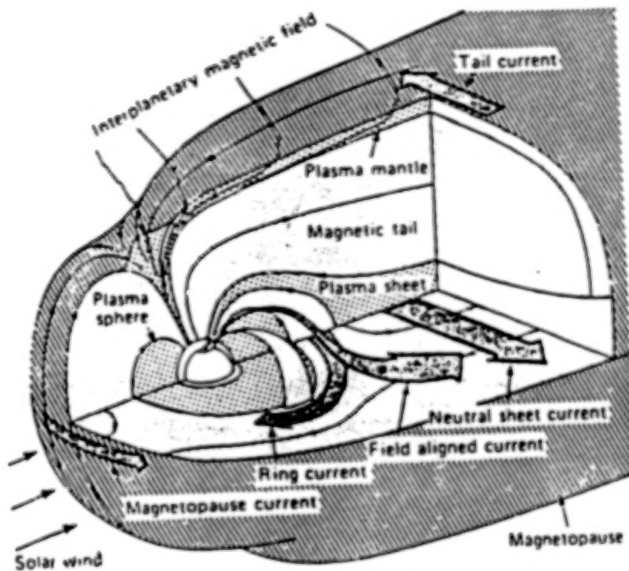
C. K. Purvis
NASA Lewis Research Center
Cleveland, Ohio

*Original figures not available at time of publication.

THE ENVIRONMENT

Near-Earth space is a complex, dynamic environment. The energies, densities, and constituents of the natural orbital environment vary with position (attitude, latitude, longitude), local time, season, and solar activity. The presence and activities of space systems modify many of the natural environment constituents (such as neutral particles and plasmas) so that the local environment may be quite different from the natural one. The local environment will interact with the system, its subsystems, surfaces, and structures. The impact of these interactions on the system must be assessed to ensure successful operation. Effects of the environment on the surface and structural materials play a crucial role in determining system function, reliability, and lifetime.

NEAR EARTH SPACE IS NOT EMPTY



THE EARTH'S MAGNETOSPHERE

IT CONTAINS

- 0 NEUTRAL ATOMS
- 0 PLASMAS
- 0 FIELDS
- 0 RADIATION
- 0 PARTICULATES

VARIABLES WITH

- 0 LOCAL TIME (DAY/NIGHT)
- 0 SOLAR CYCLE

SYSTEM PRESENCE AND OPERATIONS ALTER
LOCAL ENVIRONMENT

SYSTEM-ENVIRONMENT INTERACTIONS

- 0 INCREASE WITH SYSTEM SIZE, POWER
AND ACTIVITY
- 0 IMPACT SYSTEM/SUBSYSTEM
 - FUNCTIONAL
 - OPERATIONS
 - RELIABILITY
 - LIFETIME

THE TERRESTRIAL SPACE ENVIRONMENT

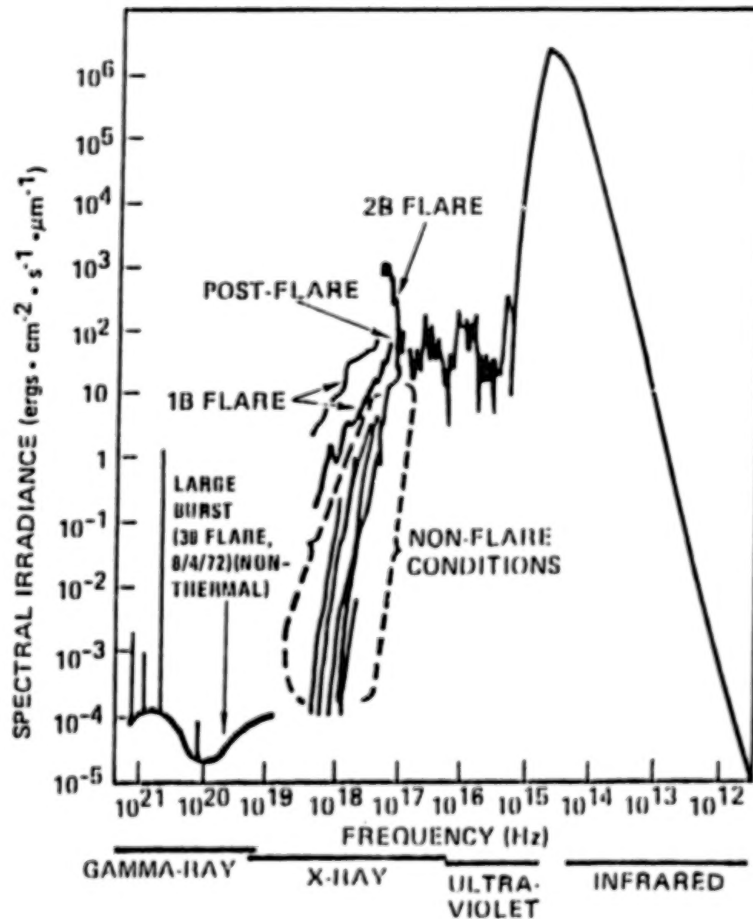
The terrestrial space environment comprises many factors, each of which can have important effects on space systems. These effects must be accounted for to ensure successful designs. This chart summarizes the natural environment factors (debris is included, though not truly a "natural" factor, because it is important and not generated by the system being considered) and their effects, and notes the importance of system-generated components. The "enhanced" or threat environment is noted for completeness, but it is not considered further here. Many of the effects listed are materials related. It is the environment factors associated with these effects on which we now focus. These are solar radiation, meteoroids and debris, neutral atmosphere, plasmas, trapped radiation, and system-generated contaminants. In what follows, each of these environments is overviewed briefly. More details will be found in the individual "environment" sections of the Workshop's focus sessions.

-EFFECTS ON SPACE SYSTEMS-

<u>ENVIRONMENTAL FACTOR</u>	<u>EFFECTS</u>
GRAVITY	ACCELERATION, TORQUES
SUNLIGHT & ALBEDO	HEATING, POWER, DRAG, TORQUES, PHOTOEMISSION, MATERIAL DAMAGE, SENSOR NOISE
METEORIDS & DEBRIS	MECHANICAL DAMAGE, ENHANCED PLASMA INTERACTIONS
NEUTRAL ATMOSPHERE	DRAG, TORQUE, MATERIAL DEGRADATION, HEATING
FIELDS	TORQUES, DRAG, SURFACE CHARGES, POTENTIALS
PLASMAS	CHARGING, INDUCED ARCING, POWER LOSSES, POTENTIALS, ENHANCED CONTAMINATION, CHANGE OF E-M REFRACTIVE INDEX, PLASMA WAVES & TURBULENCE
FAST CHARGED PARTICLES	RADIATION DAMAGE, ARCING, SINGLE EVENT UPSETS, NOISE, HAZARD TO MAN
SYSTEM GENERATED	SYSTEM DEPENDENT: NEUTRALS, PLASMAS, FIELDS VIBRATION, TORQUES, RADIATION, PARTICULATES
ENHANCED	EMP & RELATED

THE SOLAR SPECTRUM

This chart gives an overview of the solar spectrum, from the gamma ray out to the far infrared. Some 99.5% of the Sun's radiant energy is in the 1200Å to 10 μm wavelength (2.5×10^{-15} - 3×10^{-13} Hz) range. The flux levels in the visible and near-ultraviolet (UV) are relatively stable, whereas those in the extreme ultraviolet (EUV), X, and gamma ray region are highly variable and depend on solar activity.

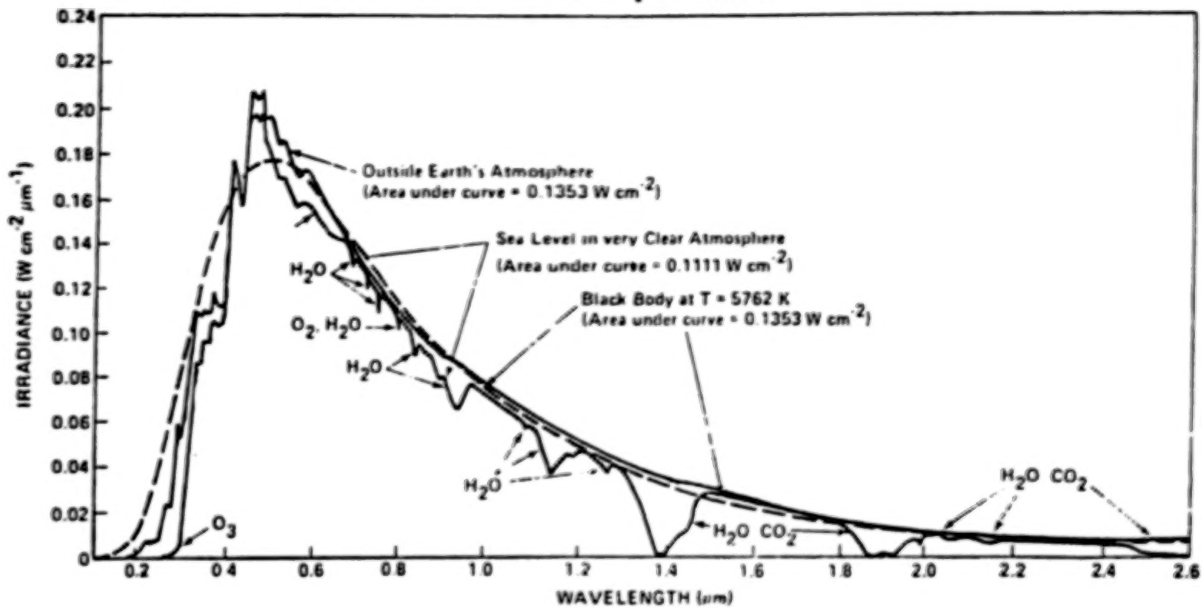


NASA-GODDARD SPACE FLIGHT CENTER
GREENBELT, MARYLAND
AUGUST, 1976

SOLAR IRRADIANCE

The solar irradiance spectrum in orbit in the UV through IR range is well approximated by black body radiation for a $T = 5762^{\circ}\text{K}$ object.

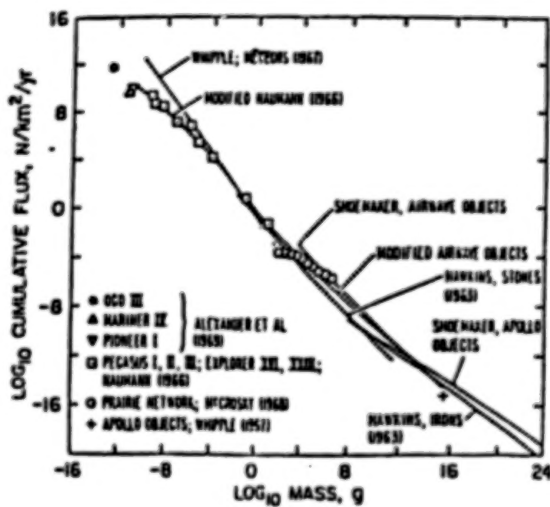
The Solar Spectrum



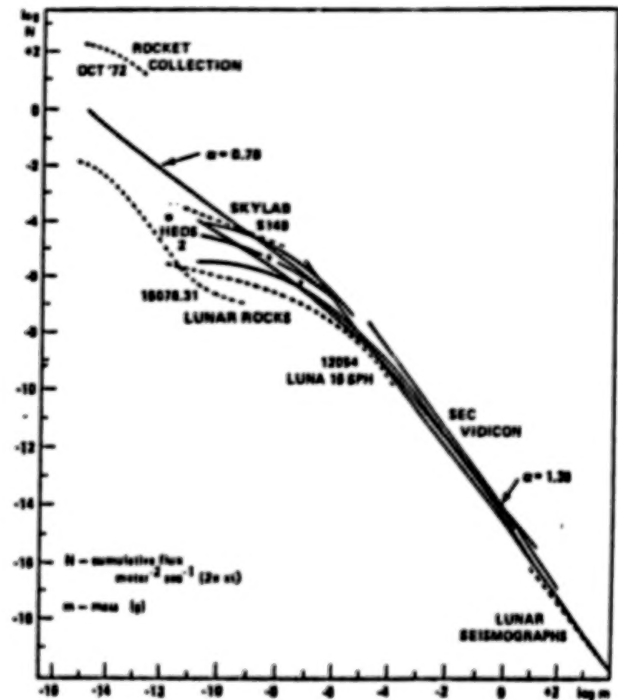
Normally incident solar radiation at sea level on very clear days, solar spectral irradiance outside the Earth's atmosphere at 1 AU, and blackbody spectral irradiance curve at $T = 5762^{\circ}\text{K}$ (normalized to 1 AU)

METEOROID ENVIRONMENT

Meteoroids are an obvious potential source of mechanical damage to spacecraft materials. Total mass influx of meteoroids is estimated as 10^{10} gm/year. Average velocity of meteoroids is considered in the models to be 20 km/second and density is considered to be approximately $.5 \text{ gm/cm}^3$ for cometary meteoroids and approximately 2 gm/cm^3 for asteroidal ones. The figures show one-year average estimates of cumulative number fluxes from various sources. In modeling this environment, N is taken to be of the form $N = \text{Const}/m^\alpha$ where α is a slowly varying parameter of order unity (see right-hand figure).



Terrestrial mass-influx rates of meteoroids. N is the flux of particles with mass greater than m (2-28).



Cumulative particle fluxes from various data sources

METEOROID IMPACTS

Estimates of frequency of meteoroid impacts can be made using formulas given in NASA SP-8013 and SP-8042. These models are old but are still used for design.

NASA SP-8013 GIVES COMETARY METEOROID FLUX N AT 1AU AS:

$$\begin{aligned} \log_{10} N &= -14.37 - 1.213 \log_{10} M & 10^{-6} \leq M \leq 10^0 \\ \log_{10} N &= -14.34 - 1.584 \log_{10} M - 0.063 (\log_{10} M)^2 & 10^{-12} \leq M \leq 10^{-6} \end{aligned}$$

N = # OF IMPACTS OF MASS M GRAMS AND LARGER PER SQUARE METER PER SEC.

MULTIPLY BY DEFOCUSING FACTOR G_e AND EARTH SHIELDING FACTOR $J'(R)$

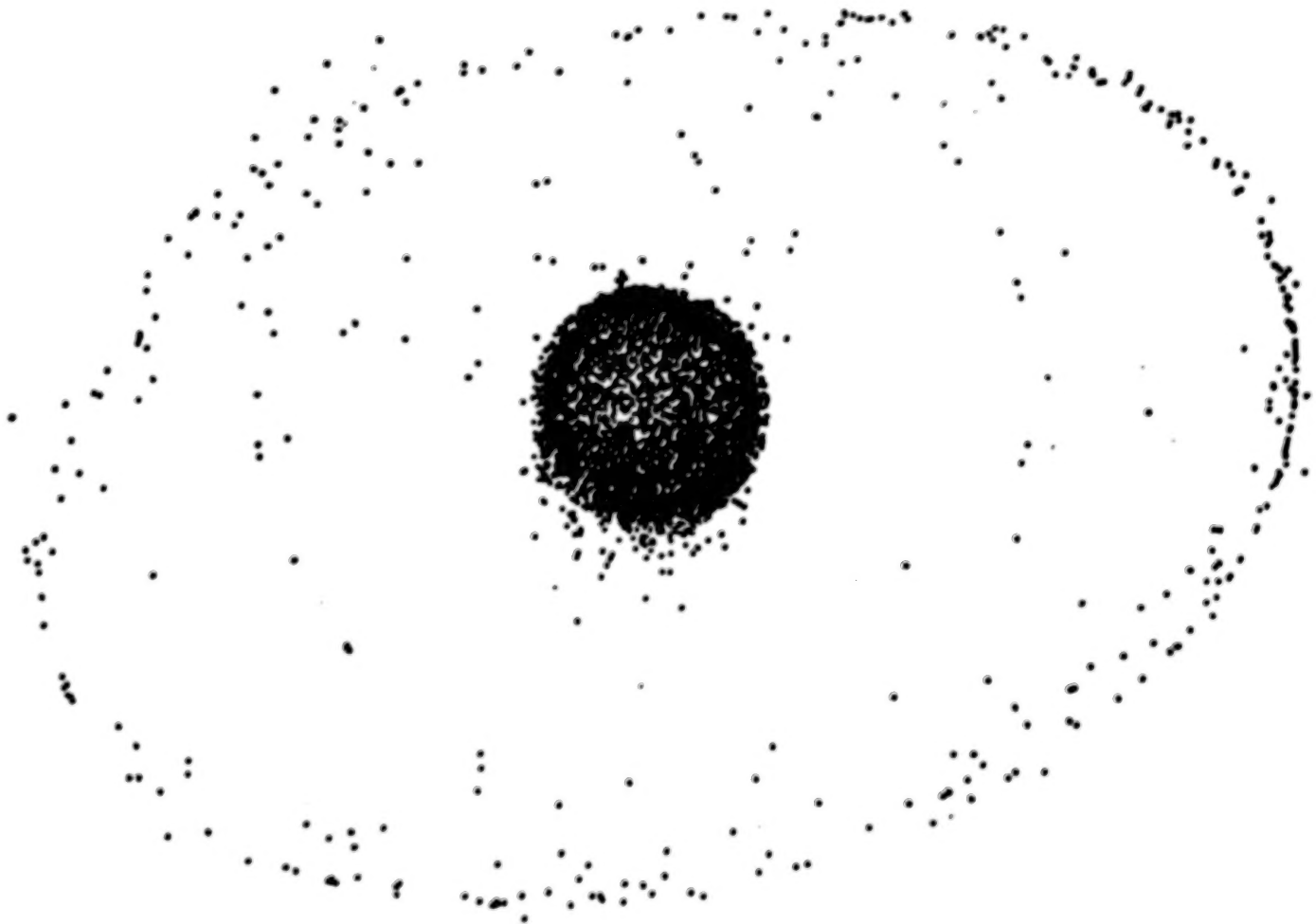
EXAMPLES:

$M(\text{GM})$	$N_{1\text{AU}} (\text{m}^{-2} \text{s}^{-1})$	$R(R_e)$	$N_R (\text{m}^{-2} \text{s}^{-1})$	$N_R (\text{m}^{-2} \text{yr}^{-1})$
1	3.9×10^{-15}	1.05	2.1×10^{-15}	6.6×10^{-8}
		1.5	2.9×10^{-15}	9.1×10^{-8}
		6	2.5×10^{-15}	7.9×10^{-8}
10^{-6}	7.9×10^{-8}	1.05	4.3×10^{-8}	1.4
		1.5	5.8×10^{-8}	1.8
		6	5.4×10^{-8}	1.6
10^{-12}	4.0×10^{-5}	1.05	2.2×10^{-5}	6.9×10^2
		1.5	3.0×10^{-5}	9.4×10^2
		6	2.6×10^{-5}	8.2×10^2

[SEE ALSO NASA SP-8042 "METEOROID DAMAGE ASSESSMENT", 1970]

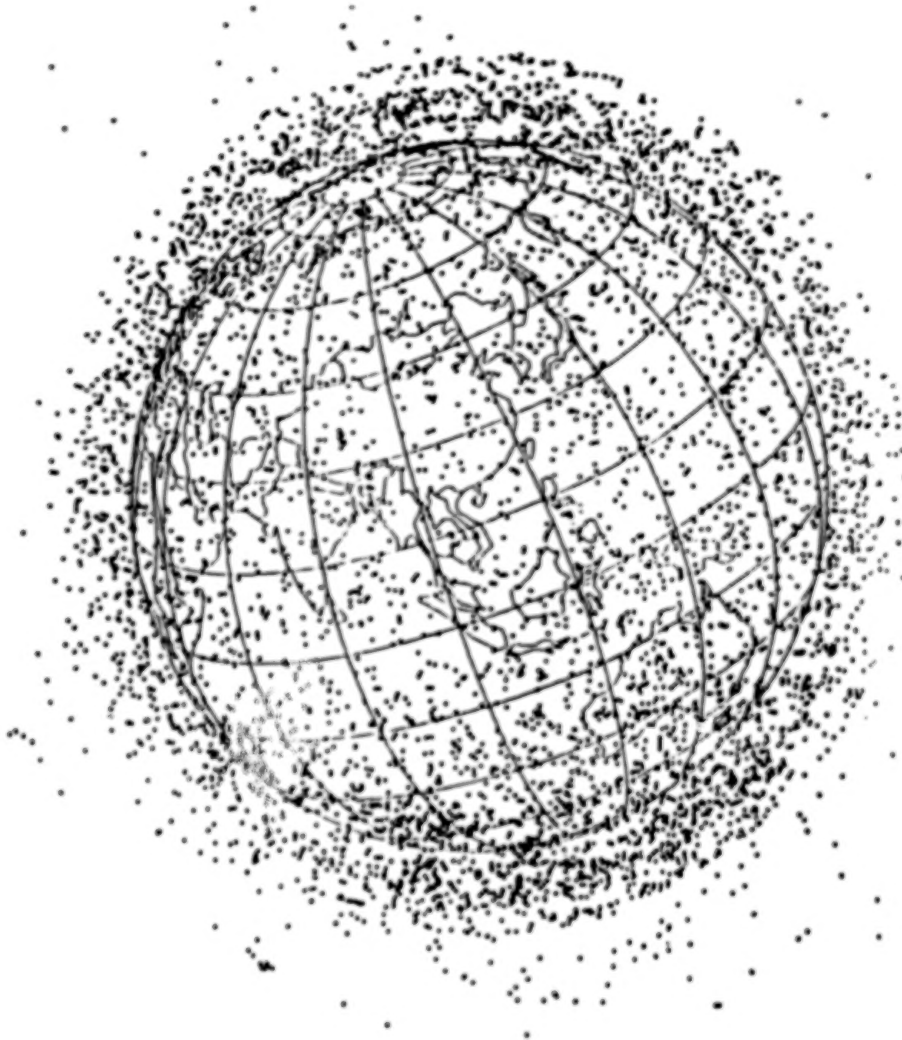
DISTRIBUTION OF DEBRIS IN EARTH ORBIT

This chart shows a representation of the distribution of debris in Earth orbit. The "ring" is at geosynchronous. Sources of debris include spent stages, nonfunctional spacecraft, fragments from staging operations, exploded stages, collision, disposed wastes, and residues from engine burns.



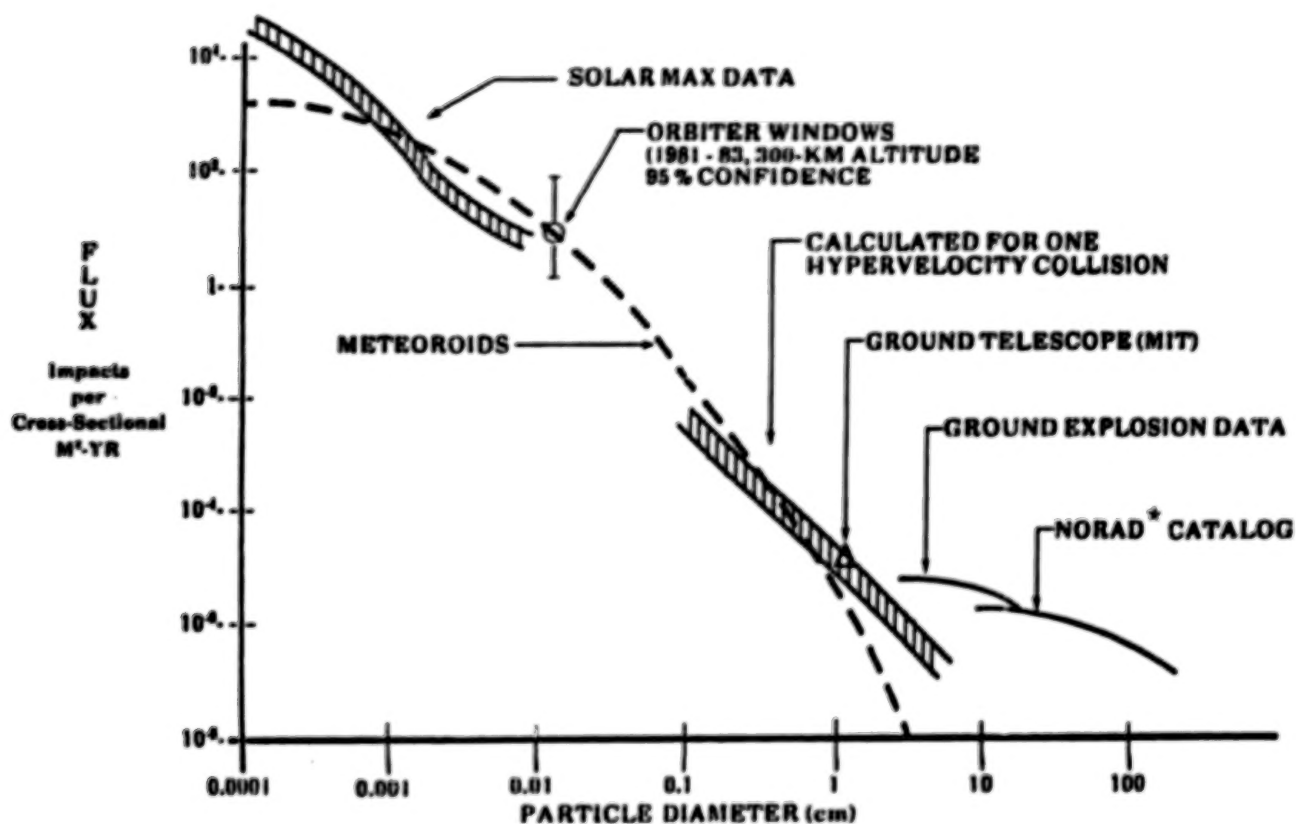
CLOSER VIEW OF DEBRIS DISTRIBUTION

A closer view illustrating the relative uniformity of debris distribution in low Earth orbit (LEO). Density of the debris falls off at altitudes ≥ 1500 km.



ORBITAL DEBRIS MEASUREMENTS COMPARED TO METEOROID FLUX

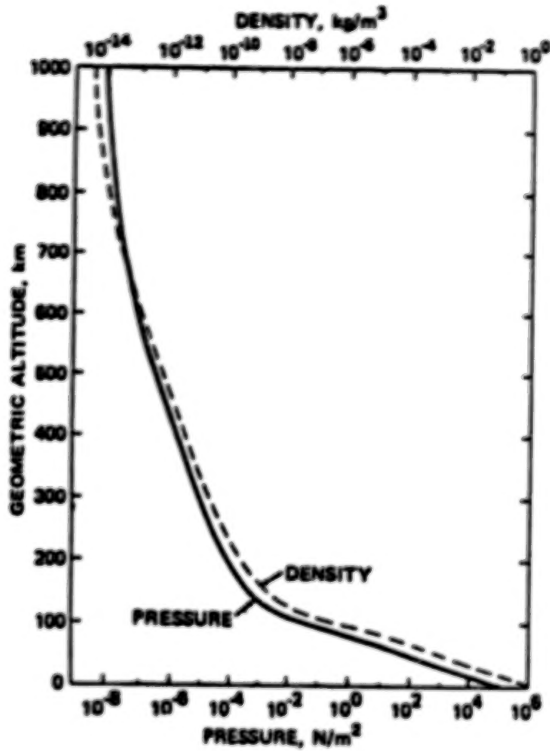
This shows a comparison of meteoroid and debris fluxes for various particle diameters. Debris is a more serious threat than meteoroids at the small and large extrema. Data on debris fluxes in the 1-mm to 1-cm diameter range is lacking.



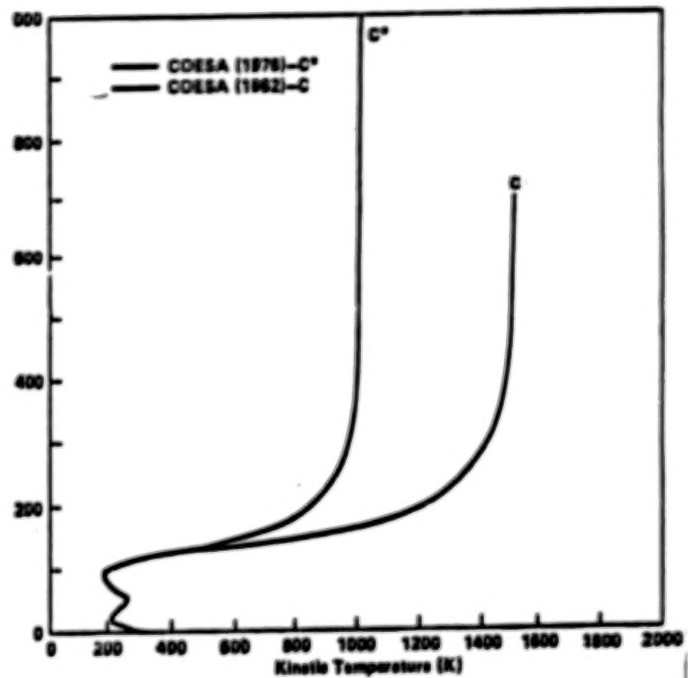
* North American Air Defense Command

NEUTRAL ATMOSPHERE

Atmospheric pressure and density decrease rapidly in suborbital regions (≤ 200 km), while kinetic temperature increases. At orbital altitudes, the residual atmosphere is tenuous enough to be essentially collisionless.



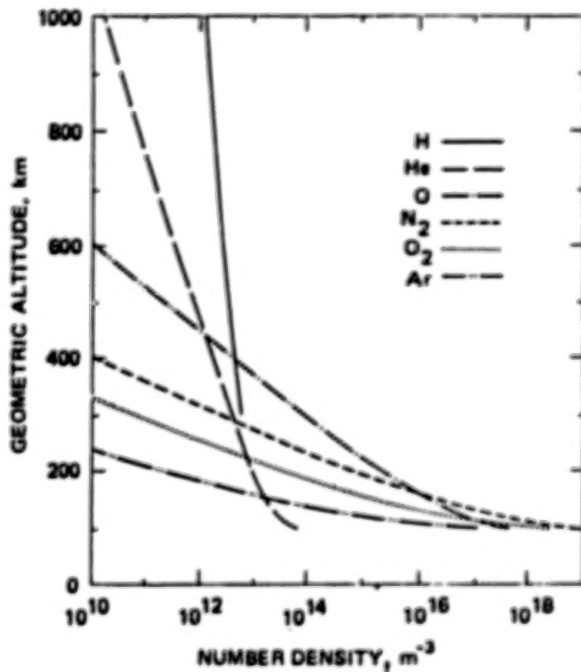
Total pressure and mass density as a function of geometric altitude



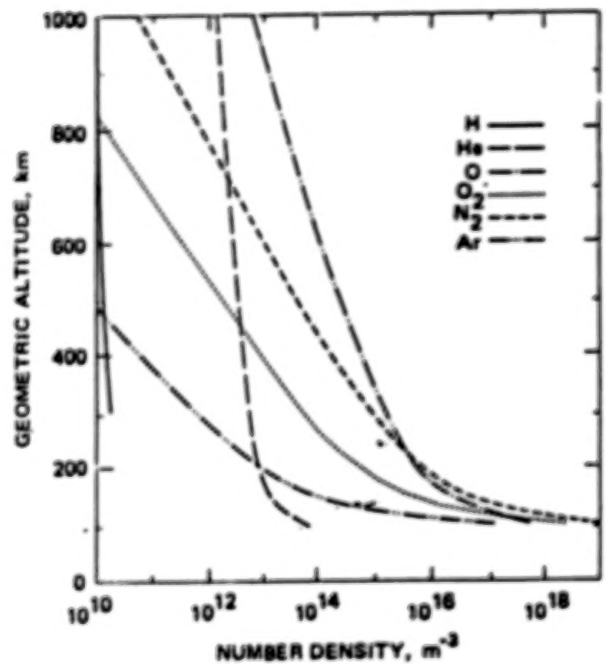
Kinetic temperature versus altitude

STANDARD ATMOSPHERE

The density, composition, and temperature of the residual atmosphere vary with solar activity. In recent years the reactivity of atomic oxygen, which is the dominant constituent of the residual atmosphere at LEO, has been recognized as a serious threat to materials exposed to its ram flow. The motion of spacecraft through the residual atmosphere in LEO at velocities of the order 7.5 to 8 km/sec results in an equivalent impingement energy for O of 4.5 to 5 eV. Rapid degradation of some materials in this environment has been observed on STS.



Relative concentrations of atmospheric constituents during periods of minimum solar activity

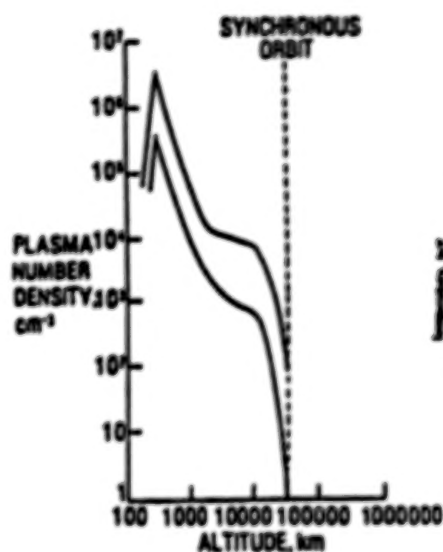


Relative concentrations of atmosphere constituents during periods of maximum solar activity

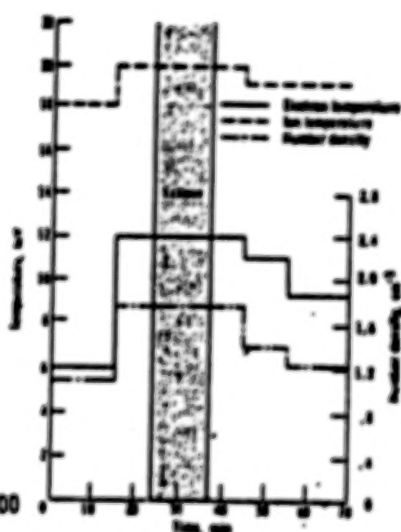
ENVIRONMENTAL INTERACTIONS

Near-Earth plasma regimes include the cold (~ 1 eV) relatively dense (to $\sim 10^6/\text{cm}^3$) ionospheric plasmas whose densities gradually fall off with altitude; the hot ($\sim \text{KeV}$ to ~ 10 's of KeV), tenuous ($\leq 1/\text{cm}^3$) plasmas observed at geosynchronous and associated with geomagnetic substorm activity; and the fluxes of hot electrons due to these geosynchronous plasma injections which travel down magnetic field lines and precipitate in the auroral zones. The latter two plasma environments can charge spacecraft surfaces to kilovolt potentials; the cold ionospheric component interacts strongly with spacecraft power systems.

NEAR EARTH PLASMAS



IONOSPHERIC
PLASMAS



GEOSYNCHRONOUS
MODEL SUBSTORM

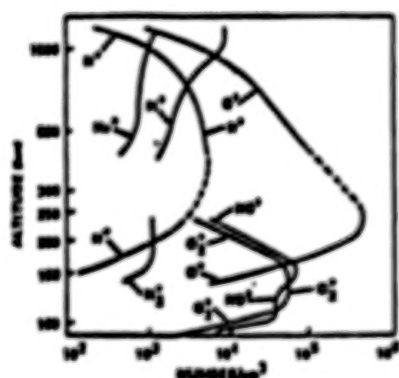


AURORAL PLASMAS
HIGH LATITUDES

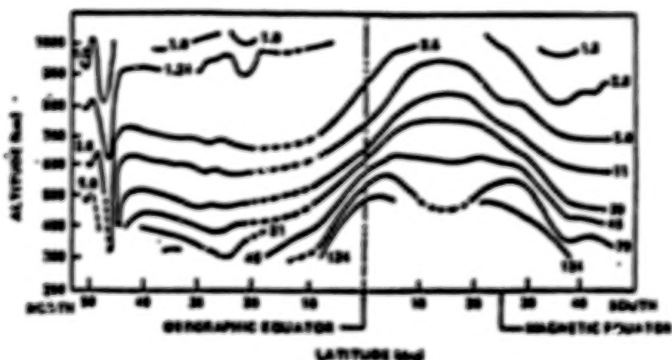
PLASMA DENSITY AND COMPOSITION IN THE IONOSPHERE

Plasma density and composition in the ionosphere vary daily, seasonally, latitudinally, and with solar activity, as is illustrated in these figures.

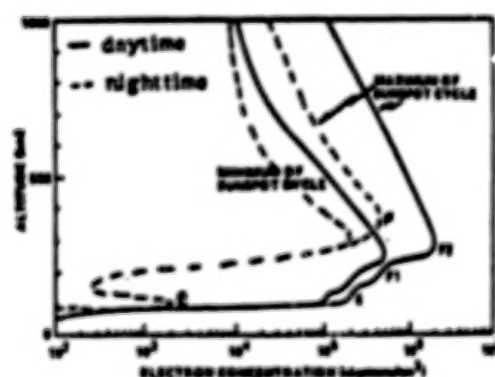
IONOSPHERE



ionic composition of the solar wind
daytime winter ionosphere (3-14).



Daytime equi-electron-density contours (N_e in 10^{11} km^{-3}) (3-18).



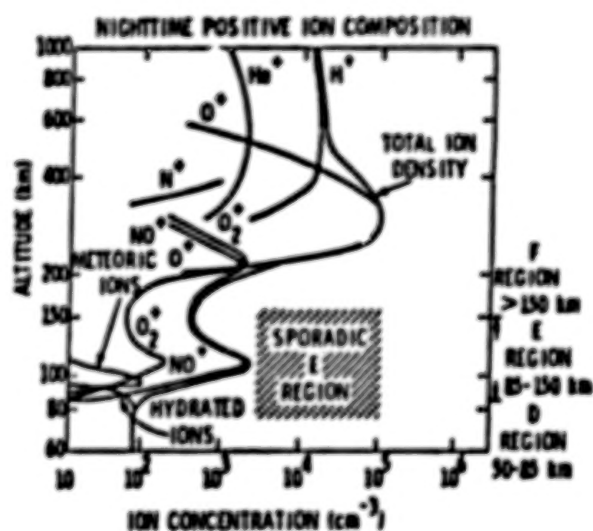
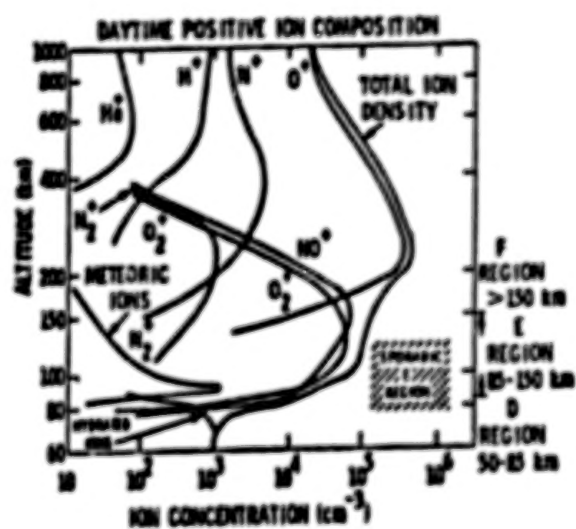
Normal electron distribution

DIURNAL VARIATION IN ION DENSITY AND COMPOSITION

This figure illustrates the diurnal variation in ion density and composition for solar maximum at mid-latitude.

MID LATITUDE ION COMPOSITION

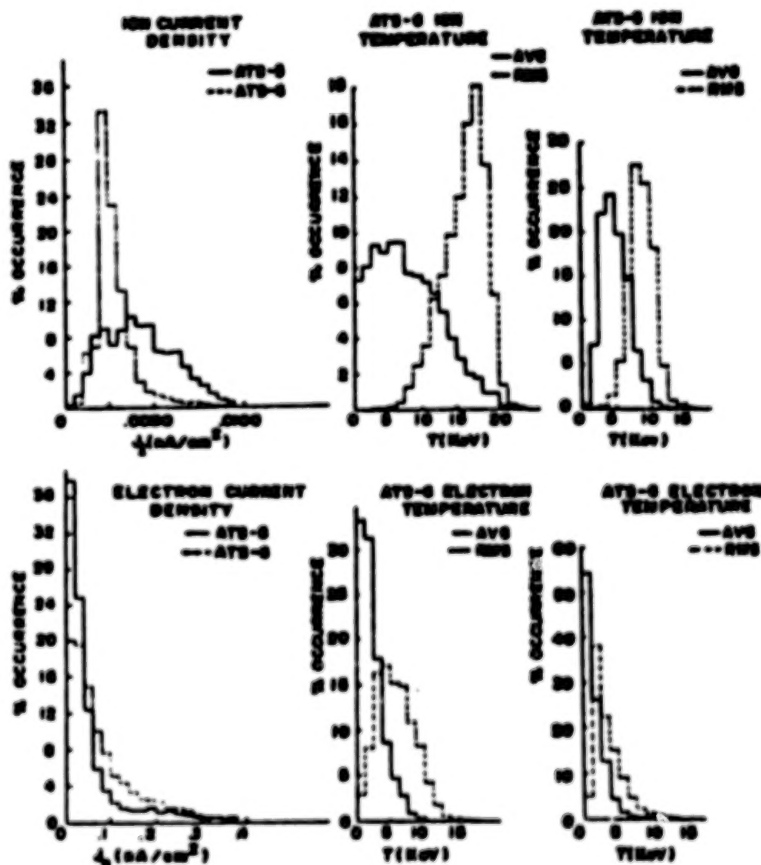
SOLAR MAXIMUM



GEOSYNCHRONOUS PLASMA ENVIRONMENT

This figure shows histograms of the occurrence frequencies of the electron and ion temperatures and current at geosynchronous orbit measured by Applications Technology Satellite (ATS)-5 and ATS-6. $T(\text{AVG})$ is two-third's the ratio of energy density to number density; $T(\text{RMS})$ is one-half the ratio of particle energy flux to number flux.

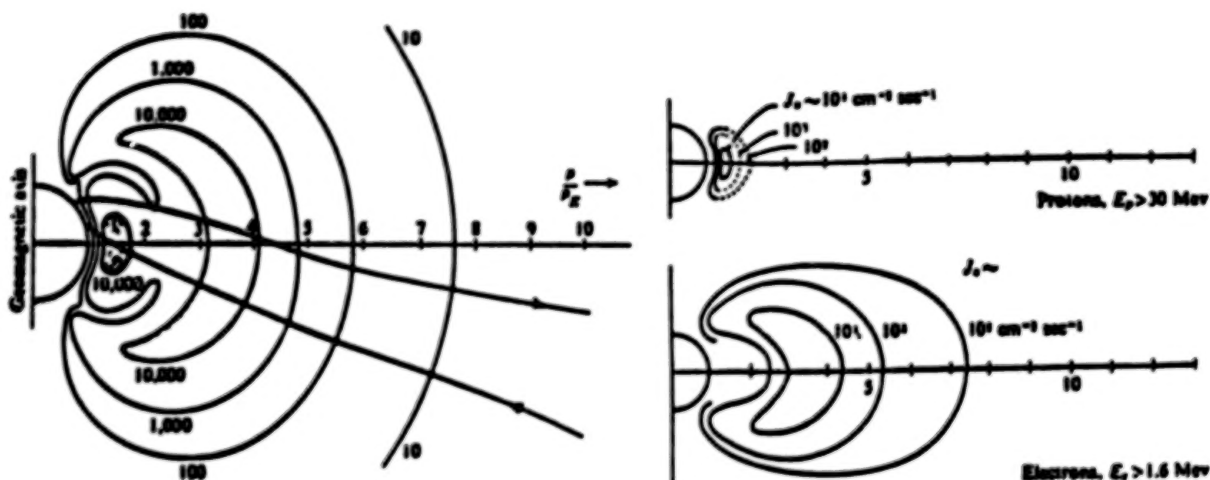
The hot plasmas were observed to charge the ATS-5 and ATS-6 spacecraft to kilovolt potentials in eclipse and to hundreds of volts in sunlight. Similar charging effects are anticipated for large spacecraft in auroral zones at LFO. The DMSP spacecraft (900 km) has been observed to charge to approximately 700 volts during auroral passage. Charging potentials are negative because electron fluxes dominate the process.



Histograms of the Occurrence Frequencies of the Electron and Ion Temperatures and Current at Geosynchronous Orbit as Measured by ATS-5 and ATS-6. $T(\text{AVG})$ is 2/3's the ratio of energy density to number density; $T(\text{RMS})$ is one-half the ratio of particle energy flux to number flux

TRAPPED RADIATION: THE VAN ALLEN BELTS

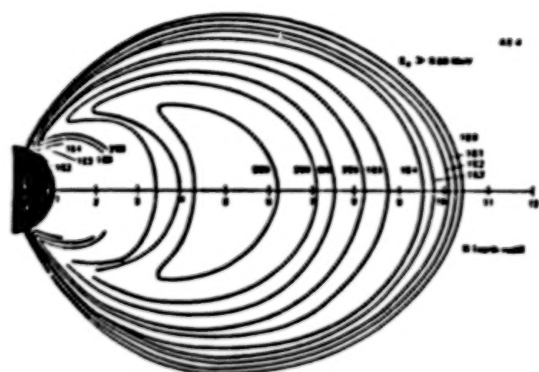
This figure shows Van Allen's first map of the radiation belt, showing the inner and outer zones of high count rate. The contours are labeled by the count rate of a Geiger counter of about 1 cm^2 area covered by 1 gm/cm^2 of lead.



Van Allen's first map of the radiation belt, showing the inner and outer zones of high count rate. The contours are labeled by the count rate of a Geiger counter of about 1 cm^2 area covered by 1 gm/cm^2 of lead (23).

NSSDC TRAPPED RADIATION MODELS

Trapped radiation models are available from the National Space Sciences Data Center (NSSDC).



SYSTEM GENERATED ENVIRONMENT

The system-generated environment is system-specific and may be quite complex. It is generally considered to be the main source of contaminants which can impact the system.

DEPENDS ON SYSTEM CHARACTERISTICS

- 0 NEUTRALS: OUTGASSING, THRUSTER EJECTA, DUMPS, RAM/WAKE
 - CHEMICAL REACTIONS: DEGRADATION, CONTAMINATION
 - LOCALLY ENHANCED PRESSURES
- 0 PLASMAS: PHOTOIONIZATION OR CHARGE EXCHANGE OF NEUTRALS, DIRECT, RAM/WAKE
 - ENHANCED PLASMA INTERACTIONS
 - COUPLING TO AMBIENT: POTENTIAL CHANGES
- 0 ENERGETIC CHARGED PARTICLES: ELECTRON OR ION BEAMS
 - BEAM-PLASMA INTERACTIONS: HEATING, WAVES, EMI*
 - INTERACTIONS WITH NEUTRALS: EXCITATION, IONIZATION, BPD†
 - ENHANCED PLASMA INTERACTIONS
 - CURRENT BALANCE ALTERATIONS: POTENTIAL CHANGES
- 0 ELECTRIC AND MAGNETIC FIELDS: EXPOSED V's, CURRENTS, RESIDUALS, $\vec{V} \times \vec{B}$
 - TORQUES AND FORCES: ATTITUDE CONTROL
 - PLASMA SHEATH EFFECTS: PLASMA INTERACTIONS
 - STIMULATION OF WAVES, INSTABILITIES: EMI, PLASMA INTERACTIONS

*Electromagnetic interference

†Beam plasma discharge

SUMMARY

The orbital environment is complex, dynamic, and comprised of both natural and system-induced components. Several environment factors are important for materials. Materials selection/suitability determination requires consideration of each and all factors, including synergisms among them. Understanding and evaluating these effects will require ground testing, modeling, and focused flight experimentation.

ORBITAL ENVIRONMENT IS COMPLEX

- O NATURAL
- O SYSTEM-INDUCED

ENVIRONMENT FACTORS IMPORTANT FOR MATERIALS INCLUDE:

- O SOLAR RADIATION
- O METEORIDS AND DEBRIS
- O NEUTRAL ATMOSPHERE
- O PLASMAS
- O TRAPPED RADIATION
- O SYSTEM-GENERATED CONTAMINANTS

MATERIALS SELECTION/SUITABILITY DETERMINATION REQUIRES CONSIDERATION OF ALL FACTORS

STRUCTURAL MATERIALS FOR SPACE APPLICATIONS

Darrel R. Tenney
Materials Division
Langley Research Center

ABSTRACT

The long-term performance of structural materials in the space environment is a key research activity within NASA. The primary concerns for materials in low Earth orbit (LEO) are atomic oxygen erosion and space debris impact. Atomic oxygen studies have included both laboratory exposures in atomic oxygen facilities and flight exposures using the Shuttle. Characterization of atomic oxygen interaction with materials has included surface recession rates, residual mechanical properties, optical property measurements, and surface analyses to establish chemical changes. The Long Duration Exposure Facility (LDEF) is scheduled to be retrieved in 1989 and is expected to provide a wealth of data on atomic oxygen erosion in space. Hypervelocity impact studies have been conducted to establish damage mechanisms and changes in mechanical properties. Samples from LDEF will be analyzed to determine the severity of space debris impact on coatings, films, and composites.

Spacecraft placed in geosynchronous Earth orbit (GEO) will be subjected to high doses of ionizing radiation which for long term exposures (20-30 years) will exceed the damage threshold ($\sim 10^9$ Rads) of many polymeric materials. Radiation interaction with polymers can result in chain scission and/or cross-linking. For highly cross-linked 177°C cure epoxies, the primary mechanism of radiation degradation appears to be chain scission. The formation of low molecular weight products in the epoxy plasticize the matrix at elevated temperatures and embrittle the matrix at low temperatures. This affects both the matrix-dominated mechanical properties and the dimensional stability of the composite.

Plasticization of the matrix at elevated temperatures can result in permanent residual strains in composites exposed to such temperatures. Embrittlement of the matrix at low temperatures results in enhanced matrix microcracking during thermal cycling. Matrix microcracking changes the coefficient of thermal expansion (CTE) of composite laminates and produces permanent length changes. Residual stress calculations have been performed to estimate the conditions necessary for microcrack development in unirradiated and irradiated composites. These calculations show that microcracking in the transverse plies of an irradiated [0/90]_s Gr/epoxy laminate is predicted to occur at temperatures substantially higher than those predicted for an unirradiated laminate. Microcracking measurements were made for standard 177°C cure Gr/Epoxy, rubber toughened Gr/Epoxy, Gr/Polyimide, and Gr/Thermoplastic composites. The effects of thermal cycling and irradiation followed by thermal cycling on the mechanical and physical properties of the epoxy composites were consistent with the predicted responses. The effects of UV and electron exposure on the optical properties of transparent polymer films has also been examined to establish the optimum chemical structure for good radiation resistance. Results are presented which show that these polymers have excellent resistance to both electron and UV radiation compared to more conventional polymer films, such as FEP Teflon.

Accelerated testing of space materials is a topic of great interest for the spacecraft community and is a central issue for long-life certification. Thoughts on approaches to establishing accelerated testing procedures are discussed in this paper.

TYPICAL SPACECRAFT MATERIALS

Research on advanced materials development for spacecraft applications has generally been focused on three classes of materials: polymer films, coatings, and composites. High-performance polymer films such as Kapton and Mylar are widely used on current spacecraft (fig. 1). The recent concern about atomic oxygen degradation of polymer materials on spacecraft placed in low-Earth orbit (LEO) has focused attention on the development of new polymer films or coatings which are resistant to atomic oxygen erosion. Another area of research at Langley has been the development of transparent polyimide films which have very good UV and electron radiation resistance. Highlights of this research will be covered in a later section of this paper.

Coatings consist of a variety of organic-base paints, metallic materials, and ceramic materials. An extensive data base exists on the development and testing of paints that range in color from black to white. The degradation in optical properties of white paints by UV, electron and proton radiation was extensively studied in the 1960's and early 1970's. The white paint designated S13GLO is generally considered to be the best white paint available today for spacecraft applications where a low solar absorptance and high emittance are required. Atomic oxygen degradation of coatings is an area of considerable interest within NASA because space durable materials are required for Space Station (30 year design life time). Aluminum foil bonded to composite tubes has been shown to have resistance to atomic oxygen erosion. However, other metals such as silver which has been used for silver interconnects on lightweight flexible solar arrays must be protected from atomic oxygen.

Composite materials have been extensively used for spacecraft structural applications because of their combination of lightweight, high stiffness, and low thermal expansion. Composites of interest for spacecraft applications include Gr/Polymer, Gr/Al, Gr/Mg, and Gr/glass. Some of the issues and concerns with these materials will be discussed in subsequent charts.

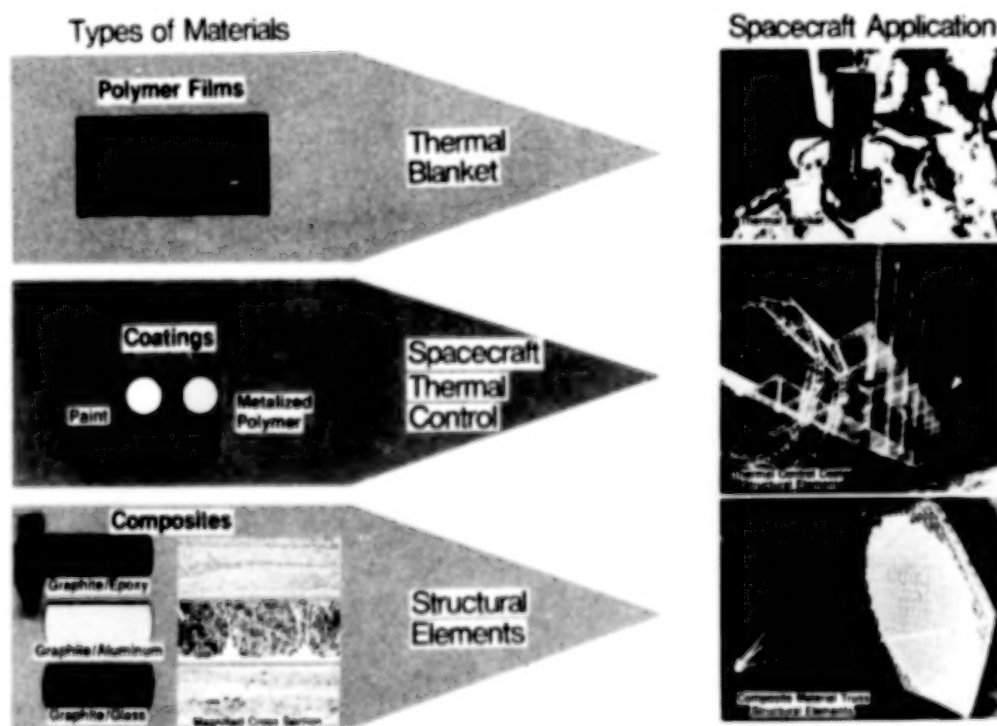


Figure 1

STRUCTURAL MATERIALS FOR SPACE APPLICATIONS

The two major topics to be covered in this paper are space environmental effects on structural materials, and new materials development (fig. 2). Highlights of on-going NASA research will be presented to illustrate the type of issues currently being addressed for NASA missions. Examples of new materials development will also be presented to illustrate some of the approaches being pursued to develop improved materials for space applications.

Topics

- Examples of space environmental effects on structural materials
 - Composites
 - Films
 - Coatings
- New materials development
 - Research focus
 - Testing issues
 - Long-life certification

Figure 2

SPACE ENVIRONMENT

The space environment is a hostile environment. It consists of atomic oxygen, ultraviolet radiation, high-energy electron, and proton radiation as well as solar flare protons, and micro-meteoroids and space debris (fig. 3). For spacecraft located in low Earth orbit, atomic oxygen erosion of polymeric materials is a primary concern. This, of course, is a function of the ambient density of the atmosphere which varies with sunspot activity. Atomic oxygen degradation is a significant issue for Space Station,* which is expected to operate for 20-25 years in low Earth orbit. This topic will be covered in detail by other speakers at this symposium and therefore will not be further discussed in this paper.

Another concern for structures placed in low Earth orbit is micrometeoroids or space debris impact. Predictions based on models of the space debris environment indicate that the population density of small particles is expected to get progressively worse over the next several years. In the smaller diameter sizes the population density of space debris is expected to exceed that of micrometeoroids.

Spacecraft placed in geosynchronous earth orbit or in a high polar orbit will be subjected to high doses of electron and proton radiation. For long life missions (25-30 years) the total absorbed dose to typical composite structural elements may exceed the threshold level for damage (10^9 rads) for most polymeric materials. Of particular concern are changes in mechanical and physical properties of structural composites and optical properties of thermal controlled coatings or polymeric films.

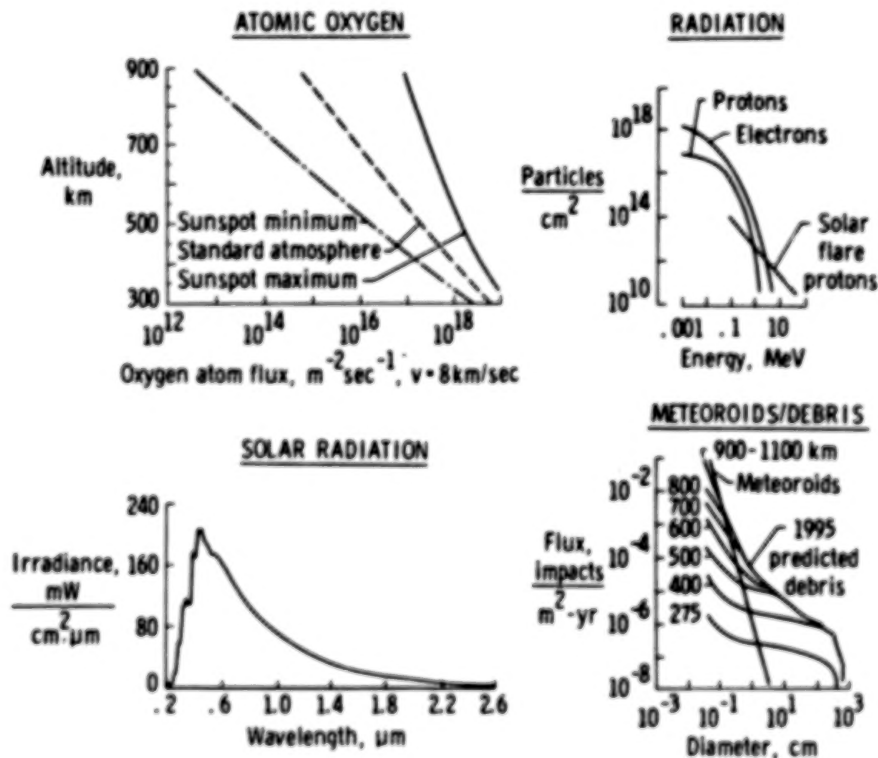


Figure 3

*Space Station Freedom

MATERIALS TECHNOLOGY NEEDS FOR SPACE SYSTEMS

The development of long-life space materials must strongly consider the dominant environmental conditions expected for the orbit where the spacecraft will be displayed. Some of the key differences for materials to be used on spacecraft placed in low Earth orbit (LEO) and Geosynchronous Orbit (GEO) are listed in figure 4. To successfully design for long-life space missions, space materials durability must be treated as a critical design requirement in the same way as requirements for mechanical, physical, or optical properties. One of the most difficult challenges in trying to engineer long life is the uncertainty associated with accelerated testing. This issue will be further discussed in a later section of this paper.

<u>Space Station - LEO</u>	<u>Antenna - GEO</u>
● Atomic oxygen stability	● Radiation stability (UV, e^- and p^+)
● Damage tolerance and toughness	● Low expansion-high precision
● Stable optical properties	● High stiffness and damping capacity
● Low outgassing	● Low outgassing

Figure 4

COMPOSITE TUBE AS A SYSTEM

The successful development of long-life structures in space must be based on a thorough understanding of the loads and environments that the structure will be subjected to during design lifetime. For a composite truss structure this means that the performance of composite tubes used to build the structure must be understood. The basic composite tube may be considered as a system (fig. 5) composed of: (1) the fiber-matrix composite laminate, (2) coatings for UV and atomic oxygen protection and for thermal control, (3) end fittings to attach to joints in the structure, (4) adhesives used to bond end fittings to composite laminate, and in some cases to bond coating to composites (i.e., Al foil to composite tube).

The long-term thermal and mechanical response of the tube is dependent on the performance of each of these elements. Factors which can lead to changes in the thermal response of the tube include: (1) changes in solar absorptance or emittance of coating either due to contamination or radiation degradation will alter the maximum and minimum thermal cycle that the tube will experience, loss of coating could result in UV and/or atomic oxygen erosion of composite laminate; (2) matrix microcracking resulting from thermal fatigue will change the coefficient of thermal expansion (CTE) of the composite laminate; (3) thermal fatigue failure of adhesive joints would affect both thermal and mechanical properties of the tube; (4) contaminating of coating surfaces, matrix microcracks, and coating separation from the composite laminate would change the thermal conductivity properties which could alter the temperature distribution of the composite tube as the structure goes into and out of the Earth's shadow. The long-term mechanical performance of the composite tube is obviously dependent on the properties of the composite laminate coatings, adhesives, and end fittings.

- Major Components
 - Composite Laminate
 - Coating
 - End Fittings
 - Adhesives
 - End Fittings
 - Coatings
- Response
 - Thermal
 - Coating optical properties
 - CTE of composite laminate and end fittings
 - Thermal conductivity of coatings and composite
 - Mechanical
 - Composite properties
 - Adhesive strength
 - End fittings properties

Figure 5

CTE MISMATCH IN ADHESIVE JOINTS

Coefficient of thermal expansion (CTE) mismatch in adhesive joints can result in high residual stresses and thermal fatigue failure. The truss structure of Space Station will be thermally cycled between approximately 150° and -100°F 175,000 times during 30 years in low Earth orbit. The current baseline for this structure is high-stiffness graphite/epoxy composite tubes with Al end fittings and joints. Thermal cycling tests are currently being conducted on representative composite/metal joints to evaluate their thermal fatigue resistance. CTE and elastic modulus data for three composites, high- and low-temperature adhesives, and Al and Ti are tabulated in figure 6.



MATERIAL	MMC (GR/AL)	CerMC (GR/GL)	PMC (GR/EP)	L.T. ADHESIVE (350F EPOXY)	H.T. ADHESIVE (PI)	AL	TI
CTE, IN/IN/°F X 10 ⁻⁶	0.8* (15)**	-0.3 (3.6)	-0.6 (18)	30	20	13	5
ELASTIC MODULUS, PSI X 10 ⁶	47	31	39	0.6	0.5	10	17

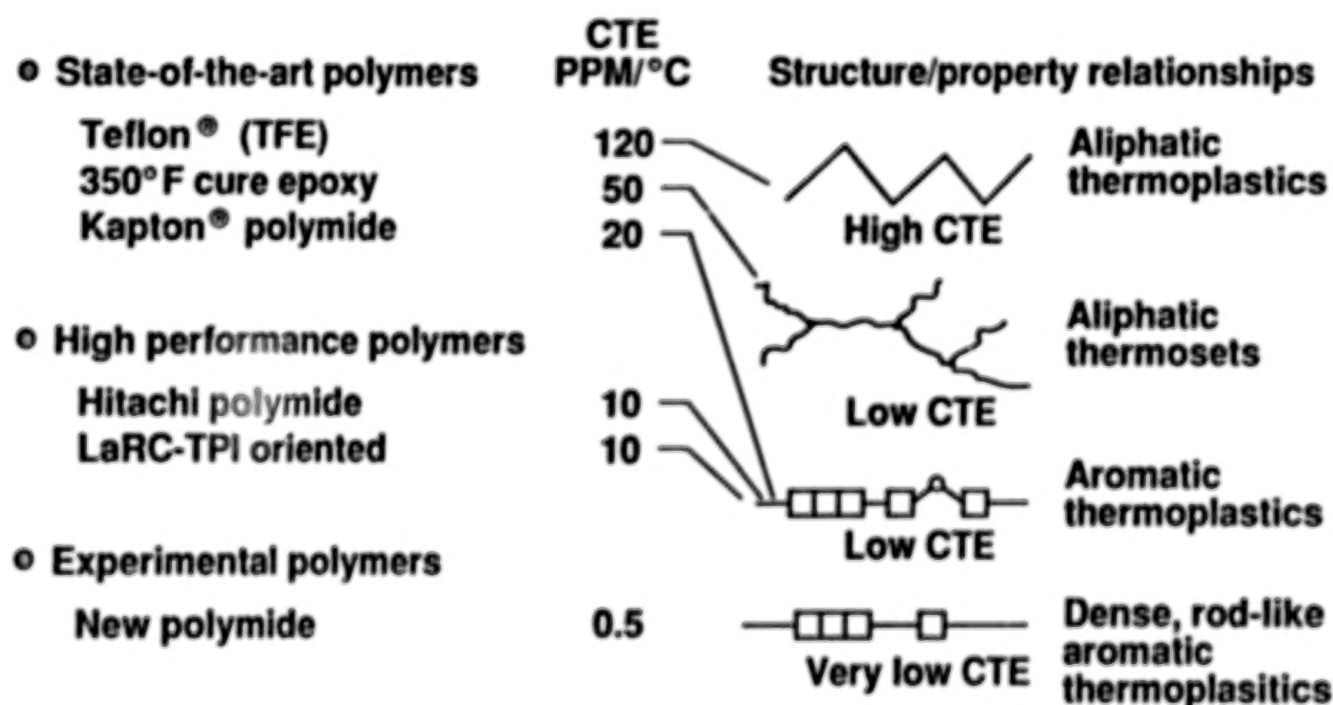
*LONGITUDINAL **TRANSVERSE

Figure 6

LOW EXPANSION POLYMER RESINS

Residual stresses in composites are a function of the differences in coefficients of thermal expansion of the matrix resin and fibers, the elastic modulus of the matrix and fibers, and the ΔT , temperature change between the cure temperature of the composite and the use temperature of the composite. The coefficient of expansion (CTE) of some typical state-of-the-art polymers, high performance polymers, and an experimental polyimide are shown in figure 7. This chart shows that the potential exists to synthesize very low CTE ($0.5 \times 10^{-6}/^{\circ}\text{C}$) polymers. However, the aromatic thermoplastics and the dense rod-like aromatic thermoplastics must be processed at much higher temperatures than the typical 177°C cure epoxies typically used for space structures. Also the modulus of the rod-like polymers can be much higher (1-2msi) than that of the typical epoxy (0.5msi).

The combination of higher processing temperatures and higher modulus may more than offset the benefit of lowering the CTE of the polymers. Research is needed to establish the degree to which each of these properties can be varied and experimental lots of material synthesized for composite fabrication and testing. Research of this nature is currently underway at NASA Langley. The near term focus of this research is directed at understanding the structure-property relationships that determine the coefficient of thermal expansion of polymers. Promising concepts will be further explored to synthesize enough resin to fabricate composites for testing.



Conclusion: Potential exists for synthesizing very low CTE resins

Figure 7

PRECISION SEGMENTED REFLECTOR

During FY 88 NASA initiated a Precision Segmented Reflector Technology program at Jet Propulsion Laboratory (JPL) and Langley Research Center (LaRC) as part of NASA's new Civil Space Technology Initiative. The primary reflector shown in figure 8 is made up of hexagonal panels, each two meters in size. The panels are supported by a deployable or erectable truss backup structure and surrounded by a sunshield to keep direct solar radiation from the primary surface. Significant technical challenges exist in the areas of lightweight deployable structures, lightweight structural composite mirrors, and the control of pointing, vibration, and figure (ref. 1).

The development of lightweight, low-cost reflector panels that demonstrate high surface precision and thermal stability is considered a critical enabling technology for precision reflectors. Some of the key requirements for the reflectors panels are: aerial density $\leq 10 \text{ Kg/m}^2$; surface roughness $< 3 \text{ }\mu\text{m}$; out-of-plane CTE $\leq 2 \text{ ppm/K}$; long-term stability in orbit $< 1 \text{ }\mu\text{m}$; low outgassing; good radiation stability. Much of the work to date has focused on the fabrication of lightweight honeycomb panels with Gr/Epoxy face sheets. Both E-glass and standard aluminum honeycomb core have been utilized. Coatings and polishing techniques have also been developed to improve a fabricated surface precision from $3 \text{ }\mu\text{m}$ to approximately $1 \text{ }\mu\text{m}$.



Figure 8

EFFECT OF MATRIX CTE ON LAMINA PROPERTIES

A significant part of the Precision Segmented Reflector (PSR) program is the development of lightweight ($<10 \text{ Kg/m}^2$) low-cost composite panels with a surface roughness less than $0.03 \mu\text{m RMS}$. These panels must be thermally stable during long-term (10-year) service at cryogenic temperatures in space. To accomplish these objectives research is underway to develop low expansion resins for resin matrix composites and establish fabrication procedures which minimize residual stresses in composites. Reducing through-the-thickness CTE of polymer matrix composites would help to minimize distortions in composite panel face sheets. Figure 9 shows that a reduction of CTE by an order of magnitude (CTE EP/10) would reduce the through thickness expansion of a typical graphite/epoxy laminate to approximately 1/3 the value of a Gr/Ep laminate fabricated with a typical 350°F cure epoxy. The results of figure 9 also show that the modulus of the graphite reinforcement fiber does not affect the through-the-thickness (T-T-T) CTE. Graphite/glass also has a very low T-T-T CTE which makes it a candidate material for PSR applications.

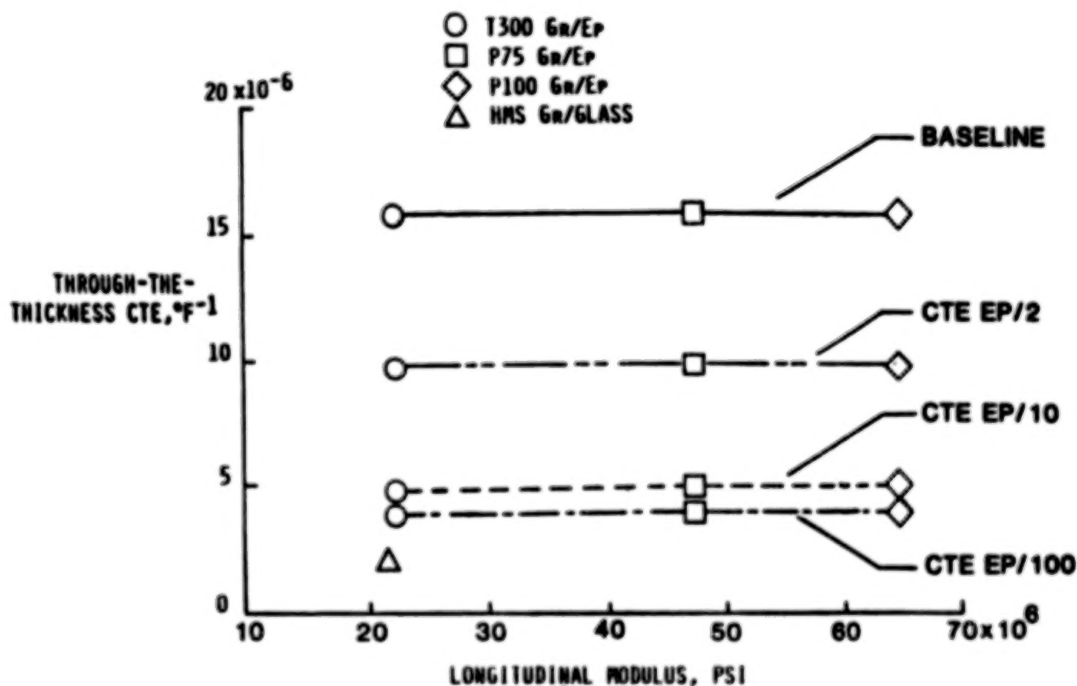


Figure 9

MICROSTRUCTURES OF HMS Gr/BOROSILICATE GLASS

Graphite-reinforced glass is a leading candidate composite material for space applications where good dimensional stability and radiation resistance are important design considerations. The microstructure of a typical Gr/glass laminate (ref. 2) fabricated by United Technologies Research Center is shown in figure 10. Each ply of continuous fiber material is separated by a 2 mil layer of graphite scrim which was used to improve handleability of the plies prior to composite consolidation. The glass matrix is a Corning borosilicate glass (type 7740) and the reinforcing fiber was Hercules HMS, a 55 msi modulus PAN base graphite fiber. The fiber volume fraction of this laminate was approximately 0.45 ± 0.03 .

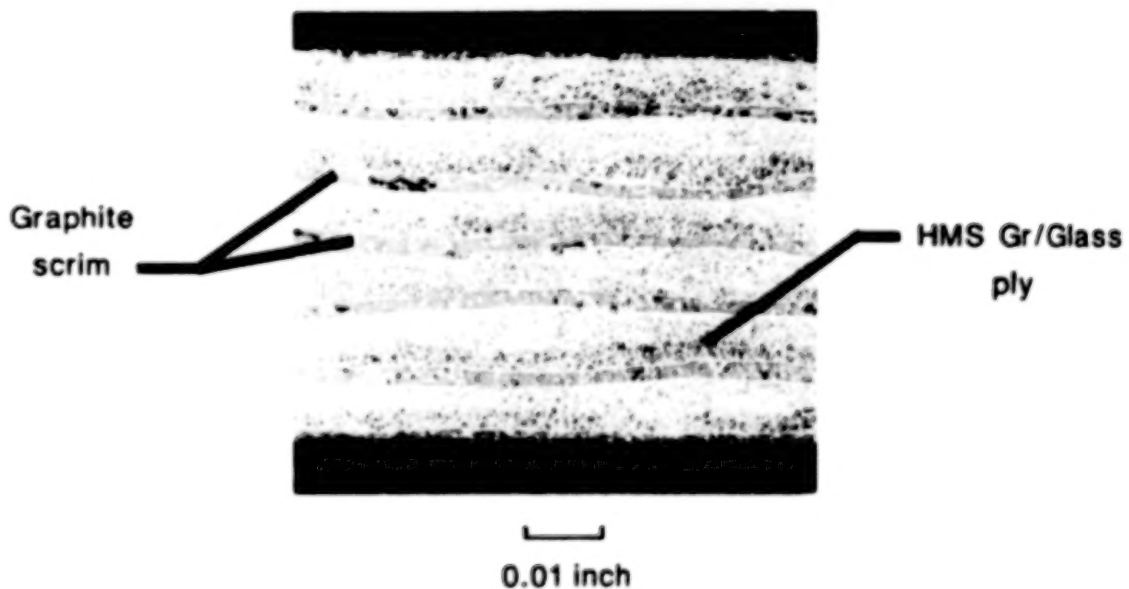


Figure 10

THERMAL EXPANSION OF $(0/\pm 60)_S$ HMS/BOROSILEATE GLASS LAMINATE

The thermal expansion behavior in the x-direction of a quasi-isotropic Gr/glass laminate measured in the dimensional stability laboratory at NASA Langley (ref. 2) is shown in figure 11. The near zero CTE is evident from the slope of the stress-strain curve. Thermal cycling did not have a significant effect on the thermal expansion behavior. However, the strain hysteresis loop of $25\text{--}30 \times 10^{-6}$ was unexpected. This behavior is generally believed to be associated with either damage development in the graphite paper interply layers or changes in residual curing stresses in the laminates. Similar hysteresis phenomena was also observed for chopped fiber mat Gr/glass composites (fiber vol. fraction of $33 \pm 3\%$). The magnitude of the hysteresis was on the order of $15\text{--}25 \times 10^{-6}$. Thermal cycling of unidirectional Gr/glass samples showed that in the longitudinal direction the expansion behavior was linear and did not change with thermal cycling (100 cycles). Values of residual strain were quite low and did not change with thermal cycling. The residual strain was much more pronounced in the transversely oriented specimens. Large values were noted on the first cycles but tended to decrease in magnitude in later cycles. However, the specimen increased in length (transverse direction) during each cycle and net cumulative strains of up to 200×10^{-6} were observed after 100 cycles. The reason for this behavior has not been established but could be associated with the development of micro damage in the composite laminate. However, microscopic and x-ray examination of the specimens after testing did not reveal any cracks.

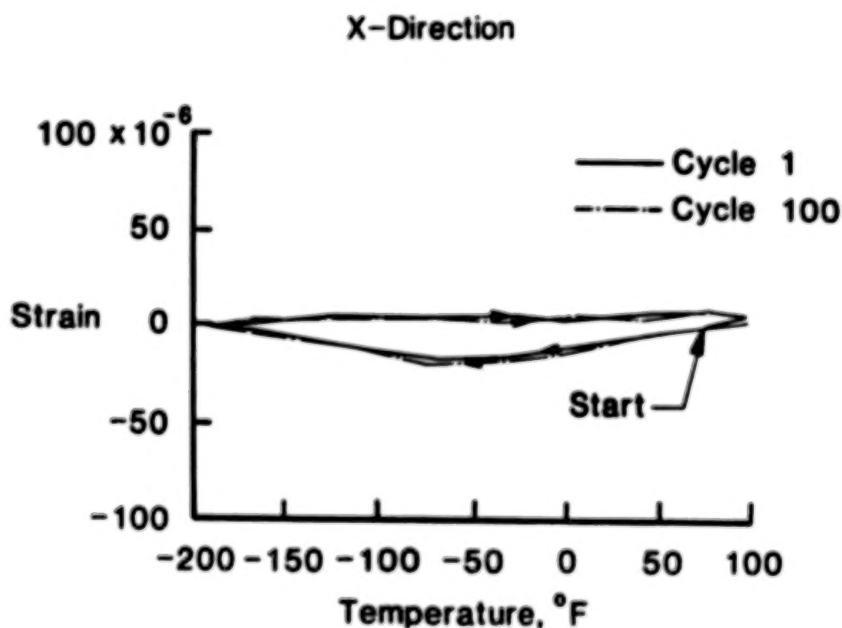


Figure 11

THERMAL EXPANSION OF (± 8)_s P100-AZ91C/AZ61A LAMINATES

Graphite reinforced magnesium composites are of interest for space structures because of their high specific stiffness, low thermal expansion, no outgassing, and excellent radiation resistance. The thermal expansion behavior of a typical Gr/Mg composite (ref. 2) is shown in figure 12. The composite laminate was fabricated with layers of precursor wires (Union Carbide P100 graphite fibers infiltrated with magnesium alloy AZ91C) separated by interply foils of 1.7 mil thick AZ61A Mg alloy and AZ61A Mg surface foils 2.5 mil thick. The finished panel was 80 mils thick with a fiber volume fraction of 0.47. The fiber orientation was $\pm 8^\circ$.

The thermal expansion measurements shown in figure 12 were made in a high precision Fritzeau type laser interferometric dilatometer which had a strain resolution of 1×10^{-6} . The results for the first thermal cycle were made by thermally cycling the specimen in the dilatometer by heating from room temperature to 100°F , then cooling to -200°F then reheating to room temperature. After the first cycle, the specimen was removed from the dilatometer, thermally cycled in a separate chamber and then reinserted into the dilatometer for thermal expansion measurements.

The nonlinear thermal strain behavior is attributed to plastic deformation of the matrix alloy due to thermal stress created by differential thermal expansion between the fibers and matrix alloys. The first thermal cycle produced a permanent residual strain in the specimen of 103×10^{-6} . The residual strain produced on the 5th thermal cycle was 5×10^{-6} and on the 100th thermal cycle 8×10^{-6} . The cumulative strain after 100 cycles was 167×10^{-6} . The coefficient of thermal expansion was small ($-.04 \times 10^{-6}$ to $0.16 \times 10^{-6}/^\circ\text{F}$) at room temperature.

The large hysteresis loop and permanent residual strains produced in the composite clearly show that this composite could not be used for applications where it would be cooled to -200°F . Tests of this composite over a reduced temperature range of 70°F to -100°F showed that a small hysteresis loop was still present but there was no evidence of residual strain following cycling. The linear thermal expansion range of this composite can be increased by heat treating the composite to increase the yield strength of the matrix alloy or by using a higher yield strength alloy for the matrix.

X-Direction

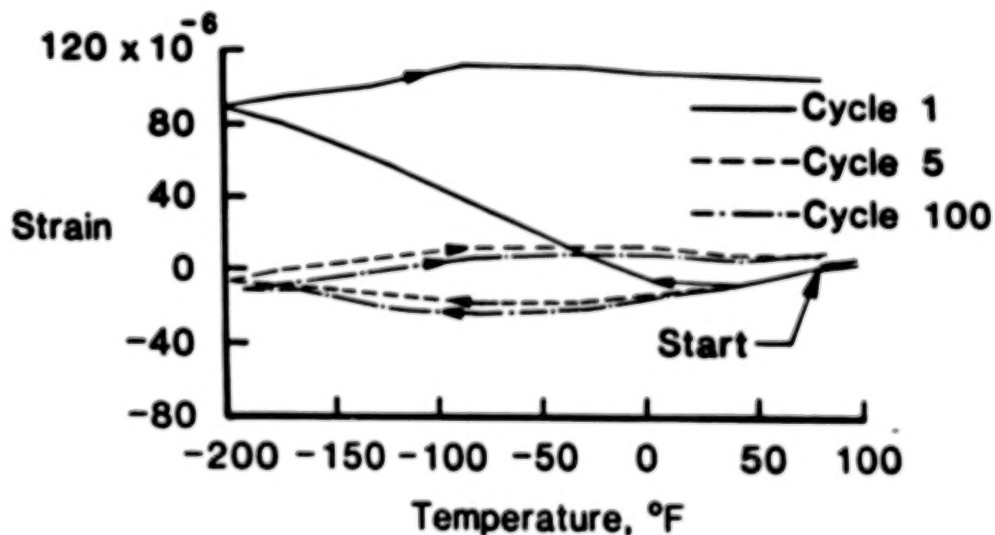


Figure 12

ELECTRON DOSE RATE IN GRAPHITE EPOXY COMPOSITE

The high energy electrons and protons present in the trapped radiation belts of the Earth can cause significant property changes in many polymer materials if the total cumulative dose exceeds approximately 1×10^9 rads. The calculated electron dose rate for a typical graphite/epoxy composite in rads/day is plotted as a function of attitude (circular orbit at zero inclination) in figure 13. The dose rate at the surface, and at 3, 6, and 15 mils below the surface are plotted. For low Earth orbit applications, such as Space Station (~550 KM), the cumulative dose over even a 30 year lifetime would not be expected to effect composite properties. However, for spacecraft placed in high Earth orbit (above 1000 KM) the absorbed dose at the surface would be approximately 7×10^9 rads in 20 years and approximately 10^{10} rads in 30 years. Because these levels are above the known damage threshold levels of many polymeric materials radiation damage is a significant environment factor which must be considered in material selection for long-life structures to be placed in high Earth orbits.

Selected highlights of an ongoing research program on radiation degradation of polymer matrix composites conducted at NASA Langley Research Center will be presented in subsequent figures.

Circular orbits at zero inclination

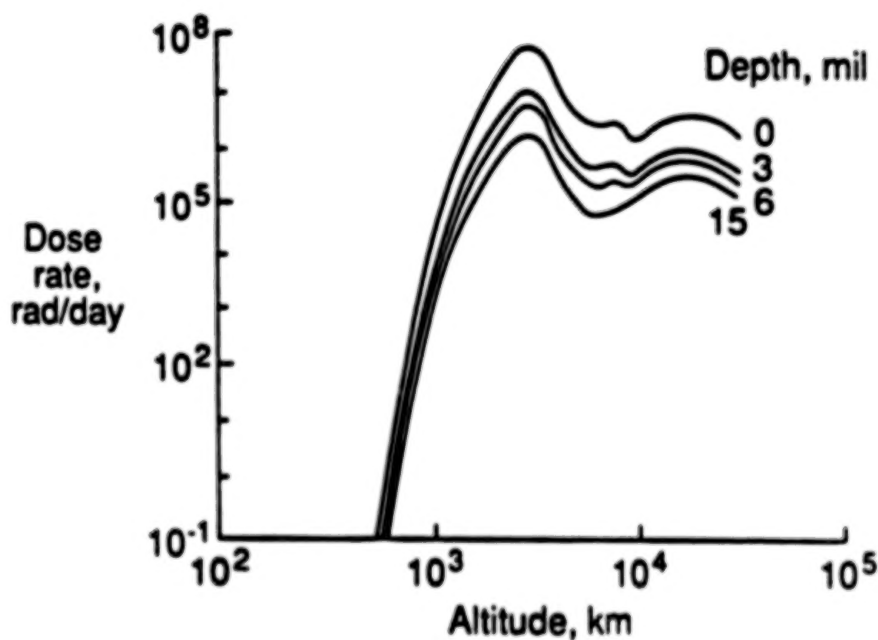


Figure 13

EFFECT OF ELECTRON RADIATION ON AXIAL RESPONSE OF [45°] OFF-AXIS Gr/Ep COMPOSITES

The effect of high energy (1 MeV) electron radiation on the shear properties of a typical 177°C cure graphite epoxy composite (T300/934) is shown in figure 14. Composite specimens 0.5 inch wide by 6 inches long were cut from a 4-ply unidirectional composite laminate such that the fibers were at a 45° angle to the axis of the specimen. The specimens were dried and irradiated in vacuum (2×10^{-7} Torr) to 1 MeV electrons at a dose rate of 5×10^7 rad/h and a total dose of 10^{10} rads. Unirradiated and irradiated specimens were tested at room temperature, +121°C and -157°C.

The results (ref. 3) in figure 14 show that radiation changes the stress strain behavior of the composite laminate at all three temperatures examined. At low temperature (-157°C) the strength and strain-to-failure of the composite are significantly reduced. At room temperature the strength and modulus are increased by irradiation and the strain-to-failure was only slightly reduced. At elevated temperature (+121°C) radiation damage of the epoxy matrix caused large reductions in strength and stiffness and a significant increase in strain-to-failure.

These changes in mechanical properties are consistent with changes expected if the primary radiation damage mechanism were chain scission. Chemical characterization tests revealed the presence of low molecular weight species in irradiated composites not found in unirradiated composites. These low molecular weight species, resulting from chain scissions, plasticize the matrix at elevated temperatures and embrittle the matrix at low temperatures. They can also have a significant effect on thermal expansion behavior which will be illustrated in subsequent figures.

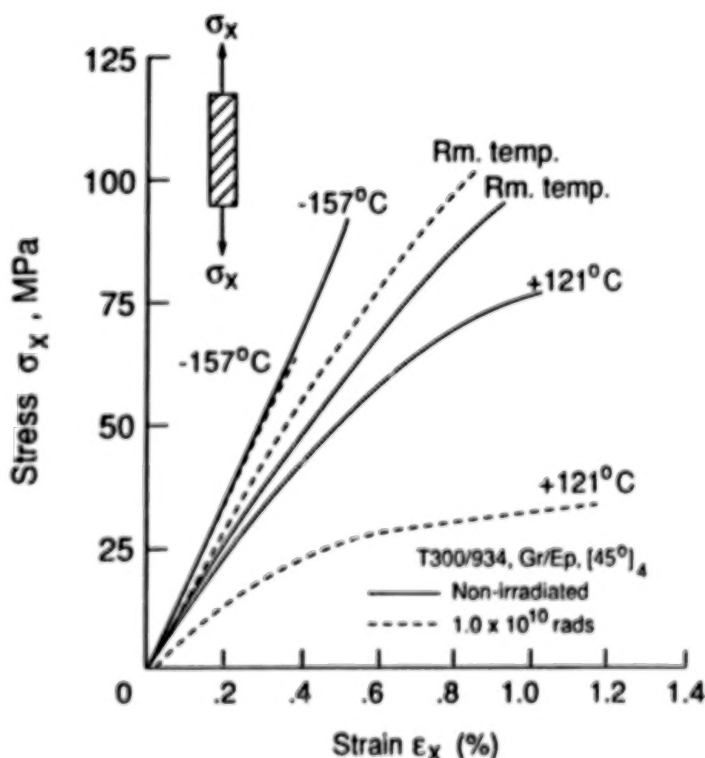


Figure 14

EFFECT OF ELECTRON RADIATION ON COMPRESSIVE RESPONSE OF Gr/Ep COMPOSITES AT ROOM TEMPERATURE

The effect of irradiation on the compressive response of $[0]_8$ and $[90]_8$ laminates of T300/934¹² was measured (ref. 3) at -157°C , RT, and 121°C . Irradiation had very little effect on the compressive properties at -157°C and caused only a small reduction in the strength properties at room temperature, -3% axial and -13% transverse. However, irradiation caused a severe reduction in the strength of both the $[0]_8$ and $[90]_8$ laminates (-62% and -54%, respectively) at elevated temperatures. The elevated temperature stress-strain curve for the $[90]_8$ laminate in figure 15 clearly shows that the matrix has been degraded by irradiation. For the $[0]_8$ laminate the matrix stiffness is sufficient at room and cold temperature to prevent microbuckling of the fibers such that the strength of the $[0]_8$ composite reflects the strength of the fibers. However, at elevated temperatures the matrix stiffness is reduced to the point where lateral support for the fibers is not sufficient to achieve full fiber properties. These results are consistent with results for neat resin specimens tested at elevated temperatures with and without irradiation exposure. The DMA results for baseline and irradiated T300/934 showed that the average molecular weight and cross-link density of this material were reduced by irradiation. Both of these effects would be expected to reduce the elevated temperature stiffness of the resin and thus degrade the compressive properties of the composite.

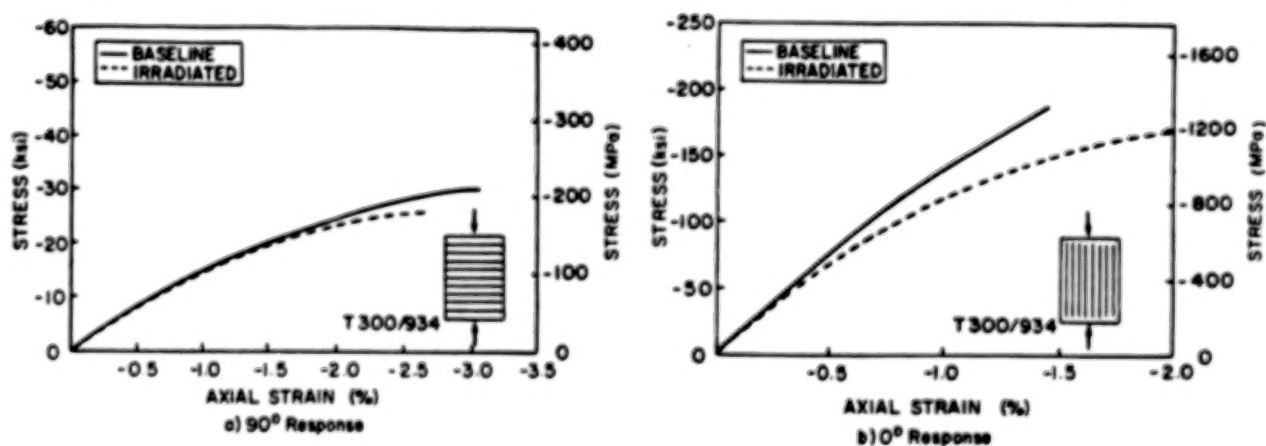


Figure 15

THE EFFECT OF ELECTRON RADIATION AND THERMAL CYCLING ON MICROCRACK FORMATION IN T300/934 Gr/Ep

The effects of sequential radiation and thermal cycling on induced microdamage in the T300/934 Gr/Ep (ref. 4) are presented in figure 16. This figure shows typical X-ray radiographs of 4-ply [0/90/90/0] laminates after (1) 500 thermal cycles, after (2) 500 cycles followed by irradiation (10^4 Mrads), and after (3) irradiation followed by 500 thermal cycles. In each case the thermal cycles consisted of cycling the specimen between -156°C and 121°C using a 20-minute cycle period. The specimens that were thermally cycled only and thermally cycled and then irradiated had approximately 7 cracks/cm in the 0° and 90° directions. However, the specimen that was irradiated and then thermally cycled developed approximately 30 cracks/cm.

The effect of radiation on matrix microcracking was found to be even a worse problem in an elastomer-toughened 121°C epoxy system (CE 339). Exposure to 1 MeV electrons caused severe degradation of the matrix at moderate doses of radiation (ref. 5). At a total dose of 10^{10} rads the residual ultimate tensile strengths of irradiated fiber-dominated specimens were about 50 percent of those of unexposed specimens. Microcracking in irradiated and thermal cycled specimens was extensive. The elastomer used to toughen the matrix in this composite system was found to be extremely sensitive to radiation and underwent crosslinking at low ($10^7 - 10^8$ rads) total doses.

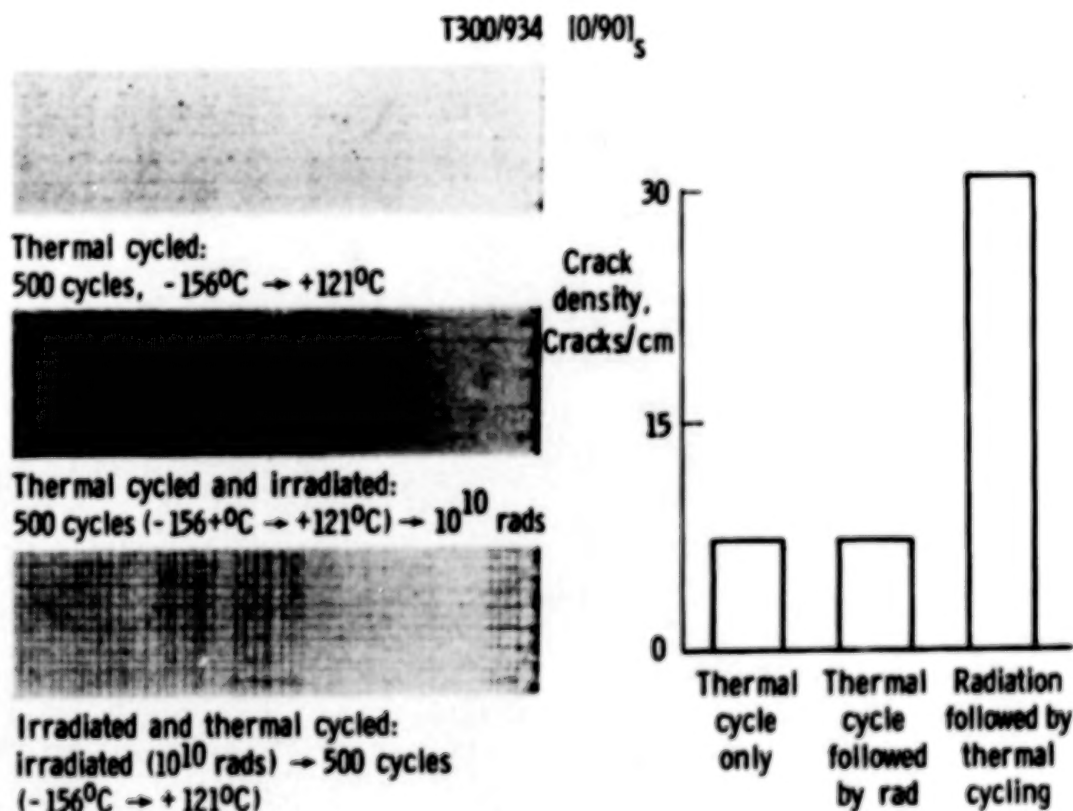


Figure 16

EFFECT OF THERMAL CYCLING ON CTE IN THE 0° DIRECTION

During thermal cycling of graphite epoxy composites microcracking can result as illustrated in figure 16 from the combination of residual fabrication stresses and the thermal stresses induced by the mismatch in thermal expansion between the fibers and matrix and between adjacent plies of different orientations. Radiation damage to the resin matrix can further contribute to microcracking by creating low molecular weight polymer products which embrittle the matrix at low temperatures. The combined effect of thermal cycling and radiation damage on the CTE of a [0, 90, 90, 0] T300/934 composite laminate is shown in figure 17. The composite was cycled up to 500 times between -156°C and 121°C in a baseline (or unirradiated) condition and after exposure to 1 MeV electrons for a cumulative exposure of 10^{10} rads. The CTE of the baseline material was essentially unchanged after 500 thermal cycles indicating that no significant damage was developed in the composite as a result of thermal cycling. However, the CTE of the irradiated composite laminate was substantially reduced by thermal cycling indicating development of damage in the composite.

X-ray microradiography of the composites showed that the crack density in the 90° plies was approximately 30 cracks/cm after 500 cycles. Microcracks in the 90° plies reduce the CTE of the laminate in the 0° direction because the 0° plies have a more dominant role than when there are no cracks in the 90° plies.

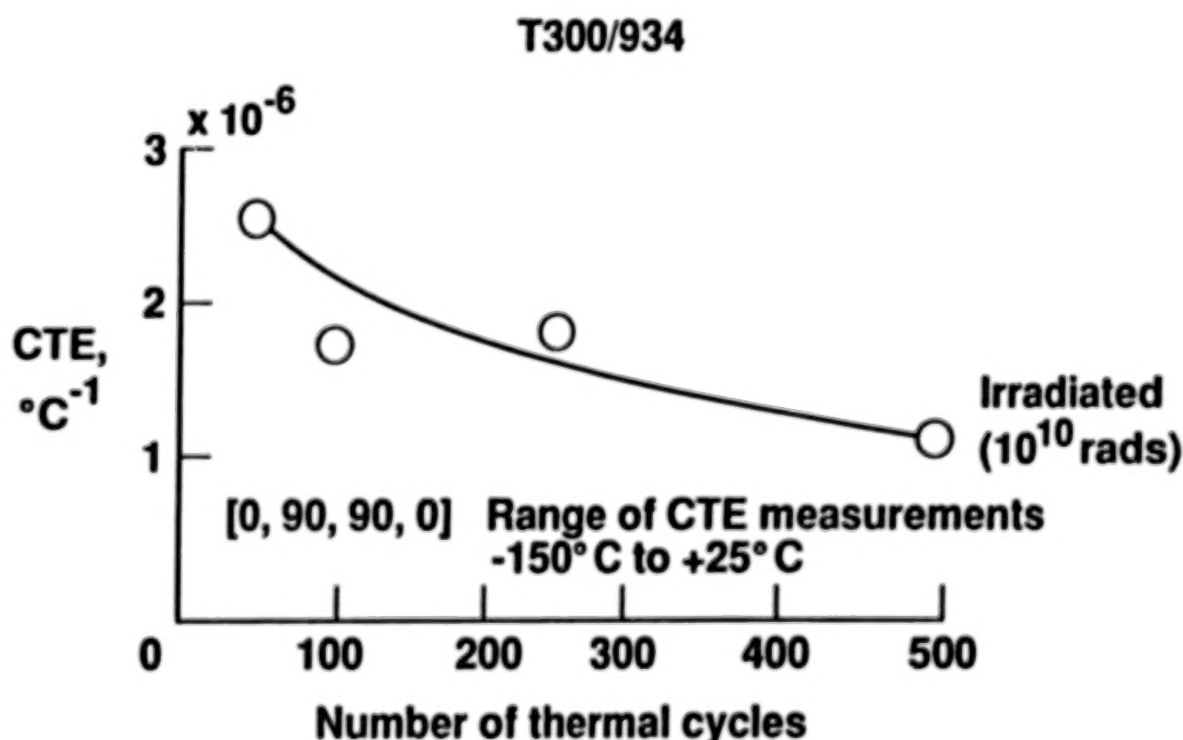


Figure 17

EFFECTS OF RADIATION ON THERMAL EXPANSION

Radiation degradation of matrix resins combined with a cyclic thermal environment can affect the dimensional stability of polymer matrix composites in two ways. Radiation-induced chain scission can produce degradation products that plasticize the matrix at elevated temperatures which can change the way in which residual curing stresses are relieved in the composite, and degradation products can embrittle the matrix at low temperatures, resulting in matrix micro-cracking. Irradiation can also result in additional cross-linking which can embrittle the matrix resin.

Figure 18 shows the effects of radiation degradation products on the thermal expansion behavior (ref. 6) of a typical 177°C cure Gr/Ep composite $[(0_2/90_2)_5]$ T300/S208). The irradiated specimen shows a pronounced nonlinearity at elevated temperature and a permanent negative residual strain of approximately -67×10^{-6} at room temperature after one thermal cycle to -157°C . Repeated cycles over the same temperature range give a strain response parallel to the unirradiated curve, but displaced by the permanent residual strain present after the first cycle. However, if the specimen was cycled to a higher maximum temperature, an additional change in slope of the thermal strain curve occurs which results in an additional permanent residual strain.

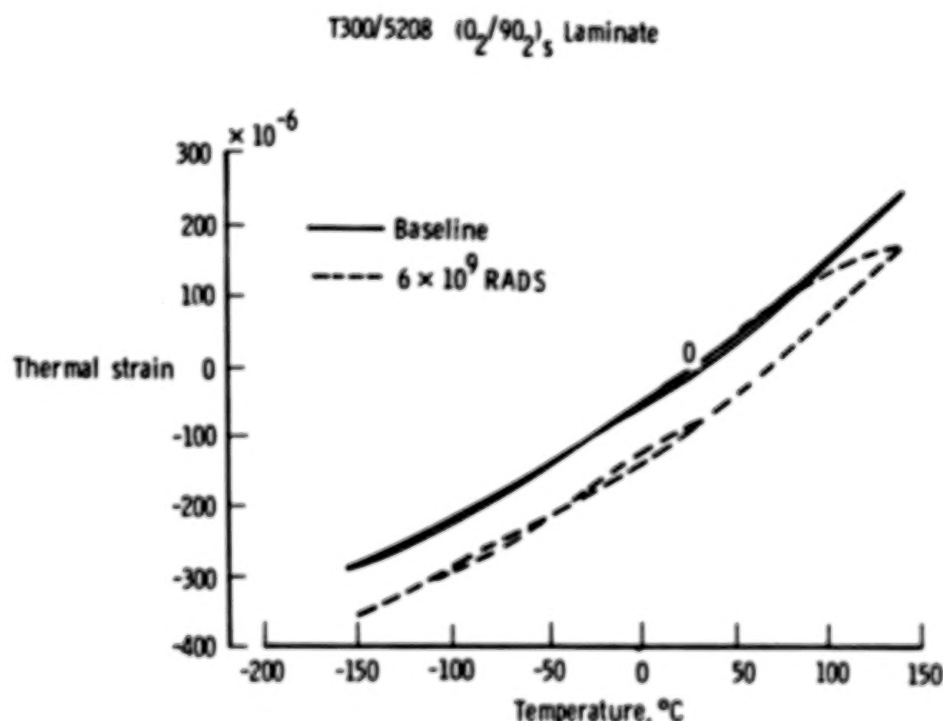


Figure 18

DYNAMIC MECHANICAL ANALYSIS OF T300/5208 GRAPHITE EPOXY

The elevated temperature nonlinear strain response and subsequent permanent residual strain at room temperature shown in figure 18 are related to radiation degradation products plastifying the matrix and can be explained by the DMA results (ref. 7) presented in figure 19. The damping data for the irradiated composite show that the T_g is lowered by approximately 22°C and a broad "rubbery region" is produced compared to the unirradiated composite sample. During the thermal cycling tests the specimen was heated into the region where the matrix could flow, thus relieving residual tensile curing stresses resulting in a more fiber-dominated response at high temperature (nonlinear region) and permanent negative residual strains at room temperature. On subsequent thermal cycles no additional changes were measured. The reason for this behavior may be related to the procedure used to run the thermal expansion tests. The heating process in these tests occurred slowly in 22°C increments, with 30-minute holds at each temperature. In the 107°-138°C temperature range, chemical changes apparently took place resulting in a movement of the "rubbery region" back to higher temperatures out of the thermal expansion test range. Thus on subsequent thermal cycles to the same temperature no additional changes were measured.

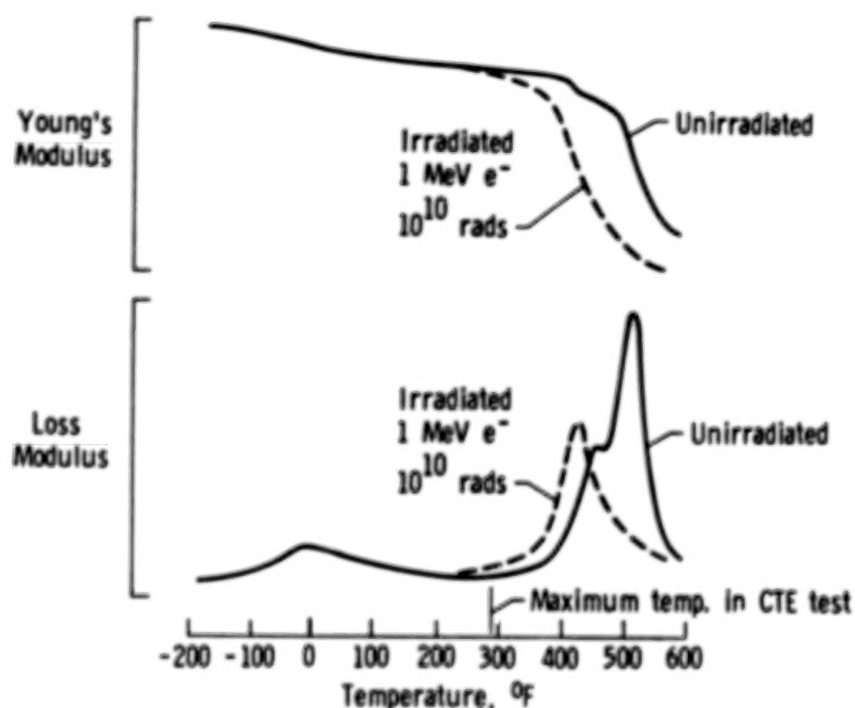


Figure 19

FLEXIBLE SECOND-SURFACE MIRROR (SSM) THERMAL CONTROL COATING

Polymeric second-surface mirror coatings are so named because the reflecting coating is on the second surface (non-sun-facing side) of the polymeric film as illustrated in figure 20. To obtain a high reflectance (low solar absorptance) the polymeric film must be highly transparent to the solar spectrum from 250 to 3000 nanometers since sunlight passes through the film and is reflected back through the film into space. The reflecting coating is typically an opaque thickness of silver or aluminum with a thin over-coating of stainless steel to provide corrosion protection. An adhesive is applied to the stainless steel side of the SSM for bonding the SSM to a spacecraft.

Although the polymeric film is transparent in the solar wavelength region, it possesses infrared absorption bands characteristic to all polymers. These IR absorption bands give rise to the thermal emittance characteristics needed for this SSM to perform as a thermal control coating. As the thickness of the polymeric film increases, the emittance also increases to some limiting value near 0.9. Solar absorptances as low as 0.08 with emittance values of 0.92 have been obtained with polymeric second-surface mirror coatings.

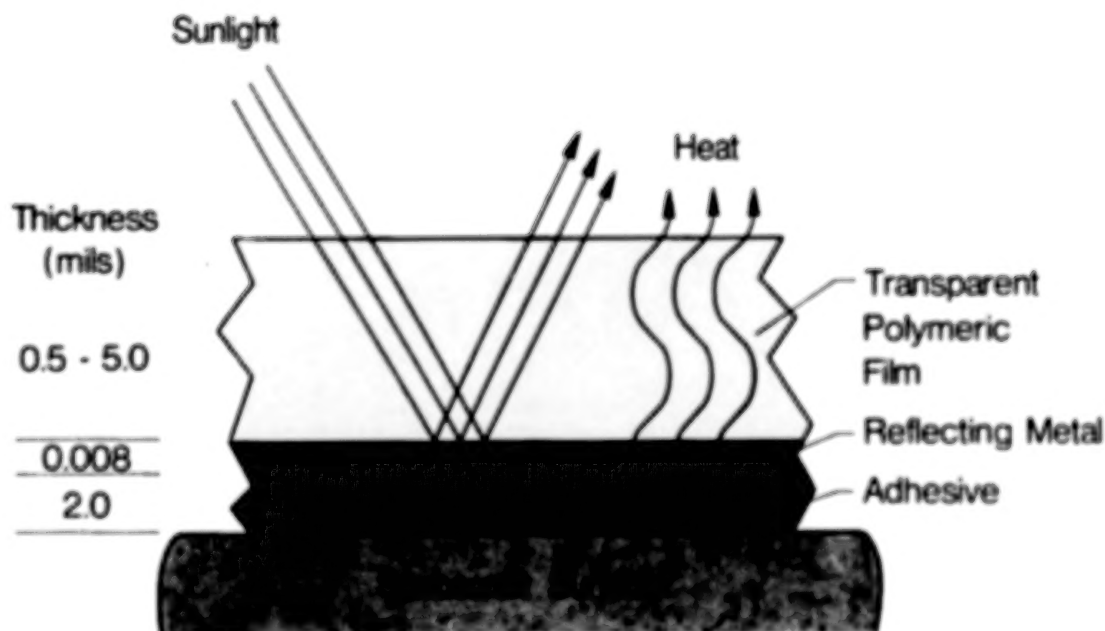


Figure 20

TRANSPARENT POLYIMIDE FILMS

Space durable polymeric films which have high optical transparency in the 300-600 nm range of the electromagnetic spectrum are needed for applications such as second-surface thermal control coatings, solar cell covers, and multilayer insulation blankets. Although several classes of polymers which are transparent/colorless are available, such as polyesters, aliphatic polyimides and FEP Teflon, these materials have limited long-term stability in the space environment, especially in orbits where high energy ionizing radiation is present. Aromatic polyimides have good toughness and flexibility, good thermal stability, high mechanical strength, and good radiation resistance but these polymers generally have poor transparency in the visible range. Commercial aromatic polyimide film is approximately 70% transparent (depending on thickness) in the 500 nm wavelength range which is the wavelength of interest for space applications. The transparency will also decrease with exposure time in space.

A new series of highly optically transparent linear aromatic polyimide films has been synthesized (refs. 8-9) with variations in the polymer molecular structure aimed at reducing electronic interactions between polymer chains to increase optical transparency. Polymerizations were performed with highly purified monomers with the result that several polymers were produced with good optical transparency compared to commercially available polyimide films such as Kapton as illustrated in figure 21. The more transparent films were evaluated for use in the space environment and typical results are shown in figure 22.

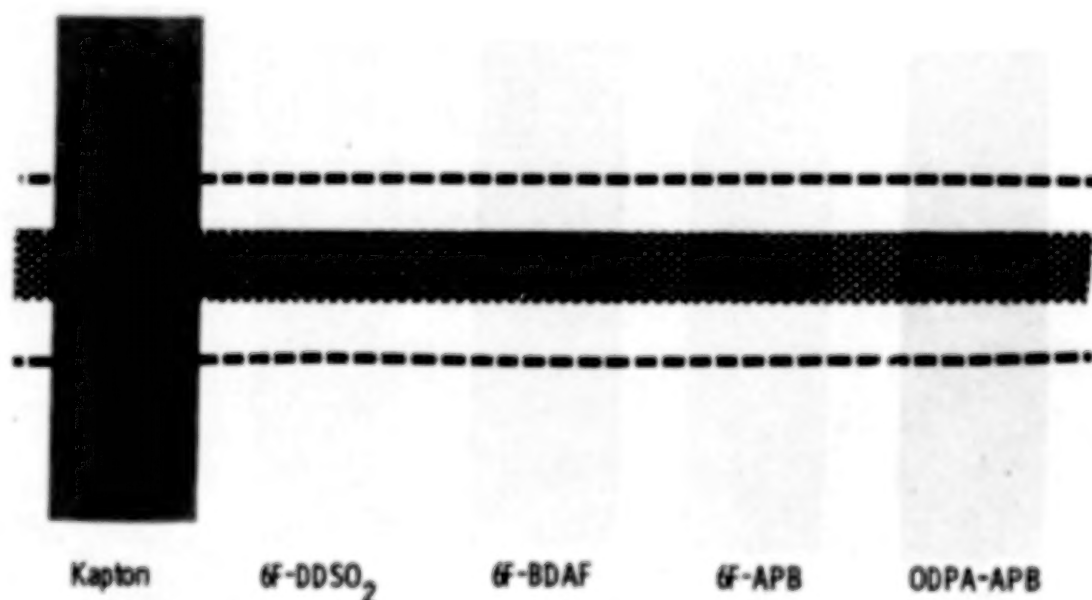


Figure 21

EFFECT OF ELECTRON RADIATION ON TRANSMISSION OF TRANSPARENT POLYIMIDE FILMS

Several series of linear aromatic polyimide films have been synthesized and characterized before and after simulated space exposure (ref. 10). To maximize optical transparency, highly purified monomers were used and several changes were made in the molecular structure to reduce the color intensity. The properties of the films were fully characterized including determination of glass transition temperatures (T_g), polymer decomposition temperature, transmission UV-visible spectra, infrared spectra, and solubility in selected organic solvents. Typical UV-visible spectra of the 6F-containing films before and after the films were exposed to 1 MeV electrons for a total dose of 5×10^9 rads representative of 20-25 years in an orbit in the trapped radiation belts such as Geosynchronous Earth Orbit (GEO) are shown in figure 22. Transmission spectra of 6F dianhydride-containing films are compared to commercially available Kapton H film. The 0.5-mil-thick films were approximately 95% transparent at 500 nm before electron exposure and were 85 to 91% transparent after exposure to 5×10^9 rads. The 6F+3,3'-ODA polyimide was especially radiation stable and showed only a 2% reduction in transparency at 500 nm after electron exposure. All of the films remained flexible after radiation exposure and no changes in molecular structure were detectable by Fourier transform infrared spectroscopy. The combination of good radiation (UV and electron) stability, good thermal stability, high optical transparency, and solubility make these polymers very attractive for space applications either as polymer films or spray coatings.

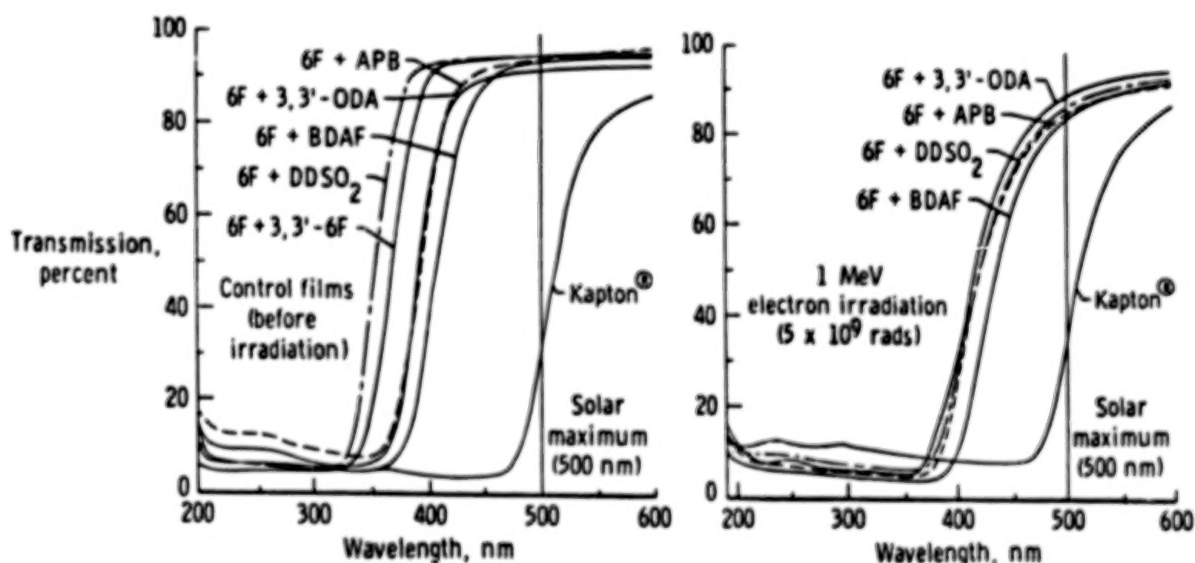


Figure 22

SPACE MATERIALS DEVELOPMENT

Space materials research and development is a continuing research thrust (fig. 23) within NASA. The objectives of this work are to develop new and improved materials for future NASA space science instruments and spacecraft for the civil space industry. The desire to increase design lifetimes combined with stringent requirements on precision, structural weight and performance have established guidelines for development of new long-life materials. However, materials development is a long-lead activity and requires long-range research programs to not only develop the materials but also conduct simulated space exposure testing to establish the long-term durability of these materials in the space environment. Short-term (2-3 yrs) "Advanced Development Programs" similar to that conducted for Space Station are not adequate to develop, test, and certify long-term space durability on new materials.

- NASA's charter is to develop technology to advance the civil space program
- NASA's customers are the civil space industry and space science community
- Materials focus should be on development of new and improved materials and long-life certification of selected existing materials
- Materials development needs to be a long-term continuing R&D effort - 2 to 3 years "Advanced Development Programs" are generally not adequate

Figure 23

NEW MATERIALS DEVELOPMENT

One of the most fundamental needs in new materials development is a clear definition of the material requirements (fig. 24) and the relative importance of each requirement. These requirements need to be as specific as possible. For example, simply to specify high strength and stiffness for structural composites is not very useful to the materials engineer. He really needs to have target mechanical, physical, optical, and electrical properties so that he can select the appropriate fibers, resins, layups, and coatings to achieve high stiffness, low CTE, good compressive strength, high resistance to thermal fatigue, low outgassing, and other critical properties as required. It is also important to define the service environment to insure that service life simulations are conducted in realistic exposure conditions. A fresh new look is needed to develop test standards for space qualification of materials for long-term (20-25 yrs.) service in space.

Testing Issues

- Mechanical, physical, optical property requirements
- Material property data base - What is required and when is it developed?
- Test standards - Are existing space qualification guidelines adequate?

Figure 24

LONG-LIFE CERTIFICATION

Established test procedures for long-life certification of space structures do not exist. Spacecraft have been designed and built for relatively short lifetimes, 3-8 years, based on limited test data. Nearly all of the environmental effects data in the literature are for exposure to a single environmental parameter such as ultraviolet radiation, electron radiation, micrometeoroid impact, etc. Very little combined exposure data exist. Also the chemical formulation of many of the polymers and composites of interest for space hardware have changed over the past decade.

For long-life (20-25 yrs.) certification acceleration methodologies (fig. 25) are required for realistic combined exposure conditions. These methodologies must be based on a fundamental understanding of damage mechanisms in the materials. Benchmark flight experiments are required to verify ground-based simulations to insure that damage mechanisms observed under accelerated exposure conditions are the same as produced in space. Space environmental effects testing is very time consuming and expensive and new approaches are required to insure that data generated on existing materials will be useful for certification of tomorrow's materials.

- Acceleration methodology - must be based on knowledge of damage mechanisms
- Benchmark flight experiments are required to verify ground-based simulations
- Long-life certification process must be cost effective -
How do we accomplish this?

Figure 25

REFERENCES

1. Mahoney, M. J., editor: Report of the Asilomar III LDR Workshop, JPL Publication 88-23, August 15, 1988.
2. Tompkins, Stephen S.; Ard, K. E. and Sharp, G. Richard: Thermal Expansion Behavior of Graphite/Glass and Graphite/Magnesium. Presented at 18th International SAMPE Technical Conference, October 7-9, 1986.
3. Reichmanis, Elsa, and O'Donnell, James H., editors: The Effects of Radiation on High-Technology Polymers, Chapter 14: Radiation Durability of Polymeric Matrix Composites by Darrel R. Tenney and Wayne S. Slempe. ACS Symposium Series 381, 1989.
4. Tenney, D. R., Sykes, G. F. and Bowles, D. E.: Composite Materials for Space Structures. Proceedings of the Third European Symposium on Space Materials in Space Environment European Space Agency SP-232, Nov. 1985, pp. 9-15.
5. Sykes, George F. and Bowles, David E.: Space Radiation Effects on the Dimensional Stability of a Toughened Epoxy Graphite Composite, SAMPE Quarterly, vol. 17, no. 4, July 1986, pp.39-45.
6. Bowles, D. E.; Tompkins, S. S. and Sykes, G. F.: Electron Radiation Effects on the Thermal Expansion of Graphite Resin Composites. J. of Spacecraft and Rockets, vol. 23, no. 6, Nov.-Dec. 1986, pp. 625-629.
7. Tenney, Darrel R.; Tompkins, Stephen S. and Sykes, George F.: NASA Space Materials Research. Large Space Antenna Systems Technology Conference - 1984, Dec. 4-6, 1984.
8. St. Clair, A. K.; St. Clair, T. L. and Shevket, K. I.: Proceedings of the Division of Polymeric Materials Science and Engineering, vol. 51, p. 62, 1984.
9. St. Clair, Anne. K. and Slempe, Wayne S.: Evaluation of Colorless Polyimide Film for Thermal Control Coating Applications. SAMPE Journal, July/August 1985, pp. 28-33..
10. St. Clair, A. K.; St. Clair, T. L. and Slempe, W. S.: Optically Transparent/Colorless Polyimides in Recent Advances in Polyimide Science and Technology, W. D. Weber and Mr. R. Gupta, eds., 1987, pp.16-36.

RADIATION EFFECTS IN SPACECRAFT ELECTRONICS*

James P. Raymond
Mission Research Corporation
San Diego, California

In this presentation effects on the internal spacecraft electronics due to exposure to the natural and enhanced space radiation environment will be reviewed. The emphasis will be placed on the description of the nature of both the exposure environment and failure mechanisms in semiconductors. Understanding both the system environment and device effects is critical in the use of laboratory simulation environments to obtain the data necessary to design and qualify components for successful application.

*Work was partially supported by MRL under Contract N00014-85-C-2642

Energy Deposition

For the internal electronics of a spacecraft the radiation exposure is characterized in terms of the energy deposited in critical regions of the piece parts. In modern electronic systems, the most sensitive pieceparts of the discrete semiconductor devices and microcircuits. It follows, therefore, the critical materials of interest are silicon and silicon-dioxide.

The absorbed energy is described in units of radiation absorbed dose for the material, or rad(Silicon) in this case, as shown in Figure 1. The energy can be absorbed in the semiconductor material by either ionizing or nonionizing means. For exposure by x- or gamma-rays (important principally in laboratory simulation environments) the energy deposition is almost exclusively by ionization. For the high energy electrons of the space radiation environment, energy deposition is principally by ionization. For the high energy electrons of the space radiation environment, energy is deposited by both ionization and nonionizing atomic displacements. For neutron exposure (important in laboratory simulation of displacement damage) the absorbed energy is almost exclusively in displacement damage, although the neutron exposure is always associated by concomitant ionizing gamma rays. It will be shown that ionizing radiation effects, both by accumulated effects and that of a single particle, are of principal concern to the internal spacecraft electronics.

■ Absorbed Energy – rads(Silicon)

- One rads(Si) = 100 ergs/gram(Silicon)

■ X-/Gamma Rays: Ionization Exclusively

■ Electrons: Principally Ionization

■ Protons: Ionization and Atomic Displacement

■ Neutrons: Principally Atomic Displacement

FIGURE 1

System/Simulator Exposure Environments

Space radiation environments can be initially scoped by the electron-induced accumulated ionizing radiation for both the natural environment and an environment enhanced (i.e., pumped-up) by the trapped electrons of a high-altitude nuclear weapon detonation, as shown in Figure 2. Also shown is the range of exposure levels typical for exposure using a laboratory Cobalt-60 source for the simulation of ionizing radiation effects.

The system environments represent the absorbed dose behind a 100 mil, semi-infinite slab of aluminum, for orbital altitudes ranging from 150 to 60,000 km, and for orbital inclinations of 0, 30, 60, and 90 degrees. System exposure to the natural environment was assumed over the range of one to thirty years. The enhanced environment is summarized for an exposure of 180 days [courtesy of Mr. S.C. Rogers, JAYCOR, and the Defense Nuclear Agency].

The lower ranges of exposure are representative of the environments at low earth or geosynchronous orbit, while the peak exposures are for environment roughly between 1,000 and 20,000 km in altitude. Additional shielding will further reduce the exposure levels, but shielding of the electron dose is limited by the production of gamma rays by bremsstrahlung.

It should be noted that the exposure rate for the natural environment is substantially lower than that typical of Cobalt-60 simulation exposures, and that the levels of exposure for the enhanced environment are both substantially greater and at a higher intensity than the natural environment exposure.

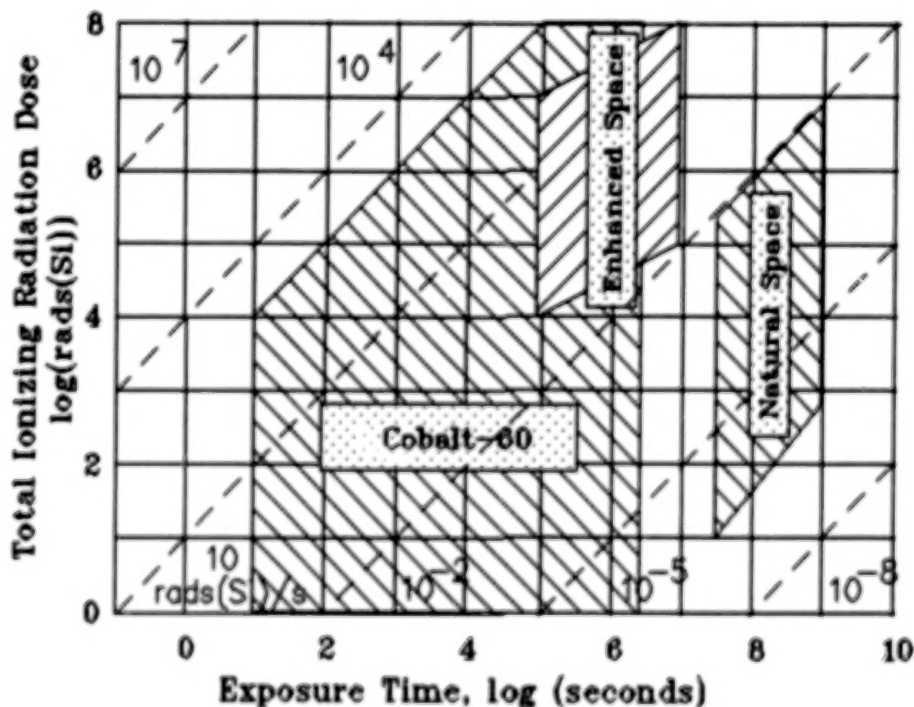


FIGURE 2

Summary of Semiconductor Device "Total Dose" Susceptibility

There has been extensive characterization of the permanent damage effects of ionizing radiation exposure of semiconductor microcircuits and devices for evaluation and qualification in systems required to survive space or nuclear weapon radiation exposure. The estimated ranges of observed hardness on a variety of semiconductor devices are shown in Figure 3 (Refs. 1,2).

In summary, the minimum level of concern for ionizing radiation exposure is on the order of 1,000 rads(Si) for the most sensitive devices; virtually all microcircuit technologies may be suspect at exposure levels of 10,000 rads(Si), and, with hardening and performance downscoping, an electronic system can be realized that can perform after exposure to greater than 1 Mrad(Si).

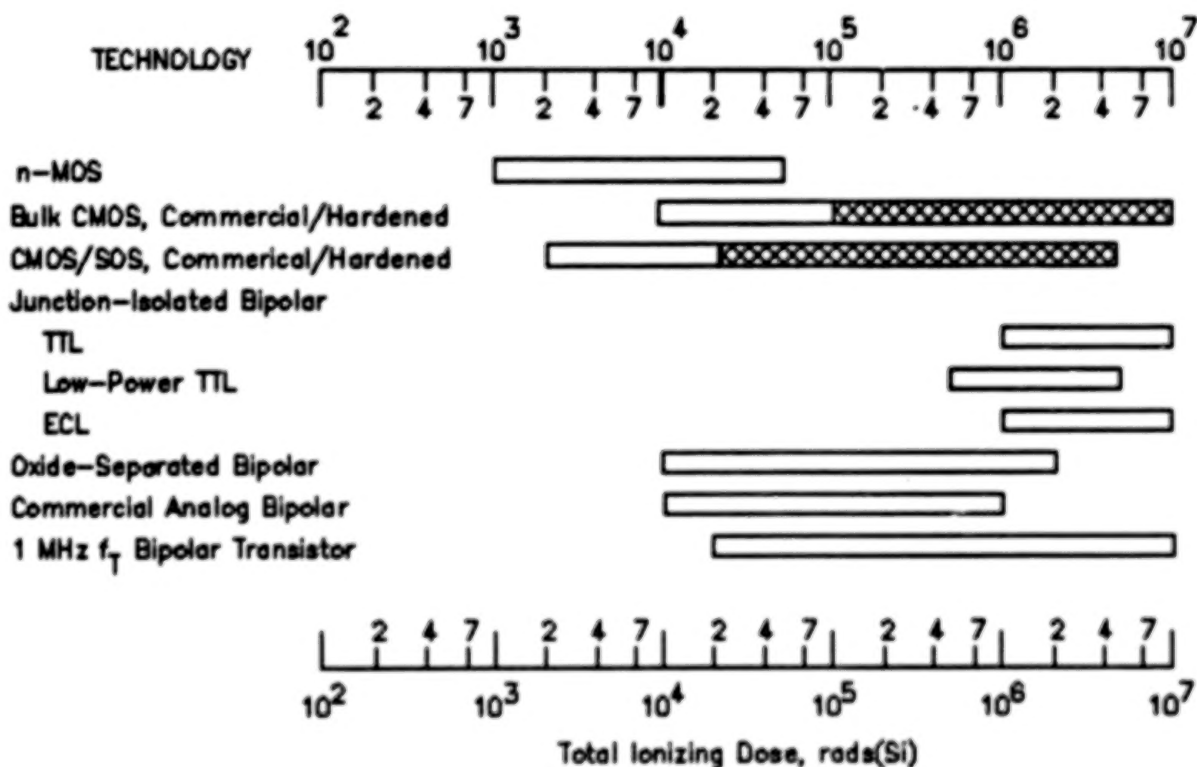


FIGURE 3

Accumulated Ionization Failure Mechanisms

The basic failure mechanisms of accumulated ionization damage in semiconductor devices, as summarized in Figure 4, are the result of hole-electron pair generation in critical silicon-dioxide isolation layers. The first failure mechanism is the result of holes being trapped in the oxide layer after the electrons are swept out by the applied electric field. The second failure mechanism is the result of an increased density of interface states formed at the active-silicon:silicon-dioxide interfaces. The manifestations of these basic failure mechanisms in the microcircuit elements include threshold voltage shift of the MOS transistors, gain degradation of the bipolar transistors, and a general increase in junction leakage currents (Ref. 3). At the overall circuit level, the result is degradation of overall performance such as drive capability and switching speed. Eventually, with sufficient exposure, the damage becomes sufficient to cause functional failure of the microcircuit.

■ Accumulated Ionization

- Oxide Trapped Charge
- Interface States
 - Threshold Voltage Shift
 - Increased Leakage Current

■ Parameter Degradation

■ Functional Failure

FIGURE 4

CMOS Inverter Failure Modes

The nature of the observed failure of even simple microcircuits in application can be relatively complex. For example, considering a hypothetical illustration of the threshold voltage shift of the n-MOS and p-MOS transistors of an inverter pair, as shown in Figure 5, circuit failure can occur in at least three different ways depending on the circuit application. In the first case, if the application is very sensitive to power supply leakage current, failure will be observed as soon as the threshold voltage of the n-MOS transistor becomes less than zero. If the design is tolerant to power supply leakage current, at a higher exposure level (in this example) failure may be the result of an unacceptably large shift in the p-MOS transistor threshold voltage. Finally, if tolerant to the first two, functional failure in the inverter will inevitably result when the sum of the n-MOS and p-MOS threshold voltages exceeds the power supply voltage.

To further complicate the situation, the threshold voltage shifts of the MOS transistors are functions of the applied bias during radiation exposure as well as the intensity (or dose rate) of the exposure. The point here is that to interpret the observed effects in a complex microcircuit it is necessary to understand the basic nature of the effects in the individual element technology.

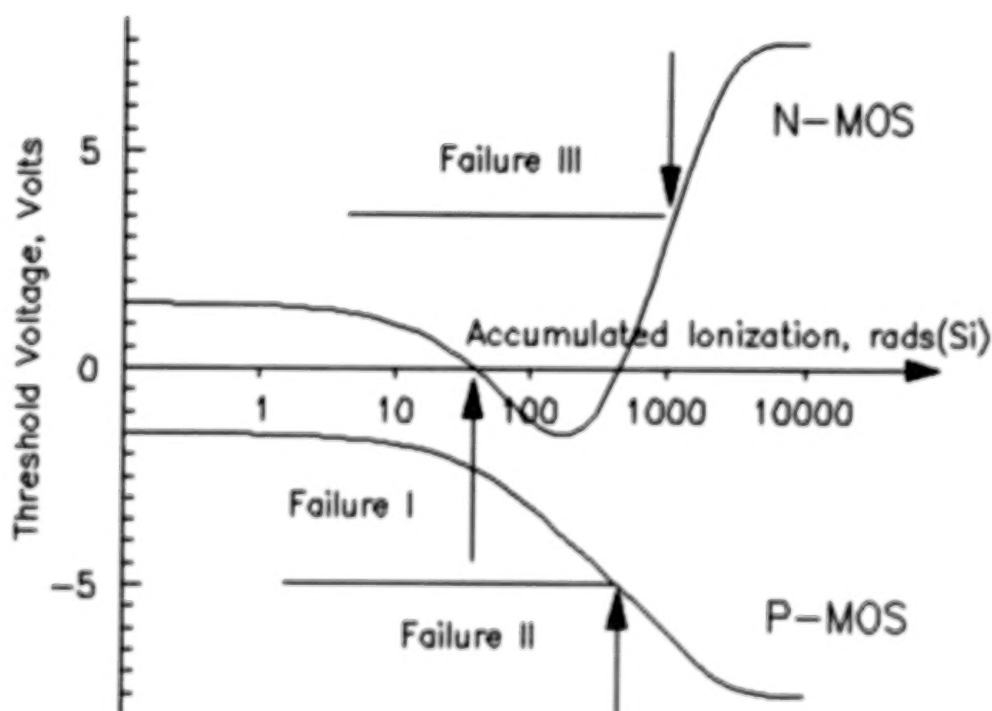


FIGURE 5

N-MOS Transistor Threshold Voltage Shift

To illustrate, consider the basic nature of variations in the threshold voltage shift of an n-MOS transistor, illustrated in Figure 6. As mentioned previously, the two basic failure mechanisms involved are trapped charge and interface states (Ref. 3). As it turns out, in an n-MOS transistor, the trapped charge results in a negative shift of the threshold voltage and the interface state buildup results in a positive shift of the threshold voltage. During ionizing radiation exposure, both trapped charge and interface states are created continuously. Also during a long exposure (e.g., greater than seconds) the trapped charge anneals and the interface state density tends to accumulate. As a result, the observed threshold voltage shift with exposure is a strong function of the time dependencies of trapped hole annealing and interface state buildup. As shown, only the relative rate of interface state buildup is varied. If the interface state buildup is rapid, the effects of trapped charge are nicely compensated and the minimum threshold voltage of the transistor remains greater than zero. Conversely, if the interface state buildup is slow, the negative excursion of the threshold voltage is substantial. It should be noted that, at least in this hypothetical example, for sufficiently long exposures, eventually the interface state buildup will dominate and the threshold voltage shift will increase above its initial value.

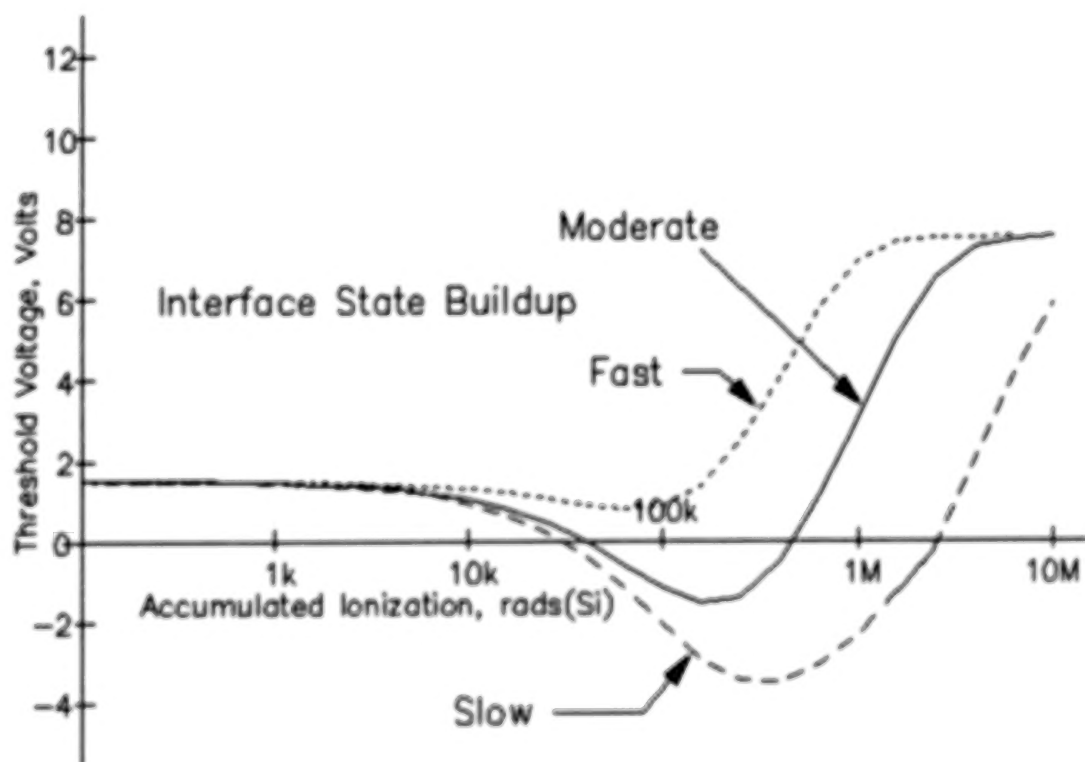


FIGURE 6

Variations in Microcircuit Hardness

As an example of the significance of the exposure environment on the effective microcircuit hardness, consider a hypothetical (and somewhat contrived) example of the effective failure level of three different microcircuits (Figure 7). It will be assumed that each of the three types was measured at an effective hardness of 100,000 rads(Si) for a 10,000 second exposure in a Cobalt-60 source. If the microcircuit hardness is essentially determined by interface states (as might be the case for some MOS microcircuits), the failure level will be highest for high-intensity exposures at short times following radiation exposure. As the exposure time increases, the effect of the interface states will increase and the effective hardness will monotonically decrease. On the other hand, if the effective hardness is essentially determined by trapped charge in the oxide, annealing effects (as might be the case in advanced recessed-oxide bipolar microcircuits (Ref. 4)), are small for high-intensity exposures and at short times following exposure, will limit the hardness. As the exposure time is increased, annealing of the trapped charge becomes more effective and the effective hardness increases. Finally, in what perhaps is the worst-case, if both interface states and trapped charge are important, the effective failure level can be lower than that observed in the Cobalt-60 characterization at either higher-intensity or longer-duration exposures (Refs. 5,6).

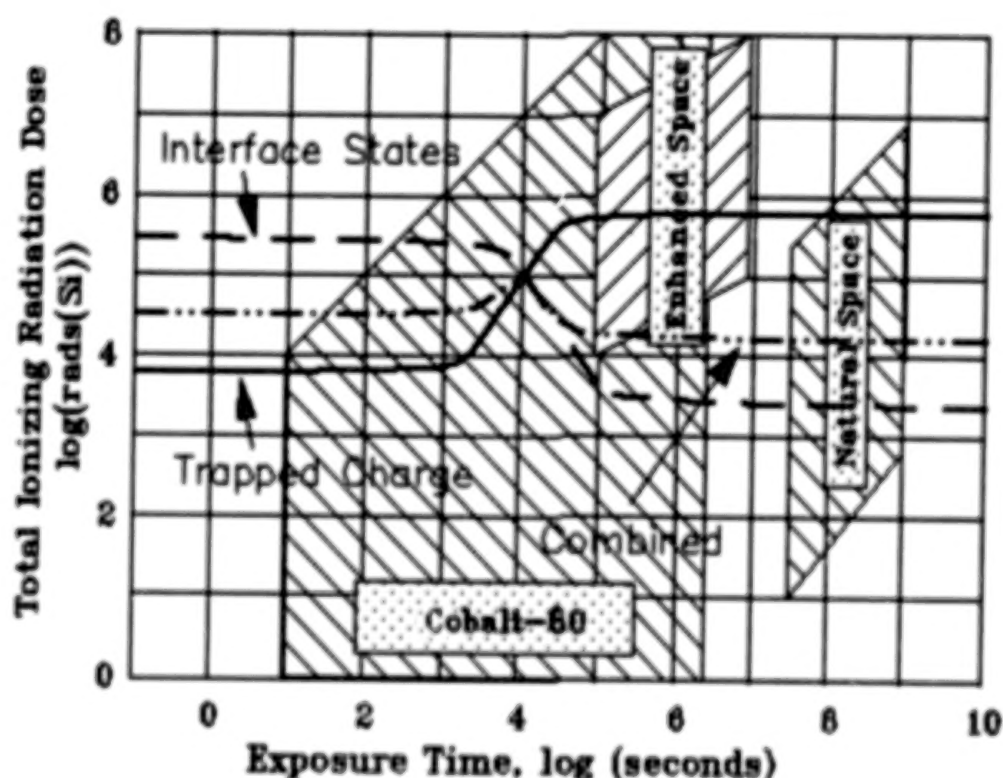


FIGURE 7

Displacement Damage Failure Mechanisms

In addition to accumulated ionizing radiation effects, exposure to the high-energy space proton environment causes atomic displacement damage in semiconductor devices and microcircuits, summarized in Figure 8. The basic failure mechanism of the atomic displacements is an accumulated reduction in the silicon minority carrier lifetime which, in turn, degrades the current gain of bipolar transistor elements and increases junction leakage currents (Ref. 3). The observed effects of the element degradation are accumulated performance degradation of the microcircuit and, eventually, functional failure.

■ Displacement Damage

- Minority Carrier Lifetime Degradation

- Bipolar Gain Degradation
- Increased Leakage Currents

■ Parameter Degradation

■ Functional Failure

FIGURE 8

Range of Neutron Damage Susceptibilities

Almost all the data on semiconductor device susceptibility to radiation-induced atomic displacement damage have been obtained by exposure to the neutron environment of nuclear reactors. This work has been done to support the hardened design of military systems that must survive a nuclear weapon radiation environment. Shown in Figure 9 are the estimated ranges of neutron damage susceptibility for the same semiconductor device technologies shown previously for accumulated ionization damage (Refs. 1,2). In terms of relative susceptibility, the MOS technologies, not critically dependent on high minority carrier lifetime for performance, are very tolerant to neutron exposure. Those technologies depending critically on high minority carrier lifetime such as the wide-base power transistor, commercial analog microcircuits using wide-base lateral pnp transistors, and older digital microcircuits are relatively susceptible to displacement damage. Modern digital microcircuits (and hardened analog microcircuits) use very fast bipolar transistor elements and are much less susceptible to displacement damage.

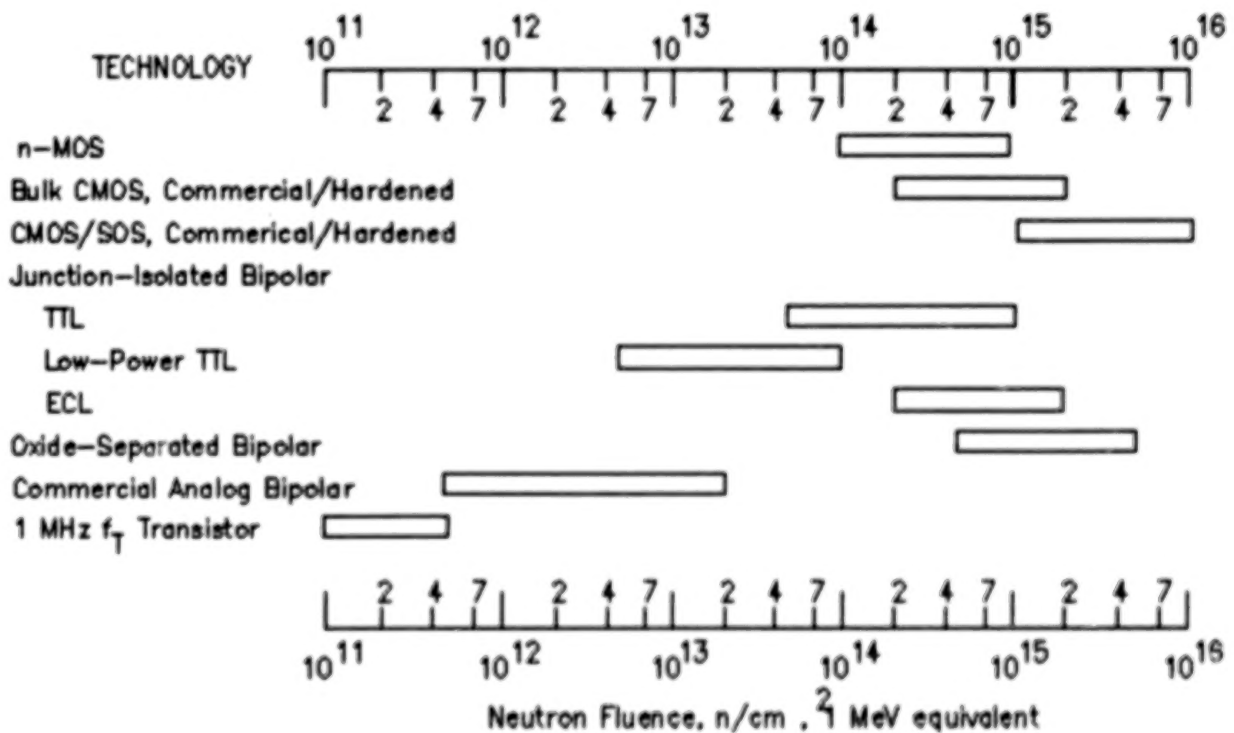


FIGURE 9

Schematic Representation of Device Susceptibility

Determination of the dominant failure mechanisms in electronics piece parts is important in the determination of the laboratory facilities required to evaluate and qualify candidates. Through careful analyses and experimental validation, the relative effects of ionization and displacement damage have been established for both the high-energy protons and electrons of the space radiation environment (Refs. 7,8). The ionizing contribution can then be related to device failure levels as observed in laboratory exposures such as with the use of a Cobalt-60 source. The displacement damage contribution can then be related to the device failure levels resulting from nuclear reactor exposure. Shown in Figure 10 are the device failure ranges. The lines represent the ratio of displacement damage and ionization damage for high energy protons and electrons. With a little reflection, it can be seen that if the device failure range falls above the particle equivalent line, the dominant failure mechanism is ionization (Ref. 2). Conversely, if the device failure range falls below the particle equivalent line, the dominant failure mechanism is displacement damage. As shown, ionization is the dominant failure mechanism for virtually all semiconductor technologies for high energy electron exposure. The exception is the susceptibility of the solar cells that are very sensitive to displacement damage and insensitive to ionization damage. For proton exposures, either displacement and ionization failure mechanisms can be dominant, but only for those technologies most susceptible to displacement damage. For virtually all modern digital microcircuit technologies, the dominant failure mechanism is ionization.

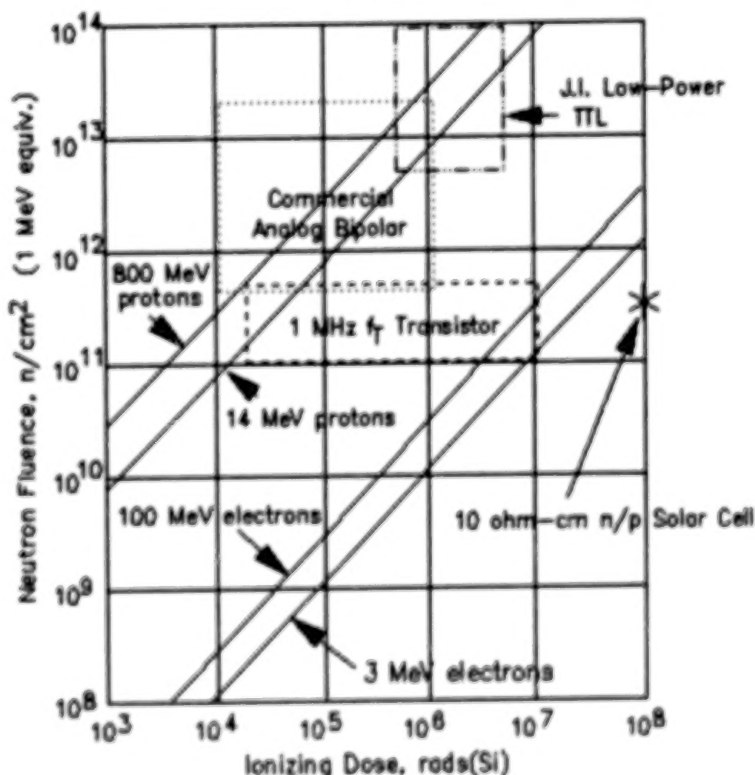


FIGURE 10

Single Particle Interactions in a P-N Junction (Ref. 9)

Single event effects in semiconductor devices, as shown in Figure 11, are the result of the intersection of the particle ionization path with a p-n junction. The result is a junction transient current that determines the overall device effect. The ionization track of the particle is characterized by its Linear Energy Deposition and range. For a high-energy cosmic ray (such as a 100 MeV lithium ion) the particle range is long compared to the semiconductor device dimensions. On the other hand, high energy proton effects are the result of energy deposition produced by the atomic product of a nuclear interaction between the proton and an atom of the semiconductor material such as a silicon recoil or product alpha particle.

Because the junction transient current is a very fast pulse (typically less than 1 ns) the circuit or device effect can be characterized in terms of a critical charge. The charge collected is determined by the particle LET and the effective collection volume of the junction. The overall susceptibility of the device or circuit is characterized by a cross section, typically in units of inverse square centimeters (i.e., cm^{-2}). The probability of observation of the effect is the product of the particle fluence and the cross section.

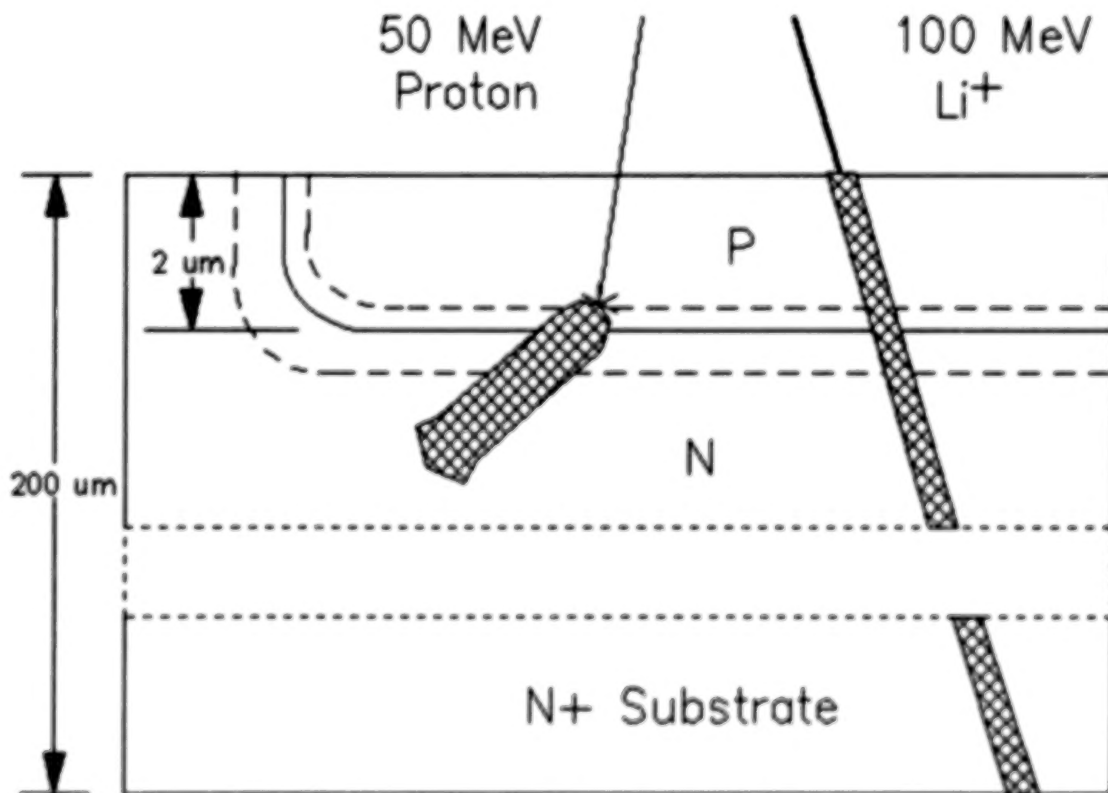


FIGURE 11

Single Particle Failure Mechanisms (Refs. 10-14)

The basic failure mechanisms of a single particle in a semiconductor device, summarized in Figure 12, are the ionization produced by the primary or secondary particles. The failure mechanisms observed in the overall device include the upset of stored data and potential damaging effects of latchup or device burnout. The data upset can be the result of a particle-induced change-of-state (i.e., flip) in a memory cell or flip-flop, or an electrical transient that can be interpreted as valid data by a latch. The most sensitive devices to bit upset effects are dynamic random-access memories, which are generally unacceptable for space applications. Bit upset rates for very sensitive semiconductor memories in space can be as great as $1\text{E-}4$ upsets per bit-day, that is an average of one bit upset for every 10,000 bits of stored data in a single day, to less than $1\text{E-}8$ upsets per bit-day in hardened semiconductor memories.

Latchup has been observed as a result of high-energy heavy-ion (i.e., cosmic ray) exposure in a number of junction-isolated CMOS memories. Dielectric-isolated memory technologies such as CMOS/SOS or CMOS/SOI can be designed to be latchup immune.

Single particle-induced burnout has been observed in n-channel power MOSFET transistors and electrically-alterable programmable read-only memories. The burnout susceptibility of the n-Power MOSFETs is a strong function of margin between the operating voltage and the d-c junction breakdown voltage. The burnout susceptibility of the EEPROMs has been observed only during the application of high-voltage during the write cycle when altering the stored data.

■ Single Event Effects

- Particle Ionization Track
- High-LET Particle Production

■ Memory Bit Upsets

■ Latch Data Upsets

■ Parasitic Latchup

■ Burnout - Power MOSFET's

- Elec. Er. PROM's

FIGURE 12

Bit Upset in a Read/Write Semiconductor Memory

The number of bit upsets in a read/write memory increases with particle exposure, as shown in Figure 13, until the memory is reset. Typically, the upset is that of a single memory cell. However, depending on the memory design, a single hit at specific locations can cause either clusters of upsets, or upsets along a row or column of the memory.

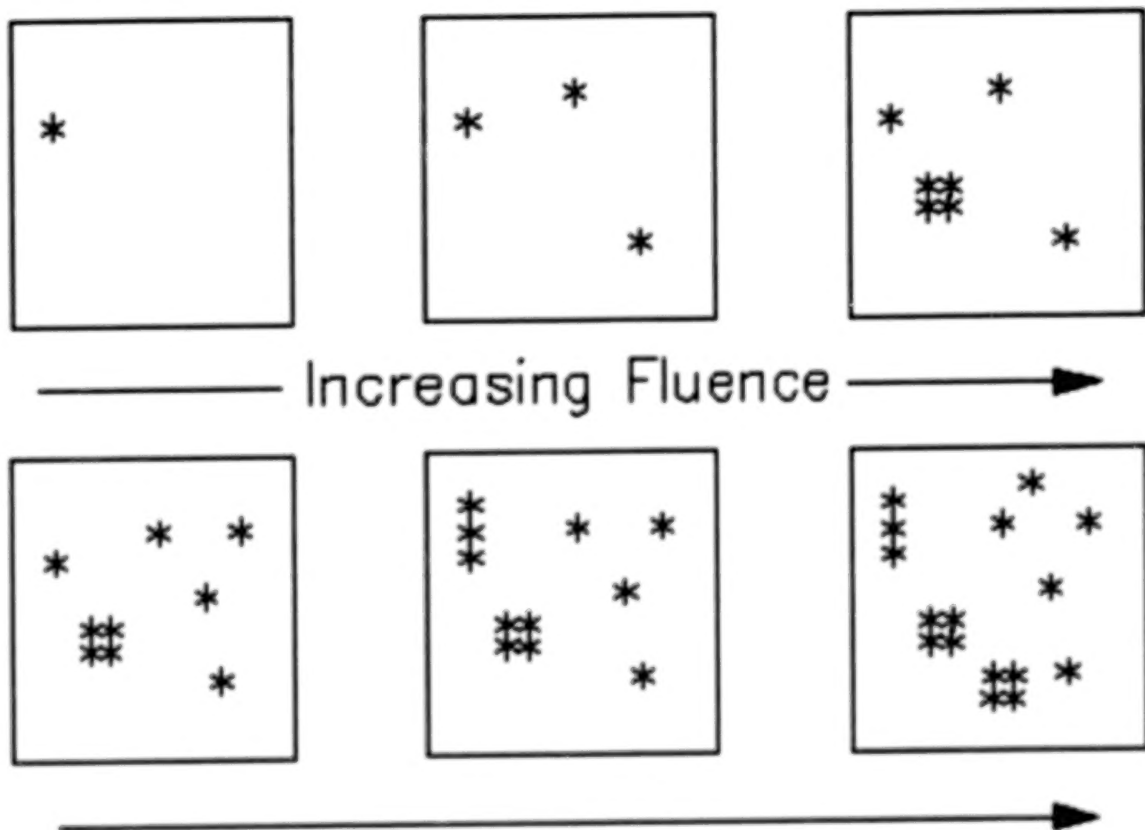


FIGURE 13

Bit Upset in a Complex Microcircuit

An important issue in the characterization of single-particle-induced upsets in complex microcircuits is that of the observability of the effect. Figure 14 illustrates cases where the induced upset can either be unobservable or can result in a large number of observed data errors.

The observed effects of an upset in the scratch-pad memory or data latches of a complex microcircuit are a strong function of the location of the upset and subsequent processing of the erroneous data. As the data is processed, the error can propagate down multiple paths. In some cases, these paths never reach an observable output and no upset is observed. The error was present, but under the test conditions used, was simply not observed.

On the other hand, the propagation of the original single upset can result in a multiplicity of paths, each of which, in the worst-case, produces errors at a number of microcircuit outputs. From the observable data, the determination of the actual number of internal upsets can be very challenging but is essential to determine the basic susceptibility of the microcircuit. In practice, careful modeling of the basic cells and a comprehensive selection of test conditions must be used.

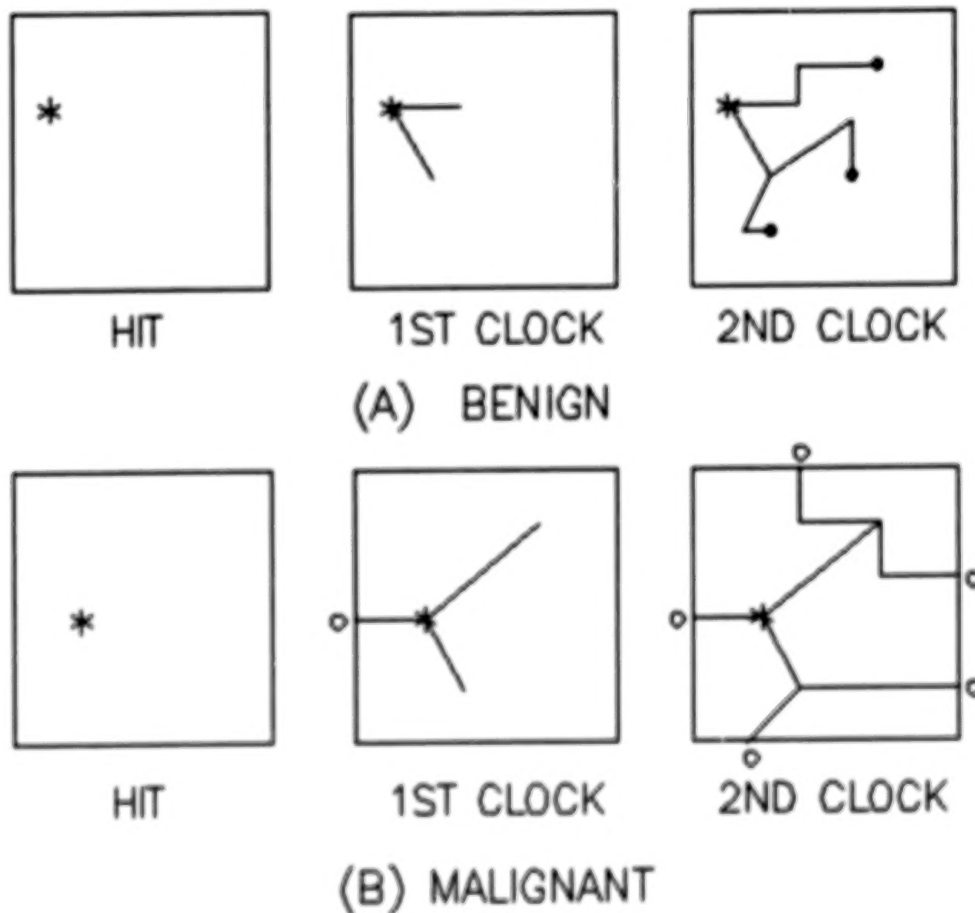


FIGURE 14

Single Event Upset Rate vs Altitude for Circular Orbits

The observed bit upset rate of microcircuits is a function of the satellite orbit as well as the microcircuit technology, as shown in Figure 15 (Ref. 9). At low and high altitudes, the bit upset rate is dominated by the cosmic ray environment. At altitudes from approximately 700 to 3,000 nautical miles, the bit upset rate is dominated by high-energy protons (for a circular orbit). The orbital dependence as shown, scales with the fundamental bit upset rate of a given microcircuit technology. A highly susceptible technology might have a bit upset rate on the order of $1\text{E-}4$ upsets per bit-day. On the other hand, a less susceptible (or hardened) technology might have a bit upset rate on the order of $1\text{E-}8$ upsets per bit-day or less.

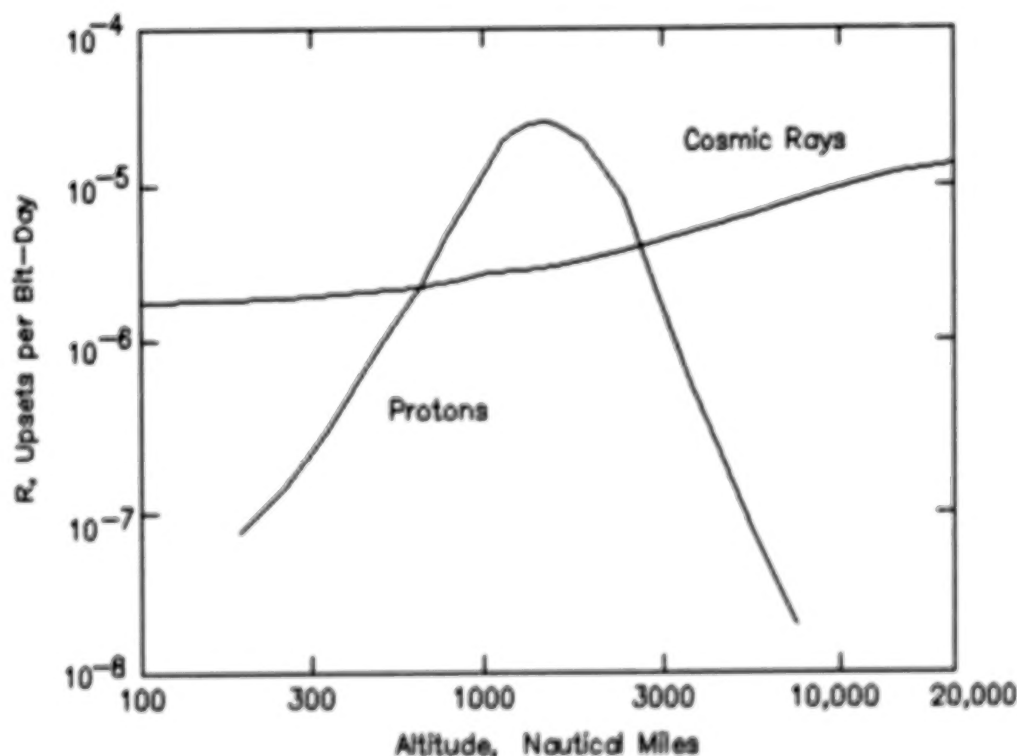


FIGURE 15

Microcircuit Parasitic PNPN Latchup Path

The mechanism of single-particle-induced latchup in a microcircuit is the regenerative action of an internal parasitic pnpn path when triggered by the particle-induced transient current pulse, as shown in Figure 16. Latchup will result when the transient current pulse is sufficiently large to initiate regenerative switching, and if there is an allowable current operating point at a dc current above the I-V characteristic holding current. The most susceptible microcircuit to single-particle-induced latchup is junction-isolated CMOS (Ref. 11). Latchup is also possible in junction-isolated bipolar, but has not yet been observed. Dielectric isolated technologies such as CMOS/SOS or CMOS/SOI are latchup-free.

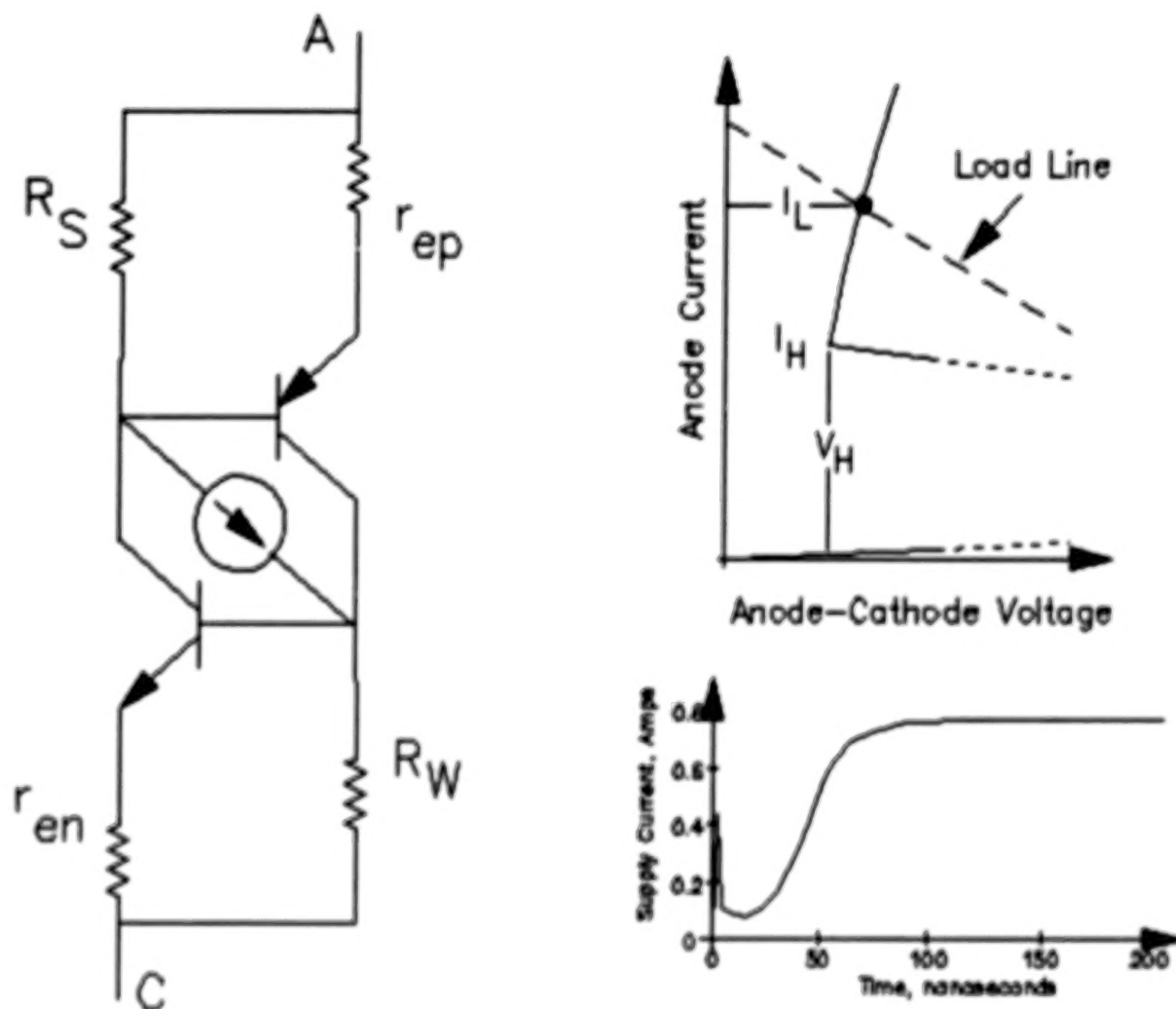


FIGURE 16

Power MOSFET Cross Section

The single-particle-induced burnout susceptibility of a Power MOSFET (shown in cross section in Figure 17, courtesy of John Adolphson, NASA Goddard) is the result of avalanche multiplication of carrier generated in the ionization track which results in current-mode second-breakdown (Ref. 12). Burnout will occur if the drain bias voltage is above the second-breakdown sustaining voltage (which can be substantially lower than the dc drain-source breakdown voltage).

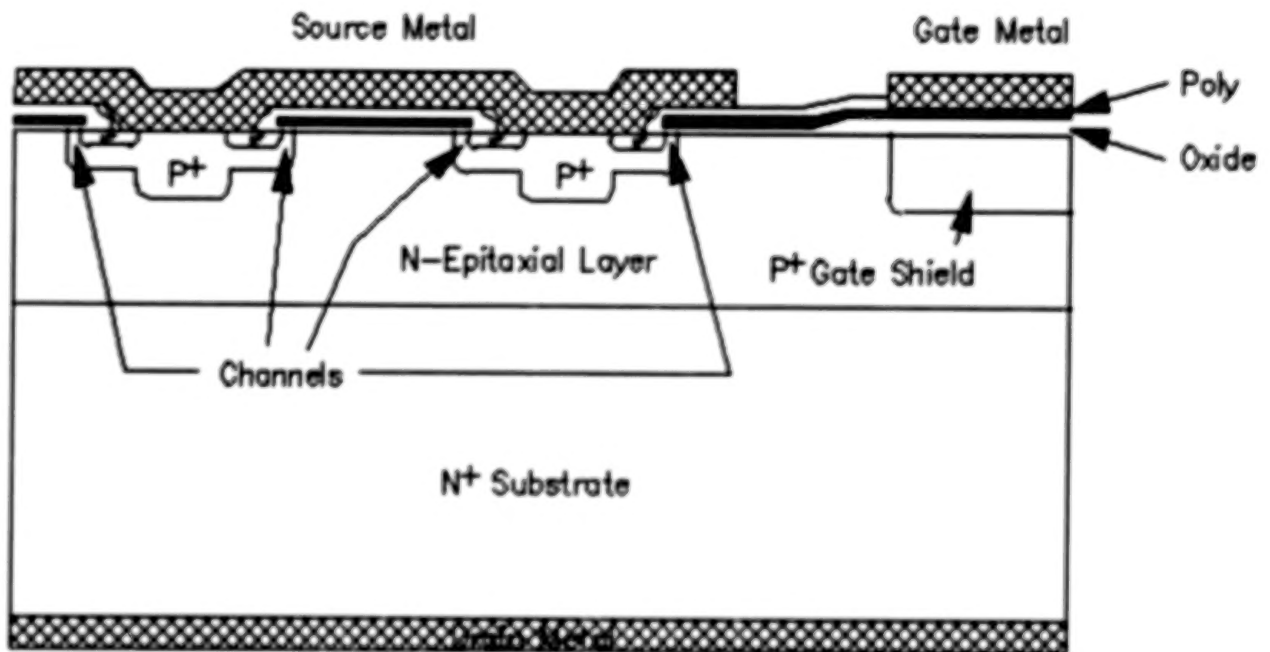
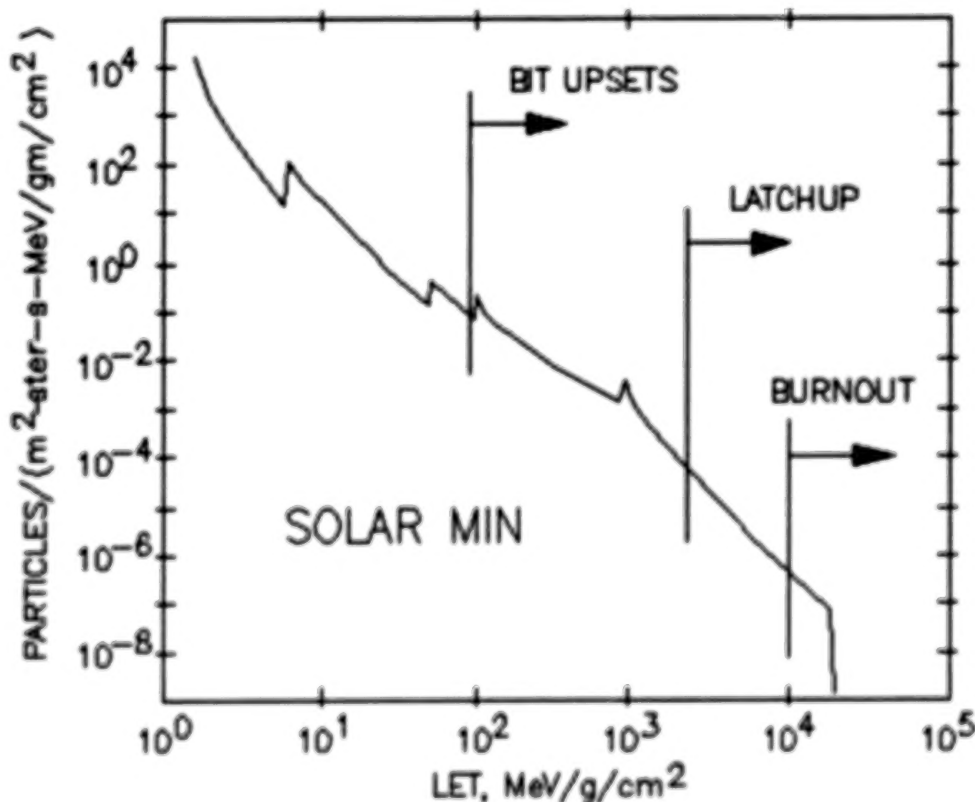


FIGURE 17

Cosmic Ray LET Spectra with Device Failure Mechanism Thresholds

Cosmic ray effects in semiconductor devices and microcircuits can be characterized by the energy deposition of the particle in the bulk semiconductor (i.e., Linear Energy Transfer or LET), and the cross section which is the probability of the effect normalized by particle fluence. Figure 18 shows the LET spectrum of cosmic rays (Ref. 15) with estimated thresholds for the various failure mechanisms presented. Clearly, bit upsets are quantitatively of greatest concern. The LET threshold for latchup is much greater than that for bit upset, and that for burnout is even greater than that of latchup. While latchup and burnout are much less likely than bit upset, it should be noted that the consequences of these effects on system performance can be much more severe.



•NRL Memorandum Report 4864, August 1982

FIGURE 18

Hardening Approaches

There are three basic hardening approaches that can be used for spacecraft electronics, as summarized in Figure 19. The first, of course, is the selection of components of minimum susceptibility. Unfortunately, however, it is very difficult to realize both very high hardness and very high electrical performance.

Shielding, for some aspects of the environment, can be very effective. Careful placement of the sensitive components can take advantage of the shielding of existing, less sensitive, spacecraft materials. Additional shielding can be added as necessary (until a fundamental limit is reached) at either the individual semiconductor device or the subsystem electronics box. It is important to note that while shielding is very effective for electrons and low-energy protons, the shielding to electrons is limited by the generation of bremsstrahlung gamma rays which are much more difficult to shield. Shielding is generally quite ineffective to reduce the effects of high-energy protons, and can be counter-effective for the shielding of cosmic rays. For the cosmic rays, shielding tends to be ineffective and even somewhat counter-productive.

Hardening techniques can be employed that include well known redundancy and error detection and correction techniques to reduce the effect of bit upsets. Hardening techniques for latchup and burnout effects on the system level can include current limiting, but hardened device selection is probably the preferred approach.

■ Component Selection

■ Shielding - Self-Shielding

- Spot Shielding
- Box Shielding
- Note: Shielding Limitations

Electrons - Bremsstrahlung limit

High-energy Protons

Cosmic Rays

■ System Hardening - Redundancy

- Error Detection and Correction
- Current Limiting (Latchup/Burnout)

FIGURE 19

References

1. Electronics Radiation Response Information Center, Kaman TEMPO, P.O. Drawer QQ, Santa Barbara, CA 93102
2. "Comparison of Neutron, Proton, and Gamma Ray Effects in Semiconductor Devices, J.P. Raymond and E.L. Petersen, IEEE Trans. on Nuclear Science, vol. NS-34, no. 6, pp. 1622-1628; December, 1988
3. "Basic Mechanisms of Radiation Effects in Electronic Materials and Devices," F. Barry McLean and Timothy R. Oldham, Harry Diamond Laboratories Report HDL-TR-2129; September, 1987
4. "Total Dose Effects in Recessed Oxide Digital Bipolar Microcircuits," R.L. Pease, R.M. Turfler, D. Platteter, D. Emily and R. Blice, IEEE Trans. on Nuclear Science, vol. NS-30, no. 6, pp. 4216-4223; December, 1983
5. "Super Recovery of Total Dose Damage in MOS Devices," A.H. Johnston, IEEE Trans. on Nuclear Science, vol. NS-31, no. 6, pp. 1427-1433; December, 1984
6. "Physical Mechanisms Contributing to Device 'Rebound'," J.R. Schwank, P.S. Winokur, P.J. McWhorter, F.W. Sexton, P.V. Dressendorfer and D.C. Turpin, IEEE Trans. on Nuclear Science, vol. NS-31, no. 6, pp. 1434-1438; December, 1984
7. "Correlation of Particle-Induced Displacement Damage in Silicon," G.P. Summers, C.J. Dale, E.A. Burke, E.A. Wolicki, P. Marshall, M.A. Gehlhausen and M.A. Xapos, IEEE Trans. on Nuclear Science, vol. NS-34, no. 6, pp. 1134-1139; December, 1987
8. "High Energy Electron Induced Displacement Damage in Silicon, C.J. Dale, P.W. Marshall, E.A. Burke G.P. Summers and E.A. Wolicki, presented at the 1988 IEEE Nuclear and Space Radiation Effects Conference, Portland, Oregon; July 12-15, 1988
9. "Single Effect Phenomena in the Space and SDI Arenas," Edward Petersen and Paul Marshall, to be published in the Journal of Radiation Effects: Research and Engineering. vol. 6-2, November, 1988.
10. "Suggested Single Event Upset Figure of Merit," E.L. Petersen, J.B. Langworthy and S.E. Diehl, IEEE Trans. on Nuclear Science, vol. NS-30, no. 6, pp. 4533-4539; December, 1983
11. "Recent Trends in Parts SEU Susceptibility from Heavy Ions," D.K. Nichols, L.S. Smith, W.E. Price, R. Koga and W.A. Kolasinski, IEEE Trans. on Nuclear Science, vol. NS-34, no. 6, pp. 1332-1337; December, 1987
12. "Burnout of Power MOS Transistors with Heavy Ions of Californium-252," A.E. Waskiewicz, J.W. Groniger, V.H. Strahan and D.M. Long,

IEEE Trans. on Nuclear Science, vol. NS-33, no. 6, pp. 1710-1713; December, 1986

13. "SEU Sensitivity of Power Converters with MOSFET's in Space," G.J. Brucker, P. Measel, D. Oberg, J. Wert and T. Criswell, IEEE Trans. on Nuclear Science, vol. NS-34, no. 6, pp. 1792-1795; December, 1987

14. "Cosmic Ray Induced Permanent Damage in MNOS EAROMs," J.T. Blandford, Jr., A.E. Waskiewicz and J.C. Pickel, IEEE Trans. on Nuclear Science, vol. NS-31, no. 6, pp. 1568-1570; December, 1984

15. "Calculation of Cosmic-Ray Induced Soft Upsets and Scaling in VLSI Devices," P. Shapiro, E.L. Petersen and J.H. Adams, Jr., NRL Memorandum Report 4864; August 26, 1982

ENVIRONMENTAL EFFECTS ON SPACECRAFT MATERIALS
J. W. HAPFNER
ROCKWELL INTERNATIONAL
SEAL BEACH, CA 90740

This is a summary of some results of Phase I work on an AFGL* contract to study the effects on the natural space environments on materials which may be used for SDI† applications. Phase I was a study of the current state-of-the-art knowledge of those effects, and was carried out by a literature search, a questionnaire mailing, and some visits to NASA and Air Force research facilities. Phase II will be a study of what materials may be used for SDI applications and to what natural space environments they may be vulnerable. Deficiencies in knowledge of the effects of the natural space environments on these materials are to be identified and recommendations are to be made to eliminate these knowledge deficiencies.

* Air Force Geophysics Laboratory

† Strategic Defense Initiative

ENVIRONMENTAL EFFECTS ON SPACECRAFT MATERIALS

PHASE I - STUDY EFFECTS

LITERATURE SEARCH
QUESTIONNAIRE MAILING
FACILITY VISITS

PHASE II - STUDY APPLICATIONS

ISSUE IDENTIFICATION
DEFICIENCY DETERMINATION
RECOMMENDATIONS

Permanent Material Effects Due To Environments

The space environment includes several components - vacuum, residual gasses, solar ultraviolet light, energetic charged (Van Allen, solar flare, and cosmic ray) particles, hot and/or cold electrical plasma and solid objects (micrometeoroids and space debris). The results of the Phase I work showed that these environments produce various effects on different types of material. For example, the space vacuum permits materials to outgas, the residual atomic oxygen erodes ram-facing exposed organics, ionizing radiation decreases mechanical strength (in most materials) and electrical conductivity (in non-insulators), etc. Other effects are surface electrical charging (due to hot plasma) electrical charge neutralization (due to ionosphere), and surface erosion and punctures (due to micrometeoroids and debris objects). While effects due to the space vacuum, solar photon radiation, and micrometeoroids are not greatly dependent on spacecraft altitude, atomic oxygen and ionospheric effects are significant only at low altitudes; hot plasma and solar flare particle effects are high altitude/latitude phenomena, while Van Allen and space debris effects have their own altitude dependences.

PERMANENT MATERIAL EFFECTS DUE TO ENVIRONMENTS

ENVIRONMENT	MATERIAL	EFFECTS
VACUUM	ALL, ESP. ORGANICS	OFFGASSING, OUTGASSING
RESIDUAL GASSES (ATOMIC OXYGEN)	ORGANICS	SURFACE EROSION, GLOW
RESIDUAL GASSES (ATOMIC OXYGEN)	SOME METALS	EMBRITTLEMENT
SOLAR U.V.	ORGANICS	SURFACE DISCOLORATION
VAN ALLEN BELTS	ALL, ESP. ORGANICS	DISCOLORATION, WEAKENING
SOLAR FLARE PARTICLES	CONDUCTORS, SEMICONDUCTORS	THERMAL, ELECTRICAL RESISTIVITY
IONOSPHERE	INSULATORS	CHARGE NEUTRALIZATION
HOT PLASMA	INSULATORS	HIGH VOLTAGES, DISCHARGES
HOT PLASMA	CONDUCTORS	ELECTRIC CURRENT, HEATING
MICROMETEOROIDS & DEBRIS	ALL, ESP. OPTICS	SURFACE EROSION, PITS. PUNCTURES

Synergistic Effects Involving Sunlight (Including UV)

Based upon the Phase I work, a summary has been compiled of the synergistic effects on materials due to combinations of two environments. This is a summary of those effects which involve sunlight.

Sunlight effects include thermal cycling (for many spacecraft surfaces) as well as discoloration and mechanical damage in many organics. Sunlight pressure can also produce torques on a spacecraft if the center of pressure is not in line with the center of mass. The combination of sunlight with other torque-producing environments (the gravitational and magnetic fields of the earth, the residual atmospheric gasses) can produce unusual spacecraft rotations and/or require special attitude control measures. Sunlight plus vacuum increases organic outgassing and cross-linking (a major effect) while sunlight heating helps anneal out the damage caused by nuclear radiation (especially in semiconductors). Photoelectric currents due to sunlight decrease the voltages and currents due to hot plasma charging, while both sunlight and solid objects can act to change the solar absorptance α_s and/or reflectivity of radiators and mirrors. For exposed coatings, the thermal cycling due to sunlight poses the threat of coating damage/decoloration especially for substrates vulnerable to any of the other environments.

SYNERGISTIC EFFECTS INVOLVING SUNLIGHT (INC UV)

ENVIRONMENTS	EFFECTS	MATERIALS/PARTS
SUNLIGHT + G. FIELD	TORQUES MODIFIED	ENTIRE SPACECRAFT
SUNLIGHT + B. FIELD	TORQUES, DRAG MODIFIED	ENTIRE SPACECRAFT
SUNLIGHT + VACUUM	INCREASED OUTGASSING, CROSS-LINKING	EXPOSED ORGANICS
SUNLIGHT + NUCLEAR RADIATION	INCREASED ANNEALING	EXPOSED SEMICONDUCTORS
SUNLIGHT + SOLID OBJECTS	DECREASED REFLECTIVITY	EXPOSED RADIATORS, MIRRORS
SUNLIGHT + IONOSPHERE	LOWER VOLTAGE, INCREASED DISCHARGES	EXPOSED CONDUCTORS
SUNLIGHT + HOT PLASMA	DECREASED CHARGING	EXPOSED INSULATORS
SUNLIGHT + NEUTRAL GASSES	INCREASED EROSION, TORQUES	RAM-EXPOSED ORGANICS

Synergistic Effects Involving The Gravity Field

The Earth's gravity field not only controls the orbit parameters of a spacecraft (position and velocity as functions of time) but also affects the orientation (spacecraft like to have their principal axis aligned with local vertical). Thus, the other torque-producing environments (magnetic field, residual gasses) can combine with the gravity field to modify the stable orientation. The space vacuum permits orientation changes to persist since it provides no damping. The gravity-modified spacecraft orientation affects the drag due to the ionosphere and the residual gasses, while the impact of a solid object can change the velocity and the orientation/spin of a spacecraft. There does not appear to be any obvious synergistic effect due to the combination of the gravity field and nuclear radiation, since the ambient nuclear radiations in space (Van Allen belts, solar flare particles) are quasi-isotropic and produce essentially zero torques on spacecraft. Conversely, the nuclear radiation effects on materials and parts are not affected by the presence or absence of the Earth's gravity field.

SYNERGISTIC EFFECTS INVOLVING THE GRAVITY FIELD

ENVIRONMENTS	EFFECTS	MATERIALS/PARTS
G. FIELD + B. FIELD	TORQUES MODIFIED	ENTIRE SPACECRAFT
G. FIELD + VACUUM	NO TORQUE DAMPING	ENTIRE SPACECRAFT
G. FIELD + NUCLEAR RADIATION	NO OBVIOUS EFFECT	
G. FIELD + SOLID OBJECTS	PROJECTED AREA/VELOCITY MODIFIED	EXPOSED MIRRORS, RADIATORS
G. FIELD + IONOSPHERE	IONOSPHERIC DRAG MODIFIED	ENTIRE SPACECRAFT
G. FIELD + HOT PLASMA	SUNLIGHT EXPOSURE MODIFIED	EXPOSED INSULATORS
G. FIELD + NEUTRAL GASSES	TORQUES, RAM EXPOSURE MODIFIED	EXPOSED ORGANICS

Synergistic Effects Involving The Magnetic Field

The major effects of the geomagnetic field will be to produce potentials and torques on current loops. Thus, the voltages produced will have a modification (small) on the voltages produced by other space environments (hot plasma, ionosphere) and will modify the torques produced by other environments (sunlight, gravity gradient, residual neutral gasses). In addition, the geomagnetic field limits the energies as a function of direction which solar flare and galactic particles can reach a given spacecraft orbit. If the torques modify the orientation of the spacecraft, the impacts rates due to stream meteoroids and orbiting debris particles will be modified. Finally, the presence of the geomagnetic field will modify the ionospheric drag.

SYNERGISTIC EFFECTS INVOLVING THE MAGNETIC FIELD

ENVIRONMENTS	EFFECTS	MATERIALS/PARTS
B. FIELD + VACUUM	NO TORQUE DAMPING	ENTIRE SPACECRAFT
B. FIELD + NUCLEAR RADIATION	SOLAR, GALACTIC CUTOFF MODIFIED	SEMICONDUCTOR ELECTRONICS
B. FIELD + SOLID OBJECTS	PROJECTED AREA/VELOCITY MODIFIED	EXPOSED MIRRORS, RADIATORS
B. FIELD + IONOSPHERE	IONOSPHERIC DRAG MODIFIED	ENTIRE SPACECRAFT
B. FIELD + HOT PLASMA	SUNLIGHT EXPOSURE MODIFIED	EXPOSED INSULATORS
B. FIELD + NEUTRAL GASSES	TORQUES, RAM EXPOSURE MODIFIED	EXPOSED ORGANICS

Synergistic Effects Involving Space Vacuum

In addition to facilitating outgassing, the vacuum of space does not limit many environmental parameters (speed, temperature, voltage, etc.) as the earth's atmosphere does. Thus, solid objects hit at higher velocities, the temperatures produced by sunlight (or its absence) are more extreme (no convective cooling), and the electron densities in hot or cold plasmas are greater than would be the case in air. Many materials exhibit increased tolerance for ionizing radiation in vacuum (broken chemical bonds have time to reform) but some atomic oxygen effects are enhanced (ions and radicals live longer). Since organic materials outgass more and have weaker chemical bonds than most inorganic materials, they tend to be the most vulnerable to these effects. Finally, space vacuum and hot plasma can combine to produce more surface contamination than the vacuum would produce alone.

SYNERGISTIC EFFECTS INVOLVING SPACE VACUUM

ENVIRONMENTS	EFFECTS	MATERIALS PARTS
VACUUM + NUCLEAR RAD.	INCREASED RADIATION RESISTANCE	EXPOSED ORGANICS, TEFLON
VACUUM + SOLID OBJECTS	INCREASED IMPACT DAMAGE	EXPOSED SURFACES
VACUUM + IONOSPHERE	INCREASED DISCHARGING (MORE ELECTRONS)	EXPOSED VOLTAGES, INSULATORS
VACUUM + HOT PLASMA	INCREASED CONTAMINATION	EXPOSED INSULATORS
VACUUM + NEUTRAL GASSES	IONS, RADICALS LIVE LONGER	EXPOSED ORGANICS, SENSORS

Synergistic Effects Involving Nuclear Radiation

The major effect of nuclear radiation is to randomize the structure of materials, decreasing their ability to transmit stress (some materials become brittle), electrical current, and thermal energy. However, electrical insulators become more conductive, decreasing the discharge rate in hot plasma. Fluid containers are more easily punctured by solid objects if they have been weakened by nuclear radiation. The presence of residual gasses (atomic oxygen) at low altitudes increases the surface damage produced by ionizing nuclear radiation, especially in organic materials on the front (ram) side of the spacecraft.

SYNERGISTIC EFFECTS INVOLVING NUCLEAR RADIATION

ENVIRONMENTS	EFFECTS	MATERIALS/PARTS
NUCLEAR RAD. + SOLID OBJECTS	DECREASED PUNCTURE RESISTANCE	FLUID CONTAINERS (ORGANICS)
NUCLEAR RAD. + IONOSPHERE	DECREASED DISCHARGE RATE	EXPOSED INSULATORS
NUCLEAR RAD. + HOT PLASMA	DECREASED DISCHARGE RATE	EXPOSED INSULATORS
NUCLEAR RAD. + NEUTRAL GASSES	DECREASED RADIATION RESISTANCE	RAM-EXPOSED ORGANICS

Synergistic Effects Involving Solid Objects

Solid objects (micrometeoroids and space debris) not only erode and puncture surfaces (affecting mirrors, radiators, fluid containers, etc.), but also can produce changes in spacecraft orientations and orbit. If the erosion, punctures, or reorientations expose surfaces or substrates to environments for which they were not designed, additional effects can follow. Thus, a hole in an insulating coating can expose a high voltage substrate to the ionosphere with considerable consequent current leakage, while a hole in an oxide coating can expose a non-oxide substrate to atomic oxygen attacks, and a hole in a conducting coating can increase discharge rates due to hot plasma. On the other hand, the voltages produced by solid object impacts will be reduced by the presence of the ionosphere.

SYNERGISTIC EFFECTS INVOLVING SOLID OBJECTS

ENVIRONMENTS	EFFECTS	MATERIALS/PARTS
SOLID OBJECTS + IONOSPHERE	IMPACT VOLTAGES DECREASED	EXPOSED SURFACES
SOLID OBJECTS + HOT PLASMA	EXPOSE SUBSTRATES	INSULATING SUBSTRATES
SOLID OBJECTS + NEUTRAL GASSES	EXPOSE SUBSTRATES	ORGANIC SUBSTRATES

Synergistic Effects Involving The Ionosphere

Since the ionosphere is a cold plasma, it acts to limit the effects of electric or magnetic fields produced by spacecraft. At low altitudes the debye lengths are measured in millimeters so the ionosphere can "see" small spacecraft features. At high altitudes the ionosphere is much less dense and has meter-sized debye lengths so it can be overwhelmed by hot (kev) plasma. Nevertheless, the ionosphere does act (along with sunlight) to decrease the hot plasma charging rate. The ionosphere also co-exists with the residual gasses (at low altitudes) and with the Van Allen belts (at high altitudes) where it acts to produce more ions and radicals than would otherwise be present.

SYNERGISTIC EFFECTS INVOLVING THE IONOSPHERE

ENVIRONMENTS	EFFECTS	MATERIALS/PARTS
IONOSPHERE + HOT PLASMA	DECREASED CHARGING RATE	EXPOSED INSULATORS
IONOSPHERE + NEUTRAL GASSES	MORE IONS, RADICALS PRODUCED	EXPOSED ORGANICS

Synergistic Effects Involving Hot Plasma

Since all other combinations of two environments have been discussed, the only combination left is that of hot plasma and neutral gasses. The presence of the neutral gasses (principally atomic oxygen) will increase the electrical discharge rate, due to the hot plasma, by providing additional atoms and ions. This increased discharge rate will be observed on ram-facing organic insulators in the dark. Since hot plasma is primarily a high altitude environment, while neutral gasses occur primarily at low altitudes, this effect will be small.

SYNERGISTIC EFFECTS INVOLVING HOT PLASMA

ENVIRONMENTS	EFFECTS	MATERIALS/PARTS
HOT PLASMA + NEUTRAL GASSES	INCREASED DISCHARGE	RAM-FACING ORGANIC INSULATORS

Summary Of Synergistic Effects On Materials

This matrix lists each environment along both the vertical (left side) and the horizontal (top) axis. The spacecraft (s/c), the types of surfaces (e.g. exposed, high voltage, etc.) and the types of materials (e.g. organics, conductors, semiconductors, or insulators) most affected by the environmental combinations are listed in the boxes. Thus, the combinations of gravity and magnetic fields will affect the entire spacecraft by producing torques, while the combination of sunlight and solid objects will be especially severe on optical surfaces (mirrors, radiators). Neutral gasses plus almost all other environments primarily affect ram-facing organics while hot plasma plus other environments affect insulators. The zero for the combination of gravity field and nuclear radiation indicates the absence of any obvious synergistic effect.

SUMMARY OF SYNERGISTIC EFFECTS ON MATERIALS

	SUNLIGHT (UV)	GRAVITY FIELD	MAGNETIC FIELD	SPACE VACUUM	NUCLEAR RADIATION	SOLID OBJECTS	IONOSPHERE	HOT PLASMA	NEUTRAL GASSES
SUNLIGHT (INC UV)	---	S/C	S/C	ORG	SEMI	OPTICS	COND	INS	ORG
GRAVITY FIELD		---	S/C	S/C	0	OPTICS	S/C	INS	ORG
MAGNETIC FIELD			---	S/C	SEMI	OPTICS	S/C	INS	ORG
SPACE VACUUM				---	ORG	EXP	HV	INS	ORG
NUCLEAR RADIATION					---	ORG	INS	INS	ORG
SOLID OBJECTS						---	EXP	INS	ORG
IONOSPHERE							---	INS	ORG
HOT PLASMA								---	ORG
NEUTRAL GASSES									---

S/C = SPACECRAFT
COND = CONDUCTORS
HV = HIGH VOLTAGES

ORG = ORGANICS
INS = INSULATORS

SEMI = SEMICONDUCTORS
EXP = EXPOSED SURFACES

Summary - Conclusions

Based on the work carried out to date, it is possible to conclude that the effects of a single space environment are either currently understood or currently being investigated. Thermal cycling, ultraviolet light degradation and radiation pressure have been studied for over two decades. The torques and $v \times B$ effects of the earth's gravity and magnetic fields are studied in freshman college physics courses. Contamination, especially that due to rocket exhaust plumes and organic material outgassing/offgassing/shedding is an active research field. Nuclear radiation, which is primarily of interest to semiconductor electrical engineers and thermal control coating specialists, produces generally well-known effects. Solid objects (especially debris) environments are under active investigation, as are the effects of neutral atomic oxygen. Plasma effects are a maturing technology after a decade of intense work.

It is the effects of multiple space environments that will probably hold some surprises, since all of the problems of studying single environments in the laboratory (energy, flux, and angular distribution simulation plus accelerated testing) are compounded. It is expected that exposed organics, optical surfaces and insulators will be especially vulnerable. This paper was an attempt to indicate some of these effects of multiple space environments and a call for more attention to them.

SUMMARY - CONCLUSIONS

EFFECTS DUE TO SINGLE ENVIRONMENTS (EITHER UNDERSTOOD OR BEING STUDIED)

- SUNLIGHT (INC UV) - EFFECTS BEING STUDIED
- FIELDS (GRAVITY, MAGNETIC) - ENVIRONMENT, EFFECTS KNOWN
- VACUUM (INC CONTAMINATION) - EFFECTS BEING STUDIED
- NUCLEAR RADIATION
 (VAN ALLEN, S. FLARE, GALACTIC) - EFFECTS BEING STUDIED
- SOLID OBJECTS (MICROMETEORIDS, DEBRIS) - DON'T KNOW
 ENVIRONMENT YET
- PLASMA (IONOSPHERE, HOT) - ENVIRONMENT QUITE VARIABLE
- NEUTRAL GASSES (ESP ATOMIC O) - DON'T KNOW EFFECTS YET

(MANY NOT UNDERSTOOD)

EFFECTS DUE TO MULTIPLE ENVIRONMENTS (FEW BEING STUDIED)

ORGANICS)
INSULATORS) ESPECIALLY VULNERABLE IF EXPOSED
OPTICS)

SURFACE TREATMENT USING METAL FOIL LINER

RAY GARVEY
OAK RIDGE NATIONAL LABORATORY

FOIL LINER TECHNOLOGY

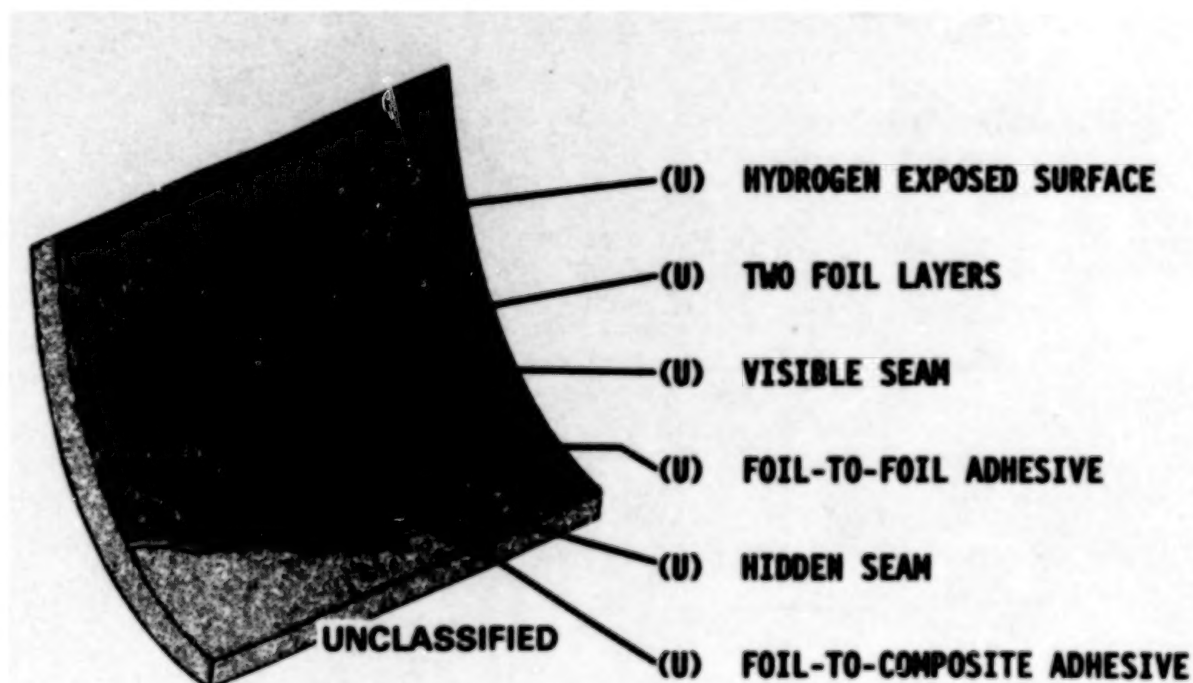
A metal foil liner can be used to seal large area surfaces. This will provide all the characteristics of a metal structure even when using organic matrix composites.

- **SEALING LARGE AREA SURFACES**
- **PROTECTION FROM ATOMIC OXYGEN OR OTHER HOSTILE ENVIRONMENTS**
- **CONTAMINATION CONTROL**
- **THERMAL MANAGEMENT USING ANODIZED FOIL**

LINER CONFIGURATION (U)

(U) It has been proposed that two 0.001-in.-thick layers of aluminum foil which are intimately bonded to the composite laminate will provide the desired liner performance. This schematic diagram shows two layers of foil with two helical seams. The visible seam is offset the maximum distance from hidden seam. Seam gaps are minimized, and overlaps are not permitted.

(U) The two-layer configuration which is shown has high reliability because flaws in the foil are prevented from exposing the composite. An alternate configuration using a helical overlap will trade reliability for weight savings.



PRODUCIBILITY DEMO - VARIOUS PARTS (U)

(U) The aluminum foil liner is easily fabricated into shapes with a uniform axial cross section. This photograph shows that the liner can be installed on the inside and outside of surfaces. Flat plates have also been successfully lined.

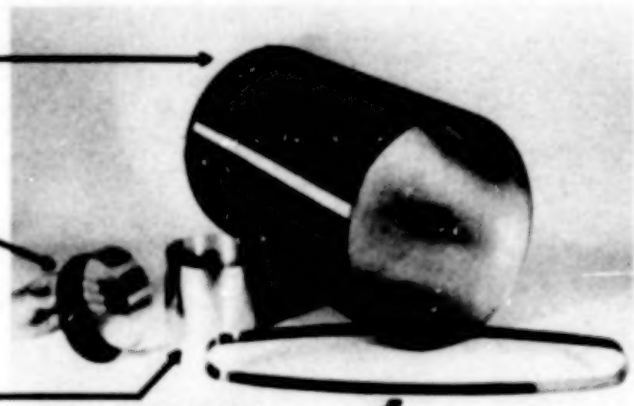
(U) It is reasonable to expect that a part with uniform taper can also be successfully lined with current materials and modified techniques. However, double-curved shapes, such as corners and fillets, present problems that will take time to overcome. This is a critical area for future development.

(U) 14-IN.-DIAM IM6/ERL2258
CYLINDER WITH ID LINER

(U) 6-IN.-DIAM IM6/ERL2258
CYLINDER WITH OD LINER

(U) 6-IN.-DIAM IM6/ERL2258
CYLINDER WITH ID AND OD
LINERS

(U) IM6/ERL2258 ELLIPSE WITH
2-IN.-DIAM CORNERS AND
180-IN.-DIAM SIDES HAVING
ID LINER



UNCLASSIFIED

LINER CHARACTERISTICS - FOIL (U)

(U) Relatively pure aluminum alloys, such as AA 1100, can be rolled into high-quality foil, which can be coated and slit for liner applications. It has been shown that the H19, half-hard, or dead-soft conditions can all be used with varying degrees of handling difficulty. A small effort was spent considering alternate alloy foil materials. The metals shown are considered to be good candidates for coating and slitting. They will have varying degrees of bond strength. Copper is likely to be the best with, aluminum second, in bond characteristics.

(U) The foil thickness and foil quality must be selected to meet aerial weight, quality, and processing requirements. It is fortunate that there is a variety of commercially available foils that will satisfy the needs for impermeability and chemical compatibility. One would find it quite difficult to get a special product made by the metal foil supplier due to small tonnage quantities needed for this application.

(U) BASELINE FOIL -- AA1100 H19 OR HALF HARD OR DEAD SOFT.

(U) ALTERNATE FOIL (NOT EVALUATED) -- INVAR, ZIRCONIUM, COPPER, NICKEL, TITANIUM, OR STAINLESS STEEL.

(U) BARE FOIL THICKNESS --

(U) MINIMUM TO ELIMINATE INCLUDED PINHOLES IN ALUMINUM IS 0.001 IN.

(U) MINIMUM TO HANDLE IN DEAD SOFT CONDITION IS 0.002 IN.

(U) FOIL QUALITY --

(U) ACCEPTABLE EDGE CURL - SLITTING RELATED.

(U) ACCEPTABLE EDGE WAVINESS - SLITTING RELATED.

(U) ACCEPTABLE WEB DEFLECTION - CLEANLINESS AND HEAT TREAT RELATED.

(U) NO SURFACE TREATMENT REQUIRED FOR CERTAIN ALLOYS.

FOIL-TO-FOIL AND FOIL-TO-COMPOSITE (U)

(U) This micrograph shows the cross section of two 1-mil layers of AA 1100 H19 aluminum bonded to each other and to the graphite/epoxy composite substrate with adhesive. In each of the micrographs in this report, the bottom of the cross section will be the innermost region (ID) and the top will be the outermost region (OD). The sample was cut from an IM6/ERL2258 cylinder which had been cured at 350°F. It was then dipped in liquid helium (10x for most samples). It was also sprayed with liquid helium on the foil surface in the vicinity of the seams to impose a thermal gradient through the laminate. The samples which are labeled "EXPOSED" in this report have been through this sequence.

(U) This photomicrograph shows that there is no breach in the integrity of the two adhesive bond lines in spite of the severe thermal shock of liquid helium exposure.

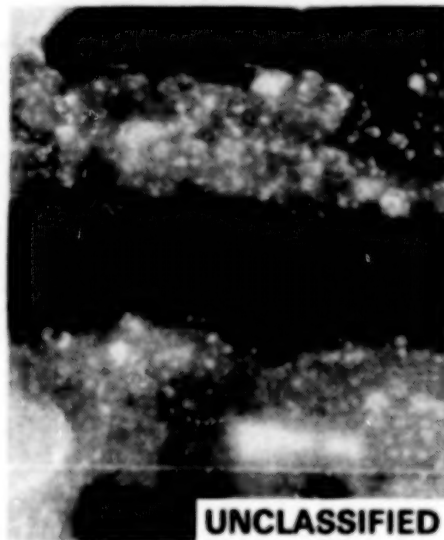


FOIL-TO-FOIL (U)

(U) This photomicrograph shows a close-up view of the epoxy foil-to-foil adhesive layer. The very small ($<10^{-5}$ in.) separation in the adhesive is damage caused by heating the electron microscope beam. Both surfaces of foil are completely wetted, and there was no breach of foil-to-foil bond integrity even after liquid helium exposure.

FOIL-TO-FOIL (U)

EXPOSED



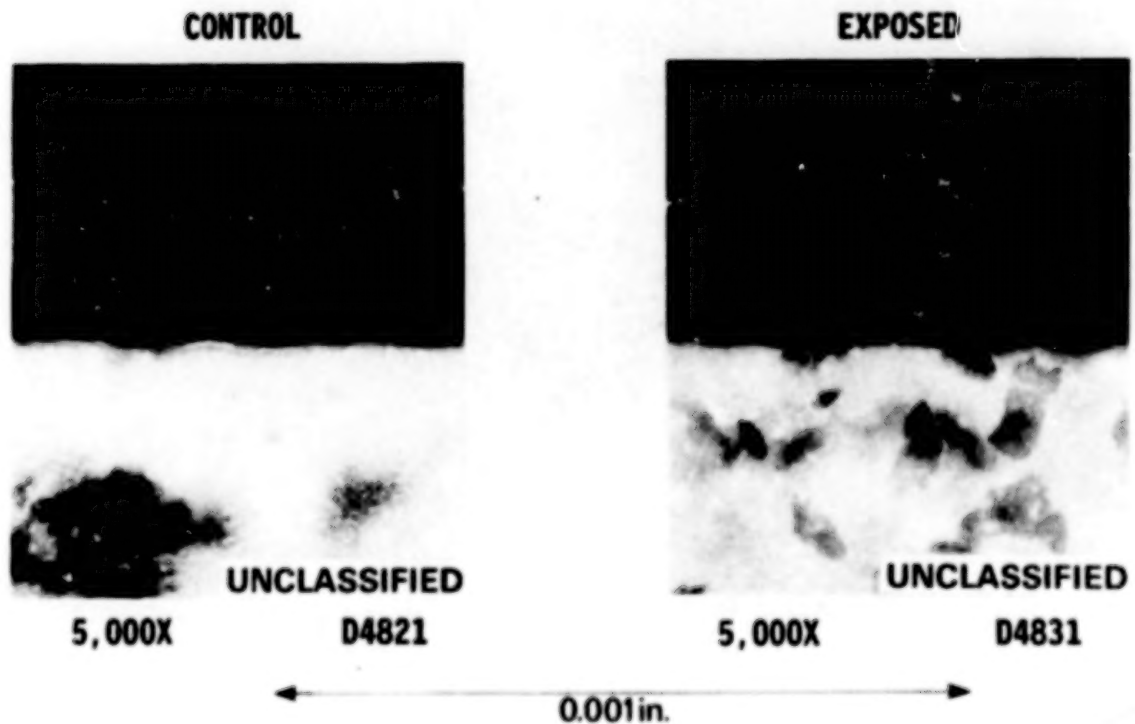
5,000X

D4833

0.001in.

FOIL-TO-COMPOSITE (U)

(U) These photomicrographs show a magnified view of the foil-to-composite interfaces. Compatibility (chemical and cure cycle) between the adhesive coating on the foil and the laminate resin is directly related to bond performance.



VISIBLE SEAM (U)

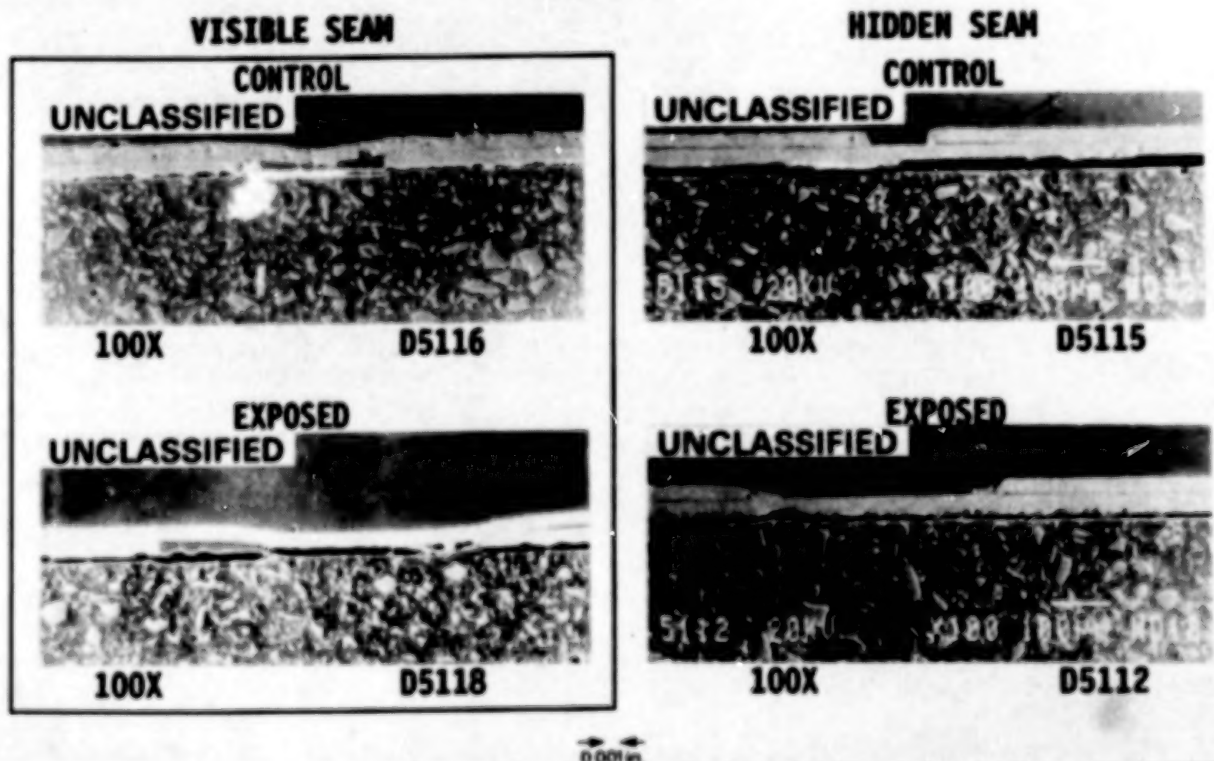
(U) These four photomicrographs show the visible and hidden seams for control and exposed samples. Observing the seams on the left half of the viewgraph, one will notice an 0.010-in.-wide gap in the upper picture and an 0.023-in.-wide gap in the lower one. In the double layer foil configuration, overlaps are not permitted, and gaps are permitted to be ≤ 0.030 in.

(U) The visible seam tends to draw a lot of attention. However, this should not be of much concern because this seam is entirely backed up by the second layer of foil. One should be more concerned about the quality of the hidden seam addressed later in this report.

(U) It is not unusual for the foil-to-foil interface in the vicinity of the visible seam to be unbonded for a region 0.005 to 0.020 in. away from the seam. This is caused by contamination during processing. Areas such as this have been unchanged through 0 psig liquid helium immersion. One may speculate that liquid hydrogen at 25 psig is a worse case. Pressurized liquid hydrogen testing is being performed at Arnold Engineering Development Center (AEDC) using a permeation test cell which is described later in this report.

(U) The distance from the visible seam to the hidden seam is maximum of one-half the width of the foil. Seams were separated by 1 and 2 in. for this study to include both in a single test specimen. The next figure will magnify the visible seam before addressing the hidden seam.

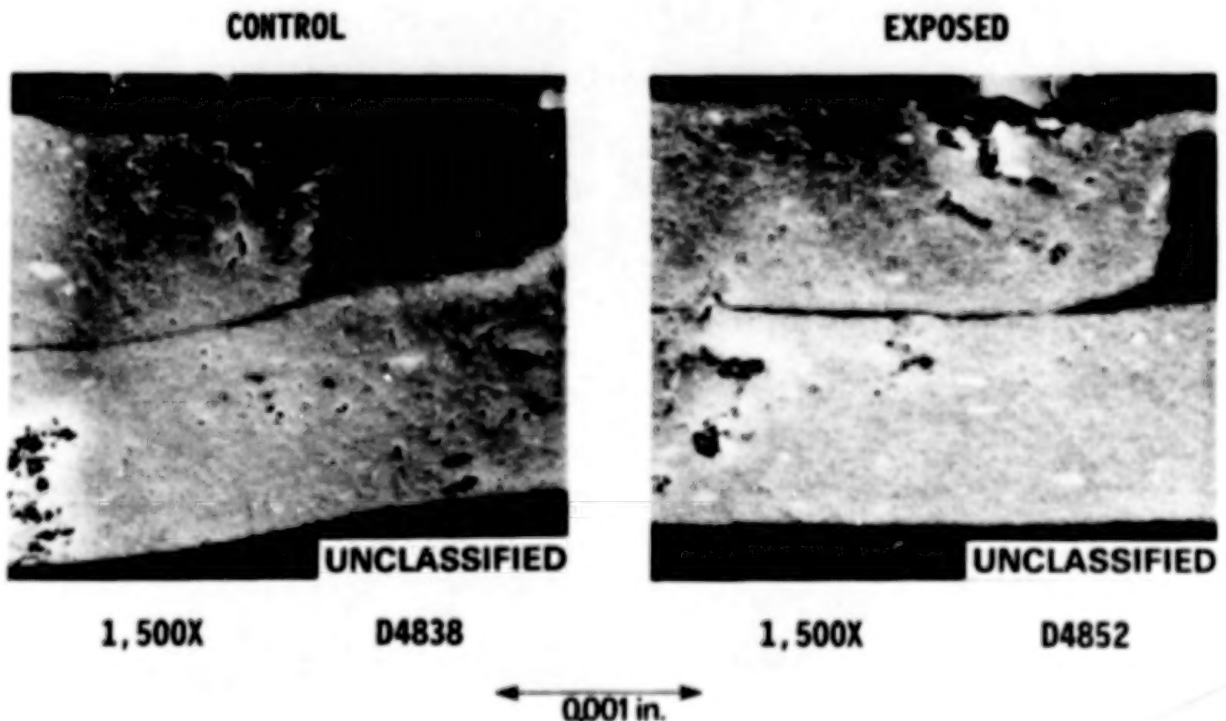
SEAMS (U)



VISIBLE SEAM (U)

(U) The higher magnification of these pictures shows the importance of foil edge condition to foil liner performance. Aluminum tends to stretch and to smear very easily at the edges during slitting. If precision shearing is not performed, the edge of the foil will not be successfully bonded, and the second layer of foil may get damaged as well. One will notice that the foil-to-foil adhesive flows to accommodate small imperfections in the foil edge condition.

(U) Both the control and exposed samples appear to have inclusions in the foil. (However, it is possible that this is damage resulting from the polishing operation.). Aluminum foil 0.0003-in. thick has frequent pinholes resulting from material flaws such as inclusions. It is generally accepted that 0.001-in.-thick foil will not have any pinholes resulting from material microstructure. Pinholes in 0.001-in. and thicker foils are normally the result of debris in the rolling and winding equipment.



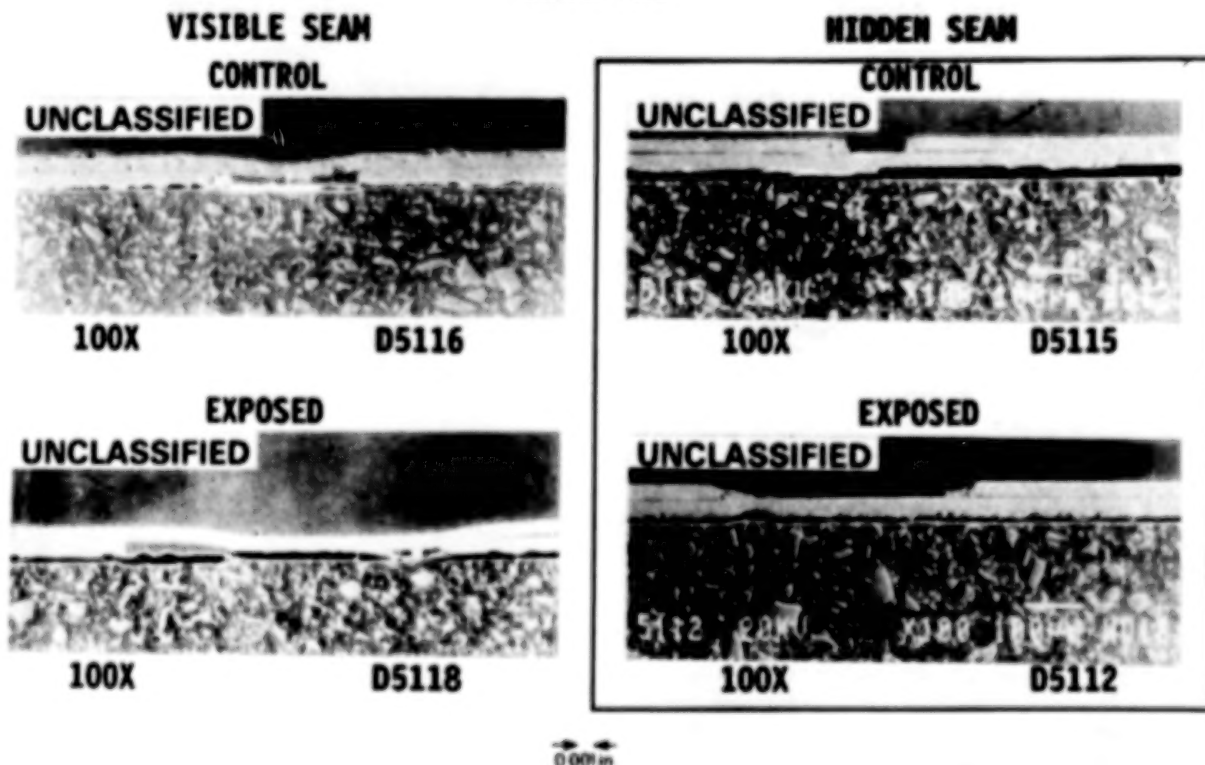
HIDDEN SEAM (U)

(U) The hidden seam is the most critical zone in the liner. Defects in this region lead directly to the underlying composite. The performance of the liner in this area is strongly affected by foil edge quality, adhesive flow, gap control, composite quality, and material compatibility.

(U) The photomicrographs on the right half of the viewgraph are typical cross sections of hidden or subsurface seams. Note that the potting compound in the bottom of the picture has separated from the foil surface leaving the black line below the inside surface of the foil. Once again, the seam gaps are different for the two samples (0.005 and 0.018 in.). Like the visible seam, the hidden seam may not overlap and may have up to 0.030-in. gap.

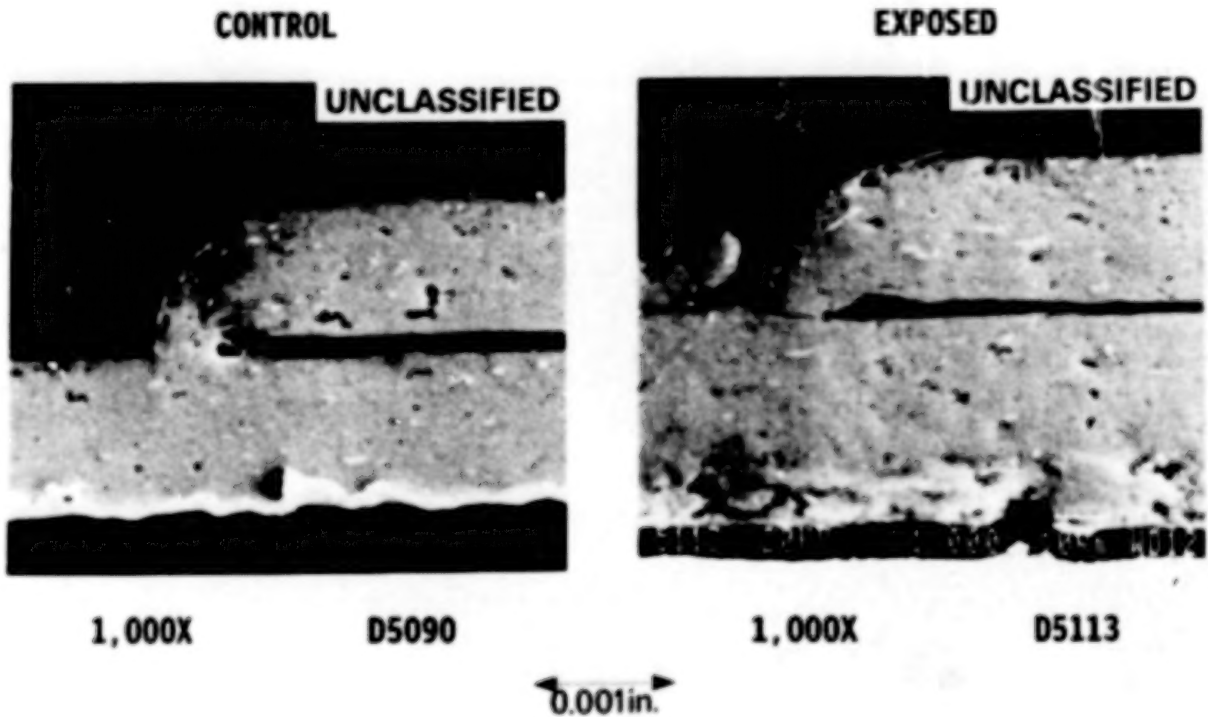
(U) As fabricated, the hidden seam will normally be unnoticeable except at the ends of the composite. Defects in the hidden seam will become visibly obvious immediately following a thermal cycle without backing support (die or mandrel). The defect will show up as a pucker or a series of puckers following the path of the hidden seam. These local puckers will not spread but will crack as a result of cyclic plastic strain.

SEAMS (U)



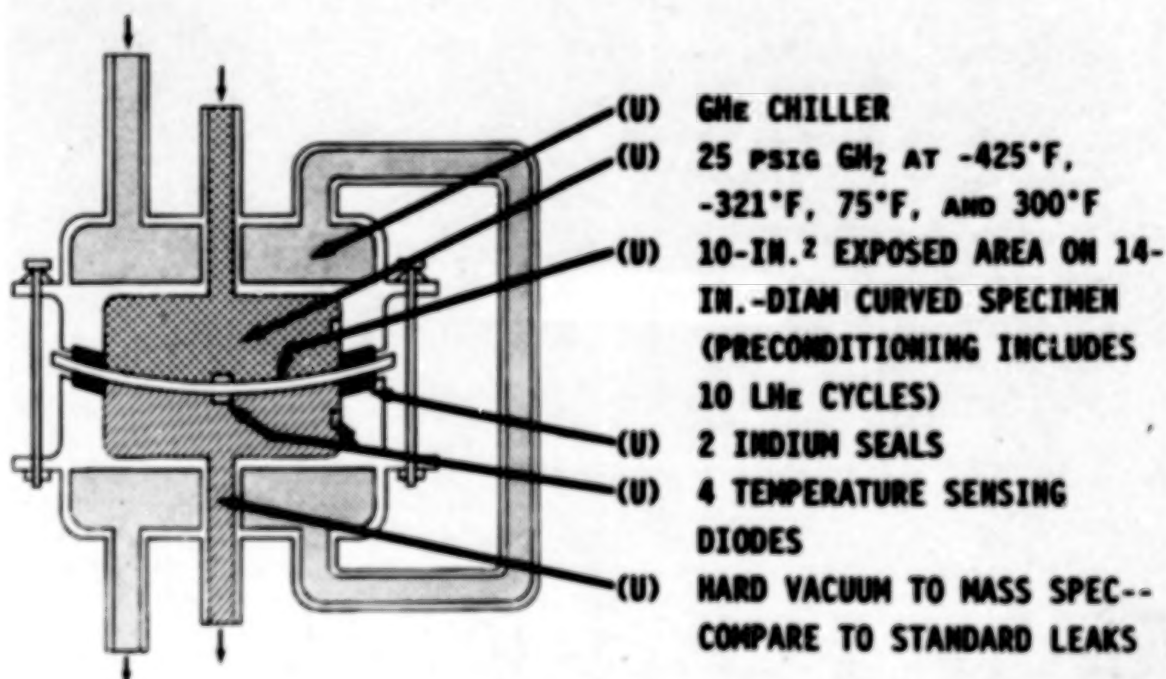
HIDDEN SEAM (U)

(U) These photomicrographs show a close-up view of the subsurface or hidden seam. Although there is evidence of some edge curl, the liner performed well through thermal exposure.



PERMEATION TEST CELL (U)

(U) Permeation testing is currently under way at AEDC using a fixture similar to that which is shown to test 14-in.-diam curved composite specimens. The test cell shown is operated in a vacuum chamber. Leakage around the indium seal on the inside contour should not influence the downstream measurements. AEDC personnel have elected to flow gaseous hydrogen into the fixture and then condense it on the test specimen at -425°F using gaseous helium.



THE LONG DURATION EXPOSURE FACILITY
MATERIAL EXPERIMENTS

William H. Kinard
and
James L. Jones, Jr.
NASA Langley Research Center
Hampton, Virginia

LONG DURATION EXPOSURE FACILITY

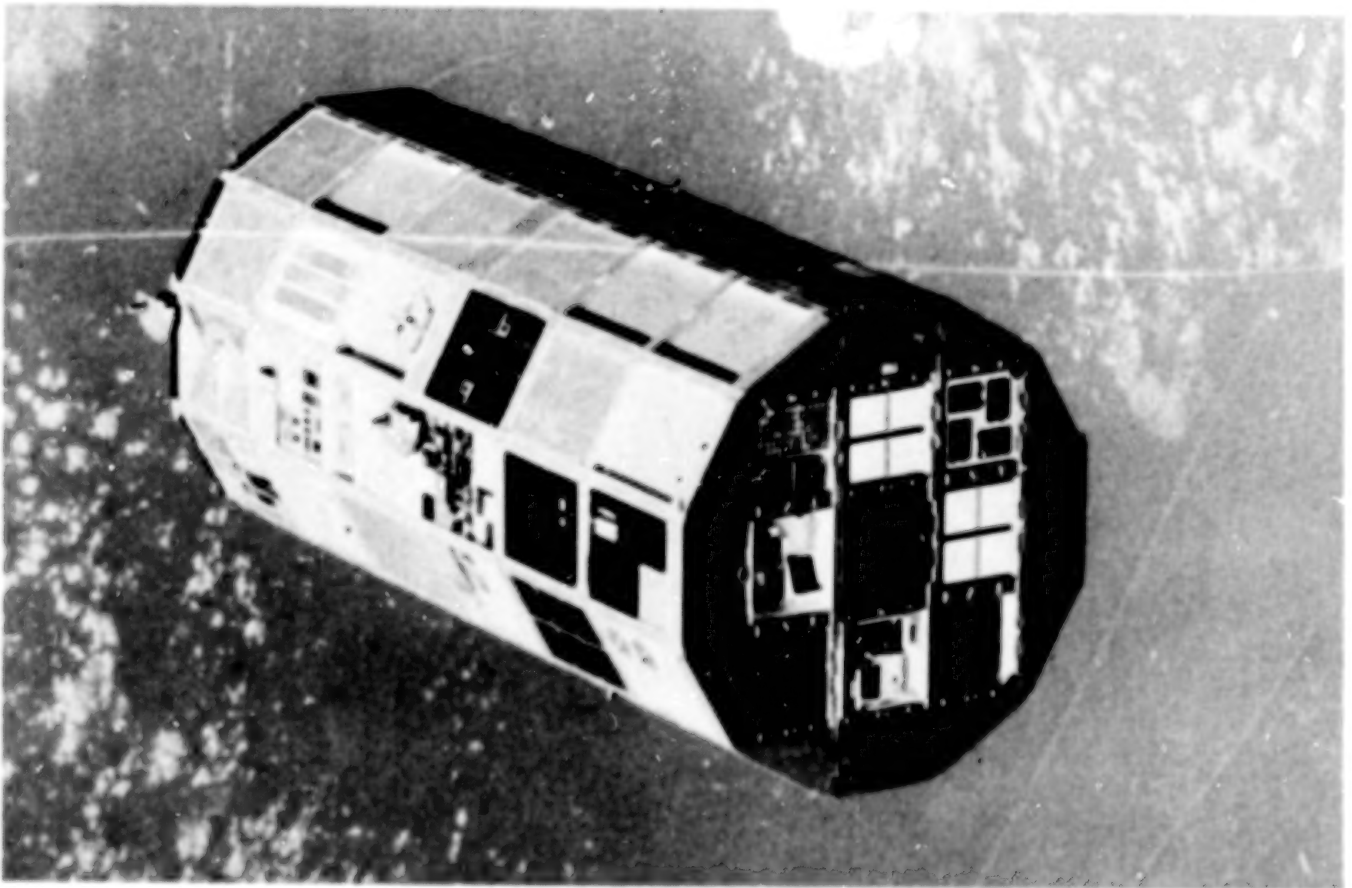
MATERIALS EXPERIMENTS

INTRODUCTION

In the early 1970's, the NASA Office of Aeronautics and Space Technology (OAST) approved the Long Duration Exposure Facility (LDEF) Project. The LDEF project provided NASA and other U.S. and foreign research organizations with opportunities to perform critical technology and science experiments in space using the LDEF and the Space Shuttle. Many of the experiments which were developed and are flying on the first LDEF mission are experiments to investigate the effects of the space environment on materials. This paper provides an overview of these materials experiments.

The LDEF, which is shown free-flying in the photograph below, was placed in orbit by the shuttle orbiter Challenger in April 1984, and it was to have been retrieved approximately 1 year later. The Challenger accident, however, has delayed the retrieval more than 4 years. The LDEF retrieval is now manifested on Flight 32 in July 1989. Since the facility and experiments will have been in space almost 5-1/4 years when they are retrieved, they will be a national trove of science and technology data.

LDEF IN ORBIT



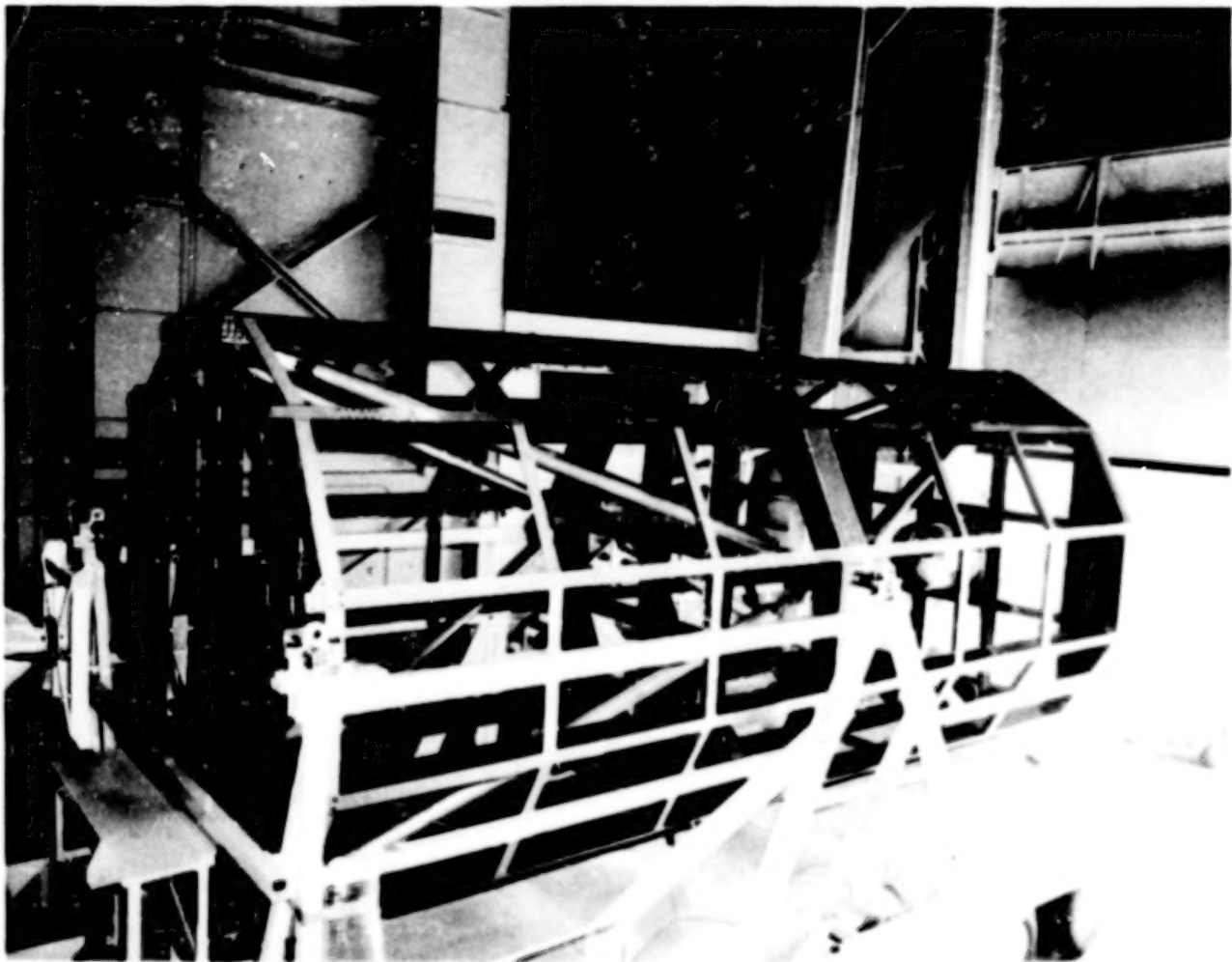
DESCRIPTION OF THE FACILITY

The LDEF is an 8,000 pound cylindrical structure, 14 feet in diameter and 30 feet in length, on which approximately 12,000 pounds of tray mounted experiments can be transported to space, exposed for long periods of time, and retrieved using the Space Shuttle. The reusable LDEF structure is gravity gradient stabilized in three axes when free-flying with the cylindrical axis Earth pointing and one edge always facing in the direction of the velocity vector. Fifty-six experiment trays are mounted on the facility.

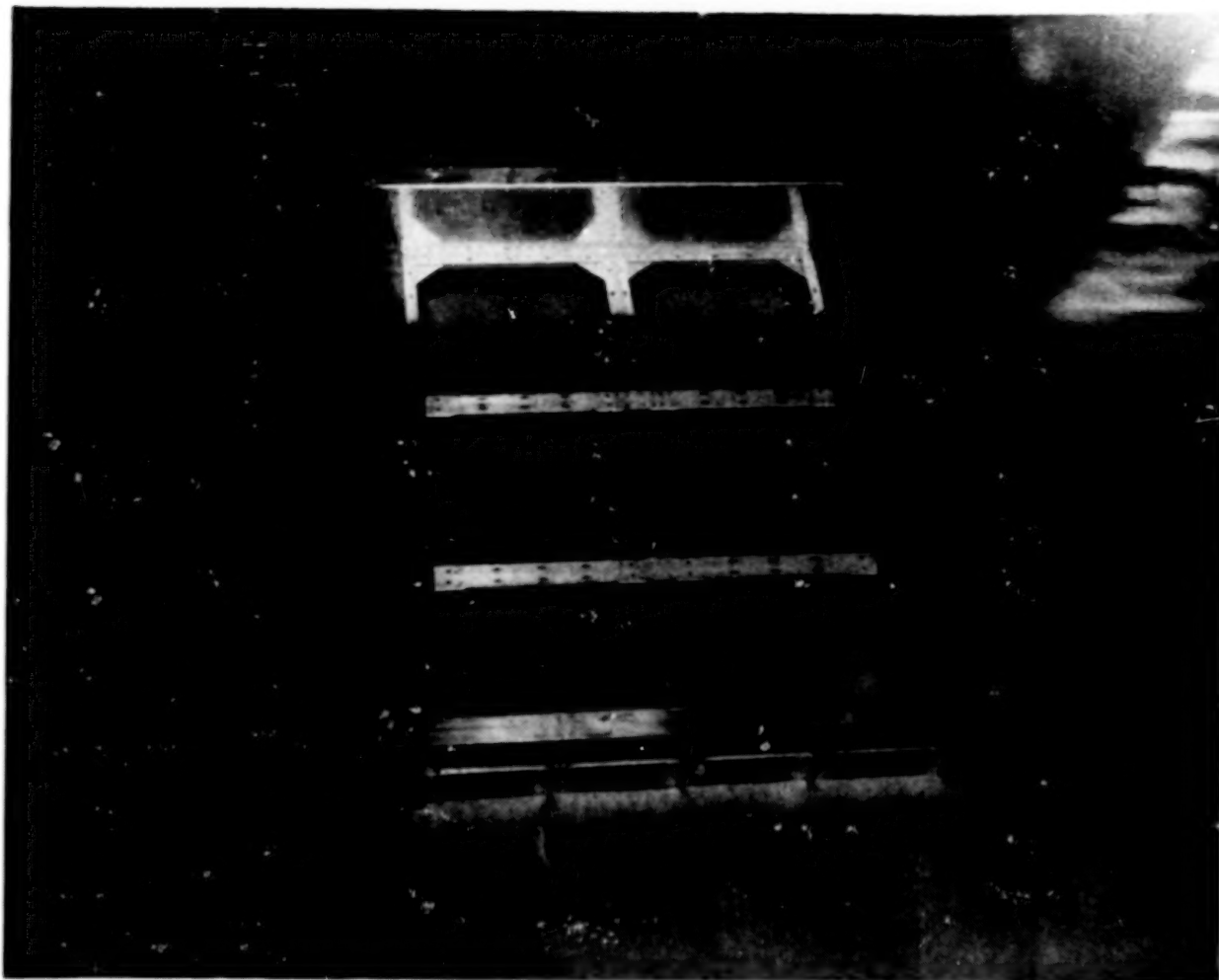
The LDEF experiments are self-contained in trays. Many are completely passive, depending on postflight laboratory investigation for data results. The active LDEF experiments have individual power and data systems incorporated in their respective trays. The LDEF provides signals to initiate the active experiment systems once in orbit.

The LDEF structure and a typical LDEF experiment tray are shown below and on the following page.

LDEF STRUCTURE



LDEF EXPERIMENT TRAY



FIRST LDEF MISSION EXPERIMENTS

The 57 science, application, and technology experiments now flying on the LDEF are listed below. Those experiments whose objectives are to provide data on space environmental effects on materials have been marked with an asterisk. Discussions of typical examples of the materials experiments are presented in the following material with a brief abstract of each of the materials experiments presented in the addendum to this paper. The Principal Investigators for the materials experiments on LDEF are from NASA, DOD, other U.S. government organizations and from U.S. universities and industries. Foreign Principal Investigators are also involved.

Detailed postflight investigations of the retrieved LDEF hardware and LDEF systems and experiment hardware will also provide additional data on the effects of long term exposure to the space environment. A discussion of the plans for such investigations are also presented in the following material.

CRYSTAL GROWTH

ATOMIC OXYGEN OUTGASSING

ATOMIC OXYGEN INTERACTION

HIGH-TOUGHNESS GRAPHITE EPOXY

RADAR PHASED-ARRAY ANTENNA

COMPOSITE MATERIALS FOR SPACE STRUCTURES

EPOXY MATRIX COMPOSITES

COMPOSITE MATERIALS

METALLIC MATERIALS UNDER ULTRAVACUUM

GRAPHITE-POLYIMIDE AND GRAPHITE-EPOXY

POLYMER MATRIX COMPOSITE MATERIALS

SPACECRAFT MATERIALS

BIOSTACK

BALLON MATERIALS DEGRADATION

THERMAL CONTROL COATINGS

SPACECRAFT COATINGS

THERMAL CONTROL SURFACES

TEXTURED AND COATED SURFACES

VARIABLE CONDUCTANCE HEAT PIPE

VACUUM-DEPOSITED OPTICAL COATINGS

TRAPPED-PROTON ENERGY SPECTRUM

HEAVY COSMIC RAY NUCLEI

SOLAR ARRAY MATERIALS

MICROABRASION PACKAGE

METEOROID IMPACT CRATERS

DUST DEBRIS COLLECTION

CHEMISTRY OF MICROMETEORIDS

MEASUREMENTS OF MICROMETEORIDS

INTERPLANETARY DUST

SPACE DEBRIS IMPACT

INFRARED MULTILAYER FILTERS

METAL FILM AND MULTILAYERS

SOLAR RADIATION ON GLASSES

SPACE ENVIRONMENT EFFECTS

HEAVY IONS

ULTRA-HEAVY COSMIC RAY NUCLEI

COATINGS AND SOLAR CELLS

SOLID ROCKET MATERIALS

RULED AND HOLOGRAPHIC GRATING

OPTICAL FIBERS AND COMPONENTS

SESSION 2: SPACECRAFT EXPERIENCE

Chairman: J. Triolo
NASA Goddard Space Flight Center

SOME EXAMPLES OF THE DEGRADATION
OF PROPERTIES OF MATERIALS IN SPACE

Frederick E. Betz
and
Joseph A. Hauser
Naval Research Laboratory
Washington, D.C. 20375-5000

SOLRAD 11 SPACECRAFT

An artist's conception of one of the two Naval Research Laboratory (NRL) SOLRAD 11 satellites that were launched on 14 March 1976 from Cape Canaveral is shown in figure 1. These spacecraft, the 65th and 66th launched by NRL, were in a 63,000 nautical mile circular orbit, spin stabilized and sun pointing. The prime power was provided by four deployed solar panels and four body mounted panels insulated from the body with a multi-layer insulation blanket.

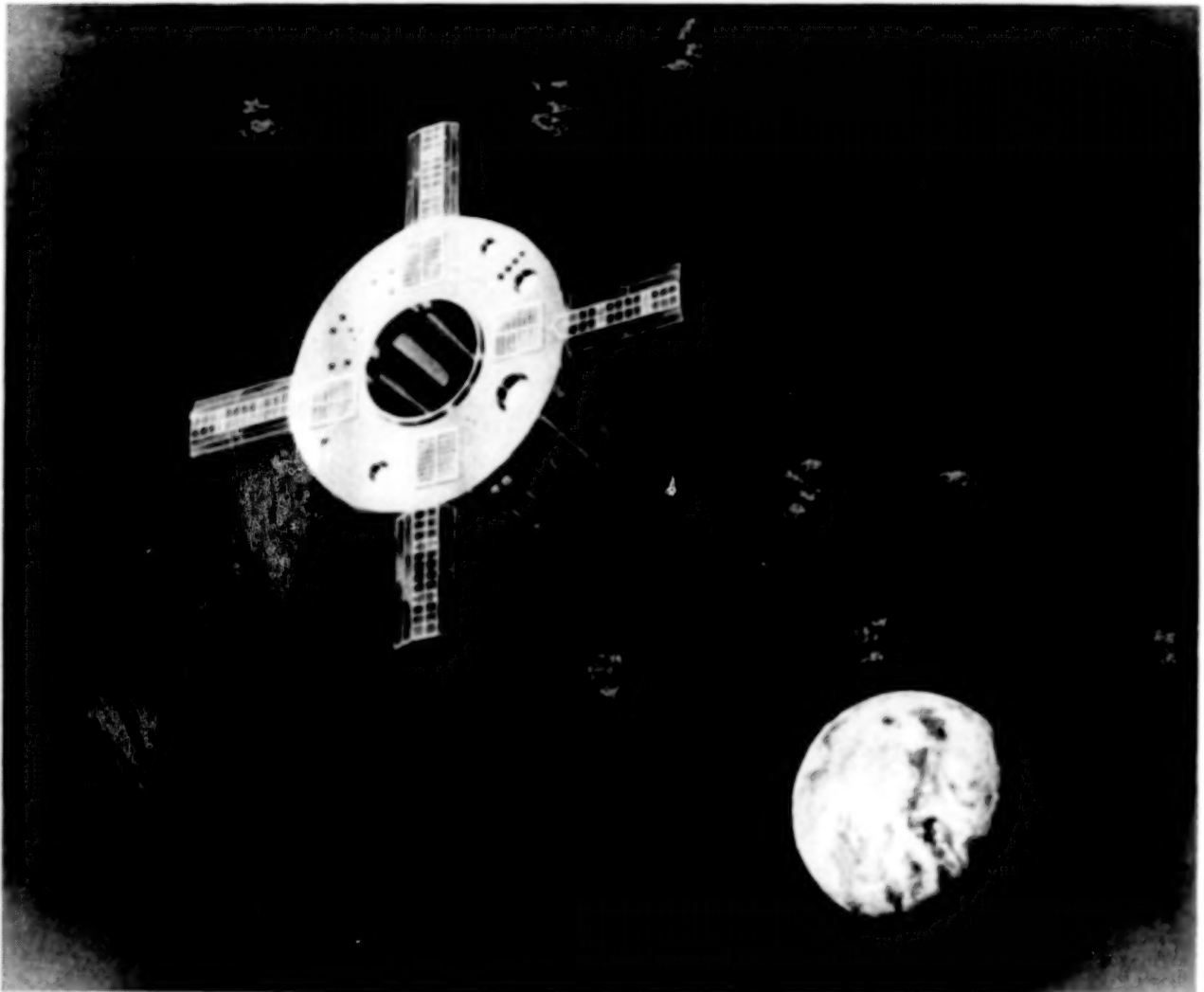


Figure 1

SOLAR CELL AND SILVER TEFLON PANEL LAYOUT

One of the four body mounted panels is depicted in figure 2. Overall dimensions of the panel were 25.4 cm (10.0 in) by 33.0 cm (130 in). On the panel was mounted an 80 cell series circuit of 2 cm by 2 cm solar cells and the non-cell area was covered with .13 mm (.005 in) thick silver teflon for thermal control. The solar cells, terminals, etc., accounted for 42.1%, and silver teflon 57.9% of the panel area. As I recall, the design operating temperature was about 50°C.

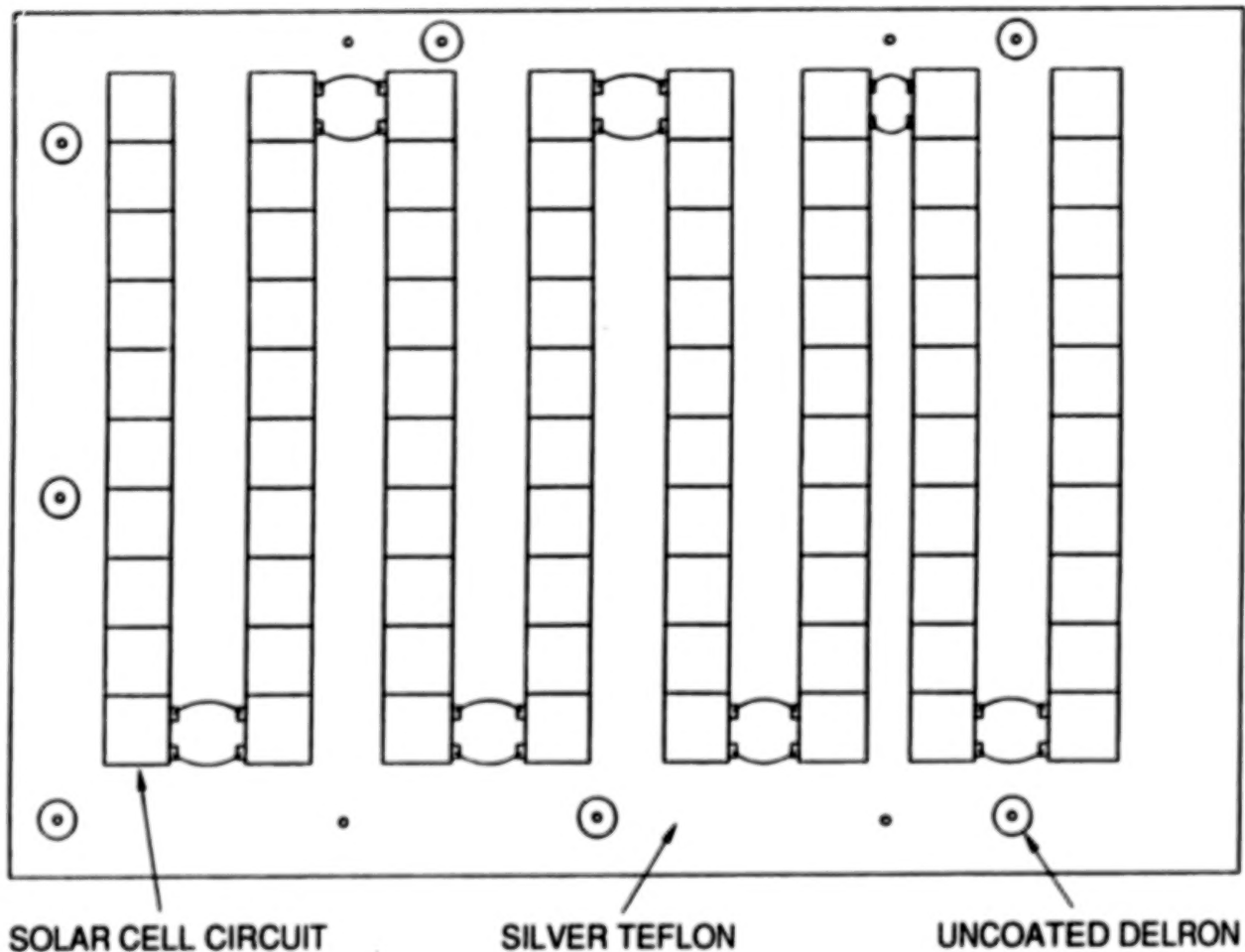


Figure 2

SOLRAD 11B SOLAR PANEL TEMPERATURE

Figure 3 is a smoothed plot of the insulated solar panel temperature versus time in orbit. The "waves" are caused by the annual variation in solar intensity due to the Earth's slightly elliptical path around the sun. Solar panel electrical output was reduced due to a non-optimum operating voltage resulting from the elevated temperature. Mission impact was minimal since higher voltage was only needed to recharge batteries after eclipses, which occurred about 30 times each year. Understanding the increase in temperature was a greater concern.

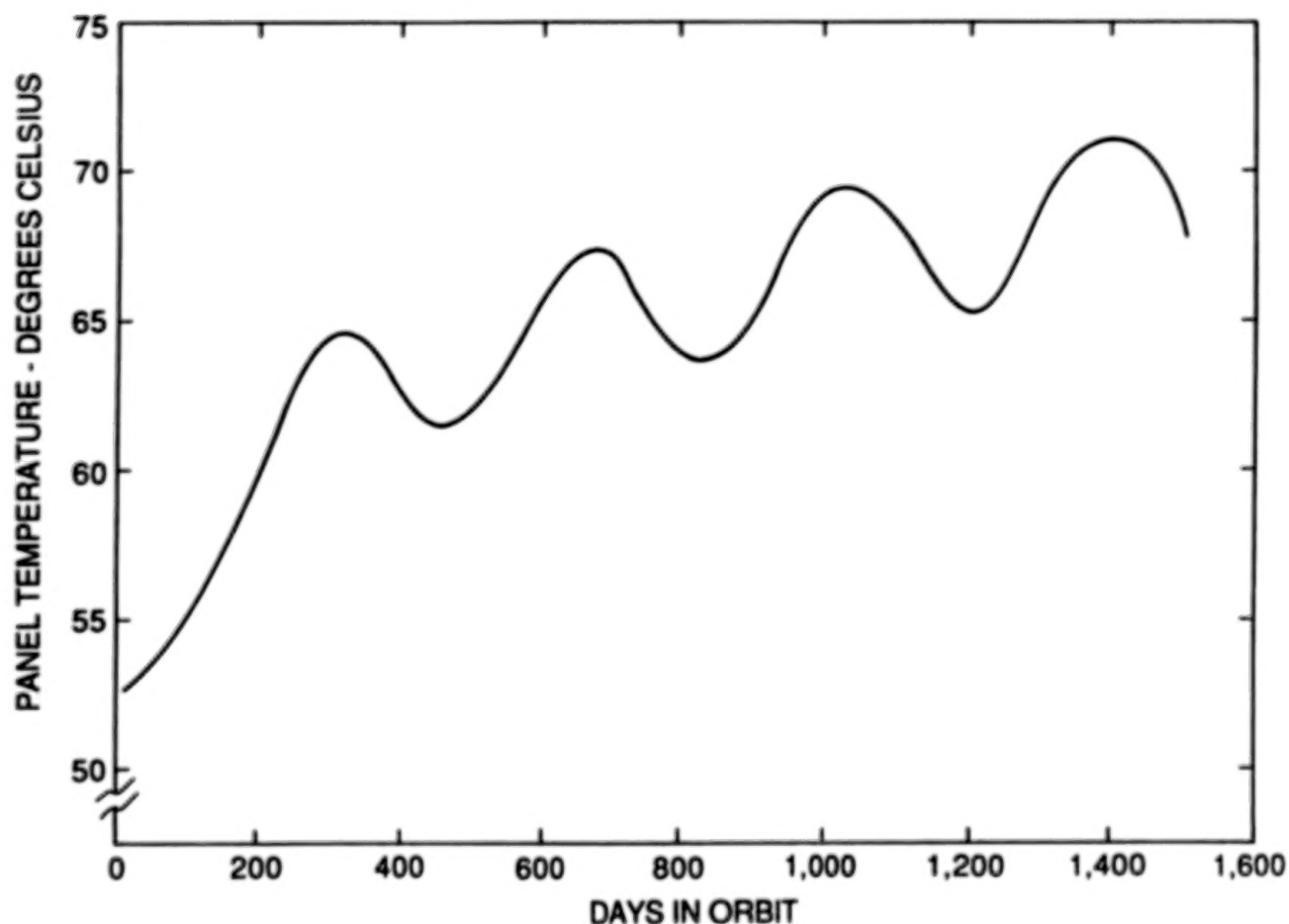


Figure 3

ESTIMATED CHANGE IN SILVER-TEFLON SOLAR ABSORBANCE

It is reasonable to assume that the temperature increase is driven by an increase in the solar absorbance of the silver teflon. I am not aware of changes occurring in material emittance. Inorganic silicon solar cell absorbance, already high, should not increase; and the reduction in solar cell efficiency is negligible. A least squares fit of the absorbance value, derived from panel temperature, is shown in figure 4 over a period of 1500 days in orbit.

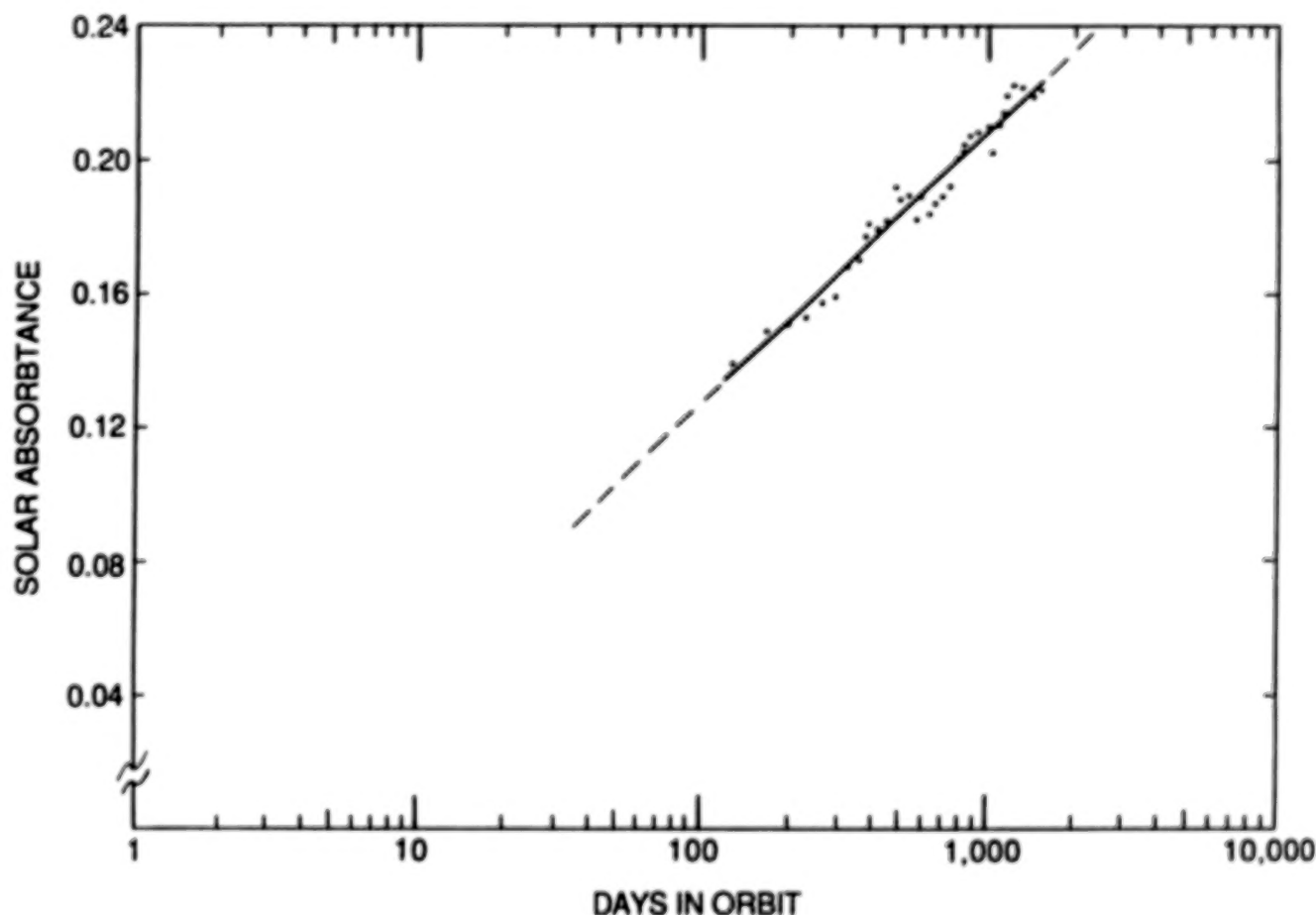


Figure 4

NAVIGATION TECHNOLOGY SATELLITE-2 (NTS-2)

While data was accumulating from SOLRAD 11, NRL was preparing NTS-2 for launch. Thermal design and engineering was contracted to the A.D. Little, Inc. Both Optical Solar Reflections (OSR) and silver teflon were incorporated for thermal control. Additionally, NASA Goddard Space Flight Center had a thermal control coatings experiment aboard with eight sample materials including OSR's and silver teflon. Internal deck temperatures exceeded the worst case temperature based on predicted degraded optical properties and maximum solar constant after less than two months on orbit.

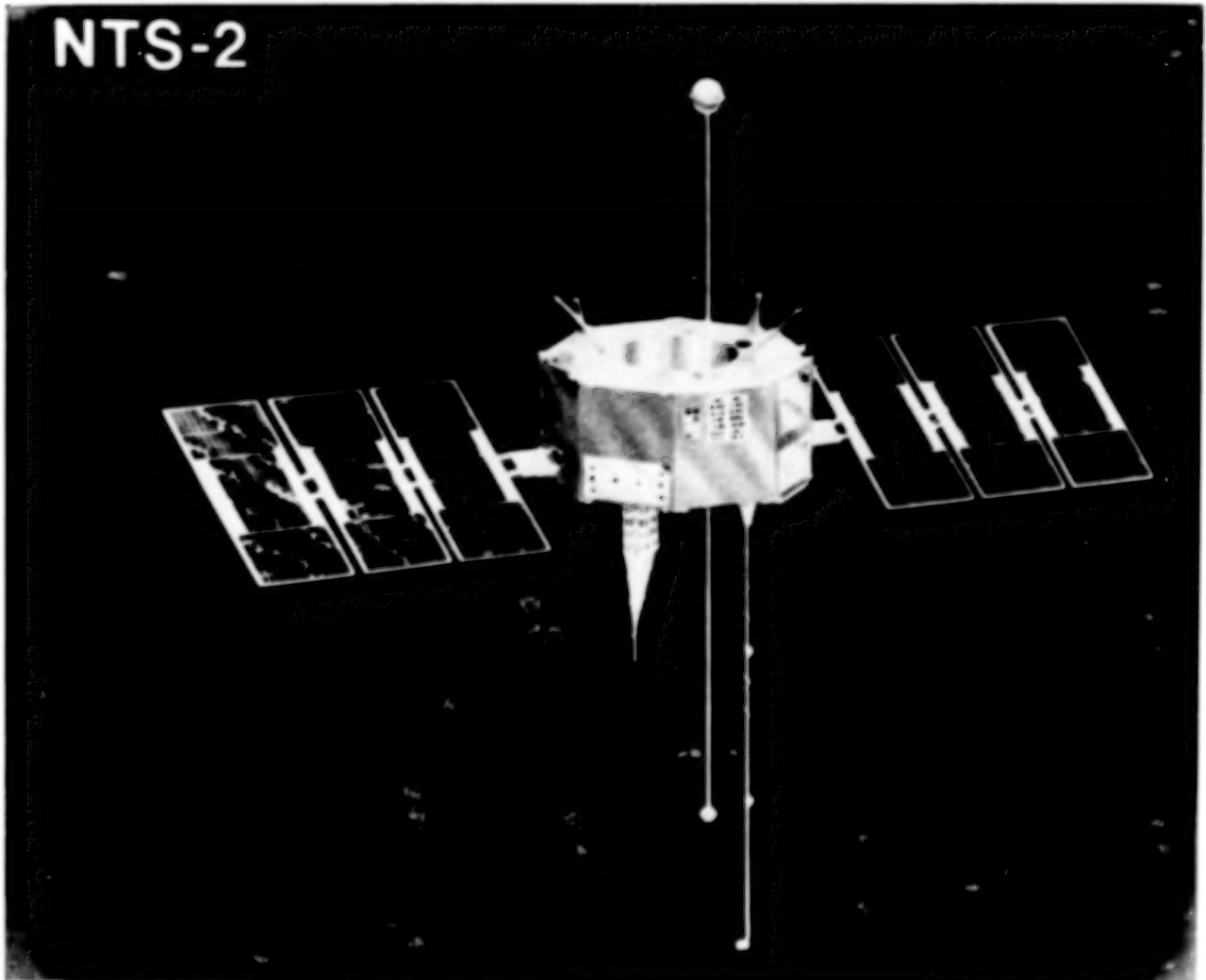


Figure 5

MEASURED DEGRADATION IN SOLAR ABSORBANCE
OF OSR AND SILVER TEFLON ON NTS-2

Figure 6 combines data from the NASA-GSPC experiment and thermal analysis of NTS-2 spacecraft equipment, deck, and radiator temperatures. D.W. Almgren of A.D. Little, Inc., concluded that the nonlinear nature of the data suggested contamination and, in an internal technical report, described four conceivable contamination mechanisms. Three mechanisms were based principally on "desorptive transfer". The solar panels were folded around the vehicle for launch and the first 14 days on orbit and provided the intermediate transfer surface. (The figure is from D.W. Almgren's report).

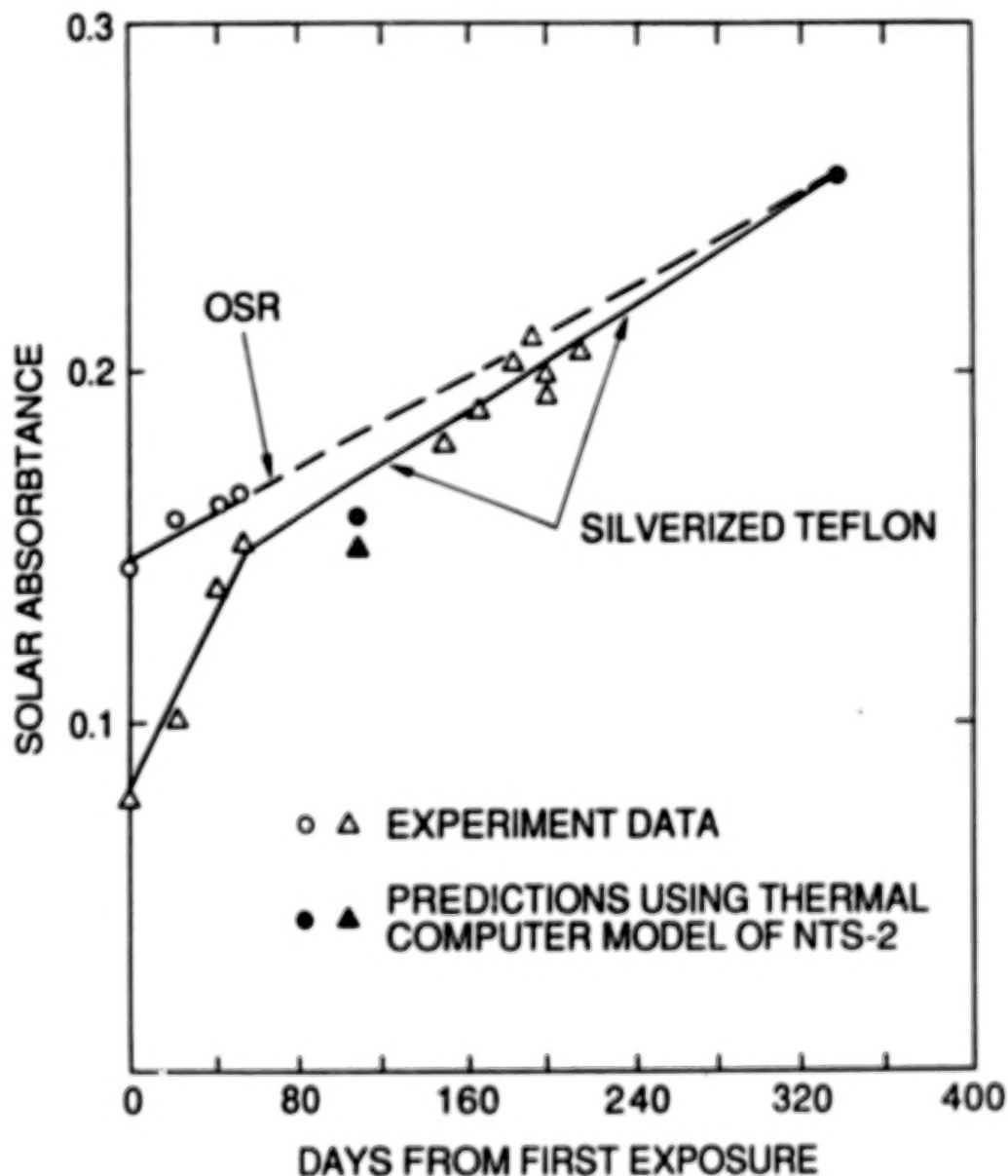


Figure 6

TEMPERATURE OF A SILVER TEFLON COVERED,
EARTH FACING, RADIATOR FOR SEVEN YEARS IN LOW EARTH ORBIT

Thermal analysis of the change in temperature of an Earth facing radiator over a seven year period, as shown in figure 7, resulted in an estimated change in solar absorptance of 0.27. Assuming an initial 0.08 absorptance, the final value totaled 0.35. A similar vehicle with only 4.5 years in orbit has shown an increase in absorptance of only 0.13 based on thermal analysis. Interestingly, the thermal analyst finding these results displeasing, performed a "sensitivity" analysis, adjusting heat flow and temperature change interpretation to reduce the change in absorptance by more than a factor of two.

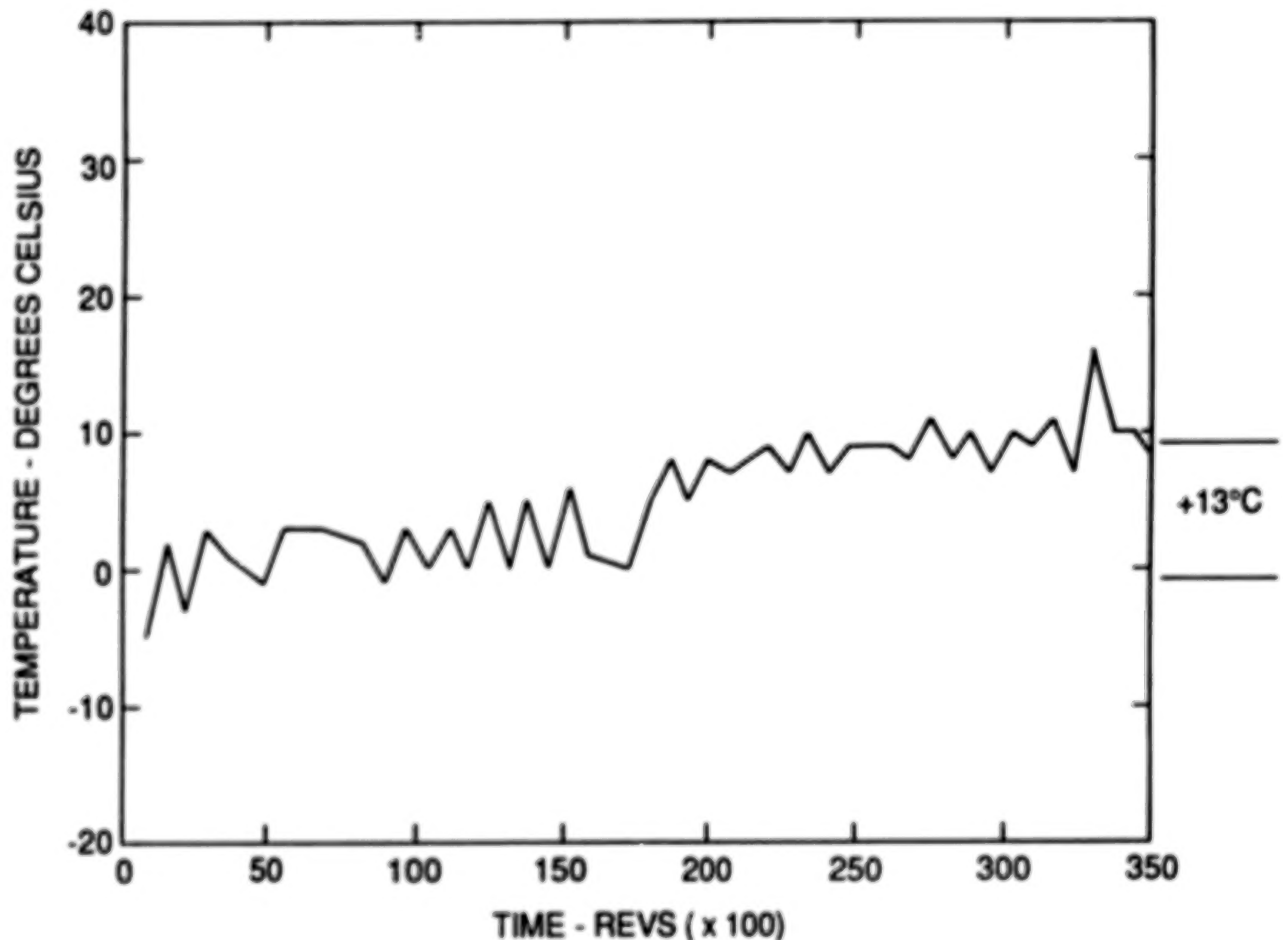


Figure 7

EXPERIMENTS 3 AND 4, SOLAR CELL SHORT CIRCUIT CURRENT DEGRADATION

NTS-2 also carried solar cell experiments. Shown in figure 8 is the difference in percent of initial on orbit short circuit current of identical solar cell and cover slide circuits. The only difference was that experiment 3 coverslide had anti-reflective coating and ultra-violet filters and was bonded with space quality organic adhesive DC 93-500, while experiment 4 cover slide had no coatings or filter and was bonded with fluorinated ethylene propylene (FEP) teflon. The data is from NRL Memorandum Report 4580 (ref 1).

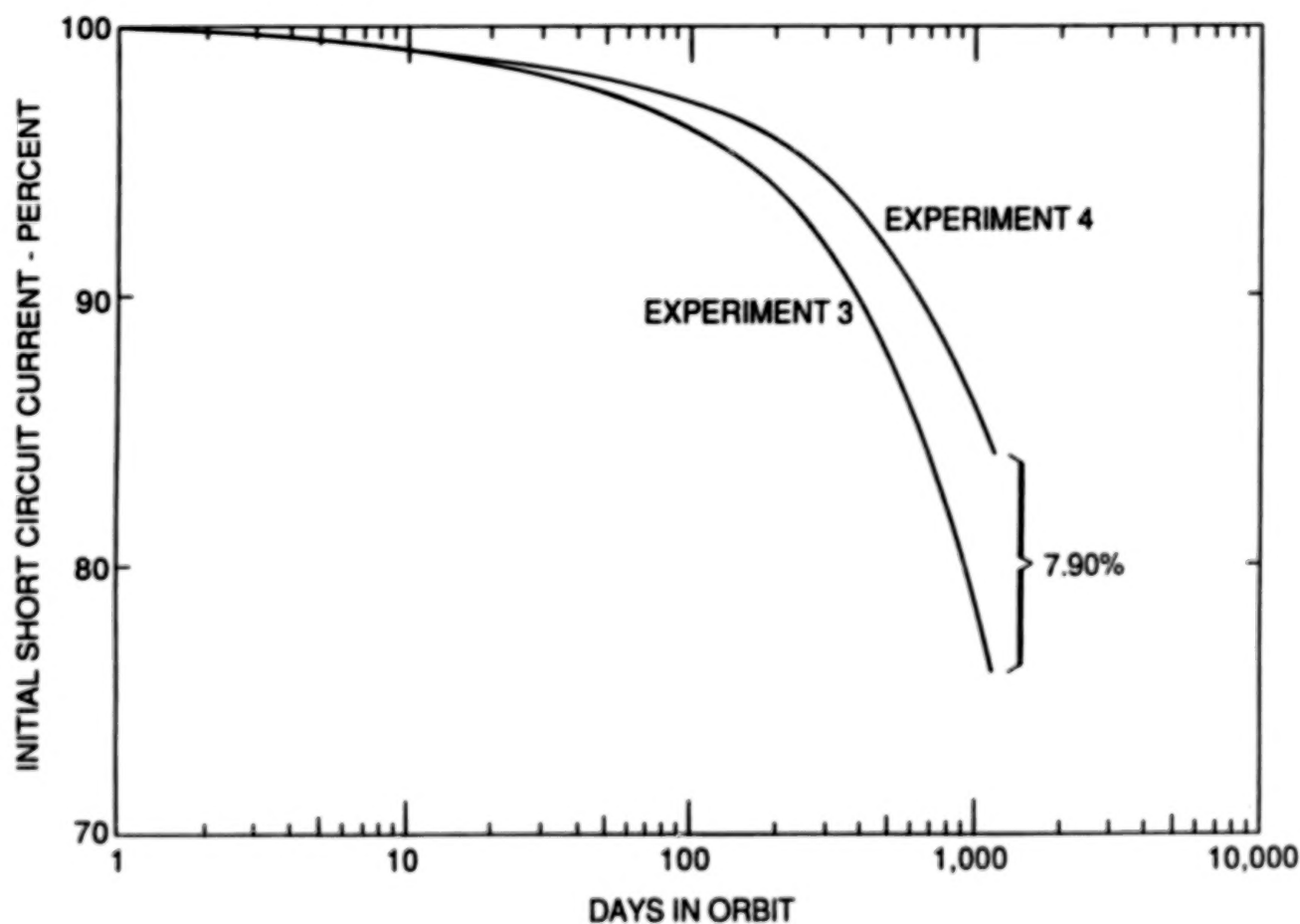


Figure 8

EXPERIMENTS 1 AND 13 SOLAR CELL SHORT CIRCUIT CURRENT DEGRADATION

Similarly, experiments 13 and 1, also contained identical cells. Experiment 1 had its cover slides bonded with organic adhesive R63-489 while experiment 13 had its cover slides electrostatically bonded without any other adhesive. Is it possible that we are throwing away 5% to 10% of available solar power because of degrading adhesive on solar array covers? It is noted that these data (ref 1) contradict data taken on the Applications Technology Satellite (ATS)-6 solar cell experiment in geostationary orbit (ref 2).

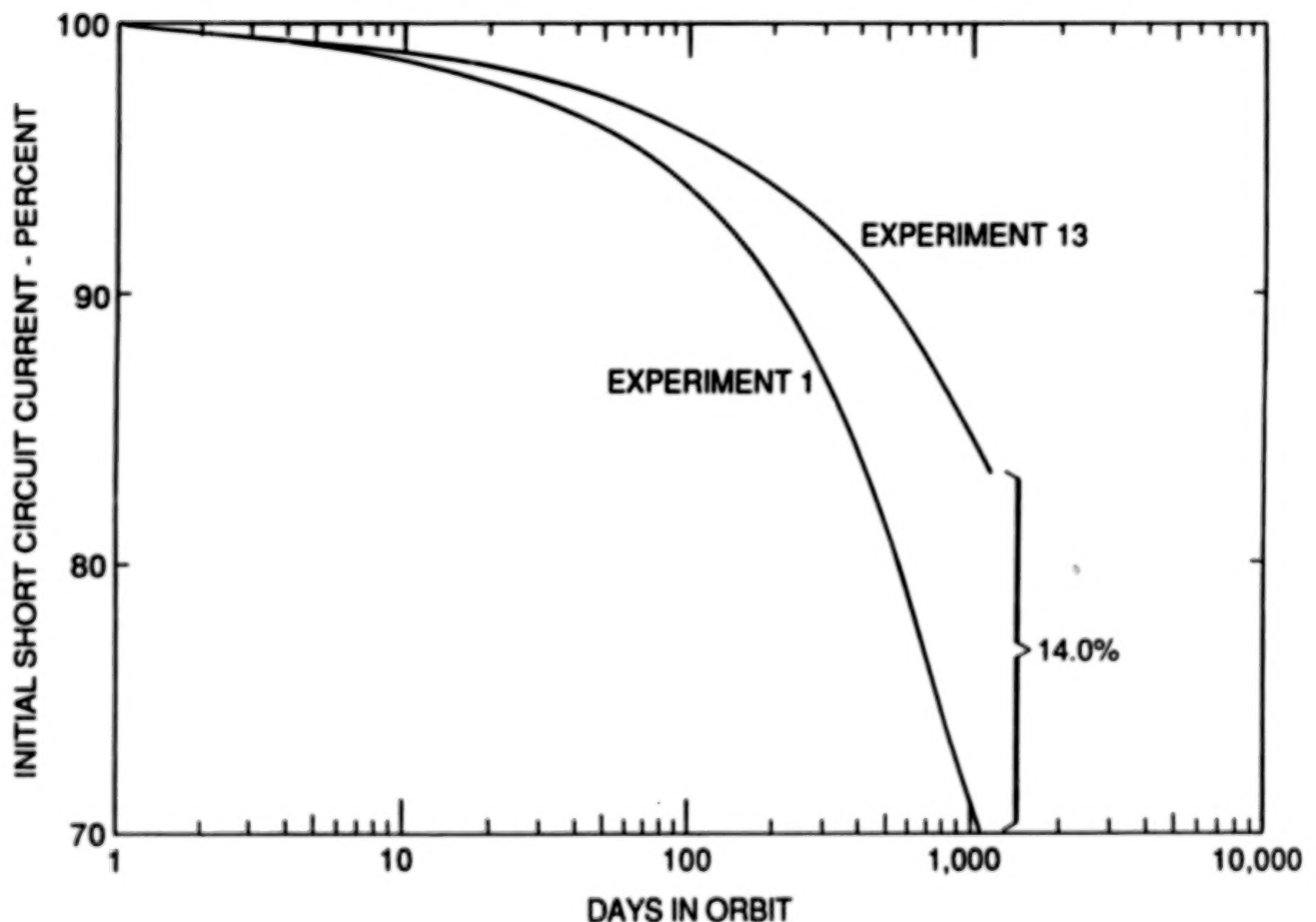


Figure 9

SHUTTLE LAUNCH DISPENSER (SLD) SPACECRAFT SHOWING PROPELLANT TANKS

Although, to our knowledge, NRL has not experienced debris or meteoroid damage, the threat is a design consideration for our space platforms. As an example, when designing the Shuttle Launch Dispenser (SLD), shown in figure 10, the design requirement was that there be greater than 0.99 probability that the propellant tanks would survive the expected meteoroid environment. This was accomplished by performing an analytical study that addressed the problem. First, using perforation equations, the minimum size particle that would penetrate the tank was determined. Then using a flux equation for our orbit, the probability of encountering a particle of this size or larger was determined. Using this approach the tank wall thickness was evaluated. Also, because Multi Layer Insulation thermal blankets were being used, it was decided to use a one-inch standoff for the blankets which produced a "Whipple Meteoroid Bumper" effect and provided additional protection for the tanks. Based on this analysis our tanks have a survival probability of greater than 0.999.

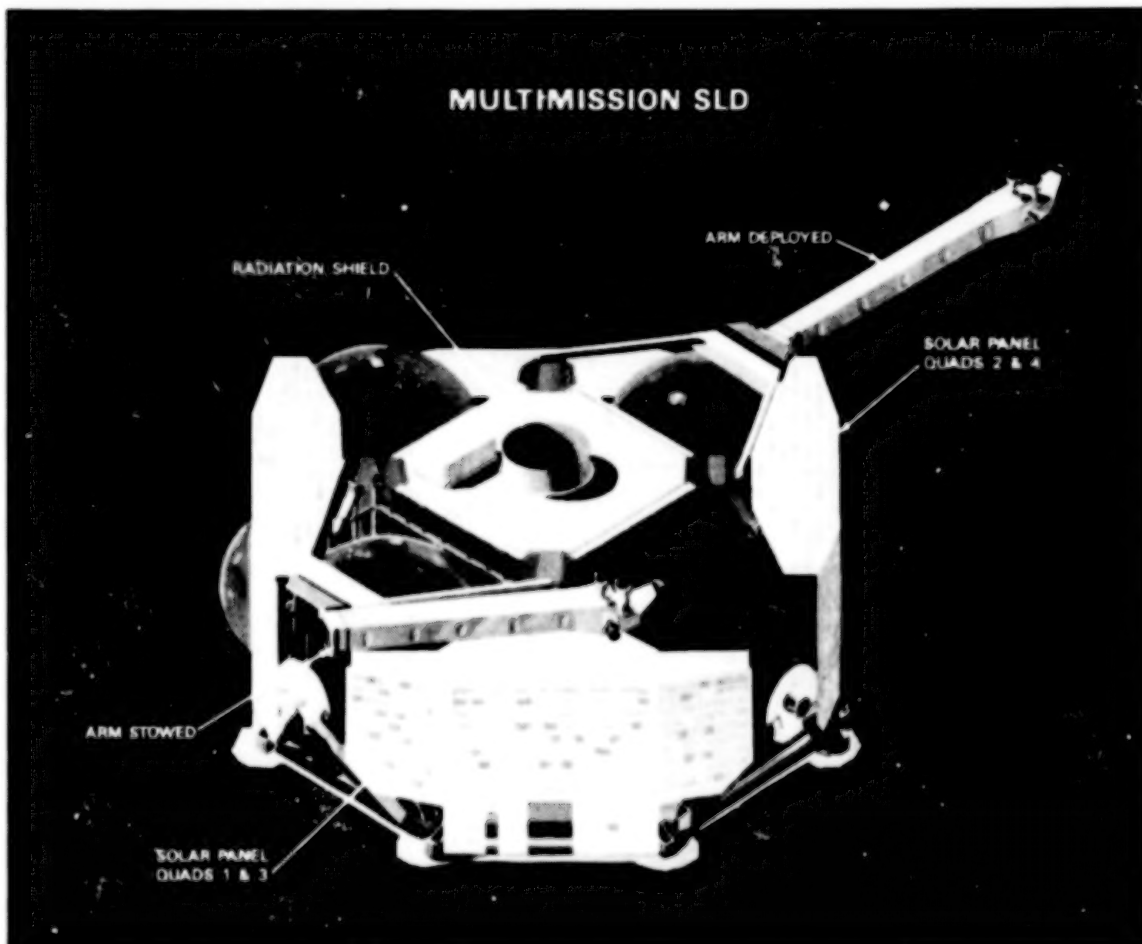


Figure 10

RELATIVE SOLAR PANEL AND SOLID ROCKET MOTOR POSITIONS

A rough correlation of the contamination of solar panels from solid rocket motor plume has been attempted. A comparison is made from pre-launch solar panel calibration output and post plume exposure data. Data samples are from several satellites. When the data was consolidated and normalized, panel 1, located behind the nozzle, was assigned 100%. Panel 2 averaged 97.0% and panel 3 averaged 97.9% of the panel 1 value.

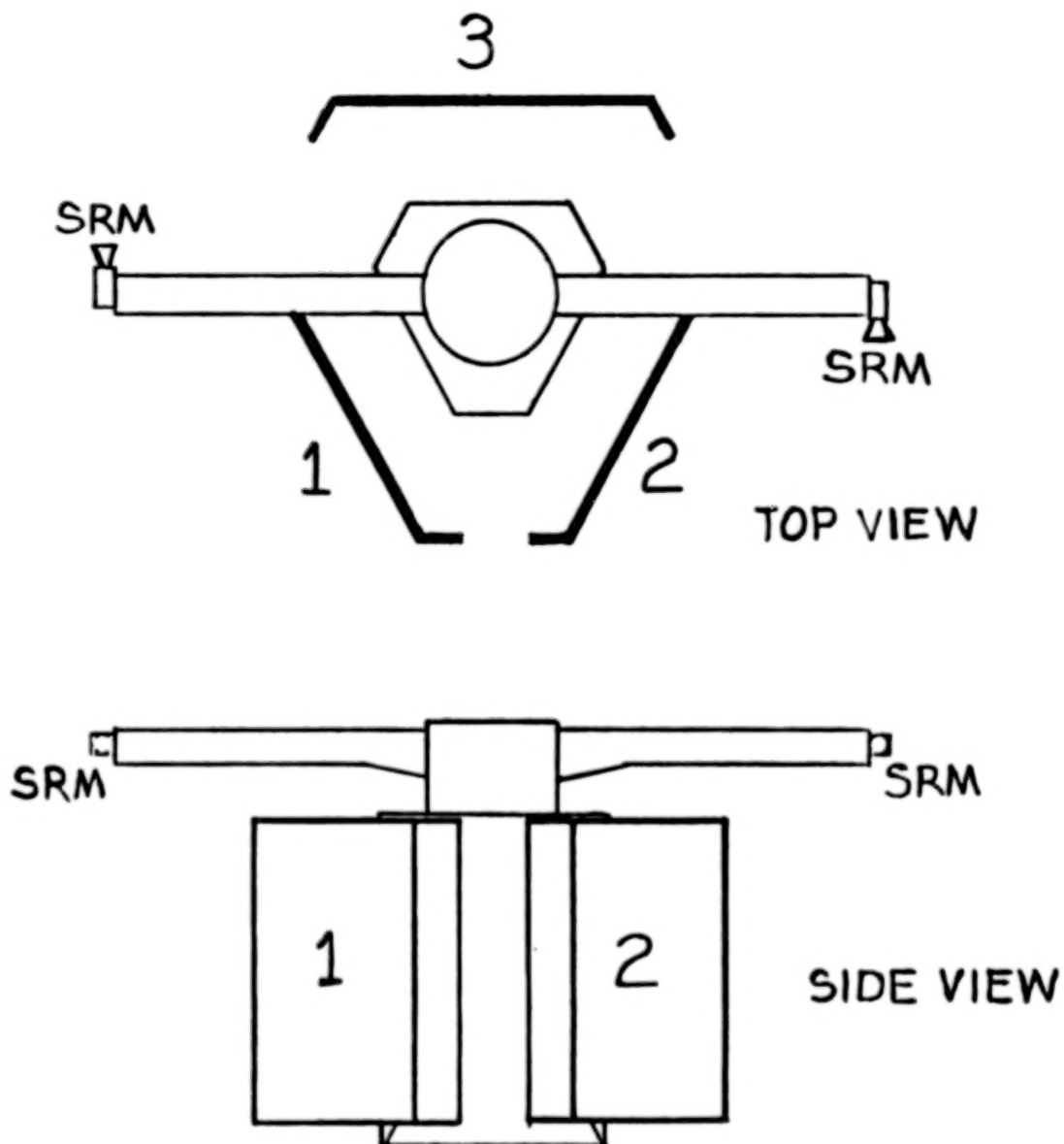


Figure 11

REFERENCES

1. Walker, D.H.; Performance of The Solar Cell Experiments Aboard the NTS-2 Satellite After Three Years in Orbit. NRL Memorandum Report 4580, July 30, 1981.
2. Goldhammer L.J.; ATS-6 Solar Cell Experiment/Improvement. Final Report, NAS Contract NAS 5-22873, 31 January 1977.

BEST COPY AVAILABLE

TRENDS IN ENVIRONMENTALLY INDUCED SPACECRAFT ANOMALIES

Daniel C. Wilkinson

National Oceanic and Atmospheric Administration
National Geophysical Data Center
Solar-Terrestrial Physics Division
Boulder, Colorado 80303

ABSTRACT

The Spacecraft Anomaly Data Base maintained at NOAA's National Geophysical Data Center has been useful in identifying trends in anomaly occurrence. Trends alone do not provide quantitative testimony to a spacecraft's reliability, but they do indicate areas that command closer study. An in-depth analysis of a specific anomaly can be expensive and difficult without access to the spacecraft. Statistically verified anomaly trends can provide a good reference point to begin anomaly analysis.

Many spacecraft experience an increase in anomalies during the period of several days centered on the solar equinox, a period that is also correlated with sun eclipse at geostationary altitude and an increase in major geomagnetic storms.

Increased anomaly occurrence can also be seen during the local time interval between midnight and dawn. This local time interval represents a region in Earth's near space that experiences an enhancement in electron plasma density due to a migration from the magnetotail during or following a geomagnetic substorm.

THE SPACECRAFT ANOMALY DATA BASE

The National Oceanic & Atmospheric Administration (NOAA) is the main U.S. civilian agency responsible for the operation of monitoring spacecraft. Its responsibilities include the (GOES)* series of geostationary weather and space environment monitoring satellites and the lower altitude, polar orbiting NOAA/TIROS satellites. Long and productive spacecraft lifetimes are of major importance to NOAA.

NOAA also operates a system of national data centers. The National Geophysical Data Center (NGDC) in Boulder, Colorado has responsibility for collecting, archiving, analyzing, and disseminating solar-terrestrial data and information. NGDC, under the auspices of World Data Center A for Solar Terrestrial Physics, services a worldwide interest in data and information about the origin of solar activity, the transfer of energy from the Sun to Earth, and its effects in interplanetary and near-Earth space. In line with these services, NGDC has made a deliberate effort to apply these data resources to the problem of spacecraft interaction with the the near space environment.

A data base of spacecraft anomalies is maintained at the Solar-Terrestrial Physics Division of NGDC in Boulder, Colorado. It includes the date, time, location, and other pertinent information about incidents of spacecraft operational irregularity due to the environment. These events range from minor operational problems which can be easily corrected to permanent spacecraft failures. It currently contains 2779 anomalies from 1971 to the present with contributions from seven countries: Australia, Canada, Germany, India, Japan, United Kingdom, and the United States. Data suppliers are asked to provide the anomaly type and diagnosis.

*Geostationary Operational Environmental Satellite

The data base is maintained on an IBM compatible personal computer. To facilitate access to the information, software has been written to perform a full range of functions for managing and displaying the contents. Satellite users can use the Spacecraft Anomaly Manager (SAM) software to create a data base containing only their anomalies and forward the data to NGDC on floppy disk for inclusion in the archive. In order to preserve confidentiality, when necessary, spacecraft may be identified by aliases.

SAM also includes two important functions to test anomaly collections for environmental relationships. Histograms of local time and seasonal frequency show distinct patterns for spacecraft susceptible to static charge build-up and subsequent discharge. The current version of the software does not perform statistical validation but the user may convert the data to a standard ASCII file that can be uploaded to any computer and processed by user supplied software.

STATISTICAL METHODS

Grajek and McPherson (ref. 1) point out the value of using statistical methods for analyzing apparent trends in anomaly occurrence. The Chi-square test for randomness can determine the probability that a given histogram, or one with similar deviations from the mean, could occur randomly.

The Pearson Product-moment Correlation Coefficient can determine both the strength of a correlation and the probability of error in establishing a correlation where none exists. A coefficient of 1 indicates perfect correlation, 0 indicates no correlation, and -1 indicates perfect anticorrelation.

These two methods were used to analyze each of the following histograms with the help of public domain software (ref. 2). The results are reported in the discussions that follow.

SEASONAL TRENDS

Figure 1 shows the basic definition of 'seasonal'. The histogram displays the apparent solar declination on the 15th of each month in whole degrees. The cartoon shows the sun-earth geometry that causes a variety of environmental effects on spacecraft in near-Earth-space. This distribution is used to test for seasonal correlations in the anomaly data.

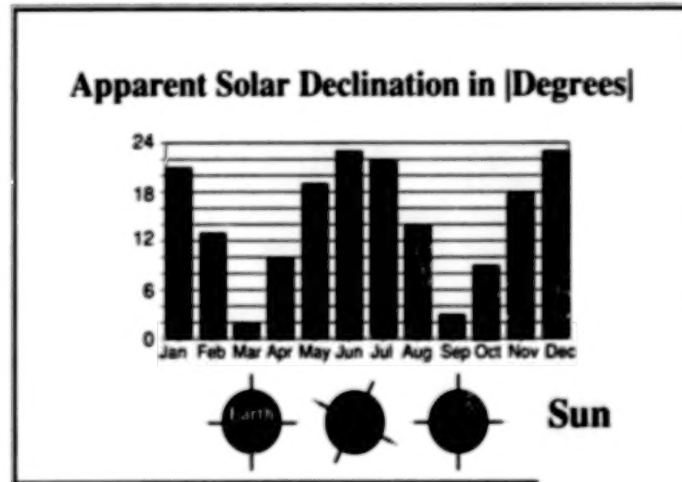


FIGURE 1

One effect of the variation in apparent solar declination on spacecraft is the periods of eclipse that occur at spacecraft in geostationary orbit as shown in figure 2. These periods of earth-shadowing occur at the spring and fall equinox near midnight local time. The periods of darkness cause an interruption in the charge balancing phenomenon that relies on the photoelectric boiling off of electrons. During equinox a spacecraft at geostationary altitude will encounter magnetotail plasma boundaries more often.

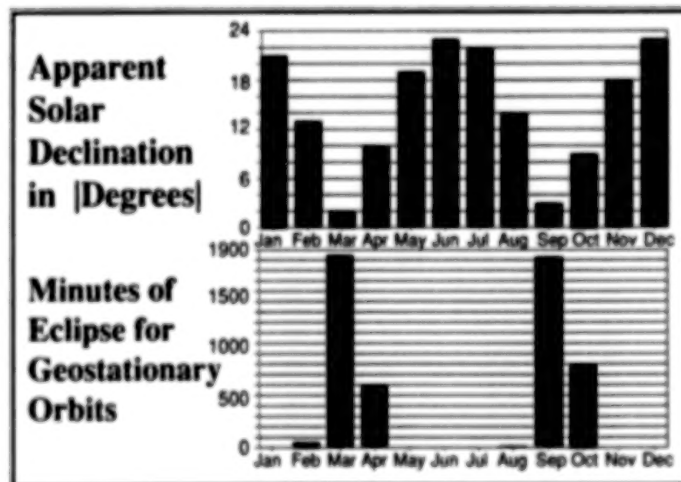


FIGURE 2

The distribution of major magnetic storms is shown in figure 3. It has a very low probability of being random (.00042) and a moderately high anticorrelation to the histogram of declinations (-.89) with a very small probability that the correlation is wrong (.00011).

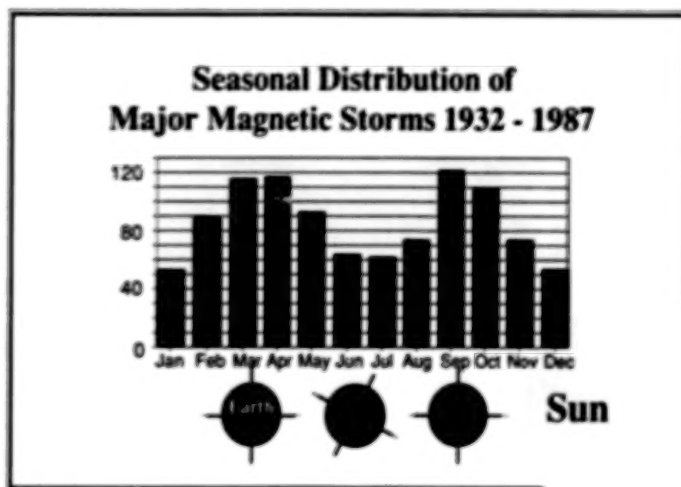


FIGURE 3

Figure 4 displays the seasonal distribution of all 2779 data base anomalies and shows a distinct increase around the spring and fall solar equinoxes. This anomaly distribution has a very low probability of being random (.0000018) and a moderately high anticorrelation to the histogram of declinations (-.86) with a very small probability that the correlation is wrong (.00011).

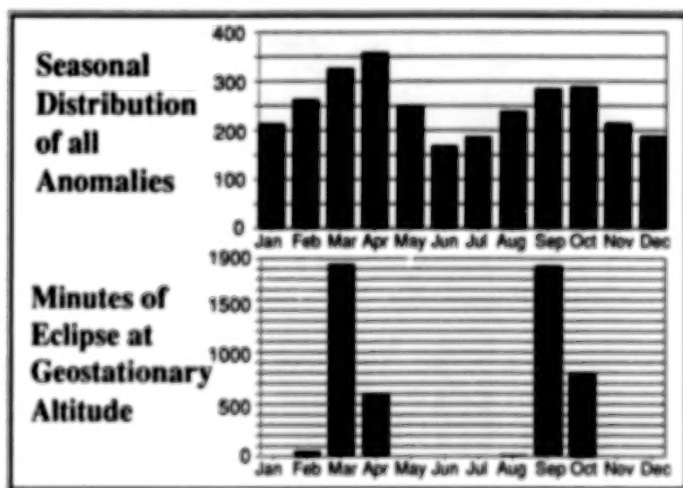


FIGURE 4

The GOES-4 & -5 phantom command anomalies shown in figure 5 are a prime example of a seasonal dependence. The phantom commands have been diagnosed as a surface charging problem which is consistent with the seasonal phenomenon. These charging events have a moderately high anticorrelation to the histogram of declinations (-.72) with a very small probability that the correlation is wrong (.0073)

The GOES-4, -5, and -6 telemetry anomalies also shown in figure 5 have been diagnosed as Single Event Upsets (SEUs). This anomaly distribution has a good probability of being random (.26) and a weak anticorrelation to the histogram of declinations (-.23) with a large probability that the correlation is wrong (.47). Since galactic cosmic ray fluxes are random in the seasonal context, the statistics validate the SEU diagnosis made for the GOES telemetry errors.

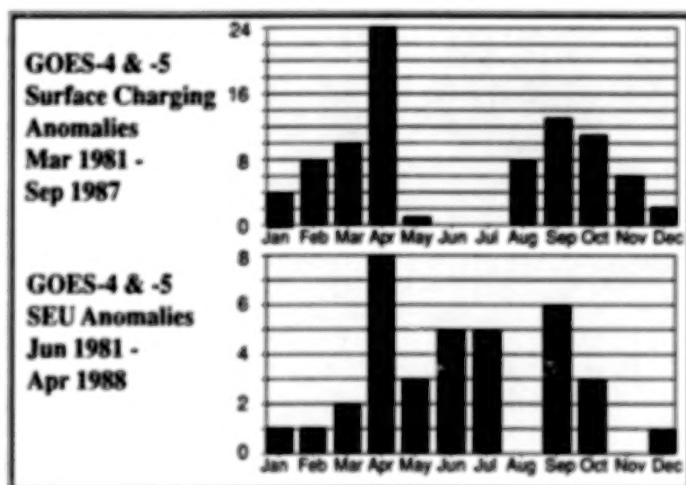


FIGURE 5

Tracking and Data Relay Satellite System (TDRSS-1) anomalies shown in figure 6 show no distinct seasonal variation in anomaly occurrence. This anomaly distribution has a very good probability of being random (.44) and a moderately weak anticorrelation to the histogram of declinations (-.55) with a small probability that the correlation is wrong (.062). However, the TDRSS SEUs show twice the seasonal correlation the GOES SEUs do.

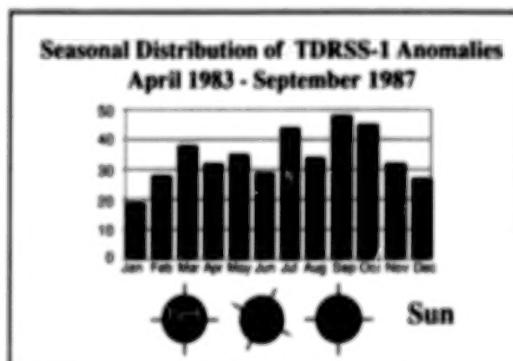


FIGURE 6

LOCAL TIME TRENDS

Figure 7 shows the local time distribution of the 2272 anomalies in the data base that have sufficient information for a local time calculation. This anomaly distribution has a small probability of being random (.00035). There is the expected midnight to dawn bump and two additional bumps, one centered at 12 LT* and one centered at 17 LT. The smaller enhancements may be explained later when a Sun-Vehicle-Earth (SVE) angle calculation is added to the anomaly entries. For specific spacecraft designs there are SVE angles that allow parts of a spacecraft to cast shadows on itself, causing a partial eclipse situation.

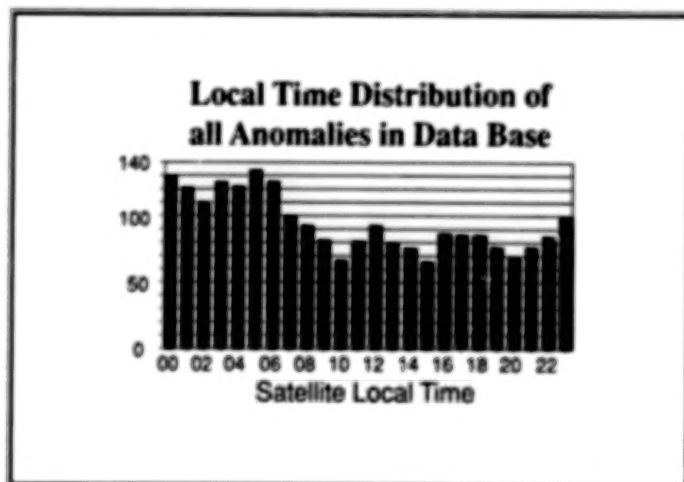


FIGURE 7

In figure 8 the GOES surface charging anomalies show a classic midnight to dawn grouping with a small probability of being random (.0000022). The GOES SEU anomalies show no such grouping and have a very high probability of being random (.94), consistent with SEUs.

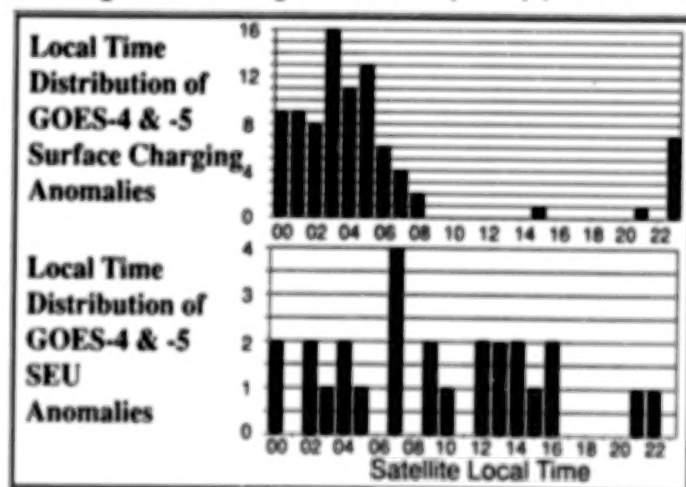


FIGURE 8

*Local Time

Figure 9 shows a clock face plot that distinctly displays the grouping of GOES surface charging anomalies between midnight and dawn. This type of grouping is due to a migration of KeV electrons from the magnetotail during magnetically disturbed periods and illustrates the extremely low probability of randomness (.0000022).

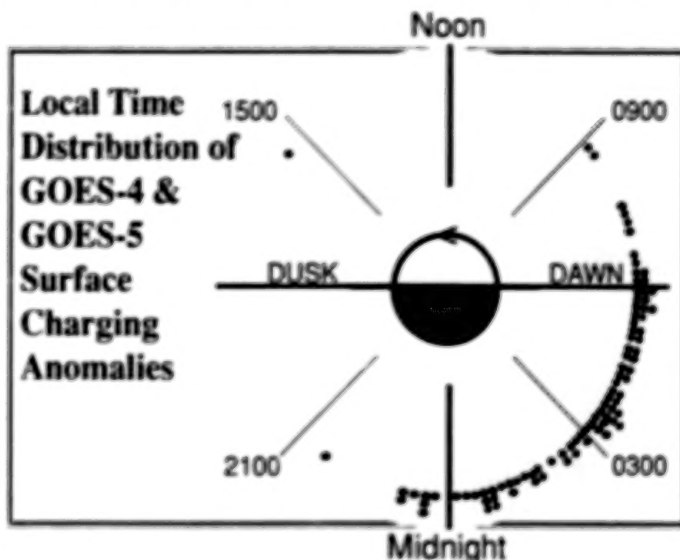


FIGURE 9

TDRSS-1 anomalies show no increase of anomaly occurrence during the midnight to dawn local time interval and have a very high probability of being random (.97), consistent with SEUs.

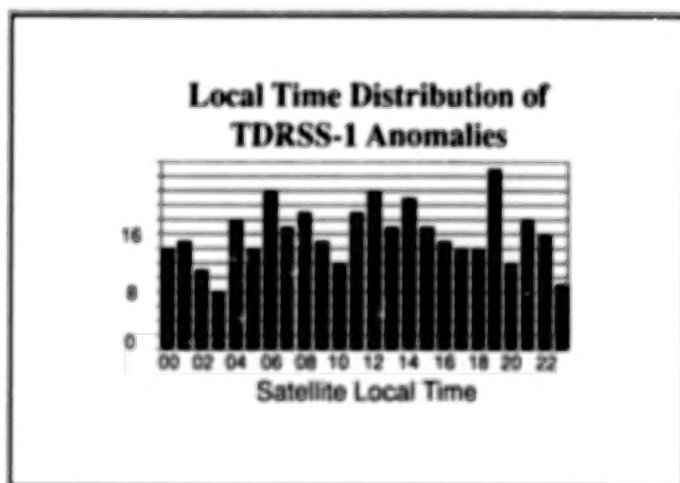


FIGURE 10

CONCLUSION

There is value in studying the trends, or their absence, in populations of spacecraft anomalies. This is only possible if there is a systematic recording of operational spacecraft anomalies and a willingness to merge those records with a common body of data for correlative study. The Spacecraft Anomaly Data Base and software for managing and studying the data are available from NGDC for these purposes.

REFERENCES

1. Grajek, Michael A.; McPherson, Donald A.: Geosynchronous Satellite Operating Anomalies Caused by Interaction with the Local Spacecraft Environment. NASA NAS3-21048.
2. Gustafson, Tracy L.: EPISTAT Statistical Package for the IBM Personal Computer, version 2.1. 1983.

RETURNED SOLAR MAX HARDWARE DEGRADATION STUDY RESULTS

Jack J. Triolo
Gilbert W. Ousley
Goddard Space Flight Center

ABSTRACT

The Solar Maximum Repair Mission returned with the replaced hardware that had been in low Earth orbit for over four years. The materials of this returned hardware gave the aerospace community an opportunity to study the realtime effects of atomic oxygen, solar radiation, impact particles, charged particle radiation, and molecular contamination. The results of 16 participants in these studies are summarized.

INTRODUCTION

The Solar Maximum Mission (SMM) spacecraft, built at the Goddard Space Flight Center, was launched in February 1980 with solar flare research its primary objective. Launched near the peak of the 11-year solar cycle, the SMM was put in a 310 nm, nearly circular orbit with 28.5° inclination. The spacecraft's longitudinal axis was pointing at the Sun in a 3-axis stabilized mode, so that the seven instruments aboard the spacecraft could monitor the activities of the Sun. Some of the instruments required very fine pointing accuracy and stability to obtain high-resolution data. During the initial period, the pointing accuracy of the SMM was better than 2 arc-sec with stability less than 1 arc-sec.

The following instruments were carried by the SMM spacecraft:

- Active Cavity Radiometer Irradiance Monitor
- Coronagraph/Polarimeter (C/P)
- Gamma Ray Spectrometer
- Hard X-Ray Burst Spectrometer
- Hard X-Ray Imaging Spectrometer
- Ultraviolet Spectrometer/Polarimeter
- X-Ray Polychromator

Six of the instruments were designed to observe solar flares in regions of the electromagnetic spectrum ranging from visible light through ultraviolet and x-ray emission to gamma rays. The seventh instrument, the Active Cavity Radiometer Irradiance Monitor, monitored the Sun's total radiation.

Equipment and Instrument Failures

The first months of the mission were very successful. The spacecraft and the instruments operated flawlessly with hundreds of flares monitored and recorded. In September 1980, about 6 1/2 months after launch, one of the three gyro channels (Channel C) of the NASA Inertial Reference Unit failed. The required attitude control was maintained, however, without performance degradation by the two remaining gyro channels (A and B) until November 1980, when three fuses burned out in the reaction wheel control circuits. In December 1980, a yaw magnetic torquer also failed. A coarse attitude control mode was established using the remaining magnetic torquers. The spacecraft was spin stabilized at a rotation rate of 1 deg/sec with a coning motion that moved the Sun pointing spacecraft axis up to 15° off the Sun line. Only two of the seven instruments were 100% operational (Gamma Ray Spectrometer and Hard X-Ray Burst Spectrometer) since they did not require precise pointing. One instrument functioned with limited capability (Active Cavity Radiometer Irradiance Monitor). Two of the instruments were not able to operate due to the backup attitude control mode (Ultraviolet Spectrometer/Polarimeter and X-Ray Polychromator) and two others had failed and were inoperative (Coronagraph/Polarimeter and Hard X-Ray Imaging Spectrometer).

Solar Maximum Repair Mission

The Solar Max spacecraft was the first spacecraft designed to be serviced and repaired in space by the Space Shuttle crew. The Modular Attitude Control System (MACS) module was designed to be an orbital replacement unit, but the instrument repair was more complex because the Instrument Module (IM) was not designed to be repaired or replaced in orbit. Of the two failed scientific instruments, only the C/P was considered repairable. An identical spare MACS module was available from the Landsat program and a new C/P Main Electronics Box (MEB) was built specifically for the repair mission.

The Solar Maximum Repair Mission (SMRM) was performed by the crew of the STS flight 41-C in April 1984. By this time the SMM orbit altitude had decayed to 265 nm. Attempts by the astronaut using the Manned Maneuvering Unit (MMU) to dock to the spacecraft and to stop its rotation failed. The docking attempts imparted to the spacecraft uncontrollable roll, pitch and yaw rates. After the spacecraft was stabilized using specially uplinked software, the spacecraft was grappled by the Orbiter's Remote Manipulator System (RMS) and placed on the Flight Support System (FSS) located in the Orbiter Bay.

The MACS module was removed from the SMM and placed on its temporary storage fixture on the FSS. After the new module was mounted on the SMM, the old module was secured in its landing location on the lower starboard side of the FSS. The entire MACS module replacement took less than an hour.

The replacement of the Main Electronics Box of the Coronagraph/Polarimeter was the next repair operation. The MEB was replaced successfully, even though it was not designed for servicing. The faulty MEB was stowed in a storage area in the FSS tool locker for return to Earth.

After the replacement of the faulty equipment, the SMM was checked out and deployed to provide more data near the Sun's least active solar flare period. The Orbiter landed two days later on April 14, 1984.

Post-Flight Handling of Returned Equipment

After landing at Edwards Air Force Base in California, the Orbiter and its returned payload were flown on the 747 to the Kennedy Space Center (KSC). After three days in the Orbiter Processing Facility (OPF), the FSS with MACS attached was removed from the Orbiter and transported to the Operations and Checkout (O&C) building.

Because of concern that contamination may mask the environmental effects on the returned equipment, the MACS and the MEB were bagged while in the O&C building and under QA control with rigid handling limitations. The MACS and MEB were removed from the FSS and placed in their respective storage containers. A one square foot wash plate and a fallout grid/surface had been attached to the MACS in the OPF before removal from the Orbiter to monitor molecular and particulate contaminants deposited from the time the MACS was taken out of the Orbiter bay to when it was unpacked at GSFC. The same procedure was used with MEB but the sequence started at the O&C building where the MEB was removed from the FSS tool locker.

Clean room attire was used by the handling personnel at all times. Except for the time when the units (MACS & MEB) were packed in their separate shipping containers, the units were protected from contamination by bagging made of Capran 518. When the wash plates and fallout plates were removed after unpacking the units at the GSFC, analyses indicated that the protected surfaces were in better condition than required by Mil Std 1246A level 100A.

The returned hardware was stored in a class 10,000 cleanroom at the GSFC. Thermal blankets were carefully cut and removed, then stored in display containers.

Post-Flight Analysis

The returned MACS unit and the MEB of the Coronagraph/Polarimeter offered an opportunity to examine the hardware in an effort to determine the causes of the failures and to study the effects of 50 months exposure to the Low Earth Orbit (LEO) environment. Natural orbital environments, such as solar ultraviolet radiation, charge particles, atomic oxygen, and micrometeoroids have been demonstrated to degrade thermal radiative properties like solar absorptance, and material mechanical properties such as elongation and tensile strength. More subtle effects on surface electrical properties have also been observed. Similar effects can be caused by self-induced environments, such as molecular and particulate contamination and by space debris carried into orbit (or created) by the launch vehicle, the spacecraft, or the payload.

The atomic oxygen and space debris effects were for the most part noted from experiments on STS-3 to 8. The contrasts in effects should provide a gauge to assess the reliability of Orbiter based testing of materials for higher altitude and longer term predictions.

HARDWARE ANALYSES

Main Electronic Box

The Main Electronic Box (MEB) provides the control and data handling functions for the Coronagraph/Polarimeter (C/P) instrument. The coronagraph creates an artificial total eclipse of the Sun by using a series of external disks to prevent direct sunlight from falling on the objective lens of the telescope. The C/P operated successfully taking pictures of Sun's corona for 5 months after launch before the first failure occurred. Fortunately, the failed microcircuit could be bypassed by ground software. The second failure in the electronics occurred about a month later, August 8, 1980, but the instrument was kept operating with only an occasional loss of data. The third electronics failure occurred in early September, but a solution to prevent unnecessary shutdowns was found by modifying the onboard software. The terminal failure in the electronics occurred on September 23, 1980, which rendered the instrument inoperative.

Subsequent post-flight analysis showed that all the failures occurred in one type of integrated circuit MM54C161J/883B manufactured by National Semiconductor. There were a total of 21 such microcircuits in use of which three failed. Electrical testing of two of the devices isolated the failures to short circuited transistors. The third device could not be tested because of damage during removal from the PC board. The short circuits were caused by defects in the gate oxide material as a result of time, temperature and applied bias voltage. Several oxide defects were also observed in the third device.

In addition, nine National Semiconductor MM54C161J microcircuits were removed from the MEB and tested. All nine devices had been operating properly on the MEB. Two of the devices failed marginally the initial electrical tests. One device failed catastrophically a static burn-in test at 125°C for 24 hours. The failures were similar to the in-orbit failures of the parts of the same type. Also the parts had similar defects in the gate oxide material, which indicates a lot related problem. There is some question about the burn-in of these devices before delivery. A proper burn-in is an accepted determinant of a parts reliability and will usually weed out weak devices.

Radiation Effects of Selected MEB Electronic Parts

A total of 29 parts of 9 different types were submitted to static, dynamic and functional electrical tests. The tested parts included flight parts and residual parts from the same date code lot as the original flight parts. The flight parts had been under power or bias for the first 8 months and about 10% of the time thereafter. These parts also had a year to anneal at ambient room temperatures on the ground.

The flight electronic parts showed no adverse effects due to the low Earth orbit radiation environment. Complex linear devices (μ A108A) begin to degrade at low doses and dose rates and will be susceptible to failure at higher altitudes and/or longer exposures. More detailed evaluation of electronic parts in orbit will be possible from the CRRES mission planned for 1986 and from the Space Station. Radiation detectors will then actually measure the environment experienced by electronic parts which will be simultaneously monitored for electrical performance.

Selected Hardware Studies

The evaluation was performed on the returned module retention system preload bolts, MEB honeycomb panel epoxy film adhesive and the thermal louver blade polyimide adhesive.

The two returned bolts were tested for yield strength and ultimate tensile strength. The tests showed no degradation in either category and the results were comparable to those of an unflown bolt.

The MEB honeycomb panel evaluation produced a conclusion that there was no degradation in room temperature bond strength of the epoxy film adhesive.

The returned louver polyimide blade adhesive was tested for lap shear strength and compared with unflown specimens. The results showed an average of 65% reduction in shear strength as compared to the unflown specimens. However, the reduction was not considered a severe one as evidenced by the bonding which survived the action and environments in good condition.

The returned thermal louver blades had red nodules on both sides of the blades. Evidence suggests that the red nodules represent regions of pure polyimide resin cured in space.

Infrared reflectometer measurements were performed on the returned louver blades and compared with those of unflown spare louver blades. The results showed no degradation of infrared reflectivity. Also the louver blade open and close temperature settings showed no degradation. The measured post-flight settings were well within the specification limits.

NASA Standard Inertial Reference Unit (DRIRU II)

The returned unit was the first production DRIRU II (S/N 1001) used as one of the subsystems of the Modular Attitude Control System (MACS). The DRIRU is a self contained, strapdown, three axis, dual redundant attitude rate sensing unit. Three orthogonally mounted, two-degree-of-freedom gyros and a triplication of electronic modules and power supplies are used to provide full operational capability with any two of the three channels. The gyros in the DRIRU II are Teledyne SDG-5 Dynamically Tuned Gyros.

The investigation concluded that gyro channel C failed because of an intermittent electrical short in the motor control logic. Because the failure occurred near the South Atlantic Anomaly, much effort was devoted to determine if the failure could have been caused by radiation. After extensive tests, it was concluded that radiation was not a probable cause of the failure. Subsequent tests at the GSFC Parts Analysis Laboratory showed that the failures occurred in three logic devices. Two of the devices failed because of an electrical overstress. As of this date, the cause of the overstress has not been determined. The third device most likely failed because time, temperature, and an out-of-tolerance logic supply voltage created a short at a latent defect of the device. The defect apparently was caused by an irregularity in the manufacturing process. (See 'DRIRU II Electronics Parts Analysis.')

After the system was reassembled with two substitute electronic modules, a full series of tests were performed to evaluate the stability of the unit over the full operating temperature range. Also the repeatability of the parameters as compared to the delivered state was investigated. The test series were designed to repeat the complete 1978 acceptance tests.

The physical condition of the system was excellent with no apparent materials degradation. There was no evidence of system performance degradation due to operational and other environments. The system had excellent long-term stability of performance parameters over the launch, orbital operation and retrieval environments during a 74-month period.

There was no measurable degradation of the shock/vibration isolators as evidenced by the excellent alignment stability of the gyro axes through launch environments and over an extended time period.

There was no evidence of structural or mechanical changes and no apparent outgassing or degradation of exposed surfaces.

Examination at Teledyne found that the gyro ball bearings showed no excessive wear to raceways, balls, or retainers. However, there was some dark colored, viscous residue mainly in the ball tracks and the retainer ball pockets. (See 'DRIRU Bearings and Lubricant' for summary of GSFC analysis.)

DRIRU Bearings and Lubricant

One of the DRIRU gyroscopes was disassembled and the bearings were returned to GSFC for examination. The gyroscopes had been running continuously in orbit for 4 years at 6000 RPM.

The bearings showed some wear in the form of tiny pits and scratch-line deformations. Numerous tiny particles were observed clinging to the bearing parts after the case and the hysteresis ring were removed. The particles had originated from the pits of the bearing races and the balls.

The lubricant for the bearings is contained in the retainers which are made from a porous, phenolic material. Examination showed that the bearings were lubricated.

The conclusion was that the bearings showed little wear and had a sufficient amount of lubricant left to perform without problems for their predicted life of 5 years.

DRIRU II Electronics Parts Analysis

The failed part in the gyro channel C of the DRIRU II unit was an RCA CD4017AK microcircuit, a decade counter. The part was submitted to the GSFC Parts Analysis Laboratory for failure analysis. The tests determined that the failure was due to a short circuit through an oxide defect underneath the output metalization. The defect was the result of a manufacturing irregularity during processing.

Two other devices, an RCA CD4049AK and a CD4081BK, both microcircuits of the DRIRU II gyro motor control logic, were submitted to the GSFC Parts Analysis Laboratory for failure analysis. Both devices had failed in flight due to a fused open die metalization track. A pin on each of the devices was open circuited to all other pins. The fused open metalization was a result of electrical overstress.

Remote Interface Unit

The Remote Interface Unit (RIU) was designed and built by the Fairchild Space Company. The first application of the RIU was on the SMM spacecraft. The unit provides two-way communications between electronic packages on the spacecraft and a central command and telemetry unit (CU) which decodes and distributes commands and generates telemetry formats. The CU communicates with the On-Board Computer (OBC) through the Standard Interface and with the ground via the RF equipment.

The standard MACS module carries two redundant RIU's which have three operational modes: 'OFF,' 'Standby 1,' and 'Standby 2.' The last two are sub-modes of the 'ON' mode. During the flight, Unit A was operating in the full 'ON' mode (Standby 2). Unit B was operating in the 'OFF' mode (only Bus Receiver/Control Logic and Power Converter continuously powered). Throughout the flight, no malfunctions of the Units were indicated.

The RIU's were returned to Earth with the MACS module and Unit B underwent a post-flight engineering evaluation from December 1984 until April 1985. The pre-flight tests were performed in 1979.

Post-flight external and internal visual inspection revealed no degradation. Besides the visual inspection, RIU B underwent two other kinds of engineering tests. Automated test equipment was used to qualify the unit as a whole ('GO - NO GO'). In the other test, a parametric test,

each parameter was evaluated separately. The parametric evaluation included user telemetry interface circuitry (active and passive analog linearity), phase lock loop performance, pulsed output current and width, serial digital commands, serial digital telemetry, and power dissipation.

The tests were performed at ambient temperature, -20°C , and $+60^{\circ}\text{C}$. The cold and hot temperatures are the qualification limits. All parameters evaluated were found to be within specification. When compared to pre-flight test data, in many categories the post-flight data showed some improvement. The test results qualify the unit for reuse in another mission.

Three Axis Magnetometers

Magnetometers are used to sense spacecraft attitude with respect to Earth's magnetic field. Two Three Axis Magnetometers, designated as the primary and secondary magnetometer, are part of the standard MACS module. The magnetometers are fluxgate magnetometers which produce three analog signals proportional to the magnetic field components along their input axes.

The magnetometers together with the magnetic torquers provided an important function during one part of the SMRM when they were used to stabilize the spacecraft's attitude. Only one of the magnetometers was used during the SMM. The other, serving as a backup unit, was never used because the primary unit did not malfunction.

After the magnetometers were returned to the manufacturer, they were subjected to the same performance tests which were performed before the flight. The post-flight tests showed that the magnetometers still satisfied the original specification requirements. The post-flight test data nearly duplicated the pre-flight data.

Standard Reaction Wheels

The four Standard Reaction Wheels are components of the MACS module and are used for attitude control and stabilization. They are essentially flywheels and work on the principle of exchanging angular momentum with the spacecraft body. Normally, three of the wheels are aligned with the principal axes of the spacecraft. The fourth, a redundant skewed wheel, is used to replace any of the orthogonal wheels in case of a wheel failure. In normal operation it is run at a bias speed to keep the other three wheels away from zero speed and to maximize bearing life.

After the return of the wheels to the manufacturer on January 24, 1985, they were subjected to visual examination, preliminary electrical checks, performance tests at ambient, hot and cold temperature environments, and internal pressure measurements. One wheel, which showed a slightly deteriorated performance, was selected for teardown.

Visual examination found the wheels in good condition. Preliminary electrical tests, continuity, bonding, and isolation were satisfactory. The bonding resistance for two of the four units was slightly above the requirements but was not considered excessive.

The internal pressure measurements indicated that the pressures were far below atmospheric, confirming that the vacuum seal was still intact.

All four units successfully passed the performance tests with the exception of the 500 RPM torque noise test using a .1 rad/sec high pass filter. However, the units met the torque noise test with the 0.3 rad/sec high pass filter in the test circuit.

Individually, two of the units showed very similar performance results as compared to pre-flight tests. One unit showed decreased bearing drag torques and extended coastdown times. Another unit had a 45% increase in drag torques and reduced coastdown times, although it met all requirements. It had been exposed to a no-load overtemperature (60°C) for approximately 3 hours due to a software problem.

Teardown analysis of the overtemperature-exposed unit showed an 'as new' appearance of the internal components and surfaces. The lubrication analysis showed a greater lubrication loss in the floating cartridge system than in the fixed cartridge system. An investigation package including contamination wipes, lubricant samples, bearing components and photographs of some items was sent to NASA GSFC for analysis.

NASA Standard Star Trackers

The MACS module includes two Fixed Head Star Trackers (FHST) which are used together with the inertial reference unit and the on-board computer to determine and maintain the spacecraft's attitude with the required accuracy. Because the star tracker is a very sensitive instrument, its image dissector tube must be adequately protected from high level light sources such as the Sun. This was done by providing light shades and a shutter operated by a bright object sensor. At the time of the grappling attempt, the trackers and the shutter were powered-off. They remained in this condition until recovery.

The cathode of the image dissector tube detector was extensively damaged by the Sun following the attempts by the astronaut to dock with the spacecraft using the Manned Maneuvering Unit (MMU). The spacecraft was tumbling out of control for many hours before it was finally stabilized so that it could be grappled by the Remote Manipulator System. The tumbling exposed the sensitive cathode to the Sun causing permanent degradation. This prevented proper operation of the tracker after return to Earth and made comparison with pre-flight characteristics impossible. Otherwise, the tracker functioned nominally during testing at the GSFC and the Kennedy Space Center.

The trackers performed flawlessly during the Solar Maximum Mission. Because of inconsistencies in the flight data, some questions arose about the position calibration and alignment. The inconsistencies were attributed partly to a new calibration method and partly to the scarcity of flight data.

During the period from the spacecraft failure to just prior to recovery, the trackers were used occasionally, but were always adequately protected by the shutter.

The tests discovered that the 'tracks' made by the Sun across the cathode were insensitive regions which could not produce an adequate signal to track a star. It was also discovered that the lens of tracker S/N 001 had on its surface large peelings from the lens coating.

MATERIALS ANALYSES

Materials analyses have been performed on materials retrieved from the Solar Max thermal control system, and on various impact particles that were imbedded in the thermal control materials. The materials analyzed were aluminized Kapton and Mylar, and Dacron netting from the multilayer insulation (MLI) blankets, and silver Teflon used on a thermal radiator and as trim on louver assemblies.

MLI is used to thermally insulate various spacecraft components. The portions of the MLI returned to Earth are primarily from the blankets used to insulate the MACS. Other pieces are from the blanket that covered the Main Electronics Box of the Coronagraph/Polarimeter. Aluminized Kapton is used for the top layer of the MLI. Other layers of the MLI are aluminized Kapton (MACS) or aluminized Mylar (MEB) separated by Dacron netting. A summary of the analyses is reported in the following section.

Silver Teflon is used on spacecraft components to increase the thermal radiation performance of exposed surfaces. The silver Teflon removed from the MACS is from the thermal louver assembly.

The chemistry of various impact particles, both natural and man made, has been analyzed. These impact particles were found imbedded in the MLI and in the thermal louvers. A summary of these analyses is reported in section 'Impact Particles.'

Insulation Materials

There are two different forms of MLI insulation blankets returned to Earth from the Solar Max. In both forms, the top layer is made of Kapton with an aluminum layer vapor deposited on the inside surface. The bottom layer, the layer facing the spacecraft systems, is also made of aluminized Kapton, with the aluminum facing the inner layers of the MLI. In both forms, every layer is separated and supported by a Dacron mesh.

The MLI blankets that covered the MACS are composed entirely of aluminized Kapton. The top and bottom layers are made of 2 mil Kapton. There are six to ten inner layers of 1/4 mil Kapton, aluminized on both sides. The MLI taken from the Main Electronics Box is made of aluminized Kapton and aluminized Mylar. The top layer is 3 mil Kapton and the bottom layer is 1 mil Kapton. There are fifteen inner layers of 1/4 mil Mylar, aluminized on both sides.

The MLI materials have been analyzed by various investigators primarily using optical microscopes and Scanning Electron Microscopes (SEM). In addition, infrared spectroscopy was used to detect potential changes in the Kapton polymer structure, and a solar reflectometer measured solar absorptance. Measurements have been made of Kapton samples by exposing them to low pressure atomic oxygen discharge, to a microwave discharge rich in ultraviolet and to a 3 Kv argon ion beam under high vacuum conditions.

Aluminized Kapton Degradation

The most apparent change in the MLI is the dull appearance of the top Kapton layers as compared to the shiny surface of new Kapton samples. Thus, studies of the MLI samples have concentrated on a possible degradation of the Kapton material. Observations show the outer Kapton surface to be eroded, thereby creating the dull appearance. This finding is similar to the results of tests performed on-orbit during the STS-8 mission. Findings on STS-8 as well as SMM indicate that changes in the Kapton are most likely due to the presence of atomic oxygen.

Degradation of the Kapton surface appears to be greater in areas cleaned during preflight operations with an alcohol based solvent. The same study has revealed tunnel-like substructures under the Kapton surface in the region of the interface between the alcohol wiped and non-wiped areas. It is believed that this is caused by the diffusion of atomic oxygen through the surface and reaction with the underlying polymers. Associated with the thin tunnel surfaces are small holes believed to be the result of atomic oxygen and UV interaction.

Infrared spectroscopy indicates that while there is obvious degradation in the Kapton, the actual polymer structure has not changed. Measurements of thickness of the top Kapton layer from the front of the MACS indicate that the Kapton suffered mass losses ranging from 0.54 percent to 31.4 percent. One sample from the bottom of the MACS suffered a 41 percent mass loss.

In order to more specifically determine the cause of the Kapton mass losses, Kapton samples were exposed to a variety of atomic oxygen sources, ion sources and ultraviolet (UV) sources. These tests suggest that the greatest surface etching is due to a combination of atomic oxygen coupled with exposure to UV. The angle at which the surface is exposed to these elements is probably significant.

Studies of the back side of the top Kapton layer from the MEB have revealed areas where the deposited aluminum is missing. These areas include scratches most likely caused by the handling of the MLI. Other areas are pinhole in size in a regular pattern, causing the illusion of penetrations in the transparent Kapton layer. These transparent pinholes appear to correspond with the knots in the underlying Dacron mesh, leading to the speculation that the knots have rubbed the aluminum off. While some surface holes appear to be the result of atomic oxygen and UV interaction or the illusion of transparent Kapton, other surface holes appear to be the result of particle impacts. Not all of these holes show a total penetration. The subject of particle impacts is discussed in section 'Impact Particles.'

The significance of the Kapton degradation to spacecraft designers lies in potential changes in the MLI performance. Measurements have been made of solar absorptance of the Kapton material. The solar absorptance of the Kapton material is typically 0.37 to 0.41 prior to on-orbit exposure. The post-flight measurements indicate that the solar absorptance of the SMM Kapton samples has increased by 0.03 to 0.04. This increase is probably due to the optical scattering effect of the degraded Kapton surface. This small increase should have little effect on the performance of the MLI insulation blankets. However, greater degradation of the top Kapton layer that may significantly affect the performance of the MLI, cannot be ruled out in future missions.

Inner Layer Material Degradation

An examination has been made of the aluminized Mylar films and the Dacron mesh from the inner layers of the MLI which was used to cover the MEB. Optical microscopes of up to 400 power have revealed no erosion in these materials. The only apparent damage to these materials was caused by the impact particles (see 'Impact Particles').

Silver Teflon

Silver Teflon is a thin Teflon film on which a layer of silver is vapor deposited. A layer of Inconel is deposited on the silver for protection from the environment. The Teflon film used on the SMM spacecraft is 5 mils thick with a 1500 Angstrom thick layer of silver and a 100 Angstrom thick layer of Inconel. Silver Teflon is used in the thermal protection system to increase the thermal radiative performance of various exposed surfaces. The film is normally applied so that the Teflon side is exposed to the orbit environment.

All silver Teflon samples given to investigators for analyses were exposed to the orbit environment on the Teflon side. Some material was also exposed on the silver/Inconel side, due to its unique application as trim on the MACS louver system (see 'Post-Flight Photographs'). It has been found in both cases that the surfaces were affected by the long duration exposure.

The silver Teflon has been analyzed, as in the case of aluminized Kapton, primarily with optical and Scanning Electron Microscopes. The absorptance of exposed samples has been measured and Energy Dispersive X-Ray Analysis (EDAX) has been used in conjunction with SEM to detect the presence of trace elements. Some samples have been tested with exposure to low pressure atomic oxygen discharge, and other samples have been subjected to tensile strength testing.

Teflon Surface Degradation

Observations of Teflon exposed surfaces show evidence of a reaction to the orbit environment. Unexposed Teflon is smooth in appearance, while the exposed Teflon has been described as having a 'bristle-like' reaction pattern.

The bristle-like structures in exposed Teflon have also been described as cone-like structures. These adjacent cones are easily visible in magnified views of Teflon samples exposed to atomic oxygen and UV. The cause of this Teflon degradation has been studied by exposing a new sample of silver Teflon to atomic oxygen alone. Although the Teflon surface was no longer smooth, it did not have the deep cone structures of the SMM samples. There is speculation that a combination of atomic oxygen fluence and UV exposure will cause a more severe Teflon reaction than atomic oxygen alone, resulting in the cone structures.

Teflon is a fluorocarbon polymer. It has been found that exposure to atomic oxygen depletes Teflon of fluorine. This is evidenced by an increase in the detected carbon/fluorine ratio. Further study is required to determine if longer on-orbit exposures would result in any further breakdown of Teflon.

Silver/Inconel Surface Degradation

The samples exposed on the silver/Inconel surface also show reaction to the orbit environment. Reactions range from cracks in the Inconel layer to a total depletion of silver and Inconel. In the later case, the exposed Teflon surfaces of some samples have developed the cone structures discussed earlier.

Many samples show the whole range of reactions. Between the extremes, a grain pattern of silver/Inconel was formed. Nearing the silver depleted regions, the grain bodies become smaller with the pattern of cracks more widespread.

The cracks in the Inconel surface may be due to temperature cycling under varying orbit conditions. Other evidence has indicated that the reaction of Inconel with atomic oxygen causes removal of the Inconel layer. Silver oxide deposits have been found on sample surfaces. The silver oxide may have come to the Inconel surface through the apparent cracks after the exposed silver reacted with atomic oxygen. Exposure tests indicate that the silver/Inconel depletion may be caused by exposure to atomic oxygen alone, or to a combination of atomic oxygen and UV. This suggests a mechanism for the loss of Inconel and silver. First, the atomic oxygen and temperature cycling causes the loss of Inconel and the formation of cracks. Silver oxide (and perhaps silver peroxide) forms and then flakes off in response to temperature cycling. This cycle continues until Teflon is exposed, and the Teflon reacts to atomic oxygen and UV resulting in the formation of the cone structures.

Tensile strength tests have shown that samples with eroded surfaces have no resilience. Abrupt breaks appear to have occurred in the same direction as thermal expansion/contraction. It was found that the tensile modulus of silver Teflon exposed to atomic oxygen decreased by about 15%, while the modulus of samples exposed to atomic oxygen and UV decreased by about 30%.

Measurements have been made of solar absorptance of the returned Teflon material. The solar absorptance of the Teflon film is typically 0.05 to 0.07 prior to on-orbit exposure. The Teflon samples having the greatest absorptance change, appear to be those exposed to the orbit environment on both sides of the film, and those contaminated by spacecraft outgassing. In these samples, the solar absorptance has increased by as much as 0.22 to 0.29. This large change in absorptance indicates a potentially large change in the performance of the Teflon film. The solar absorptance of Teflon film samples with non-eroded silver/Inconel surfaces had increased by a maximum of 0.04.

Impact Particles

A survey of approximately one-half square meter of MLI has revealed over 1500 impact sites. Of these, 432 impacts resulted in craters in the Kapton greater than 40 microns in diameter. In the 75-micron thick Kapton (MEB), craters greater than 100 microns in diameter are

perforations through the Kapton layer. In the 50 micron Kapton (MACS), craters larger than 70 microns in diameter penetrate through the Kapton. When the survey totalled approximately 0.7 square meters of Kapton surface, about 160 impact craters penetrating the Kapton layer were found.

A number of particles completely penetrated all of the MLI layers. One particle penetrated the MLI near a star tracker, making an impression in the star tracker's aluminum shield. Approximately half of the particles that impacted the MACS louvers penetrated the first of the two aluminum sheets, as evidenced by impressions in the second sheet.

Chemical analyses of a number of the impacts has shown that sources of the particles fall into one of four groups. The first group of particles is meteoric material, evidenced by the elements silicon, magnesium, iron, calcium, aluminum with minor amounts of iron-nickel sulfide. The second group of particles is paint particles. This is characterized by titanium and zinc, and the chemistry includes potassium, silicon, aluminum and chlorine. The third group of particles is aluminum droplets, probably from the MLI. The fourth group of particles is waste particles as evidenced by one impact that penetrated three layers of MLI. The chemistry includes sodium, potassium chlorine, phosphorus and minor amounts of sulfur. Investigators believe that this particle may have come from the Orbiter's waste management system.

Two of the large impacts have been investigated in more detail. In both cases, the impact particle apparently disrupted upon impact with the outer Kapton layer of the MLI. The disrupted material was sprayed inward in a cone shaped pattern, lodging on the second layer of the MLI.

In the case of the first impact particle, a small portion of disrupted material penetrated the second layer of the MLI. This impact particle caused a hole 280 microns in diameter with a raised rim. The second MLI layer has a ring of tiny holes and craters surrounding a roughed up area of about 5 millimeters in diameter. Particles from the back of the first layer and from the front of the second layer have been analyzed showing that about 75% are fragments or melted droplets of Kapton. Of the non-Kapton particles, most are composed of magnesium, silicon and iron. Next in number were aluminum particles. Investigators believe that the aluminum is derived from the MLI. Other particles are composed of iron, sulfur and nickel.

The second reported impact particle caused a crater 355 microns in diameter with a raised rim in the Kapton layer. The second layer has a wedge shaped pattern of concentric, elongated holes. Particles of the second impact are composed primarily of iron, sulfur and nickel.

INTRODUCTION

SMM FLEW FOUR YEARS IN LEO PRIOR TO REPAIR

- LAUNCHED TO 310 NM
- REPAIRED AT 265 NM

SMRM RESULTED IN THE RETURN OF:

- ATTITUDE CONTROL SUBSYSTEM MODULE
- CORONOGRAPH/POLARIMETER MAIN ELECTRONICS BOX

THIS PRESENTATION DESCRIBES FLIGHT HISTORY, OBSERVATORY ELEMENTS AND ATTITUDES, RECOVERED HARDWARE, AND STUDIES PERFORMED ON THE RETURNED HARDWARE, ELECTRONICS, AND THERMAL MATERIALS

SMM FLIGHT HISTORY

LAUNCH TO 310 N.M.

FEBRUARY 1980

3-AXIS STABILIZED
SUN-POINTING

ATTITUDE CONTROL FAILURE

NOVEMBER 1980

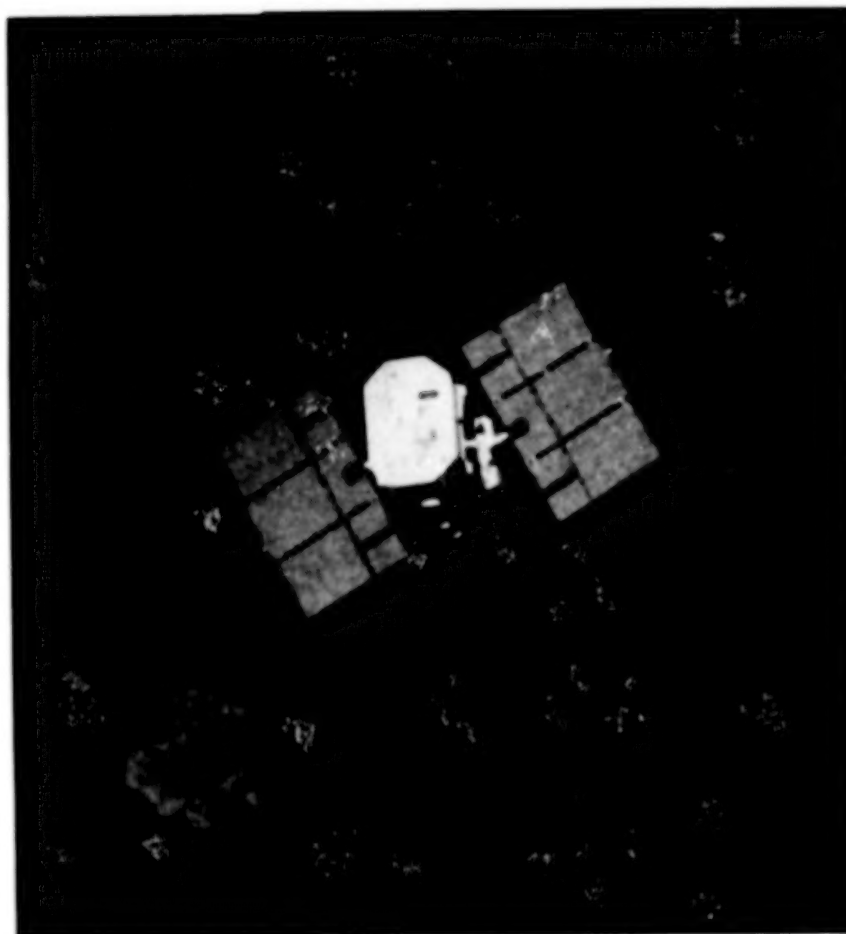
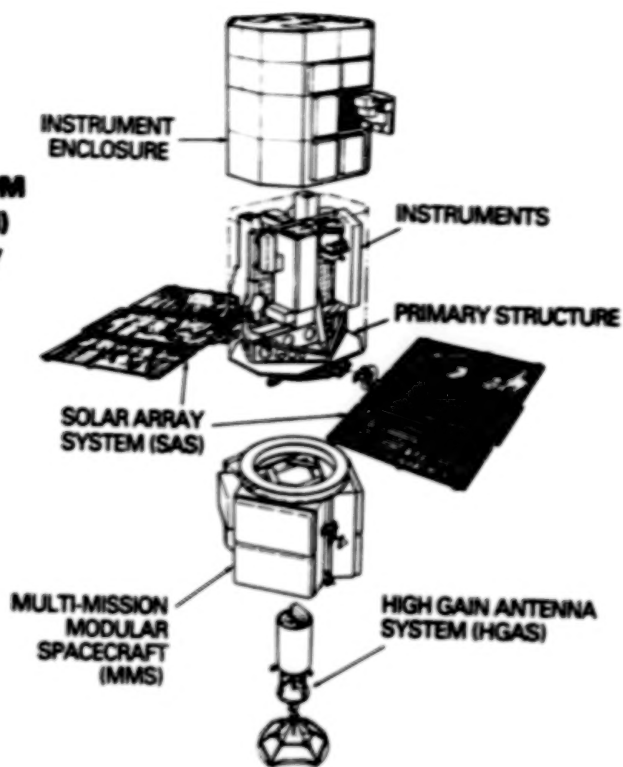
WOBBLE UP TO 15° OFF SUN
ROTATING AT 1°/SEC

SMM REPAIR AT 265 N.M.

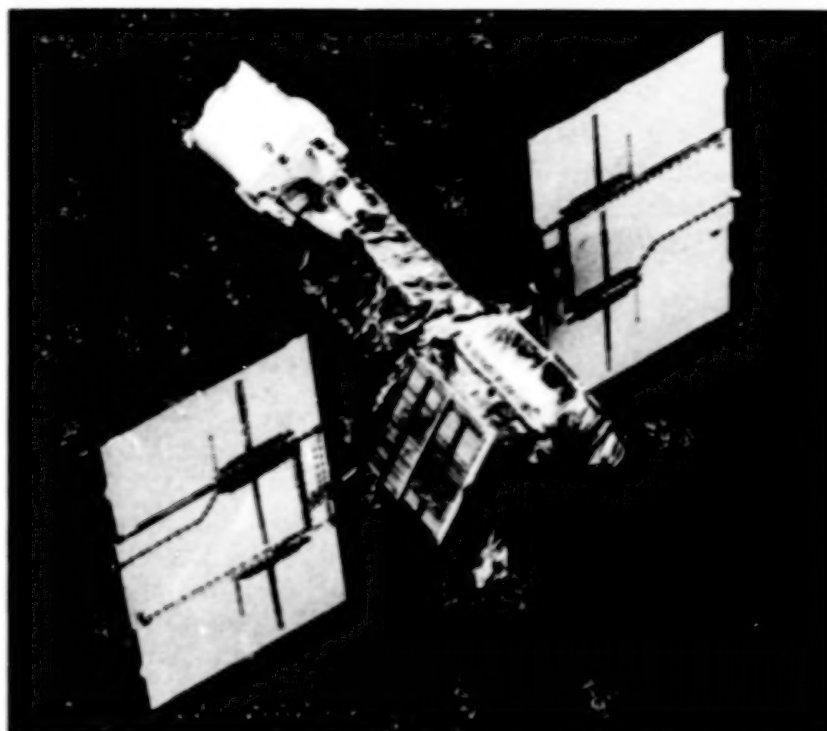
APRIL 1984

ACS, MEB RETURNED

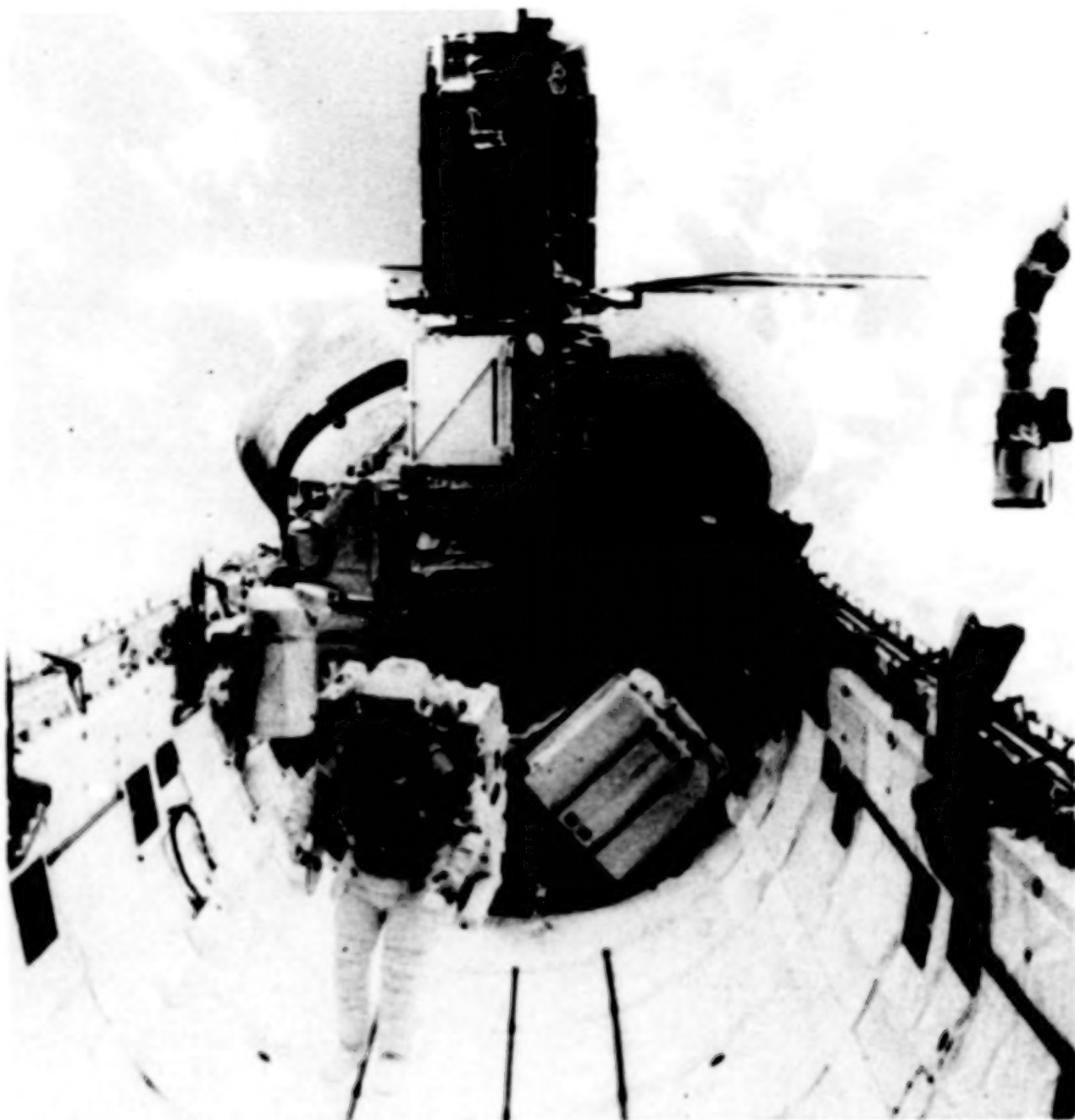
**SOLAR MAXIMUM
MISSION (SMM)
OBSERVATORY**



SMM as seen by the Sun in the post-failure attitude (15° wobble).



View of MACS module after unsuccessful dock attempt. Most louvers are closed. Degradation of the bottom-facing trim (Teflon) can be seen.



SMM in-bay after repairs completed.

DEGRADATION STUDY WORKSHOP CHRONOLOGY

MAY 1984: ISSUED INVITATION ON ALL AEROSPACE COMPANIES,
NASA CENTERS, DOD ORGANIZATIONS AND UNIVERSITIES

JUNE 1984: FIRST WORKSHOP MEETING WITH INTERESTED
PARTICIPANTS

- RESEARCH TASKS PROPOSED AND DISCUSSED
- RESPONSIBILITIES ASSIGNED
- BEGAN DISTRIBUTION OF MATERIAL AND HARDWARE

JULY 1984 TO
APRIL 1985: RESEARCH INVESTIGATIONS CARRIED OUT BY WORKSHOP
PARTICIPANTS

MAY 1985: STUDY RESULTS PRESENTED BY PARTICIPANTS AT GSFC

JUNE/JULY 1985: FINAL DETAILED REPORT SUBMITTED BY EACH
PARTICIPANT

SMM STUDIES SUMMARY

SURFACE MATERIAL STUDIES

<u>PRINCIPAL INVESTIGATOR</u>	<u>ORGANIZATION</u>	<u>SUBJECT</u>
W. STUCKEY	AEROSPACE	TEFLON ANALYSIS
R. FRISTROM	APPLIED PHYSICS LAB	KAPTON OXYGEN EROSION AND OTHER SURFACE EFFECTS
R. LIANG	JPL	TEFLON BULK PROPERTY DEGRADATION BY OXYGEN
A. WHITAKER	MSFC	KAPTON EROSION RATES AND MECHANISMS
M. MCCARGO	LOCKHEED	TEFLON, KAPTON SURFACE AND BULK EFFECTS
B. SANTOS	LANGLEY	TEFLON, KAPTON SURFACE CHEMISTRY, THERMAL EFFECTS
D. KESSLER	JSC	BLANKETS, LOUVERS SPACE PARTICLE IMPACTS
J. PARK	GSFC	TEFLON, KAPTON, CONTAMINATION

SMRM STUDIES SUMMARY

PARTS COMPONENTS HARDWARE

<u>PRINCIPAL INVESTIGATOR</u>	<u>ORGANIZATION</u>	<u>SUBJECT</u>
C. UPTON	SHONSTEDT	MAGNETOMETER ELECTRICAL AND MAGNETIC PERFORMANCE
H. FRANKEL	FAIRCHILD	RIU ELECTRICAL; MEM; HONEYCOMB, LOUVERS MECHANICAL
J. RITTER	TELEDYNE	DRIRU ELECTRICAL, MECHANICAL PERFORMANCE
J. UBER	GSFC - METALLURGY	DRIRU BEARING WEAR AND OIL DEGRADATION
R. LEE	GSFC/HAO	MEB BOX FAILURE ANALYSIS
A. ANSTEAD	GSFC - PARTS	DRIRU AND MEB PARTS MICROSCOPIC ANALYSIS
R. MAURER	APL	COMPARISON OF IRRADIATED "NEW" PARTS TO FLOWN PARTS
C. SUTTER	SPERRY	WHEEL TORQUE AND POWER STUDIES; MEASURE LUBRICANT LOSS
P. NEWMAN	GSFC - ACS	STAR TRACKER SENSITIVITY AND ELECTRICAL PERFORMANCE

VERIFICATION OF IN-FLIGHT ANOMALIES

POST-LANDING ACS FUNCTIONAL TEST

- DETECTED OPEN FUSE ON 28V SUPPLY TO DRIRU CHANNEL C
- OBSERVED SYMPTOMS OF FUSE FAILURE THAT DISABLE REACTION
WHEELS

C/P MEB - BAD LOT OF NATIONAL MM54C161 MICROCIRCUITS

- 21 OF THESE PARTS IN MEB, OF WHICH 3 FAILED ON-ORBIT
- DEFECTS IN GATE OXIDE MATERIAL CAUSED TRANSISTOR SHORTS

DRIRU CHANNEL C FAILURE ANALYSIS

- MANUFACTURING DEFECT CAUSED SHORT IN A RCA MICROCIRCUIT
- ELECTRICAL OVERSTRESS CAUSED FAILURE OF TWO OTHER RCA PARTS

OTHER ELECTRONIC BOXES

ACS MAGNETOMETER AND REMOTE INTERFACE UNIT SHOWED NO ELECTRICAL DEGRADATION

DRIRU CHANNELS A & B HAD NO SIGNIFICANT CHANGES IN MECHANICAL OR ELECTRICAL PERFORMANCE

STAR TRACKER ELECTRONICS HAD NO CHANGES IN PERFORMANCE DETECTOR CATHODES DAMAGED DURING REPAIR MISSION

RADIATION EFFECTS ON PARTS

DYNAMIC AND FUNCTIONAL TESTS PERFORMED ON 27 PARTS OF 7 DIFFERENT TYPES

- COMPARISON OF FLOWN PARTS TO RESIDUAL INVENTORY
- SOME RESIDUAL PARTS WERE IRRADIATED AND RETESTED

NO ADVERSE EFFECTS FOUND ON 6 PART TYPES, INCLUDING CMOS

COMPLEX LINEAR DEVICE (LM 108 OP AMP) SHOWED SLIGHT RADIATION DEGRADATION

- WOULD BE SUSCEPTIBLE TO FAILURE AT HIGHER DOSES

BEARING AND LUBRICATED COMPONENTS

DRIRU BEARING SHOWED MINIMAL WEAR AFTER TEN BILLION REVOLUTIONS

- SOME SCRATCHES AND FINE METAL PARTICLES
- GYRO MECHANICAL PERFORMANCE SHOWED NO DEGRADATION

ALL FOUR REACTION WHEELS REMAINED WITHIN SPEC

- THREE WHEELS SHOWED NO DEGRADATION IN DRAG TORQUE

ROLL-AXIS WHEEL DRAG TORQUE INCREASED BY 45 PERCENT

- HAD EXPERIENCED TEMPERATURE > 60°C DURING FLIGHT
- DISASSEMBLY SHOWED 10 PERCENT LUBE LOSS AFTER 4 YEARS IN SPACE

DEGRADATION OF MECHANICAL PROPERTIES

MODULE PRELOAD BOLTS HAD NO CHANGE IN REMOVAL TORQUE

- NO DEGRADATION IN YIELD OR ULTIMATE STRENGTH

MEB HONEYCOMB PANEL ADHESIVE BOND STRENGTH WAS UNCHANGED

ACS LOUVERS SHOWED NO CHANGES IN ACTUATION TEMPERATURES

SPACE PARTICLE IMPACTS

1500 PARTICLE IMPACTS FOUND IN 1/2 M² OF BLANKET

- 10 PERCENT OF PARTICLES PENETRATED ONE LAYER OF KAPTON

SPACE DEBRIS IMPACTS OUTNUMBERED MICROMETEORIDS BY 2 TO 1

- PAINT PARTICLES, ALUMINUM, WASTE PARTICLE
- ONE PARTICLE PENETRATED 17-LAYER BLANKET

ALUMINUM LOUVER BLADES (1M²) HAD 64 PENETRATIONS

- NO PARTICLES PENETRATED BACK SIDE OF BLADE

JSC SPONSORED CONSORTIUM HAS BEEN STUDYING REMAINDER OF MATERIAL

OXYGEN/UV EFFECTS ON THERMAL SURFACES

KAPTON MASS LOSS SIMILAR TO STS EXPERIENCE

- EROSION PATTERN MUCH SMOOTHER
- MATERIAL STRENGTH UNAFFECTED
- SOLAR ABSORPTANCE INCREASE BY 10%

REACTIONS OF UNSUPPORTED SILVER TEFLON

- THERMAL CYCLING CAUSED CRACKS IN SILVER LAYER
- NEGLIGIBLE EFFECT ON THERMAL PROPERTIES WHEN SILVER IS NOT EXPOSED
- SILVER WAS REMOVED BY OXYGEN REACTION WHEN EXPOSED

TEFLON SIDE ALSO EXPERIENCED SOME EROSION

- MUCH MORE EROSION WHEN EXPOSED TO UV
- SOME EROSION DUE TO REACTION OF HYDROCARBON IMPURITY



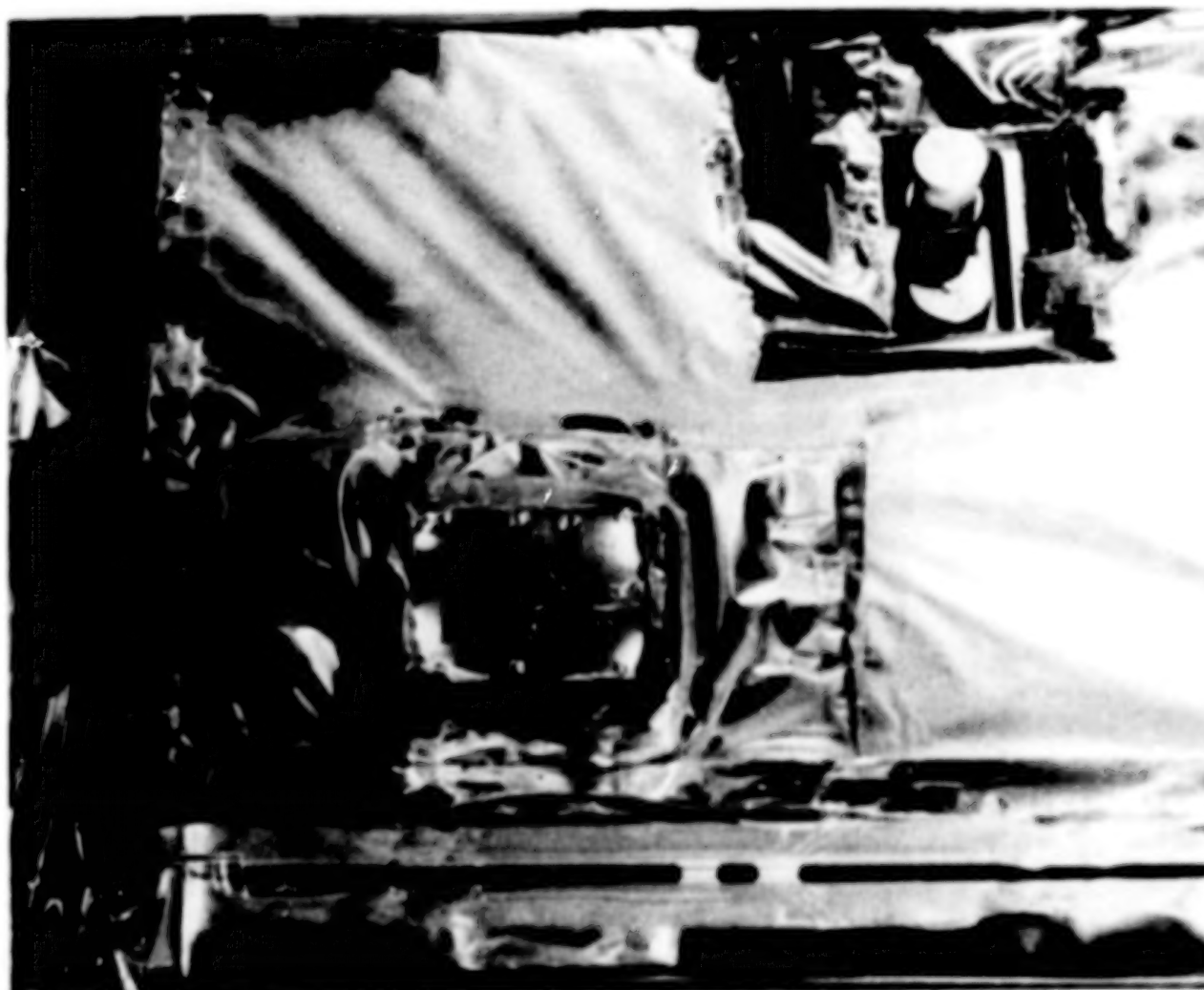
Close up of the degraded silver Teflon louver trim on the "bottom" side to solar radiation and the atomic oxygen fluence on the silver/Inconel side of the silver Teflon.

SELF-INDUCED CONTAMINATION

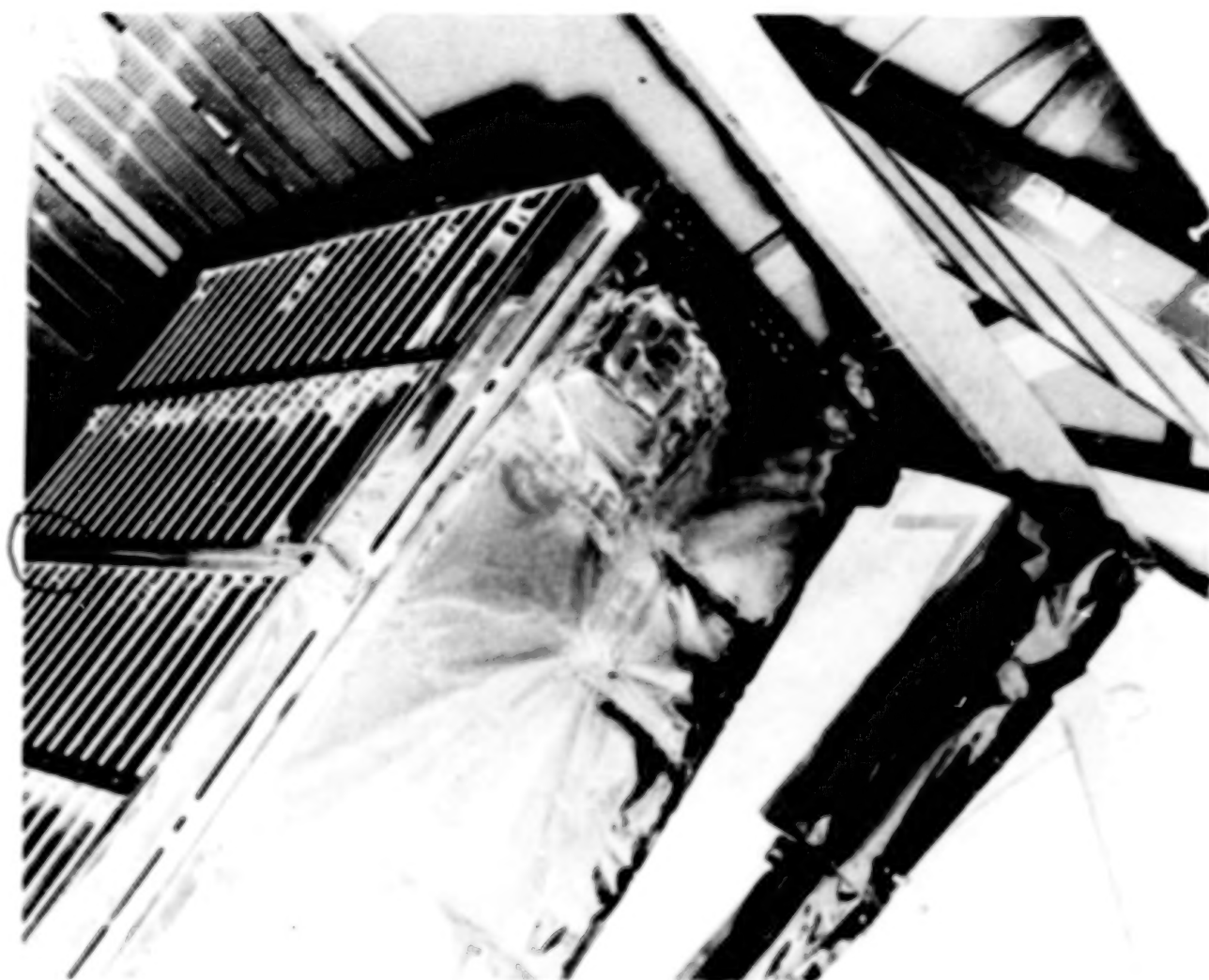
ACS MODULE SAW FOUR THERMAL VAC CYCLES AT MODULE QUALIFICATION
- TEMPERATURE 10°C MORE EXTREME THAN FLIGHT

WHITE SUBSTANCE ON FINE SUN SENSOR, COMPOSITION UNKNOWN
- CONDENSED ON COLD SURFACE FROM WARM INTERIOR OF MODULE

SILICA BASED RESIDUE ON LOUVER FRAME NEAR MODULE VENT
- OUTGASSING DEPOSIT FROM OIL, THERMAL GREASE, STAKING, ETC.
- SIMILAR CONDENSATE AROUND VENT BETWEEN STAR TRACKERS



White powder residue from unintentional vent on sun sensor radiator.



Silica based residue (circled) on louver frame.

CONCLUSION

IN-FLIGHT ANOMALIES WERE VERIFIED: OTHER ELECTRONICS BOXES DID NOT DEGRADE

RADIATION DEGRADATION WAS DISCOVERED IN ONE PART TYPE

CYRO AND WHEEL BEARINGS IN GOOD SHAPE

THE EFFECT OF SPACE PARTICLE IMPACTS MUST BE CONSIDERED IN DESIGN OF FUTURE SPACECRAFT

EXPERIENCE INDICATED A NEED FOR AWARENESS OF UNINTENTIONAL VENTING IN CONTAMINATION CONTROL DESIGN CONSIDERATIONS

COMPARISON OF SMM AND STS RESULTS DEMONSTRATED VALIDITY AND LIMITATIONS OF PREDICTING LONG-TERM LEO EFFECTS FROM STS BASED STUDIES

**EnviroNET: SPACE ENVIRONMENT
FOR STRATEGIC DEFENSE INITIATIVE EXPERIMENTS**

**MICHAEL LAURIENTE
NASA GODDARD SPACE FLIGHT CENTER, MD 20771**

INTRODUCTION

EnviroNET is a service/facility intended to provide users with on-line, dial-up technical information concerning environmental conditions likely to be encountered by instruments and experimental arrangements carried aboard the Space Shuttle and the Space Station Freedom. The database also has wider applicability for information on environments encountered by other satellites in both low altitude and high altitude (including geosynchronous) orbits. This information--which is DISTINCT FROM "REQUIREMENTS"--is intended to help scientists and engineers design equipment to operate successfully in the (somewhat hostile) space environment (fig .1).

ENVIRONET

- CENTRALIZED COMPUTER-BASED INFORMATION ON NATURAL AND INDUCED ENVIRONMENTS OF SHUTTLE AND SPACE STATION
- BASED ON MEASURED DATA (SHUTTLE) AND EMPIRICAL MODEL VALIDATED BY DISCIPLINE PANELS
- FOR SCIENTISTS AND ENGINEERS USE IN THE DESIGN AND DATA ANALYSIS OF FLIGHT HARDWARE
- MAINTAINED CURRENT BY NASA THROUGH COOPERATIVE EFFORTS OF INDUSTRY, OTHER GOVERNMENT AGENCIES, THE EUROPEAN SPACE AGENCY, ACADEMIA, AND THE NASA COMMUNITY

Figure 1

EnviroNET incorporates at present a combination of expository text and numerical tables amounting to about two million characters (bytes), plus FORTRAN programs that model the neutral atmosphere, magnetic field and ionosphere. This text is under continuous review, correction, and augmentation by ten subpanels of technical experts: one for each of the database's main topics. The information contained in EnviroNET is shown in Figure 2. The aim is to keep information as accurate and current as possible. The EnviroNET files are stored on a MicroVAX II computer at GSFC and may be accessed on a 24 hour dial-up basis, at 1200 baud with ordinary telephone connections and at 9600 baud for users on the Space Physics Analysis Network, SPAN (ref. 1). SPAN is available via more than 1000 space science computer systems throughout the U.S., Canada and Europe.

BACKGROUND

Early in the development of the Space Shuttle, payload planners recognized the need for a detailed picture of environmental impacts on Shuttle payloads. The extreme complexity and size of the Shuttle made it very difficult to characterize these environments by computation. At the urging of the NASA payload community, the Shuttle Program agreed to fly instruments (in early Orbital Flight Tests) that would measure various elements of payload environment. In the fall of 1982, NASA conducted its first Shuttle Environment Workshop (ref. 2) to describe what had been learned from these measurements. This led to concerns voiced with regard to the need for information, on a continuing basis, about these and new concerns. To address the issues, NASA's Office of Space Science and Applications (OSSA) requested that a focal point be established for this environmental information, and that the activity be coordinated with other NASA centers, government agencies and the user community. As might be expected, initial tests did not answer all the questions and concerns raised by the payload community.

In mid 1983, Shuttle Payload Engineering Division asked that Goddard Space Flight Center (GSFC) lead an Agency-wide effort to identify Shuttle environment data that could be used by Shuttle payload planners and developers. It also suggested that the data obtained from this activity be put into an electronic database which could be accessed by any interested user.

ENVIRONET MAIN TOPICS		
Section	Chapter	Page
1.0	INTRODUCTION	1-1
2.0	THERMAL AND HUMIDITY	2-1
3.0	VIBRATION AND ACOUSTICS	3-1
4.0	ELECTROMAGNETIC INTERFERENCE	4-1
5.0	LOADS AND LOW FREQUENCY DYNAMICS	5-1
6.0	MICROBIAL AND TOXIC CONTAMINANTS	6-1
7.0	MOLECULAR CONTAMINATION	7-1
8.0	NATURAL ENVIRONMENT	8-1
9.0	ORBITER MOTION	9-1
10.0	PARTICULATE ENVIRONMENT	10-1
11.0	SURFACE INTERACTIONS	11-1
12.0	DEFINITIONS AND ACRONYMS	12-1

Figure 2

THE WORKING GROUP

As a consequence, a multi-center Shuttle Environment Working Group was organized through the efforts of OSSA and GSFC, with the Working Group establishing the charter and framework within which this group would function (fig. 3).

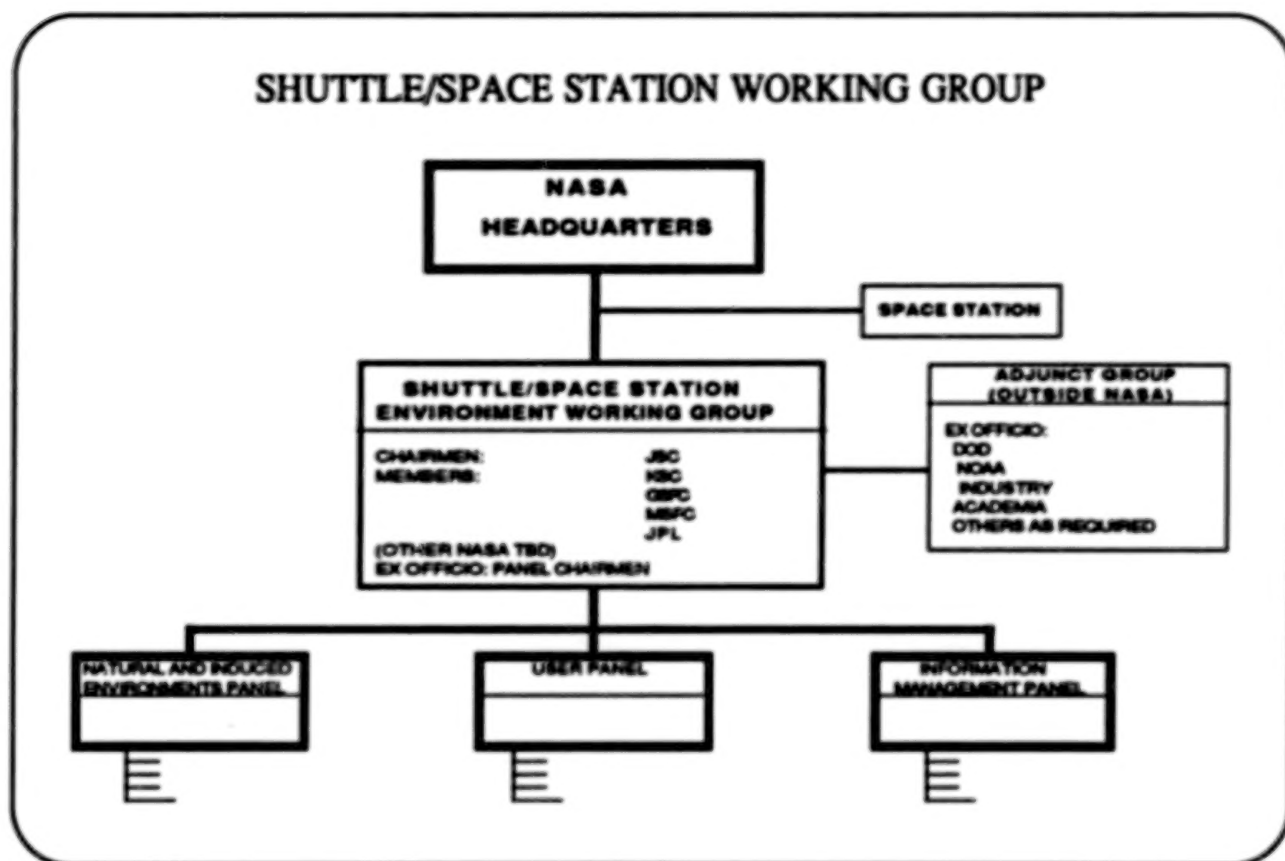


Figure 3

The goal of the Working Group was to have a comprehensive database established of current information regarding the Shuttle Environment, readily accessible in a user-friendly format. Specific objectives for the Shuttle Environment Working Group included:

- 1) Assessing the user requirements for environmental data at all stages of the experiment definition and development.
- 2) Obtaining and distilling the available and pertinent environmental data from the sources.
- 3) Working with the sources to obtain a common database that is acceptable and will be reviewed by those concerned.
- 4) Developing an information accessing system that is user-friendly.
- 5) Providing a network accessible by a wide variety of existing computer terminals and peripherals.
- 6) Coordinating these activities with other NASA centers, government agencies, and the user community.

With these objectives in mind, the Working Group began organizing in late 1983 and on into early 1984. A structure of panels and subcommittees was established and the task of staffing began. Three major panels were established with the functions and duties as follows:

- 1) The Natural and Induced Environments Panel (fig. 4) gathers and organizes data for input into the database. Duties: Make preliminary assessment of the reliability and traceability of the data for the database; assess the state of the data and determine if it is directly useful to the user.
- 2) The User Panel (fig. 5) provides for interaction between disciplines and users. Duties: Identify user requirements and needed environmental data; provide an interface between the scientific community and the environmental data panel; and identify gaps in the information base, also noting the urgency of the requirements for this data.

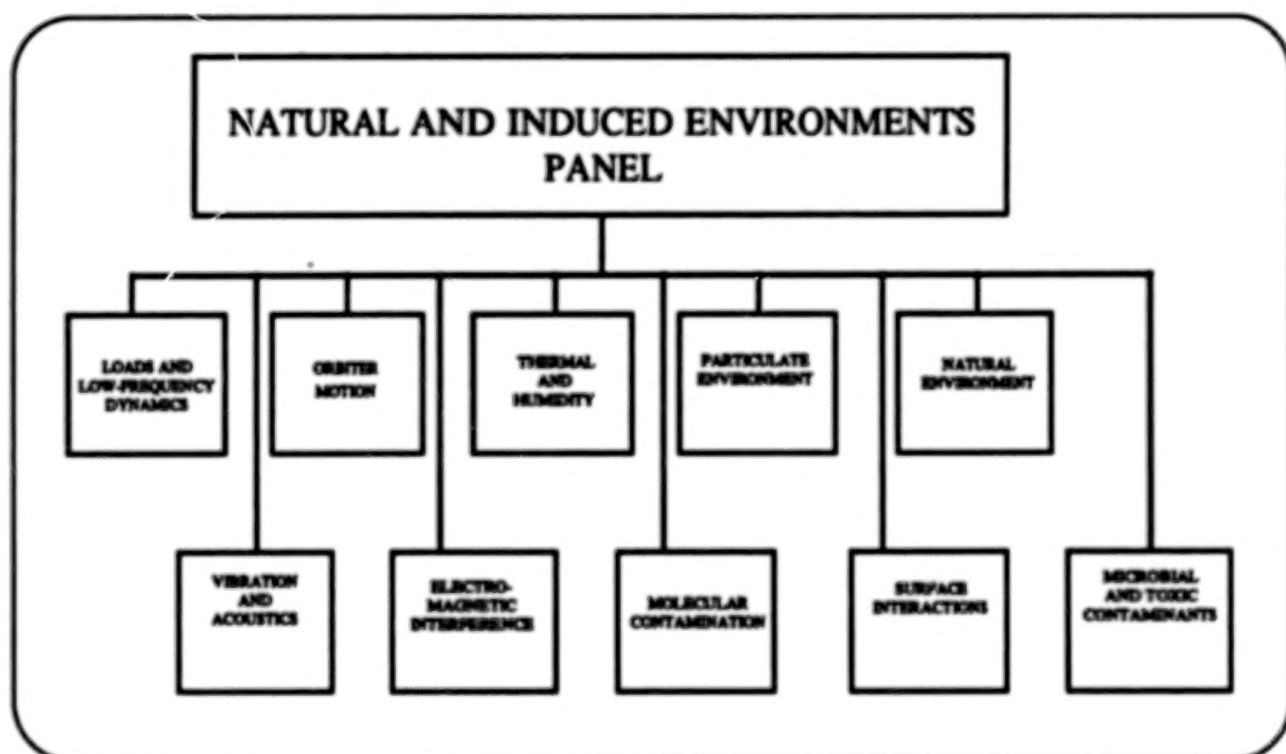


Figure 4

- 3) The Information Management Panel (fig. 6) provides the database structure and manages the database. Duties: Create a system for compiling, storing, and cataloging the information in the database; edit information; and coordinate network activities.

In August 1984, the Working Group, joined by the European Space Agency (ESA), sponsored its first Shuttle Environment Workshop, and the process of gathering data for the requested database began in earnest (ref. 3). The database was arranged by sections (or "chapters") along the key disciplines and named "EnviroNET." Also, database management procedures were outlined: The subpanels decide what data to collect; obtain and edit the data; and submit it to the Working Group for validation. Following validation, the Working Group gives the data to the Information Management Panel for inclusion in the electronic database. As a result of these considerable efforts, EnviroNET has evolved into a reasonable, mature and comprehensive database.

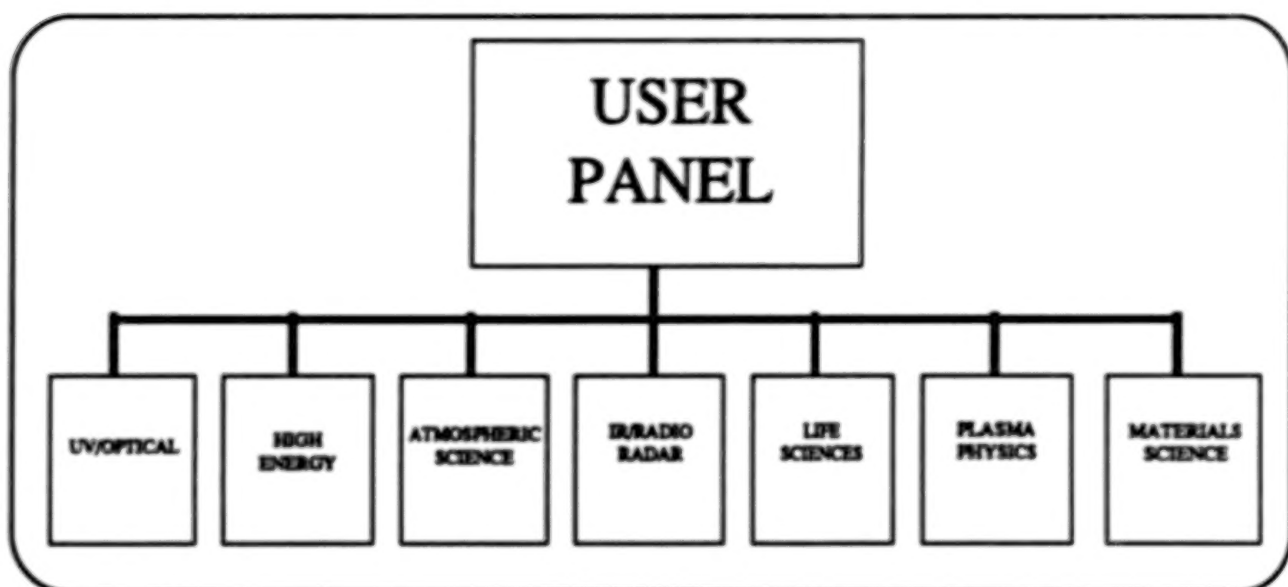


Figure 5

EnviroNET Displays

Plans for improving the services of EnviroNET are shown in Figure 7. Software from commercial sources are constantly evaluated for feasibility. Where necessary, in-house software is developed. The main menu system (ref. 4), which controls the EnviroNET activity on the MicroVAX II, is frequently updated in response to user suggestions and changing needs of the database activity. This main menu (fig. 8) allows one to run BROWSE, access the data files, download graphics and text, send mail to the system manager, read bulletin board notices, use the models or exit the system.

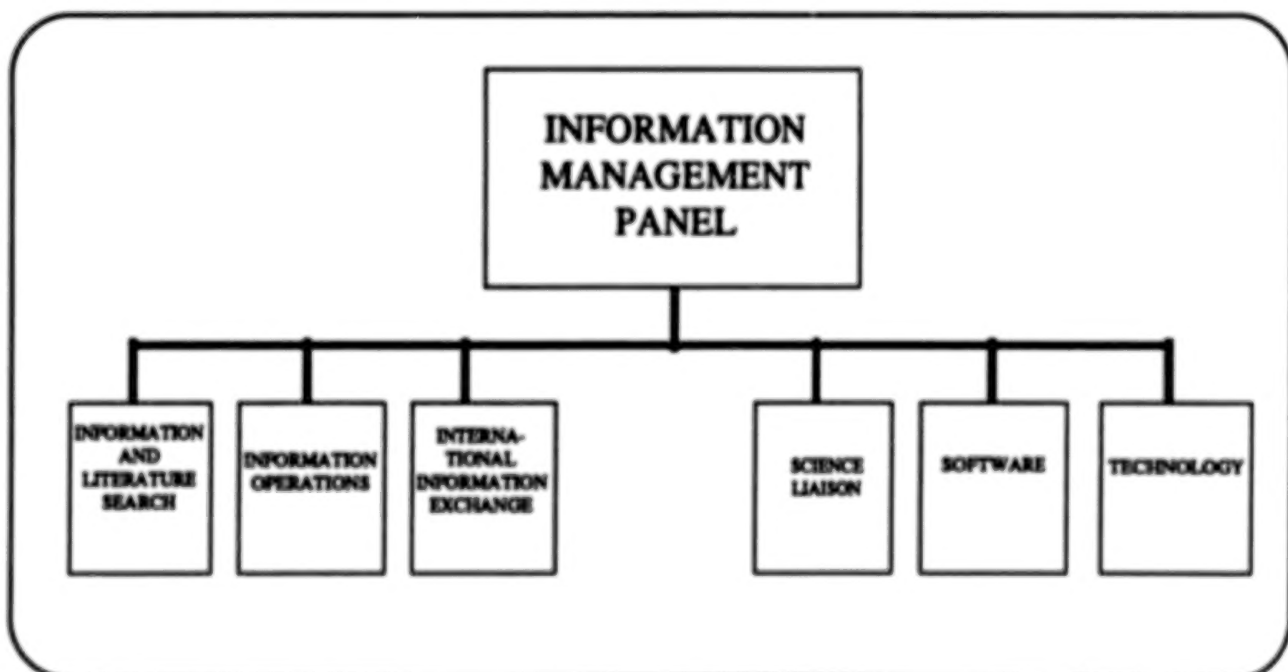


Figure 6

PLANS

- Consider options for improving service
 - Software
 - Graphics
 - Modeling
 - Network Servers (NSSDC, SPAN...)
- Newsletter
- Telescience
- Workshops

Figure 7

ENVIRONET MAIN MENU *****

B -> BROWSE - Text Retrieval Subsystem (Requires VT100 emulation)
U -> User Message Service - Leave messages for other users
N -> Bulletin Board Notices - Changes to the database
D -> Download Specific Chapter
M -> Mail System - Mail us your comments about the system
F -> Function Calculation System - Natural Environment Models
G -> Graphics - Download high resolution graphs
L -> Logoff - End ENVIRONET session
Enter appropriate letter, followed by RETURN :

Figure 8

The principal retrieval program, called BROWSE, is continually being updated in response to user and subpanel suggestions. With BROWSE, simple command choices allow one to page through the EnviroNET database sequentially, or jump to points of interest. To use BROWSE, one must have a VT100 compatible terminal or emulation. BROWSE has three menus: Main Topics, Data and Table of Contents/Index. One can move among the three menus to any part of the database, or back to the EnviroNET main menu with a single keystroke. As you BROWSE about the database and change menus, the information on the terminal screen will change, but the basic layout of the screen will remain the same. Information is displayed in three "windows": the page window at the top right, the data window at the center, and the option window at the bottom (fig. 9).

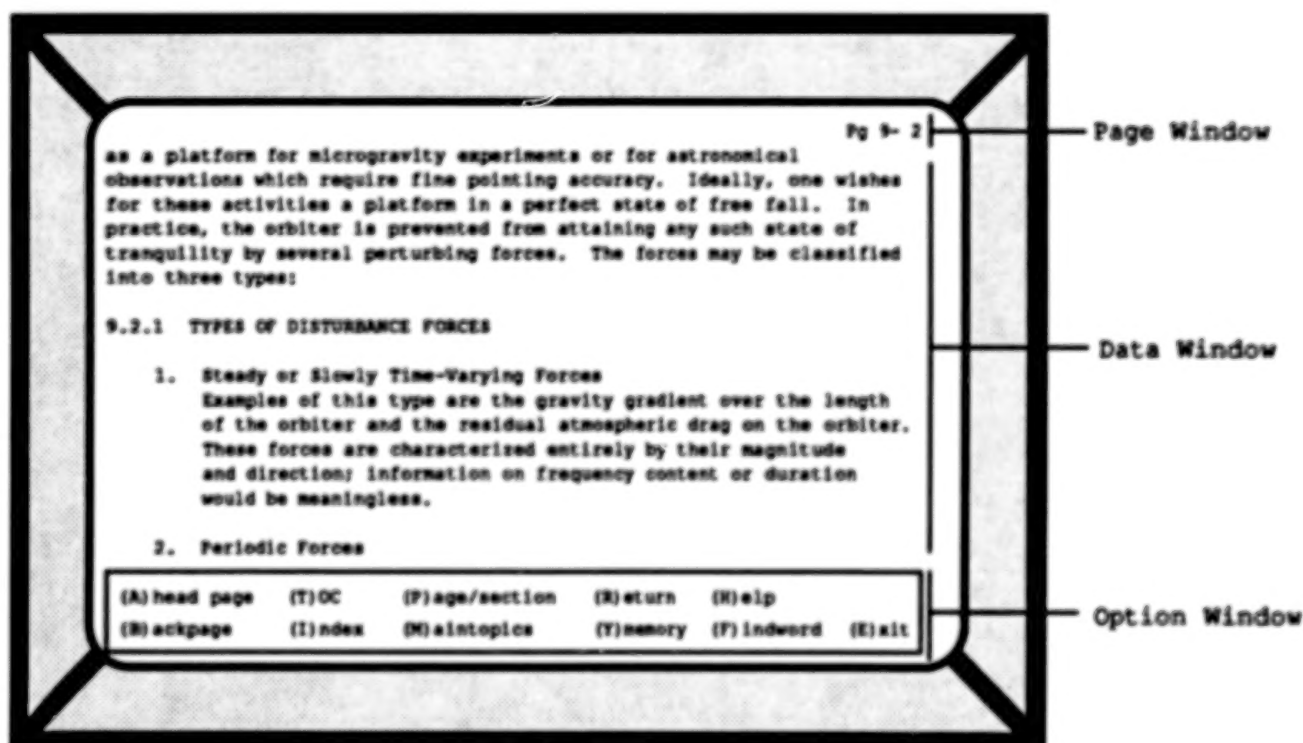


Figure 9

GRAPHICS

Graphics display of database figures is slowed because of the high number of bits in the bit map and the 1200 baud rate of the communication system. All possible avenues for circumventing or coping with this problem are under continuing investigation. In the interim, the text is designed for minimal dependence upon graphics, although "text graphics" are displayed when suitable. The immediate graphics effort is to deliver high resolution graphical data accompanied with textual data to the user with a minimum of user effort and familiarity with the system. A near-term goal is to provide graphical data in an easy and convenient format. To accomplish this objective, certain components—such as POPGRAPH—are being developed. POPGRAPH is a user friendly program being written in-house to facilitate easier access to the graphical data while viewing the textual data. It resides in memory and can be invoked instantly by pressing

a sequence of three keys. When finished viewing the graphical data, the user can immediately return to the text with a single keystroke.

The Enhanced Graphics Adapter (EGA) is a standard high-resolution graphics adapter used on the IBM PC and compatibles. It provides a resolution of 640 pixels by 350 pixels. Since the Color Graphics Adapter (CGA), has a resolution of 640 pixels by 200 pixels, which is not always sufficient for some of the more detailed graphs, there is a need to upgrade to the EGA. Currently, the EGA image size is 28 kilobytes. Downloading one of the images from the MicroVAX to a PC will require an average of 1 second per kilobyte at 9600 baud.

At 1200 baud, the download time will increase proportionately, thus compaction protocol to squeeze the 28 kilobyte image down to about 10 kilobytes will be undertaken to cut the down load time by as much as 60%. A typical high-resolution graph available for viewing (fig. 10) shows contamination during ascent. The long-term goals are first, to accommodate more users by expanding to different graphics cards on the IBM PCs, and by expanding to different machines, such as Macintosh computers; and second, to integrate textual data and graphical data into one format so that a user will not have to switch from one to the other as at present. To sum up: most IBM PCs and compatibles use one of the three following graphics cards. They either have a Color Graphics Adapter (CGA), an Enhanced Graphics Adapter (EGA), or a Video Graphics Array card (VGA), or compatibles of these adapters. Currently, only CGA and EGA users are

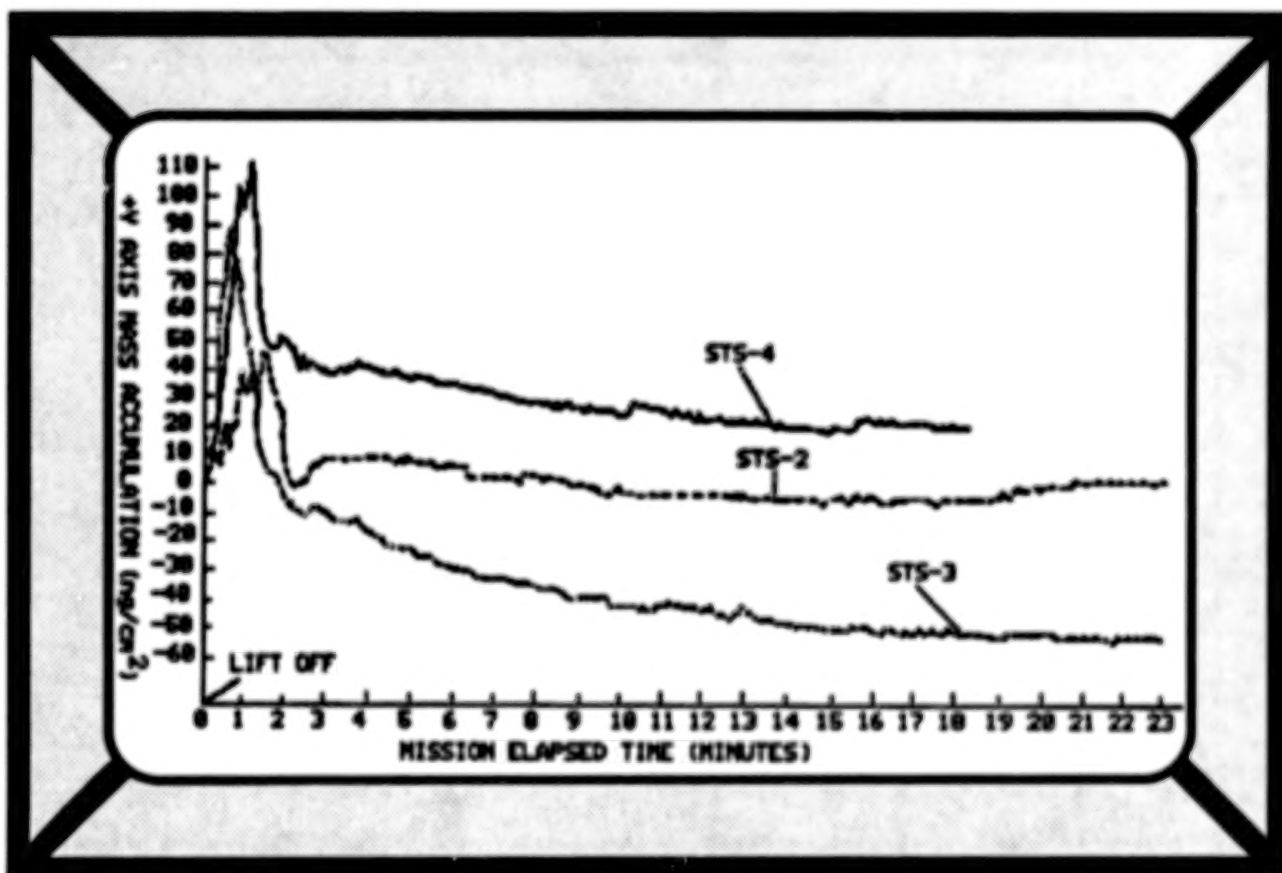


Figure 10

supported. Eventually, the system will support users of the VGA adapters as well as users of the Macintosh computer. Currently, if a user of EnviroNET is reading textual data, and he sees a reference to a piece of graphical data, he must log off, run the display program to view the graphical data, and log in again to continue viewing textual data. This is a very inconvenient and time-consuming process. POPGRAPH makes things easier by allowing the user to switch between textual data and graphical data and vice versa.

MODELS

EnviroNET has expanded its activity by adding interactive models of the natural environment. The models include neutral atmosphere density and temperature (refs. 5, 6), ionosphere, electron temperature and density, the magnetic field vector, and energetic particle or radiation flux. These models are based on data from satellites which orbit the Earth in the thermospheric and exospheric regions of the atmosphere. The thermosphere is the region above approximately 85 km (depending on season and other factors) where temperature increases sharply with altitude, turbulent mixing of different molecular species ceases, and ultraviolet (UV) and extreme ultraviolet (EUV) flux from the sun dissociate the molecules and ionize the constituents to form the ionosphere. Above roughly 500 km, the thermosphere gradually merges into the exosphere where the mean free path of molecules is longer than the vertical scale height. The temperature in the upper thermosphere and lower exosphere approaches an asymptote called the exospheric temperature. The ineffectiveness of mixing processes above about 105 km results in a situation called diffusive equilibrium, where the individual atmospheric constituents decrease with a scale height inversely proportional to their individual molecular weights, and the mean molecular weight decreases monotonically with altitude. Atomic oxygen is a major constituent of the upper thermosphere along with molecular nitrogen and helium. Hydrogen becomes a major constituent in the exosphere. Argon, molecular oxygen, and atomic nitrogen are minor constituents in the upper thermosphere. The structure of the thermosphere has been determined by a number of satellite, rocket, and ground based techniques and the data summarized in various empirical models. The density, temperature, and composition of the thermosphere are found to depend on time (year, day of year, and time of day), position (latitude, longitude, and altitude), solar generated or triggered energy inputs (solar UV and EUV, magnetospheric particles, and magnetospheric electric fields and currents), and to some degree on the state of the lower atmosphere upon which the thermosphere rests.

Winds are an important part of the environment at orbital altitudes. Wind speeds may reach 1000 meters per second at high latitudes, driven indirectly by magnetospheric electric fields, but are usually less than 100 meters per second at low latitudes. Wind measurements have only recently been summarized in the same fashion as density and temperature measurements. There are five major types of variations in the thermosphere at orbital altitudes. The temperature and densities of all the constituents except hydrogen increase strongly with increases in solar EUV flux. Total density has a diurnal maximum in the early afternoon, but temperature and the various constituents all have diurnal maxima at different times of the day. The temperature and individual constituents have strong seasonal variations which are out of phase for the heavier and lighter constituents, resulting in only a minor seasonal variation for total density. A significant global semiannual variation, with density maxima near the equinoxes, is present for all constituents and varies from year to year for unknown reasons. Magnetospheric energy input in the auroral regions (magnetic storms) increases total density and temperature over the whole globe, but preferentially at high latitudes, while the lighter constituents decrease at high latitudes.

Wave activity originating in the auroral zone and also the lower atmosphere is present everywhere in the thermosphere, but primarily at high latitudes with density variations up to 15%. The occurrence of waves can only be described statistically and limits the accuracy of model predictions. The solar 10.7 cm radio flux, which can be measured from the ground, is used as an index of solar UV and EUV flux. The 10.7 cm flux correlates quite well with major EUV emissions, but less well with other EUV emissions and UV wavelengths. The EUV and radio flux vary from day to day with major periods of 27 days and 11 years. Both the daily value of the 10.7 cm flux and a several month average of the flux have proved useful in empirical models. Energy input from the magnetosphere, which can change rapidly in less than an hour, not only heats the atmosphere (particularly at high latitudes), but also causes variations in the magnetic field measured at the ground (magnetic storm). These variations are summarized in a number of magnetic indices. The three hourly ap or kp planetary magnetic indices (kp is derived from ap by a pseudo-logarithmic transformation) and their daily averages (ap and kp) are used by most empirical models as their index for magnetospheric energy input. The prediction of either the 10.7 cm flux or magnetic indices for future times is subject to large errors because it depends on the meteorology of the sun and nonlinear processes in the magnetosphere, and constitutes the major uncertainty in predicting the future state of the thermosphere.

Historical values of the 10.7 cm flux and magnetic indices can be found in standard references (ref. 7 and ref. 8). For rough estimates, the 10.7 cm flux index can be taken as 70, 150, or 230 for low, medium, and high solar activity respectively and the Ap (Kp) index can be taken as 4 (1), 27 (4), or 400 (9) for low, medium, and extremely high magnetic activity respectively.

Two empirical models can be accessed through the EnviroNET menu and allow calculation of density, temperature, and composition based on user specifications for time, position, and energy input, as discussed above. The first is the MSFC/J70 model (ref. 4) chosen as the design standard for Shuttle and Space Station. This model is based directly on total densities derived from changes in satellite orbits as a result of atmospheric drag. However, the data were gathered before 1970 and do not provide unique information about temperature or composition. The second model is the MSIS-86 model (ref. 5) chosen for the 1976 Committee on Space Research (COSPAR) International Reference Atmosphere. This model is based primarily on in situ mass spectrometer composition and temperature measurements, and ground-based radar temperature measurements. Total densities of the MSIS model basically agree with drag models, while providing more accurate predictions for the temperature and individual constituents. The models generally have an accuracy for total density on the order of 15% to 20%. The natural atmosphere models, which are run from the EnviroNET main menu, will be expanded to include topics such as gravity, radiation, and meteoroids. In addition, a model is being developed to provide parameters at given points along a space shuttle or space station orbit as well as integrated doses. Graphics display of the model parameters along given orbits will also be developed. The computer screen display for the MSIS model is shown in Figure 11. After input parameters (left) are entered, the computer calculates the output displayed on the right.

NETWORK SERVERS

SPAN (ref. 1) uses Digital Equipment Corporation computers as network nodes (usually already paid for by NASA for a wide number of missions), and communicates over a combination of leased circuit switches and packet switching lines using the DECnet protocol. The SPAN topology, (fig. 12) features four primary routing centers in the

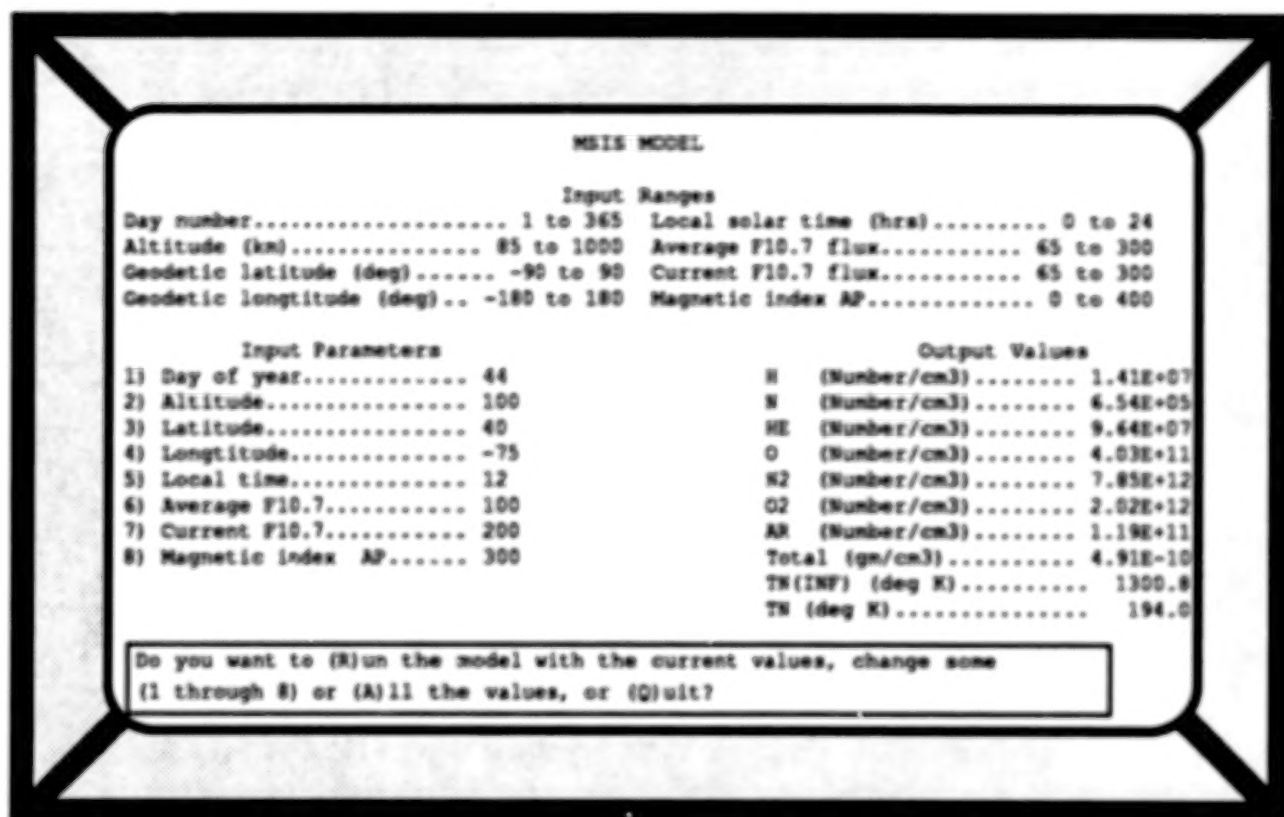


Figure 11

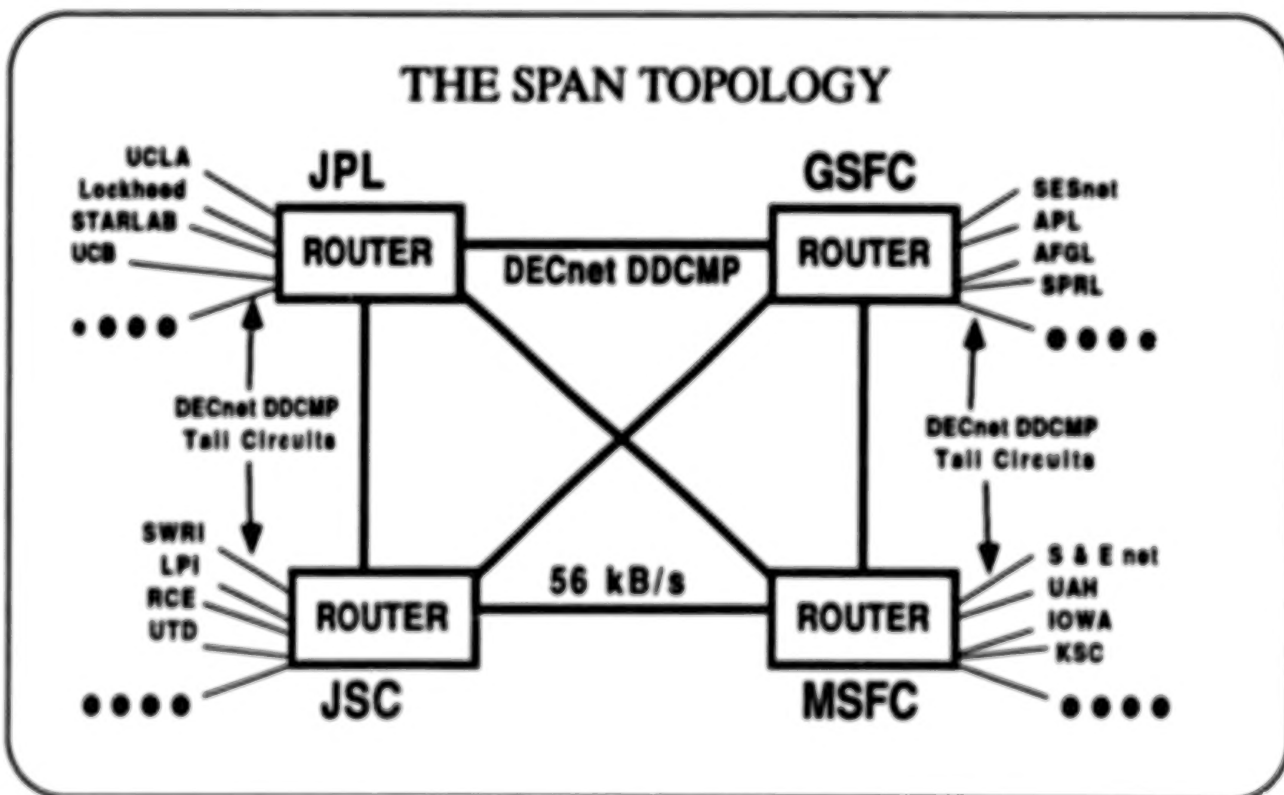


Figure 12

United States: Goddard Space Flight Center (GSFC), Johnson Space Flight Center (JSC), the Jet Propulsion Laboratory (JPL), and Marshall Space Flight Center, (MSFC), as well as one routing center at the European Space Operations Center (ESOC) in Darmstadt, Germany. There are approximately 1200 registered SPAN nodes. EnviroNET may be accessed via modem-equipped terminals, SPAN, or network servers at the routing centers.

The SPAN system brings the space scientific community together in a common working environment. The network supports the transmission and reception of manuscripts. Data and Graphics files can be transferred between network nodes. SPAN now supports several types of network-to-network connections which provide access to SPAN (ref 9). These are shown in Figure 13. Each oval represents an entire network of computer nodes (ref. 1).

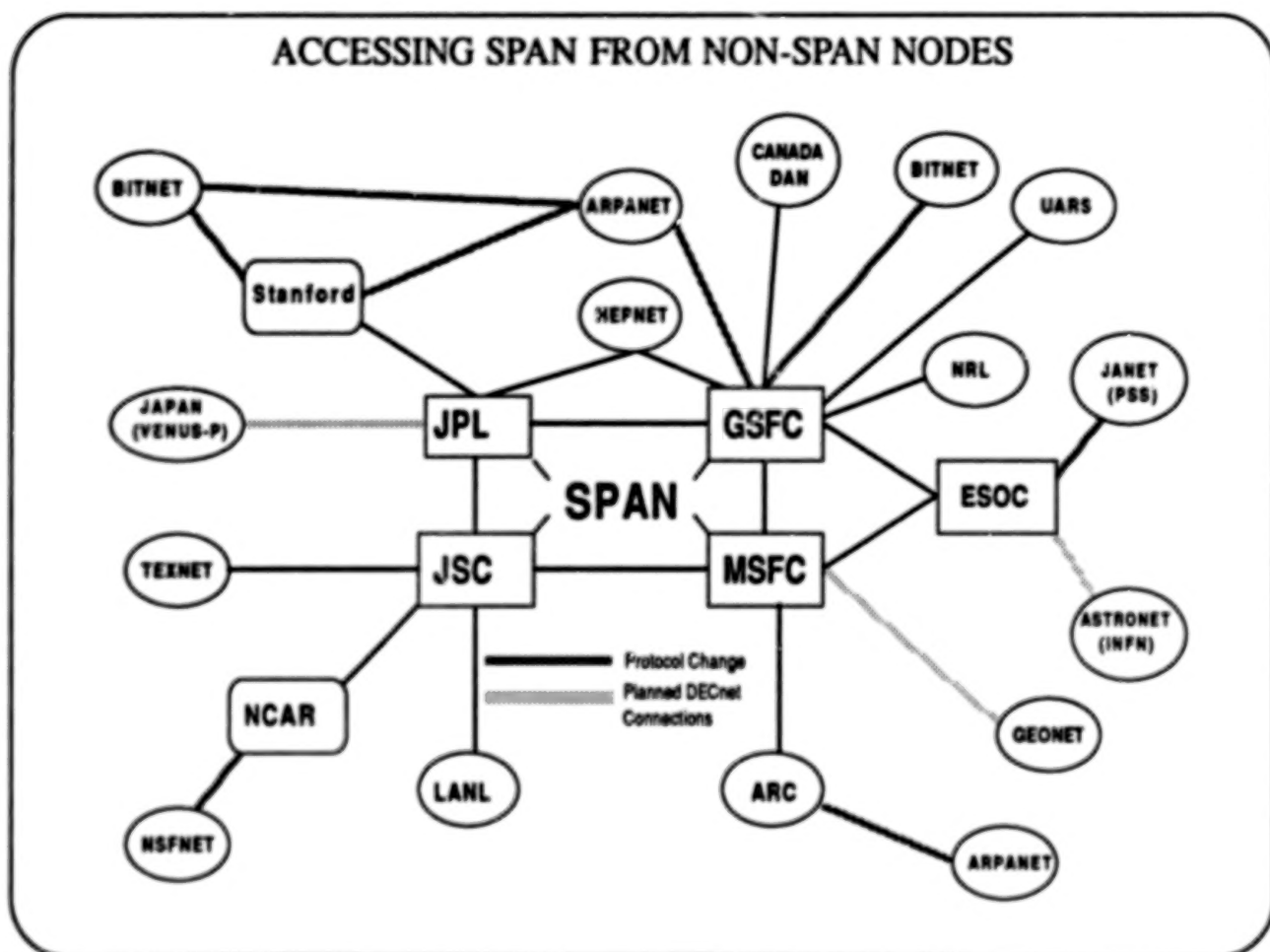


Figure 13

TELESCIENCE

EnviroNET is ideally suited for investigators to cooperate from their "remote" home laboratories and computers with their colleagues by computer networking. This is an expansion of the concept started with the Atmosphere Explorer and Dynamics Explorer programs when many scientists were connected over dedicated phone lines to a central "remote" computer site containing their data and computer programs. With the advent

of SPAN, the remote Dynamics Explorer scientists could communicate with one another directly and offload calculations and data analysis to their home systems, thereby improving productivity with simultaneous analysis on remote, distributed computer systems. EnviroNET is being upgraded to permit the users to conduct teleanalysis, i.e., perform analyses using Space Shuttle/Space Station environment data and the models on computers at remote institutions. EnviroNET has always drawn on the NASA centers, other government laboratories, industry, and universities. The academic community is especially involved because it provides important opportunities for testing and evaluating new ideas, techniques and concepts before they have reached the state of maturity considered by contractors and project managers suitable for implementation. A testbed program like EnviroNET provides a valuable way of training graduate students who represent the future scientists and engineers of the nation, and who need to be at the leading edge of our SPAN technology.

WORKSHOPS

Workshops are conducted periodically for the panel leaders and subpanels. The results of these workshops are printed as informal documents for the purpose of feedback of information essential to the improvement of the services to users and to take advantage of the advancements in communications. These documents are available upon request.

CONCLUSION

EnviroNET is an operational system available to the SDI experimenters who have access to a terminal or dial-up port. It is a tail node on SPAN accessible directly or through the national networks via NPSS.

Some of the benefits to using EnviroNET include:

- 1) Validated NASA environmental information and interactive space models
- 2) Facilitating the payload integration process
- 3) Easy access to expert assistance
- 4) Potential for time and cost savings

ACKNOWLEDGMENTS

The information on modeling was contributed by D. Bilitza, J. Green, A. Hedin, and J. Vette of NASA/GSFC. The author acknowledges indirect but valuable contributions gained from the Working Group through many telecons, meetings, and general exchange of unpublished information. Funding was provided by NASA Headquarters, the Air Force Geophysical Laboratory (AFGL) Space Systems Environmental Interaction Technology Office, and by the U.S. Air Force Systems Command, Space Division.

REFERENCES

1. Green, James L. The Space Physics Analysis Network. Computer Physics Communication 49, pp. 205-213, North-Holland, Amsterdam, 1988.
2. Proceedings: The Shuttle Environment Workshop. Prepared for NASA by Systematics Corp., Contract NAS5-27326, Feb. 1983.
3. Wilkerson, Thomas D., Michael Lauriente, and Gerald W. Sharp. Space Shuttle Environment. Library of Congress Catalog No.: 85-81606, ISB No-939204-28-2
4. The EnviroNET User's Guide. Code 410.1, NASA/GSFC, Greenbelt, MD 20770.
5. Johnson, D .L. and R. E. Smith. The MSFC/J70 Orbital Atmosphere Model and the Data Bases for the MSFC Solar Activity Prediction Technique. NASA TM-86522, 1985.
6. Hedin, Alan E. The MSIS-86 Thermospheric Model, J. Geophys. Res., vol. 92, pp. 4648-4662, 1987.
7. Solar-Geophysical Data Part I (prompt reports), issued monthly by National Geophysical Data Center, NOAA/NESDIS, E/GC2, 325 Broadway, Boulder, CO 80303.
8. Journal of Geophysical Research (Space Physics), issued monthly by American Geophysical Union, 2000 Florida Ave, N.W., Washington, D.C. 20009.
9. Accessing SPAN From Non-SPAN Nodes, National Space Science Center (NSSDC)/Work Data Center-A for Rockets and Satellites (WDC-A-R&S), NASA GSFC, Greenbelt, MD 20771.

SESSION 3: ATOMIC OXYGEN

Chairmen: L. Leger and J. Visentine
NASA Lyndon B. Johnson Space Center

ENVIRONMENTAL DEFINITION OF THE EARTH'S NEUTRAL ATMOSPHERE

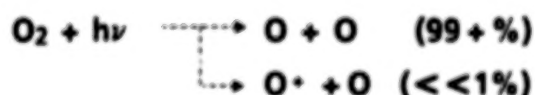
**JAMES T. VISENTINE
NASA LYNDON B. JOHNSON SPACE CENTER
HOUSTON, TEXAS**

ENVIRONMENTAL DEFINITION OF THE EARTH'S NEUTRAL ATMOSPHERE

- ALTHOUGH NUMBER DENSITIES ARE LOW (10^6 - 10^9 PARTICLES/ cm^3) AT ALTITUDES WHERE SPACECRAFT TYPICALLY OPERATE, HIGH ORBITAL SPEEDS (8 km/s) RESULT IN INCIDENT FLUXES (10^{14} - 10^{15} atoms/s cm^2) AND COLLISIONAL ENERGIES (TRANSLATIONAL ENERGIES EQUIVALENT TO $\sim 60,000$ °K) LARGE ENOUGH TO INTERACT WITH AND DEGRADE MATERIAL SURFACES
- DURING PREVIOUS STS MISSIONS (STS-5, -8, AND -41G), SURFACE RECESSIONS AS HIGH AS $0.5 \mu\text{m}$ PER ORBIT HAVE OCCURRED FOR ORGANIC MATERIALS EXPOSED TO THE FLIGHT ENVIRONMENT
- SIMILAR EFFECTS HAVE BEEN OBSERVED FOR SOME METALS, MOST NOTABLY OSMIUM AND SILVER, WHICH BECOME HEAVILY OXIDIZED DURING LEO (LOW-EARTH ORBIT) EXPOSURE
- STS POST-FLIGHT RESULTS ARE CONSISTENT WITH AN ATOMIC OXYGEN-BASED MECHANISM

ATOMIC OXYGEN PRODUCTION MECHANISM

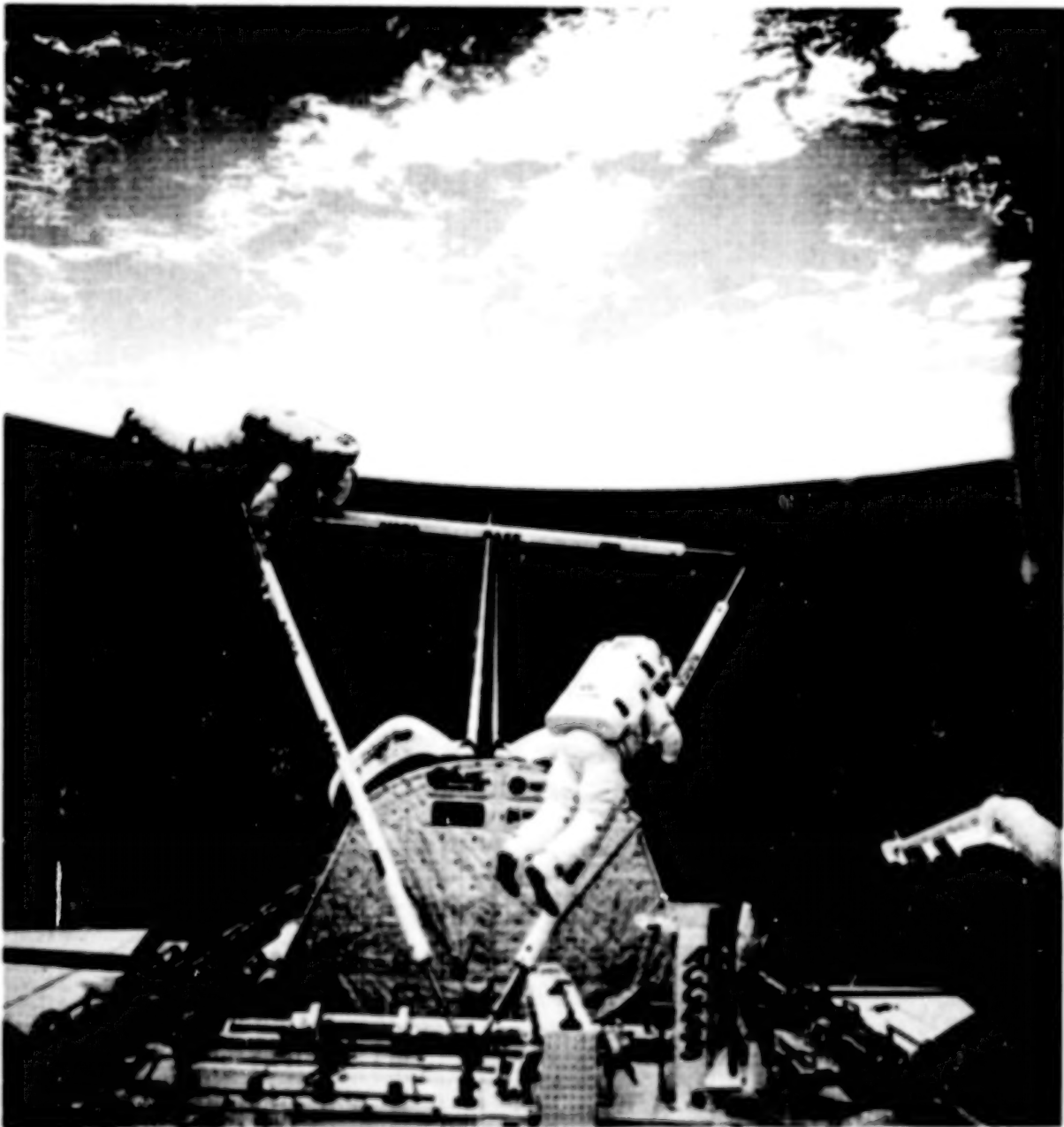
- EARLIER SATELLITE MEASUREMENTS HAVE SHOWN ATOMIC OXYGEN IS THE PREDOMINANT SPECIES IN THE UPPER ATMOSPHERE (200 TO 600 km) -- IT IS FORMED AT ORBITAL ALTITUDES THROUGH THE DISSOCIATION OF O_2 BY ULTRAVIOLET (100 TO 200 nm) RADIATION:



- DIURNAL AND SEASONAL VARIATIONS IN ATOMIC OXYGEN NUMBER DENSITY MAY BE PREDICTED USING GLOBAL MODELS OF THE EARTH'S UPPER ATMOSPHERE

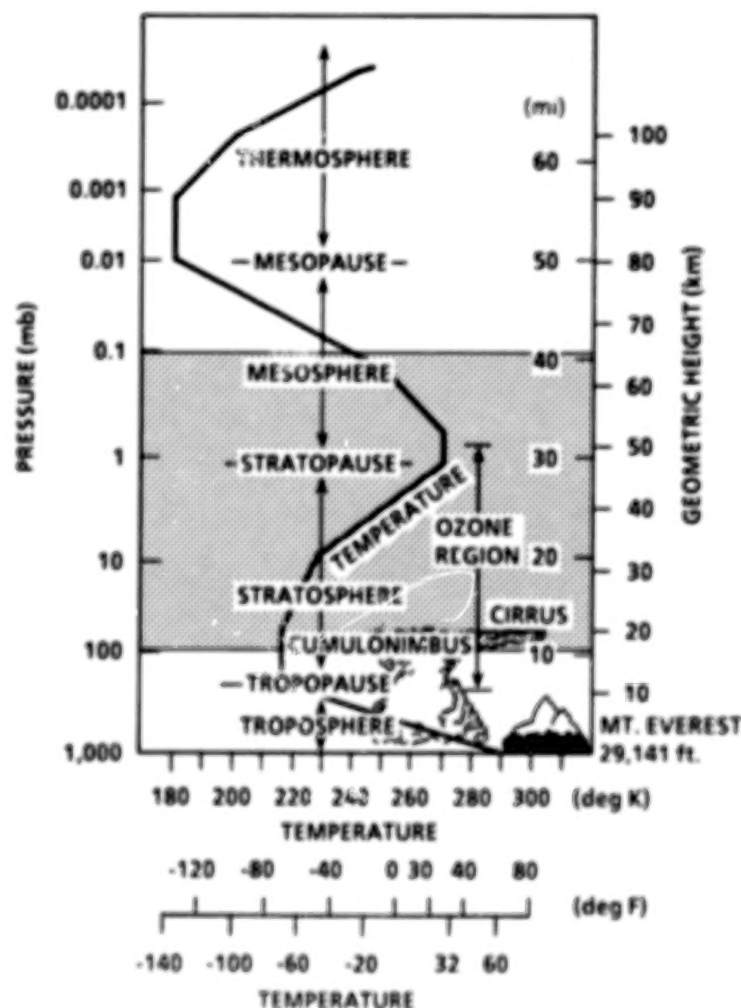
View of the Earth and Its Atmosphere as Observed from Space

The visible atmosphere shown in this photograph was obtained from Shuttle Mission 61-B during December 1985. In this photograph, Mission Specialists Jerry L. Ross and Woody Spring are shown assembling the EASE (Experimental Assembly of Structures in Extravehicular Activity) flight experiment. The lower atmosphere appears as a thin glow above the surface of the Earth. This glow results from emissions produced as excited oxygen molecules decay to their ground state, and extends upward to the edge of the mesosphere, or mesopause. The Earth's upper atmosphere begins above the region where the visible glow disappears, or about 85 km in altitude.



Vertical Temperature Distribution in Earth's Atmosphere from Surface to 100 km Altitude, Giving Nomenclature of Atmospheric Regions

The Earth's atmosphere is divided into specific regions. In the most commonly used system, these regions are differentiated by thermal stratification. The lowest region, extending from sea level to the first temperature minimum, is called the troposphere. The stratosphere, or second region, extends upward to the level of highest temperature. The upper atmosphere may be defined as the region above the mesopause, or upper temperature minimum, and extends from about 85 km to geostationary altitudes. Global thermospheric models are designed to operate within this region of the atmosphere. Their specific formulations give accurate estimates of temperature, density, and composition and are based on in situ measurements from the Atmospheric Explorer and Dynamics Explorer satellites. The upper atmosphere may be further divided into the thermosphere (85 to 500 km), and the exosphere (500 km and above). Spacecraft normally operate in the upper atmosphere at altitudes above 300 km to reduce drag effects, which are significant at lower altitudes, and minimize requirements for re-boost propulsion systems.



GLOBAL THERMOSPHERIC MODELS

- MOST RECENT GLOBAL MODELS INCLUDE J77 (JACCHIA, 1977), AND MSIS-86 (MASS SPECTROMETER AND INCOHERENT SCATTER, 1986)
- EARLIER JACCHIA MODELS (J70) WERE BASED SOLELY ON SATELLITE DRAG DATA AND DID NOT ACCURATELY REPRESENT CONSTITUENT DENSITY VARIATIONS ASSOCIATED WITH GEOMAGNETIC DISTURBANCES
 - THESE VARIATIONS WERE ASSUMED TO BE UNIFORM OVER THE GLOBE, WHILE MORE RECENT DATA HAVE SHOWN THEY HAVE VERY SIGNIFICANT GLOBAL STRUCTURE, MAINLY IN RELATION TO GEOMAGNETIC LATITUDE
- J77 RESOLVED EARLIER DISCREPANCIES BY INCORPORATING SATELLITE MASS SPECTROMETER MEASUREMENTS AND INCLUDING A HIGH-RESOLUTION MODEL OF GEOMAGNETIC VARIATIONS IN THE THERMOSPHERE (85-500 km) AND OUTER ATMOSPHERE, OR EXOSPHERE (500 km AND ABOVE)
- IN FORMULATING MSIS-86, TERMS WERE ADDED TO MSIS-83 TO BETTER REPRESENT SEASONAL VARIATIONS IN THE POLAR REGIONS UNDER BOTH QUIET AND MAGNETICALLY DISTURBED CONDITIONS
- MSIS-86 AND J77 AVERAGE TEMPERATURE AND TOTAL DENSITY ESTIMATIONS AGREE TO WITHIN 10% OF ONE ANOTHER

MSIS 86 THERMOSPHERIC MODEL

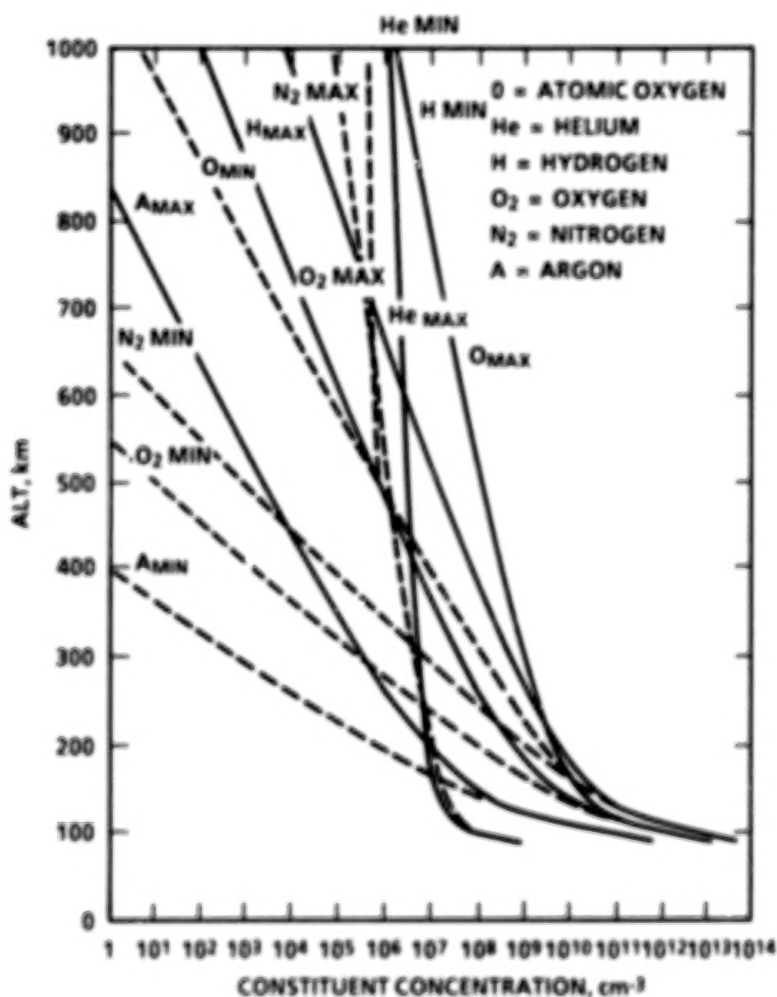
- THE MSIS 86 MODEL, DEVELOPED BY GSFC, IS FREQUENTLY USED TO PREDICT CONSTITUENT NUMBER DENSITIES FOR SHUTTLE AND SPACE STATION ATOMIC OXYGEN INTERACTION STUDIES
- MODEL IS BASED ON IN-SITU DATA FROM SATELLITES, SUCH AS ATMOSPHERIC EXPLORER AND DYNAMICS EXPLORER, AND GROUND-BASED INCOHERENT SCATTER STATIONS:
 - OUTPUT DATA INCLUDE BOTH TEMPERATURE PROFILES AND CONSTITUENT (N_2 , N, O_2 , O, He, H, Ar) NUMBER DENSITIES WITHIN A 85-750 km ALTITUDE RANGE
 - MODEL ASSUMES TURBULENT MIXING OCCURS BELOW THE TURBOPAUSE (NOMINALLY 105 km), AND DIFFUSIVE EQUILIBRIUM EXISTS AT HIGHER ALTITUDES:
 - MESOSPHERE - 50-85 km
 - THERMOSPHERE - 85-500 km
 - EXOSPHERE - 500- ∞ km
- HEAVIER GASES (N_2 , O_2 , Ar) HAVE SMALLER SCALE HEIGHTS AND DECREASE MORE RAPIDLY WITH INCREASING ALTITUDE -- LIGHTER GASES (H, He, O) HAVE LARGER SCALE HEIGHTS AND DECREASE MORE SLOWLY WITH ALTITUDE
- CONSTITUENT CONCENTRATIONS ARE STRONGLY INFLUENCED BY SOLAR ACTIVITY CONDITIONS AND GEOMAGNETIC DISTURBANCES WHICH VARY WITH THE 11-YEAR SOLAR CYCLE

SOLAR ACTIVITY VARIATIONS IN CONSTITUENT NUMBER DENSITIES

- **EXOSPHERIC TEMPERATURE AND NUMBER DENSITY OF ALL CONSTITUENTS, EXCEPT HYDROGEN AND MOLECULAR OXYGEN, INCREASE WITH SOLAR ACTIVITY**
- **AS SOLAR ACTIVITY INCREASES, ATMOSPHERE EXPANDS AND REGIONS OF HIGH DENSITY RISE TOWARD HIGHER ALTITUDES TO REPLACE REGIONS OF LOWER DENSITY**
- **GEOMAGNETIC STORMS OCCUR WHEN CLOUDS OF CHARGED PARTICLES INTERACT WITH THE EARTH'S MAGNETOSPHERE -- DENSITY INCREASES PRIMARILY IN THE POLAR REGIONS, BUT EFFECTS ARE ALSO SEEN AT LOWER LATITUDES**
- **UNDER MAGNETICALLY QUIET CONDITIONS, N₂, O₂, AND Ar DENSITIES INCREASE TOWARD THE POLES WHILE O, N, He, and H DECREASE IN DENSITY**

Plot of Constituent Number Density in Earth's Atmosphere
from
100 to 1,000 km Altitude

At altitudes where LEO (low-Earth orbital) spacecraft typically operate (300 to 500 km), constituent number densities vary in direct proportion to solar activity. Higher atomic oxygen number densities result in higher fluxes incident on spacecraft surfaces and, consequently, in higher surface recession rates for reactive materials. During conditions of high solar activity (Curve O_{MAX} shown in the figure below), the O-atom number density varies from 10^9 to 10^8 atoms/cm³ over an altitude range of 300 to 500 km. During conditions of low solar activity, variations over these altitudes are reduced to 10^8 to 10^6 atoms/cm³. Consequently, spacecraft launched during times of minimum solar activity experience less exposure to the neutral O-atom environment than spacecraft launched during times of high activity. Typically, a Space Shuttle mission is flown at an altitude near 300 km. For these missions, the atomic oxygen number density varies between 10^8 and 10^9 atoms/cm³ during the 11-year solar cycle. Spacecraft flown at a higher altitude of 500 km would encounter much lower number densities (10^6 to 10^8 atoms/cm³) during the same exposure period.



MIN SOLAR CONDITIONS: 0400 hr USING $F_{10.7} = 70$ & $A_p = 0$

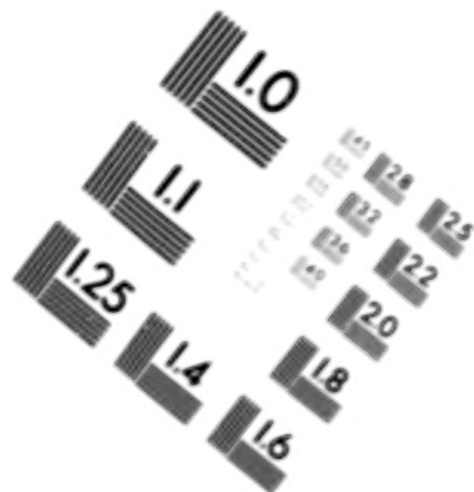
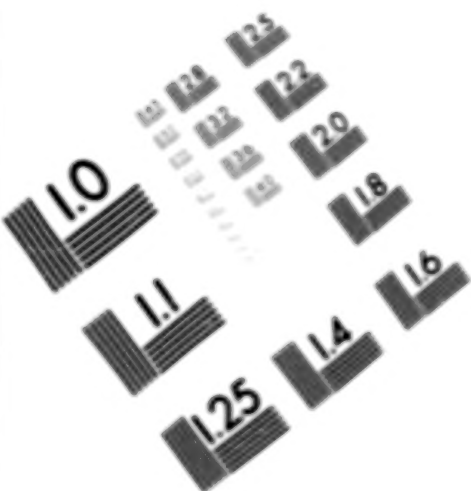
MAX SOLAR CONDITIONS: 1400 hr USING $F_{10.7} = 230$ & $A_p = 35$



AIM

Association for Information and Image Management

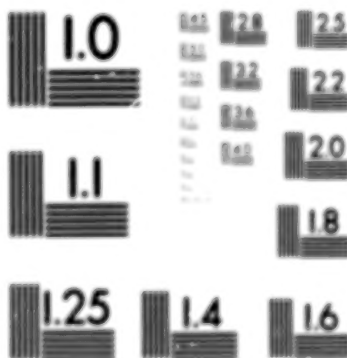
1100 Wayne Avenue, Suite 1100
Silver Spring, Maryland 20910
301/587-6202



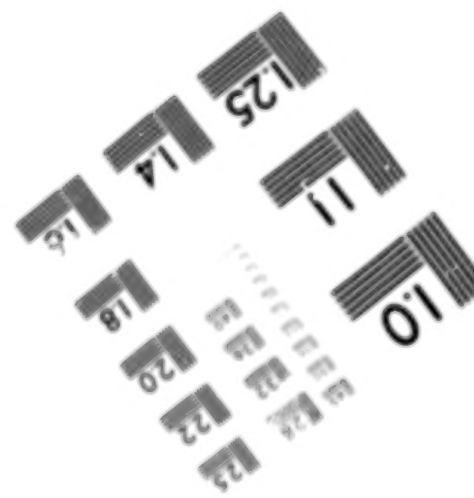
Centimeter



Inches



MANUFACTURED TO AIM STANDARDS
BY APPLIED IMAGE, INC.

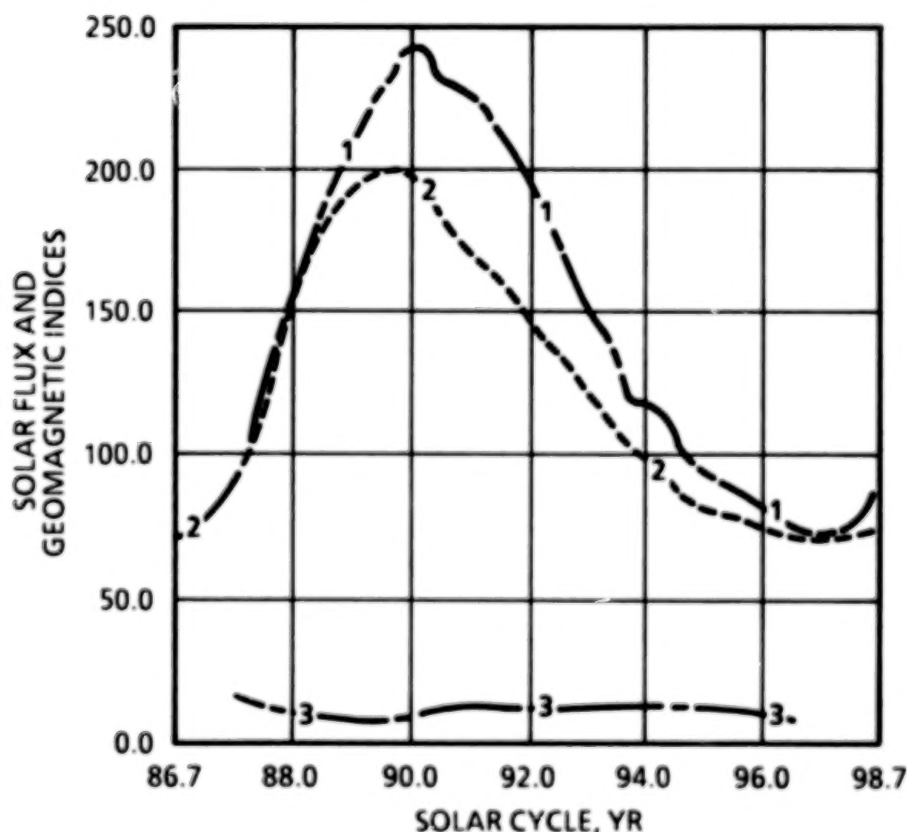


Solar Activity Predictions for Cycle 22

In the thermosphere, the density is strongly influenced by changing levels in solar activity. Both radiant energy and charged particles are emitted by the Sun's surface. It is largely the ultraviolet (UV) and extreme ultraviolet (EUV) radiation emitted by the Sun that heats the upper atmosphere and produces changes in the constituent number density. One component of this radiation relates to the active regions on the solar disk and varies from day-to-day in direct proportion to the ebb and flow of sunspot activity. The other component relates to the solar disk itself and moves more slowly with the 11-year solar cycle. The intensity of this component is measured directly by the $F_{10.7}$ number, which is shown in the figure below. This number represents the radio flux density (in units of 10^4 Jansky, or 10^{-22} watts/m²/S/bandwidth) at 10.7 cm wavelength, and is used as a measure of solar activity because it correlates well with radiation absorbed by the upper atmosphere. The A_p number, also shown in this figure, is a measure of variations in the Earth's magnetic field intensity. Charged particles emitted by the Sun spiral along the Earth's magnetic field lines and also contribute to heating of the atmosphere, but to a much lesser extent than the Sun's radiant energy. Increases in the A_p number (geomagnetic index) result in higher number densities at any given altitude.

LEGEND

- 1 = SOLAR FLUX $F_{10.7} + 2$ SIGMA, (10^4 JANSKY)
- 2 = SOLAR FLUX $F_{10.7}$ (10^4 JANSKY) PREDICTED
- 3 = GEOMAGNETIC INDEX MEAN

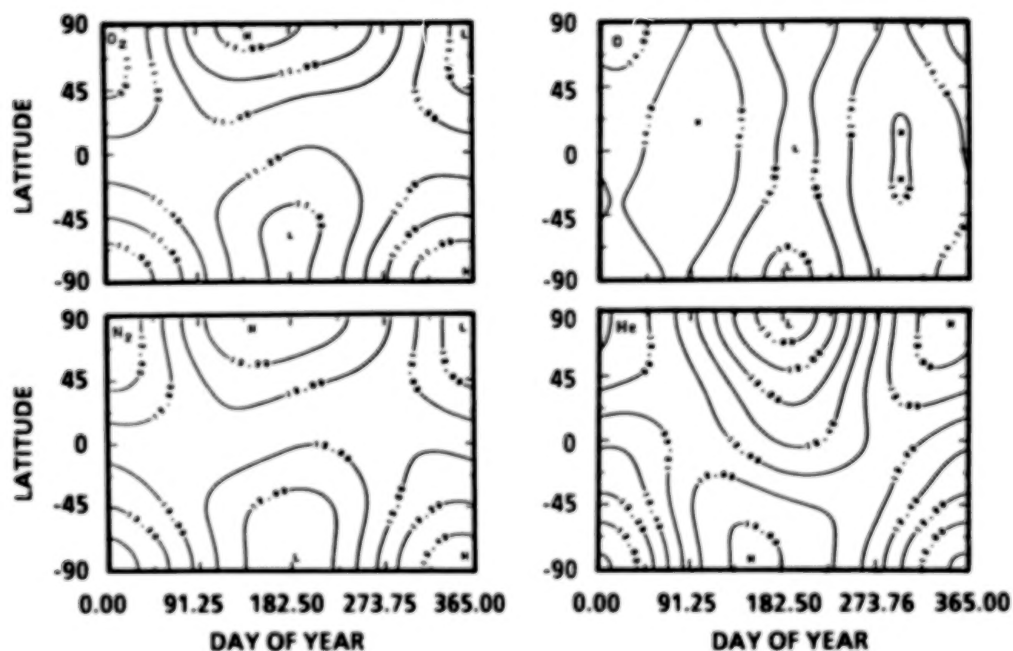


SEASONAL VARIATIONS IN CONSTITUENT NUMBER DENSITY

- **ALL CONSTITUENTS HAVE A SIGNIFICANT (5-10%) SEMIANNUAL VARIATION IN NUMBER DENSITY DUE TO SUN BEING ABOVE THE EQUATOR DURING SUMMER MONTHS, AND BELOW THE EQUATOR DURING MONTHS OF WINTER**
- **ATOMIC OXYGEN HAS A SUMMER MAXIMUM AT HIGHER ALTITUDES, AND A WINTER MAXIMUM AT LOWER ALTITUDES**
- **BOTH ATOMIC OXYGEN AND ATOMIC NITROGEN UNDERGO A SEMIANNUAL VARIATION IN NUMBER DENSITY**
- **AND AT HIGHER ALTITUDES, THEIR MAXIMUM DENSITIES OCCUR NEAR THE EQUINOXES**
- **HEAVIER SPECIES (O_2 , N_2 , Ar) EXPERIENCE LOWEST DENSITIES DURING WINTER MONTHS, AND HIGHEST DENSITIES DURING SUMMER MONTHS**
- **CONVERSELY, HIGHEST DENSITIES FOR THE LIGHTER SPECIES (H, He) OCCUR DURING WINTER MONTHS**

Contour Plots of Diurnally Averaged Number Densities of O_2 , N_2 , O and He at 400 km Altitude during Nominal Solar Activity Conditions

All constituents in the upper atmosphere have a significant (5 to 10 percent) semiannual variation in number density, which results from the Sun being above the equator during summer months and below the equator during the months of winter. Atomic oxygen behaves differently than the other species in that it experiences a winter maximum at lower altitudes and a summer maximum at higher altitudes. During months of summer, O (as well as N) exhibits maximum density near the equinoxes. In the northern hemisphere, O_2 and N_2 have highest densities during summer months and lowest densities during winter months. Conversely, He , which is a lighter species, has its highest density during winter months. These results from the MSIS-86 model are consistent with data obtained from the Explorer Satellites, which have demonstrated helium experiences a winter density bulge in the exosphere. The formation of this bulge near the polar region may be attributed to seasonal winds in the thermosphere. The mechanism of this bulge and its variation with latitude are, however, still under investigation.



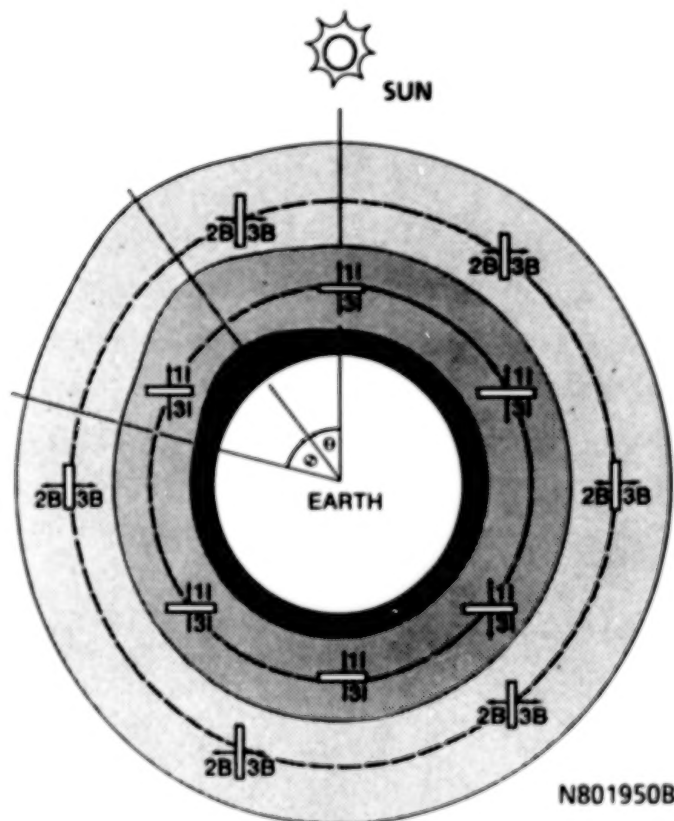
(LOGARITHM TO BASE 10) OF O_2 , N_2 , O AND He AT 400 km ALTITUDE DURING NOMINAL SOLAR CONDITIONS. NOTE O (AS WELL AS N) EXHIBITS MAXIMUM DENSITY NEAR THE EQUINOXES. IN NORTHERN HEMISPHERE, O_2 AND N_2 HAVE HIGHEST DENSITIES DURING SUMMER MONTHS; He , WHICH IS A LIGHTER SPECIES, HAS ITS HIGHEST DENSITY DURING WINTER MONTHS (SOURCE: NASA/GSFC: H. HEDIN, 1987)

DINURAL VARIATIONS IN CONSTITUENT NUMBER DENSITIES

- NEAR EQUATORIAL LATITUDES, A DENSITY BULGE DURING DAYLIGHT HOURS IS PRODUCED BY SOLAR HEATING OF THE ATMOSPHERE
- DIURNAL WINDS IN THE THERMOSPHERE CAUSE TOTAL DENSITY INCREASES TO LAG SUB-SOLAR POINT - BULGE OCCURS ABOUT 30° EAST OF SOLAR NOON AND MIGRATES NORTH AND SOUTH AS SUN'S DECLINATION ANGLE CHANGES
- CONSTITUENT NUMBER DENSITIES DO NOT EACH MAXIMIZE AT SAME LOCAL TIME
 - HELIUM EXPERIENCES A MORNING MAXIMUM IN NUMBER DENSITY
 - ATOMIC OXYGEN (AO) REACHES MAXIMUM DENSITY APPROXIMATELY 40° EAST OF SOLAR NOON
- AT ANY GIVEN HEIGHT ABOVE 120 km, MAXIMUM DENSITY OCCURS WITHIN THE CENTER OF DENSITY BULGE - SATELLITES MOVING THROUGH THIS REGION PERIODICALLY EXPERIENCE ENHANCED AO EFFECTS

Surface Orientations Relative to Atomic Oxygen Density at Solar Noon

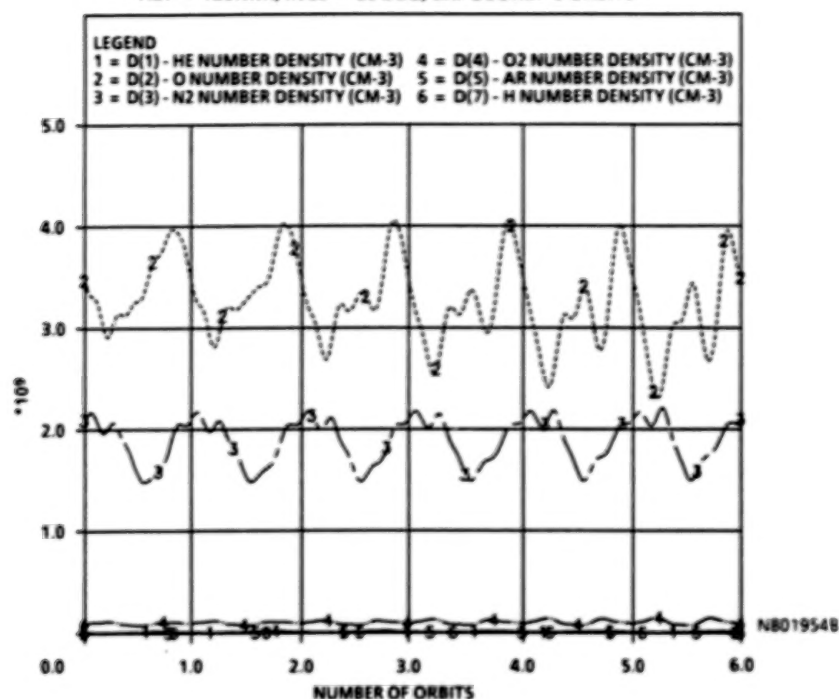
Diurnal (24 hr.) variations of density occur in the upper atmosphere and result from the Earth's rotation about its axis. During rotation, regions of the atmosphere illuminated by the Sun are warmed by its rays, and regions in darkness are cooled by radiative heat loss to space. These variations become more pronounced at higher altitudes. At an altitude of 200 km, the nightside and dayside densities are about the same. At 600 km altitude, the dayside density may become a factor of eight higher than the nightside density during conditions of high solar activity. The total density has a maximum around 1400 hrs. local solar time (30° east of solar noon) at a latitude equal to that of the sub-solar point, and a minimum around 0300 hrs. at about the same latitude in the opposite hemisphere. These effects are attributed to absorption of EUV radiation by the neutral atmosphere, followed by heat conduction downward toward lower altitudes. Diurnal winds in the thermosphere cause the densities of individual constituents to maximize at different local times. Helium maximizes during the mid-morning hours, about 30° west of solar noon. Atomic oxygen reaches its maximum density about 40° east of solar noon. Note from the figure shown below, spacecraft surfaces, such as Surfaces 3I and 2B, which fly through this bulge in atomic oxygen density will experience higher fluxes than surfaces protected from it because of wake effects.



SIMULATED SURFACES
1I: SOLAR-VIEWING
3I: ANTISOLAR
2B: SPACE-VIEWING, RAM
3B: SPACE-VIEWING, WAKE

SDIO DELTA STAR FLUENCE PREDICTIONS

ALT = 120NMI, INCL = 50 DEG, EXPOSURE: 6 ORBITS



ATOMIC OXYGEN SURFACE INTERACTION STUDIES

- PREVIOUS STS EXPERIMENTS HAVE SHOWN SURFACE RECESSION OF TYPICAL SPACECRAFT MATERIALS IS DIRECTLY RELATED TO FLUENCE, OR TOTAL INTEGRATED FLUX, DETERMINED OVER THE EXPOSURE PERIOD:
 - FLUX = NUMBER DENSITY TIMES ORBITAL VELOCITY
 - FLUENCE = FLUX TIMES EXPOSURE PERIOD
- ATOMIC OXYGEN NUMBER DENSITY MAY BE DETERMINED FOR EACH ORBITAL PASS USING GLOBAL THERMOSPHERIC MODELS
- SPACECRAFT VELOCITY IS DERIVED USING ORBITAL MECHANICS EQUATIONS
- FLUENCE PER ORBIT IS OBTAINED BY MULTIPLYING PRODUCT OF VELOCITY AND DENSITY TIMES THE ORBITAL PERIOD (NOMINALLY, 90 MINUTES) EXPRESSED IN SECONDS
- TOTAL FLUENCE IS THEN DETERMINED BY SUMMING FLUENCE OBTAINED DURING EACH ORBITAL PASS OVER THE TOTAL NUMBER OF ORBITS MADE DURING THE MISSION -- CALCULATIONS ARE STRAIGHTFORWARD FOR RAM-ORIENTED EXPOSURES
- DIFFICULTIES ARISE, HOWEVER, WHEN THE INCIDENT FLUX IS NOT ALWAYS NORMAL TO THE SURFACE, SUCH AS FOR SOLAR INERTIAL OR SUN-SYNCHRONOUS SATELLITES

FLUENCE COMPUTATIONAL MODEL

- COMPUTATIONAL PROGRAMS ARE AVAILABLE TO COMPUTE FLUENCES INCIDENT ON SPACECRAFT SURFACES IN LOW-EARTH ORBIT FOR A VARIETY OF EXPOSURE ATTITUDES
- MODEL IS GENERALIZED AND INCLUDES CONDITIONS OF EITHER NORMAL OR OBLIQUE (SWEEPING) IMPINGEMENT -- SURFACE ORIENTATIONS AND INITIAL ORBITAL CONDITIONS DEFINED PRIOR TO PROGRAM EXECUTION:
 - SURFACES ARE SPECIFIED BY: (1) SPACECRAFT ALTITUDE, (2) ORBIT INCLINATION, (3) EARTH LONGITUDE AND LATITUDE OF FIRST NODAL CROSSING, (4) LOCAL SOLAR TIME, (5) YEAR, MONTH, AND DAY SIMULATION WILL BEGIN, AND (6) MISSION DURATION
 - SPACECRAFT IS PERMITTED TO ADVANCE THROUGH ITS ORBIT IN DISCRETE STEPS -- AVERAGE AO DENSITY MIDWAY THROUGH PATH DISTANCE TRAVELED IS OBTAINED USING MSIS-86 THERMOSPHERIC MODEL
 - EQUATIONS ARE USED TO DETERMINE ORBITAL VELOCITY NORMAL TO EACH SURFACE UNDER STUDY
 - AO FLUENCE IS DETERMINED USING VALUES OF AVERAGE DENSITY, RELATIVE VELOCITY, AND EXPOSURE DURATION ALONG EACH PATH-LENGTH TRAVELED
 - INCREMENTAL EXPOSURES OBTAINED DURING PROGRAM OPERATION ARE THEN SUMMED OVER DURATION OF SIMULATION TO OBTAIN TOTAL FLUENCE INCIDENT ON EACH SPACECRAFT SURFACE UNDER STUDY

SPACECRAFT FLUENCE PREDICTIONS

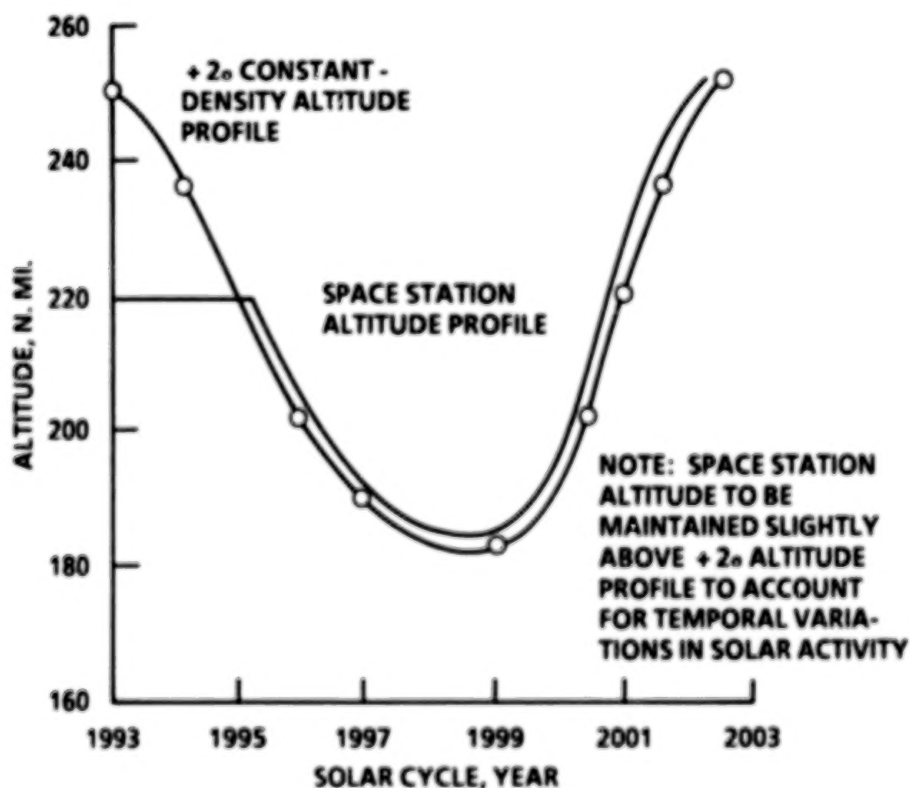
SPACECRAFT PROGRAM	EXPOSURE ALTITUDE, NMI	ORBIT INCLINATION	MISSION DURATION	ATOMIC OXYGEN FLUENCE, ATOMS/cm ²	ESTIMATED SURFACE RECESSON, MILS (KAPTON)*
DELTA STAR	120	50°	7 DAYS	1.5 X 10 ²¹ (RAM)	1.8
DELTA STAR	176	50°	3 MONTHS	9.0 X 10 ²⁰ (SI)	1.1
DELTA STAR	176	50°	1 YEAR	3.5 X 10 ²¹ (SI)	4.1
SPACE TELESCOPE	320-260	28.5°	5 YEARS	4.0 X 10 ²¹ (RAM)	4.7
SPACE TELESCOPE	320-260	28.5°	5 YEARS	1.4 X 10 ²¹ (SI)	1.7
SPACE STATION	250-180	28.5°	30 YEARS	1.5 X 10 ²² (RAM)	177
SPACE STATION	250-180	28.5°	20 YEARS	5.5 X 10 ²² (SI)	65

* SURFACE RECESSON = **MATERIAL REACTION EFFICIENCY (cm³/atom) X AO FLUENCE (atoms/cm²), WHERE

** REACTION EFFICIENCY = VOLUME OF MATERIAL LOSS PER INCIDENT OXYGEN ATOM (3.0 X 10⁻²⁴cm³/atom FOR KAPTON)

Space Station Freedom Altitude Strategy for Surface Interaction Studies

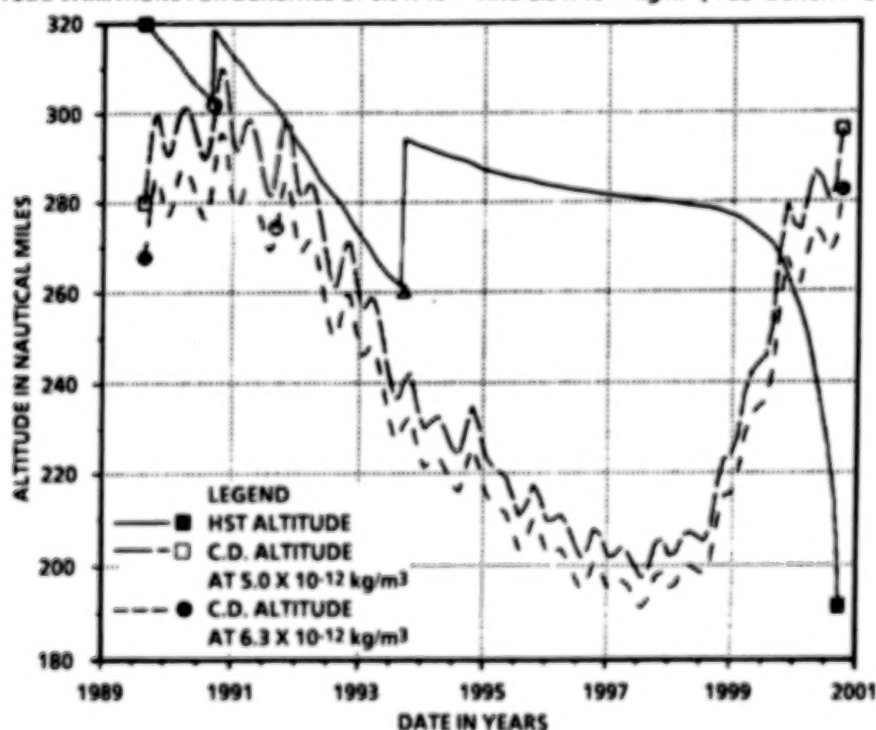
During conditions of high solar activity, the atmosphere expands and the drag on spacecraft surfaces increases substantially. Spacecraft flying at low altitudes during solar maximum experience higher deceleration forces and must be re-boosted to higher altitudes to remain in stable orbit about the Earth. Not only does drag often dictate requirements for re-boost capability, but it usually restricts use of sensitive microgravity experiments. As is illustrated in this figure, a variable altitude strategy has been baselined for Space Station Freedom which reduces the amount of atmospheric drag it will experience during the next solar cycle. During periods of high solar activity, Space Station Freedom will be operated at high altitudes (220 to 250 nmi) to minimize deceleration forces on its sensitive microgravity experiments. As solar activity decreases, the altitude of Space Station Freedom will be reduced to maintain number density constant. Since variations in orbital velocity over this altitude range are very small, constant density will result in constant aerodynamic drag. At Solar minimum, Space Station Freedom will have attained its lowest (180 nmi) altitude. As solar activity increases to its maximum level, aerodynamic drag will once again be controlled by boosting Freedom to higher altitudes at rates which maintain the number density constant. This strategy will result in significant savings in STS operations costs -- it will reduce the number of Shuttle resupply flights for Space Station Freedom because the Orbiter can deliver more payload weight to lower altitudes than it can to higher altitudes. However, when compared to a constant altitude strategy, the constant density strategy will increase the atomic oxygen fluence on Space Station surfaces by about a factor of four. Thus, when compared to a constant altitude strategy, the need for protective coatings to limit AO surface interactions becomes even more significant.



Hubble Space Telescope Predicted and Constrained Orbital Altitudes

The Hubble Space Telescope (HST) is a Shuttle-launched and serviced satellite designed to have an operational life over many years. To meet these lifetime requirements, on-orbit maintenance is planned, with major refurbishment accomplished by retrieval and return to Earth. The HST is designed to operate in a 28.5° inclined circular orbit at altitudes from 320 to 215 nmi (593 to 398 km). The satellite will be deployed at an altitude just high enough so that "worst case" aerodynamic drag will not cause it to decay below 215 nmi at the end of a 5-year period. Lifetime predictions are strongly dependent on assumptions made about the degree of solar activity, as high activity increases the atmospheric density at a given altitude, thereby increasing the drag force and shortening vehicle life. Given current solar activity predictions (see constant density curves shown below), the HST must be reboosted twice by the Space Shuttle during its 5-to 7-year lifetime. The first reboost will occur approximately 1 year after launch, and is required to maintain the satellite above the 6.3×10^{-12} kg/m³ density curve encountered early-on during its mission. Assuming a reboost flight is delayed by several months, reaction wheels aboard the HST will have to spin at higher speeds to maintain attitude control within the high aerodynamic drag environment, and excessively long times will occur between target acquisitions. Even longer delays would saturate the reaction wheels, and attitude control would then be lost altogether. To avoid these problems, NASA will dedicate a Shuttle flight to reboost the HST early in its mission. Also note from this figure, a second reboost flight will occur approximately 4 years after the HST is delivered to orbit, during which time its batteries and solar arrays will be changed out to extend its lifetime.

STS LAUNCH DATE OF 8/31/89, $F_{10.7}$ (PEAK) = 245
ALTITUDE VARIATIONS FOR DENSITIES OF 5.0×10^{-12} AND 6.3×10^{-12} kg/m³ (+ 2σ DENSITY CURVES)



SOURCE: NASA/MSFC; V. BUCKELEW

CONCLUSIONS

- **ATOMIC OXYGEN IS THE MOST ABUNDANT CONSTITUENT IN THE LOW-EARTH ORBIT ENVIRONMENT:**
 - **AT ORBITAL ALTITUDES, NEUTRAL ATMOSPHERE CONSISTS PRIMARILY OF 80% ATOMIC OXYGEN AND 20% MOLECULAR NITROGEN**
 - **INCREASES IN SOLAR ACTIVITY LEAD TO HIGHER ATOMIC OXYGEN NUMBER DENSITIES**
 - **OXYGEN DENSITY DECREASES EXPONENTIALLY WITH INCREASING ALTITUDE**
- **GLOBAL THERMOSPHERIC MODELS, WHEN COMBINED WITH ORBITAL MECHANICS MODELS, MAY BE USED TO PREDICT ATOMIC OXYGEN FLUENCE, OR TOTAL INTEGRATED FLUX, INCIDENT ON SPACECRAFT SURFACES:**
 - **RAM-ORIENTED SURFACES RECEIVE MORE FLUENCE THAN SOLAR INERTIAL SURFACES**
 - **MISSIONS OF LONG DURATION MORE SEVERELY AFFECTED THAN MISSIONS OF SHORT DURATION**
 - **MISSIONS CONDUCTED DURING PERIODS OF LOW SOLAR ACTIVITY LESS SEVERELY AFFECTED THAN MISSIONS DURING HIGH ACTIVITY**
- **FLUENCE PREDICTIONS, WHEN USED WITH STS MATERIAL REACTIVITY MEASUREMENTS, PROVIDE RELIABLE ESTIMATES OF THE OXIDATIVE EFFECTS ON SPACECRAFT SURFACES**

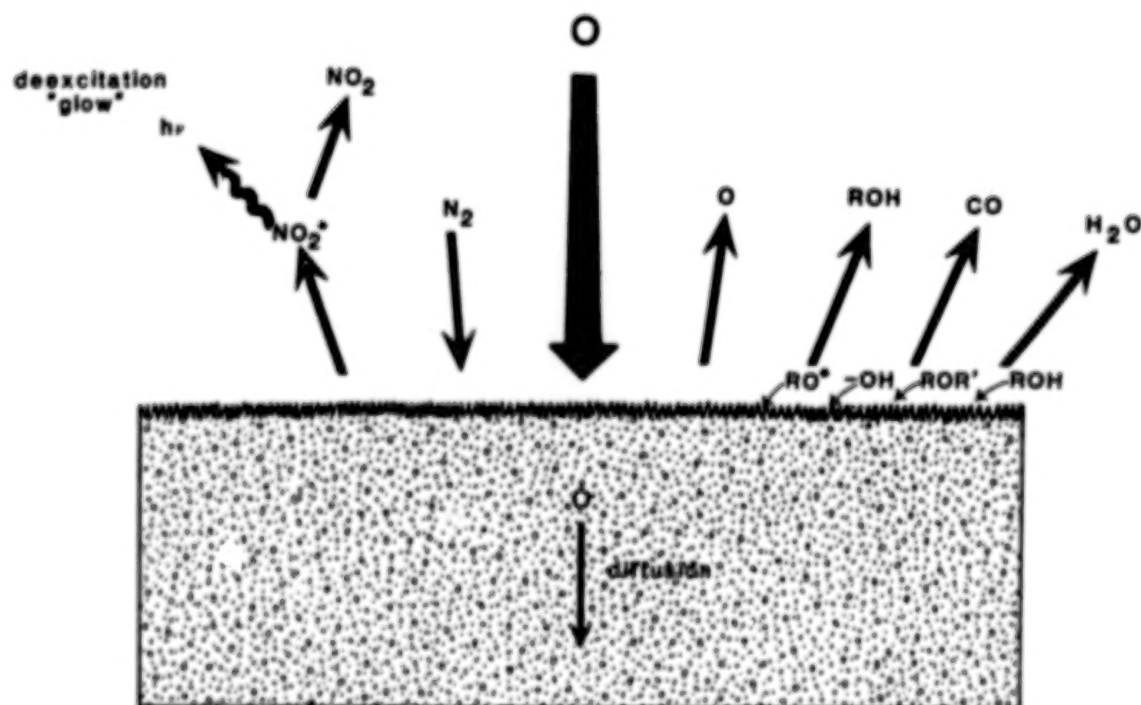
ATOMIC OXYGEN EFFECTS ON MATERIALS *

Bruce A. Banks, NASA Lewis Research Center
Sharon K. Rutledge, NASA Lewis Research Center
Joyce A. Brady, Sverdrup Technology, Inc.
Cleveland, Ohio
James E. Mellow, Ohio University
Athens, Ohio

*Original photographs not available at time of publication.

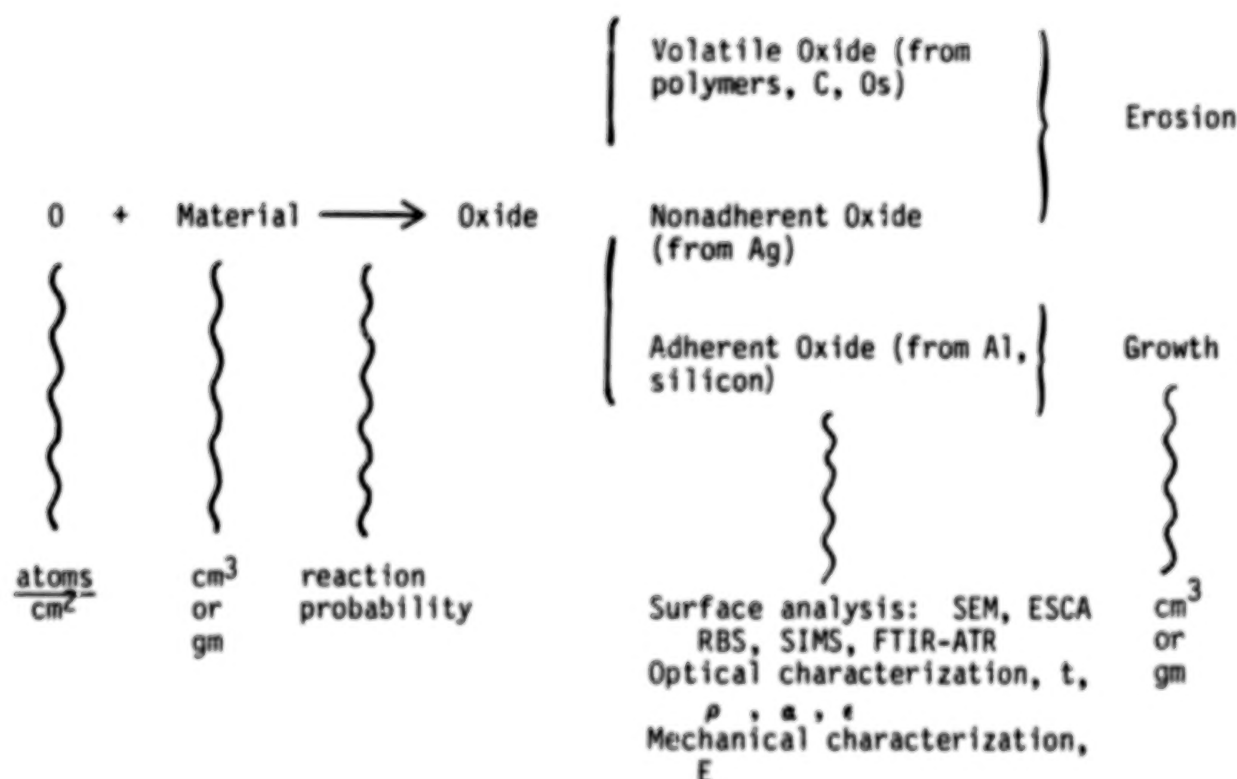
ATOMIC OXYGEN SURFACE INTERACTION PROCESSES

Atomic oxygen with an energy level of 4 - 5 eV may initiate numerous chemical and physical events on the surface it impacts. The atomic oxygen may simply be scattered or it may chemically react with nitrogen, also incident upon the surface, to form nitrous oxide in an excited state, which can de-excite to produce a glow. If atomic oxygen reacts with an organic material, volatile fragments, such as short chain oxidation products, may leave the surface. The surface may also be populated with excited state fragments, radicals, or polymeric molecules with oxygen-containing functionalities. The oxygen may also, as in the case of silver, diffuse into the bulk of the material.



QUANTIFICATION OF ATOMIC OXYGEN EFFECTS ON MATERIALS

The quantification of atomic oxygen interaction with materials has generally been performed by measuring the atomic oxygen flux and multiplying it by the duration of exposure, which results in an atomic oxygen fluence in terms of atoms per square centimeter. The material is usually measured in terms of weight or volume, and the probability that oxygen will react with the material can be measured (for some materials) in terms of reaction probability. The chemistry of the surface which is reacting with the incident oxygen may cause the formation of volatile oxides from polymers, carbon, and osmium; or oxides which are not adherent and tend to spall, as in the case of silver, may form. Both of these types of surface oxides contribute to net erosion of the surface. If the surface material being impinged by atomic oxygen forms an adherent oxide, such as aluminum forming aluminum oxide or silicones forming silicon dioxide on the surface, then the surface may grow. The chemistry of the remaining or reacted surface may be analyzed by surface analysis, optical characterization, and mechanical characterization (in terms of modulus and elasticity). If net erosion of the material surface occurs, the volume or mass loss is quantified and used to calculate an erosion or recession per incident oxygen atom, generally in units of cubic centimeters per incident oxygen atom.



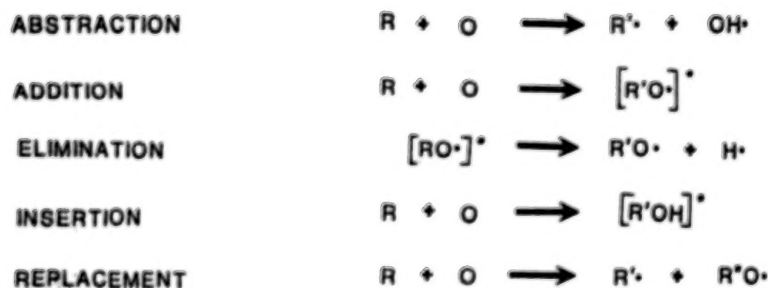
ATOMIC OXYGEN REACTION PROBABILITIES

The probability of atomic oxygen reacting with a given material can be calculated for those materials which form known or simple oxides. Using erosion yield numbers from space tests, one finds that atomic oxygen has a rather low probability (approximately 13%) of reacting with carbon to form carbon monoxide. However, in the case of silver, a very high fraction of the incident atomic oxygen reacts with the silver to form silver oxide. Because the silver oxide may tend to shield from further oxidation or be a catalyst surface for recombination of atomic oxygen on the surface, the reaction probability for silver is expected to drop as the degree of oxidation on the surface becomes higher.

<u>MATERIAL</u>	<u>EROSION YIELD, cm³/atom</u>	<u>REACTION PROBABILITY, %</u>
Carbon	1.2×10^{-24}	13
Silver	10.7×10^{-24}	62

ATOMIC OXYGEN REACTION MECHANISMS WITH POLYMERS

Various mechanisms have been suggested for the reactions of atomic oxygen with polymers based on studies with simple organic compounds. Basic processes are labeled as abstraction, addition, elimination, insertion, and replacement reactions. Abstraction is the process by which atomic oxygen "abstracts" an atom, such as hydrogen, from the compound. "Addition" describes the process by which an oxygen atom adds or attaches itself to an organic compound. This has been observed for the reaction with a typical alkene, and the initial product is a vibrationally excited molecule which can then undergo "elimination" of a hydrogen atom. Atomic oxygen has also been observed to "insert" between two bound atoms, such as carbon and hydrogen in an organic molecule. "Replacement" is the mechanism by which an oxygen atom attaches to the molecule and a portion of the original molecule departs (usually as a radical). Oxygen, in effect, replaces a group originally present on the molecule producing an alkoxy radical and an alkyl radical.



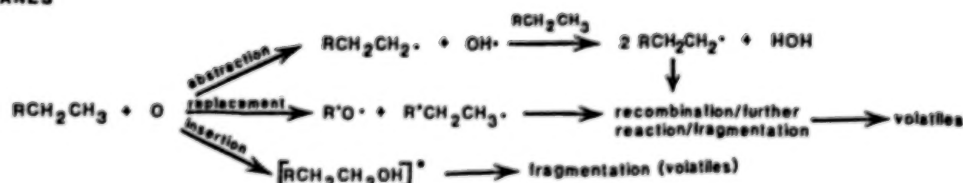
ATOMIC OXYGEN REACTION MECHANISMS

Reactions of atomic oxygen with polymers have been shown to occur by various mechanisms. Under thermal energy conditions, it is known that ground state atomic oxygen $O(^3P)$ abstracts hydrogen from saturated organic molecules. Singlet atomic oxygen $O(^1D)$ at thermal energy, inserts into C-H bonds in saturated organic molecules to form alcohols. Another suggested mechanism is replacement to form alkyl radicals and alkoxy radicals. These primary reaction products undergo further reactions which lead to fragmentation of the reactants. The fragmentation products form weakness of bonds. Under high vacuum conditions, moderate molecular weight oligomers and fragments are volatile.

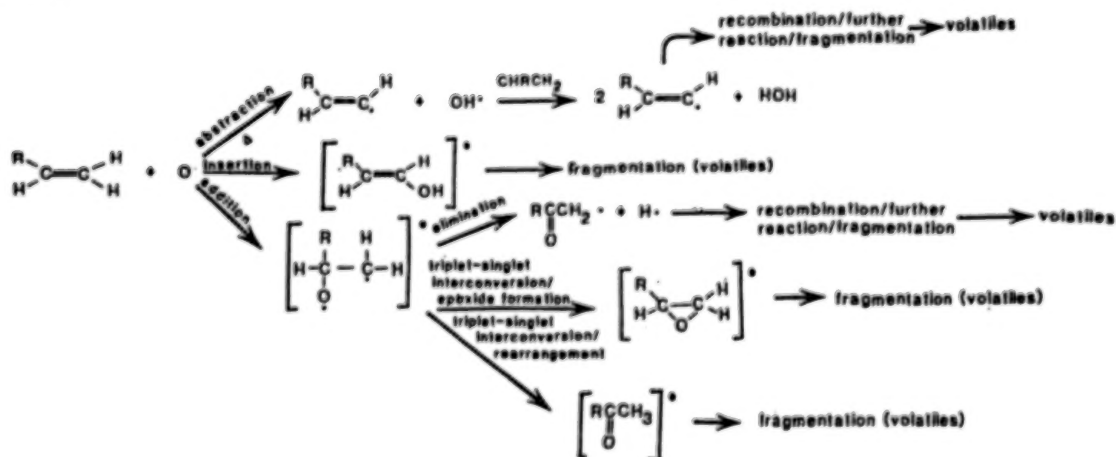
Unsaturated organic molecules show different pathways leading to formation of fragments and volatiles. $O(^3P)$ adds to carbon-carbon double bonds, forming metastable triplet biradical intermediates which can undergo further reaction to form epoxide, aldehyde, and ketone products. The favored pathway for the reaction of the triplet biradical is hydrogen elimination to form a carbonyl-containing radical. $O(^1D)$ inserts into C-H bonds in alkenes and the resulting metastable species undergoes further reaction. At high temperatures, hydrogen abstraction may compete with O atom insertion.

It is important to note that at high energy, $O(^3P)$ acts similarly to $O(^1D)$ and it is more difficult to distinguish between them.

ALKANES



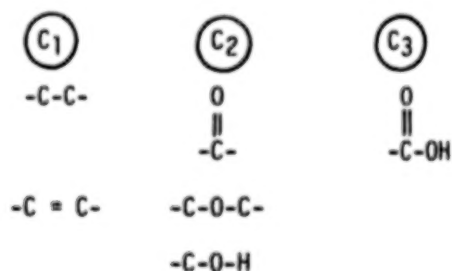
ALKENES



ESCA ANALYSIS OF POLYETHYLENE SURFACE

Surface chemical analysis by means of ESCA has been performed on polyethylene surfaces exposed to atomic oxygen in low Earth orbit. Such analyses performed by Coulter, Liang, Chung, Smith, and Gupta have indicated that olefin formation is not an important process in atomic oxygen interaction with polyethylene.

	C ₁	C ₂	C ₃	O
Theoretical	100.0	--	--	--
Control	99.2	--	--	0.8
Exposed	81.5	4.5	3.1	9.9



EROSION YIELDS OF VARIOUS MATERIALS EXPOSED TO ATOMIC OXYGEN IN LOW EARTH ORBIT

The erosion yields of various materials exposed to atomic oxygen are listed along with their sources for all the references known to the authors at the present time.

MATERIAL	EROSION YIELD, $\times 10^{-24}$ cm ³ /ATOM	REFERENCE
Aluminum (150 Å)	0.0	1
Aluminum-coated Kapton	0.01	2
Aluminum-coated Kapton	0.1	2
Al ₂ O ₃	<0.025	3
Al ₂ O ₃ (700 Å) on Kapton H	<0.02	4
Apiezon grease 2 μm	>0.625	5
Aquadag E (graphite in an aqueous binder)	1.23	6
Carbon	1.2	7, 1, 8, 9
Carbon (various forms)	0.9 - 1.7	10
Carbon/Kapton 100XAC37	1.5	11
401-C10 (flat black)	0.30	12

MATERIAL	EROSION YIELD, $\times 10^{-24}$ cm ³ /ATOM	REFERENCE
Chromium (123 Å)	partially eroded	14
Chromium (125 Å) on Kapton H	0.006	15, 16
Copper (bulk)	0.0	17
Copper (1,000 Å) on sapphire	0.007	15, 16
Copper (1,000 Å)	0.0064	14
Diamond	0.021	17
Electrodag 402 (silver in a silicone binder)	0.057	6
Electrodag 106 (graphite in an epoxy binder)	1.17	6
Epoxy	1.7	10, 16
Fluoropolymers:		
FEP Kapton	0.03	18
Kapton F	<0.05	6
Teflon, FEP	0.037	5
Teflon, FEP	<0.05	10

MATERIAL	EROSION YIELD, $\times 10^{-24}$ cm ³ /ATOM	REFERENCE
Teflon, TFE	<0.05	10, 6
Teflon, FEP and TFE	0.0 and 0.2	15, 19
Teflon, FEP and TFE	0.1	15
Teflon	0.109	19
Teflon	0.5	15
Teflon	0.03	15
Teflon	<0.03	9
Gold (bulk)	0.0	17
Gold	appears resistant	20
Graphite Epoxy:		
1034 C	2.1	10
5208/T300	2.6	10
GSFC Green	0.0	1
HOS-875 (bare and preox)	0.0	1
Indium Tin Oxide	0.002	15, 16
Indium Tin Oxide/Kapton (aluminized)	0.01	2
Iridium Film	0.0007	17

MATERIAL	EROSION YIELD, $\times 10^{-24}$ cm ³ /ATOM	REFERENCE
Lead	0.0	1
Magnesium	0.0	1
Magnesium Fluoride on glass	0.007	15, 16
Molybdenum (1,000 Å)	0.0056	4
Molybdenum (1,000 Å)	0.006	15, 16
Molybdenum	0.0	1
Mylar	3.4	10
Mylar	2.3	15, 19
Mylar	3.9	15, 19, 9
Mylar	1.5 - 3.9	15
Mylar A	3.7	18
Mylar A	3.4	21, 6
Mylar A	3.6	6
Mylar D	3.0	6
Mylar D	2.9	21
Mylar with Antiox	heavily attacked	22
Nichrome (100 Å)	0.0	1

MATERIAL	EROSION YIELD, $\times 10^{-24}$ cm ³ /ATOM	REFERENCE
Nickel film	0.0	17
Nickel	0.0	8
Niobium film	0.0	17, 1
Osmium	0.026	10
Osmium	heavily attacked	20
Osmium (bulk)	0.314	17
Parylene, 2.5 μ m	eroded away	22
Platinum	0.0	1
Platinum	appears resistant	20
Platinum film	0.0	17
Polybenzimidazole	1.5	10, 7
Polycarbonate	6.0	8
Polycarbonate resin	2.9	17
Polyester - 7% Poly- silane/93% Polyimide	0.6	10
Polyester	heavily attacked	10, 22
Polyester with Antiox	heavily attacked	10, 22
Polyester (Pen-2,6)	2.9	23
Polyethylene	3.7	10, 21, 16, 15

MATERIAL	EROSION YIELD, $\times 10^{-24}$ cm ³ /ATOM	REFERENCE
Polyethylene	3.3	18, 6
Polyimides:		
BJPIPSX-9	0.28	23
BJPIPSX-9	0.071	24
BJPIPSX-11	0.56	23
BJPIPSX-11	0.15	24
BTDA-Benzidine	3.08	23
BTDA-DAF	2.82	23
BTDA-DAF	0.8	24
BTDA-mm-DOSO2	2.29	23
BTDA-mm-MDA	3.12	23
BTDA-pp-DABP	2.91	23
BTDA-pp-DABP	3.97	23
Kapton (black)	1.4 - 2.2	15, 12
Kapton (TV blanket)	2.0	15
Kapton (TV blanket)	2.04	19
Kapton (OSS - 1 blanket)	2.55	15
Kapton (OSS - 1 blanket)	2.5	15

MATERIAL	EROSION YIELD, $\times 10^{-24}$ cm ³ /ATOM	REFERENCE
Kapton H	3.0	10, 15, 19, 4, 6, 9
Kapton H	2.4	15, 19
Kapton H	2.7	15, 18
Kapton H	1.5 - 2.8	15
Kapton H	2.0	18
Kapton H	3.1	18
ODPA-mm-DABP	3.53	23
PMDA-pp-DABP	3.82	23
PMDA-pp-MDA	3.17	23, 24
PMDA-pp-ODA	4.66	23
Polymethylmethacrylate	3.1	16
25% Polysiloxane, 45% Polyimide	0.3	10
25% Polysiloxane-Polyimide	0.3	9
Polystyrene	1.7	10, 16, 9
Polysulfone	2.4	10, 16
Polyvinylidene Fluoride	0.6	9

MATERIAL	EROSION YIELD, $\times 10^{-24}$ cm ³ /ATOM	REFERENCE
----------	---	-----------

Pyrrone:

PMMA-DAB	2.5	23
S-13-GLO, white	0.0	12
SiO ₂ (650 Å) on Kapton H	0.00103	4
SiO _x /Kapton (aluminized)	0.01	2

Silicones:

DC1-2577	0.055	21
DC1-2755-coated Kapton	0.05	15
DC1-2775-coated Kapton	<0.5	15
DC6-1104	0.0515	20
Grease 60 μ m	intact but oxidized	25
RTV-560	0.443	21
RTV-615 (black, conductive)	0.0	20
RTV-615 (clear)	0.0625	5
RTV-670	0.0	1

MATERIAL	EROSION YIELD, $\times 10^{-24}$ cm ³ /ATOM	REFERENCE
----------	---	-----------

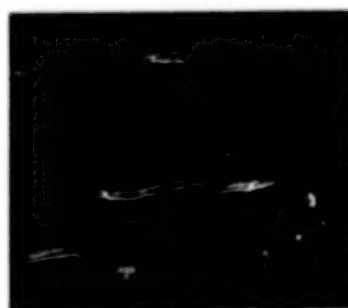
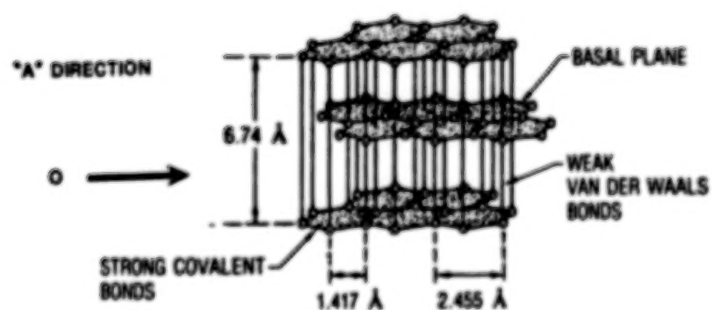
RTV-5695	1.48	11
RTV-3145	0.128	1
T-650-coated Kapton	<0.5	15
Siloxane Polyimide (25% Sx)	0.3	7
Siloxane Polyimide (7% Sx)	0.6	7
Silver	10.5	5
Tantalum	appears resistant	20
Tedlar	3.2	10
Tedlar (clear)	1.3 and 3.2	15
Tedlar (clear)	3.2	18, 6
Tedlar (white)	0.4 and 0.6	15
Tedlar (white)	0.05	15
TiO ₂ , (1,000 Å)	0.0067	5
Trophet 30 (bare and preox)	0.0	1
Tungsten	0.0	8
Tungsten Carbide	0.0	8
YB-71 (ZOT)	0.0	7

EROSION YIELD TABLE
REFERENCES

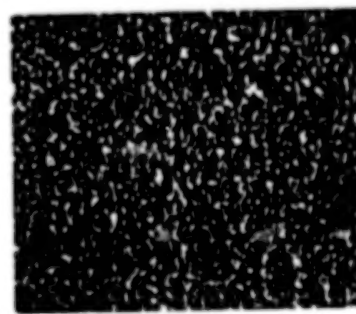
1. Marshall Space Flight Center
2. Smith, K. A. Evaluation of oxygen interaction with materials (EOIM) - STS-8 atomic oxygen effects. AIAA-85-7021. November, 1985.
3. Durcanin, J. T., and Chalmers, D. R. The definition of low earth orbital environment and its effect on thermal control materials. AIAA-87-1599. June, 1987.
4. Banks, B. A., Mirtich, M. J., Rutledge, S. K., and Nagra, H. K. Protection of solar array blankets from attack by low earth orbital atomic oxygen. 18th IEEE Photovoltaic Specialists Conference. October, 1985.
5. Purvis, C. K., Ferguson, D. C., Snyder, D. B., Grier, N. T., Staskus, J. V., and Roche, J. C. Environmental interactions considerations for space station and solar array design. Preliminary - December, 1986.
6. Visentine, J. T., Leger, L. G., Kuminecz, J. F., and Spiker, I. K. NASA JSC STS-8 atomic oxygen effects experiment. AIAA 23rd Aerospace Sciences Meeting. January, 1985.
7. Langley Research Center
8. University of Alabama at Huntsville
9. Coutler, D. R., Liang, R. H., Chung, S. H., Smith, K. O., and Gupta, A. O-atom degradation mechanisms of materials. Taken from Proceedings of NASA Workshop on Atomic Oxygen Effects. June 1, 1987, p. 42.
10. Leger, L. G., Santos-Mason, B., Visentine, J. T., and Kuminecz, J. F. Review of LEO flight experiments. Proceedings on the NASA Workshop on Atomic Oxygen Effects. November, 1986, p. 6.
11. British Aerospace
12. Whitaker, A. F. LEO atomic oxygen effects on spacecraft materials.
13. Martin Marietta
14. Lewis Research Center
15. Leger, L. J., Spiker, I. K., Kuminecz, J. F., Ballentine, T. J., and Visentine, J. T. STS Flight 5 LEO effects experiment - Background description and thin film results. AIAA-83-2631-CP. October, 1983.
16. Jet Propulsion Laboratory
17. Gregory, J. C. Interaction of hyperthermal atoms on surfaces in orbit: The University of Alabama Experiment. Proceedings of the NASA Workshop on Atomic Oxygen Effects. November, 1986, p. 31.
18. Leger, L. J., Visentine, J. T., and Kuminecz, J. F. Low earth orbit.
19. Leger, L. J. Oxygen atom reaction with shuttle materials at orbital altitudes - Data and experiment status. AIAA-83-0073. January, 1983.
20. Goddard Space Flight Center
21. Johnson Space Center
22. Washington University
23. Slomp, W. S., Santos-Mason, B., Bykes, G. F., Jr. and Witte, W. S., Jr. Effects of STS-8 atomic oxygen exposure on composites, polymeric films and coatings. AIAA-85-0421. January, 1985.
24. Santos, B. The dependence of atomic oxygen resistance on polyimide structures. (Preliminary results of STS-8). NASA Headquarters. January 23-24, 1984.
25. Aerospace Corporation

ATOMIC OXYGEN ATTACK OF PYROLYTIC GRAPHITE, A-PLANE (STS-8)

Atomic oxygen attack of both polymers and graphite tends to cause the development of microscopic cone-like surface structures. Such cone-like structures develop in the "A" or prismatic plane direction for pyrolytic graphite. Pronounced structures are evident for RAM-only attack. However, only minor roughening occurs under sweeping atomic oxygen incidence.



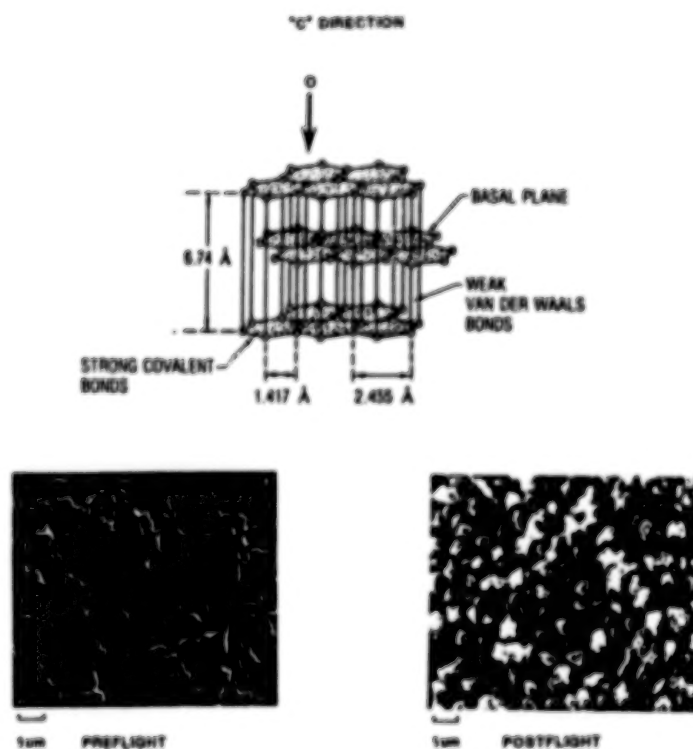
1 μm preflight



1 μm postflight

ATOMIC OXYGEN ATTACK OF PYROLYTIC GRAPHITE, C-PLANE (STS-8)

Atomic oxygen bombardment of the C-plane or basal plane of graphite also causes the formation of surface texture, even though there is no apparent rationale for such development with respect to differential erosion yields for amorphous compared to graphitic regions, as may occur in polymeric materials such as Kapton, Mylar, and fluoropolymers.



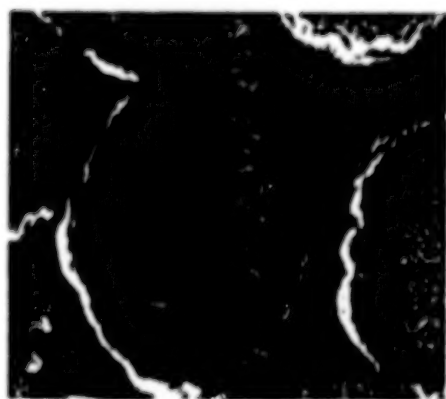
CARBON FIBERS IN EPOXY MATRIX EXPOSED TO ATOMIC OXYGEN (STS-8)

Differences in erosion yield for graphite or carbon fiber epoxy composites result in exposure of the carbon fibers because of more accelerated erosion of the epoxy matrix material.



PAN FIBERS IN EPOXY EXPOSURE TO ATOMIC OXYGEN (STS-8)

PAN fibers (polyacrylonitrile derived) also develop a cone-like microscopic surface morphology. In fact, pitch and PAN based fibers both develop a cone-like morphology upon RAM attack by atomic oxygen. In general, all bulk materials with volatile oxidation products tend to develop cone-like surface morphology upon RAM attack.



1 μm
PREFLIGHT



1 μm
POSTFLIGHT

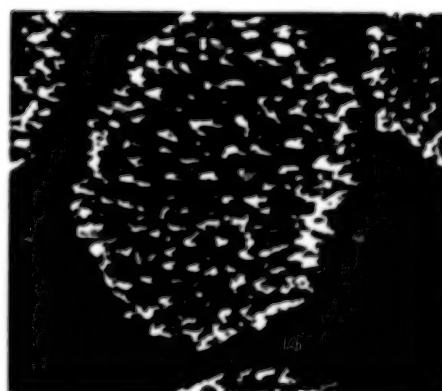
KEVLAR POLYIMIDE FIBERS IN EPOXY EXPOSURE TO ATOMIC OXYGEN (STS-8)

Kevlar polyimide fibers develop a surface texture very similar to Kapton polyimide.



2 um

PREFLIGHT

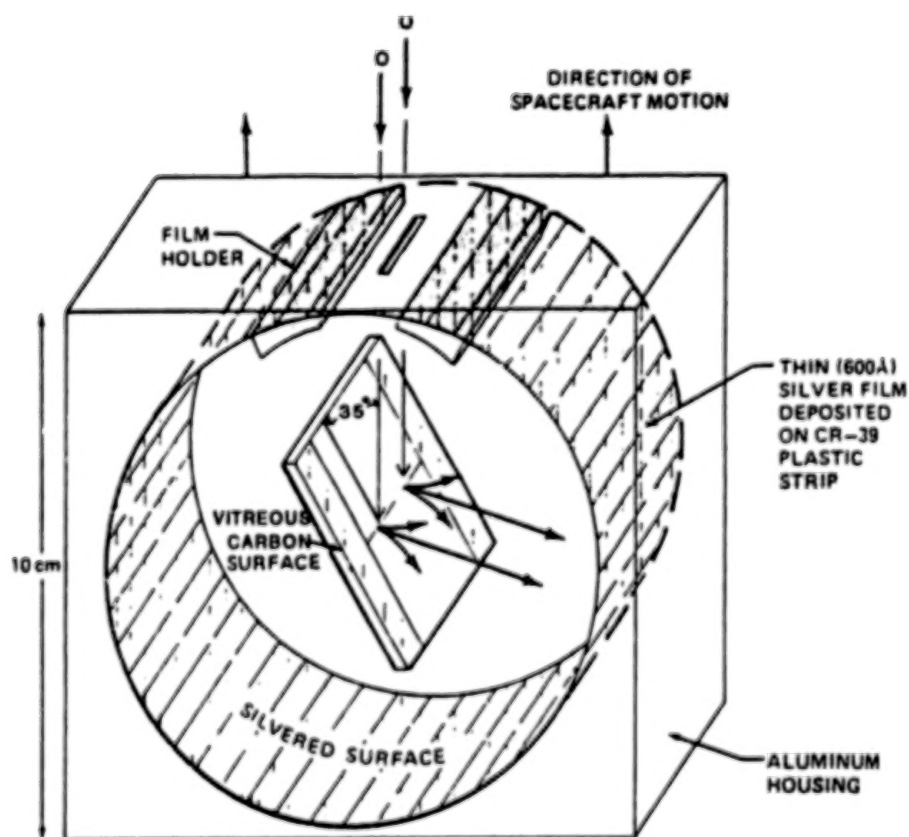


2 um

POSTFLIGHT

OXYGEN ATOM REFLECTOMETER FLOWN ON SHUTTLE STS-8

Atomic oxygen which does not react with a surface may accommodate to the surface or specularly scatter off the surface. Gregory performed an interesting experiment in space on STS-8 which gives some insight into these processes. Atomic oxygen was allowed to enter a slit in a short cylindrical segment which contained a silvered plastic strip to permit optical density measurements to determine the magnitude and direction of reactive species leaving a vitreous carbon target surface.



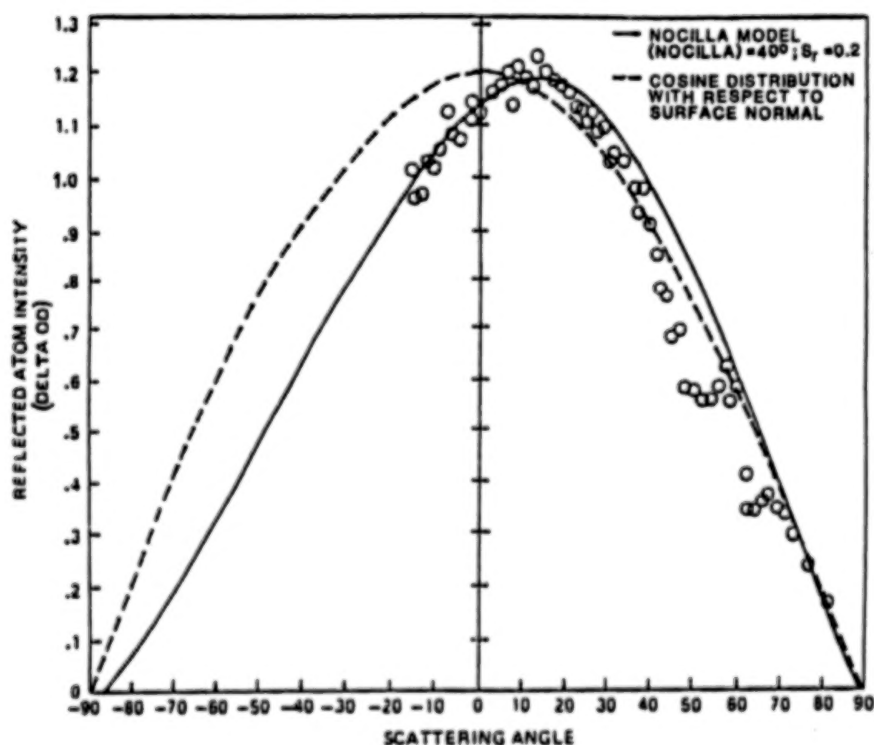
THE JENKINS MODEL OF THE STRUCTURE OF GLASSY CARBON

The vitreous carbon target used for this experiment does not have a preferential direction or plane because it is a woven tangle of graphine ribbons of random orientation.



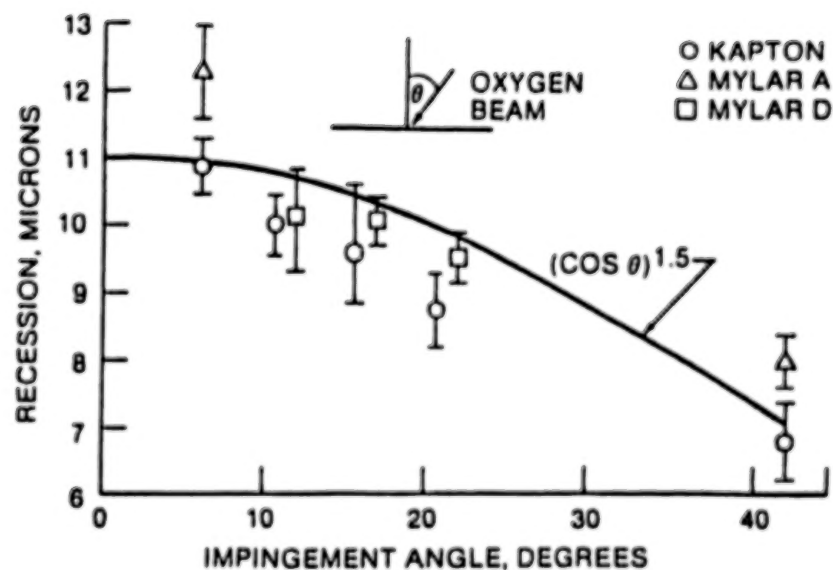
SCATTERED ATOMIC OXYGEN

Atoms of oxygen which do not react with the glassy carbon target surface appear to be ejected with a slight preferential forward specular scattering, indicating that at least a certain portion of the atoms do not totally accommodate to the surface. The facts that the ejection occurs at wide angles and that the probability of reaction is low on the first bounce contribute to a general concern that we must deal with atomic oxygen not only from the RAM direction, but from multiple bounce arrival to assure durability of reactive surfaces.



SURFACE RECESSION DEPENDENCE UPON ATOMIC OXYGEN IMPACT ANGLE

The angle of impact of the atomic oxygen affects the rate of surface erosion with an angular sensitivity proportional to the cosine of the angle with respect to the surface normal to the 1.5 power as opposed to the cosine to the 1 power, as would normally be expected. This may be an indicative that highly inclined surfaces may have a higher probability of specular scattering. The role that the microscopic cone formation on the surface plays with respect to this angular sensitivity is not clearly understood.



ATOMIC OXYGEN EROSION YIELD TEMPERATURE DEPENDENCE

Atomic oxygen erosion is a function of the temperature of a material as shown in this activation energy expression. The activation energies for several materials tested in space are shown on this chart.

$$\text{Erosion Yield} \propto e^{-\frac{\Delta E}{RT}}$$

ΔE = Activation Energy, calories/mole

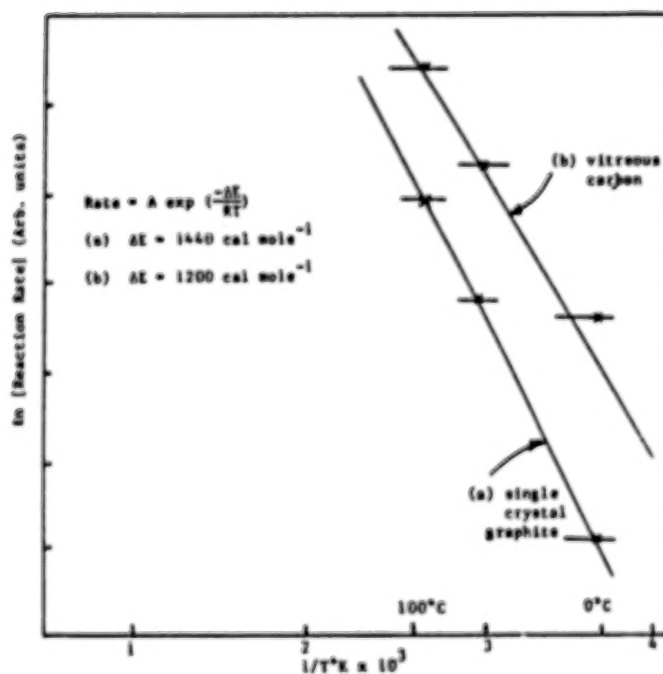
R = Gas Constant, 1.986 calories/(mole K)

T = Absolute Temperature, K

<u>MATERIAL</u>	<u>ACTIVATION ENERGY ΔE, CALORIES/MOLE</u>
Vitreous carbon	1,200
Graphite	1,400
CR-39 (bisallyl diglycol carbonate, an optical plastic)	1,050

EFFECT OF TEMPERATURE ON OXIDATION RATE OF CARBON ON STS-8

Heated vitreous carbon and single crystal graphite samples on STS-8 were used to make an Arrhenius plot to determine the activation energies for these materials.



POLYMERIC FILMS AT VARIOUS TEMPERATURES ON STS-8

Efforts to measure the effect of sample temperature on erosion yield of Kapton, Mylar A, Mylar D, and clear Tedlar on STS-8 have not resulted in the discovery of measurable dependencies greater than the uncertainty of the temperatures used for the experiment.

MATERIAL	THICKNESS, μm (MILS)	EXPOSED SIDE	SURFACE RECESSION, μm	
			STRIP SAMPLES	
			121°C	65°C
KAPTON	12.7 (0.5)	AIR ROLL	9.5	10.5
			11.8	10.3
KAPTON	25.4 (1.0)	AIR ROLL	9.8	10.7
			9.9	9.0
KAPTON	50.8 (2.0)	AIR ROLL	11.1	10.6
			11.1	11.1
MYLAR A	12.7 (0.5)	AIR	12.7	12.3
MYLAR A	40.6 (1.6)	AIR	12.1	11.9
MYLAR D	50.8 (2.0)	AIR ROLL	9.9	10.2
			11.0	10.4
CLEAR TEDLAR	12.7 (0.5)	AIR	10.9	11.5

ACTIVATION ENERGY, ΔE , CALORIES/MOLE

This table compares activation energies calculated from space experiments with laboratory experiments performed by various researchers. The data may suggest that the level of understanding of activation of energies in space and in the laboratory simulation of space is rather low. However, data obtained in ground experiments occasionally are consistent with the results obtained in space experiments.

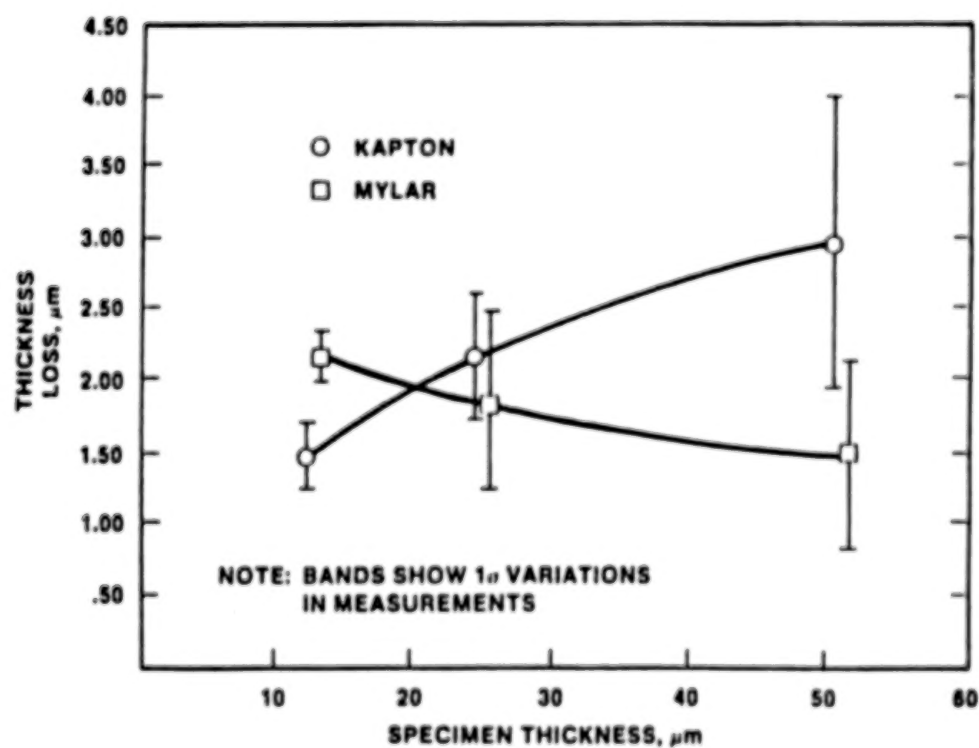
<u>MATERIAL</u>	<u>SPACE</u>	<u>LABORATORY</u>
Graphite	1400 ^A	2300 ^C
		3580 ^E
		1437 ^E
Kapton H	72 ^B	
Kapton HN		1325 ^E
FEP	Indeterminate ^B	369 ^E

SOURCES:

A-J. Gregory, STS-8
 B-J. Visintine, STS-8
 C-C. Park
 D-G. Arnold and D. Peplinski-1ev
 E-S. Rutledge - RF Asher

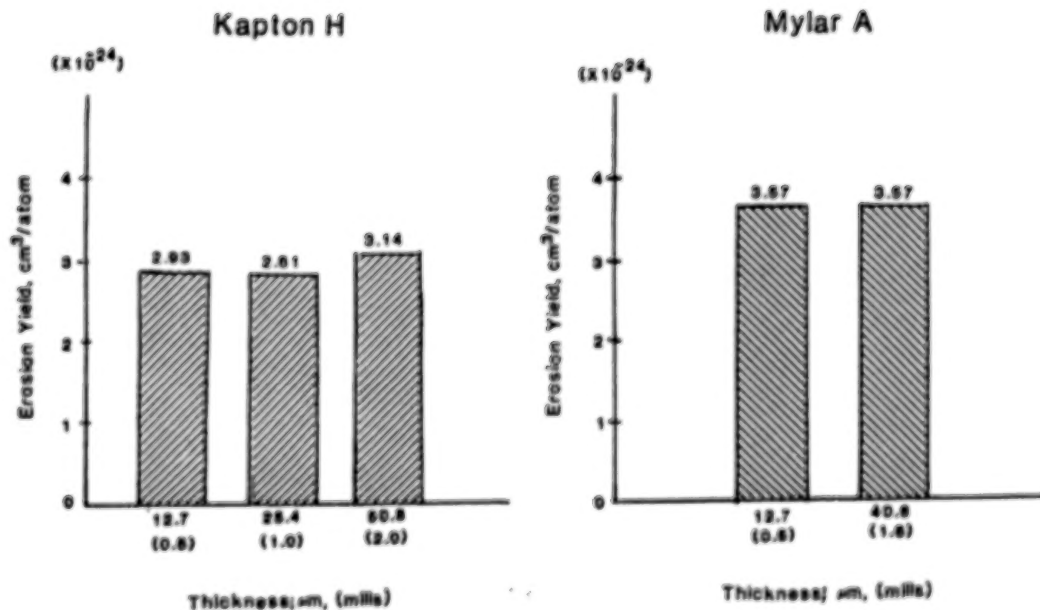
ATOMIC OXYGEN EROSION DEPENDENCE UPON POLYMER FILM THICKNESS (STS-5)

Measurements taken on STS-5 indicate a slight erosion yield dependence of polymer thickness on Kapton and Mylar.



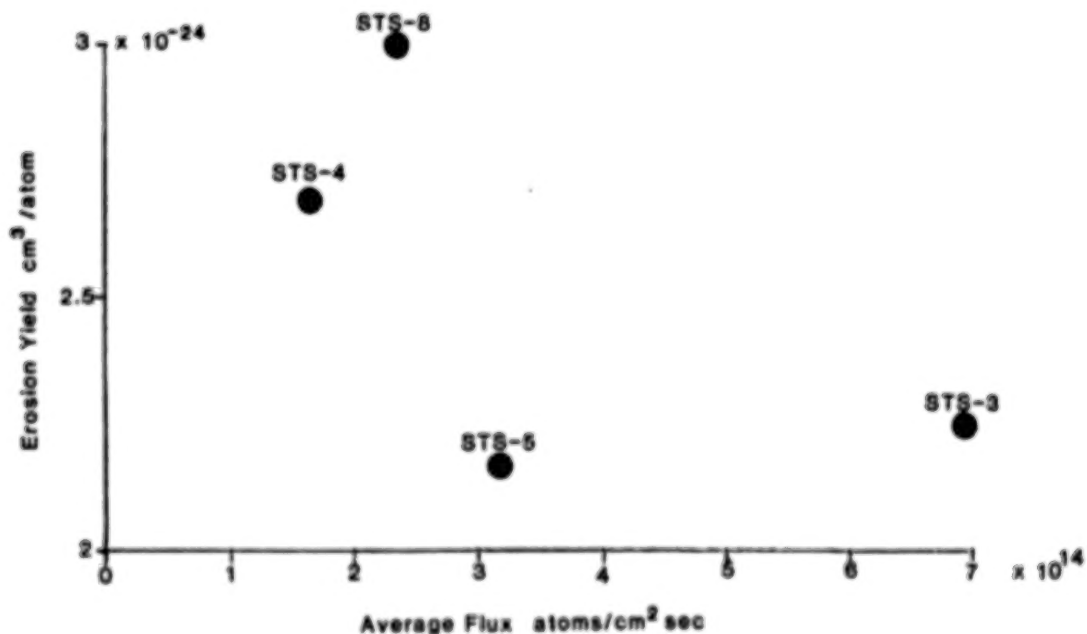
EROSION YIELDS AS A FUNCTION OF POLYMER FILM THICKNESS (STS-8)

Measurements taken on STS-8 indicate a far smaller sensitivity to polymer film thickness than was previously observed on STS-5. Film thickness may play an indirect role because of film processing materials which may be present on the surface of polymers to varying degrees depending upon the thickness of the specific polymer. Such surface contaminants may act as atomic oxygen barriers until sufficiently large fluences remove them.



ATOMIC OXYGEN EROSION YIELD FOR KAPTON H AS A FUNCTION OF FLUX

One can make a plot of the erosion yield versus the average flux for several of the STS flight experiments to find that there is significant data scatter, but that some trend of reduced erosion yield as a function of increasing flux can be observed. However, it is very difficult to draw any definite conclusion because the average flux may be the result of averaging a high flux and near zero flux and comparing that with a moderate flux from another flight. One can make arguments that erosion yield should increase with flux due to interaction of radicals and metastables with each other, and also that erosion yield should decrease with increasing flux due to increases in nonreactive scattering of the incident atomic oxygen upon oxygen resident at the surface. The effects of RAM versus sweeping atomic oxygen impingement may also contribute to difficulty in data interpretation.



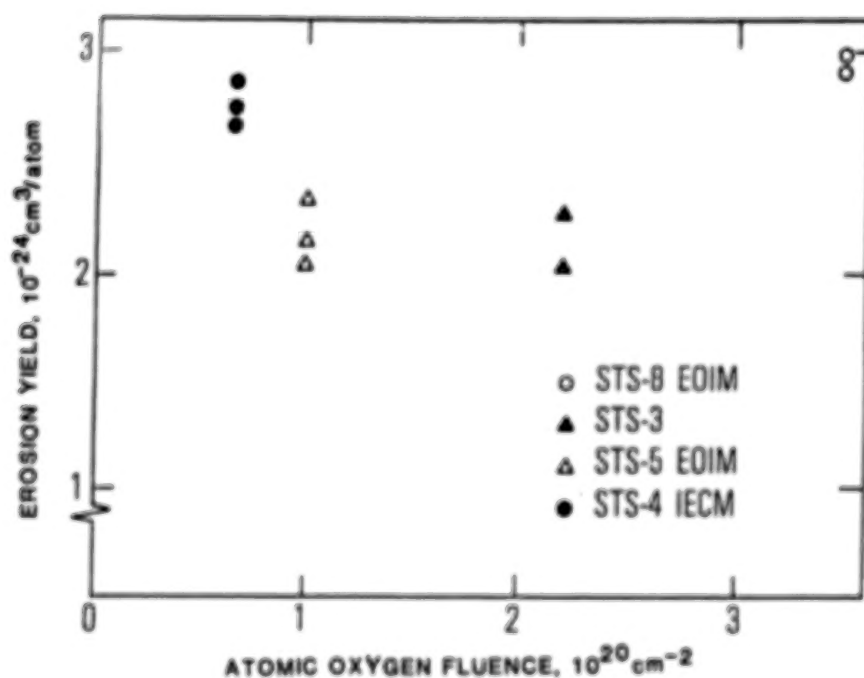
EFFECT OF SOLAR RADIATION ON EROSION YIELD

The question of whether or not atomic oxygen is synergistically affected by solar radiation has been addressed, with the resulting conclusion that if there is any effect, it is very small, and not within measurable significance for the data taken to date. If one assumes graphite is a material whose erosion yield is independent of solar radiation effects, then one finds most of the polymers have erosion yields in the sun which are lower than in the dark. However, if one makes calculations based on fluence estimates, the ratio of erosion yield in the day to erosion yield at night appears to close to 1 or slightly positive, indicating that there may be some slight synergistic effect, but of questionable magnitude relative to the uncertainty.

<u>MATERIAL</u>	<u>DAY EROSION YIELD</u> <u>NIGHT EROSION YIELD</u>	
	<u>ASSUMING GRAPHITE REACTIVITY</u> <u>IS INDEPENDENT OF SOLAR RADIATION EFFECTS</u>	<u>BASED ON</u> <u>FLUENCE ESTIMATES</u>
Graphite	≈ 1.0	1.2-1.7
Polyethylene	0.8	0.9-1.3
Kapton H	.9	1.0-1.5
Mylar A	.9	1.0-1.5
Kapton F	Indeterminate	Indeterminate

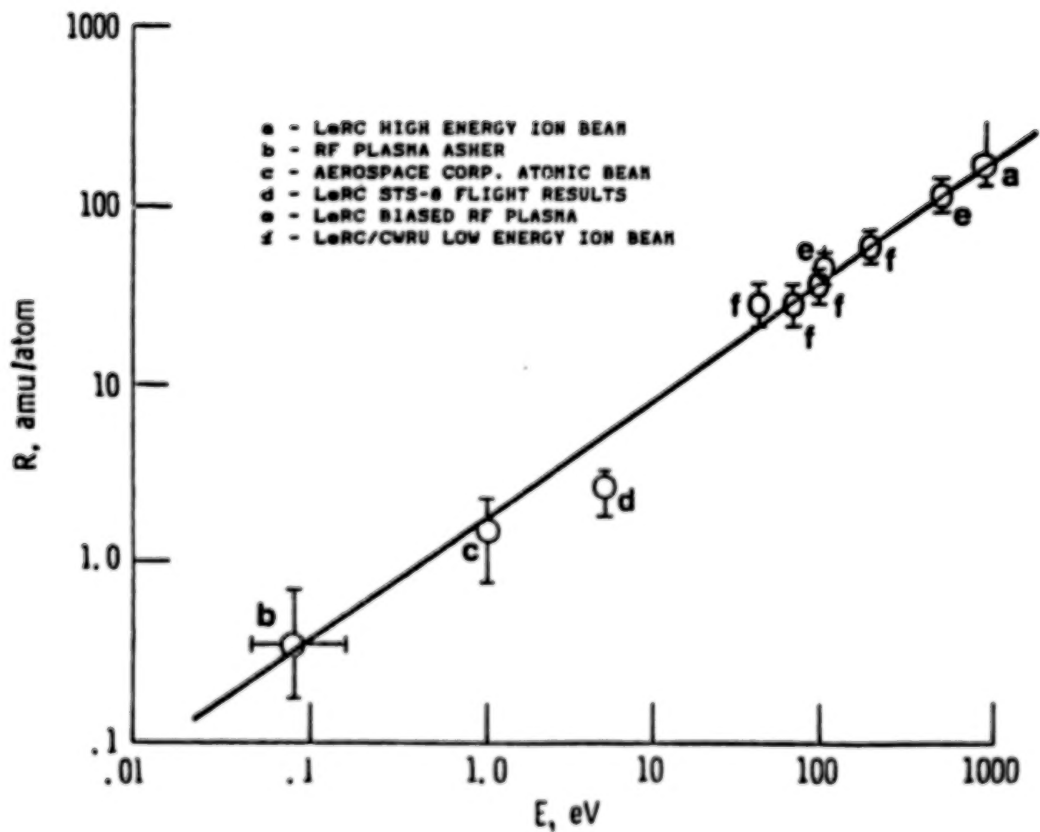
EROSION YIELD OF KAPTON H AS A FUNCTION OF ATOMIC OXYGEN FLUENCE

Erosion yield sensitivity to fluence is also widely scattered, indicating no clear trend. In the case of erosion yield fluence dependence, one could make argument that induction mechanisms may cause erosion yield to increase once a certain level of polymeric degradation is achieved by virtue of the arrival of a sufficiently high fluence.



KAPTON MASS LOSS RATES VS. OXYGEN ENERGY

The erosion yield may also be dependent upon energy, as shown in this plot, which combines space data with low energy thermal asher data and high energy ion beam data. As one can see, there appears to be a very definite increase in the yield with kinetic energy.



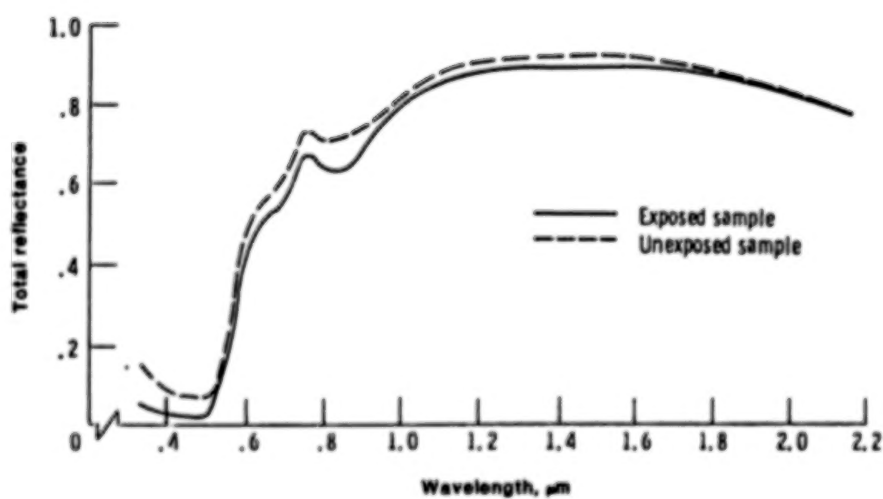
DEPENDENCE OF EROSION YIELD ON PRESENCE OF ATMOSPHERIC OXYGEN IONS

The dependence of erosion yield on whether or not oxygen is charged has been addressed by Gregory using carbon, and by Gull using osmium. Because the charge population of atomic oxygen is so low in low Earth orbit, one would not expect to see any measurable dependence. Although no effect was seen on STS-8, the question is very relevant with respect to simulation systems where either ions or neutrals may be chosen for low Earth orbital simulation.

- . No measureable effect on STS-8
- . LEO ionic oxygen population too low ($\frac{O^+}{O} \sim 10^{-4}$)
to measure a dependence

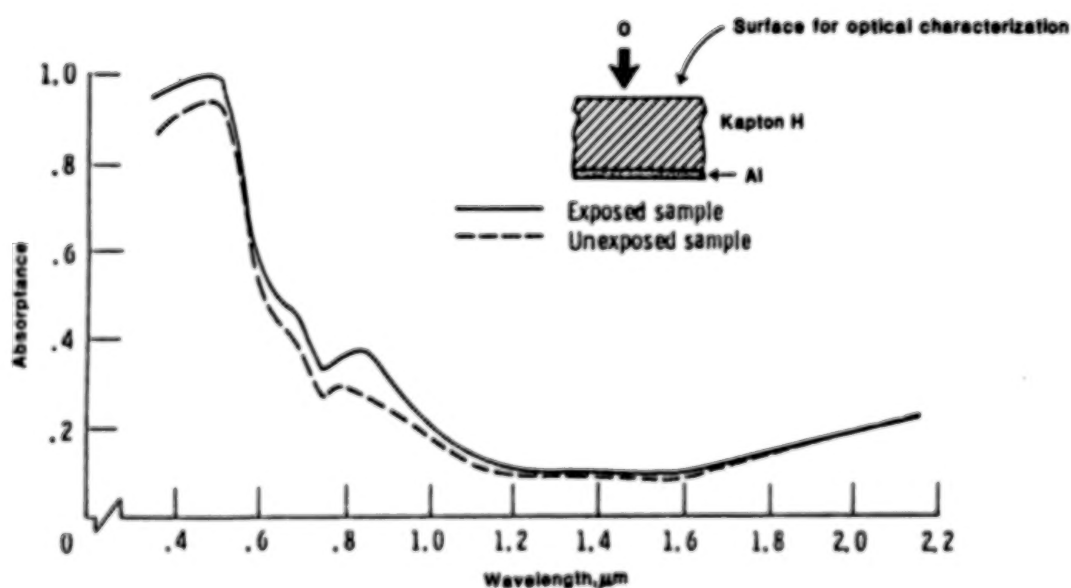
EFFECT OF ATOMIC OXYGEN ON TOTAL REFLECTANCE OF BACK ALUMINIZED KAPTON H (STS-8)

Polyimide Kapton H shows only a slight reduction in total reflectance as a result of atomic oxygen exposure.



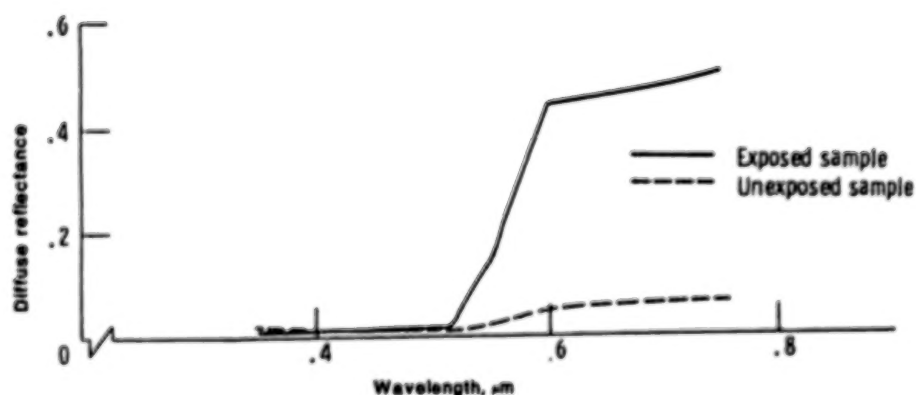
EFFECT OF ATOMIC OXYGEN ON ABSORPTANCE OF BACK ALUMINIZED KAPTON H
(STS-8, FLUENCE = 3.5×10^{20} atoms/cm²)

Similarly, there is a slight increase in absorptance as a result of atomic oxygen exposure. Much of this may be due to the fine cone-like structures on the surface contributing to a slight reduction in reflectance and an increase in absorptance.



EFFECT OF ATOMIC OXYGEN ON DIFFUSE REFLECTANCE OF BACK ALUMINIZED KAPTON H (STS-8)

The dominant optical change for Kapton and all polymers is the optical consequence of the microscopic surface structures contributing substantially to the diffuse reflectance and subsequent reduction in specular reflectance. It is the increase in diffuse reflectance that makes all the polymer surfaces appear matte-like and diffuse with respect to transmittance as well as reflectance.



EFFECT OF LEO ATOMIC OXYGEN ON OPTICAL PROPERTIES OF MATERIALS

The changes in solar absorptance and reflectance of various materials are listed in this table. As can be seen, the most significant changes occur for those materials which allow organic surfaces to be exposed to atomic oxygen. Thermal blanket materials such as aluminized Kapton or aluminized FEP Teflon display changes in solar absorptance and thermal emittance which would alter their performance as thermal blankets or radiator materials.

<u>Material</u>	<u>Change in Optical Properties due to A/O</u>		
	<u>Solar</u> <u>Absorptance</u>	<u>Emittance</u>	<u>Reflectance</u>
Kapton H (aluminized)	0.041	-	-0.051
Urethane (black, conductive)	0.042	0.55	-
Z853, yellow	-0.34	-	-
Chemglaze Z302 (glossy, black)	0.011	-	-0.01
Chemglaze A276 (white)	-0.005	0.03	-0.039
Silicone RTV-670	-0.004	-	0.001
Silicone (black, conductive)	0.0	-0.005	-
GSFC (green)	-0.002	-	-
Aluminum (150 Å)	0.0	0.0	0.0
SiO ₂ (650 Å on Kapton H)	0.0	0.0	0.0
Silicone RTV-650+TiO ₂	0.001	-0.01	-
Aluminum (chromic acid oxidized)	0.0	0.0	0.0
AlMgF ₂	-	-	0.0
Silicone SiO ₂	-0.022	-0.02	-
Chemglaze A276 (w/modifiers)	-0.006 to 0.016	0.02	-
Chromium (123 Å)	0.0	0.0	0.0

<u>Material</u>	<u>Change in Optical Properties due to A/O Solar</u>		
	<u>Absorptance</u>	<u>Emittance</u>	<u>Reflectance</u>
Al ₂ O ₃	0.0	-	0.0
Silicate MS-74	0.01	0.0	-
Urethane inhib A-276	0.0	0.01	-
FEP Teflon with silver undercoat	0.006	0.0	-
Bostic 463-14	0.01	0.0	-
Indium Tin Oxide coated Kapton H with aluminized backing	0.006	0.004	-
Kapton with aluminized backing	0.048	0.018	-
Nickel	0.005	0.0	-
Polyurethane A-276	0.023	0.01	-
Silicone RTV-602/Z302	-0.004	-	-
S13 - GLO	-0.005	0.0	-
YB-71	0.005	0.0	-
Z306 (flat black)	-0.022	0.0	-
Black, carbon-filled PTFE impregnated fiberglass (0.127 mm thick)	-0.16	-0.05	-
Aluminized Kapton, second surface mirror, uncoated (0.052 mm thick)	-0.23	-0.59	-
Aluminized FEP Teflon, second surface mirror (0.025 mm thick)	0.05	-0.19	-
Siloxane coating, RTV 602/ 0 on aluminized Kapton, second surface mirror substrate (0.008 mm thick coating) (0.052 mm thick Kapton)	0.0	0.0	-

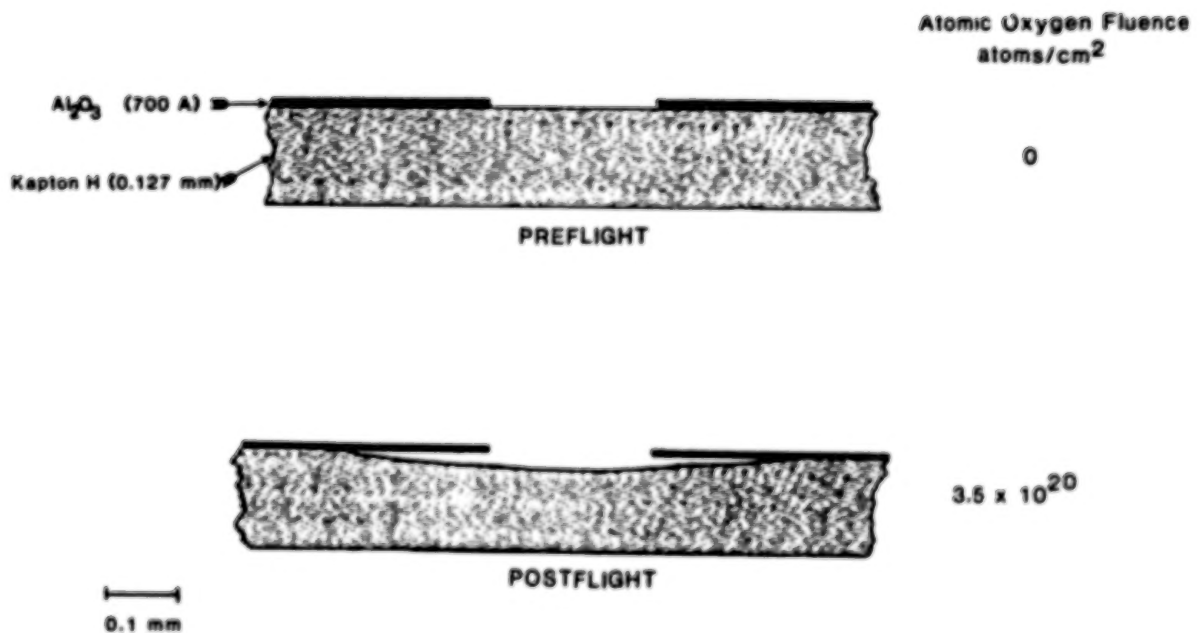
DIMENSIONAL CHANGES DUE TO ATOMIC OXYGEN REACTION

Atomic oxygen may cause dimensional changes in either the surface or the bulk of some materials. In the case of silver, a slight oxidation can be tolerated. However, significant oxidation with diffusion into the bulk causes the formation of an oxide which expands and does not remain adherent to the unreacted silver. In the case of silicone, the bombarded surface tends to form silicon dioxide with the loss of surface organic groups so that surface contraction and cracking occurs. Depending on the thickness of the silicone, underlying organic material below the coating may become exposed to atomic oxygen.

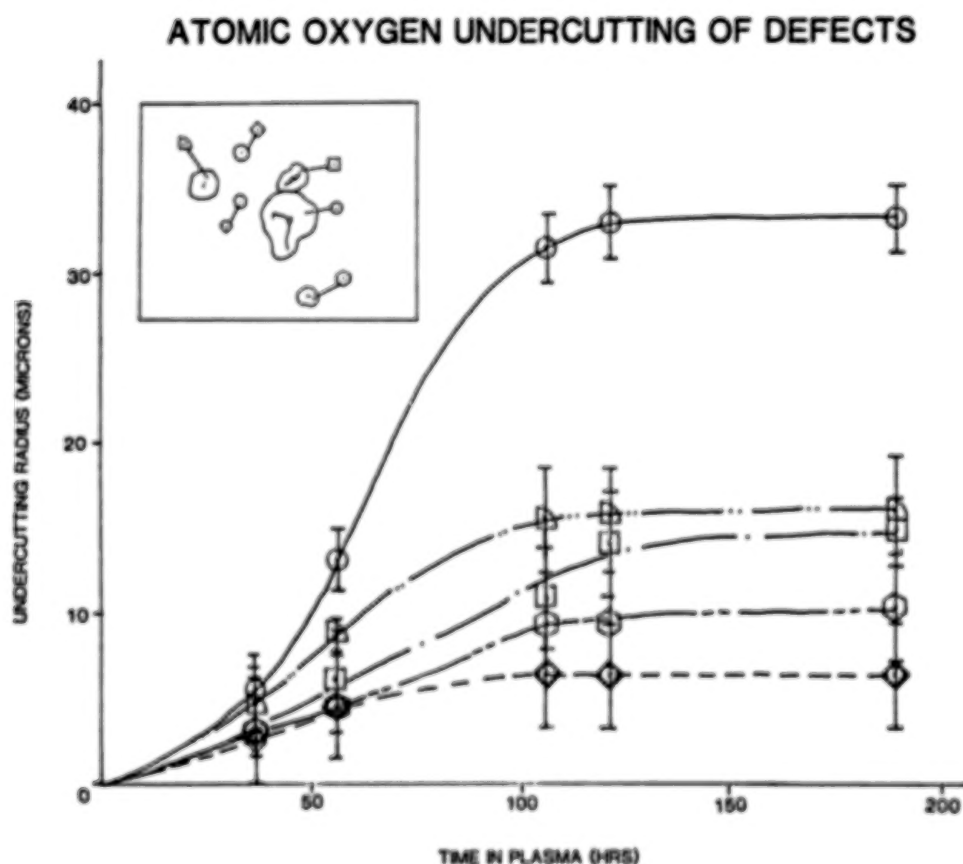
- Silver + O \rightarrow Silver Oxide (expansion + spalling)
- Silicone + O \rightarrow Surface Oxidation (contraction + cracking)

ATOMIC OXYGEN UNDERCUTTING - STS-8

Atomic oxygen undercutting has been observed in samples on STS-8 as shown in this scale drawing of a cross section of a defect which was initially on the surface prior to atomic oxygen exposure in space. The wide undercutting could be a problem depending on the population density of surface defects, whether caused by fabrication procedures, handling, micrometeoroids, or debris.

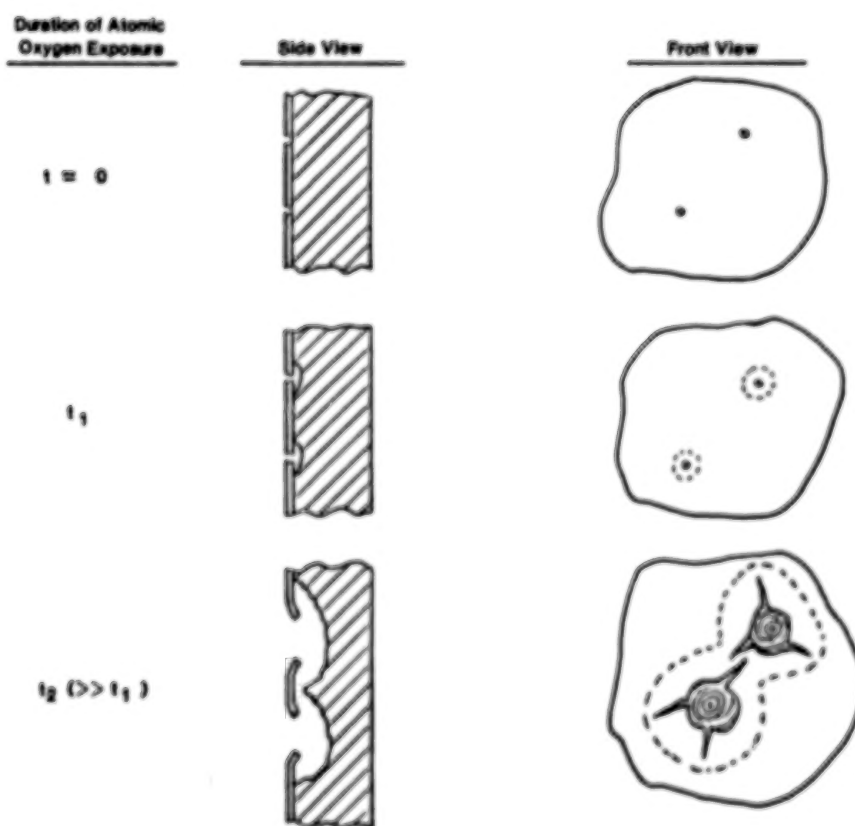


Measurement for defects in thin film protective coatings over polyimide Kapton have disclosed approximately 22,000 atomic oxygen transparent defects per square centimeter. If undercutting occurs without end, bulk failure of tensile-loaded polymeric blankets would eventually occur. However, as can be seen in this plot, in simulation tests performed in laboratory plasma ashers, undercutting tends to terminate. Thus, the survivability of atomic oxygen protective coatings may perhaps more depend on defect density than the fluence.



PROTECTIVE COATING FAILURE MODE

This viewgraph depicts the observed atomic oxygen undercutting failure scenario which occurs if the thin-film protective coating tears as the undercutting increases. Thus, not only is it necessary to control the defect density within limitations, but the nature of the coating must be such that tearing does not occur, even though undercutting may self-limit.



SUMMARY

Understanding of the basic processes of atomic oxygen interaction is currently at a very elementary level. However, measurement of erosion yields, surface morphology, and optical properties for low fluences have brought about much progress in the past decade. Understanding the mechanisms and those factors that are important for proper simulation of low Earth orbit is at a much lower level of understanding. The ability to use laboratory simulations with confidence to quantitatively address the functional performance and durability of materials in low Earth orbit will be necessary to assure long-term survivability to the natural space environment.

ATOMIC OXYGEN EFFECTS ON SPACECRAFT MATERIALS
THE STATE OF THE ART OF OUR KNOWLEDGE

Steven L. Koontz
NASA Lyndon B. Johnson Space Center
Houston, Texas

SPACE EXPOSURE DATA BASE - ATOMIC OXYGEN EFFECTS ON
SPACECRAFT MATERIALS

THREE SPACE SHUTTLE FLIGHT EXPERIMENTS
ONE RECOVERED SATELLITE

Flight	Altitude (Inclin.)	Exposure Time	Fluence* (Attitude)
STS - 5	222 km(28.5°)	44 hours	1 x 10 ²⁰ (VAR)
STS - 8	222 KM(28.5°)	41.75 hours	3.5 x 10 ²⁰ (RAM)
STS - 41G	225 km(57°)	38 hours	3 x 10 ²⁰ (RAM)
SMRM	574 - 491 km	50 months	2 x 10 ²¹ (VAR)

* Fluence is in atoms/cm²

- Detailed descriptions of the flight experiments can be found in References 1 through 21.

SHUTTLE FLIGHT EXPERIMENT ATOMIC OXYGEN EFFECTS DATA BASE

- About 300 different materials have been evaluated and several mechanism studies have been conducted during STS-5, STS-8, and STS-41G.
- Atomic Oxygen Effects were determined by post flight measurements on returned samples; no real time rate data was obtained; only limited variable exposure time data is available.
- Reaction efficiency obtained from flight experiment data provides a measure of material susceptibility to atomic oxygen attack.
 - Reactivity is expressed as the volume or mass of material lost per incident oxygen atom.
 - If the atom fluence is known for a future mission, then surface recession or mass loss can be estimated.

$$\text{RECESSION} = \text{FLUENCE} \times \text{REACTIVITY}$$

- Atomic oxygen effects data obtained from Space Shuttle flight experiments can be found in References 1 through 20. Oxidation reactions, not sputtering, are responsible for reactivity.
 - Polymeric materials containing C-H bonds, diamond and graphite have reactivities on the order of 10^{-24} cm³/atom.
 - Of the metals, only silver and osmium are rapidly attacked by formation of volatile reaction products or surface oxides layers which spall (peel off) readily.
 - Silicones and teflon appear inert.
 - Silicones react to form a protective surface oxide layer (SiO₂).
 - Teflons (pure fluorocarbons) show very low reactivities; The C-F and C-C bonds in these materials appear inert.
 - Surface temperature can influence reactivity.
 - Organic materials show a characteristic surface damage morphology.

REACTION EFFICIENCIES OF SELECTED MATERIALS WITH ATOMIC OXYGEN IN LOW EARTH ORBIT

MATERIAL	REACTION EFFICIENCY, cm ³ /ATOM	MATERIAL	REACTION EFFICIENCY, cm ³ /ATOM
KAPTON	3 x 10 ⁻²⁴	SILICONES	
MYLAR	3.4	RTV-560	0.2*
TEDLAR	3.2	DC6-1104	0.2*
POLYETHYLENE	3.7	T-650	0.2*
POLYSULFONE	2.4	DC1-2577	0.2*
GRAPHITE/EPOXY		BLACK PAINT Z306	0.3-0.4*
1034C	2.1	WHITE PAINT A276	0.3-0.4*
5208/T300	2.6	BLACK PAINT Z302	2.03*
EPOXY	1.7	PERFLUORINATED POLYMERS	
POLYSTYRENE	1.7	TEFLOW, TFE	<0.05
POLYBENZIMIDAZOLE	1.5	TEFLOW, FEP	<0.05
25% POLYSILOXANE/45%			
POLYIMIDE	0.3	CARBON (VARIOUS FORMS)	0.9-1.7
POLYESTER 7%			
POLYSILANE/93% POLYIMIDE	0.6	SILVER (VARIOUS FORMS)	HEAVILY ATTACKED
POLYESTER	HEAVILY ATTACKED	OSMIUM	0.026
POLYESTER WITH			
ANTIOXIDANT	HEAVILY ATTACKED		

*UNITS OF mg/cm² FOR STS-8 MISSION. LOSS IS ASSUMED TO OCCUR IN EARLY PART OF EXPOSURE; THEREFORE, NO ASSESSMENT OF EFFICIENCY CAN BE MADE.

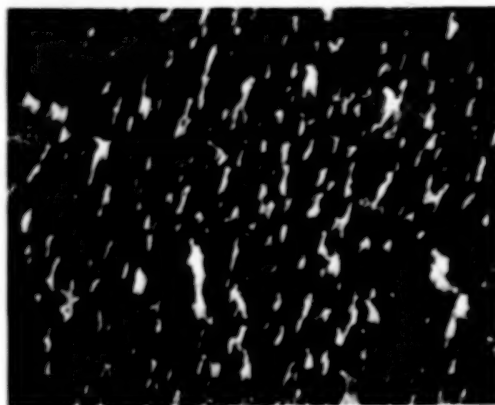
SURFACE DAMAGE MORPHOLOGY FROM LEO EXPOSURE

Many organic materials develop a characteristic surface damage morphology ("carpet" morphology) when exposed to atomic oxygen ram flux in low Earth orbit. Fluence dependent changes in the appearance of the carpet have been observed but do not seem to affect the reactivity of the material. At high fluence, the depth of the carpet is much less than the loss in thickness of the material.

COMPARISONS OF STS-8 KAPTON SPECIMENS (12.7 μm) BEFORE AND AFTER ATOMIC OXYGEN EXPOSURE, NORMAL IMPINGEMENT



UNEXPOSED, SEM: 10 000X



EXPOSED, SEM: 10 000X

LIMITATIONS OF CURRENT SPACE SHUTTLE FLIGHT EXPERIMENT DATA BASE

- Atom fluences were not measured during flight but calculated using the MSIS model of the thermosphere (Ref. 19); it follows that model errors are included in the flight experiment data base.
- The data base provides only limited basis for understanding the kinetics and mechanism of hyperthermal atom - surface reactions.
- Reaction efficiencies have been obtained at low fluence.
 - STS flights: 10^{19} to 10^{20} atoms/cm² in about 40 hours at 222 to 225 km altitude
 - Space Station: 10^{22} to 10^{23} atoms/cm² in 30 years (2.6×10^5 hours at 340 to 475 km altitude)
- The data base provides only a limited basis for evaluating effects of other space environment factors on oxygen reactivity.
 - Solar ultraviolet (UV) radiation (especially Lyman alpha at 121.6 nm) and high energy charged particles should influence the magnitude of atomic oxygen effects in some materials through photochemical and radiochemical mechanisms.
 - At 222 km altitude, the high atomic oxygen flux may wash out synergistic effects.
 - Synergistic effects cannot be evaluated with the available data base.
 - No data is available in the polar orbit environment.
- The validity of extrapolation to high fluence conditions or radically different orbital environments is unknown at this time.
 - Components of the Solar Maximum Satellite (altitude 574 to 491 km, inclin. 28.5°) recovered in April 1984 showed surface recession in crude agreement with predictions made using the data base. Teflon appeared to be more reactive than anticipated; kapton reactivity was in agreement with data base (Ref. 20).

LABORATORY SIMULATION AND MODELING OF ATOMIC OXYGEN EFFECTS
ON SPACECRAFT MATERIALS

- Ground based simulation and test systems are needed to support (1) interpretation and understanding of environmental effects and (2) development and flight qualification of long life spacecraft materials and components.
- A complete understanding of the kinetics and mechanism of hyperthermal atom surface reactions does not exist. Without the understanding produced by laboratory simulation and modeling studies, we cannot develop accelerated test methods with high confidence, and we cannot understand synergistic effects.
- An ideal laboratory test and simulation system would provide a pure, well collimated beam of neutral oxygen atoms with a kinetic energy of 5 eV (8km/sec) and an atom flux greater than 10^{14} atoms/cm²*sec. No such system exists at this time.
 - Nearly all the neutral atom test methods under development fall into one of four categories.
 1. Thermal atom sources: Oxygen atoms are produced in radio frequency (RF) or microwave discharges to produce high oxygen concentrations at thermal or near thermal energies.
 2. Plasma torch, atomic beam sources: Oxygen atoms are generated in a high temperature plasma; then, free jet or supersonic expansion converts sensible heat to velocity: Atom energies of 1 to 2 eV (possibly 4 eV) have been achieved.
 3. Ion beam methods: Positive or negative atomic ion beams are produced, accelerated, and focused to proper velocity, then neutralized to give a nominal 5 eV oxygen atom beam.
 4. Laser sustained plasma, atomic beam sources: Lasers are used to produce high temperature/high pressure plasmas which expand as free jets or supersonic beams. Atom kinetic energies of 1 to 12 eV have been reported with atom fluxes of 10^{15} to 10^{18} atoms/cm²*sec.

BEAM SOURCES UNDER DEVELOPMENT

Type	Location, PI	Species	Energy
Ion beam	LeRC, Furgeson	$O^+(O_2)$	0 - 50 eV
Ion beam	JPL, Chutjian Boing, Rempt	O	5 eV
Ion beam	MSFC, Carruth Martin(Denver)	O^+	5 eV
Ion beam	Vanderbilt, Tolk	O^+	100 eV
Ion beam	G.E., Amore	O^+/O_2^+	3 - 10 eV
Ion beam	LeRC, Banks	O^+, O, O_2	3 - 15 eV
Ion beam	Princeton U.	O, O_2, N, N_2	10 eV
Ion beam	Aerospace, Mahadaven	O, O_2, N, N_2	3 - 100 eV
ESD	LaRC, Outlaw	O	5 eV

• All the above sources produce fluxes of less than 10^{14} atoms/cm²sec at 5 eV. Those below produce greater fluxes.

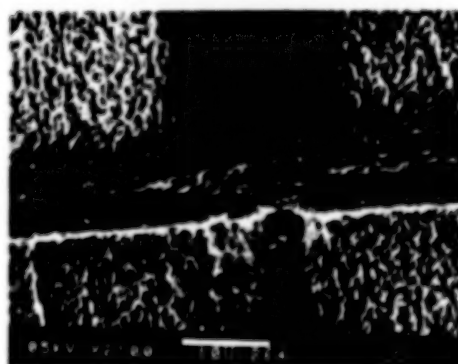
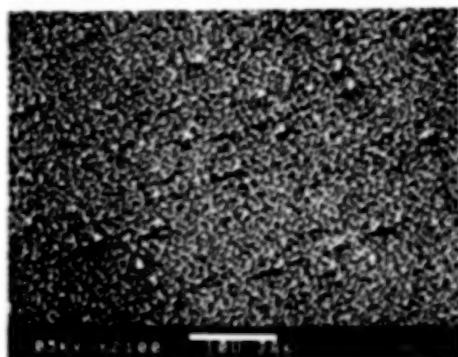
Plasma torch, atom beam	UTIAS, Tennyson	O, O_2, He	1 - 4 eV
ECMD, atom beam	Aerospace, Arnold	O, O_2, He	0.2 eV
Plasma torch, atom beam	ARI, Freeman	O, O_2, He	1.3 eV
Laser Disch. atom beam	PSI, Caledonia	O, O_2	2 - 14 eV
Laser Disch. atom beam	LANL, Cross	O, O_2, He	1 - 5 eV
Laser Disch. atom beam	JPL, Brinza	O	2 - 7 eV

LABORATORY SIMULATION AND TEST SYSTEM EVALUATION

- The following data are necessary for a complete evaluation of the test system:
 - Direct measurement of atom flux and velocity
 - Direct measurement of beam purity
 - Reaction efficiency measurements on materials in the flight experiment data base
 - Reaction efficiency measurements on the LeRC "round robin" materials set
- No ideal, completely characterized system exists; however, the laser sustained plasma, atomic beam systems offer the best approximations.
 - Los Alamos National Laboratory (Ref. 21)
 - Continuous beam (CW laser sustained discharge)
 - 1.5 to 5 eV O atoms; 10^{15} to 10^{17} atoms/cm²sec
 - Beam purity varies; in situ diagnostics measure O₂, inert gas and UV radiation content; ions and electrons and O atom excited states are negligible.
 - Kapton reactivity and surface damage morphology are in reasonable agreement with the flight data base.
 - Teflon appears more reactive than in flight.
 - Physical Sciences Incorporated (Ref. 22)
 - Pulsed beam (Pulsed laser sustained discharge)
 - 2 to 14 eV O atoms; 10^{15} to 10^{17} atoms/cm²sec (instantaneous fluxes much higher, about 10^{21})
 - Beam purity measured with in situ diagnostics; 98% O atoms, negligible UV, ions, electrons, and O₂; O atom excited states negligible
 - Kapton and teflon reactivities and surface damage morphology in reasonable agreement with flight data base

SURFACE DAMAGE MORPHOLOGY FROM LANL BEAM

Samples of organic materials exposed to the atomic oxygen beam at Los Alamos National Laboratory (LANL) develop carpet morphology similar to that developed in low Earth orbit. As the three SEM images shown below demonstrate, the appearance of the carpet depends on the fluence. From top to bottom these samples experienced 7.2×10^{19} , 1.4×10^{20} , and 4.0×10^{20} atoms/cm². The atom flux was 8×10^{15} atoms/cm² sec with a nominal atom kinetic energy of 1.5 eV.



SUMMARY

- In flight materials exposure data base
 - Extensive quantitative data is available from limited exposures in a narrow range of orbital environments.
 - More data is needed in a wider range of environments as well as longer exposure times.
 - Synergistic effects with other environmental factors
 - Polar orbit and higher altitude environments
 - Real time materials degradation data is needed to understand degradation kinetics and mechanism
- Laboratory simulation and modeling
 - Almost no laboratory data from high fidelity simulations of the LEO environment; simulation and test system under development; data base scanty
 - Theoretical understanding of hyperthermal atom surface reactions in the LEO environment not good enough to support development of reliable accelerated test methods
 - The laser sustained discharge, atom beam sources are the most promising high fidelity simulation-test systems at this time

REFERENCES

1. Leger, L.J. Oxygen Atom Reaction With Shuttle Materials at Orbital Altitudes, Nasa TM-58246, May 1982.
2. Leger, L.J. Visentine, J.T., and Schliesing, J.A., A Consideration of Atomic Oxygen Interaction with Space Station, AIAA Paper 85-0476, AIAA 23rd Aerospace Sciences Meeting, Reno, Nevada, January 14-17, 1985.
3. Leger, L.J., et al., STS Flight 5 LEO Effects Experiment - Background Description and Thin Film Results, AIAA Paper 83-2631, AIAA Shuttle Environment and Operations Meeting, Washington, DC, October-November 1983.
4. Whitaker, A.F., et al., LEO Oxygen Effects on Spacecraft Materials, AIAA Paper 83-2632, AIAA Shuttle Environment and Operations Meeting, Washington, DC, October-November 1983.
5. Park, J.J., et al., Effects of Atomic Oxygen on Paint and Optical Coatings, AIAA Paper 83-2634, AIAA Shuttle Environment and Operations Meeting, Washington, DC, October-November 1983.
6. Zinner, E., et al., Erosion of Mylar and Protection by Thin Metal Films, AIAA Paper 83-2636, AIAA Shuttle Environment and Operations Meeting, Washington, DC, October-November 1983.
7. Liang, R. and Gupta, A., Mechanistic Studies of Kapton Degradation in Shuttle Environments, AIAA Paper 83-2656, AIAA Shuttle Environment and Operations Meeting, Washington, DC, October-November 1983.
8. Visentine, J. T., et al., STS-8 Atomic Oxygen Effects Experiment, AIAA Paper 85-0415, AIAA 23rd Aerospace Sciences Meeting, Reno, Nevada, January 14-17, 1985.
9. Whitaker, A.F., Orbital Atomic Oxygen Effects on Thermal Control and Optical Materials STS-8 Results, AIAA Paper 85-0416, AIAA 23rd Aerospace Sciences Meeting, Reno, Nevada January 14-17, 1985.
10. Banks, B.A., et al., Ion Beam Sputter-Deposited Thin Film Coatings for Protection of Spacecraft Polymers in Low Earth Orbit, AIAA Paper 85-0420, AIAA 23rd Aerospace Sciences Meeting, Reno, Nevada January 14-17, 1985.
11. Liang, R.H., and Gupta, A., Mechanistic Studies of Interaction of Materials With Energetic Oxygen Atoms in Low Earth Orbit, AIAA Paper 85-0422, AIAA 23rd Aerospace Sciences Meeting, Reno, Nevada January 14-17, 1985.
12. Gull, T.R., et al., Effects of Optical Surfaces at Shuttle Altitudes, AIAA Paper 85-0418, AIAA 23rd Aerospace Sciences Meeting, Reno, Nevada January 14-17, 1985.

13. Gregory, J.C. and Peters, P.W., Measurement of Reaction Rates and Activation Energies of 5 eV Oxygen Atoms With Graphite and Other Solid Surfaces, AIAA Paper 85-0417, AIAA 23rd Aerospace Sciences Meeting, Reno, Nevada, January 14-17, 1985.
14. Smith, K., Evaluation of Oxygen Interaction with Materials (EOIM) - STS-8 Atomic Oxygen Effects, AIAA Paper 85-7021, AIAA Shuttle Environment and Operations II Conference, Houston, Texas, November 1985.
15. Whitaker, A.F., et al., Protective Coatings for Atomic Oxygen Susceptible Spacecraft Materials - STS41-G Results, AIAA Paper 85-7017, AIAA Shuttle Environment and Operations II Conference, Houston, Texas, November 1985.
16. Fromhold, A.T., et al., Reaction of Metals in Lower Earth Orbit During Space Shuttle Flight 41-G, AIAA Paper 85-7018, AIAA Shuttle Environment and Operations II Conference, Houston, Texas, November 1985.
17. Zimcik, D.G. and Maag, C.R., Results of Apparent Atomic Oxygen Reactions With Spacecraft Materials During Shuttle Flight STS41-G, AIAA Paper 85-7020, AIAA Shuttle Environment and Operations II Conference, Houston, Texas, November 1985.
18. Peters, P.W., Gregory, J.C., and Swann, J.T., Effects on Optical Systems From Interactions With Oxygen Atoms in Low Earth Orbits, Applied Optics, Vol. 25, No. 8, April 15, 1986.
19. Visentine, J.T. and Leger, L.J., Material Interactions With the Low Earth Orbital Environment: Accurate Reaction Rate Measurements, AIAA Paper 85-7019, AIAA Shuttle Environment and Operations II Conference, Houston, Texas, November 1983.
20. Proceedings of the SMRM Degradation Study Workshop. The Satellite Servicing Project, Goddard Space Flight Center 408-SMRM-79-0001, May 9-10, 1985.
21. Visentine, J.T. and Leger, L.J., Atomic Oxygen Effects Experiments: Current Status and Future Directions, NASA TM, JSC, May 18, 1987.
22. Caledonia, G.E., Krech, R.H., and Green, B.D., A High Flux Source of Energetic Oxygen Atoms for Material Degradation Studies, AIAA J. 25, 59 (1987); also Caledonia, G.E., and Krech, R.H., Energetic Oxygen Atom Material Degradation Studies, AIAA-87-0105, 25th Aerospace Sciences Meeting, Reno, Nevada, January 1987.

SESSION 4: MICROMETEORIDS AND DEBRIS

Chairman: Andrew Potter
NASA Lyndon B. Johnson Space Center

THE LONG-TERM EFFECTS OF THE MICROMETEOROID AND ORBITAL
DEBRIS ENVIRONMENTS ON MATERIALS USED IN SPACE

Burton G. Cour-Palais
NASA Lyndon B. Johnson Space Center
Houston, Texas

Introduction

The purpose of this report is to discuss the long-term effects of the orbital debris and micrometeoroid environments on materials that are current candidates for use on space vehicles. In addition, the limits of laboratory testing to determine these effects are defined and the need for space-based data is delineated. The impact effects discussed are divided into primary and secondary surfaces. Primary surfaces are those that are subject to erosion, pitting, the degradation and delamination of optical coatings, perforation of atomic oxygen erosion barriers, vapor coating of optics and the production of secondary ejecta particles. Secondary surfaces are those that are affected by the result of the perforation of primary surfaces, for example, vapor deposition on electronic components and other sensitive equipment, and the production of fragments with damage potential to internal pressurized elements. The report defines the material properties and applications that are required to prevent or lessen the effects described.

Encounter Dynamics and Typical Damage

In dealing with the long-term effects of the micrometeoroid and orbital debris environments on materials used in space, we have to know something about these solid particles that pack so much energy. Kessler, (Reference 1), presented a detailed look at these environments, but let us look at what an encounter with a micrometeoroid or an orbital debris particle means.

Micrometeoroids, as most of you know, can have Earth encounter velocities of 11 to 73 km/sec. However, the most probable encounter velocity for a spacecraft in Earth orbit is about 17 km/sec. For modeling purposes, the meteoroid cumulative flux-mass curve given for NASA use (SP 8013) is tied to an average velocity of 20 km/sec. Similarly, the average mass density of meteoroids given by the same model is 0.5 gm/cc. The flux of these particles is altitude dependent, and they are omni-directional.

Orbital debris particles by definition, have a relative encounter velocity of 0 to 16km/sec for a spacecraft in Earth orbit. In fact, there is a velocity distribution and the average encounter velocity is 11 km/sec. Most orbital debris particles are postulated to be aluminum fragments from explosions in space, and therefore have a mass density of 2.8 gm/cc. What do these velocities and mass densities mean for the surface of an object in space that encounters a micrometeoroid or an orbital debris particle? First, these particulates are very energetic. The specific kinetic energy for a micrometeoroid at 20km/sec is 2×10^5 joules/gm, and for orbital debris at 10 km/sec, 6×10^4 . So micrometeoroids are several times more energetic than orbital debris particles, but we must also be concerned with the relative number of particles of each that are encountered.

Table 1 lists the number of micrometeoroids and orbital debris particles encountered per square meter of surface area in 10 years. For the particle sizes of interest in this study, the fluxes of the two environments cross over to make one or the other dominant. However, we are concerned with the total number of impacts.

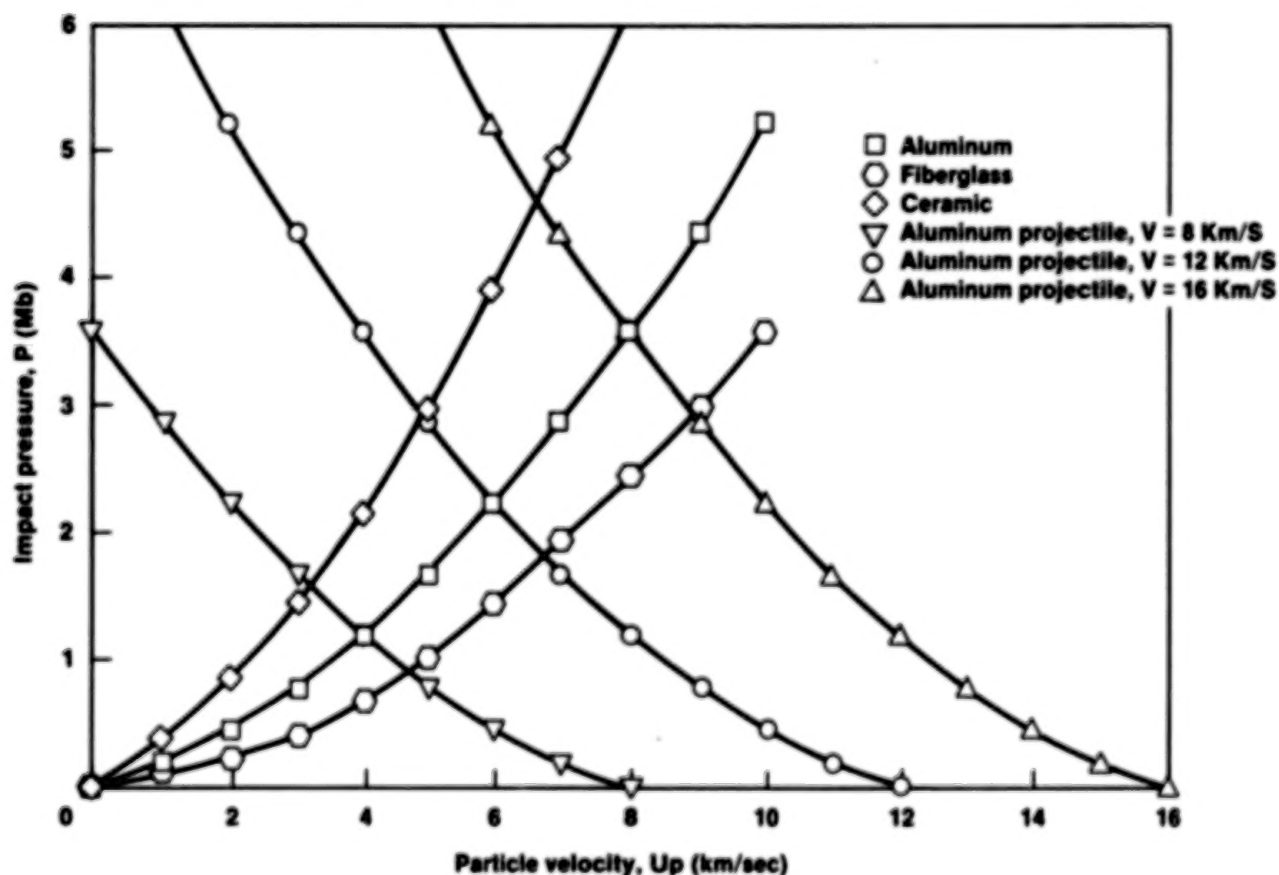
Table 1

NUMBER OF MICROMETEORIDS AND ORBITAL DEBRIS PARTICLES ENCOUNTERED IN 10 YEARS (1996 - 2005).

DIAMETER (cm)	ORBITAL DEBRIS (number/sq.meter)		MICROMETEORIDS (number/sq.meter)	
	385-475km	800km	385-475km	800km
0.001	5100	12000	2400	2600
0.01	16	37	49	53
0.10	0.051	0.120	0.019	0

Secondly, a characteristic of an encounter with these particles is the very high impact pressures and shocks associated with them. For a micrometeoroid, the average impact pressure is 2.5 megabars and for the orbital debris, 1.9 megabars, a megabar being equal to 14.5×10^6 psi. Figure 1 shows a graphical means of determining the initial impact pressure as a function of the particle or shocked material velocity. The intersections of the left-running projectile curves and the right-running target curves denote the impact pressure. Three aluminum projectiles are shown at 8, 12 and 16 km/sec, and the target materials are graphite-epoxy, aluminum and a ceramic.

Initial Shock Pressure Effect of Shield Material Density



Graphical Solution for the Initial Impact Pressure.

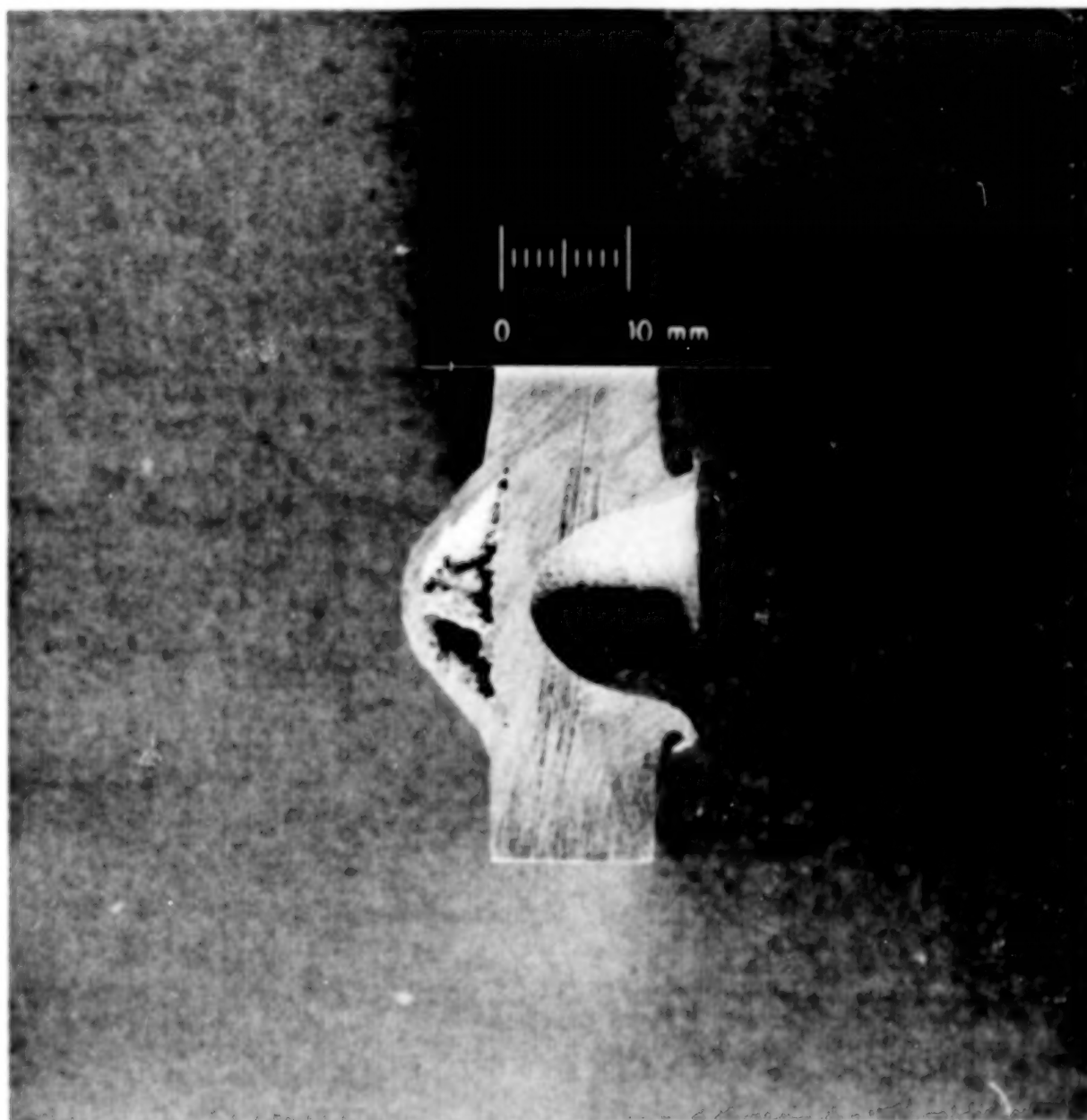
Figure 1

These very high pressures decay rapidly but remain well above the material strength so that the elements close to the impact point flow like a liquid. In addition, the impact process of instantaneous compression followed by slower release of pressure causes the projectile and target material to be locally heated due to an increase of entropy. The temperatures generated are always high enough to melt the materials in contact, and quite often to vaporize them. Table 2 shows some metallic materials of interest with their melting and vaporization temperatures, and the impact pressures and velocities required to achieve these states, (Reference 2).

Table 2
IMPACT SHOCK HEATING

MATERIAL	TEMPERATURE		INCIP. MELT		COMP. MELT		INCIP. VAPOR	
	Melt ₀ C	Vap ₀ C	Mbar	Km/s	Mbar	Km/s	Mbar	Km/s
Aluminum	660	2057	0.65	5.6	0.90	6.6	1.67	10.2
Cadmium	321	767	0.40	3.0	0.60	3.9	0.88	5.2
Steel	1535	3000	1.80	7.9	2.10	8.8		>>9
Lead	327	1620	0.30	2.0	0.35	2.6	0.90	4.8
Titanium	1800	>3000	1.30	7.6		>>8		

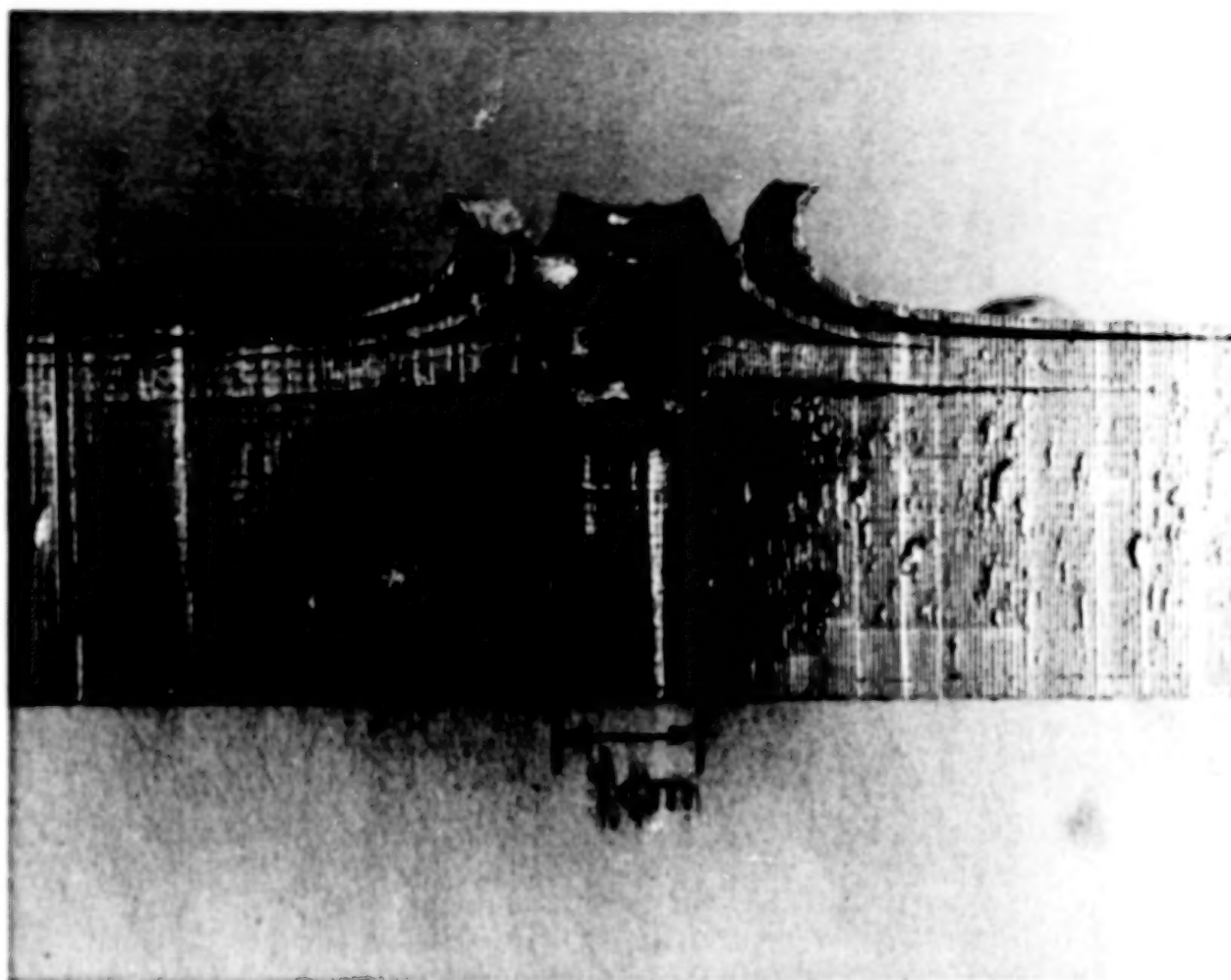
Figure 2 shows a cross-section of a laboratory impact crater formed in an aluminum 1100-0 alloy plate by a 45 milligram aluminum projectile at just over 6 km/sec. The near hemispherical shape and raised lip is characteristic of a hydrodynamic impact crater. In this case, the impact shock pressure is 0.8 megabars, and from Table 2 one would expect the material to have been melted. Another feature illustrated in Figure 2 is the near spallation of the rear surface. A thin segment of the aluminum plate has separated due to the tensile stress induced by the shock after reflection. The rarefaction or release stress wave reflected off the rear surface was still high enough to cause this alloy to fail in tension. Incidentally, the specific KE was about 2×10^4 joule/gm.



Hypervelocity Impact Cross-section: 1100-F Aluminum Alloy Plate.

Figure 2

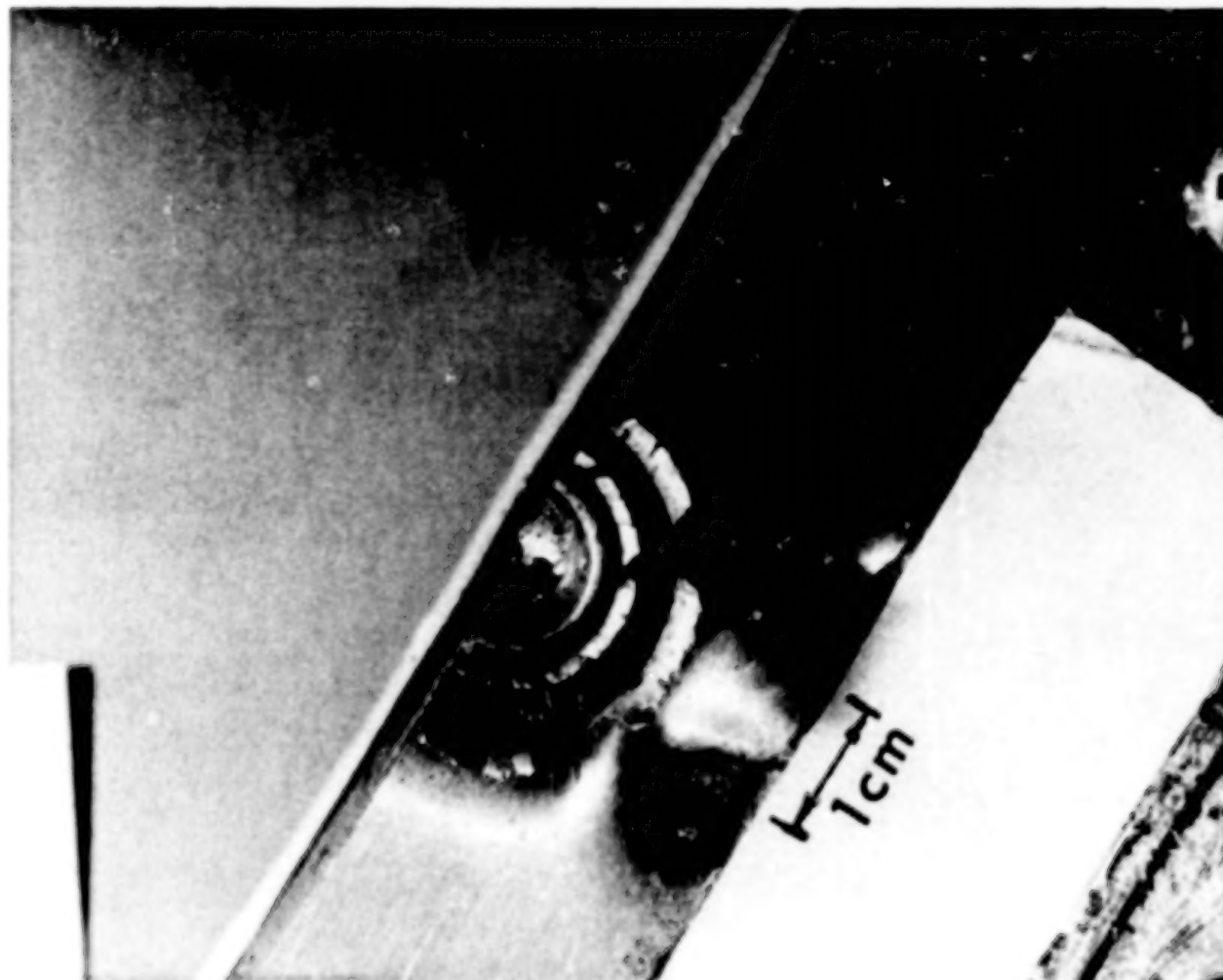
In Figure 3, we see a cross-section of an impact into laminated aluminum plates held together mechanically. It is a useful illustration of the impact forces that cause the problems seen in hypervelocity encounters with the first surface of a spacecraft. We see delamination of the upper layers, peeling under the influence of shearing forces at edges of the crater, shock compression in the layers and the rebound of a significant proportion of the target.



Side View Sectioned Hypervelocity Impact into an Aluminum Alloy Laminate.

Figure 3

In Figure 4, the top view, we see the splitting of the material in the process of peeling back of the upper layers. These two views are important in understanding the basic processes taking place in delamination and ejection of surface materials, such as coatings and atomic oxygen barriers, etc., examples of which will be shown shortly. This impact occurred at 7 km/sec using a Pyrex glass projectile so the impact pressure was over 1 megabar and the specific KE, 2.5×10^4 joules/gm.

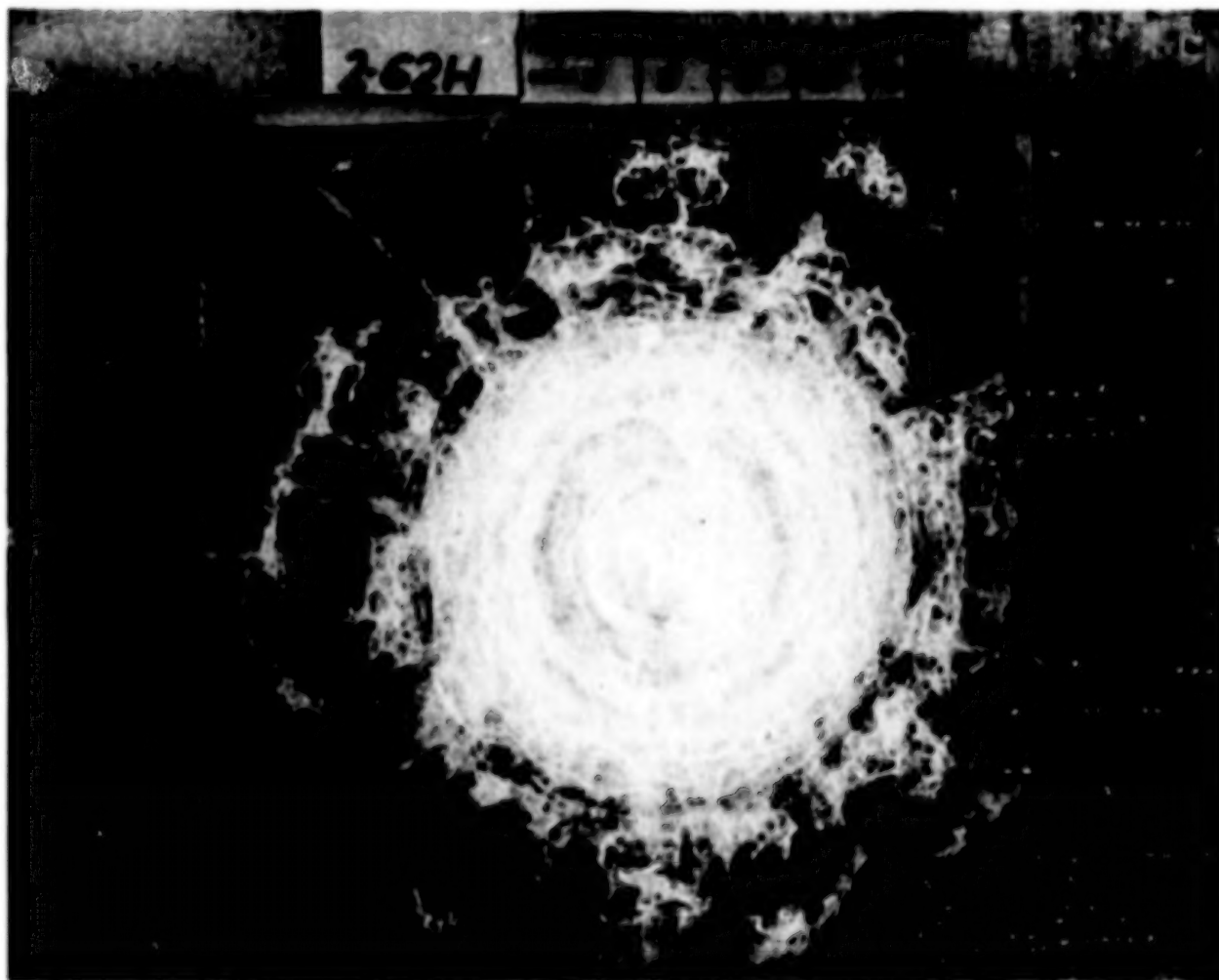


Top View of Figure 3.

Figure 4

The target described previously is a reasonable analogue of the front surface of a glass or similar brittle material that has been impacted by a hypervelocity projectile. In this aluminum target there is a residual crater as is usually seen in glass targets, (Figure 5) and there are two levels of ejected spall rings, also seen in the glass target. Also the deeper layer of the aluminum stack separated from the main body is analogous to the sub-surface fracture zone present in most glass targets at laboratory impact velocities. The glass target was impacted by a 0.16 cm glass (2.3 gm/cc) projectile at 7.3 km/sec. This is approximately the same impact pressure as for the aluminum laminated target.

This completes our quick look at the dynamic characteristics of hypervelocity impacts and some of the typical effects on the spacecraft first surface.



Damage to a 2 cm thick Glass Target by a 0.15 cm Projectile at 7.3 km/sec.

Figure 5

Long-term Damage Effects

Let us now discuss the long-term effects of the micrometeoroid and orbital debris environments on typical materials used in space. Impact effects will be divided into those that could cause a problem to the first or outer surface of a spacecraft, and those that can also affect the surface or region behind it.

First surfaces are primarily affected by the smaller particles in both environments, and Table 3 lists the penetration depths and diameters that can be expected for orbital debris in aluminum and glass. The equations used were developed during the Apollo program, (Reference 3), and the spall diameters are consistent with the target shown in Figure 5. For typical large spacecraft that have aluminum first surface thicknesses of 0.16 to 0.25 cm as bumper shields, particles under 1 mm would not penetrate.

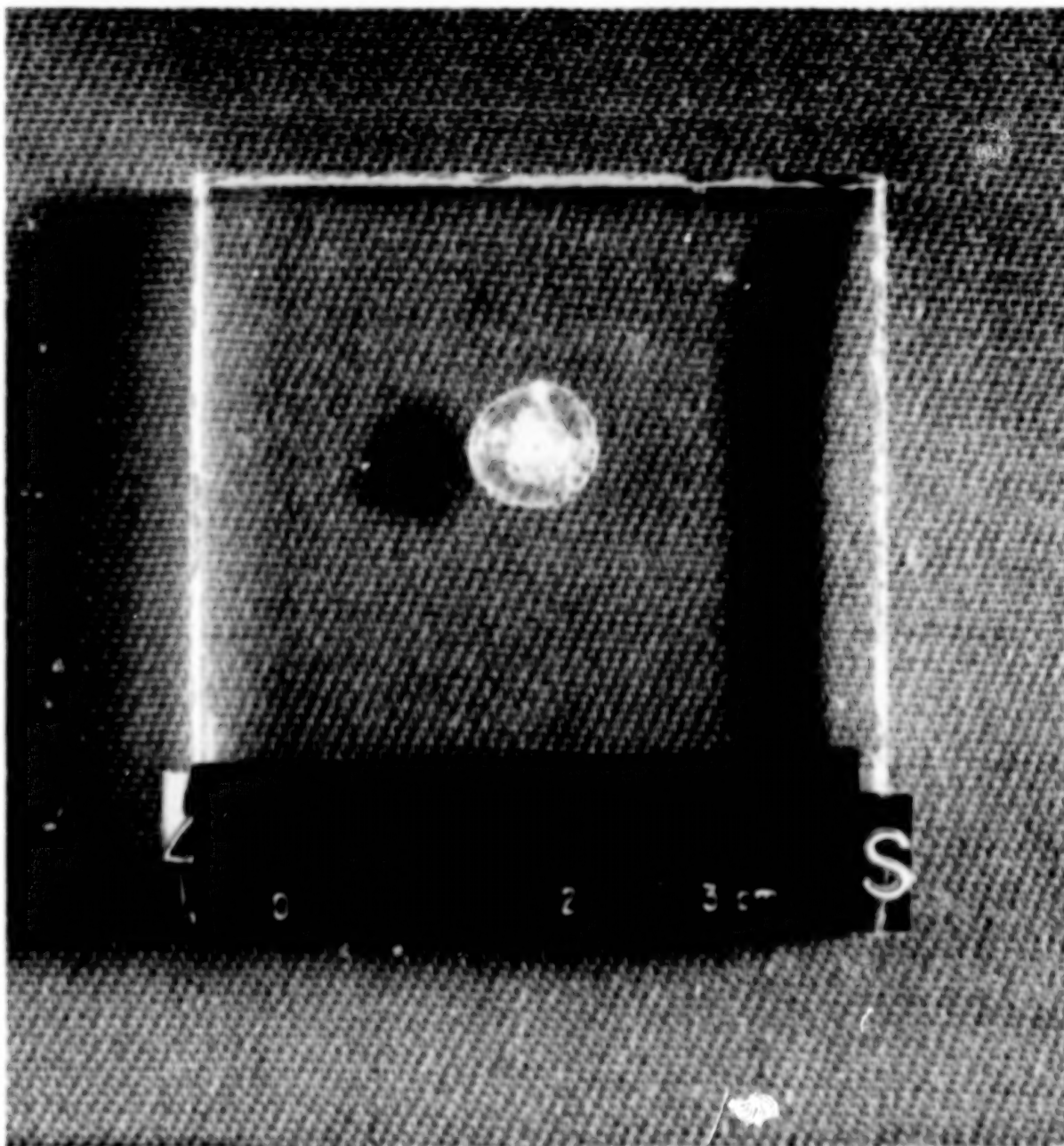
PENETRATION DEPTHS AND CRATER DIAMETERS
IN ALUMINUM AND GLASS SURFACES.

MATERIAL	PROJECTILE DIAMETER (cm)	CRATER DEPTH (cm)	INNER SPALL DIAMETER (cm)	OUTER SPALL DIAMETER (cm)	CRATER DIAMETER (cm)
Aluminum (2024T3)	0.001	0.0017	-----	-----	0.0034
	0.010	0.0194	-----	-----	0.0390
	0.100	0.2210	-----	-----	0.4420
Aluminum (1100-F)	0.001	0.0025	-----	-----	0.0050
	0.010	0.0287	-----	-----	0.0570
	0.100	0.3271	-----	-----	0.6540
Glass (7940)	0.001	0.0012	0.012	0.024	-----
	0.010	0.0138	0.138	0.276	-----
	0.100	0.3615	3.620	7.230	-----

Table 3

The types of impact problems to be expected on first, or for that matter any single surface such as solar panel or radiator paddles, are discussed next.

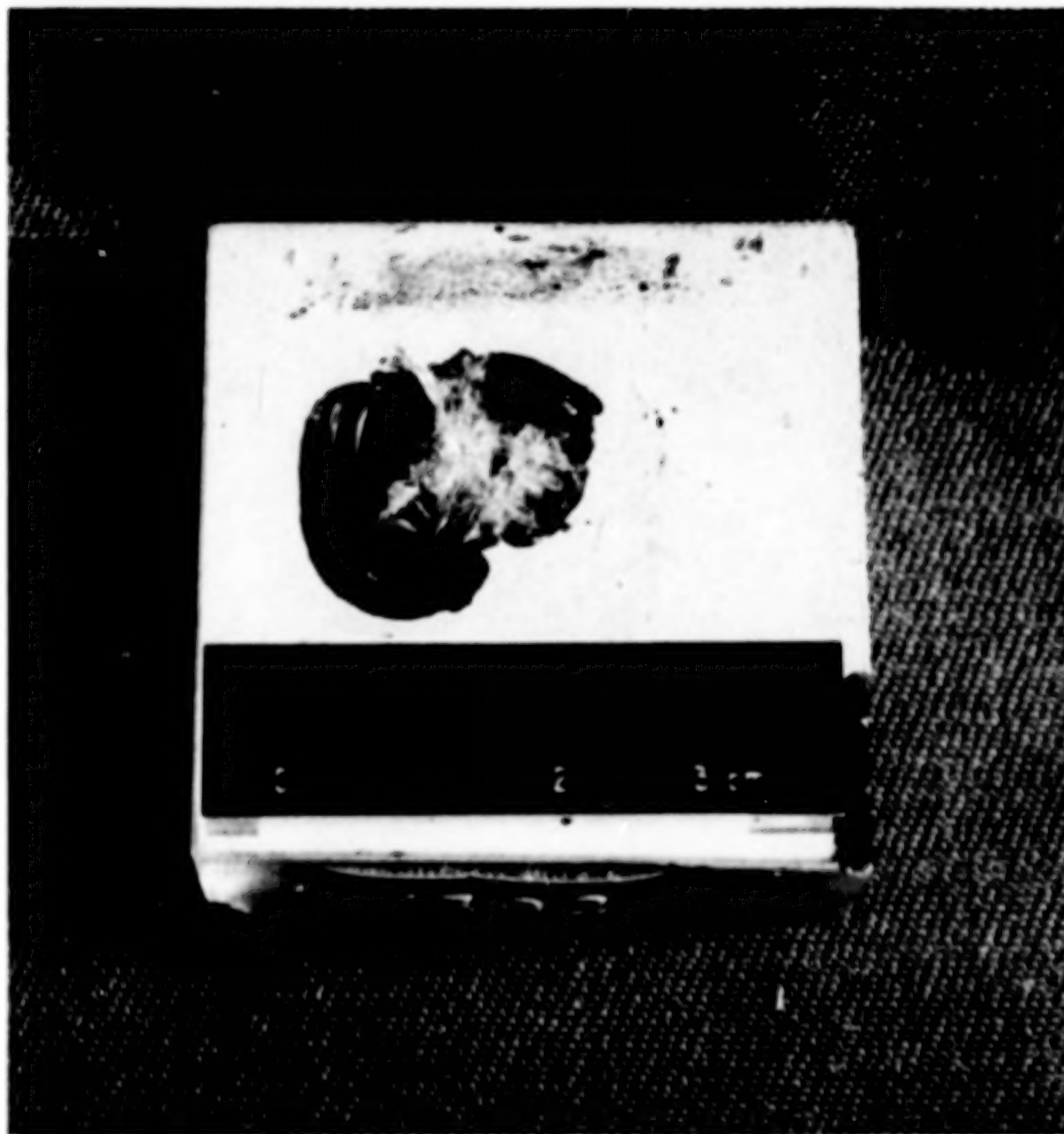
Erosion, pitting and degradation of optical transmissibility as shown in Figure 6. This impact damage resulted from a 0.4 mm glass projectile (2.3 gm/cc) at 7.4 km/sec. The shock damage diameter is 7 mm which gives an obscured diameter of about 0.4 sq.cm. Although there would only be between 2 and 3 impacts of this size per square meter in ten years for the combined environments, the summation of the crater areas for this size and all smaller sizes could present a problem.



Impact Damage Area caused by a 0.04 cm Projectile at 7.4 km/sec.

Figure 6

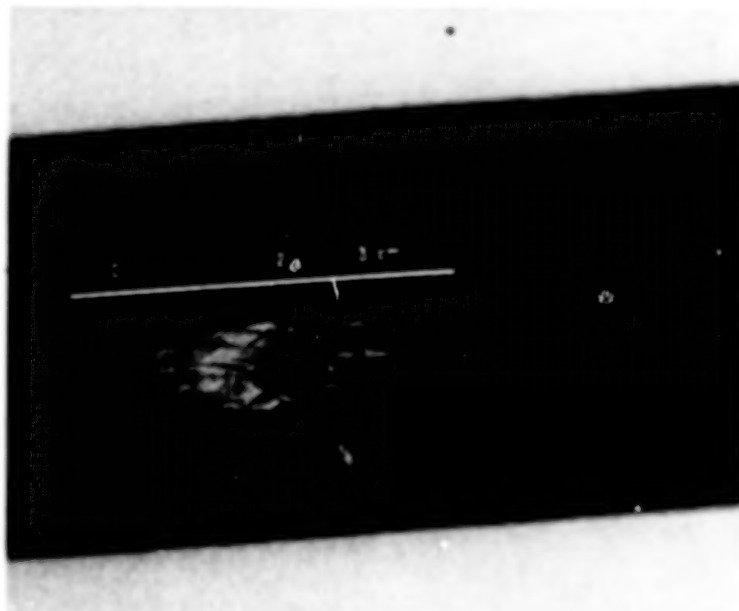
Ejection of mirror surfaces and optical coatings by impact spallation is shown in Figure 7. The particular target shown resulted from a double impact of 0.17 mm tungsten-carbide projectiles at over 6 km/sec and it is illustrative of the effect of impacts on mirrored surfaces. The actual damage areas will be similar to the values quoted for pitting discussed previously.



Impact Damage to a Mirrored Glass Surface by Hypervelocity Impact.

Figure 7

Delamination of composite materials by shock effects. Figures 8a (entry) and 8b (exit) show the results of a 2.4 mm aluminum projectile impacting a graphite-epoxy tube at 7.48 km/sec. The entry side breaks up the projectile like a bumper and the impact of the debris plume causes the extensive damage seen on the exit side. This size of impact has a 70% chance of occurring at least once in 10 years for a tubular structure area the size of the Phase 1 Space Station Freedom.



Graphite-Epoxy Tubular Strut: Hypervelocity Impact Entry.

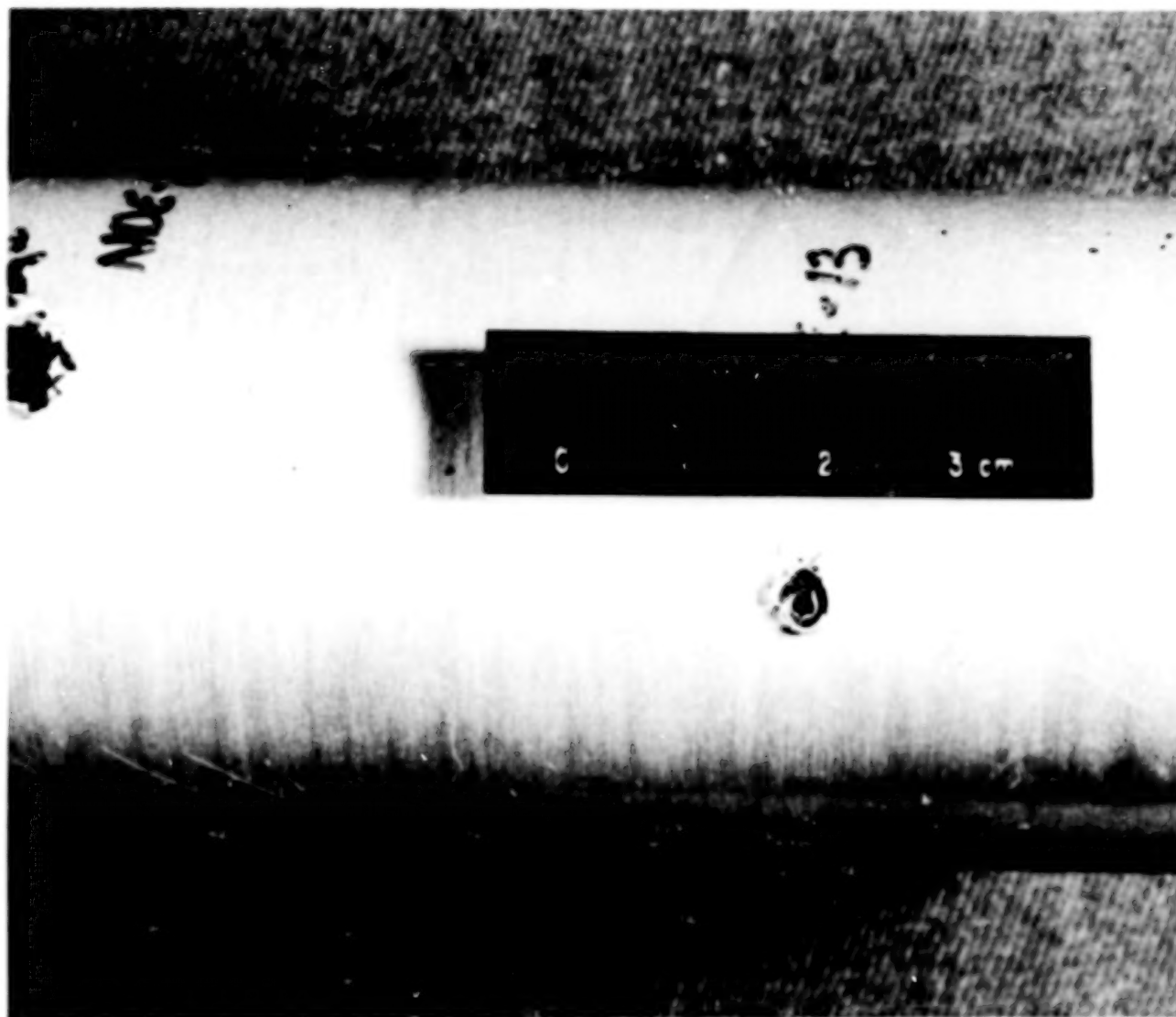
Figure 8a



Graphite-Epoxy Tubular Strut: Hypervelocity Impact Exit.

Figure 8b

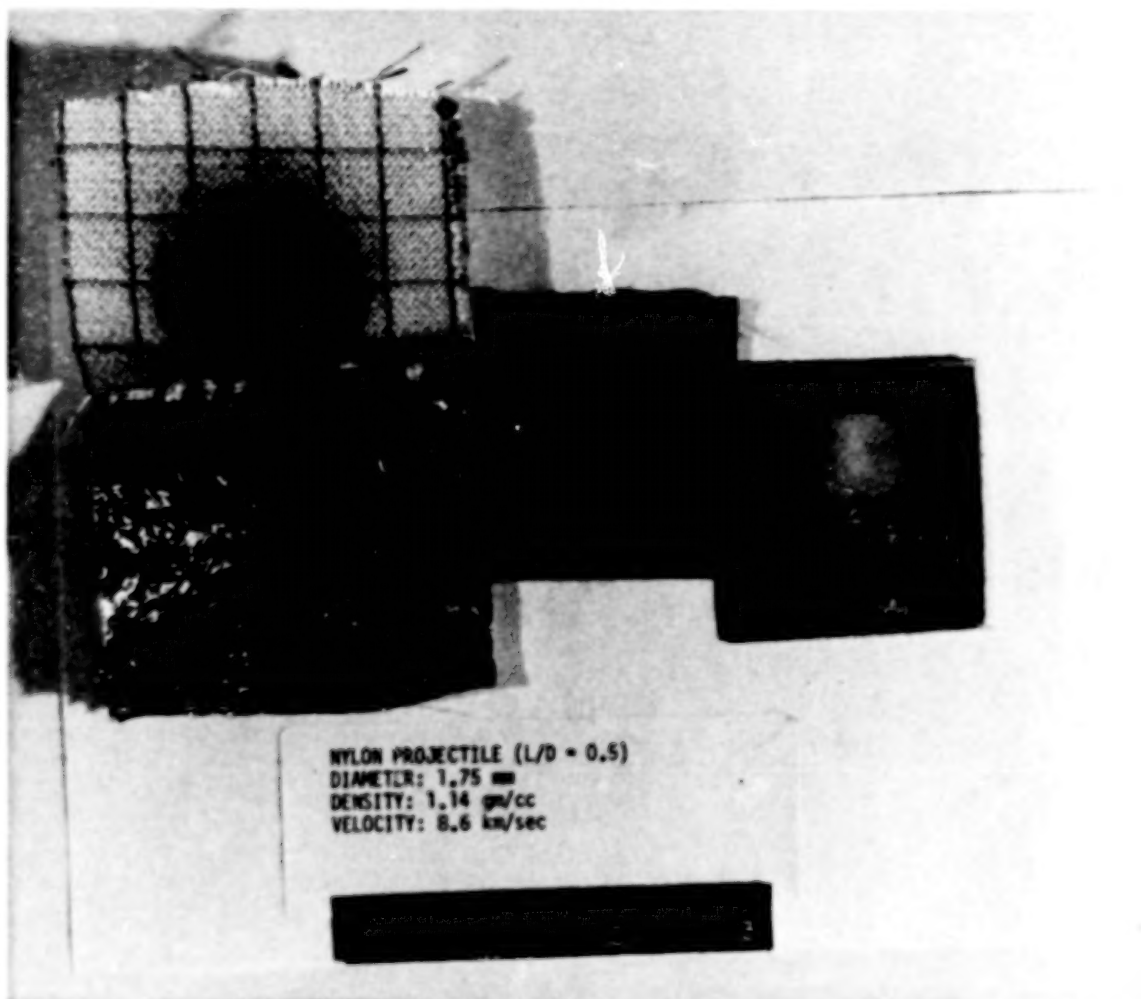
Perforation and peeling of barrier layers used to protect materials subject to atomic oxygen erosion. These impact effects are shown in Figure 9. The smaller one is the result of a 0.77 mm glass projectile impact at 4.7 km/sec, and the larger one is due to a 1.5 mm aluminum projectile at 6.7 km/sec. The barrier layer was a 0.05 mm thick aluminum 2024-T3 bonded sleeve on a 35×10^6 modulus tube. Orbital debris particles equivalent to these sizes can be expected to impact the Phase 1 Space Station Freedom several times in a 10 year period.



Aluminum-coated Graphite-Epoxy Strut: Impact Damage to Coating.

Figure 9

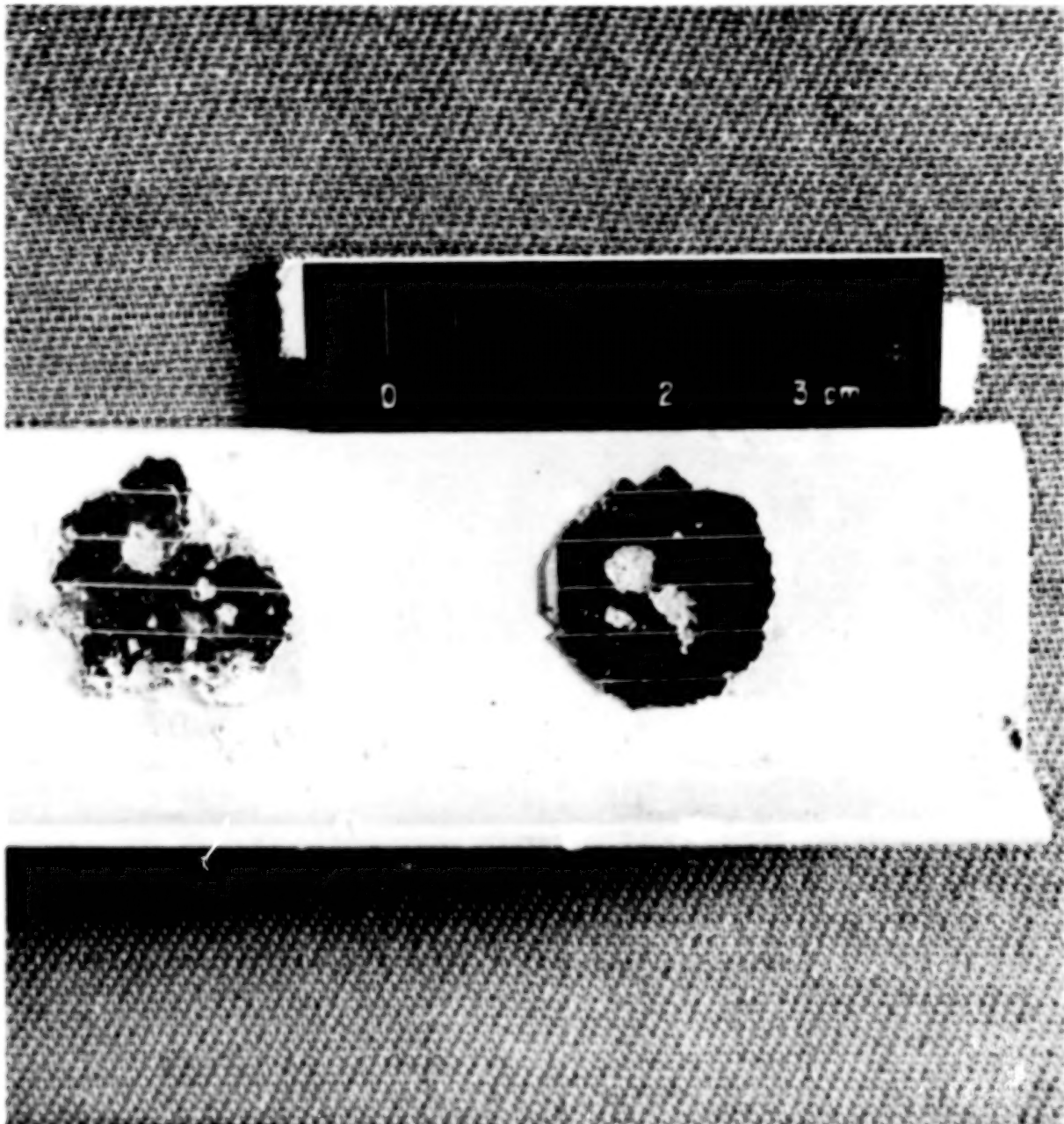
Flammability, vapor deposition and toxicity. Figure 10 is a view of a space-suit element with the outer thermal barrier material folded back to reveal the large hole in the aluminized mylar insulation layer, the hole and blackening of a kapton felt layer and the delamination of a fiberglass laminate. The projectile in this test was a 1.75 mm nylon projectile that impacted at 8.6 km/sec.



Space-suit Element showing Damage to Materials in the Layup.

Figure 10

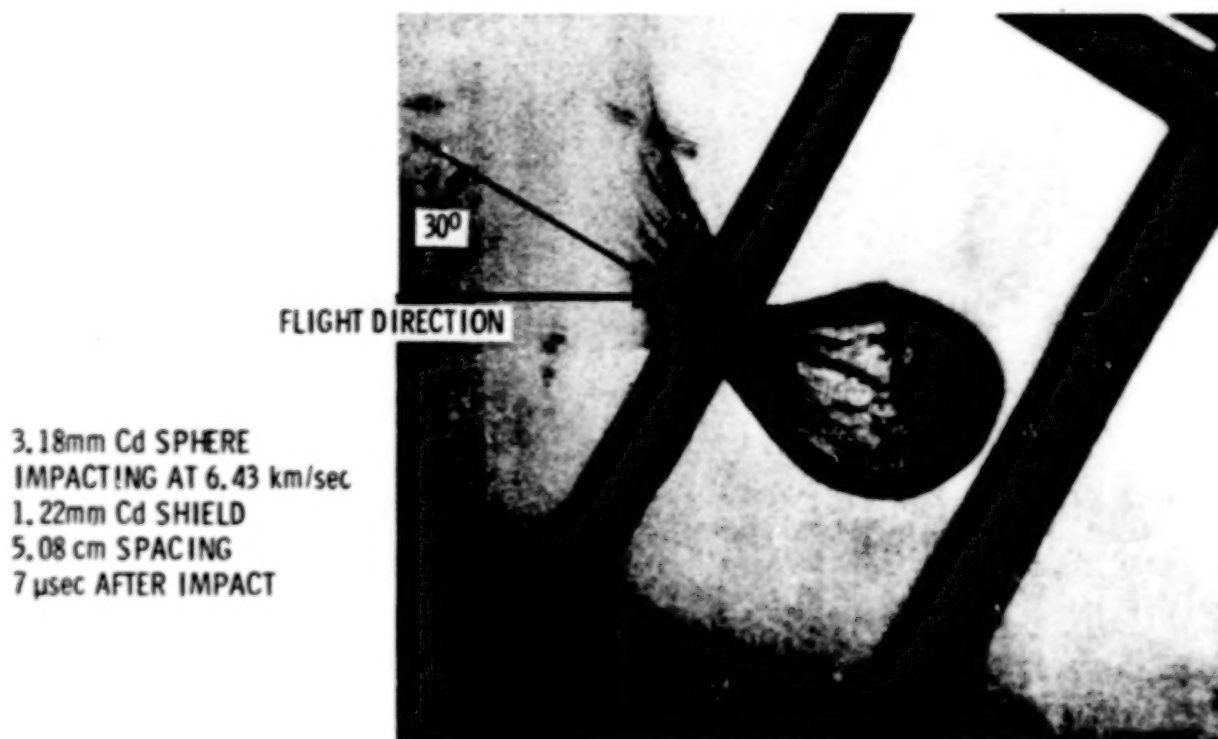
Impacts, molten splatter and vapor deposition result from an impact on a first surface. Oblique impacts are the norm and there will be ejecta from the impact site that will affect other spacecraft components or sensors in the line of flight. Figure 11 is an illustration of secondary impacts on solar cell elements bonded to an aluminum L-section. The damage to the cells is extensive, and the magnification factor for brittle materials can be seen by comparison with the impacts on the aluminum substrate. One impact by a micrometeoroid or an orbital debris particle can result in thousands of secondary impacts on another surface in the way.



Effect of Impact Ejecta on Solar-cell Bonded to Aluminum Substrate.

Figure 11

Second or subsequent surfaces are those that are exposed to the results of perforation of the first surface. The high-speed photograph, Figure 12, from Reference 4. It shows a projectile debris plume generated by an impact on the first sheet of a dual-sheet target and illustrates how the second sheet and the void between can be affected. The plume can be a vapor, molten droplets or even solid fragments. Generally, the second surface is the component that is being protected, but in some instances it could be vulnerable system components.



Flash X-Ray Showing Effect of Oblique Impact

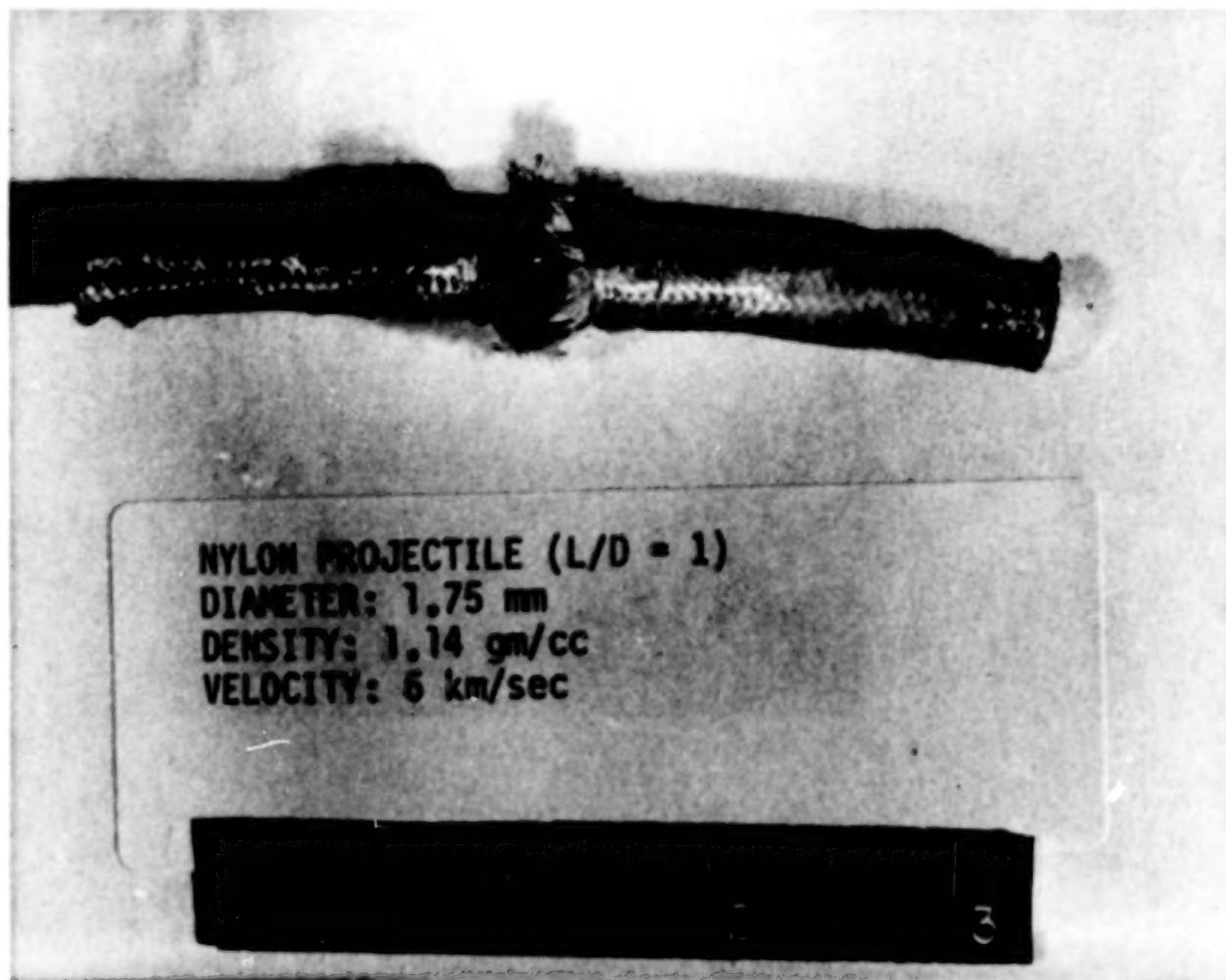
Oblique Impact in Two-sheet Target showing Debris Plume.

Figure 12

Some of the effects of impacts by micrometeoroids or orbital debris particles are as follows:

a. Shield and projectile fragment damage to pressure vessels, wire bundles and sensitive electronic packages.

In Figure 13, a wire cable has been impacted by a large fragment from a debris plume resulting in significant damage.



Electrical Cable Impacted by a Hypervelocity Projectile.

Figure 13

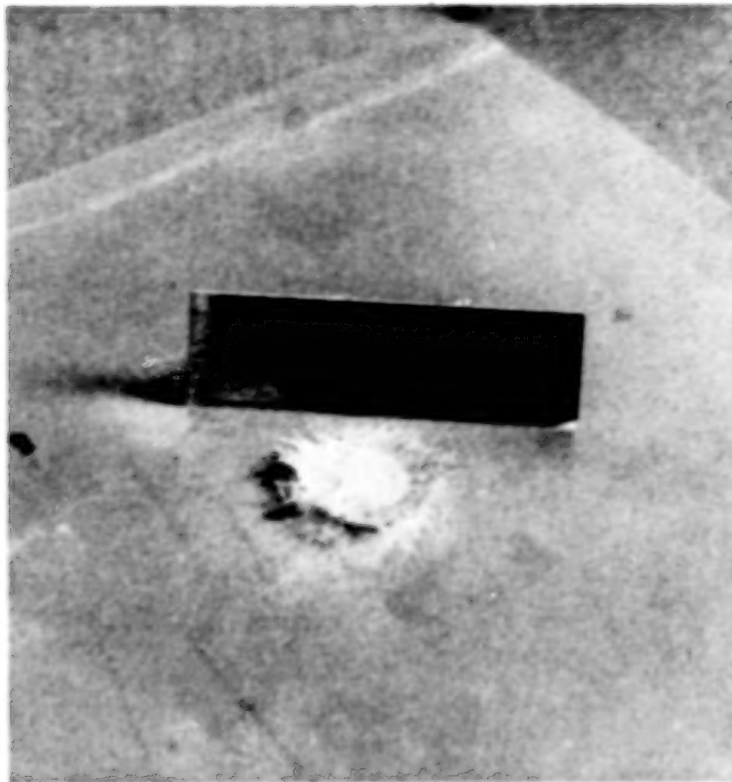
b. Molten droplet and vapor deposition on electronic components could cause shorts.

Examples of these can be seen in the next three figures. Figure 14 shows vapor deposited on the rear surface of the first sheet. A molten aluminium droplet adhering to an aluminum second sheet surface is shown in Figure 15. In Figure 16, a molten aluminum splash and vapor deposit is shown coating a copper second sheet surface.



Rear View of First Sheet Impacted showing Vapor Deposited.

Figure 14



Molten Aluminum Droplet on Aluminum Second Sheet Surface.

Figure 15



Molten Aluminum Splash and Vapor Deposit on Copper Second Sheet Surface.

Figure 16

c. Destruction of a large area of multi-layer thermal insulation (MLI) barriers often placed in the void behind the first surface to protect the second surface.

This effect can be seen in Figure 10, where the aluminized MLI is part of the thermal protection in a space suit.

d. Thermal effects such as burning, charring and toxic by-products.

These effects are also visible in Figure 10.

Material Properties and Practices for Space Durability

The information presented above should lead to a better understanding of how some of the material properties and environmental shielding practices can be improved upon or avoided for long-term space applications. However, the following list of avoidable materials is offered as a starting point:

a). Brittle materials such as glass for mirrors and uncovered windows or lenses, and monolithic ceramic shields. Tough, transparent, optically acceptable synthetic materials respond very well to laboratory hypervelocity impacts.

b). Deposited optical coatings will be easily delaminated and ejected over an area 20 to 30 times the size of the impacting particle. The use of tinting in conjunction with the suggested materials in (a) above would be a solution.

c). Laminated materials can be used provided that impact-caused delaminations do not present a problem. The nonmetallic laminates would be beneficial first surfaces from the secondary impact effects standpoint.

d). Low vaporization temperature materials to avoid vapor coating components that would malfunction.

e). Glass mirrors. Metal mirrors should be the rule as far as possible.

f). Laminated first surfaces with oriented fibers dictated by strength requirements should have an external layer of basket-woven fibers bonded to it. This prevents the peeling along the oriented fibers that results from a hypervelocity impact.

g). Electronic and electrical components should be protected by a double shield to prevent short circuits due to molten droplets or vapor from a first surface impact debris plume.

Spaceflight Experiment Requirements

There is a definite need for in-situ experiments to determine the long-term effects of micrometeoroid and orbital debris impacts on materials used in space. As is indicated by the numbers of impacts as a function of size given in Table 1, test panels required to obtain data on particles 1 mm and larger would be prohibitively large. For instance, a 100 sq. meter test panel exposed for 10 years would collect between 7 and 14 total impacts of this size, depending on orbital altitude. It is however, reasonable to consider flight testing materials subjected to the smaller particles. A 10 sq. meter panel would collect a total of 630 to 900 impacts of the 0.1 mm particle size, and probably 1 or 2 of the 1 mm size, in 10 years of exposure. Obviously, shorter durations of 2 or 3 years would still yield useful data for the 0.1 mm and all smaller sizes. Laboratory hypervelocity impact facilities cannot launch projectiles in the range of sizes between 0.1 mm and 0.01 mm at velocities greater than 6 km/sec.

Although it is not reasonable to expect dedicated flight experiments for micrometeoroid and orbital debris impacts for sizes larger than 2 mm, it should be possible to use reserved areas of the Space Station Freedom truss structure to attach test panels requiring a long exposure.

Laboratory hypervelocity impact facilities have successfully launched 0.2 mm projectiles when required, although normal testing calls for 0.8 to 3.2 mm. The velocity ranges most readily obtained for all these sizes are between 5.5 and 7.5 km/sec. As a result, ground-based hypervelocity testing of new materials for space use could be a part of an overall plan to develop space durability for the impact environments.

Conclusion

The long-term effects of the micrometeoroid and orbital debris environments on materials that are commonly used in space are dominated by the particles smaller than 1 mm in size. These particles are numerous enough to cause erosion of surface layers, optical degradation by pitting and vapor deposition, the destruction of coated and mirrored glass surfaces, the delamination and penetration of anti-atomic oxygen coatings and impact ejecta effects on surrounding structure. If a penetration of an outer layer of a spacecraft occurs, the impact debris plume can cause damage to electrical and electronic elements by solid particulate matter, molten droplets, and vapor deposition. Some materials are more susceptible to be damaged than others, and some are worse from the standpoint of secondary effects. This report presents information that could lead to enhanced long-term performance of current materials and the development of new materials designed to mitigate the effects described.

REFERENCES

1. Kessler, Donald J.; Orbital Debris Environment and Data Requirements. Space Environmental Effects on Materials - 1988. NASA CP -----, 1988
2. Swift, Hallock F.; Hypervelocity Impact Mechanics. Impact Dynamics. John Wiley and Sons., p. 226
3. Cour-Palais, Burton G.; Hypervelocity Impact Investigations and Meteoroid Shielding Experience Related to Apollo and Skylab. NASA CP 2360, 1982
4. Gehring, John W.; Impact of Thin Targets and Shields: Theory and Experiment. High-Velocity Impact Phenomena. Academic Press., p. 109

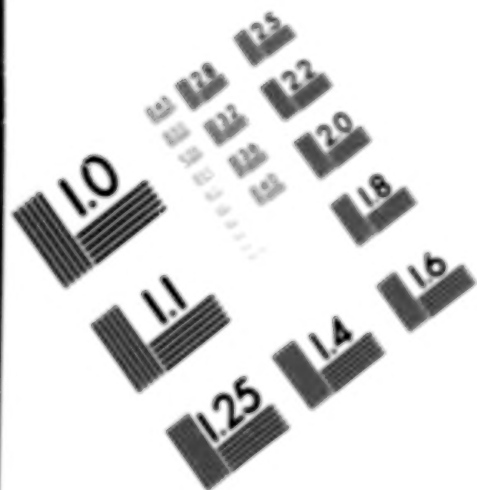
ORBITAL DEBRIS ENVIRONMENT
AND DATA REQUIREMENTS

Donald J. Kessler
NASA Lyndon B. Johnson Space Center
Houston, Texas

ORBITAL DEBRIS, CURRENT NASA INVOLVEMENT

NASA is involved with orbital debris in 4 major areas: 1. Characterizing the environment. This is accomplished with a program of measurements and modeling. This work is mostly conducted at JSC. 2. Examining implications of the environment. This is accomplished by conducting hypervelocity impact tests, determining possible failure modes for spacecraft systems, and evaluating the required shielding to obtain a desired spacecraft reliability. This work is conducted at MSFC, JSC, ARC, and LaRC. In addition, other agencies and contractors conduct independent research. 3. Developing an Agency technical plan. JSC has put together a technical plan for the review of other centers. 4. Developing Policy. NASA Headquarters has the responsibility of developing policy, with other centers providing the technical background.

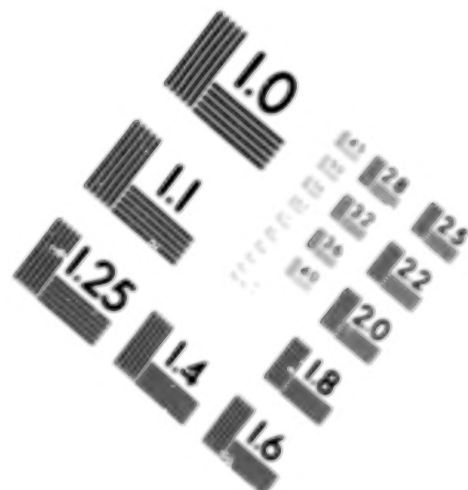
- CHARACTERIZING THE SPACE ENVIRONMENT
- EXAMINING IMPLICATIONS FOR FUTURE USE OF SPACE
- DEVELOPING AN AGENCY TECHNICAL PLAN
- DEVELOPING AGENCY POLICY



AIM

Association for Information and Image Management

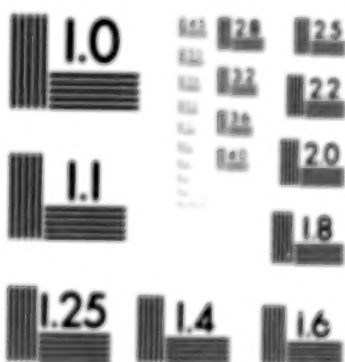
1100 Wayne Avenue, Suite 1100
Silver Spring, Maryland 20910
301/587-8272



Centimeter



Inches



MANUFACTURED TO AIM STANDARDS
BY APPLIED IMAGE, INC.



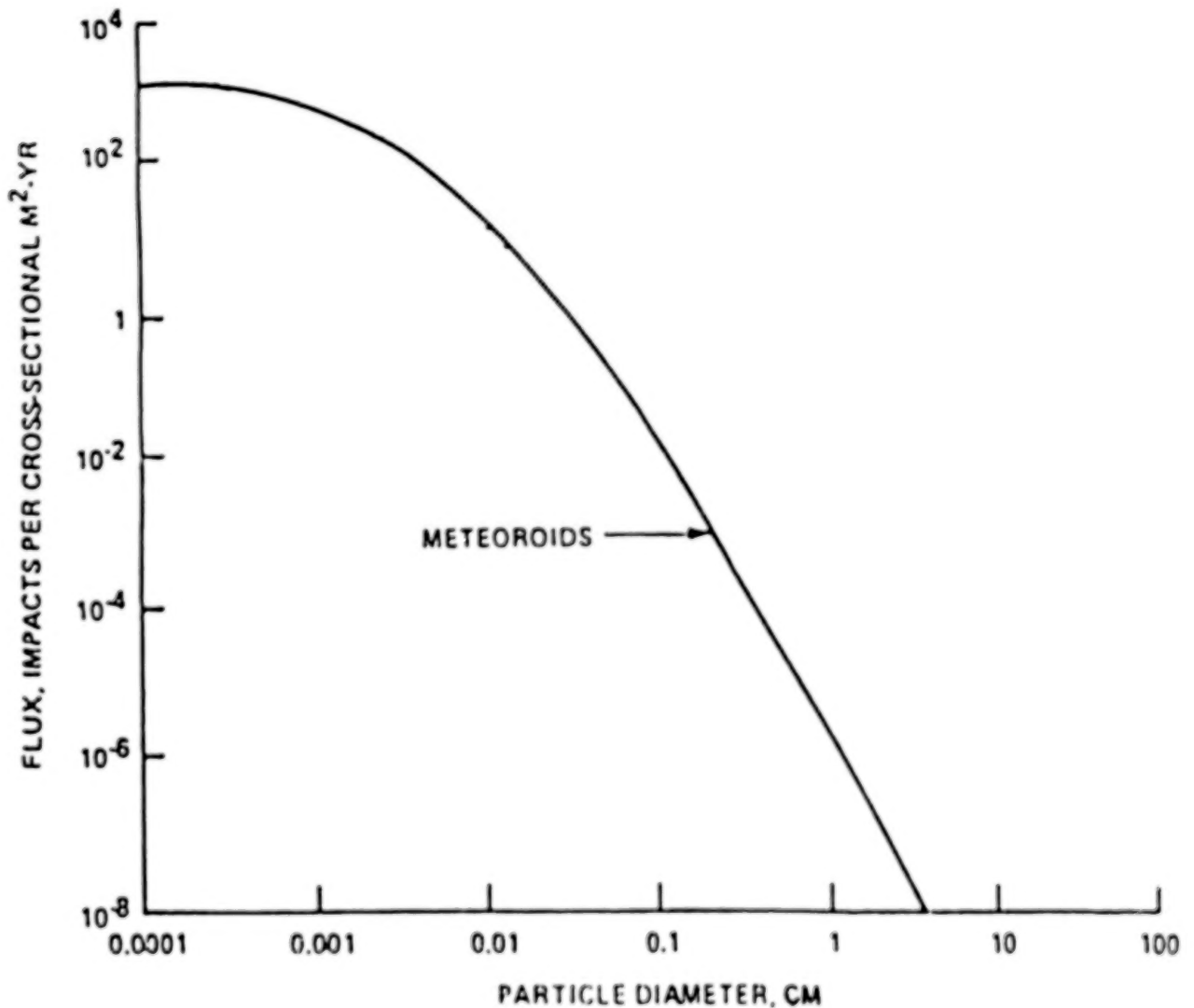
METEOROID BACKGROUND

The natural meteoroid environment has historically been a design consideration for spacecraft. Meteoroids are part of the interplanetary environment, and sweep through Earth orbital space at an average speed of 20 km/sec. At any one instant, a total of 200 kgm of meteoroid mass is within 2000 km of the Earth's surface. Most of this mass is concentrated in 0.1 mm meteoroids, with only a small fraction of the mass in sizes as large as 1 cm.

- **Meteoroid orbits pass through Earth orbital space**
- **Less than 500 lbs at altitudes below 2000 km at any one time (most approximately 0.1 mm in diameter)**
- **In the past, meteoroids have occasionally been a spacecraft design consideration**
 - Apollo, Skylab
 - size range 0.3 mm to 3 mm most important
- **In the future, meteoroids are expected to be more important**
 - larger spacecraft
 - longer exposure
 - lighter weight construction
 - size range 0.1 mm to 1 cm will be important

METEOROID FLUX

As a result of measurements by Pegasus and Explorer satellites and photographic and radar meteors, the meteoroid flux has been defined at 1 AU for about 20 years. When used for Earth orbit, both an Earth shielding factor and a gravity concentration factor must be applied to give the flux shown here, published in Planetary and Space Sciences, July, 1970, Vol. 18, No. 7, pp. 953-964.



ORBITAL DEBRIS POPULATION

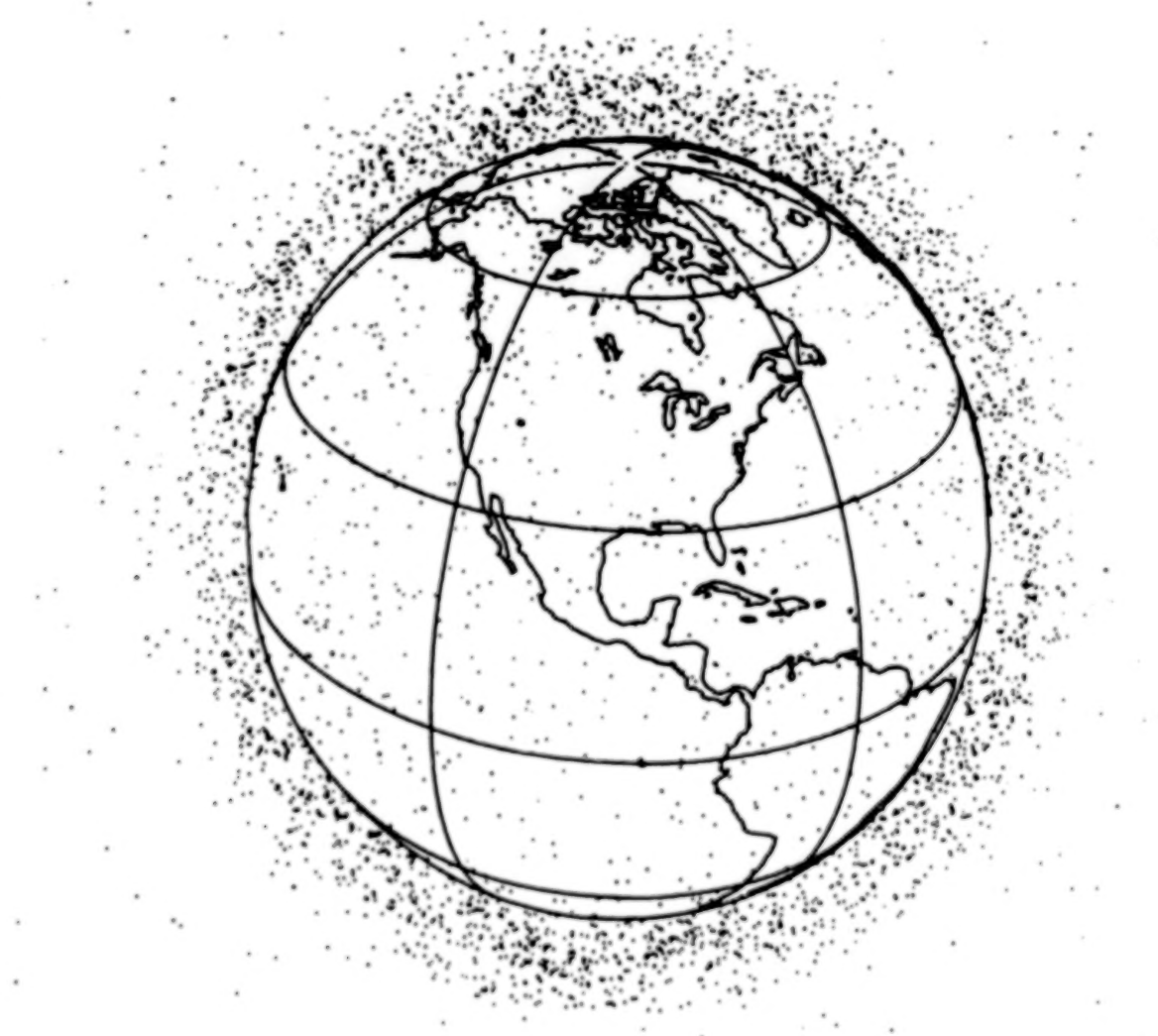
Within 2000 km of the Earth's surface, there is also an estimated 3,000,000 kgm of man-made orbiting objects. These objects are in mostly high inclination orbits, and sweep past one another at an average speed of 10 km/sec. Most of this mass is concentrated in about 3000 spent rocket stages, inactive payloads, and a few active payloads. A smaller amount of mass, about 40,000 kgm, is in the remaining 4000 objects currently being tracked by US Space Command radars. Most of these objects are the result of over 90 on-orbit satellite fragmentations. Consequently, from these considerations alone, it is likely that smaller satellite fragments exist in low Earth orbit in sufficient quantities to exceed the meteoroid flux.

- Over 6000 objects catalogued by NORAD^{*} and "permanently" in Earth orbital space (over 16,000 injected into orbit to date)
- Approximately 4,000,000 lbs at altitudes below 2000 km (most approximately 3 meters in diameter)
- High intersection angles produce high collision velocities
- If only a small fraction (0.01%) of the mass were in a smaller size range, the resulting environment would exceed the meteoroid environment in that size range. Possible sources of smaller objects are:
 - explosions
 - hypervelocity collisions
 - degradation of spacecraft surfaces
 - solid rocket motors firing in space

^{*} North American Air Defense Command

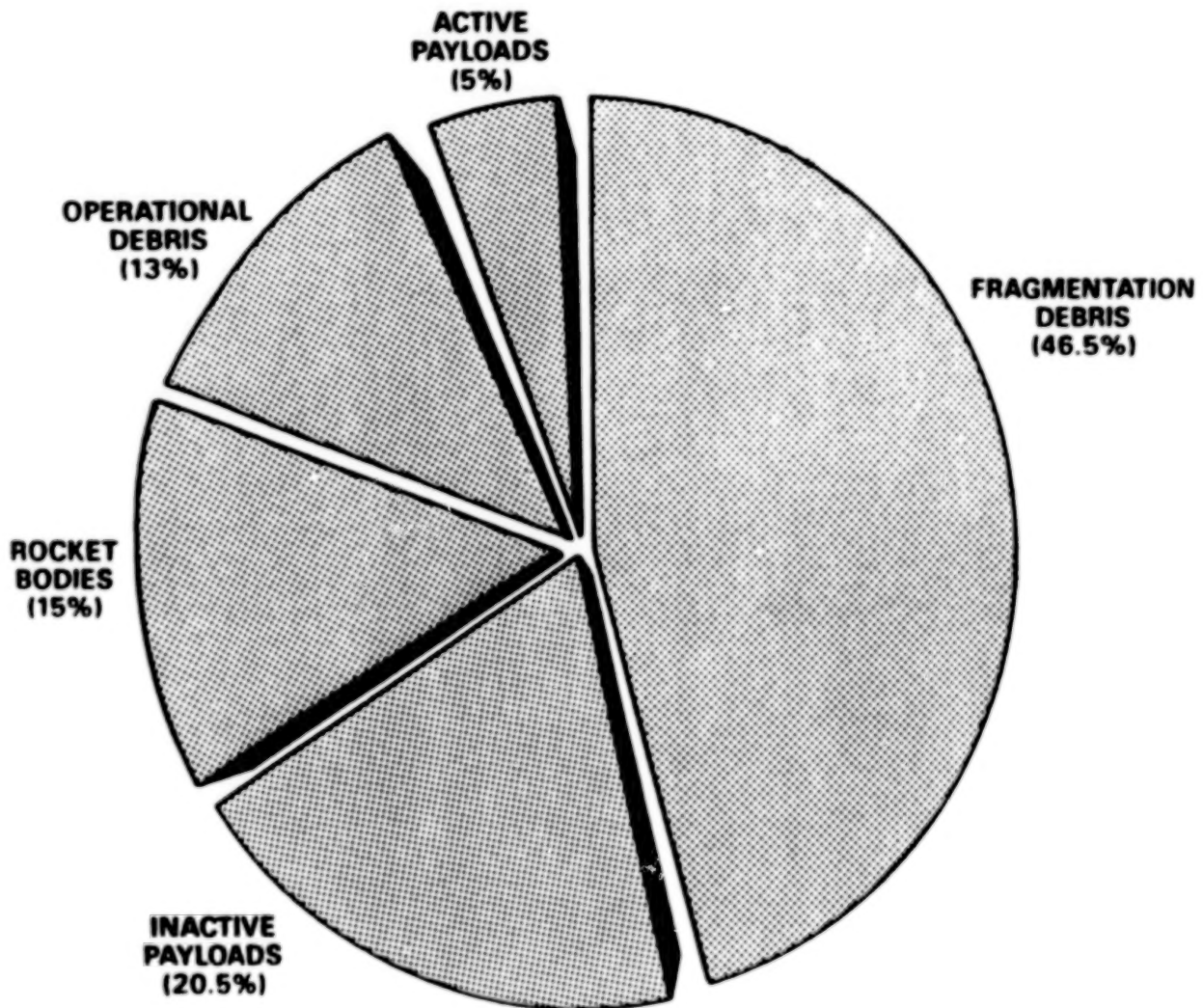
THE MAY 30, 1987 CATALOGUE AS OBSERVED FROM A POINT IN SPACE

The position of about 7000 objects cataloged by US Space Command is shown. Most objects are at altitudes less than 2000 km, and are nearly randomly distributed over the surface of the Earth. Consequently, collision probabilities are nearly independent of a spacecraft's orbital inclination, and collision velocities are high, averaging about 10 km/sec. The dots representing orbiting objects are not to the same scale as the size of the Earth; consequently, collision probabilities with the catalogued population are low, unless the spacecraft is larger than about 100 meters in diameter.



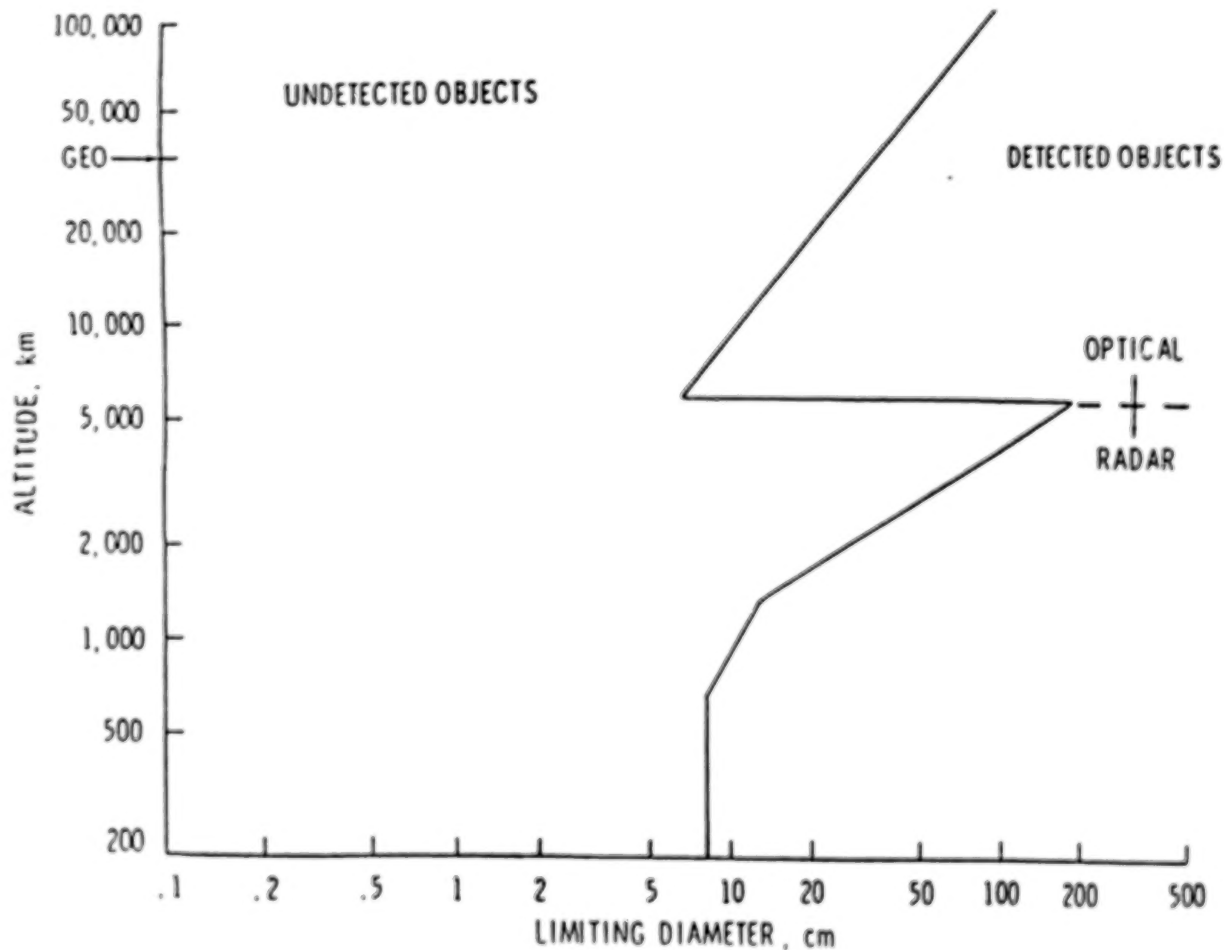
CATALOGUED EARTH SATELLITE POPULATION, 1 JANUARY 1987

Only about 5% of the catalogued population is active payloads. The remaining is orbital debris, with the largest percentage coming from on-orbit fragmentation events. Of the more than 90 events, only about 25 events contribute to more than 90% of the fragments. Because of new operations procedures, since 1981, only 1 US event has made any contribution to the accumulation of fragments in orbit; the USSR has been the major contributor in recent years.



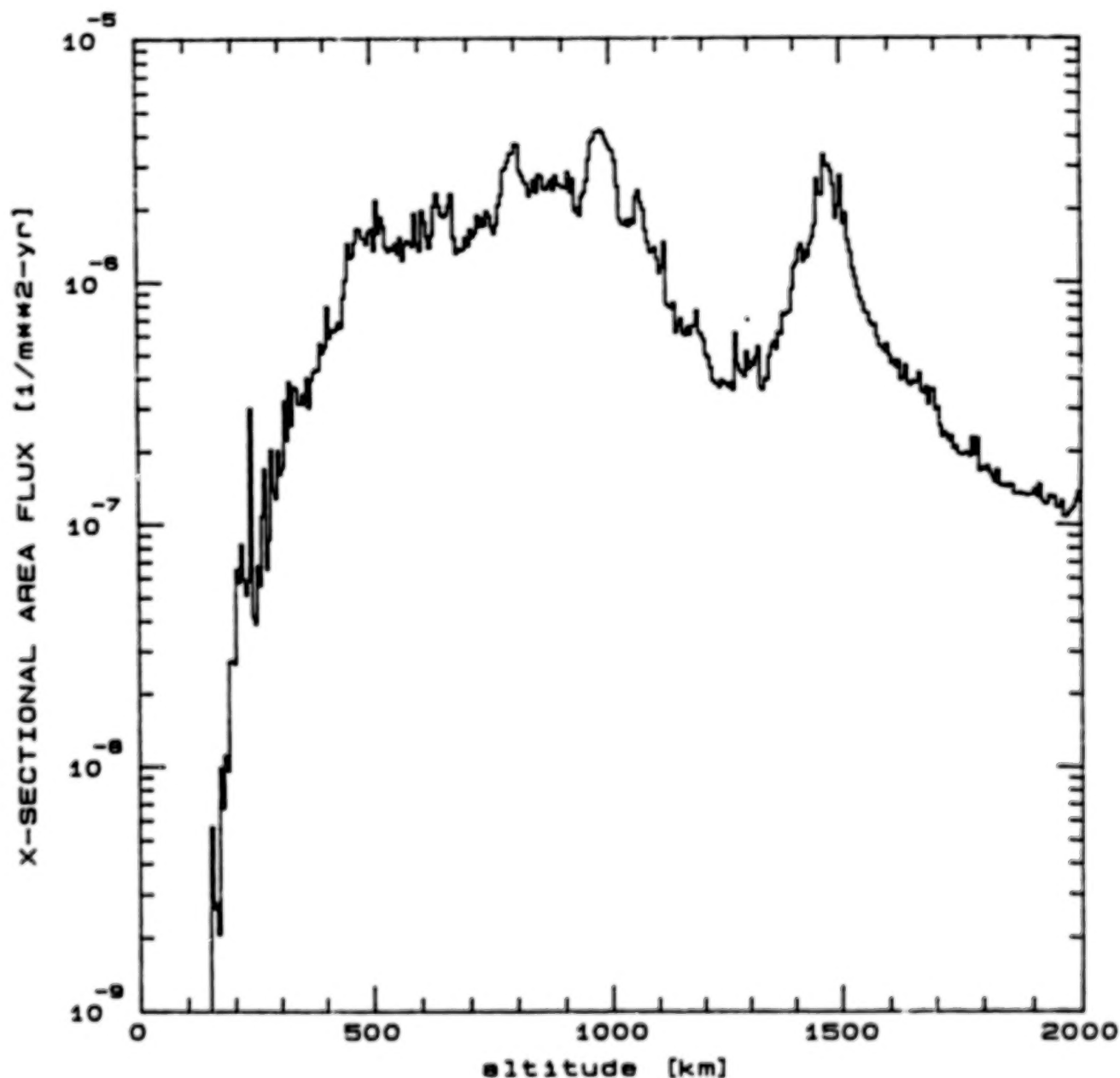
US SPACE COMMAND OPERATIONAL CAPABILITY TO DETECT SATELLITES

Because the US Space Command radars use a radar wavelength that is about 70 cm, their ability to detect and catalogue objects smaller than about 10 cm is very limited, even at low altitudes. At higher altitudes, they use optical techniques to catalogue objects. Note that an extrapolation of the optical technique to low altitudes would allow the detection (but not cataloguing) of 1 cm objects at 500 km. This technique has been experimentally used by MIT's Lincoln Labs.



US SPACE COMMAND CATALOGUED OBJECTS-JANUARY 1987

In January, 1987, the US Space Command was tracking about 6300 catalogued objects. The flux of the objects was calculated by the technique described in the publication *Icarus*, Vol. 48, 1981, pp. 39-48. To calculate the collision probability with a spacecraft, multiply the flux by the cross-sectional area of the spacecraft. For example, a very large spacecraft, 100 meters in diameter, at 500 km would have about a .015 probability per year of collision with a catalogued object. However, typically several hundred additional objects are awaiting catalogue, and these objects usually significantly increase the collision probabilities at altitudes below 500 km.



1987 SATELLITE BREAKUPS

During the year of 1987, a large number of breakups occurred. Most of these breakups occurred at altitudes below 500 km. At these lower altitudes, it is very difficult to maintain an accurate catalogue because the orbits are changing rapidly and because the objects do not pass over radar sites as frequently. Typically, more than a year is required to catalogue most of the fragments following a major breakup.

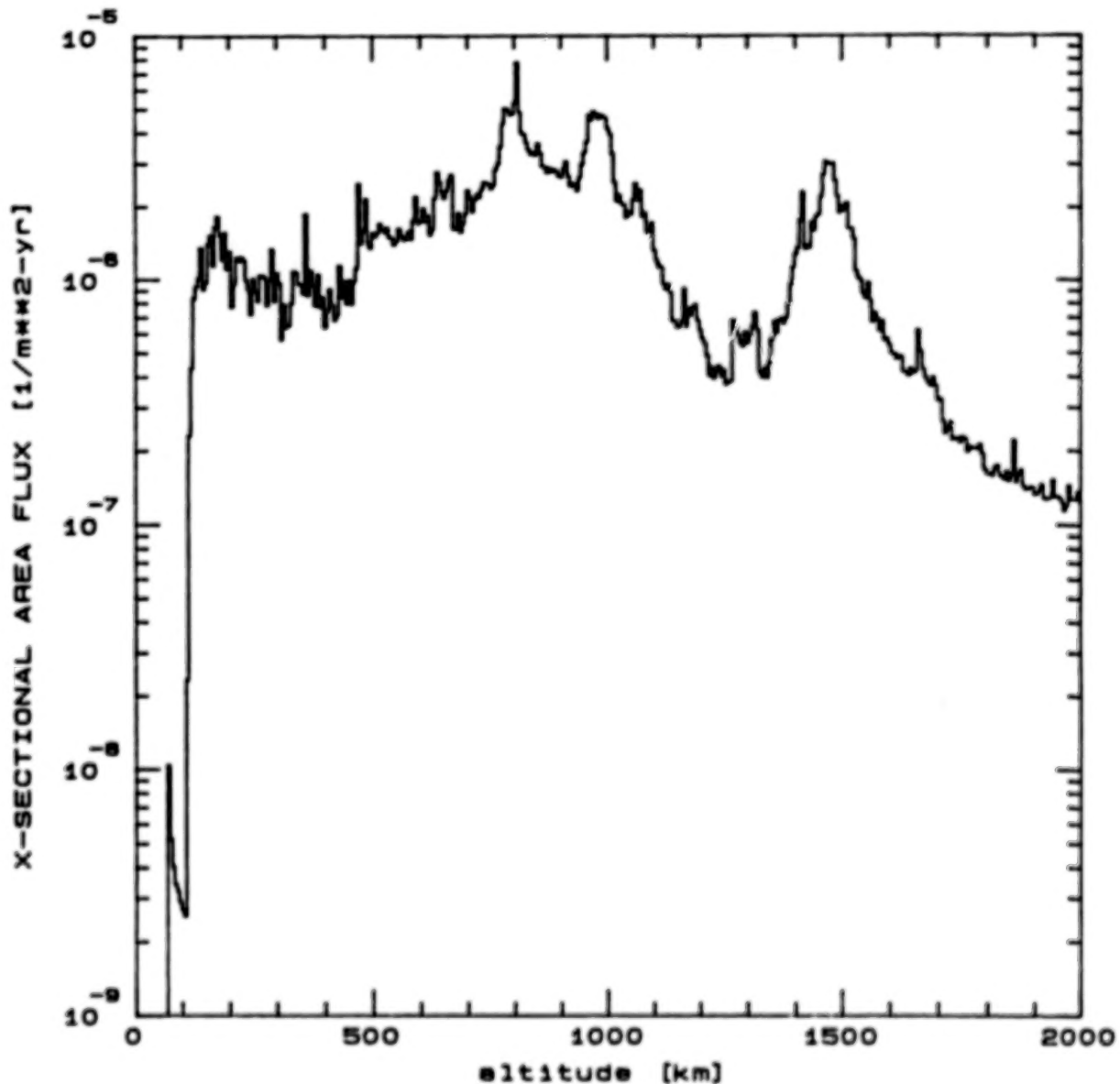
Cataloged fragments as of January 10, 1988

Breakup	Satellite	Breakup Altitude	Orbital Perigee	Orbital Apogee	Orbital Incl.	Trackable Fragments	
Date	Name	(km)	(km)	(km)	(deg.)	Estimated	Catalogued
1-28-87	COS1813	390	359	417	73	1000	190
7-26-87	COS1866	243	167	361	67	1000	9
9-18-87	ARIANE	?	246	36523	7	>15	1
9-21-87	COS1769	333	310	444	65	150	4
11-20-87	COS1646	406	401	434	65	150	25
12-17-87	COS1823	1485	1477	1523	74	>60	43

The estimated number of fragments was determined from radar data from individual radar sites.

US SPACE COMMAND CATALOGUED OBJECTS-JANUARY 1988

Although most of the fragments from the 1987 breakups were not catalogued, there was still a very large increase in the flux at altitudes below 500 km due to these breakups. At these lower altitudes, most of the fragments will reenter soon, and the flux should return to near its 1987 values within a year, assuming new breakups do not occur. However, the large increase at 800 km, which was due to the belated cataloguing of a breakup that occurred in November, 1986, will remain for 50 to 100 years.



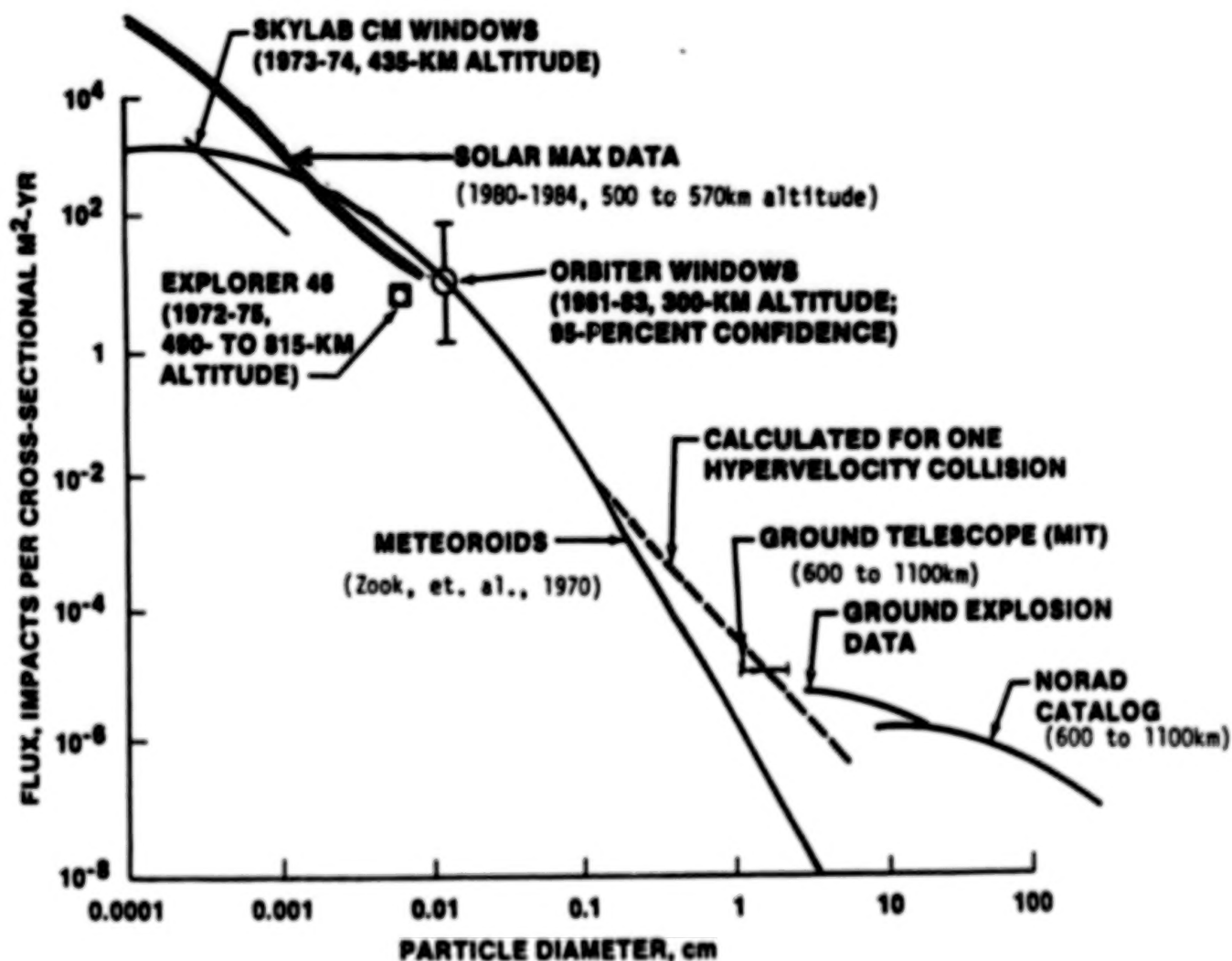
NASA'S ACTIVITIES TO DEFINE ENVIRONMENT

Because of the likelihood that a large number of objects with diameters less than 10 cm are in orbit, JSC has had a program for the last 10 years to better determine this environment. US Space Command ground radar data has been used to better understand the nature of each satellite fragmentation so that better predictions could be made concerning the total number of fragments generated. Ground telescopes have been used to detect 16th visual magnitude orbital debris and has found about 5 times the catalogued number of objects. IR measurements of satellite fragments have determined that these fragments are dark, having an albedo of about 0.1. Spacecraft surfaces, such as orbiter windows and returned Solar-Max satellite surfaces have been examined for hypervelocity impacts. A model has also been developed which predicts future orbital debris growth as a result of random collisions between satellites.

- Analysis of NORAD/ground radar data
- Acquire and analyze ground telescope data
- Acquire, analyze, and curate for research purposes returned spacecraft surfaces
- Model NASA, DoD, other traffic models
 - collision fragmentation
 - predict consequences of various activities in space

EXISTING ORBITAL DEBRIS MEASUREMENTS COMPARED TO METEOROID FLUX

All orbital debris measurements to date show an orbital debris flux that is either nearly as large as, or greater than, the meteoroid flux. The chemical composition of material found in hypervelocity pits on the Apollo/Skylab windows, the orbiter windows, and Solar-Max surfaces was used to distinguish orbital debris from meteoroids. Directionality was used to make this distinction on Explorer 46. The MIT telescopes were likely detecting 2 cm objects. Modeling hypervelocity collisions and ground explosions predict the distributions shown. However, no measurements have been made in the critical 1 mm to 1 cm size range. Modeling predicts that the amount of debris in this size range will increase significantly as the result of random collisions.



MODELING

Modeling consists of using various space traffic models, using past and predicted satellite fragmentation events to predict the future orbital debris environment. Such modeling consistently predicts that even if small debris did not already exist, it will soon exist in large quantities due to random collisions between larger orbiting objects. The most probable type of collision would be between an old rocket body, or inactive payload, and a large satellite fragment.

INPUTS

- DOD, NASA, ESTIMATED USSR TRAFFIC MODEL
- SATELLITE BREAKUP MODELS

OUTPUTS

- FLUX AS FUNCTION SIZE, ALTITUDE, TIME
- VELOCITY, DIRECTION DISTRIBUTIONS

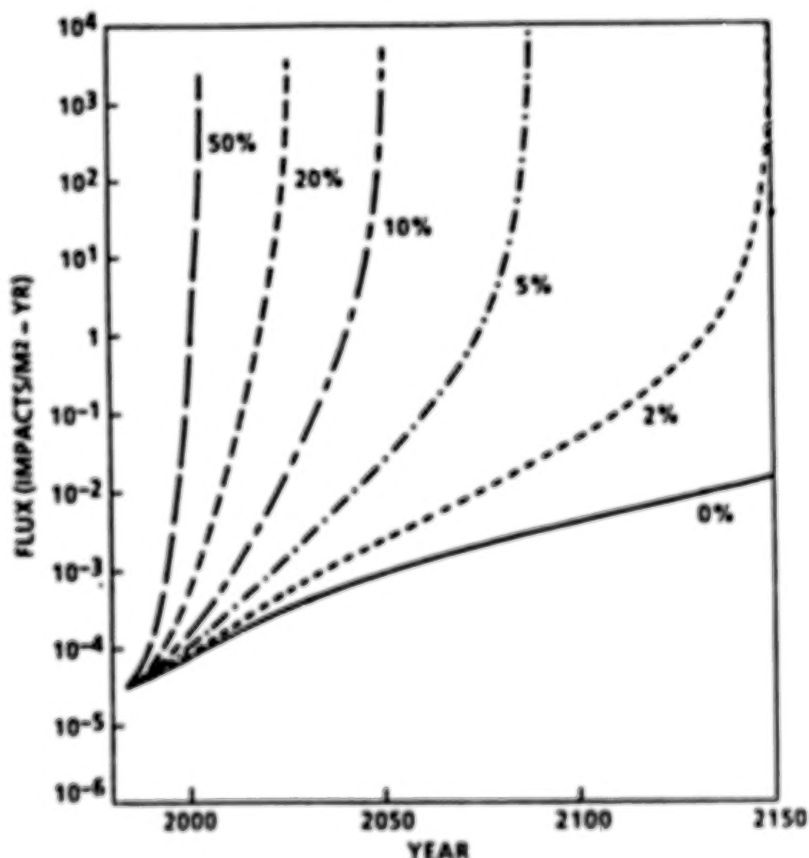
CONCLUSIONS

CASCADING EFFECT OF SATELLITE COLLISION FRAGMENTATION COULD PRODUCE AN EXPONENTIAL GROWTH IN THE 1 MM TO 1 CM POPULATION WITHIN THE NEXT 20 YEARS, DEPENDING ON

- TRAFFIC MODELS
- SATELLITE BREAKUP MODELS

DEBRIS FLUXES FROM OBJECTS 4 MM ,OR LARGER, AT 1000 KM ALTITUDE

By assuming a yearly percentage increase in the current launch rate, and that future small debris originates only from random collisions between orbiting objects (i.e., no future accidental or intentional explosions), a prediction of the future environment is made. As a result of cascading collisions, the small debris increases at a much faster rate than the launch rate alone would predict. Eventually, a critical density of larger objects would be reached, causing a very rapid increase in the rate of satellite collisions, generating small debris at a rate that would be independent of the launch rate. A 5% per year increase in the current launch rate could cause this critical density to be reached by the year 2060, while a 10% per year increase in the launch rate could cause the critical density to be reach by 2030. See the publication *Advances in Space Research*, Vol. 6, No. 7, 1986, pp. 109-117.



Debris fluxes from objects with diameter 4 mm or larger at 1000 km altitude with different increase rates of yearly traffic input.

TECHNIQUES TO OBTAIN DATA ON DEBRIS--1 CM AND LARGER

Various studies and experiments have shown that techniques to statistically sample the orbital debris environment at sizes smaller than catalogued by US Space Command can be conducted from either space based or ground based experiments. In both cases, remote sensing techniques must be used in order to provide a large effective collecting area. The cost of constructing a space based instrument is larger than a ground based instrument, and does not include the cost of launch, or the spacecraft; consequently, ground based measurements are more cost effective. Although ground telescopes have provided excellent data, they are limited by lighting constraints...for example, most sun synchronous orbits cannot be observed from latitudes closer to the equator than 45 degrees. However, a single X-band radar near the equator could sample all orbits. NASA plans to have such a radar operational by 1991.

TECHNIQUE	COST*	TECHNOLOGY RISK	DATA RETURN	COMMENTS
SPACE BASED				ALTITUDE LIMITED TO SPACECRAFT ALTITUDE
RADAR ¹	HIGH	LOW	LOW	RADAR NOT OPTIMIZED FOR PERFORMANCE
LIDAR ¹	HIGH	HIGH	LOW	
OPTICAL ¹	MED	LOW	HIGH	
IR ²	HIGH	LOW	HIGH	
GROUND BASED				ALTITUDE LIMITED TO LESS THAN 500KM
⇒ RADAR ³	LOW	LOW	HIGH	X BAND RADAR
OPTICAL ⁴	LOW	LOW	LOW	TWO 30 INCH TELESCOPES, ASSUMING HIGH ALBEDO LIGHTING CONSTRAINTS LIMITS DATA RETURN

1. G.E. STUDY, 1982; BATTELLE STUDY, 1983; JPL 1987

2. IRAS EXPERIENCE

3. BATTELLE, TELEDYNE BROWN ENG., JPL, JSC STUDIES, 1987

4. MIT DATA; INHOUSE EXPERIENCE

*COST

LOW LESS \$20M

MED \$20M TO \$50M

HIGH GREATER \$50M

TECHNIQUES TO OBTAIN DATA ON DEBRIS--1 MM AND LARGER

The cost of building a ground based system which could sample the 1 mm environment is considerably higher than the system to sample the 1 cm environment. In addition, the technology risk is higher for the required K-band radar. Consequently, the most cost effective technique of obtaining this data is a space based optical detector. JPL proposed earlier this year a configuration, called "Quicksat", which would orbit a pair of 25 cm telescopes, each with sensors consisting of 8X16 CCD "macropixels". The spacecraft and instrument would cost \$100M-- more than NASA can currently afford.

TECHNIQUE	COST*	TECHNOLOGY RISK	DATA RETURN	COMMENTS
SPACE BASED				ALTITUDE LIMITED TO SPACECRAFT ALTITUDE
RADAR ¹	HIGH	LOW	LOW	RADAR NOT OPTIMIZED FOR PERFORMANCE
LIDAR ¹	HIGH	HIGH	LOW	
⇒ OPTICAL ¹	MED	LOW	HIGH	
IR ²	HIGH	LOW	HIGH	
GROUND BASED				ALTITUDE LIMITED TO LESS THAN 500 KM
RADAR ³	HIGH	HIGH	HIGH	K BAND RADAR
OPTICAL ⁴	HIGH	LOW	LOW	TWO 300 INCH TELESCOPES, ASSUMING HIGH ALBEDO; LIGHTING CONSTRAINTS LIMITS DATA RETURN

1. G.E. STUDY, 1982; BATTELLE STUDY 1983; JPL 1987

2. IRAS EXPERIENCE

3. JPL, 1987; JSC, 1987

4. UNIV. TEXAS PROPOSAL, 1985

*COST

LOW LESS \$20M

MED \$20M TO \$50M

HIGH GREATER \$50M

TECHNIQUES TO OBTAIN DATA ON DEBRIS--1 MM AND SMALLER

Meteoroids smaller than 1 mm have been measured using satellite "impact" sensors since the 1960's. However, only recently has consideration been given to determining the trajectory of the impacting meteoroid. Being able to discriminate between orbital debris and meteoroids is essential to any type of sensor. By obtaining trajectory information, one can determine which objects are in Earth orbit. If the surface is planned to be returned for analysis, then chemical composition of material found associated with the impact can be used to determine if the object is natural or man-made. Both techniques can be used on a single experiment; that is, the trajectory could be measured, and the impact surface later returned for analysis. Such experiments may be used on the Space Station Cosmic Dust Facility.

SPACE BASED SENSORS

Techniques	Technology Risks	Debris, Meteoroid Discriminator	Flight Experience
Telemeter Data		Trajectory	No trajectory configurations:
Intrinsic Charge Sensing	HIGH		Lab experiment only
Impact Plasma Sensing	LOW		Pioneer 8, 9, Helios, Heos, Giott
Capacitive Sensing	LOW		Vega, Pegasus
Returned for Analysis		Chemical Composition	
capture cell	LOW		Solar Max, LDEF
Low density Foam	LOW		Flights scheduled

CONCLUSIONS

Orbital debris is already a major design consideration for Space Station Freedom and is becoming important to the design of unmanned spacecraft. Mathematical models predict the environment will increase with time. The amount it increases is dependent on future operations in space, and how these operations are conducted. Therefore, it is important to understand the sources of debris and which operations will minimize debris generation. This requires that debris be monitored. Currently, NASA plans to have an operational capability to monitor 1 cm debris at 500 km by 1991. However, there are currently no plans to monitor the environment of smaller debris which will be important to future spacecraft design.

- **Existing measurements indicate the current Orbital Debris Environment in Low Earth Orbit is more important to spacecraft design than meteoroid environment.**
- **Mathematical Models predicts significant increases in the orbital debris environment within the near future.**
- **Need to monitor environment of 1 cm and smaller orbital debris**

MICROPARTICLE IMPACTS IN SPACE
RESULTS FROM SOLAR MAX SATELLITE AND SHUTTLE WITNESS PLATE INSPECTIONS

David S. McKay
NASA Lyndon B. Johnson Space Center
Mail Code SN14
Houston, TX 77058

The Solar Maximum Satellite developed electronic problems after operating successfully in space for several years. Astronauts on Space Shuttle mission STS-41C retrieved the satellite into the orbiter cargo bay, replaced defective components, and re-deployed the repaired satellite into orbit. The defective components were returned to Earth for study. Scientists in the Solar System Exploration Division at Johnson Space Center in Houston have been examining the space-exposed surfaces. The approach and objectives of these studies are shown in Figure 1.

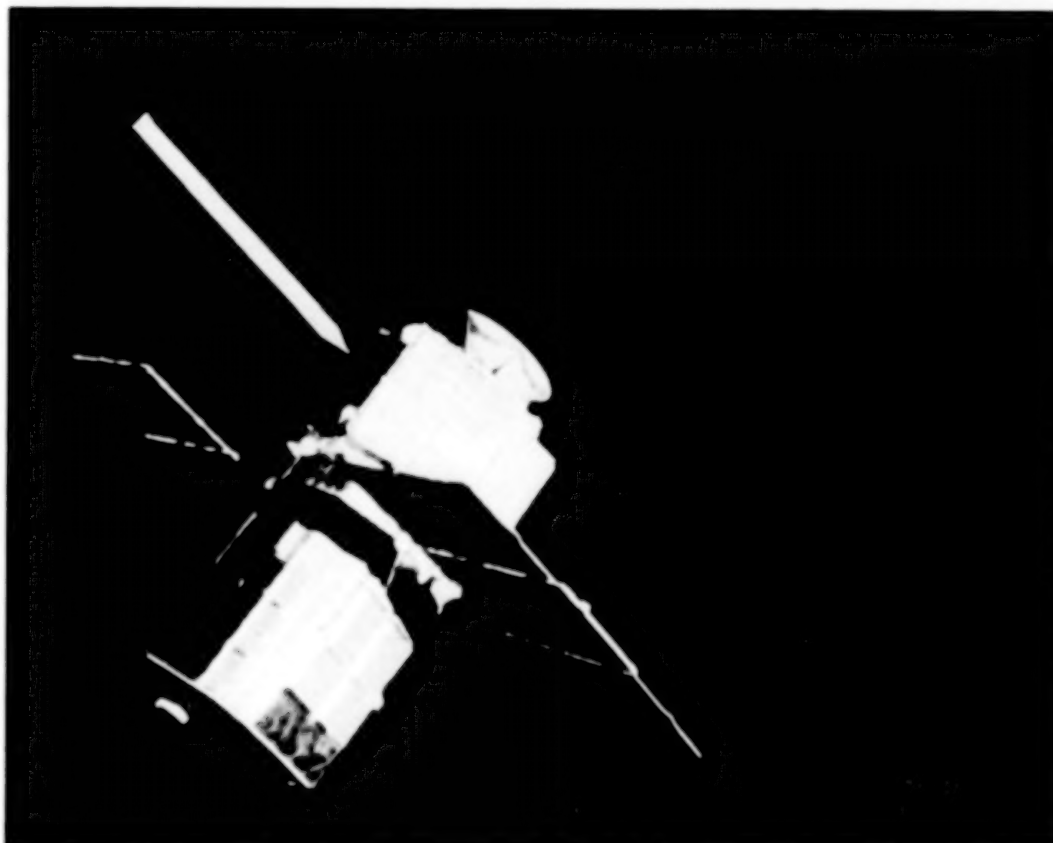
MICROPARTICLE IMPACT ON RETURNED SOLAR MAXIMUM HARDWARE

Approach and Objectives:

1. Document morphology of impact.
2. Find and analyze projectile residue.
3. Classify impact by origin.
4. Determine flux distribution.
5. Determine implications for space exposure.

Figure 1

Figure 2 illustrates the geometry and positioning of the Attitude Control Systems Box as seen before recovery and repair of the satellite. Thermal blankets and louvers exposed to space were retrieved by Shuttle astronauts during Solar Max repair mission STS-41C. These louvers and blankets have been inspected by means of scanning electron microscopy in order to determine fluxes and origins of impacting projectiles.



Attitude Control Systems Box before recovery and repair of satellite.

Figure 2

The Attitude Control Systems Box was returned from the Solar Maximum Satellite after spending 50 months in low-Earth orbit. One side of this box contained 84 aluminum thermal control louvers. These louvers had been penetrated by 64 impacts which made holes ranging from 180 micrometers to 820 micrometers in diameter. The location of these holes is shown in Figure 3. Most of these holes were made by micrometeorites as identified by chemical analysis of projectile residue associated with each hole. Micrometeorite holes are shown by open circles in this Figure. Seven of the holes were made by small particles of orbital debris. These holes are shown as filled circles on Figure 3.

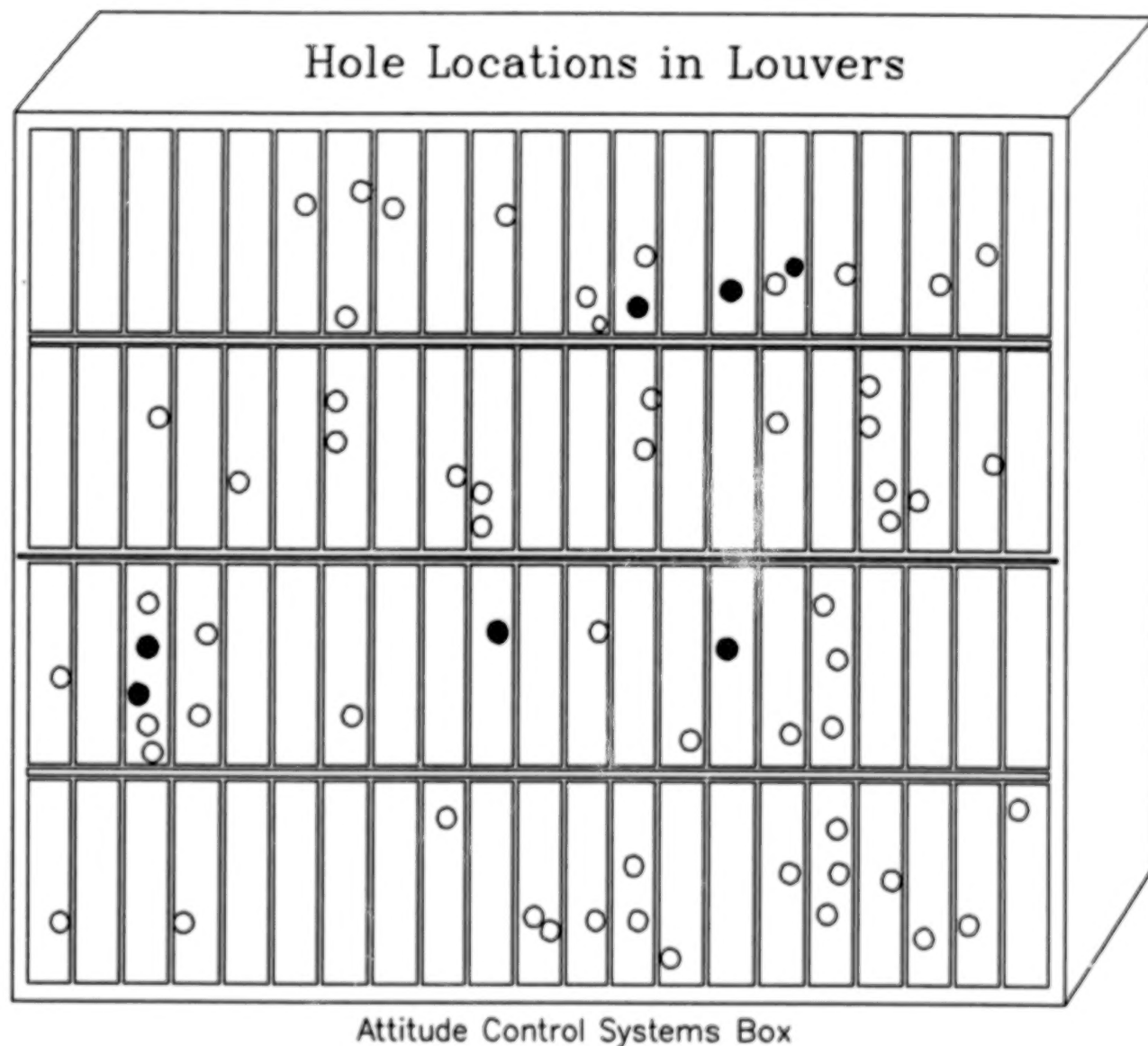


Figure 3

Figure 4 shows the structure of the aluminum louver and the morphology of a typical impact hole. The louver consists of two sheets of aluminum, each 125 micrometers thick, separated by a 3-millimeter space except at the edges and along a central support rib. A typical hypervelocity impact has three major morphologic features. The entry hole (Figure 4.1) is generally quite circular and has an upturned rim of aluminum which usually contains traces of residue from the projectile. The exit hole (Figure 4.2) also contains an overturned rim which is usually more jagged and less regular than the entry rim. All penetration holes are also associated with a spray pattern (Figure 4.3) on the second layer. This spray pattern is always much larger than the diameter of the hole, usually an order of magnitude larger in diameter and two orders of magnitude larger in area. The spray pattern is formed by the combined material from the projectile and the aluminum from the hole. Usually the aluminum from the hole is the primary constituent of the spray. The spray pattern consists of large numbers of small irregular craters which are sometimes arranged in loops and chains. Some of these small irregular craters on the second layer completely penetrate the aluminum layer, but most do not. Sometimes a secondary spray is created at the second layer which sprays tiny aluminum droplets back up to coat the bottom of the first layer (Figure 4.2) or which completely exit through the hole and create many more orbital debris microparticles in space.

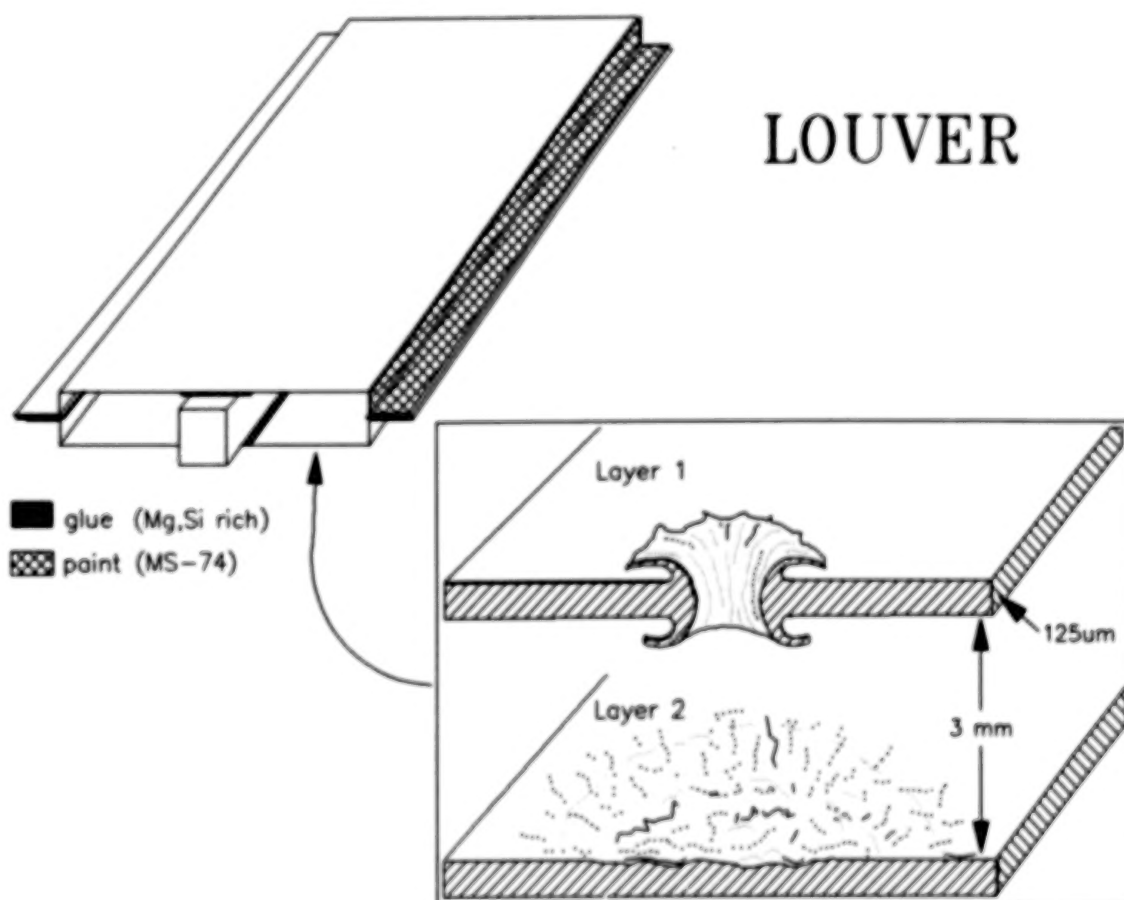


Figure 4.

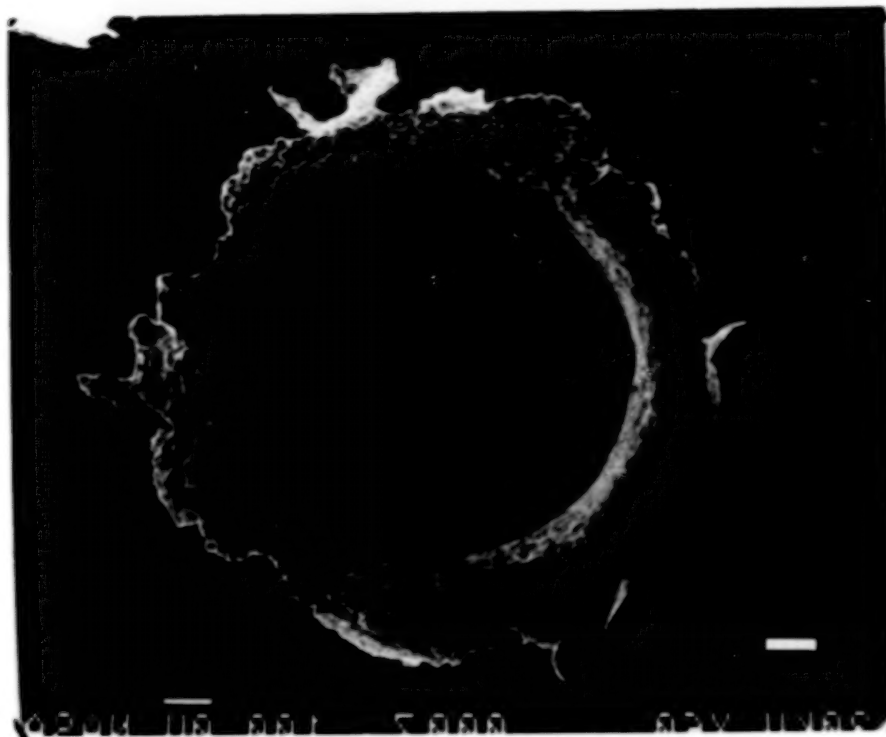


Figure 4.1 - Entry hole.

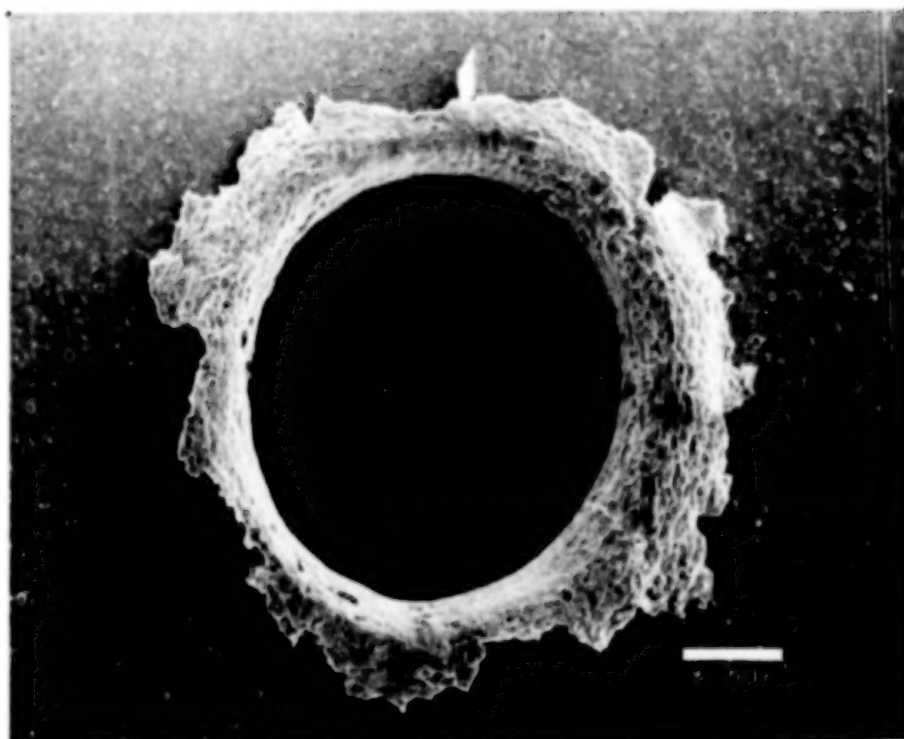


Figure 4.2 - Exit hole.

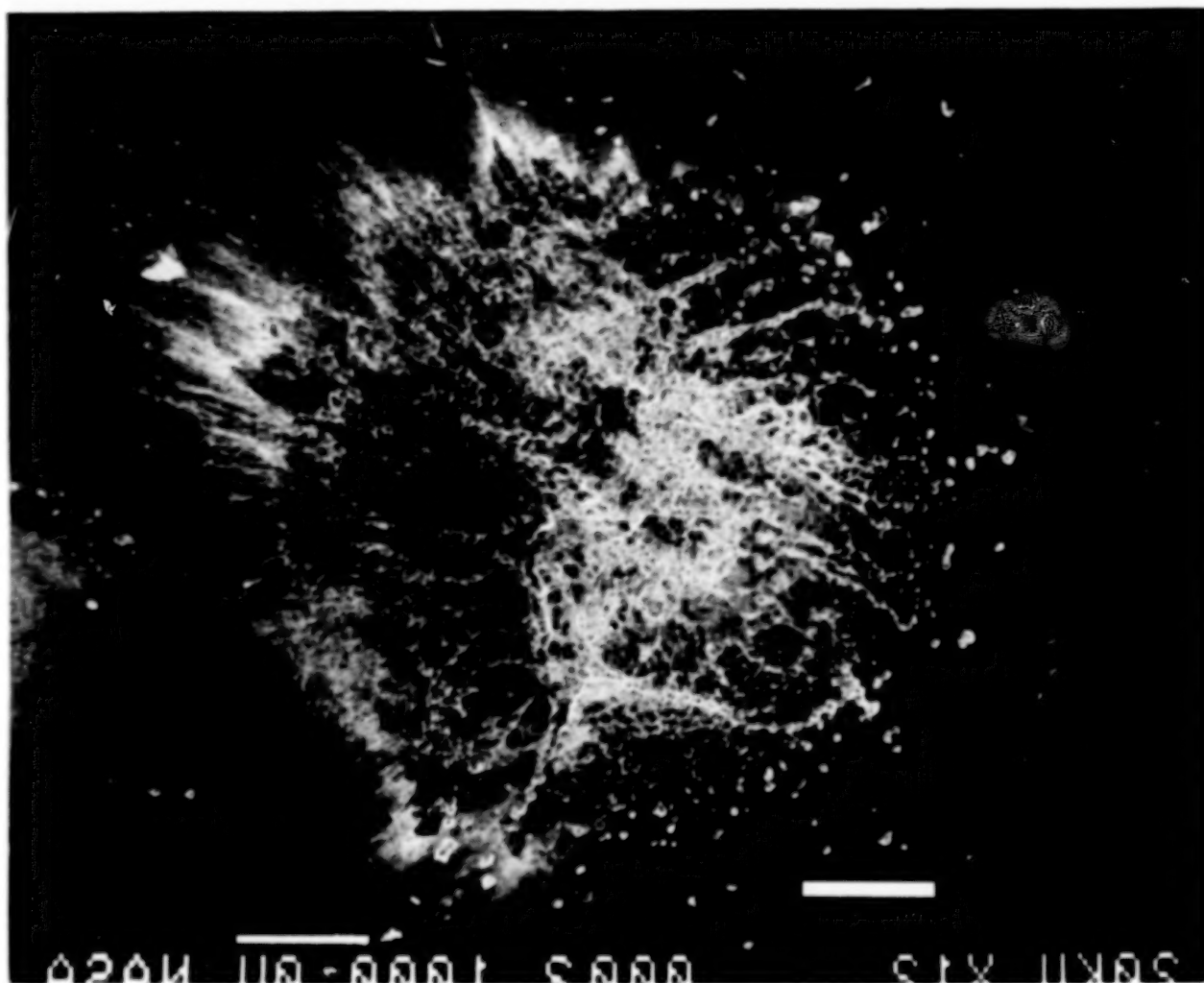


Figure 4.3 - Spray pattern.

Figure 5 shows the size distribution of holes in the aluminum louvers. Most of the holes are in the size range of 180 micrometers to 400 micrometers. Below 180 micrometers, impacts produced craters rather than holes in the 125-micrometer thick louver material. Also shown in this figure is the distribution between identified micrometeorite holes and identified orbital-debris holes. Orbital-debris holes clearly are a minority of the population in this size range. However, that is somewhat misleading. Orbital debris particles have a mean velocity relative to a satellite in low-Earth orbit of about 10 km/sec, but micrometeorites have a mean velocity of about 20 km/sec relative to the satellite. Therefore, debris particles of equal mass and density as micrometeorites are likely to make smaller holes or even craters rather than holes. Consequently, the difference between the abundance of micrometeorite holes and orbital debris holes does not accurately reflect the difference in flux between these two populations; the fluxes are more nearly equal than is indicated by the hole data.

FLUX OF LOUVER HOLES

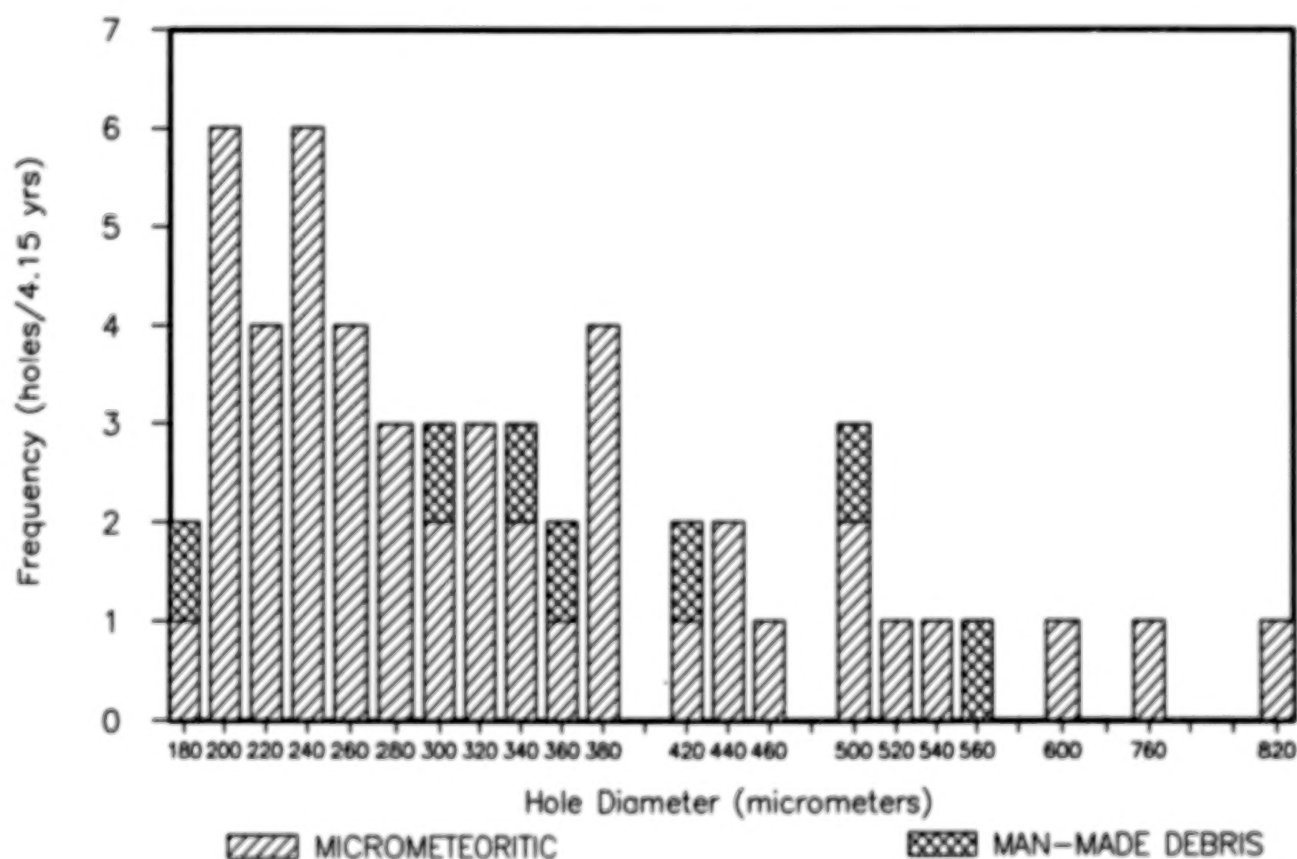


Figure 5

In Figure 6, the mass of the impacting projectile has been calculated using experimental penetration data on the louvers (Reference 1) and assumed velocities (approximately 20 km/sec for micrometeoroids, and approximately 10 km/sec for orbital-debris particles). Over most of the range, the projectile flux difference is only about a factor of three rather than the order of magnitude suggested by the hole data alone. At lower masses the two flux curves begin to diverge because the lower velocity debris microparticles are beginning to make craters rather than holes so that the flux dropoff is an artifact of the transition from holes to craters for these particles.

CUMULATIVE FLUX OF LOUVER HOLES

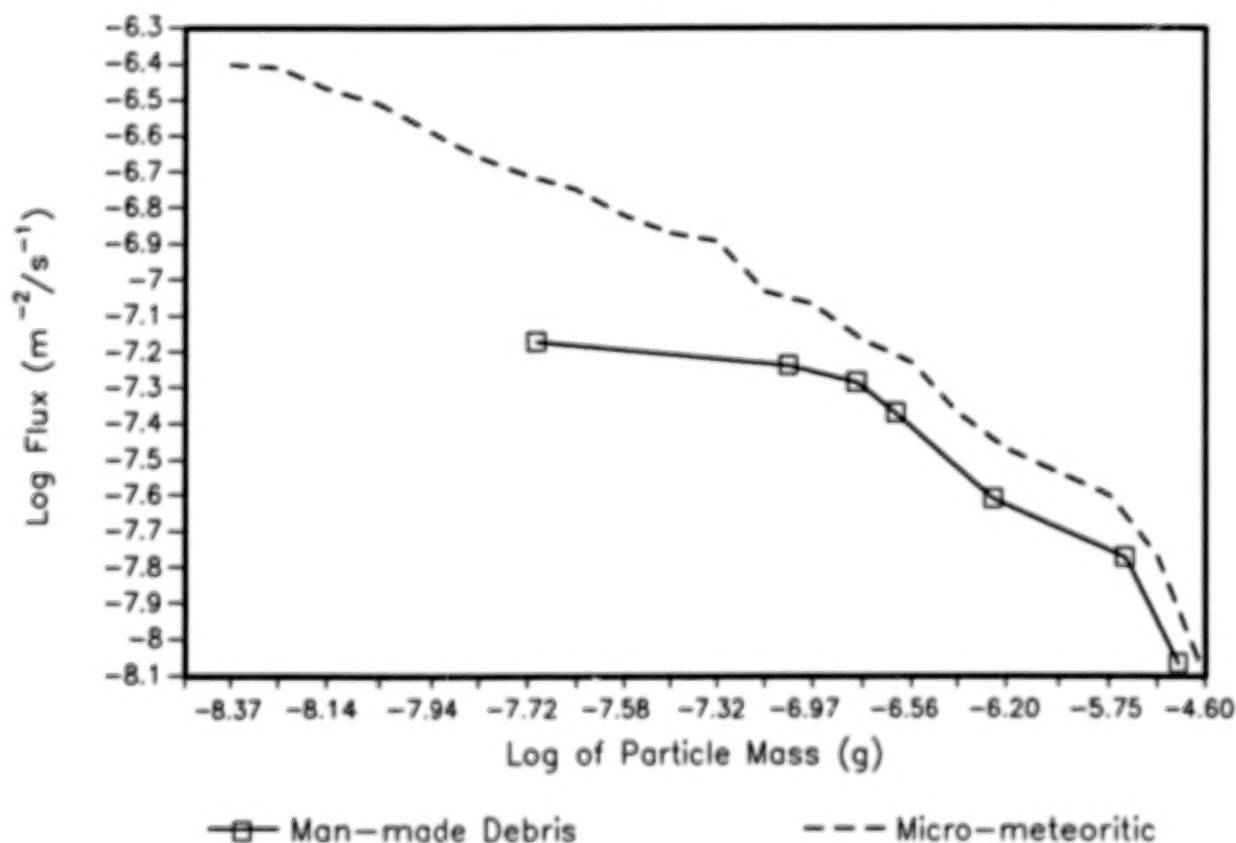


Figure 6

This diagram (Figure 7) of the louvers shows 15 areas which we selected for more detailed higher magnification study. In these selected areas we scanned the surfaces at a magnification of 10,000X designed to reveal all craters larger than 1 micrometer and, in selected subareas, all craters larger than 0.1 micrometer. The smallest observed crater was 50 nanometers in diameter. Examples of some of these craters are illustrated by Figures 7.1 - 7.5.



Figure 7

Example of Crater

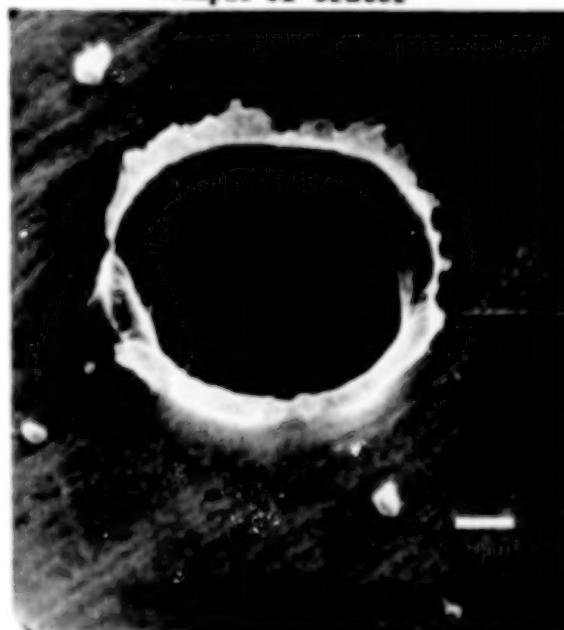


Figure 7.1

Examples of Craters

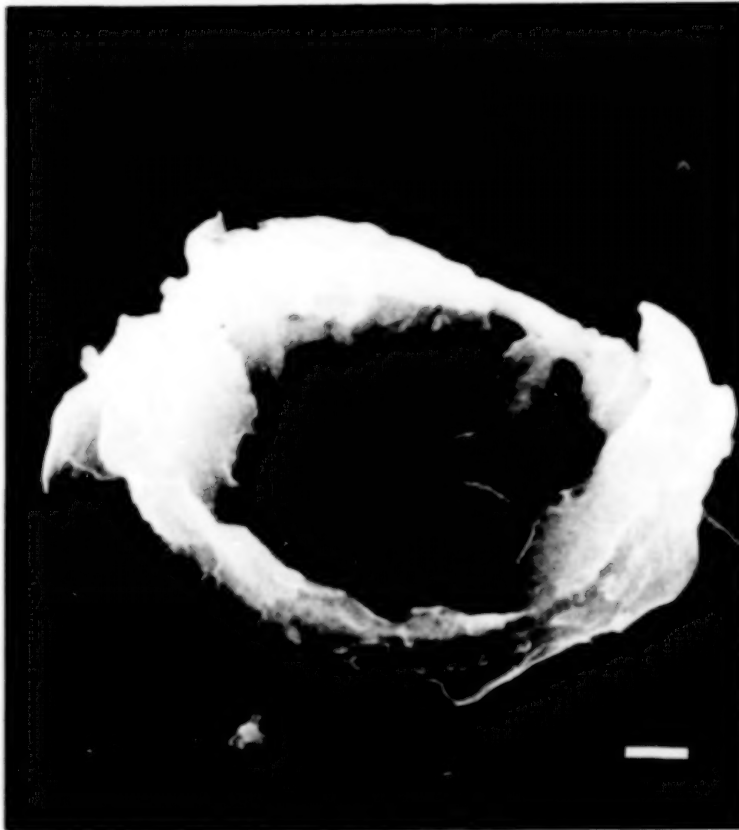


Figure 7.2

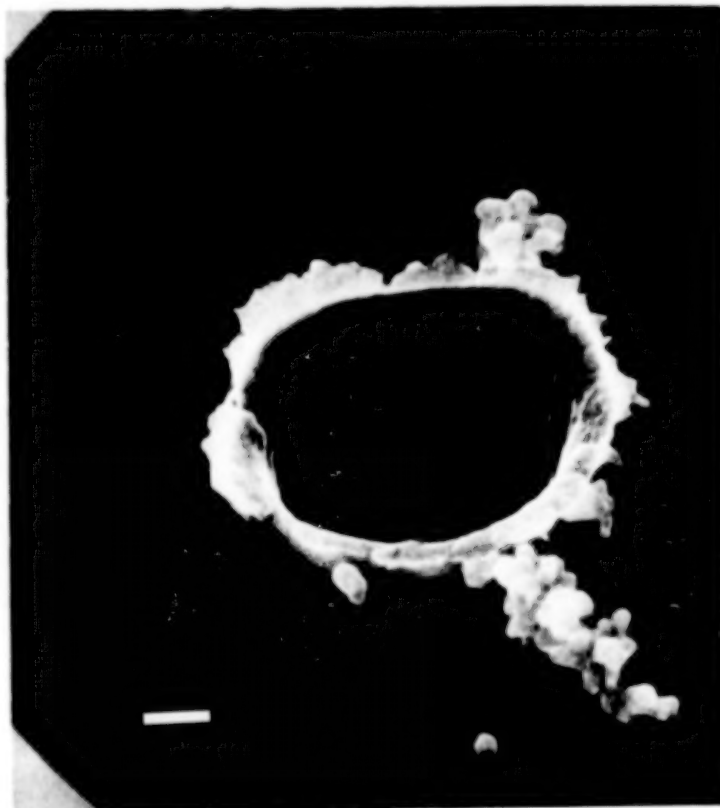


Figure 7.3

Examples of Craters (cont.)



Figure 7.4

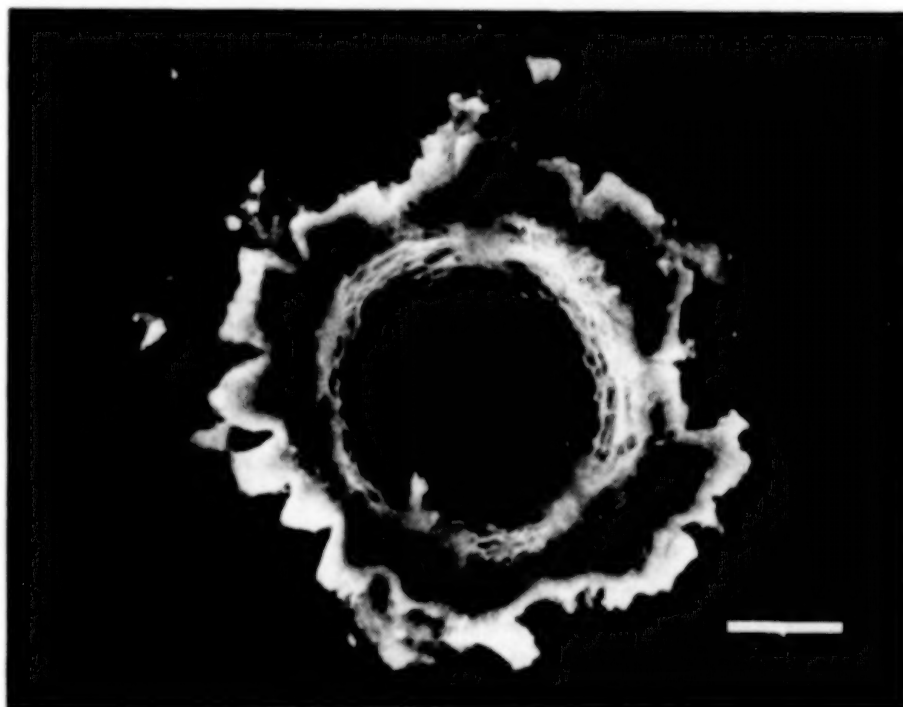


Figure 7.5

Figure 8 shows the abundance of small craters (0.1 - 0.5 micrometers) in several of the regions examined at high magnifications (Figure 7). The abundance of small craters are higher in regions 4, 5, and 6 compared to regions 9, 10, 14, and 15. Shielding calculations (Reference 2) show that regions 4, 5, and 6 have a higher proportion of the solid angle field of view obstructed by the nearby solar panel. This correlation would support an interpretation that many of these small impact craters are caused by high velocity secondary ejecta from primary impacts into the backside of the nearby solar panel while the smallest craters (less than 1 micrometer) do not contain enough detectable residue for chemical identification; the larger craters (5 - 100 micrometers) often contain detectable residue and many of these craters contain residue rich in titanium, oxygen, and sometimes zinc. These compositions are typical of pigments used in chemglaze paint on the solar panels and other parts of the spacecraft. Consequently, some of these impacts could be from secondary projectiles generated at other Solar Max surfaces, although other compositions including potassium and silicon-rich and aluminum oxide have originated on other spacecraft or from solid rocket exhaust.

LOCAL SUBMICRON CRATER FLUX

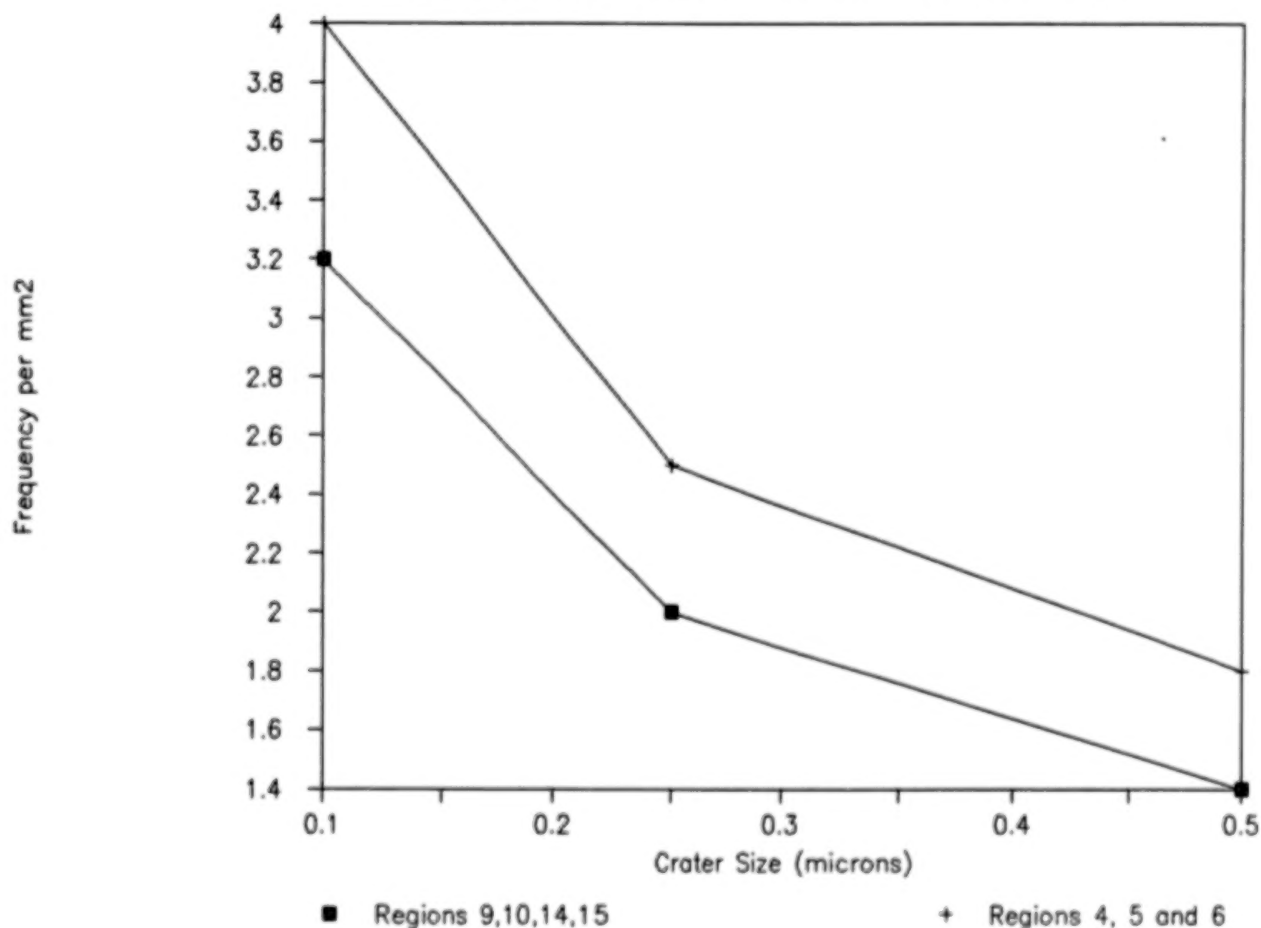


Figure 8

Figure 9 shows the abundance of adhering particulate contamination on the various examination regions of the aluminum louvers as shown in Figure 7. These particles are mostly titanium dioxide and are typically 0.2 - 0.5 micrometers in diameter. The particles occur individually and in clumps (Figure 9.1). Abundance of these particles is not random but increases systematically from regions 14 and 15 to regions 4, 5, and 6. As stated previously, regions 4, 5, and 6 shielding calculations have shown that regions 4, 5, and 6 have the largest solid angle field of view for the nearby solar panel. Consequently, we suggest that many of the surface particulates come from the solar panel and are in fact paint pigment particles. The particles are clean-appearing and lack the binder typical of unflown chemglaze paints. We suggest that the near-surface binder of this paint has been eaten away by atomic oxygen erosion and the included pigment particles have been released by thermal cycling or other mechanisms and have drifted to the louvers and have been deposited on their surfaces. Self-contamination from released paint pigment may be a widespread particulate contamination on other spacecraft.

PAINT PIGMENT CONTAMINATION FLUX

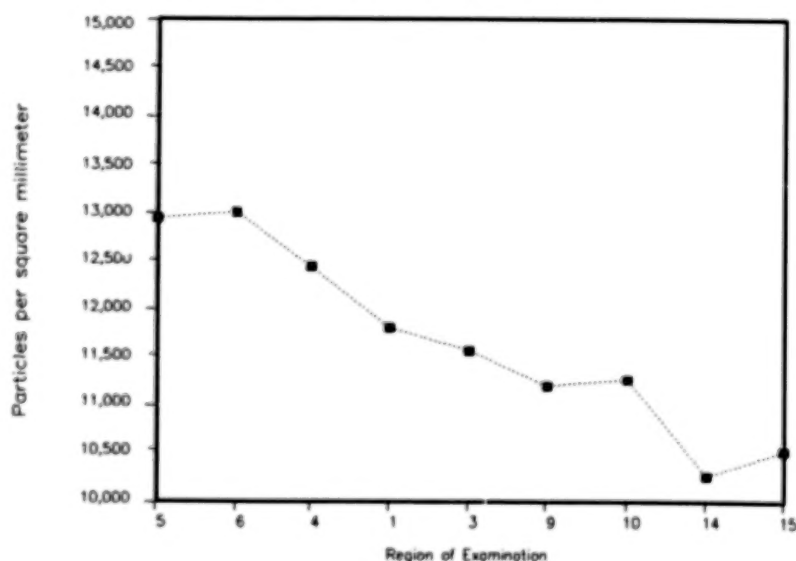
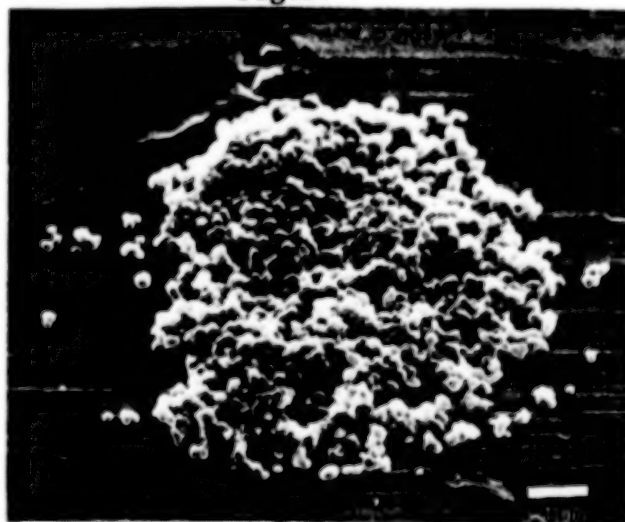


Figure 9



Example of adhering particulate contamination

Figure 9.1

Figure 10 shows the overall flux of holes and craters on the aluminum louvers over the size range from 10 micrometers to 1 millimeter. For the size region dominated by holes, the micrometeorite curve is clearly higher than the orbital-debris curve as discussed previously (Figures 4 and 5). The transition region between holes and craters is clearly shown in the region around 200 micrometers. While not shown on this figure, chemical data indicate that a high proportion of the smaller craters are formed by debris projectiles rather than micrometeorites. Therefore, the flux curves must cross over, probably in the crater region between 50 and 100 micrometers. As pointed out elsewhere in this report, the population of large (centimeters to meters) projectiles is dominated by orbital debris. Thus, based on Solar Max results, small projectiles (approximately those which make less than 50 micrometers crater diameters on aluminum) are dominated by orbital debris (mainly paint pigments with lessor aluminum oxide solid rocket exhaust), the larger projectiles (centimeters to meters) are dominated by orbital debris, and only the narrow region between (projectiles making holes or craters in aluminum from about 0.1 mm to possibly 1 cm) is still dominated by natural meteoroids.

SIZE DISTRIBUTION LOUVER CRATER AND HOLES

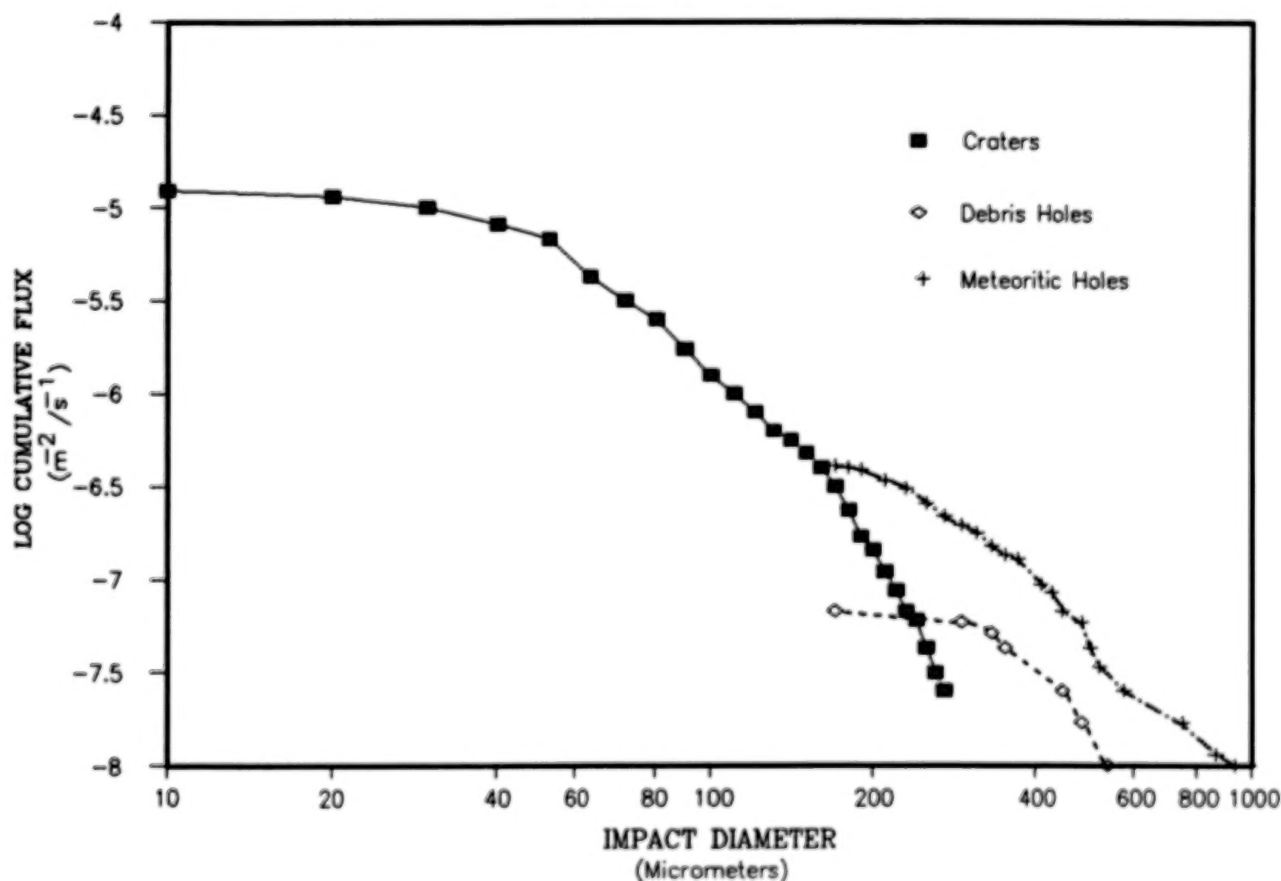


Figure 10

Figure 11 shows some of the major conclusions which have emerged from the study of Solar Maximum space-exposed surfaces having more than four years exposure to micrometeorites, atomic oxygen erosion, and orbital debris microparticle abrasion.

CONCLUSIONS

1. On Solar Max louvers, the flux of micrometeoritic holes is three times greater than orbital debris holes.
2. The majority of smaller impacts ($< 20\mu\text{m}$ in diameter) are produced by man-man debris projectiles.
3. A significant proportion of the smallest impacts are caused by secondary ejecta originating from the solar panel.
4. Low velocity projectiles (particles and clusters of paint pigments) are abundant. These most likely originate from the nearby solar panel.
5. Atomic oxygen erosion is a contributing factor to low velocity surface contamination.
6. Hardware exposed to space will be impacted by a broad mass range of both micrometeorite and orbital debris projectiles and may be further degraded by atomic oxygen erosion and effects of secondary ejecta.

Figure 11

Figure 12 shows the outline of a Shuttle experiment of material abrasion by solid rocket exhaust particles.

SHUTTLE WITNESS PLATE RESULTS

PURPOSE

DETECT IMPACTS FROM PAM D2 SOLID ROCKET MOTOR

DETERMINE FLUX AND SIZE DISTRIBUTION OF PARTICLES

DETERMINE ABRASION EFFECTS ON VARIOUS

CONDITIONS

PAM D2 ROCKET WAS 17 KM FROM SHUTTLE ORBITER

BURN DURATION WAS 96 SECONDS

RESULTS

ALUMINUM SURFACES

COPPER SURFACES

STAINLESS STEEL SURFACES

INCONEL SURFACES

QUARTZ GLASS SURFACES

Figure 12

Figure 13 shows the ratio between the diameter of the retained aluminum oxide projectile and the diameter of the resulting crater or pit in the stainless steel (15-5) witness plate. This witness plate retained 62% of the impacting projectiles. The mean projectile/pit diameter for stainless steel is 0.90 ± 0.09 . Figure 13.1 illustrates a fractured SRM projectile in a stainless steel target.

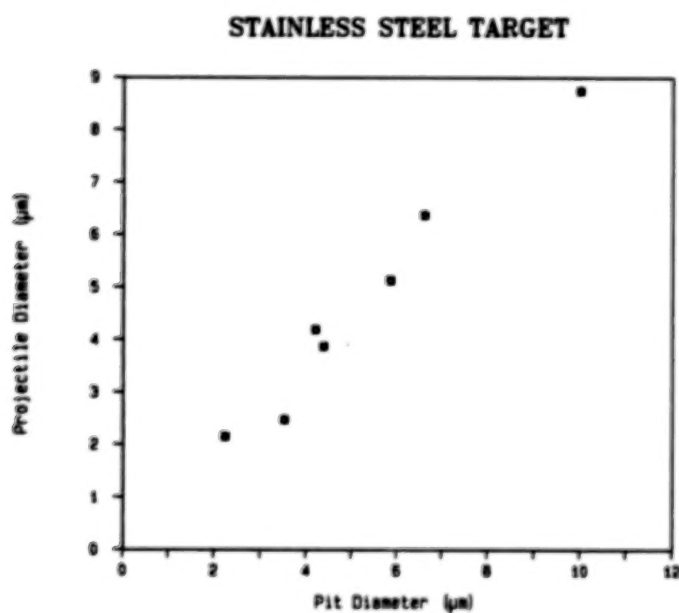


Figure 13



Fractured SRM projectile in a stainless steel target

Figure 13.1

Figure 14 shows the projectile to pit ratios for the inconel target from the Shuttle Orbiter witness plate experiment. The mean projectile/pit diameter for this target is 0.9 ± 0.09 . The inconel target retained 48% of the impacting aluminum oxide particles, the least of any of the targets.

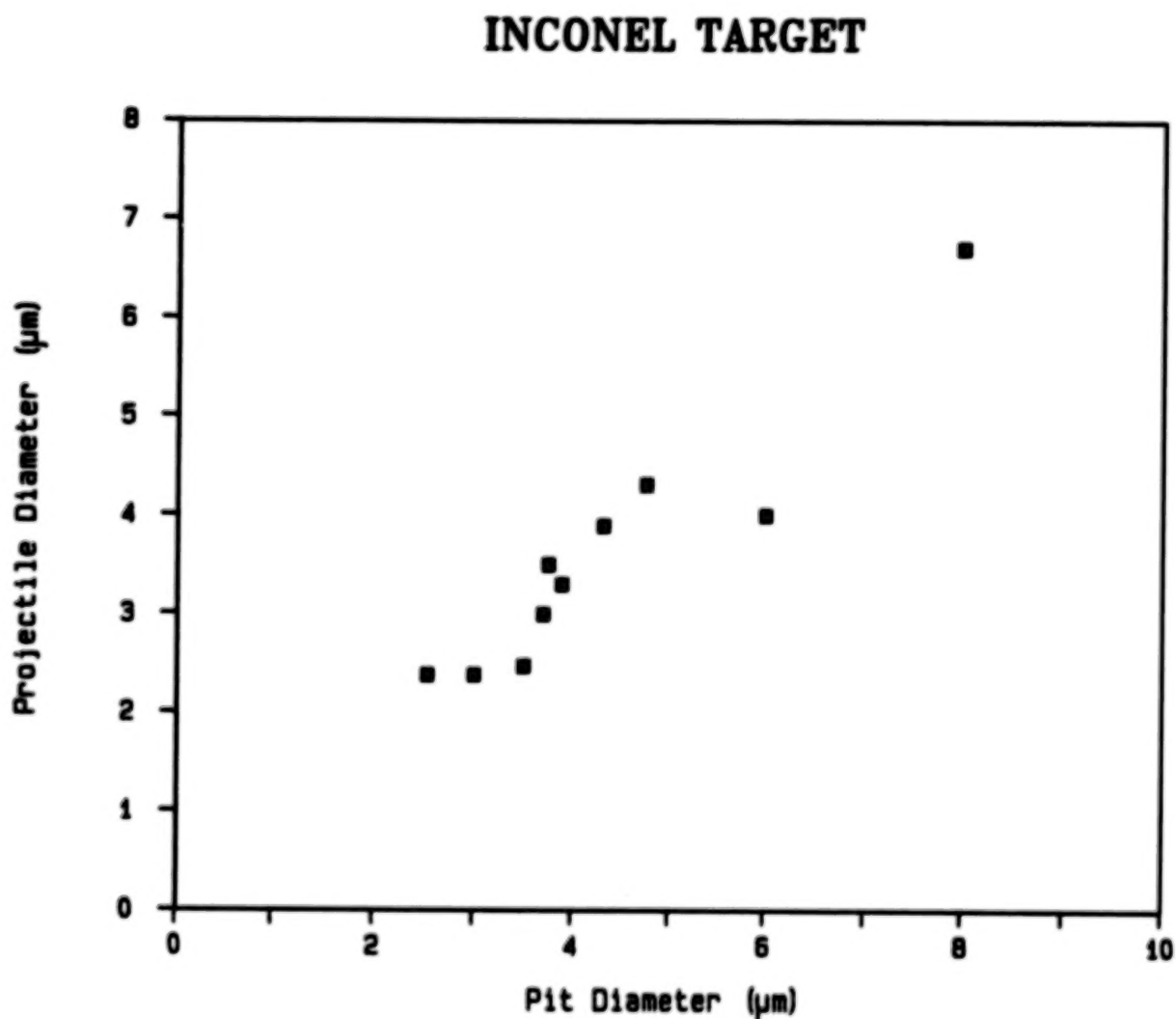


Figure 14

Shuttle witness plate impact results on scanned areas of the copper, aluminum, and quartz glass targets. The abundance of impacts per unit area is statistically equivalent for the three targets. The mean number of impacts for all pits greater than 1 micrometer in diameter is $10.25/\text{mm}^2$. If pits smaller than 1 micrometer are included, the mean impact abundance for all size ranges and all targets is 15.4 impacts/ mm^2 , (Table 1).

Table 1

MEAN IMPACTS/ mm^2 RANGING FROM 1 μm TO $>10 \mu\text{m}$ IN DIAMETER
FOR ALL TARGETS

TARGET	TOTAL IMPACTS	SURFACE AREA SCANNED (mm^2)	IMPACTS/ mm^2
COPPER	111 +/- 10.34	9.88	11.2 +/- 1.05
ALUMINUM	63 +/- 7.94	6.37	10.0 +/- 1.25
QUARTZ	23 +/- 4.80	2.97	7.7 +/- 1.61

Total	197	19.22	

$$\text{MEAN IMPACTS}/\text{mm}^2 = 197/19.22 = 10.25$$

Figure 15 shows the relationship between measured depth/diameter ratios for a number of pits (lacking retained projectiles) and the calculated impact velocity. An empirically determined relationship between stereometrically measured pit depth and projectile diameter is used (Hermann & Jones, 1962), Reference 3.

$$P/d = K_1 \times \ln(1 + K_2 V^2)$$

where P = depth of penetration
d = diameter of projectile
 $K_1 = 0.604$, constant determined for aluminum projectile and target
 $K_2 = 0.593$, constant determined for aluminum projectile and target
V = velocity (km/s)

DEPTH/DIAMETER vs. VELOCITY

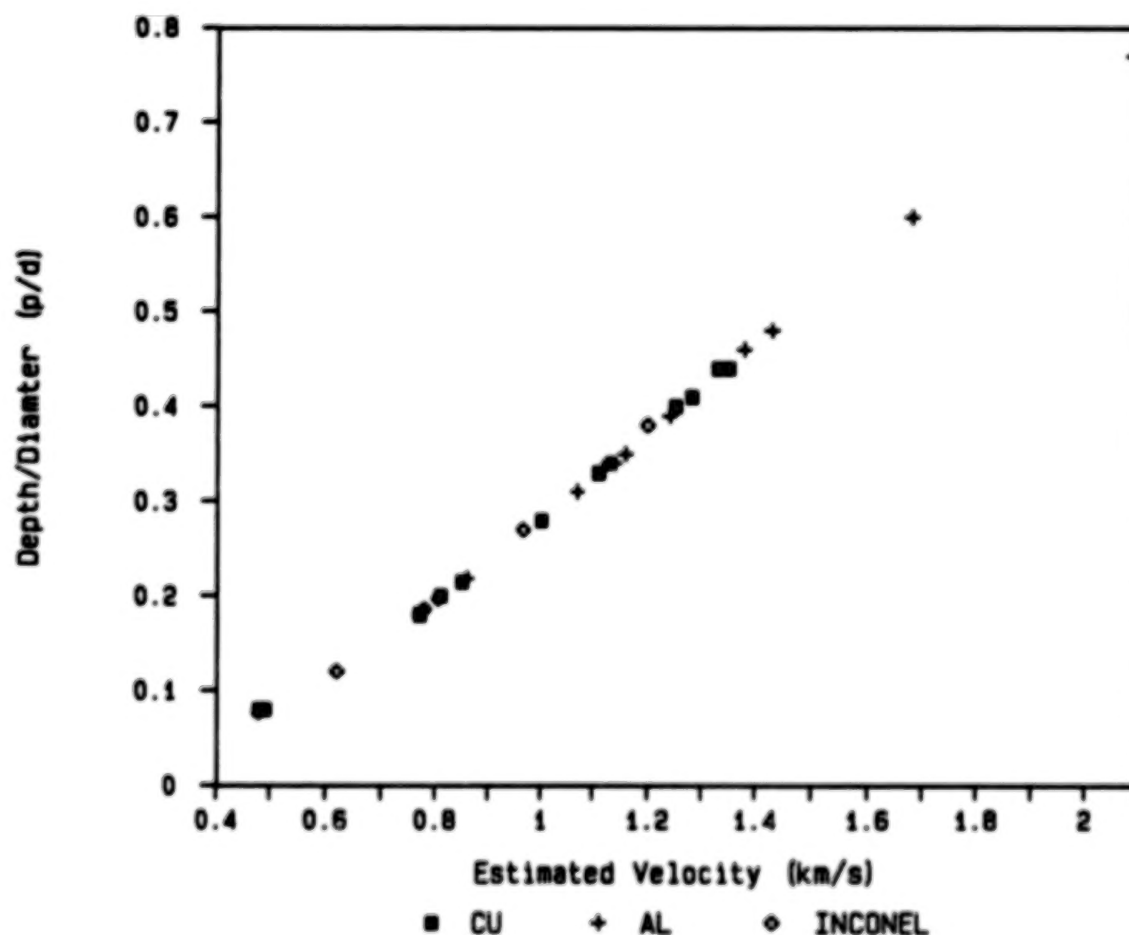


Figure 15

The size distribution of aluminum oxide particles impacting targets on the Shuttle Orbiter witness plate experiment is shown in Table 2. This distribution is strongly peaked at 1 to 5 micrometers. The smallest pit observed was 0.8 micrometers in diameter and the largest pit observed was 14 micrometers.

Table 2

SIZE DISTRIBUTION FOR IMPACT FEATURES

TARGET	SIZE RANGE (um)				TOTAL IMPACTS
	<1	1-5	6-10	>10	
Copper	69	105	6	0	180
Aluminum	20	57	6	0	83
Quartz*	10	21	1	1	33
Total	99	183	13	1	296

DISTRIBUTION
BY SIZE (%) 33.4 61.8 4.4 0.34
(All Targets)

*Dimension refers to pit diameter, not spall diameter

Table 3 shows the calculated eroded area for metal targets (aluminum, copper, stainless steel, and inconel). The calculations show that approximately 0.01% of the surfaces were eroded or destroyed by impingement of particles from the plume of the solid rocket.

Table 3

PERCENTAGE OF SURFACE AREA EROSION ON METALLIC TARGETS

Diameter Range (um)	Average Diameter (um)	Average Radius (um)	Surface Area Eroded Impact (mm ²) ¹
<1	0.9*	0.4	6.4E-7
1-5	3.0	1.5	7.1E-6
6-10	8.0	4.0	5.0E-5
>10	12.0**	6.0	1.1E-4

Surface Area Eroded/Impact x Average Impact Density² x
Size Frequency³ x Total Surface Area = Surface Area Eroded (mm²)

$$\begin{aligned}
 6.4E-7 \text{ mm}^2 \times 15.2/\text{mm}^2 \times 0.339 \times 3354.3 \text{ mm}^2 &= 0.011 \\
 7.1E-6 \text{ mm}^2 \times 15.2/\text{mm}^2 \times 0.613 \times 3354.3 \text{ mm}^2 &= 0.221 \\
 5.0E-5 \text{ mm}^2 \times 15.2/\text{mm}^2 \times 0.0445 \times 3354.3 \text{ mm}^2 &= 0.114 \\
 1.1E-4 \text{ mm}^2 \times 15.2/\text{mm}^2 \times 0.0034 \times 3354.3 \text{ mm}^2 &= 0.020 \\
 \text{Total Surface Area Eroded (mm}^2\text{)} &= 0.366
 \end{aligned}$$

Total Metallic Surface Area Exposed to the Plume = 3354.3 mm²

Area Eroded (%) = 0.366/3354.3 x 100 = 0.011

*Smallest observed size was approximately 0.8 um

**Largest observed size was approximately 14.0 um

¹Approximate Surface Area Eroded/Impact = sphere = $3.14159r^2$

²Table 2

³Table 1

Table 4 shows the calculated eroded area for the quartz glass target. The calculations show that approximately 0.34% of the glass surface was eroded or destroyed by the particle impacts. This area is more than 30 times that for the metal surfaces subjected to the same flux of aluminum oxide particles.

Table 4

PERCENTAGE OF SURFACE AREA EROSION ON NON-METALLIC TARGETS

Pit Diameter Range (um)	Ave. Pit Diameter (um)	Ave. Pit Radius (um)	Ave. Spall to Pit Ratio ¹	Ave. Spall Radius (um)
<1	0.9*	0.4	1/5.55	2.5
1-5	3.0	1.5	1/5.55	8.3
6-10	8.0	4.0	1/5.55	22.2
>10	12.0**	6.0	1/5.55	33.3

Surface Area Eroded/
Impact (mm²)²

1.96E-5
2.18E-4
1.55E-3
3.48E-3

Surface Area Eroded/Impact x Average Impact Density³ x
Size Frequency⁴ x Total Surface Area = Surface Area Eroded (mm²)

1.96E-5 mm² x 15.2/mm² x 0.339 x 1570.5 mm² = 0.159
2.18E-4 mm² x 15.2/mm² x 0.613 x 1570.5 mm² = 3.190
1.55E-3 mm² x 15.2/mm² x 0.0445 x 1570.5 mm² = 1.646
3.48E-3 mm² x 15.2/mm² x 0.0034 x 1570.5 mm² = 0.283

Total Surface Area Eroded (mm²) = 5.278

Total Non-Metallic Surface Area Exposed to the Plume = 1570.5 mm²

Area Eroded (%) = 5.278/1570.5 x 100 = 0.336

*Smallest observed size was approximately 0.8 um

**Largest observed size was approximately 14.0 um

¹Table 8

²Approximate Surface Area Eroded/Impact = sphere = $3.14159r^2$

³Table 2

⁴Table 1

Figure 16 shows modeled orbital decay times and settling times (after reaching zero horizontal velocity) for small particles. For example, a 0.5 micrometer (radius) particle released from a spacecraft at 500 km altitude will lose all of its orbital velocity in 2.2 hours as a result of air drag. During this time the particle loses altitude to about 380 kilometers. The particle then falls or settles over 6.8 more hours to the stratosphere below 100 km where the particle slows down considerably as it encounters significant air. Equation used for orbital decay is from Mueller (1981) Reference 4 and equation used for settling times is from R. Reynolds (1987), (Lockheed, JSC), [personal communication].

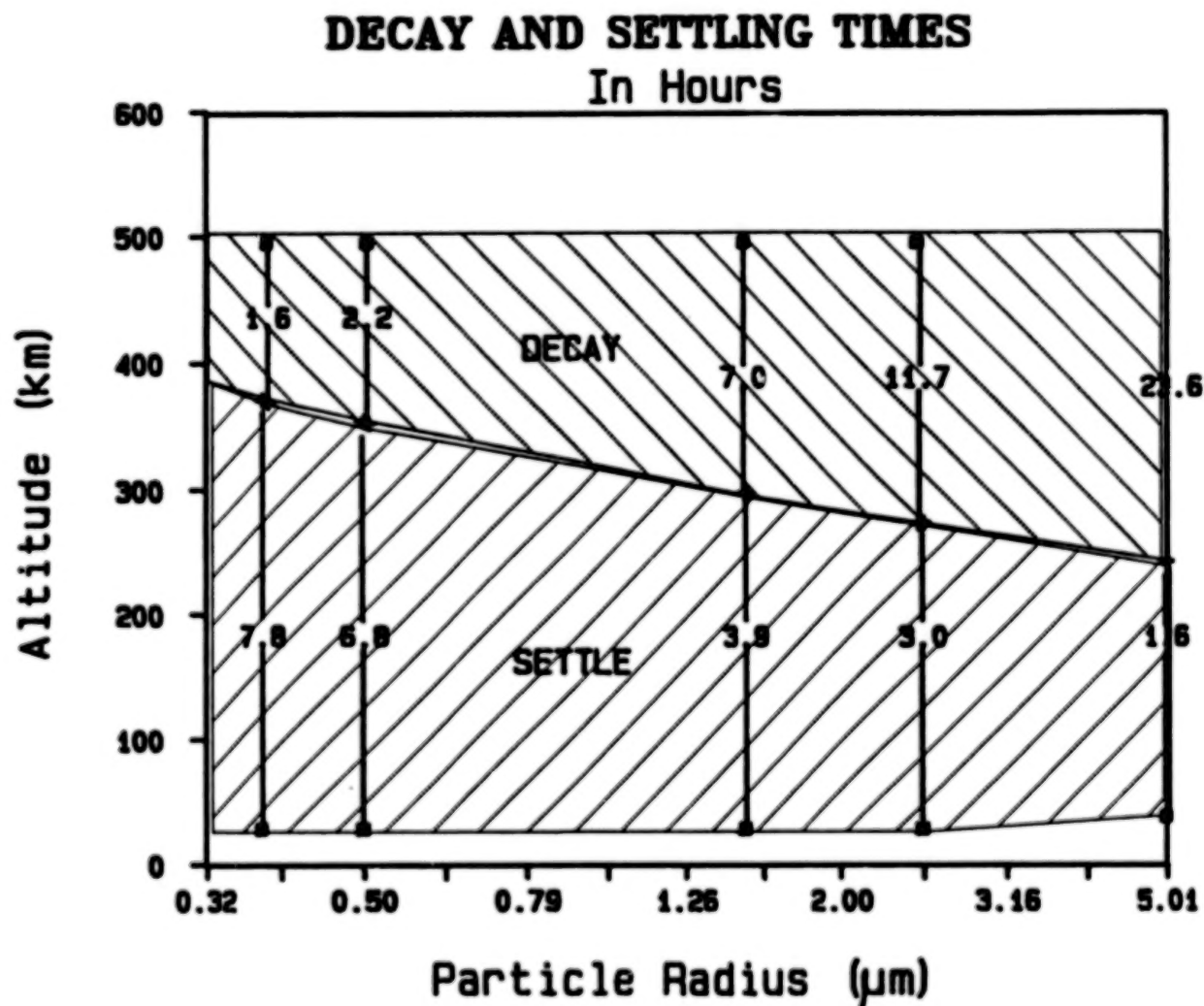


Figure 16

Figure 17 (Zolensky et al, 1988, Reference 5) shows measured abundance for aluminum-rich stratospheric dust particles in the stratosphere as collected by the NASA cosmic dust collection program. Most of these aluminum-rich particles are interpreted to be from spacecraft and rockets. The abundance of these spacecraft-derived particles increased more than an order of magnitude between 1981 and 1984, the most recently analyzed sample. Additional analysis of existing samples is needed to determine if the abundance of these particles is still increasing. Recent (June 1988) deployment of the large area collectors will greatly increase the amount of sampled stratospheric dust available for analysis.

NUMBER DENSITY OF PARTICLES IN THE STRATOSPHERE

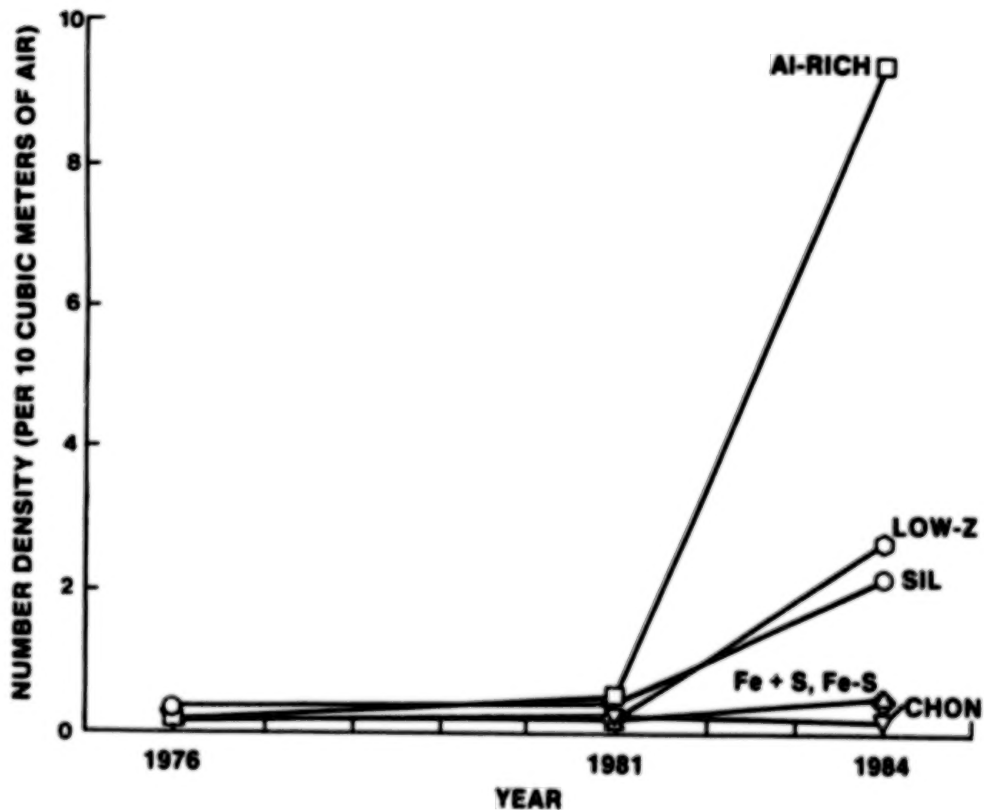


Figure 17

REFERENCES

1. Carey, W. C.: Properties and Interactions of Interplanetary Dust, pp. 131-136, 1985.
2. Warren, J.: Optical Observations of Impact Features on Solar Max Thermal Blankets and Louvers. Lunar and Planetary Science XIX, 1988.
3. Hermann, W.: Correlation of Hypervelocity Impact Data. Proceedings of the Fifth Symposium of Hypervelocity Impact (Colorado), #G-0020-62, Vol. 1, Part 2, 1962.
4. Mueller, A. C.: The Decay of the Low Earth Satellite for the Orbital Debris Study. J. O. 69-067, Lockheed 17520, 1981.
5. Zolensky, M. E.: Stratospheric Particle Abundance and Variations Over the Last Decade. Lunar and Planetary Science Conference XVII, pp. 969-970, 1986.

SESSION 5: CONTAMINATION

Chairman: C. Maag
Jet Propulsion Laboratory

Spacecraft Contamination Experience

**E. N. Borson
Materials Sciences Laboratory
The Aerospace Corporation
El Segundo, California**

OUTLINE

Definitions

Introduction

Design

Factory Operations

Launch Site Ground Operations

Launch and Ascent

Orbital Operations

Flight Measurements

Conclusions and Assessments

References

Contaminant

This definition for contaminant is very broad and could include items such as radio frequency, other forms of electromagnetic irradiation, particulate irradiation, meteoroids and debris, and atmospheric effects including atomic oxygen as well as the molecular and particulate materials that are usually considered.

The primary concern in this presentation is the molecular and particulate material that affects spacecraft system performance as a result of deposition on surfaces or being in the field of view of sensors. The contamination of sealed, internal fluid systems, gas and liquid, is not included because these subsystems are governed by well established standards and procedures. Exceptions to this are the deliberate introduction of material into the environment such as occurs during the operation of propulsion, evaporation, and other fluid systems that vent. Another area of concern is the unintentional leaking of contaminants into the environment.

It is important to consider contaminants that can deposit on spacecraft throughout the life of the hardware, from factory to the end of mission life. Spacecraft hardware may be exposed to ground environments for many years before exposure to the flight environments.

The contaminants that affect spacecraft systems are deliberately and accidentally put in or on spacecraft hardware and then can interact with the space environment even when these contaminants are added during ground environment exposures. A contaminant for one system or component may be a necessity for another. An example is the lubricant required in a bearing but that would degrade the performance of an optical system. Other examples include materials that contain molecular species that improve the processing or performance but outgas excessively.

Contamination Control

The process of achieving the required cleanliness levels requires a contamination control program that starts during the preliminary design phase and continues through to the end of mission life.

DEFINITIONS

Contaminant:

Any material, substance, or energy which is unwanted or adversely affects components and systems.

Contamination Control:

The planning, organization, and implementation of all activities needed to determine, achieve, and maintain a required cleanliness level.

Particle

Particles may be either solid or liquid. Airborne particles (aerosols) are usually small solid and liquid particles. The sizes of particles that can be carried in the air and their settling rates depend upon factors such as the particle density, shape (drag), and air velocity. Typically particles under 5 μm in size stay airborne for long periods of time, and particles over a few hundred μm in size settle out quickly.

Molecular Contaminant

Non-particulate matter (solid, liquid, or gas) has no definite shape and may exist on surfaces as uniform or non-uniform films. These contaminants may also be found as sorbed (absorbed and adsorbed) matter. The materials may also change state between solid, liquid, and gas. Particles may also change state, depending upon temperature and pressure, as well as changing to a molecular form.

NVR

NVR is usually considered to be a molecular contaminant that is found on surfaces or in liquids after evaporation of the liquid. Various test procedures are used to measure the NVR on spacecraft surfaces or on plates exposed to the ground environments. MIL-STD-1246 and NASA SN-C-0005 define NVR levels for hardware that have been in general use; however, other definitions are also used depending upon the requirements.

DEFINITIONS

Particle (Particulate Matter)

Matter of miniature size with observable,
length, width, and thickness

Molecular Contaminant

Non-particulate matter,
may be in a solid, liquid, or gaseous state

NVR (Non-Volatile Residue)

Soluble material remaining after the evaporation
of a volatile liquid or determined by special
purpose analytical instruments.

INTRODUCTION

Effective contamination control must encompass all aspects of ground and flight from design of the system through the end of mission life.

**Therefore,
Contamination control is a systems engineering function,**

**and,
a review of experience with space systems should include phases of activity from design to the end of life.**

Contamination control activities should start during the preliminary design phase of a project. This includes the initial selection of materials and preliminary analyses of the sensitivities to contamination and quantities of contaminants. If the contamination control work is delayed, required design changes will increase costs, cause schedule delays, or compromise system performance.

DESIGN 1

It is necessary to include contamination control in the design trade off studies and to initiate operational planning activities that affect the design.

Each design activity has an impact on the contamination control program and there are iterative processes that contribute to the development of the design.

The determination of system performance requirements leads to a definition of the sensitivity of the system to contaminants.

The configuration of the system defines the relationship between the elements that are sensitive to contamination and the sources of contamination. This configuration can be changed to eliminate or, at least, minimize the contamination. The sources of contaminants include materials and components on the surface of the spacecraft as well as materials and components inside the spacecraft that get out through intentional and unintentional vents. The locations of these vents are frequently a critical factor in the contamination of sensitive components.

The configuration also has a bearing on how easy or difficult it is to clean sensitive elements during the various phases of ground operations.

The selection of the materials, components, and subsystems so as to minimize outgassing and generation of particles involves tradeoffs with the need to meet the other functional requirements. These other functional requirements include temperature and radiation stability, mechanical and electrical properties, and resistance to atomic oxygen.

As the design develops it is possible to consider preliminary planning for ground and flight operations including those procedures that will minimize contamination. In this way design changes can be implemented early.

DESIGN 2

<i>Activity</i>	<i>Impact on Contamination Control</i>
Determination of Performance Requirements	Defines system sensitivities
Definition of Configuration	Defines relationship between sensitive elements and sources of contamination Ease of cleaning and protection
Selection of Materials, Components, Subsystems	Affects outgassing, particle, generation, and other functions
Planning of Operations for Factory, Launch Site, and Flight	Affects the ability to meet requirements and minimize cost

The contamination analyses are used to determine if the materials, components, and subsystems can be expected to meet the performance requirements for the system. When the analyses are performed early in the design process it is possible to make necessary changes with a minimum impact on schedule and cost. As the design develops, the analyses can be "fine tuned" for critical items.

The contamination control plan is a summary of the requirements and the procedures to be used to meet these requirements. The contamination control plan should start early in the design phase of a project. There may be many unresolved issues and blanks in the plan, but these indicate work that must be accomplished and to allow schedules to be set for implementation. One important purpose of the contamination control plan is to assure that the requirements and procedures are implemented in the working documents. It also allows all parties to review it and reach a consensus on the approaches to be followed starting early in the design activity.

Development tests should be used to get data that are needed in the design of the new space system. Typical development tests include outgassing tests on materials and components where there is a lack of data in the literature or special test conditions are required.

DESIGN 3

<i>Activity</i>	<i>Impact on Contamination Control</i>
Perform Contamination Analyses	Determines if the configuration, materials, components, and subsystems that are used are likely to result in the cleanliness levels needed to meet system performance requirements.
Prepare a Contamination Control Plan	Summarizes the requirements, goals, and procedures and is used to provide guidance to all activities that impact contamination control.
Perform Development Tests	Tests should be performed early enough to affect designs without increasing costs.

It is important to clean the hardware as it goes through the factory operations. It is especially critical to remove all oils and chips following machining, drilling, forming, and similar manufacturing operations. It is critical because particulate and molecular contaminants become trapped in enclosed (but not sealed) areas and can be released by exposure to the vibro-acoustic, vacuum, and elevated temperature environments during flight.

During the assembly operations, particles, debris, and oils should be removed before areas are closed out because it may not be possible to inspect or clean these areas again.

Many areas on a spacecraft are inaccessible even when they are not enclosed. The possibility of damaging sensitive components by performing cleaning operations late in the assembly phase may outweigh the benefits of the cleaning.

Spraying operations are particularly hazardous. Oils, paints, and solvents are frequently sprayed. Aerosols from spraying operations can be carried over long distances because the aerosols are very small, usually less than 1 μm in size.

Areas where spacecraft and components are tested have not always been cleanrooms; however, the current trend is to build new facilities, or modify old ones, to be cleanrooms. This makes the contamination control process much easier.

FACTORY OPERATIONS

Manufacturing

Clean hardware to remove oils and chips before assembling.

Clean and protect hardware through all operations.

Assembly

Clean areas that are being closed out.

Protect the hardware.

There may be no way to access areas for inspection and cleaning.

Test

Test areas should be clean facilities

Vibro-Acoustic, Thermal, Thermal-Vacuum

Thermal-vacuum tests have frequently been a cause of contamination. There has been a tendency to blame the vacuum system for many of the problems; however, outgassing from the spacecraft and test equipment have been major causes of contamination.

The design of the chamber and vacuum pumping equipment is important, but the use of operating procedures that minimizes the probability for contamination are also necessary. The pumpdown, temperature changes, and return to one atmosphere are critical procedures for protecting the spacecraft from self contamination as well as contamination from the chamber and test equipment.

Equipment failures and accidents have also caused actual or possible contamination problems. Equipment should be fail-safe so that damage can not occur as a result of a failure. Typical problems have been electrical power and cooling water failures. When vacuum pumps fail or overheat contamination is likely to occur if there is no automatic, controlled shut down and manual restart system.

Errors by personnel have also resulted in problems. Although it is not possible to prevent human errors it is possible to human-engineer a system to reduce the probability of error and to have fail-safe controls installed.

Even if it turns out that no actual contamination occurred as a result of an accident, the time spent investigating and analyzing the failure increases costs and schedule times.

THERMAL VACUUM TESTS 1

<i>Problem</i>	<i>Corrective Action</i>
Contamination from equipment	Verify prior to test Proper design and procedures
Self contamination	Proper operating procedures Monitor contamination
Equipment failure & personnel error	Design should be "fail safe" Proper operating procedures
Power & cooling water Pump failure Accident	

Many measurements and tests can be performed during the thermal vacuum test to enhance the confidence and reliability of a system. These include the measurement of outgassing rates, the measurement of contaminant deposition and effects, and evaluation of performance under simulated flight conditions.

Outgassing rates and contaminant deposition from the Inertial Upper Stage (IUS) were measured during the thermal vacuum test program at the Boeing Company. The data were compared with the results of the contamination analyses and were used to improve the models and assumptions used in the analyses.

Outgassing rates from typical electronic boxes used on the Centaur upper stage were measured at the NASA White Sands Test Facility. The results were used to determine if the outgassing exceeded the predicted maximum allowable rates, based on contamination levels predicted from the contamination analyses. From the test results it was determined that the boxes should be subjected to a vacuum bakeout to reduce outgassing rates to acceptable levels.

There have also been many instances where contamination problems were encountered during thermal vacuum tests, and corrective actions were taken prior to flight. There have also been situations where problems were encountered but not corrected before flight, often because the cause was not understood.

THERMAL VACUUM TESTS 2

Activities to Enhance Confidence and Reliability

Measure Outgassing of Equipment and Spacecraft

**Compare with the values used in the
contamination analyses**

Look for Potential Flight Problems

**Evaluate the performance under simulated
flight conditions**

Facilities for handling space systems do not always get adequate attention in comparison with the hardware which go through these facilities. The state of the art with respect to contamination control has shown a great advance since the design and construction of the older, existing facilities. Also, the cleanliness requirements for spacecraft have become more demanding. The microelectronics industry has been forced to go to Class 10 and Class 1 cleanrooms, with commensurate improvements in procedures, as solid state devices have become smaller and more sensitive to smaller particles.

Although spacecraft do not require the degree of contamination control that is necessary for the fabrication of electronic and optical devices, the technology that has been developed in areas such as air filtration, measurement, garments, procedures, and facility construction are applicable to spacecraft facilities. Greater thought in the design and planning of these facilities is necessary to protect the expensive space hardware being produced.

It appears to be cost effective to design the protection and controls into a facility that is commensurate with the cost of the hardware and cost of schedule slips.

FACILITIES

The cost of building and launching space systems is expensive. Damage, failures, and delays can result in significant cost increases. Therefore, it is cost effective to design and construct facilities that minimize operating costs and provide fail-safe protection.

Some Problems That Have Been Observed

**Overhead water pipe breaks over a long, holiday weekend and is discovered by a guard when water is seen leaking under a wall.
Overhead fire sprinkler system leaks or is turned on accidentally.
Local fire generates smoke with the potential for contaminating other hardware in the room, and the local sprinkler sprays water on some hardware.**

Air conditioning system ingests outside contaminants.

Oil vapor leaks in from adjacent machine shop.

Corrosive vapor from adjacent metal processing room.

Delays at the launch site are especially costly because all elements of payload-launch vehicle system are affected even when only one of the elements has a problem. All elements must wait for the problems to be resolved. This ties up personnel and facilities.

The Tracking and Data Relay Satellite (TDRS) on Shuttle flight STS-6 experienced a number of problems. These problems included facility and procedural failures.

LAUNCH SITE OPERATIONS 1

Problems during launch site operations have a greater impact on cost and performance than those during factory operations.

Example: TDRS (Tracking and Data Relay Satellite) on STS-6

Problems:

High winds breached the seals resulting in the ingestion of contaminants into the Payload Changeout Room (PCR).

Installation work on the forward bulkhead of the Orbiter resulted in particulate fallout on to the TDRS.

Examples of some contamination problems occurred with the TDRS on STS-6. One event was the breach of the seals between the Orbiter and the PCR during high winds in a storm. Although this was potentially a serious event, analyses of the data showed that the airborne particle counts exceeded Class 100,000 only one time during the storm. Class 100,000, as defined by FED-STD-209, means that there are 100,000 particles per cubic foot of air of sizes 0.5 μm and larger. A Class 100,000 cleanroom must never exceed Class 100,000 during normal operations. The HEPA (High Efficiency Particulate Air) filters provide better than Class 100 air into the facility, and cleanrooms can be expected to have a Class 10,000 or better environment during normal operations; therefore, Class 100,000, although the maximum allowable, is considered very high for a cleanroom.

As a result of the TDRS event and greater concerns for contamination control at NASA KSC, considerable improvements have been made in facilities and procedures that have reduced the probability of similar problems in the future.

Another problem that occurred with STS-6 was the discovery of particulate contamination and debris on the TDRS. Some occurred when work was performed on the Orbiter forward bulkhead, above the TDRS, resulting in fallout. Some was found to have been on the TDRS previous to the Orbiter work and the storm. The procedures now reflect the need to protect the payloads when Orbiter work must be performed and require inspection of payloads before NASA will accept them into the launch site processing.

LAUNCH SITE OPERATIONS 2

TDRS on STS-6

Conclusions:

Significant particulate contaminants were observed on the TDRS prior to the above events.

Airborne particle counts exceeded Class 100,000 only once during the high winds.

Cleaning in place was limited because of possible damage to the spacecraft, and return to the factory was a major impact to the program.

Corrective Actions:

Clean TDRS as well as possible under the circumstances because the risk from contamination was low.

Improvements in facilities and procedures were started at KSC.

The launch and ascent environments potentially are the greatest contamination hazard for exposed hardware. The vibro-acoustic environment will remove particles from Orbiter payload bay surfaces, or payload fairing surfaces on expendable launch vehicles. Payloads and airborne support equipment will also be sources of particles during ascent. The turbulent flow of venting gases and the vehicle acceleration will transport the particles, so it is important to consider the cleanliness and placement of all hardware within the bay or payload fairing relative to the contamination sensitive components.

Venting of gases from within hardware may also carry molecular contaminants to sensitive components, and aerodynamic heating will increase the outgassing rates from payload fairing materials.

The payload fairing used on the Titan IIIC used a low outgassing RTV to seal particulate contaminants within the faying surfaces; however, it is better to eliminate all contaminants from faying surfaces of structures during manufacture to significantly reduce problems during ascent.

Separation and deployment operations use thrusters, explosive devices, and mechanical elements. These generally produce molecular and particulate contaminants.

Measurements, using a QCM (quartz crystal microbalance), on the P74-1 mission on a Titan IIIC showed approximately $4 \mu\text{g}/\text{cm}^2$ deposition in the payload area from the solid propellant retromotor on Stage 2.

LAUNCH AND ASCENT

**The vibro-acoustic environment during ascent
will remove particles from surfaces.**

Orbiter payload bay

Spacecraft, experiments, and airborne support equipment

Payload fairing on expendable launch vehicles

Aerodynamic heating may increase outgassing rates.

**Separation and deployment activities produce molecular and
particulate contaminants.**

**Separation techniques that use explosive devices and/or
that cause materials to fracture**

Thruster operation

Operation of mechanical elements

Spacecraft in low Earth orbits are exposed to an ambient atmosphere that will affect the contaminant deposition and performance. Molecular contaminants that outgas or vent from the spacecraft can be scattered back to the spacecraft as a result of collisions with the atmosphere. This adds to the deposition from direct line of sight transport.

Solar ultraviolet irradiation will enhance contamination as a result of a photochemical deposition process.

Atomic oxygen will remove contaminants, such as hydrocarbons, that produce volatile species during oxidation. Contaminants, such as silicones, that produce solid oxides will remain. The net contaminant deposition, or removal, rate will depend upon the rates of each mechanism.

Spacecraft going to higher orbits will go into a transfer orbit. They may only spend a short time in low Earth orbit, so atmospheric effects may not be significant. There will be exposures to contaminants from additional thruster firings and separation activities.

Examples of contamination problems include the following:

Heat soaking back into the Kevlar-epoxy motor case on the IUS (Inertial Upper Stage) results in higher outgassing rates, and measures were taken to prevent the outgassing products from reaching sensitive components on spacecraft.

A contamination/collision avoidance (C/CAM) maneuver was designed for the separation of the spacecraft from the IUS to prevent outgassing products from the hot solid propellant motor from being emitted towards the spacecraft.

ORBITAL OPERATIONS 1

Low Earth Orbits

Long Exposure Times

Self-Contamination

Atmospheric Effects

Molecular back scatter increases molecular deposition.

Atomic oxygen will remove some molecular deposits.

Solar ultraviolet will enhance the molecular deposition

Micro-debris Impacts

Transfer Orbits

Atmospheric Effects

This is usually a short exposure.

Venting and Outgassing

Thrusters

Separation

As with most spacecraft contamination, the spacecraft is the primary source. Line of sight transport of molecular contaminants, directly from sources or reflection/emission from secondary surfaces, is the primary mechanism for contamination. Spacecraft electrostatic charging will also result in a return flux of molecular contaminants. This effect was predicted by analyses and then verified by the ML-12 experiment on the SCATHA (Spacecraft Charging at High Altitudes) spacecraft.

As in low altitude orbits, solar ultraviolet irradiation will enhance the deposition of molecular contaminants. This effect has been demonstrated on the ML-12 experiment and in laboratory experiments.

The electron and proton irradiation does not appear to have a large effect on contaminant deposition based on the ML-12 results. The QCM exposed only in the shadow of the spacecraft did not show the deposition that the QCM exposed to solar irradiation did.

ORBITAL OPERATIONS 2

High Earth Orbits

Long Exposure Times

Self Contamination

Spacecraft Charging

There is a return flux of charged molecular contaminants that originated from the spacecraft.

Solar ultraviolet will enhance molecular deposition.

The impact of electrons and protons on contaminant buildup is uncertain.

Contamination data can be secured from two types of measurements in flight. One type is the experiment or measurement dedicated to contamination. The other involves the use of data from spacecraft housekeeping instruments or from some payload performing another mission related measurement.

Dedicated contamination instruments have flown on Skylab, Shuttle, Titan IIIC, LDEF (Long Duration Exposure Facility), SCATHA, NOAA-7, GPS (Global Positioning Satellite), DSP (Defense Support Program), and others. The instruments have included QCMs (quartz crystal microbalances), TQCMs (temperature controlled quartz crystal microbalances), calorimeters (ratio of solar absorptance to total hemispherical emittance), and radiometers.

The performances of spacecraft and components have also revealed the effects of contamination. Temperature measurements combined with analyses using thermal models of spacecraft have shown changes in solar absorptances and thermal emittances that have been traced back to contamination.

Data from optical sensors have also shown that contamination has affected performances, and analyses of solar array power output has shown evidence of contamination.

The problem with using data from spacecraft housekeeping, sensors, and power systems arises from the fact that there may be many things that affect performance besides contamination and the usually poor precision and accuracy of the measurement.

However, if more spacecraft flight data were analyzed, better contamination information useful for future design and operation would be available. Unfortunately, flight data usually is only analyzed when problems are encountered.

FLIGHT MEASUREMENTS 1

Dedicated Instruments

Skylab: QCMs, Solar Coronagraph

Shuttle: IECM (Induced Environment Contamination Monitor),
NASA MSFC, on STS-2,3,4,9

CMP (Contamination Monitor Package), NASA GSFC, on STS-3

IOCM (Interim Operational Contamination Monitor),
AFSD/JPL, on STS-51C

PACS (Particle Analysis Camera for Shuttle), AFGL, on STS-51C

Recoverable: LDEF

Expendable: QCM on P74-1 (Titan IIIC)

ML-12 on SCATHA

TQCM, calorimeter, & UV detector on NOAA-7

Calorimeters on GPS & DSP

Performance Analyses

Thermal analyses/Optical Sensor Changes/Electrical Power Analyses

Future contamination data in flight will come from the same type of measurements as in the past, dedicated instrumentation and analyses of the performance of spacecraft and payloads.

There are plans for instrumentation on Shuttle flights. The IOCM (Interim Operational Contamination Monitor) was developed by JPL for the Air Force Space Division and is planned to fly on future Shuttle flights. It consists of separate modules that can be attached to the sides of the Orbiter bay and contains both active and passive sensors. Data are recorded in flight and analyzed after the mission. Typical active sensors are TQCMs, radiometers, and calorimeters. Passive witness plates can also be flown on an IOCM module. The IOCM has the flexibility to incorporate new active sensors to perform special measurements.

The APM (Ascent Particle Monitor) was designed and built by Martin Marietta Aerospace for the Air Force Space Division. There are three modules that can be programmed to open and close during the ascent of the Shuttle Orbiter in order to capture particles in the bay. The particles will be counted and analyzed after the return of the Orbiter. The Aerospace Corporation Materials Sciences Laboratory is responsible for the experiment, and Rockwell International is responsible for Shuttle integration activities. The NASA Goddard Space Flight Center is providing significant support to the APM experiment. The first flight of the APM is now planned to be on STS-30, the Magellan Mission, scheduled for launch in April 1989.

NASA GSFC also has a Contamination Monitor Package (CMP) that has flown on STS-3, will fly on the EOIM-III (Effects of Oxygen Interaction with Materials) experiment, and could be available for future Shuttle flights.

The IBSS/SPAS (Infrared Background Signature Survey/Shuttle Pallet Satellite) experiment planned for a Shuttle flight will provide some data on contamination in the bay and during deployment and recovery.

Unfortunately there appear to be fewer opportunities for flights on spacecraft that are not recovered. The P-888 mission contains the IAPS (Ion Auxiliary Propulsion System) experiment sponsored by the NASA Lewis Research Center. The diagnostic instrumentation includes a QCM and solar cells that will provide general contamination data as well as data on deposition and effects of the mercury ion thrusters' effluents.

FLIGHT MEASUREMENTS 2

Some Planned Flights

Shuttle: IOCM (Interim Operational Contamination Monitor)

APM (Ascent Particle Monitor)

CMP (Contamination Monitor Package)

**Spacecraft: IAPS (Ion Auxiliary Propulsion System)
diagnostic instrumentation on P-888**

An effective contamination control program will contribute to reducing cost and meeting the performance requirements of a space system. One aspect of cost control is doing what is necessary to meet performance requirements but not doing more than is necessary.

The design phase of the project can be used to make the system less sensitive to contamination as well as making the system easier to clean and keep clean. Materials and components that contribute little or no molecular and particulate contaminants should be incorporated into the design at this time.

Facilities and procedures for manufacturing, assembly, test, and ground processing are critical for maintaining cleanliness. The importance of ground facilities as a part of space systems needs to be increased. For contamination control and the overall ground operations needs, the operating costs should be considered in the requirements on the design and construction of the facilities.

The ability to understand and predict contamination processes and effects depends upon knowing what is happening on spacecraft in flight. Greater use of contamination instrumentation and more analyses of performance for operational spacecraft are needed to develop the models for use in design and mission planning. Contamination experiments in flight and complementary laboratory experiments are needed to fill in the gaps and develop new technology for operational vehicles.

The use of standards and specifications will contribute to cost reduction by providing a uniform approach and quality of work and reducing duplication of effort. In addition to DoD and federal standards, committees within organizations such as the American Society for Testing and Materials (ASTM) and Institute of Environmental Sciences (IES) have been and will continue to play a major role in the development of standards. Greater support from DoD and NASA to the appropriate committees would help the effort.

CONCLUSIONS & ASSESSMENTS

The contamination control program must cover the project from the beginning to the end.

Design systems to minimize sensitivity to contamination, ease of cleaning, and contaminant production.

Facilities and procedures are critical to maintaining cleanliness during ground operations.

Flight operations should be planned so as to minimize contamination.

More data from flights are required to assess the adequacy of designs and operations.

Standards and specifications should include contamination control requirements.

Bibliography

- Bareiss, L.E., et. al., "Shuttle/Payload Contamination Evaluation (SPACE) Program, Version II, User's Manual", NAS9-15826, MCR-81-509, Martin Marietta Aerospace, 30 Jan. 1981
- Borson, E.N. & Peterson, R.V., "Spacecraft Contamination from Propulsion Systems", AFRPL TR-84-068, 31 Aug. 1984
- Curran, D.G.T. & Millard, J.M., "Contamination/Degradation Measurements on Operational Satellite Thermal Control Surfaces", Progress in Astronautics & Aeronautics, Vol. 60, 1978
- DoD, "Product Cleanliness Levels and Contamination Control Program", MIL-STD-1246B, 4 Sept. 1987
- Ehlers, H.K.F.; Jacobs, S.; Leger, L.J.; & Miller, E., "Space Shuttle Contamination Measurements from Flights STS-1 Through STS-4", Journal of Spacecraft & Rockets, Vol. 21, No. 3, May-June 1984
- General Services Administration, "Clean Room and Work Station Requirements, Controlled Environment", FED-STD-209C, 27 Oct. 1987
- Hall, D. F.; Stewart, T. B.; & Hayes, R. R., "Photo-Enhanced Spacecraft Contamination Deposition", Proceedings, 3rd European Symposium on Spacecraft Materials in Space Environment, 01-04/10/85
- Hall, D.F., "Flight Experiment to Measure Contamination Enhancement by Spacecraft Charging", SPIE Vol. 216, Optics in Adverse Environments, 1980
- Hall, D.F. & Fote, A.A., " α_S/ϵ_H Measurements of Thermal Control Coatings Over Four Years at Geosynchronous Altitude", Progress in Astronautics & Aeronautics, Vol. 91, 1984
- D. F. Hall, T. B. Stewart, & R. R. Hayes, "Photo-Enhanced Spacecraft Contamination Deposition", Proceedings, 3rd European Symposium on Spacecraft Materials in Space Environment", 1-4 Oct. 1985, ESA SP-232, Nov. 1985
- Hetrick, M.A. & Hoffman, R.J., "CONTAM Data Analysis and Model Improvement Study (CONTAM III): Review & Assessment II: S/C Flight Data", AFRPL-TR-79-13, April 1979
- Hetrick, M.A. & Romine, G.L., "Payload Contamination Environment for Titan IIIC Launch Vehicles Using Launch Complex 40", MCR-75-118, Martin Marietta, Jan. 1975
- Huang, S. & Hetrick, M. A., "Preliminary Correlation of Spacecraft Contamination Flight Data with the Modified SPACE II Computer Model", AIAA-86-1357, Thermophysics Conf., 2-4 June 1986
- IES, "Compendium of Standards, Practices, Methods and Similar Documents Relating to Contamination Control", IES-CC-009-84, 1984

Jarossy, F. J.; Pizzicaroli, J. C.; & Owen, N. L., "Shuttle/Payload Contamination Evaluation (SPACE) Program Improvements", Shuttle Optical Environment, Proc. SPIE, V 287, pp 78-85, (1981)

Lynch, J.T., "Quartz Crystal Microbalance (QCM) Monitor of Contamination for LES-8/9, 9th Space Simulation Conference, NASA CP-2007, 26-28 April 1977

Lyon, W.C., "Thruster Exhaust Effects Upon Spacecraft", NASA-TMX-65427, Oct. 1970

Maag, C.R. & Millard, J.M., "NOAA Contamination Monitoring Instrument, Design and Performance of a Contamination Monitoring Instrument on a NOAA Satellite", AFRPL-TR-85-065, Sept. 1985

Mc Keown, D.; Fountain, J.A.; Cox, V.H.; & Peterson, R.V., "Analysis of TQCM Surface Contamination Absorbed During the Spacelab 1 Mission", AIAA-85-7008-CP, 13-15 Nov. 1985

Miller, E.R., ed., "IECM Preliminary Results from the Spacelab 1 Flight", NASA TM-86461, Aug. 1984

Rantanen, R.O. & Gordon, T.D., "Contaminant Buildup on Ram Facing Spacecraft Surfaces", Proc. SPIE V777, pp 26-33, (1987)

J. J. Scialdone, "An Estimate of the Outgassing of Space Payloads and Its Gaseous Influence on the Environment", Journal Spacecraft & Rockets, Vol. 23, No. 4, July-Aug. 1986

Scialdone, J.J., "Particulate Contaminant Relocation During Ascent", NASA TM 87794, June 1986

Scialdone, J.J., "Redistribution of Particulates During Launch", Space Simulation Conference, NASA CP 2446, 3-6 Nov. 1986

Simpson, J.P. & Witteborn, F.C. "Effect of the Shuttle Contaminant Environment on a Sensitive Infrared Telescope", Applied Optics, Vol. 16, No. 8, Aug. 1977

Stewart, T.; Arnold, G.; Hall, D.; Marvin, D.; Hwang, W.; Chandler, R.; & Martin, H., "Photochemical Self-Contamination", AIAA 88-2728, Thermophysics Conf., 27-29 June 1988.

EFFECTS OF THE CONTAMINATION ENVIRONMENT
ON SURFACES AND MATERIALS

CARL R. MAAG
JET PROPULSION LABORATORY
PASADENA, CALIFORNIA

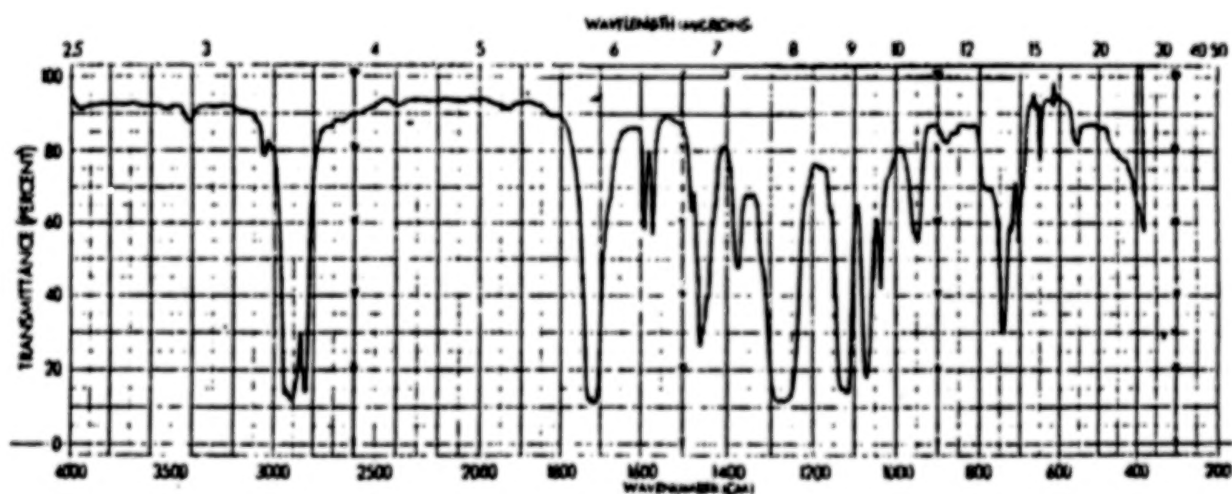
CONTAMINATION CAN BE CONSIDERED AN INDUCED ENVIRONMENTAL EFFECT. CONTAMINATION, BOTH MOLECULAR AND PARTICULATE, HAS CAUSED DEGRADATION IN BOTH OPTICAL AND THERMAL CONTROL SYSTEMS.

INTRODUCTION

- o IN ADDITION TO THE ISSUES THAT HAVE ALWAYS EXISTED, NEW DEMANDS ARE BEING PLACED ON SPACE SYSTEMS FOR INCREASED CONTAMINATION PREVENTION/CONTROL
- o OPTICAL SURVEILLANCE SENSORS ARE REQUIRED TO DETECT LOW RADIANCE TARGETS. THIS INCREASES THE NEED FOR VERY LOW SCATTER SURFACES IN THE OPTICAL SYSTEM. PARTICULATE CONTAMINATION LEVELS TYPICALLY EXPERIENCED IN TODAY'S WORKING ENVIRONMENTS/HABITS WILL MOST LIKELY COMPROMISE THESE SENSORS
- o CONTAMINATION (MOLECULAR AND PARTICULATE) CAN ALSO AFFECT THE SURVIVABILITY OF SPACE SENSORS IN BOTH THE NATURAL AND HOSTILE SPACE ENVIRONMENTS

DI-OCTYL PHTHALATE (DOP) IS A TYPICAL SPACECRAFT CONTAMINANT. DOP IS USED AS BOTH A PLASTICIZER IN POLYMERIC MATERIALS AND AS A MATERIAL TO CHECK THE EFFICIENCY OF HEPA FILTERS IN CLEAN ROOMS. IT HAS BEEN OBSERVED TO BE CARRIED DOWNSTREAM IN THE AIR FLOW OF A CLEAN ROOM AND COAT CRITICAL OPTICS. AN IR SPECTRA OF A THIN FILM IS SHOWN BELOW.

INFRARED ABSORPTION SPECTRA OF DI-N-OCTYL PHTHALATE

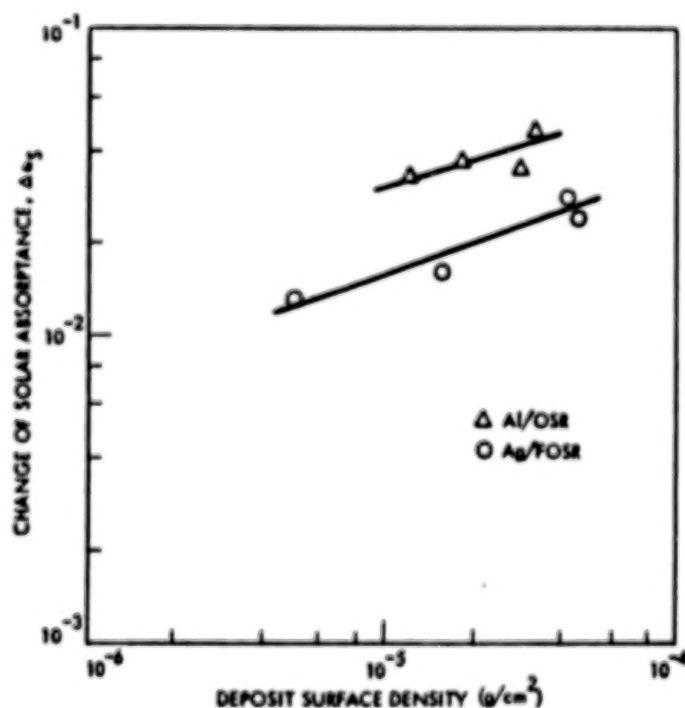


ULTRAVIOLET ABSORPTION SPECTRA OF DI-N-OCTYL PHTHALATE



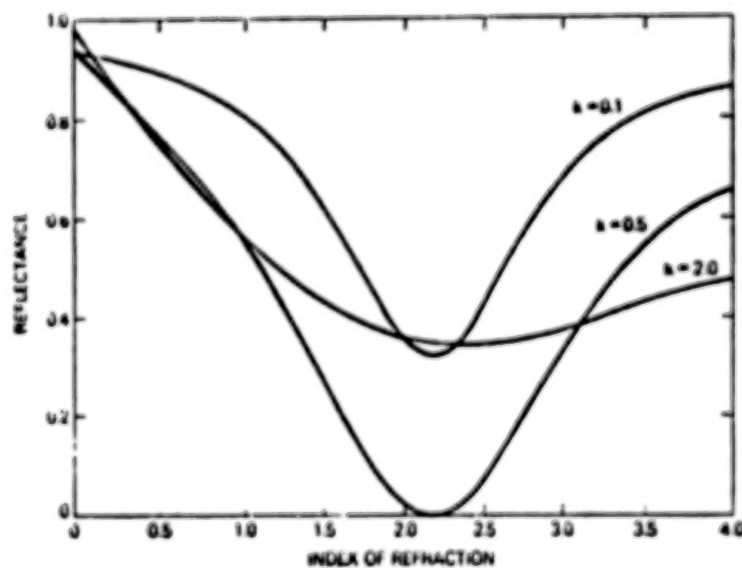
OUTGASSING PRODUCTS CAN ABSORB STRONGLY EVEN BEFORE PHOTOLYSIS CAN CAUSE ADDITIONAL DARKENING. THE FIGURE BELOW SHOWS THAT APPROXIMATELY 500Å OF RTV 560 OUTGAS PRODUCTS CAUSED A 0.03 INCREASE IN SOLAR ABSORPTANCE ON AN ALUMINIZED SECOND SURFACE MIRROR.

CHANGE OF SOLAR ABSORPTANCE BY RTV560 OUTGAS PRODUCTS



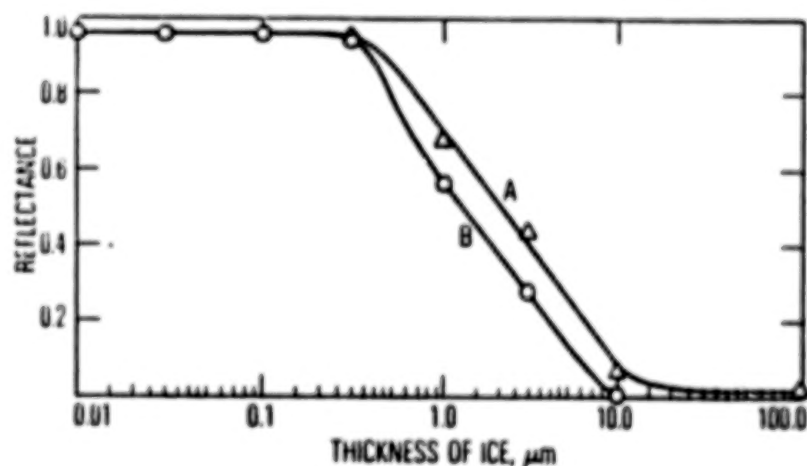
THE REFRACTIVE INDEX OF AN ORGANIC FILM CAN CAUSE GIGANTIC VARIATIONS IN REFLECTANCE IF DEPOSITED ON A MIRROR. BELOW ONE CAN SEE THE DIFFERENCES ON A FRONT SURFACE VIS/IR MIRROR.

**REFLECTANCE AS A FUNCTION OF THE INDEX OF REFRACTION
OF A CONTAMINANT FILM (550A) DEPOSITED ON A VIS/IR MIRROR**



IN ADDITION TO ORGANIC FILMS, CRYODEPOSITS OF WATER ICE HAVE BEEN OBSERVED TO CAUSE SIGNIFICANT CHANGES IN OPTICAL PROPERTIES. THE CHART BELOW SHOWS EXAMPLES OF BOTH THEORETICAL AND EMPIRICAL DATA AS DEPOSITED ON A GOLD MIRROR.

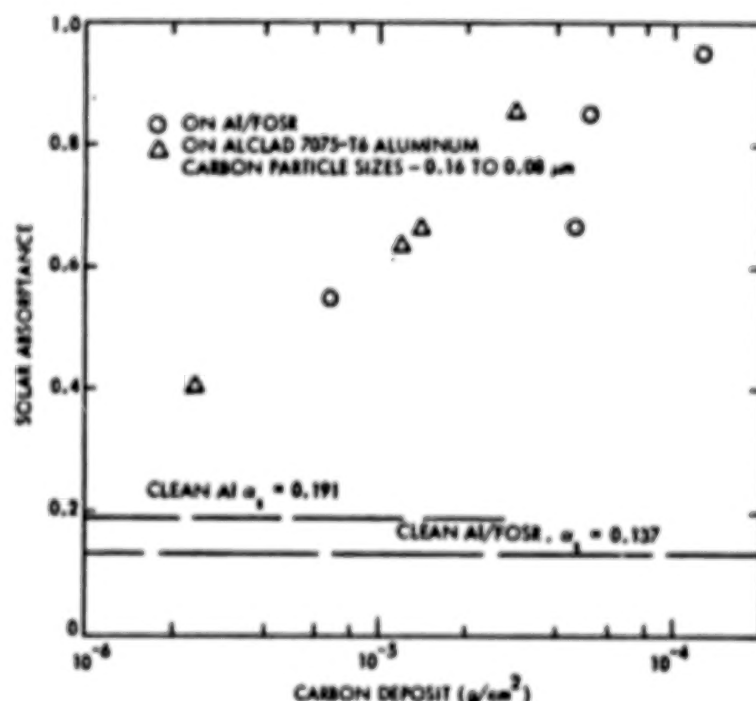
REFLECTANCE OF A GOLD MIRROR (MID IR) AS A FUNCTION OF WATER ICE THICKNESS



A = ESTIMATED AVERAGE
B = WORST CASE

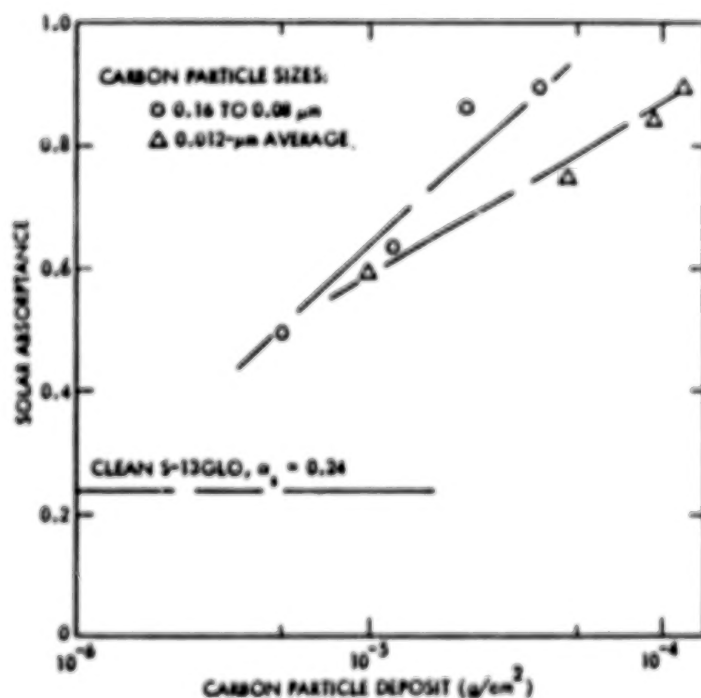
PARTICLES CAN CAUSE CHANGES IN THE RADIATIVE PROPERTIES OF THERMAL CONTROL SURFACES. AS CAN BE SEEN FROM THE FIGURE BELOW, CARBON PARTICLES ARE ONE OF THE MORE DELETERIOUS FORMS. CARBON PARTICLE DEPOSITS FROM SOLID ROCKET MOTORS (SRM'S) HAVE BEEN SEEN TO HAVE SIMILAR EFFECTS WHEN DEPOSITING ON THERMAL SURFACES.

CHANGE OF SOLAR ABSORPTANCE BY CARBON PARTICLE DEPOSIT



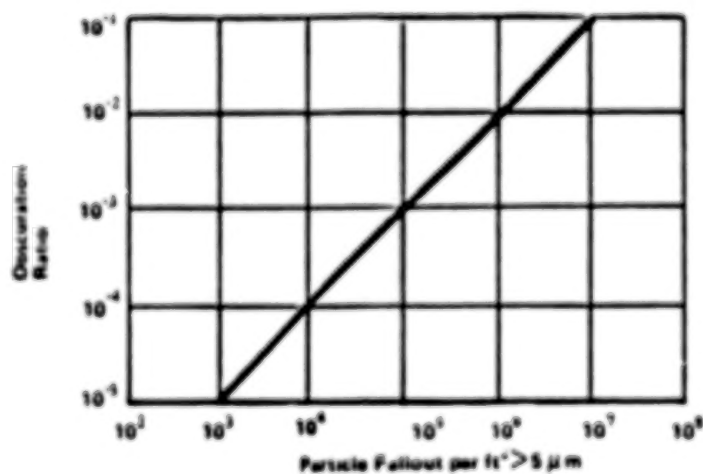
AS CAN BE SEEN, LARGER PARTICLE SIZES CAUSE GREATER CHANGES IN RADIATIVE PROPERTIES. THIS IS DUE PRINCIPALLY TO OBSCURATION. SMALLER PARTICLES, ALTHOUGH HAVING LESS IMPACT IN ANY CHANGE OF SOLAR ABSORPTANCE, CAUSE INCREASED SCATTERING.

EFFECT OF PARTICLE SIZES ON CHANGE OF SOLAR ABSORPTANCE



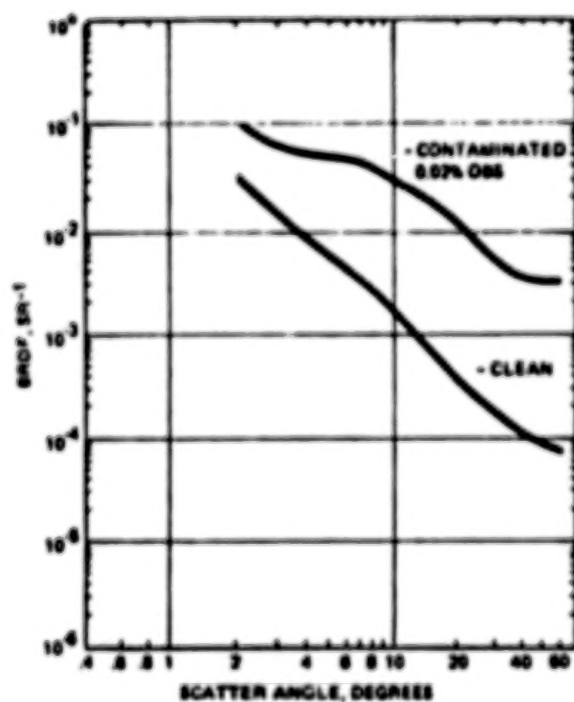
PARTICLES FIVE (5) MICROMETERS AND ABOVE CAN CAUSE SIGNIFICANT OBSCURATION AS EXHIBITED BELOW.

**OBSCURATION RATIO OF A SURFACE VERSUS NUMBER OF
PARTICLES PER FT² (>5 μ M)**



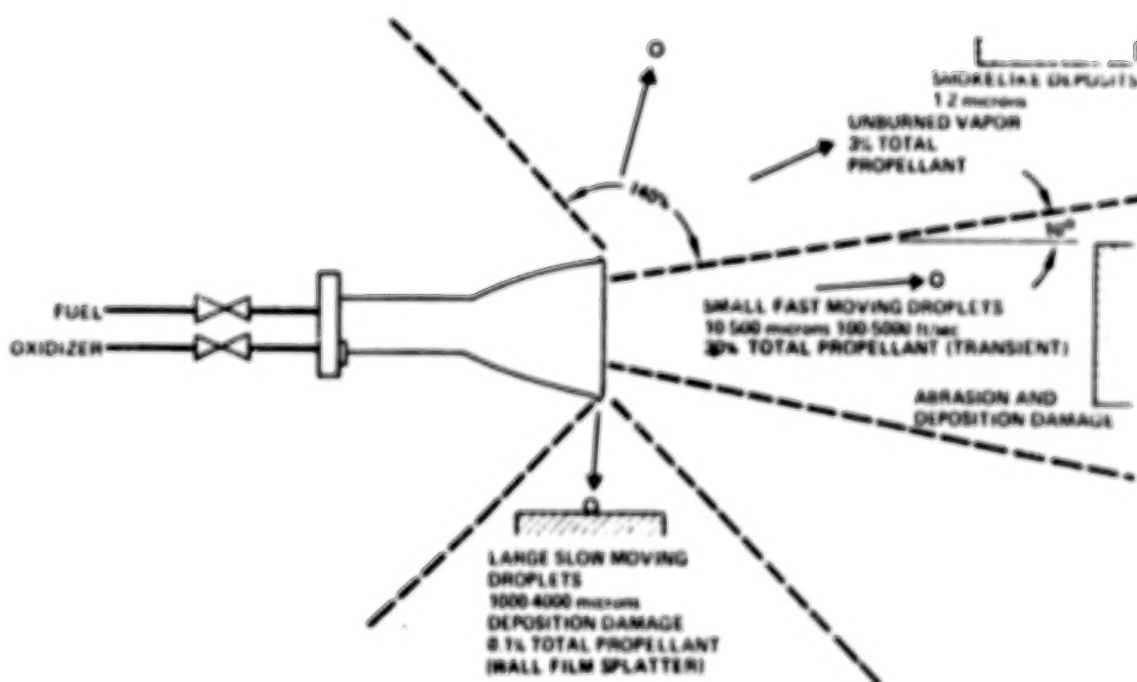
THE BI-DIRECTIONAL REFLECTANCE DISTRIBUTION FUNCTION (BRDF), A METHOD OF DESCRIBING SCATTERING ON OPTICAL SURFACES, CAN BE SIGNIFICANTLY ALTERED BY SMALL PARTICLES.

BRDF OF AN ALUMINUM MIRROR



IN ADDITION TO INDUCED CONTAMINATION FROM OUTGASSING PRODUCTS OR PARTICLE DEPOSITION, THE EFFLUENTS FROM PROPULSION SYSTEMS CAN BOTH DAMAGE SURFACES AND/OR CHANGE THEIR OPTICAL AND THERMAL PROPERTIES.

PRODUCTION AND TRANSPORT OF PLUME EFFLUENTS





Report Documentation Page

1. Report No. NASA CP-3035, Part 1	2. Government Accession No.	3. Recipient's Catalog No.	
4. Title and Subtitle NASA/SDIO Space Environmental Effects on Materials Workshop		5. Report Date May 1989	
		6. Performing Organization Code	
7. Author(s) Louis A. Teichman and Bland A. Stein, Compilers		8. Performing Organization Report No. L-16575	
		10. Work Unit No. 506-43-21-04	
9. Performing Organization Name and Address NASA Langley Research Center Hampton, Virginia 23665-5225		11. Contract or Grant No.	
		13. Type of Report and Period Covered Conference Publication	
12. Sponsoring Agency Name and Address National Aeronautics and Space Administration Washington, DC 20546-0001 and Department of Defense - Strategic Defense Initiative Organization, Washington, DC 20301-7100		14. Sponsoring Agency Code	
		15. Supplementary Notes	
16. Abstract The National Aeronautics and Space Administration (NASA) and the Strategic Defense Initiative Organization (SDIO) cosponsored a workshop on Space Environmental Effects on Materials at the NASA Langley Research Center from June 28 to July 1, 1988. The joint workshop was designed to inform participants of the present state of knowledge regarding space environmental effects on materials and to identify knowledge gaps that prevent informed decisions on the best use of advanced materials in space for long-duration NASA and SDIO missions. Establishing priorities for future ground-based and space-based materials research was a major goal of the workshop. The end product of the workshop was an assessment of the current state-of-the-art in space environmental effects on materials in order to develop a national plan for spaceflight experiments. The workshop was intended for participation by expert applied researchers, systems technologists, and program managers for spacecraft systems.			
17. Key Words (Suggested by Author(s)) Space environmental effects on materials Atomic oxygen Micrometeoroids and debris Contamination Thermal and ultraviolet (UV) radiation Particulate radiation and cosmic rays		18. Distribution Statement Unclassified - Unlimited Subject Category 23	
19. Security Classif. (of this report) Unclassified	20. Security Classif. (of this page) Unclassified	21. No. of pages 373	22. Price A16

National Aeronautics and
Space Administration
Code NTT-4

Washington, D.C.
20546-0001

Official Business
Penalty for Private Use, \$300



National Aeronautics and
Space Administration

Washington, D.C.
20546

SPECIAL FOURTH CLASS MAIL
BOOK

Postage and Fees Paid
National Aeronautics and
Space Administration
NASA-451

Official Business
Penalty for Private Use \$300



U2 901 2F3635-PT16404 120007 000
GOVERNMENT PRINTING OFFICE
LIBRARY OF CONGRESS
MAY 19 1967
WASHINGTON, D.C. 20540



POSTMASTER:

If Undeliverable (Section 158
Postal Manual) Do Not Return

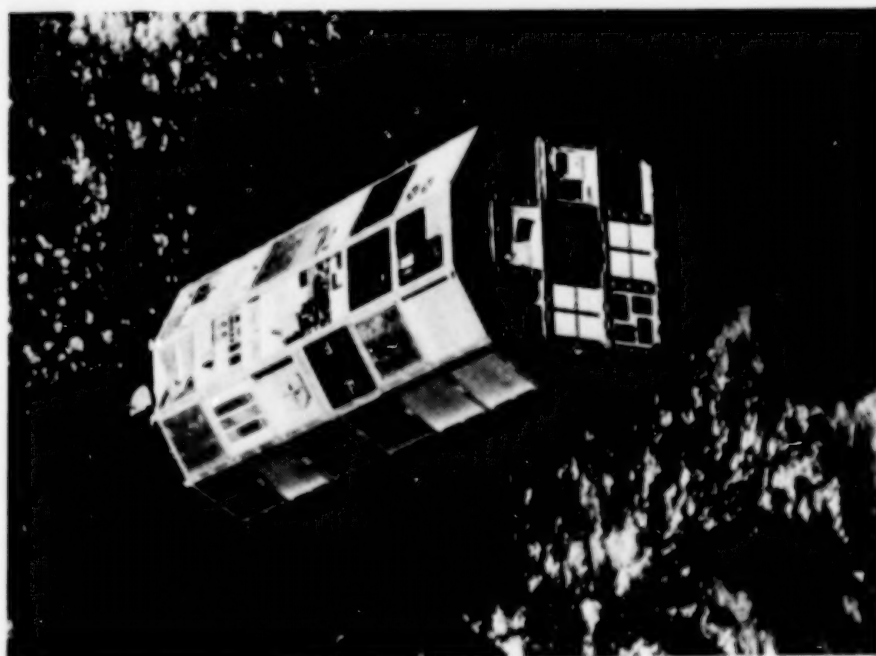
MAY 13 1988

0830-H-10
(330)

NASI. 55: 3035/pt. 2

NASA Conference Publication 3035
Part 2

NASA/SDIO Space Environmental Effects on Materials Workshop



*Proceedings of a workshop held at
NASA Langley Research Center
Hampton, Virginia
June 28-July 1, 1988*

NASA

COMPLETED

NASA Conference Publication 3035
Part 2

NASA/SDIO Space Environmental Effects on Materials Workshop

Compiled by
Louis A. Teichman and Bland A. Stein
NASA Langley Research Center
Hampton, Virginia

Proceedings of a workshop jointly
sponsored by the National Aeronautics
and Space Administration and the
Strategic Defense Initiative
Organization, and held at
NASA Langley Research Center
Hampton, Virginia
June 28-July 1, 1988



National Aeronautics and
Space Administration
Office of Management
Scientific and Technical
Information Division

1989

PREFACE

Until now, most satellites have been launched with limited life expectancies (at most 3-5 years) and the materials used and the operating orbits selected for "long-term" flights have evolved from many successful shorter duration flights. During the 1990's, the Strategic Defense Initiative Organization (SDIO) plans to launch various platforms and satellites, and NASA plans to deploy Space Station Freedom and other large space structures. All of these spacecraft are expected to remain in space for 10 to 30 years at altitudes varying from low Earth orbit to geosynchronous orbit. The materials community is concerned that these systems will be vulnerable to environmentally induced degradation that will result in reduced performance. The environments of major concern are particulate radiation, atomic oxygen, micrometeoroids and debris, contamination, spacecraft charging, and solar radiation (ultraviolet (UV) and thermal cycling).

Although many spacecraft have performed successfully for relatively short periods of time, the effects of these environments, both individually and synergistically, on long-term materials performance is virtually unknown, and terrestrial facilities and tests are unable to resolve the uncertainties. In late 1987 opportunities for piggy-back or getaway special experiments or even a dedicated spaceflight seemed possible. Immediately, questions of which experiments to conduct and in what order of priority arose.

The primary objective of this workshop was to identify and prioritize candidate spaceflight experiments; that is, which materials experiments must be conducted in space to achieve maximum assurance that SDIO and NASA space assets will survive and perform for 10-30 years.

A secondary objective was to provide concise but authoritative tutorials describing each environmental factor. These tutorials would present current knowledge on topics such as each factor's applicable orbital ranges, its variations with time, how it interacts with various materials, and the subsequent consequences to materials or system performance. In addition, assessments of the sources of this knowledge (derived from true space exposure data or from modeling and laboratory simulations), the availability and authenticity of terrestrial test facilities, and the current understanding of interactions (synergisms) between these environmental effects would be offered.

The workshop was cosponsored by SDIO and NASA. It was organized by Charles F. Bersch of the Institute for Defense Analyses; Thomas W. Crooker of the Office of Aeronautics and Space Technology, NASA Headquarters; and Bland A. Stein of NASA Langley Research Center. The papers are published in the order in which they were presented at the Workshop; Section I contains an opening overview session on Environments and Materials Effects, followed by more detailed sessions on past spacecraft experience, and each of the environmental factors mentioned above. Each session was organized by its chairman, who also led the subsequent working group session for his environmental factor and prepared the presentations reproduced in Section II.

Administrative arrangements for the Workshop, as well as the collection of papers for and preparation of these Proceedings, was accomplished under the supervision of Dr. Louis A. Teichman at NASA Langley.

The efforts of the Executive Planning Committee and the Workshop Co-Chairmen are hereby acknowledged. They provided the perspective necessary to define the objectives and to organize a multidisciplinary Space Environmental Effects Workshop. They also planned the technical content of the tutorial presentations and the interactions of the groups representing the individual environmental disciplines. As a result, the objectives of the meeting regarding overall conclusions and recommendations were successfully reached by the collective efforts of all the Workshop participants.

The Executive Planning Committee consisted of

Charles F. Bersch	Institute for Defense Analysis
Herbert A. Cohen	W. J. Schafer Associates
Burton G. Cour-Palais	NASA Marshall Space Flight Center
Thomas W. Crooker	NASA Headquarters
Raymond L. Gause	NASA Marshall Space Flight Center
William Hong	Institute for Defense Analysis
Lubert J. Leger	NASA Johnson Space Center
Ranty H. Liang	Jet Propulsion Laboratory
Carolyn K. Purvis	NASA Lewis Research Center
Fred Smidt	Naval Research Laboratories
Bland A. Stein	NASA Langley Research Center
Louis A. Teichman	NASA Langley Research Center
Jack J. Triolo	NASA Goddard Space Flight Center
James. T. Visentine	NASA Johnson Space Center

The Workshop Co-Chairmen were Charles Bersch, Tom Crooker, and Bland Stein.

The excellence of the meeting facilities at the NASA Langley Activities Center and the continued cooperation of the staff, under the supervision of Ms. Patricia Gates, contributed significantly to the success of the Workshop. Arrangements were coordinated for the Executive Planning Committee by Dr. Louis Teichman.

Mr. Charles F. Bersch provided the primary impetus to the concept and basic goals of this Space Environmental Effects on Materials Workshop. The space environmental effects community owes him a debt of gratitude for his efforts.

CONTENTS

PREFACE	iii
---------------	-----

PART I*

SECTION I - THE TUTORIALS

SESSION 1: Overview: Environments and Materials Effects

Chairman: B. Stein - NASA Langley Research Center

Overview of Environmental Factors	5
C. K. Purvis - NASA Lewis Research Center	
Structural Materials for Space Applications	25
Darrel R. Tenney - NASA Langley Research Center	
Radiation Effects in Spacecraft Electronics	53
James P. Raymond - Mission Research Corporation	
Environmental Effects on Spacecraft Materials	75
J. W. Haffner - Rockwell International	
Surface Treatment Using Metal Foil Liner	87
Ray Garvey - Oak Ridge National Laboratory	
The Long Duration Exposure Facility Material Experiments	101
William H. Kinard and James L. Jones, Jr. - NASA Langley Research Center	

SESSION 2: SPACECRAFT EXPERIENCE

Chairman: J. Triolo - NASA Goddard Space Flight Center

Some Examples of the Degradation of Properties of Materials in Space	109
Frederick E. Betz and Joseph A. Hauser - Naval Research Laboratory	
Trends in Environmentally Induced Spacecraft Anomalies	123
Daniel C. Wilkinson - National Oceanic and Atmospheric Administration	
Returned Solar Max Hardware Degradation Study Results	133
Jack J. Triolo and Gilbert W. Ousley - Goddard Space Flight Center	
EnviroNet: Space Environment for Strategic Defense Initiative Experiments	161
Michael Lauriente - NASA Goddard Space Flight Center	

*Part I presented under separate cover.

†Paper not available at time of publication.

SESSION 3: ATOMIC OXYGEN

Chairmen: L. Leger and J. Visentine
NASA Lyndon B. Johnson Space Center

Environmental Definition of the Earth's Neutral Atmosphere	179
James T. Visentine - NASA Lyndon B. Johnson Space Center	
Atomic Oxygen Effects on Materials	197
Bruce A. Banks and Sharon Rutledge - NASA Lewis Research Center	
Joyce A. Brady - Sverdrup Technology, Inc.	
James E. Merrow - Ohio University	
Atomic Oxygen Effects Applications to Spacecraft	†
Ann Whitaker - NASA George C. Marshall Space Flight Center	
Atomic Oxygen Effects on Spacecraft Materials - The State of the Art of Our Knowledge	241
Steven L. Koontz - NASA Lyndon B. Johnson Space Center	

SESSION 4: MICROMETEORIDS AND DEBRIS

Chairman: Andrew Potter - NASA Lyndon B. Johnson Space Center

The Long-Term Effects of the Micrometeoroid and Orbital Debris Environments on Materials Used in Space	257
Burton G. Cour-Palais - NASA Lyndon B. Johnson Space Center	
Orbital Debris Environment and Data Requirements	281
Donald J. Kessler - NASA Lyndon B. Johnson Space Center	
Microparticle Impacts in Space - Results From Solar MAX Satellite and Shuttle Witness Plate Inspections	301
David S. McKay - NASA Lyndon B. Johnson Space Center	

SESSION 5: CONTAMINATION

Chairman: C. Maag - Jet Propulsion Laboratory

S/C Contamination Environments Overview	†
L. Bareiss - Martin Marietta Corporation	
Spacecraft Contamination Experience	331
E. N. Borson - The Aerospace Corporation	
Effects of the Contamination Environment on Surfaces and Materials	353
Carl R. Maag - Jet Propulsion Laboratory	

PART II

SESSION 6: TRAPPED RADIATION

Chairmen: W. K. Stuckey and A. L. Vampola
The Aerospace Corporation

The Space Particle Environment	367
A. L. Vampola - The Aerospace Corporation	
Effects of Space Radiation on Electronic Microcircuits	383
W. A. Kolasinski - The Aerospace Corporation	
The Radiation Belt Mission on CRRES	†
D. Hardy - Air Force Geophysics Laboratory	

SESSION 7: SOLAR RADIATION

Chairman: Wayne S. Slemp - NASA Langley Research Center

Space Vehicle Thermal Testing: Principles, Practices, and Effectiveness	395
Donald F. Gluck - The Aerospace Corporation	
Ultraviolet Radiation Effects	425
Wayne S. Slemp - NASA Langley Research Center	
Effects of Thermal Cycling on Composite Materials for Space Structures	447
Stephen S. Tompkins - NASA Langley Research Center	

SESSION 8: SPACECRAFT CHARGING

Chairman: N. John Stevens - TRW

Dielectrics for Long Term Space Exposure and Spacecraft Charging A Briefing	473
A. R. Frederickson - Air Force Geophysics Laboratory	
An Overview of Charging Environments	495
S. B. Gabriel and H. B. Garrett - Jet Propulsion Laboratory	
Surface Phenomena in Plasma Environments	511
C. K. Purvis and D. C. Ferguson - NASA Lewis Research Center	
Influence of Charging Environments on Spacecraft Materials and System Performance	535
N. John Stevens - TRW Space and Technology Group	

SECTION II-A

WORKING GROUP ORAL PRESENTATIONS	543
--	-----

Atomic Oxygen	545
Micrometeoroids and Debris	553
Contamination	559
Trapped Radiation	565
Appendix: Trapped Particle Flux Models at NSSDC/WDC-A-R&S	569
D. Bilitza, D. M. Sawyer, J. H. King	
Solar Radiation	573
Spacecraft Charging	577

SECTION II-B

WORKING GROUP WRITTEN PRESENTATIONS	585
Atomic Oxygen	587
Meteoroid/Orbital Debris Effects on Materials	589
Contamination	↑
Trapped Radiation Effects	597
Solar Radiation	607
Spacecraft Charging	609

SECTION II-C

Conclusions and Recommendations to NASA and SDIO	621
As summarized by William Hong - Institute for Defense Analysis	

PART II

SESSION 6: TRAPPED RADIATION

Chairmen: W. K. Stuckey and A. L. Vampola
The Aerospace Corporation

The Space Particle Environment

A. L. Vampola

The Aerospace Corporation, P.O. Box 92957, Los Angeles, CA 90009

ABSTRACT

This paper is a tutorial covering the energetic charged particle environment in the Earth's magnetosphere. It provides an overview of trapped particle morphology, the geometry of the trapping regions, the radiation environmental models, the current status of these models, and future modelling requirements.

INTRODUCTION

The extensive use of space for platforms for communications, surveillance such as weather and Earth resources, science research, military objectives, and manned activities results in a critical requirement for knowledge about the energetic particle environment in space. Radiation damage to circuits and materials, background effects in sensors, hazard to personnel, spurious effects in circuits: all are the result of this energetic particle environment. Utilization of space is continuing to increase. With this increase comes an equivalent increase in the number of personnel who have to have basic knowledge about and access to information about the space particle environment. The material here is intended to provide an overview in the areas of the dynamics of the particle environment, trapped radiation morphology, current trapped radiation models, and future modelling activity in this field. The references accompanying this discussion can serve as a convenient source for more detailed information in this field.

A Geiger-Muller tube launched February 1, 1958 on Explorer I by Dr. James Van Allen is considered to have produced the discovery of the trapped radiation belts surrounding the earth, but such a phenomenon had been predicted prior to the launch of the first artificial Earth satellite. A great flurry of activity aimed at understanding the radiation belts (sometimes called the *Van Allen belts*) ensued. However the myriad of measurements initially resulted in the acquisition of data rather than the acquisition of understanding. Part of the problem was the fact that data were being organized in terms of the orbital parameters longitude-latitude-altitude, a three parameter space, and the quantity of data was insufficient to provide a sufficient density of data points in any part of space to produce a reliable picture of the particle population. In addition to the three spatial parameters, there were also energy, time, and species to contend with. Some instruments made integral energy measurements (detected everything above a particular energy threshold, such as Geiger counters which counted any charged particle which could penetrate its window or walls), some made differential energy measurements, some made unidirectional measurements using collimators, others accepted particles coming from anywhere within a 2π or 4π steradian angle. Some detectors were on spinning vehicles, other on stabilized platforms. Since the particle population is not isotropic (same intensity in all directions), further confusion was possible. The first major step toward producing order out of chaos was taken by Prof. Carl McIlwain when he introduced a new variable, L , based on the second adiabatic invariant of particle motion [1], which with the magnetic field coordinate B formed a two-parameter space to replace the three spatial coordinates used to describe satellite orbits. The variable L is discussed in the next section.

In 1965, NASA funded Dr. James Vette of the Aerospace Corporation to produce model electron and proton environments using the data then available from the various satellites. All the particle data sets available within the US were assembled and incorporated into model environments--AE1 (Aerospace Electron model environment number 1) and AP1 (Aerospace Proton model environment number 1) were the result. These initial models could not be considered to be more than educated guesses. Great effort was expended in translating the various data sets into a common parameter space. (As noted above, different variables controlled the various experimental measurements of the trapped particles.) Since with

sparse data sets differential energy measurements could be converted reliably into integral fluxes and unidirectional measurements into omnidirectional but not vice-versa, the "lowest common denominator" approach was used: fluxes were specified as integral-omnidirectional fluxes as a function of location in B,L space. This is still the mode used for most trapped particle environment models. Two to three orders of magnitude disagreement between ostensibly similar measurements were the norm rather than the exception, even in some cases where the measurements were made at the same time by different instruments on the same satellite. It was realized that producing a reliable environmental model was going to be a gargantuan task. The National Space Science Data Center was set up by NASA at the Goddard Space Flight Center with Dr. Vette as its director and a major effort at space environment modelling was begun, one that continues at a low level to this day. The models produced by those efforts will be discussed later in this presentation.

TRAPPED PARTICLE MORPHOLOGY

In this section, three subjects will be discussed: trapped particle motions, McIlwain's "L" parameter, and the general configuration of the radiation belts. The discussion is at an introductory level: no previous knowledge about the particle radiation environment is assumed. The intent is to provide sufficient background material about radiation belt morphology that the rest of this tutorial and the other presentations in these proceedings which deal with particle radiation effects will be understood in context.

Trapped Particle Motions

An understanding of the dynamics of the radiation belts requires some knowledge of the dynamics of an individual particle. The three basic particle motions in the Earth's magnetosphere with which we are concerned are gyration or cyclotron motion, bounce, and drift. The gyration is about the local magnetic field line, the bounce motion is from one end of the field line to the other (one hemisphere to the other), and the drift is around the world in longitude. These motions are a consequence of the behavior of a charged particle with forces acting on it moving in a non-uniform magnetic field.

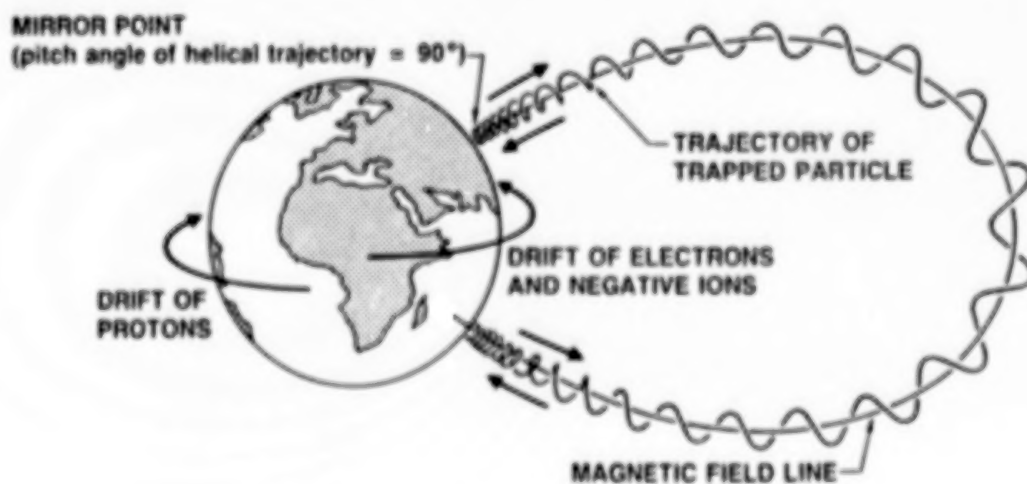


Figure 1. Geomagnetically Trapped Particle Motions

In a uniform magnetic field \mathbf{B} , a charged particle q moving with velocity \mathbf{v} experiences a force which appears as an electric field \mathbf{E} at right angles to both the direction of the field \mathbf{B} and the component of the velocity vector perpendicular to that field ($\mathbf{E} = -q \mathbf{v} \times \mathbf{B}$ in vector notation). Since at each instant this electric field tends to change the direction of the particle, which in turn changes the direction of the effective electric field, the particle executes a circular path---it gyrates about the field. This coupling of forces also results in a complementary behavior: a charged particle initially at rest in a magnetic field which has a force imposed upon it will move in a net direction perpendicular to both the force and the magnetic field

(components of force along the field are ignored here). The three basic motions of trapped particles in the magnetic field are a consequence of these force couplings and of the fact that the geomagnetic field has curvature and intensity gradients. Because of the curvature and intensity gradients, the particle's gyration path does not close upon itself, resulting in a drift motion. The motions are shown in Figure 1.

The direction of gyration follows the "right hand rule" for both electrons and ions; since the charges are opposite for the two types of particles, the direction of gyration is opposite for the electrons and ions, and therefore the direction of drift is also opposite, with electrons and negative ions drifting eastward and protons and other positive ions drifting westward. The frequency of gyration, called the *Larmor frequency*, is given by

$$f_L = \Omega_1 / 2\pi = -q B / 2\pi m_0 \gamma c \quad (1)$$

where: q = charge on the electron or ion

B = local magnetic field

m_0 = rest mass of the electron or ion

γ = relativistic mass ratio of the particle, $1/(1-v^2/c^2)^{1/2}$

v = velocity of the particle

c = velocity of light

Note that since the frequency of gyration is proportional to B , it is not constant along the field line. It is a minimum at the magnetic equator and increases as the particle moves away from the equator. Typical equatorial frequencies at 1000 km altitude are around 0.5 MHz for very low energy electrons and about 300 Hz for low energy protons. High energy particles have lower gyrofrequencies because of their greater (relativistic) mass.

The First Adiabatic Invariant

If one analyzes the path of a particle gyrating in a magnetic field, one observes that it encloses a fixed amount of flux which depends on the momentum of the particle perpendicular to the magnetic field. Under static conditions, the flux can't "leak" out of the path. This flux quantity, which is the origin of the magnetic moment of the particle, is *invariant* as long as conditions are adiabatic; i.e., the magnetic field is quiescent and no energy is added to the particle. It is called the *first adiabatic invariant*. The radius of gyration is inversely proportional to B . Thus the total flux enclosed by the path (flux density times area) is inversely proportional to the *square* of the magnetic field. But, if the magnetic field increases, thereby decreasing the radius of gyration, the perpendicular momentum of the particle has to increase to conserve the magnetic moment--to keep any of the flux from leaking out of the enclosed path. Otherwise the flux area enclosed by the gyration path would have decreased by B^2 while the flux density increased by only B . This has two interesting consequences:

First, it produces the bounce motion of particles in the geomagnetic field. A particle starting out at the equator with a component of velocity along the field line will travel a helical path to lower altitude with the field line as a guiding center. As it moves, it is moving in an increasing field. In order to maintain a constant magnetic moment, the momentum component perpendicular to the magnetic field has to increase (in the absence of such an increase, the magnetic moment would be decreasing as $1/B$). The only sources of energy to provide this perpendicular momentum increase are the magnetic field and the particle velocity. In a quiescent field, all of the momentum increase is obtained from the particle motion by converting momentum parallel to the field into momentum perpendicular to the field. When this source is exhausted, the particle motion parallel to the field line is zero and the particle is gyrating at a field intensity B_m , called the *mirror B* . The gradient in the field then reverses the process (called *mirroring*) and the particle travels a helical path to the other hemisphere where it again mirrors at a magnetic field intensity B_m exactly equal to the previous one. The two mirror points are called *conjugate* points because they are joined by the field line which is the guiding center of this helical motion. The particle actually spends most of its time at these mirror points.

The second interesting consequence which follows from conservation of the first adiabatic invariant is acceleration of the particle by an increasing magnetic field. As noted above, the only sources of energy to

maintain a constant magnetic moment in an increasing field are the particle motion and the field. If the field is changing, the particle may maintain its magnetic moment by increasing its perpendicular momentum at the expense of the magnetic field. Consider a particle that is mirroring so that all of its momentum is perpendicular momentum. If the field then increases, the field must accelerate the particle to increase the particle's perpendicular momentum (which must be done to conserve the total flux enclosed within the particle's gyration path). Note that the particle still has the same magnetic moment after it has been accelerated as it had previously, but it is now at a higher energy. The reverse process also works: a decreasing field will decelerate particles. Geomagnetic activity does both, producing radial displacements in the process. If the third adiabatic invariant, discussed below, is violated, the result is radial diffusion (a process in which particles initially on the same field line are transported to higher and lower field lines) which results in a net increase of energetic particles in the outer zone. These energetic particles then diffuse both inward and outward.

The Second Adiabatic Invariant

The bounce motion described above also has an associated invariant, called the *second adiabatic invariant*. Basically it is the total magnetic field energy contained within the envelope of the helical path between mirror points. (This function, like the other invariants, can be evaluated as a line integral. This will be discussed in more detail under *McIlwain's L Parameter*.) Note that if the magnetic field is increased, the energy density is increased. The radius of gyration is reduced to compensate (first invariant, described above), but the path length must also be reduced. Thus the mirror points must be raised. Conversely, if the field weakens, mirror points can also be lowered and the particles could be lost into the atmosphere. The bounce period is only a weak function of the equatorial pitch angle of the particle (the angle between the particle velocity and the magnetic field line at the magnetic equator) since the particles spend most of their time at the mirror points. The bounce period can be approximated by [2]:

$$2\pi/\Omega_2 = (4 L R_e / v) T(y) \quad (2)$$

where: L = McIlwain's parameter

R_e = Earth radius

$y = \sin \alpha$ where α is the equatorial pitch angle

and $T(y)$ is given by [2]:

$$T(y) = 1.3802 - 0.31985(y + y^{1/2})$$

The Third Adiabatic Invariant

Because the field has a radial gradient and curvature, the radius of curvature of the gyration or orbit about the field line is larger at the top of the orbit than at the bottom (top and bottom referenced with respect to the Earth radial direction). Thus the path does not quite close into a circle and the next orbit starts slightly eastward (for electrons) or slightly westward (for positive ions) from the previous gyration. This advance in position results in a drift motion around the Earth. After one drift period around the Earth, the particle will be back at the same location in the field where it started, provided the field is quiescent. The locus of points through which the particle passes is called its *drift shell*. The total flux enclosed by this shell must again be conserved. It is the conservation of this flux function, or *third adiabatic invariant*, that causes the particle drift shell to close after one drift period. However, during the time required for a particle to drift around the Earth (Figure 2), the magnetic field itself may change. During large magnetic storms, the change can be quite substantial, up to 1%. After one drift period, the particle may find itself on a different drift shell with a different field intensity (and therefore a different energy). The resulting violation of the third adiabatic invariant is the primary source of particle acceleration in the magnetosphere.

The drift frequency is a function of the bounce frequency (note the $T(y)$ in Eqn. 2 shows up in Eqn. 3) and can be approximately represented by [2]:

$$2\pi/\Omega_3 = -(3L/2\pi\gamma)(\gamma^2-1)(c/R_e)^2(m_0/qB_0)D(y)/T(y) \quad (3)$$

where $D(y)$ is given by

$$D(y) = 1/12[5.5208-.4381y-.6397(y \ln y + y^{1/2})]$$

and B_0 is the value of the Earth's magnetic field at the surface of the earth at the equator. Figure 2 presents a summary of approximate gyration, bounce, and drift frequencies for electrons and protons as a function of energy and L .

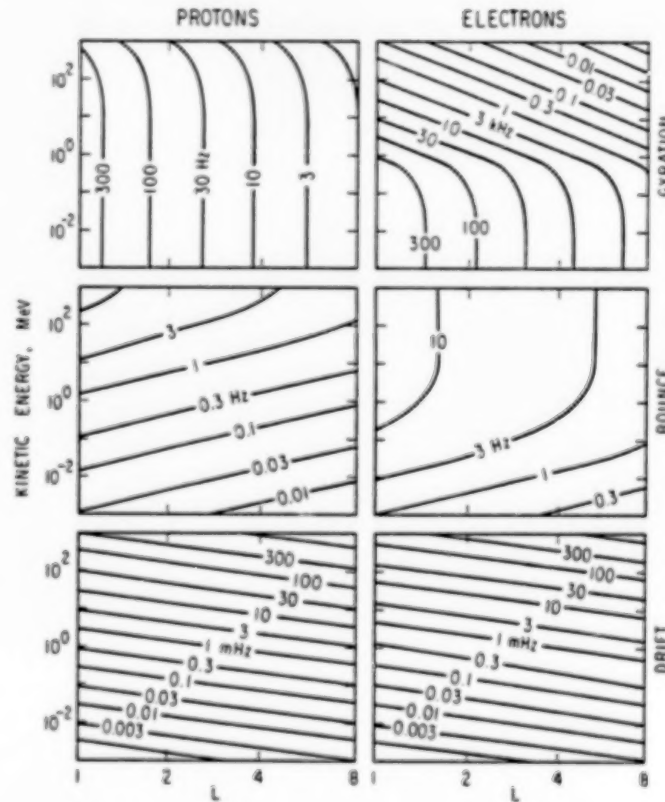


Figure 2. Gyration, Bounce and Drift Frequencies for Electrons and Protons in the Earth's Magnetic Field [2].

Mcllwain's \dot{L} Parameter

As a result of conservation of the first invariant, a particle's instantaneous pitch angle as it moves along a field line can be expressed in the form

$$\sin^2 \alpha_i / B_i = \text{constant} \quad (4)$$

where: α_i is the particle pitch angle at location i
 B_i is the magnetic field intensity at the same location

As a consequence of this relationship between B and α , if one knows the pitch angle of a particle at any point on the field line between the mirror points, one also knows B_m (which is the point at which $\alpha = 90^\circ$). The loci of these mirror points as the particle drifts around the Earth are two rings of constant B_m (one in each hemisphere). Provided one knows the unidirectional flux all along the field line below a point, the relationship expressed by the equation above permits the conversion of unidirectional fluxes to omnidirectional fluxes along the same region of the field line. In a similar manner, one can reconstruct the

unidirectional flux from the omnidirectional flux. However, in practice it is much easier to measure the unidirectional flux along the field line (it can be done from a single equatorial point by using an instrument that scans in the angle α) than to measure the omnidirectional flux distribution (which would have to be done by making measurements at closely-spaced points all along the field line).

As a particle drifts around the earth, the conservation of the second invariant results in the particle's guiding center tracing out a shell which connects the two rings of mirror points. The third invariant produces the result that the shell is closed upon itself--a particle remains on the same shell as it drifts around the earth. Of course, if the magnetic field varies during a drift period (or bounce or gyration), the adiabat associated with that motion will no longer be precisely conserved. As previously stated, such violation of conservation due to magnetic field fluctuations results in pitch angle diffusion, cross-field particle diffusion, and in changes in the energy of the particles.

Mapping of the particle population in the magnetosphere requires multi-dimensional labelling: particle species; energy; pitch-angle; altitude, latitude, longitude. The task of mapping the radiation environment is greatly simplified by reducing the three spatial coordinates to two magnetic coordinates, B and L, which are essentially the drift shells (L) and mirror rings (B_m) described above. The adiabatic invariant associated with the bounce motion, I, is obtained by integrating the function $(1-B/B_m)^{1/2}$ between the mirror points. Since this is awkward to do in a nonuniform field (the field has to be represented by a multipole expansion), an approximate relation is derived which can be related to a dipole field: $L^3 B / M = F(I^3 B / M)$. Here M is the dipole moment of the geomagnetic field. The function F can be calculated at a number of points, generating an interpolation table. L then becomes a simple calculation [1]. Note that for the real magnetic field, L is only an approximate representation of I, although a sufficiently accurate representation for mapping purposes. For a dipole, $L = R$, where R is the normalized distance from the center of the dipole to the equatorial crossing of the field line labeled "L". For our purposes, the dipole approximation will provide some understanding without belaboring the mathematics:

$$R = L \cos^2 \lambda \quad (5)$$

$$B = M/R^3 (4 - 3 R / L)^{1/2} \quad (6)$$

where R and λ are the usual radial distance and magnetic latitude in a dipole field, M is the dipole moment, and L is McIlwain's parameter. Note that R and λ are not sufficient to describe the spatial characteristics of the particle distributions since a given particle does not drift at a constant R or mirror at a constant λ except in a true dipole field where the azimuthal symmetry produces a degeneracy. The above expression shows that in a dipole field, L would correspond to the radial distance from the center of the Earth to the equatorial crossing of the magnetic field ($\lambda = 0^\circ$).

The Radiation Belts

The Earth's magnetosphere contains a wide variety of charged particles, primarily electrons and protons, with energies ranging from the thermal (less than 1 eV) to highly relativistic (tens of MeV for electrons, BeV for protons). The ionosphere contains a cold plasma, in the 1 eV energy range, with densities of the order of $10^6/\text{cm}^3$. The ionosphere is generally considered to consist of the neutral and ion components up to about 1000 km altitude, with the region above this called the plasmasphere (since the constituents there are highly ionized, forming a plasma). The plasmasphere particle density drops slowly until a boundary, called the plasmopause, is reached in which the cold plasma density drops abruptly by about 2 orders of magnitude, from 10^3 to 10^4 per cm^3 to below 100 per cm^3 . The location of the plasmopause is local-time and magnetic-activity dependent but is generally found between $L=4$ and $L=5$ and generally follows the field line to higher latitudes rather than an altitude contour. Beyond this region, hot plasma clouds, with temperatures of the order of 1 to 10 keV or more, are sometimes encountered. The plasma is heated by magnetic processes in the tail and auroral regions of the magnetosphere. In the remainder of this section, we will restrict our discussion to the energetic particle populations >40 keV. They will be discussed by location or zone and by species.

When Prof. Van Allen's detector passed through the magnetosphere in a radial direction, the count rate in the detector first increased, then decreased, and then increased again. Two distinct zones of trapped radiation were being traversed. These were named the *Van Allen belts* and are commonly referred to as the *inner zone* and the *outer zone*, with a region known as the *slot* separating them. Only for electrons are these zones distinct. Figure 3, which presents data from a period when copious fluxes of fission electrons were still present from the Starfish nuclear explosion in space, shows the minimum between the inner zone and outer zone. The inner zone, which is generally considered to cover the region $1.0 < L < 2$, has a peak in flux intensity at about $L=1.5$ for 1 MeV electrons. The region $2.0 < L < 2.8$ is generally considered the slot region where magnetospheric processes result in a low intensity of electrons during magnetically quiet periods. The process which removes the electrons is a resonant interaction between energetic electrons and whistler-mode (right circularly polarized) electromagnetic waves. The interaction results in some of the particles being scattered to lower angles (relative to the magnetic field line) such that their new mirror points are within the atmosphere. The atmosphere absorbs them. Thus the slot region normally contains relatively low fluxes of particles. At times of large magnetic storms, the slot can be refilled and quite high flux levels can be observed there for a few days. The location of the slot is quite variable: during large geomagnetic storms, the minimum between the inner and outer zone can be very narrow and may be displaced to a low L value, even centered as low as $L=2.0$. Immediately after a storm, the slot may be completely filled with electrons and so does not exist. An extensive discussion of these dynamics is available elsewhere [3]. The outer electron zone, which is extremely variable, typically peaks around $3.5 < L < 4.0$. In the outer zone, significant fluxes of electrons with energies in excess of 5 MeV are observed after major magnetic storms. During extended quiet periods, the outer zone may almost disappear at high energies. The difference in flux intensity from minimum to maximum may be as high as 5 orders of magnitude. See, for example, Figure 2 of [3] or Figure 7 of [4].

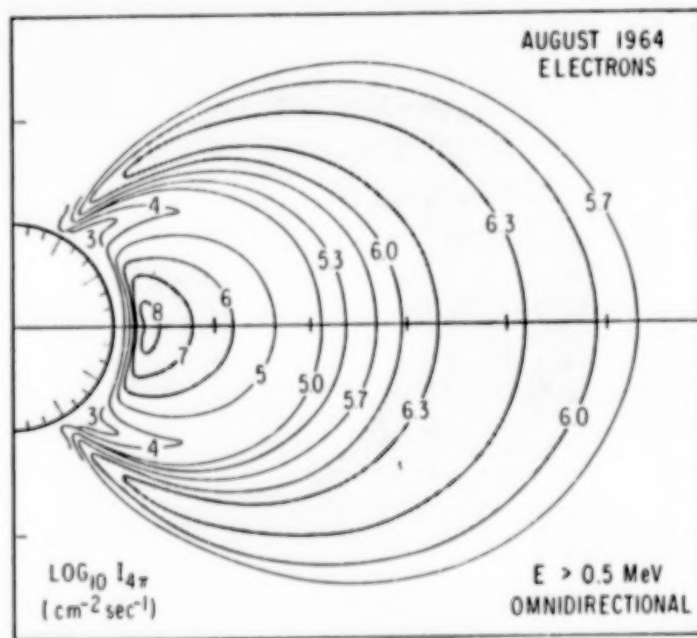


Figure 3. Inner and Outer Zone Electron Belts. The numbers on the contours are the \log_{10} of the integral omnidirectional flux, $I_{4\pi}$. The intense inner zone was due to the Starfish fission source. For times subsequent to 1968, the maximum inner zone intensity is several orders of magnitude lower.

The proton environment is sometimes separated into two constituents also, but in this case the separation is done on the basis of the energy of the protons. The same region of space that constitutes the inner zone for electrons contains very energetic protons, some with energies in excess of 200 MeV, which are also the result of the cosmic-ray albedo neutron decay described in the section on inner zone electrons.

There is another source of trapped protons. Low energy protons, from either a solar wind or ionosphere source, are accelerated similarly to the energetic electrons. Some of the initial acceleration for

ionospheric electrons is produced by electric fields, especially in the auroral zone. The low energy proton belt can be considered to be composed primarily of protons with energies below 10 MeV. These lower-energy protons are present in both the inner and outer zones. There is no slot such as occurs for the electrons. The peak in proton flux intensity depends on the energy, with lower energy protons peaking farther out. The 1 MeV proton flux is at its maximum at about $L = 3$.

TRAPPED PARTICLE POPULATIONS

In this section, we will briefly describe the four major components of the magnetospherically trapped energetic particle population---the inner and outer electron zones, the energetic proton belt, and the low energy proton population. The sources of the particles and their general flux levels as a function of L and energy will be discussed. Solar flare protons, which are discussed in the later section on modelling, will not be discussed in this section because the contribution of flare protons *which become trapped* to the fluxes observed in most orbits is negligible. Flare protons in the polar region may be a major concern for some satellites, but those particles are not trapped.

Inner Zone Electrons

The source of the inner zone electrons is a combination of cosmic-ray albedo neutron decay (CRAND) and radial diffusion through the slot from the outer zone. In the CRAND mechanism, cosmic rays interact with air molecules in the upper atmosphere, producing energetic neutrons, some of which escape back into space. Since neutrons are uncharged, they cross magnetic field lines unimpeded. However, some decay while still in the magnetosphere and the decay products, an electron and a proton, are charged and so become trapped. The end-point energy of the electron in neutron decay is slightly under 1 MeV. The contribution of the neutron's velocity to the electron's energy is small. As a result, there are few electrons with energies in excess of 1 MeV in the inner zone. Electrons with higher energies are present in small numbers, especially above about $L=1.65$ after large magnetic storms, but can be ignored as a hazard to space systems except for their background effects in sensors.

Inner zone electrons below about 1000 km have lifetimes that are primarily determined by the scale height of the atmosphere. During solar-active periods, the increased scale height results in a reduced lifetime and lower average fluxes. This is reflected in the models by having a solar maximum and a solar minimum version. Farther out in the inner zone, electrons are quite stable, with typical lifetimes of 400 days [5]. Principle loss mechanisms are probably any or all of the following: radial diffusion into the atmosphere (violation of the second and third invariants caused by magnetic storms); interaction with whistler-mode waves produced by lightning strokes (the resonant interaction between these waves, also known as cyclotron waves, and the electrons results in a lowering of the electron pitch angle, causing it to be absorbed by the atmosphere at the end of the field line); interaction with VLF waves from ground-based transmitters.

The order-of-magnitude of the electron fluxes at $L=1.45$ in the inner zone are as follows: $> 10^8$ for $E_e > 0.1$ MeV; $> 10^6$ for $E_e > 1$ MeV; $> 10^5$ for $E_e > 2$ MeV. The numbers represent the integral, omnidirectional fluxes $\text{cm}^{-2}\text{-sec}^{-1}$. Below about $L = 1.55$, the fluxes are quite stable, with little variation being observed over the solar cycle [6] except for altitudes below 1000 km where atmospheric effects are observed. Above $L= 1.6$, major magnetic storms inject electrons with energies up to at least 1.2 MeV [3]. Figure 4 shows the equatorial omnidirectional inner zone electron flux intensities as a function of L and energy.

Outer Zone Electrons

The outer zone electrons originate either as solar wind electrons in the tail of the magnetosphere or as ionospheric electrons at high latitudes which are accelerated up the field lines. Magnetic field fluctuations cause them to be diffused radially inward, energizing them. The acceleration is a consequence of the conservation of the first adiabatic invariant coupled with violation of the third invariant, discussed earlier, by magnetic activity. As the particles are transported to field lines deeper in the magnetosphere, the increase in the average field intensity has to be compensated by an equivalent increase in particle momentum, or energy. The various fluxes peak at different locations in the outer zone for different energies, with the higher energies peaking at lower L . Representative outer zone fluxes are of the order of: $> 10^8$ for $E_e >$

0.1 MeV, $L = 6$; $> 10^7$ for $E_e > 1$ MeV, $L = 5$; $> 10^5$ for $E_e > 4$ MeV, $L = 4$. Units are as described for the inner zone fluxes.

Outer zone electron fluxes are highly variable, with increases at a given energy on a given L shell being as great as 5 orders of magnitude in less than a day. These large increases are caused by major magnetic storms, where $D_{st} > -150\gamma$. D_{st} is a global magnetic field disturbance index which is generally responsive to low latitude variations caused by a magnetospheric ring current. This ring current is composed of low energy ions accelerated by the magnetic storm. Typical decay constants for outer zone electrons are of the order of 10 days. In addition to the radial diffusion of particles caused by magnetic storms, they also cause pitch-angle scattering of the particles. Thus particles which were previously stably trapped on a field line (had mirror points that were above the atmosphere everywhere along their drift paths), can be perturbed so that they now mirror within the residual atmosphere below 100 km at some point along their drift path. At this altitude, the atmosphere absorbs the particles. A low altitude satellite which is normally below the trapped radiation zones (except when traversing the South Atlantic Anomaly) may suddenly find itself bathed in large fluxes of energetic electrons at midlatitudes when it encounters these particles which show up low on the outer zone field lines (sometimes called the *horns* of the outer zone). The South Atlantic Anomaly is a region of anomalously low magnetic field strength. Since particles mirror at a constant B_m , they attain at their lowest mirror altitude in the South Atlantic Anomaly.

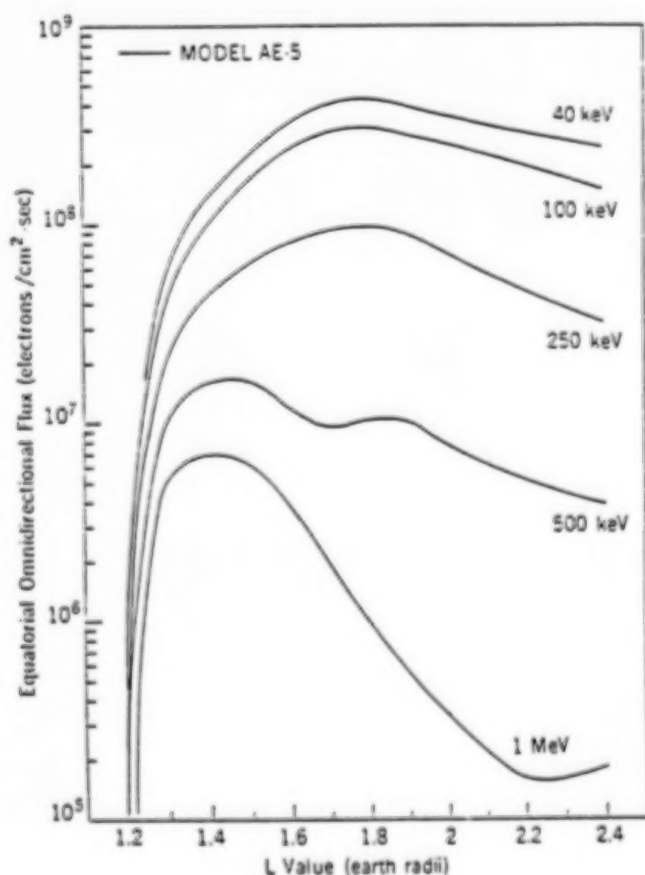


Figure 4. Inner Zone Electron Flux Intensities [6]

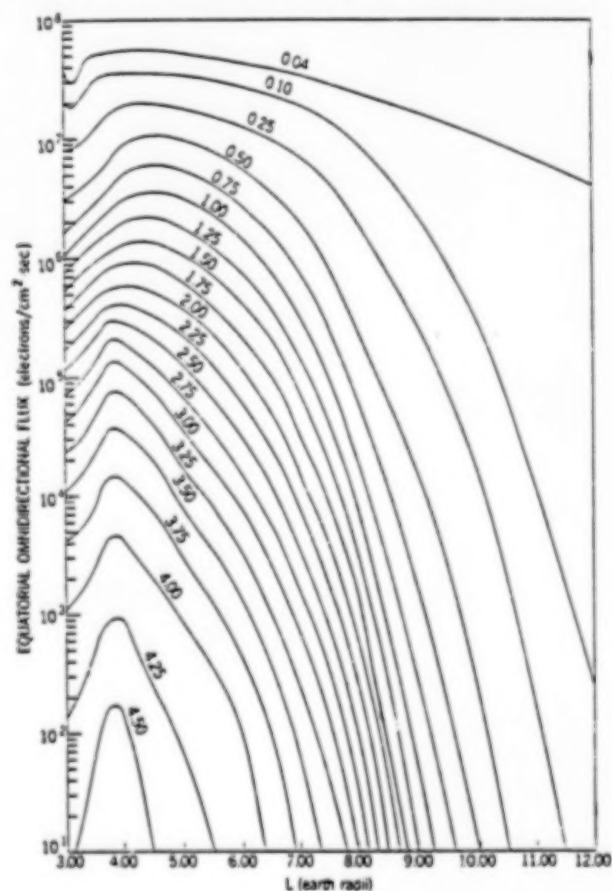


Figure 5. Outer Zone Electron Flux Intensities [7]

Energetic Protons

The source of the energetic protons which are present in the inner zone is CRAND, the mechanism mentioned previously. They are quite stable, with minor variations in intensity occurring at low altitudes due to variations in the atmospheric density due to solar activity. Typical intensities are of the order of

$> 10^4$ for $E_p > 100$ MeV and $> 10^3$ for $E_p > 300$ MeV, both at $L = 1.45$. Due to the secular variation in the magnetic field, a very slow decrease which may be an indication that the earth's field will undergo a reversal in the geologically-speaking near future (10^4 years?), the energetic proton environment is also exhibiting a small decrease (the decreasing field intensity is driving the protons into the atmosphere, again due to conservation of the adiabatic invariants). A serious problem in particle modelling due to this secular decrease in field intensity will be discussed in the section on models.

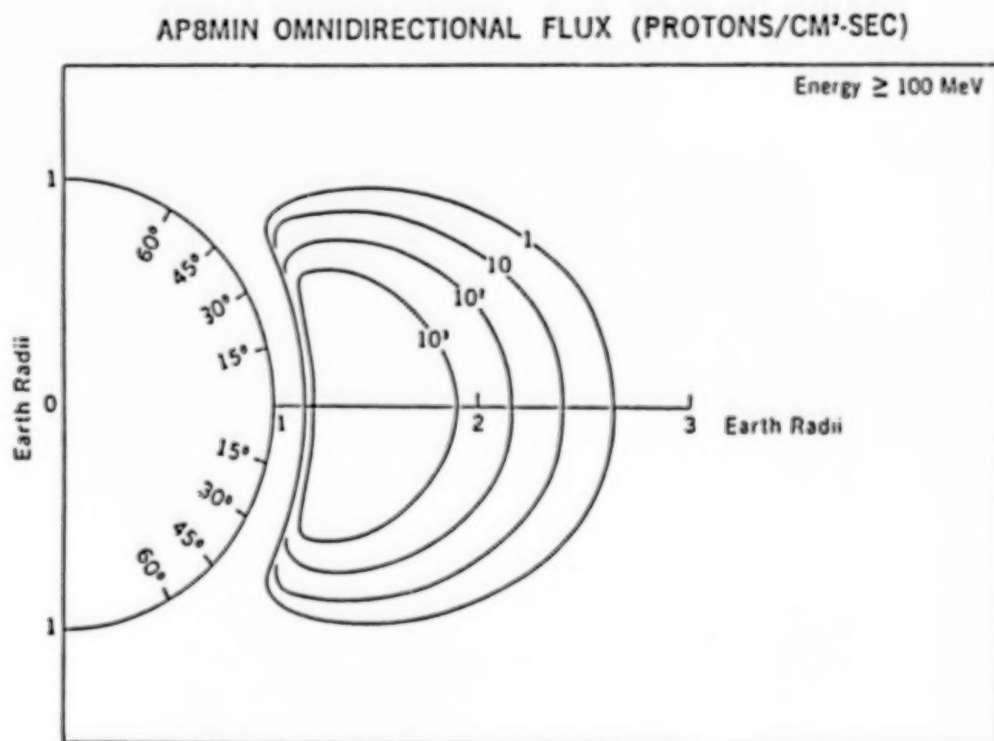


Figure 6. High Energy Protons in the Inner Zone [8]

Low Energy Protons

The low energy protons with which we are concerned here are in the 0.5 to 5 MeV range, since there are large fluxes of such particles in both the inner and outer zone and they have significant materials effects. Particles with these energies can originate in a number of sources: radial diffusion and energization of solar wind particles which enter the geomagnetic tail, similar to the outer zone electrons; ionospheric acceleration up field lines, with subsequent radial diffusion and acceleration; direct access of solar flare protons. Typical intensities in the outer zone are $> 10^8$ for $E_p > 0.1$ MeV; $> 10^7$ for $E_p > 1$ MeV; $> 10^5$ for $E_p > 10$ MeV; $< 10^2$ for $E_p > 100$ MeV. Again, these are omnidirectional, integral fluxes in units of $\text{cm}^{-2}\cdot\text{sec}^{-1}$. While the fluxes are subject to variation due to magnetic storm activity, the variations are much smaller than for electrons. The primary loss mechanisms are deenergization through collisions with the residual atmosphere and charge-exchange, which results in an energetic neutral particle which is not trapped by the magnetic field.

CURRENT STATUS OF PARTICLE MODELS

In this section, we will cover the currently recommended particle models, their ranges and estimates of accuracy, discuss briefly their sources, availability, future modelling plans, and requirements for additional data. A more extensive discussion of the modelling efforts at the National Space Science Data Center is presented elsewhere [9].

Inner Zone Electron Models

The current NSSDC models which provide useful inner zone ($L = 1.2$ to 2.4) electron data are AE5 [6], for solar minimum, AE6 [10], for solar maximum, and AE8 [9] for either solar minimum or maximum. The energy range of these models is from 0.04 MeV to 5 MeV, although present techniques can not make reliable measurements of electrons with energies above 2 MeV below about $L=1.55$ in the inner zone. They are empirical models, being based on in-situ measurements of the fluxes. To produce the models, data is acquired from investigators, corrected, edited, averaged, interpolated, extrapolated, etc; in other words, it is all very thoroughly massaged. Some estimate of its reliability is also made, but such a step is very subjective. In general, the temporal coverage for any data set is six months or longer. The measurements were made between 1964 and 1977 (although data up to 1968 include Starfish electrons). Starfish contamination has been removed from the data in generating the above models. Newer data are available for incorporation into models [9]. The accuracy of the models is very good, better than a factor of two, for energies below 1 MeV and $L < 1.65$. Above $L=1.65$, the variability of the flux levels themselves produce uncertainty. Above 2 MeV, the fluxes are extrapolations and their accuracy is unknown.

The models, and codes for running them, are available from NSSDC. In addition to a tape format, the codes are also available as files on a VAX at NSSDC. The VAX is a SPAN (Space Physics Analysis Network) node. Thus, anyone with access to SPAN or other networks which can connect to SPAN (such as TELENET, ARPANET, BITNET, etc.) can access these files to download them to their home computer via the network. Dr. James Green is in charge of SPAN at NSSDC. Alternatively, the codes can also be run interactively on the NSSDC VAX at no charge to the user (other than his own costs of connecting to the SPAN network). An alternate interactive resource is EnviroNET [11], which is resident on a MicroVAX at GSFC and is accessible as the SPAN node ENVNET. To access EnviroNET, the user name ENVIRONET and password HENNIKER are used.

Future plans for the inner zone modelling activity are to incorporate newer data bases and also perhaps include some storm-time dynamics. It may not be possible to accomplish the latter task with presently available data bases, but the CRRES mission [12] has as one of its objectives the acquisition of the data required for producing dynamic particle models.

Outer Zone Electron Models

In-situ electron flux data in the outer zone are far from satisfactory for generating electron models. Most of the data used are extrapolations in both energy and altitude. At the geosynchronous region, measurements up to 1.7 MeV have been available from ATS-1. Near the equator, S³ provided measurements from about $L=2.5$ to $L=6$, but only up to 300 keV. OGO-5 had an electron channel at 2.7 MeV but the satellite orbit inclination was 27° so it made no measurements near the equatorial region. All other satellites which traversed the equatorial region at high altitude either had no high energy electron measurements ($E_e > 1.5$ MeV) or the energy threshold and detector efficiency were not known with sufficient accuracy to be usable in modelling. The source of the orders-of-magnitude discrepancies seen in comparisons of energetic outer zone electrons (e.g., Figure 12 of [4]) are these uncertainties. All other sources of data used in the models are extrapolations of measurements made low on the field line.

The current NSSDC outer zone models ($L > 2.4$) which provide useful results are the following: AE7-Lo and AE8 for solar minimum and AE7-Hi for solar maximum or long duration missions (> 5 years). For geosynchronous satellites, another model is still relatively valid--AE3 [13]. For long term missions, AE7-Hi is probably accurate to within a factor of two, especially for $L < 6$ and $E < 5$ MeV. However, if the mission includes the period a year or two following the sunspot maximum when the magnetic storm activity is greatest, AE7-Hi will err on the low side (actual integrated fluences can be expected to be greater than the model prediction). AE7-Hi was generated in response to criticisms that the earlier models, AE4 and AE6, were deficient in high energy electrons, and seriously so. In fact, in those models the energy spectra were truncated at 5 MeV, as is also done in AE8. A comparison of the models with in-situ data [4] showed that the models predicted fluxes that were low by about a factor of three, but almost the entire deficiency was in electrons > 1.5 MeV. The result was a prediction of dose in heavily shielded satellite components that was low by an order of magnitude. AE7-Hi, which truncates the energy spectrum at 7.5 MeV, has also been criticized for truncating the spectrum, since electrons with energies up to 10 MeV have been

measured at geosynchronous orbit [14]. Figure 7 shows the equatorial flux contours as a function of L and energy which are contained in AE7-Hi [15].

AE8 exists in two forms, AE8MIN and AE8MAX, which are supposed to represent the environment during solar minimum and maximum. However, both are truncated at 5 MeV and cannot properly model the solar maximum period when large fluxes of very energetic electrons appear. AE8 uses a single outer zone model and uses AE5 and AE6 solar minimum and solar maximum inner zone models. The major difference between AE8 and AE7-Hi is in the high energy electron flux at around $L = 4$. The AE7-Hi model contains about a factor of two greater flux at 3 MeV and about a factor of 10 greater flux at 4.5 MeV. At solar minimum, there are relatively few energetic electrons and any of the later models, AE7-Hi, AE7-Lo, AE8MIN, and AE8MAX are satisfactory for any use except calculating background rates in detectors. The models are probably accurate to a factor of three for dose calculations.

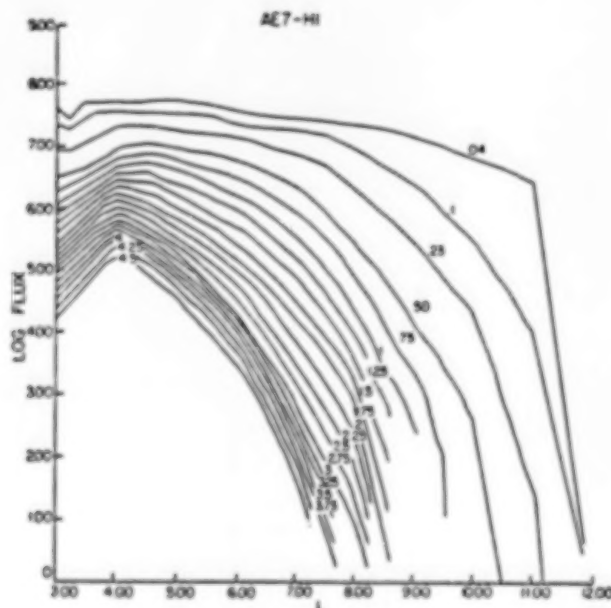


Figure 7. AE7-Hi Equatorial Electron Flux Contours [15].

As in the inner zone case, future plans are to incorporate new data in an attempt to increase the accuracy of the models and to include a dynamic model (addressing both the prediction of electron increases due to magnetic storms and the evolution of the fluxes after the increases). The Radsat portion of the CRRES mission [12] has two outer zone electron modelling goals: obtain data in the outer zone nearer to the equator than has been done previously in order to reduce the amount of extrapolation that has been necessary for model generation; obtain a data base which can be used to generate a dynamic model.

Proton Models

The current proton models are AP8MIN and AP8MAX, again representing the solar minimum and maximum periods. The major effect of the solar variation is the variation in atmospheric density at lower altitudes: at solar maximum, the higher scale height of the atmosphere decreases the energetic proton fluxes. The models are probably accurate to 50% or better. They cover the energy range from 100 keV to 400 MeV and the L range from 1.17 to 7. The data were obtained during the same time period that the inner zone electron data was obtained. Figure 8 shows the equatorial flux contours as a function of L and energy provided by AP8MIN. Since the MIN model predicts slightly more flux than the MAX model, it can be used during solar maximum or for long term missions as a conservative model.

One major problem with the energetic proton models is the fact that they are organized in terms of B,L. The secular variation in the earth's magnetic field (the dipole term is diminishing) causes the energetic proton ensemble, which is nominally very stable, to be carried to lower altitude. The model does not take into account the increased atmospheric density the protons will encounter at the lower altitude. As a result, if calculations are made with the magnetic field projected well into the future (more than ten to fif-

teen years), totally invalid results are obtained for low altitudes such as the Space Station orbit [16]. Since the source of the energetic protons is the decay of energetic neutrons produced in the upper atmosphere by cosmic rays, the geometry of the production process relative to the atmosphere will not change. The future configuration of the inner zone proton belt probably will not change relative to the present configuration, provided both are described in terms of L and B/B_0 , where B is the magnetic field at the point in question and B_0 is the equatorial intensity on the same field line. One will almost certainly get a more accurate result for a calculation of the proton environment for Space Station in the year 2025 by making the calculation with the present field model than by extrapolating the field 35 years into the future.

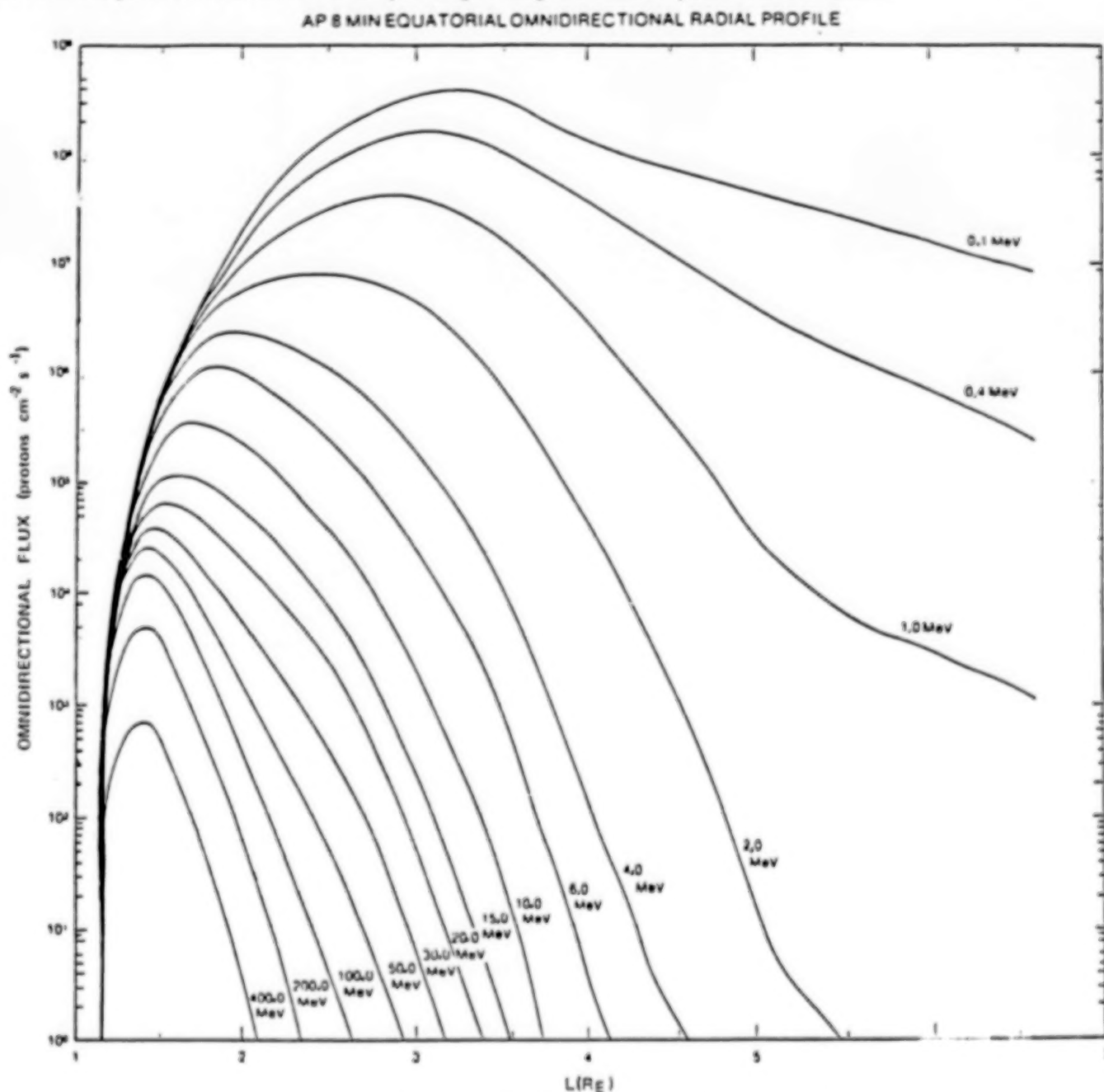


Figure 8. AP8MIN Equatorial Proton Flux Contours [15].

Solar Flare Proton Models

Solar flare protons are treated separately because they are transient and show up in the outer zone only in relatively small numbers. Their major impact is in the case of low altitude polar-orbiting satellites which normally receive relatively little particle irradiation--and almost all of that in short infrequent traversals of the South Atlantic Anomaly region. For some satellites, the major portion of the particle environment they encounter during their lifetime may occur during one or two major solar flare particle events, each lasting only a few days. In a typical solar cycle of 11 years, 90% of the energetic proton fluence is the result of a single anomalously large flare. The integrated fluence over the polar caps from the one event can be of the order of $2 \times 10^{10}/\text{cm}^2$ $P+ > 30$ MeV. Averaged over a solar cycle, the annual fluence is about $5 \times 10^8/\text{cm}^2$ $P+ > 30$ MeV over the polar cap. At 100 MeV, these numbers are about a factor of 30 lower. A low altitude polar orbiting satellite spends roughly 40% of its time at latitudes where these protons can gain access. Thus such a satellite may receive virtually all of its energetic proton dose from solar flares rather than from the magnetospherically-trapped protons.

FUTURE MODELLING REQUIREMENTS

The major efforts in modelling must be directed toward the electron environments, since the energetic inner zone protons are relatively stable and well understood and the outer zone protons can be described well statistically. Within limits, their evolution after a storm is also generally predictable. This is primarily due to the relative ease with which proton measurements can be made. Also, the studies of the physics of the protons have been more productive. The CRRES mission [12] is expected to provide additional high-quality data for the proton dynamics modelling.

While a large amount of data is available which has not yet been used to update the various trapped radiation models, there are significant gaps in the electron data bases. A major reason for this is the difficulty of separating the signal from a small flux of these particles from the large background of protons and cosmic rays. One of these gaps was mentioned previously: No useful data base has ever been obtained in the outer zone for electrons above 300 keV between about $L=2.8$ and geosynchronous orbit at geomagnetic latitudes below about 20° . CRRES will lower this limit to 10° . Above 2.8 MeV no data is available for altitudes above 8000 km except for some geosynchronous orbit measurements [14]. In the inner zone above 2 MeV, no usable measurements are available because of tremendous penetrating proton background problems in detectors. CRRES will not be able to furnish this type of data, either, because its primary radiation mission is an engineering one and electrons above 2 MeV in the inner zone can be ignored. (If you have problems measuring them, they are unlikely to cause a problem on operational vehicles.)

One major area which has not been modelled is the dynamics of the radiation belts in response to magnetic activity. One report [17] attempts to correlate the response of the outer zone to the magnetic index K_p , but the particle data were all obtained at geosynchronous orbit and the field lines that are represented in the K_p index are high latitude field lines which thread through the geosynchronous region. Hence, that study is limited in validity to the geosynchronous region. Low altitude measurements indicate that in general the outer zone does not correlate with K_p , except incidentally when major magnetic storms occur, but does have some relationship with D_{st} , the low latitude index mentioned previously. The intention is to get the type of data base from CRRES that one needs to address the dynamics modelling.

In order to be useful, the dynamics models have to address three issues *quantitatively*: a) The prediction of magnetic storms which produce increases in the outer zone energetic electron and proton populations; b) The energy spectra and L profiles of the fluxes as a function of the magnetic storm parameters; and c) The evolution of the distribution as a function of time (and magnetic activity) post-storm. The first of these requires a better understanding of the solar-terrestrial coupling physics and may have to await completion of the Global Geophysics Program (aka International Solar-Terrestrial Physics program) which is scheduled to start launching satellites in the 1993 time period [12]. A first step for b) and c) would be to make a statistical model of particle storm and post-storm behavior from a large data base. Again, CRRES is designed to provide the data base for such an effort and current plans include developing such a statistical model.

REFERENCES

- [1] McIlwain, Carl E., Coordinates for Mapping the Distribution of Magnetically Trapped Particles, *J. Geophys. Res.*, 66, 3681-3691, 1961.
- [2] Schulz, M. and L. J. Lanzerotti, *Particle Diffusion in the Radiation Belts*, Springer, New York, 1974.
- [3] Vampola, A. L., "Natural Variations in the Geomagnetically Trapped Electron Population," in *Proceedings of the National Symposium on Natural and Manmade Radiation in Space*, NASA TM X-2440, E. A. Warnan, Ed., 1972.
- [4] Vampola, A. L., J. B. Blake and G. A. Paulikas, "A New Study of the Magnetospheric Electron Environment," *J. Spacecraft and Rockets*, 14, 690, 1977.
- [5] Stassinopoulos, E. G. and P. Verzariu, General formula for decay lifetimes of Starfish electrons, *J. Geophys. Res.*, 76, 1841, 1971.
- [6] Teague, M. J., and J. I. Vette, *The Inner Zone Electron Model AE-5*, NSSDC WDC-A-R&S 72-10, 1972.
- [7] Singley, G. W., and J. I. Vette, *A Model Environment for Outer Zone Electron*, NSSDC WDC-A-R&S 72-13, 1972.
- [8] Sawyer, D. M., and J. I. Vette, *AP-8 Trapped Proton Environment*, NSSDC WDC-A-R&S 76-06, 1976.
- [9] Bilitza, D., D. M. Sawyer, and J. H. King, Trapped Particle Models at NSSDC/WDC-A-R&S, NASA CP-3035, p. 569, May 1989.
- [10] Teague, M. J., K. W. Chan and J. I. Vette, *AE-6: A Model Environment of Trapped Electrons for Solar Maximum*, NSSDC WDC-A-R&S 76-04, 1976.
- [11] Lauriente, M., EnviroNET: Space Environments for SDIO Experiments, this proceedings.
- [12] Hardy, D. A., The Radiation Belt Mission on CRRES, Presented at the Space Environmental Effects on Materials Workshop, June 1988.
- [13] Vette, J. I. and A. B. Lucero, Models of the Trapped Radiation Environment, Vol. III: Electrons at Synchronous Altitudes, NASA SP-3024, 1967.
- [14] Baker, D. N., R. D. Belian, P. R. Higbie, R. W. Klebesadel, and J. B. Blake, "Hostile Energetic Particle Radiation Environments in Earth's Outer Magnetosphere," in *The Aerospace Environment at High Altitudes and its Implications for Spacecraft Charging and Communications*, AGARD CP 406, p. 4-1, 1986.
- [15] *Handbook of Geophysics and the Space Environment*, A. S. Jursa, Ed., AFGL/AFSC, 1985. NTIS Accession No. ADA 167000.
- [16] Konradi, A. and A. C. Hardy, "Radiation Environment Models and the Atmospheric Cutoff" *J. Spacecraft and Rockets*, 24, p. 284, 1987.
- [17] Nagai, T., "Space weather forecast: Prediction of relativistic electron intensity at synchronous orbit," *Geophys. Res. Lett.*, 15, 425, 1988.

EFFECTS OF SPACE RADIATION
ON
ELECTRONIC MICROCIRCUITS

W. A. Kolasinski
Space Sciences Laboratory
The Aerospace Corporation
El Segundo, California

INTRODUCTION

Originally, as the title of my talk implies, I was going to discuss briefly the cumulative effects of radiation dose on integrated microcircuits and then cover in some detail the instantaneous Single Event Phenomena (SEP) associated with energetic, individual particles (protons or heavier ions) striking the device sensitive region(s). However, since Jim Raymond has covered in admirable fashion the subject of total dose effects in his talk yesterday, it would be presumptuous and ill-advised on my part to belabor the subject; instead, I shall avail myself of the opportunity to address topics which are more closely related to the work I am currently involved in. Before leaving the subject of total dose behind, I would like to mention that because of the large populations of energetic protons and electrons in the radiation belts, displacement damage in solid state devices can play a larger role here than in other regions of space. Furthermore, the penetrating nature of the trapped radiation precludes in general the use of shielding as a means of mitigating total dose damage.

Without further ado, let us now turn to single event effects or phenomena (SEP), which so far have been observed as events falling in one or another of the following three classes:

1. Single Event Upset (SEU),
2. Single Event Latchup (SEL) and
3. Single Event Burnout (SEB).

Single event upset is defined as a lasting, reversible change in the state of a multistable (usually bistable) electronic circuit such as a flip-flop or latch. In a computer memory, SEUs manifest themselves as unexplained bit flips. Since latchup, as discussed yesterday by Jim Raymond is in general caused by a single event of short duration, the "single event" part of the SEL term is superfluous. Nevertheless, it is used customarily to differentiate latchup due to a single heavy charged particle striking a sensitive cell from more "ordinary" kinds of latchup. Single event burnout (SEB) refers usually to total instantaneous failure of a power FET when struck by a single particle, with the device shorting out the power supply. Needless to say, an unforeseen failure of this kind can be catastrophic to a space mission.

SINGLE EVENT PHENOMENA: EARLY HISTORY

Figure 1 is a summary of the early events leading up to and resulting in our preoccupation with SEP. During the early 1960's, reverse-biased silicon diodes came into widespread use as nuclear particle detectors both on the ground and in

Early History

- 1962
 - UPSET BY COSMIC RAYS PREDICTED
- 1973
 - UPSSETS OBSERVED ON INTELSAT IV
- 1978
 - UPSSETS PRODUCED BY BEVELAC IRRON BEAM
 - PAPERS ON COSMIC RAY UPSET PUBLISHED BY SEVERAL GROUPS
- 1979
 - RESULTS OF EXPERIMENTS ON PROTON AND HEAVY ION ACCELERATORS REPORTED BY SEVERAL GROUPS
 - REPORT ON UPSSETS INDUCED BY ALPHAS FROM RADIOACTIVE DECAY

Figure 1. Early History of SEP.

space. The particle-detection process depends on the fact that an energetic ion, while passing through the depletion region of a reverse-biased p-n junction, generates electron-hole pairs along its track. These are swept out of the region by the electric field across the junction and produce a current pulse at the diode output. The amount of charge collected at the output is proportional to the energy lost by the particle in passing through the junction.

In 1962, Wallmark and Marcus¹ made the logical deduction that the same physical process which allows nuclear particle detection by semiconductor devices could lead to a spurious response by ever smaller silicon devices being used with increasing frequency in space systems. They correctly predicted that the problem would emerge when device miniaturization reached a certain critical level beyond which circuit elements would become sensitive to spurious charge

pulses created by the passage of heavy cosmic rays through vulnerable regions. D. Binder and coworkers² reported observations of upsets in JK Flip-Flops on board Intelsat IV. After a careful study they attributed these upsets to cosmic rays. In 1978 upsets of dynamic RAMs in space were reported by Pickel and Blandford³ who explained the observed upset rate in terms of the known cosmic ray environment and its effect on the devices in question. Later that year Kolasinski et al⁴ simulated directly the effect of heavy cosmic rays on solid state memories with the use of a very energetic iron beam from the Lawrence Berkeley Laboratory (LBL) Bevalac accelerator. They continued the work in 1979 using the 88-in. Cyclotron at LBL and discovered SEL in the process⁴. In approximately the same time frame investigators at the Naval Research Laboratory⁵ and the Air Force Geophysical Laboratory⁶ were actively studying upsets caused by protons with energies like those of protons trapped in the inner Van Allen belt. Since that time, numerous manifestations of the various SEP have been observed in semiconductor devices both on the ground and in space-borne systems. Figure 2 is a summary of

SEU Rates in Space
UPSETS PER 10^6 BITS PER DAY
(COURTESY OF E.C. SMITH, HUGHES AIRCRAFT CO)

PROGRAM	PART TYPE	RATE
INTELSAT IV	JK FLIP-FLOP	16.0*
PIONEER VENUS	PMOS SHIFT REGISTER	7.0
PV/O	SCHOTTKY TTL 64 BIT RAM	12.0
EO	MISC ANOMALIES	10.0
GPS	4096 BIT NMOS RAM	10.0

Fig. 2. Observations of SEU in Space.

Idealized SEU Events

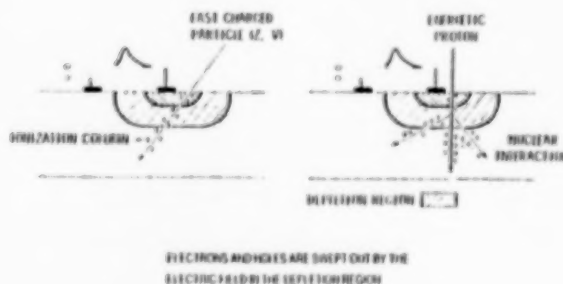


Fig. 3. Pictorial View of the SEP Process.

some of the early observations of SEU in space. An excellent review of the early days of SEP studies, together with a bibliography up to 1982 has been written by Sanderson et al.⁷

THE NATURE OF SINGLE EVENT EFFECTS

When considering any single event effect associated with an integrated circuit chip, it is important to keep firmly in mind the instantaneous and microscopic nature of the underlying process. In other words, the time during which charges are generated in the sensitive region is negligible compared with the time for charge collection; also, the initial diameter of the charge column is smaller than or comparable to the size of the sensitive region. This is in contrast to other common radiation effects such as cumulative total dose damage or response to a short burst of flash x-rays or particles, where the whole chip is bathed in radiation.

Figure 3 above depicts in schematic form the essential features of the mechanism responsible for SEP. At left on Fig.3, a heavy ion traversing the reverse-biased junction depicted on the chip produces a dense track of ionization (electron-hole pairs). The charges move to the electrodes under the electric field within the so-called depletion region, which to first order is the sensitive region for SEU. Upon being collected, the charges produce a current pulse at the circuit node. The linear charge density along the track is proportional to the rate at which the particle loses its energy, or its "linear energy transfer" (LET) in technical jargon. The higher the particle LET and track length within the sensitive region, the higher the deposited charge and hence the node current which may result in a single event upset or other phenomenon.

An upset occurs when a certain minimum amount of charge (the critical charge) has been collected at the circuit node in a time small in comparison with the circuit response time. Generally this prompt charge-collection time is in the pico-second domain, while the circuit time constants are measured in nanoseconds. The circuit critical charge divided by the longest dimension (track length) within the sensitive volume is defined as the threshold LET for a given SEP.

On the right hand side of Figure 3 we see a somewhat different phenomenon taking place. Here, an energetic proton like those trapped in the radiation belt collides with a silicon nucleus within the depletion region, and a nuclear reaction in the form of scattering, neutron emission, fragmentation etc. takes place. As we shall see in a moment, the proton LET is too low to produce enough current for an upset, but by transferring its energy and momentum to the nuclear reaction products whose LET is much higher, the proton can produce an upset. Clearly, the lower the threshold LET of the device for upset with heavy ions, the more vulnerable will the device be to upset by protons. Since the trapped radiation zones contain large fluxes of energetic protons, spacecraft traversing these zones are subject to an increased rate of SEP.

Figure 4 summarizes the process of ion interaction with matter. As we can see, dE/dx and hence LET varies as the

square of the nuclear charge (atomic number) and inversely as the square of the ion velocity. The table at the bottom of

Charged Particle Interaction with Matter

- PARTICLE LOSES ENERGY BY IONIZATION OF ATOMS IN MATERIAL BEING PENETRATED
- ENERGY LOSS PER UNIT PATHLENGTH $\frac{dE}{dx} \propto \frac{Z^2}{v^2}$
 - PARTICLE NUCLEAR CHARGE
 - PARTICLE VELOCITY
- THE VALUE OF $\frac{dE}{dx}$ RELATIVE TO HYDROGEN FOR SEVERAL IONS AT A GIVEN VELOCITY IS GIVEN IN THE TABLE

ION	$(dE/dx)_{ion} / (dE/dx)_H$
H ⁺	1
O	64
Ar	324
Fe	676
Pu	8836

Fig. 4. Ion Interaction with Matter.

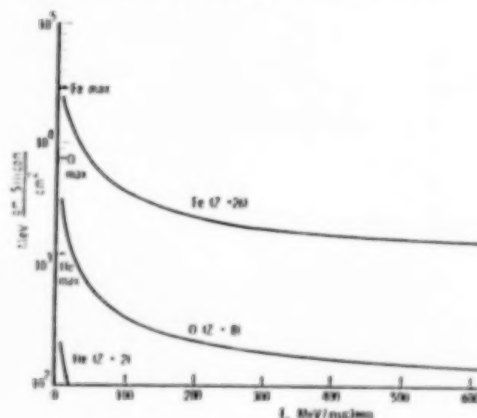


Fig. 5. Energy Dependence of LET.

Figure 4 shows the LETs of several ions relative to protons. We see that the linear charge density along an iron track is almost 700 times that produced by a proton with the same velocity. The increase of LET with increasing atomic mass can be shown more dramatically by multiplying the numerator and denominator of the expression for dE/dx in Fig. 4 by M , the nuclear mass. The denominator now becomes the ion energy, and we note that the rate of energy loss or LET varies directly as the product of ion mass and the square of its charge, and inversely with the energy. Another way of looking at the inverse-square dependence of LET on ion velocity is to remember that velocity squared is essentially energy divided by the ion mass, where the latter equals the mean bound nucleon (ie, proton or neutron) mass times the number of nucleons. Thus LET varies as the square of the nuclear charge and inversely as the energy per nucleon.

This functional form of LET is shown in Fig. 5 for the three major cosmic-ray constituents, not counting protons. Note that LET (vertical axis) is expressed here in units of MeV/(g/cm²), ie, the energy lost in traversing a thickness of material weighing 1 g/cm². In some applications it is more useful to express LET in units of pC/micron. I shall leave it as an exercise for the reader to show that 1 pC/micron in silicon is equivalent to 98 MeV/(mg/cm²). Looking at the oxygen curve in Fig. 5, we note that at 100 MeV/nucleon (1.6 GeV total energy), the oxygen nucleus loses roughly 300 MeV in traversing 1 g/cm² of silicon. To stop it completely would require several g/cm² of shielding. Thus at these energies, shielding against energetic ions in space is impractical except in a few very special cases.

SPACE-RADIATION ENVIRONMENTS RESPONSIBLE FOR SINGLE EVENT EFFECTS

Single event effects in microelectronics are caused primarily by three types of radiation environments in space: galactic cosmic rays, solar cosmic rays and trapped charged particles. While this session is devoted to the effects of trapped

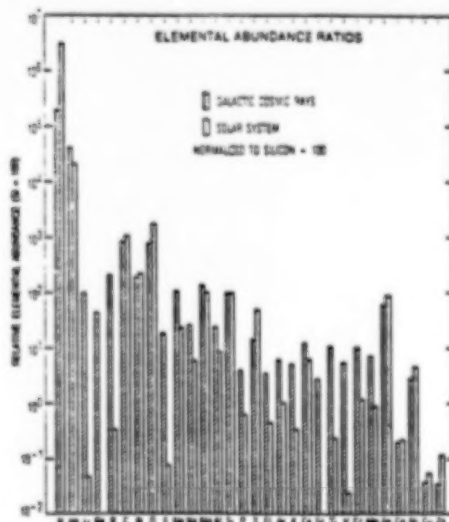


Fig. 6. Cosmic Ray Abundance Ratios.

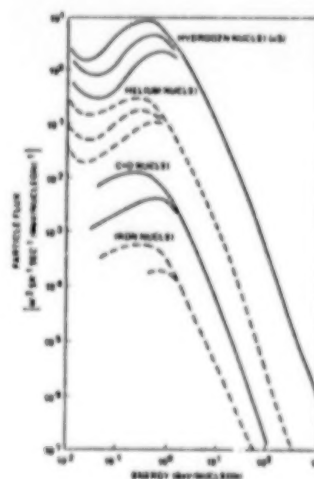


Fig. 7. Cosmic Ray Energy Spectra.

radiation, I shall briefly discuss the other two environments, since to a greater or lesser extent they coexist with the third in many regions of space and are the major contributors to SEP. In the previous talk, Al Vampola presented a very thorough description of the trapped environment, so I shall only comment briefly on its aspects pertaining to SEP.

Galactic Cosmic Rays

Figures 6 and 7, respectively, show the relative abundances and energy spectra of the galactic cosmic rays. The most prominent in this environment are protons, alpha particles, nuclei in the carbon and oxygen group and finally the nuclei with atomic numbers close to that of iron. A very exhaustive and detailed description of the environment has been given by J. H. Adams⁸, including an analytical formulation and review of the experimental data on which it is based. It is important to note that the environment is most severe at spacecraft-orbit altitudes exceeding a few thousand kilometers. At lower altitudes and inclinations below approximately 50 degrees, the earth's magnetic field keeps out a large portion of the low to medium energy flux of the heavy ions. In the polar regions, however, these ions reach low altitudes by spiralling along magnetic field lines, so that the flux intensity is not reduced very much over that at high altitude.

The galactic cosmic ray intensity is modulated by the 11-year cycle of solar flare activity, with the maximum flux occurring during minimum solar activity and vice-versa. Hence the term "solar-minimum flux" refers to the highest intensity flux and so implies the most severe environment. This can be confusing to someone uninitiated to the technical jargon. The degree of solar cycle modulation of the flux is shown by the branches in the spectra of Figure 8.

Solar Flare Particles

An example of heavy ion fluxes associated with a solar flare is shown in Fig. 8. Since solar flares occur sporadic-

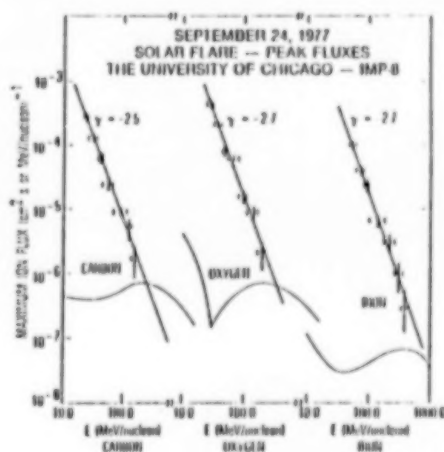


Fig. 8. Particle Fluxes in a Heavy Ion Rich Solar Flare.

ally, so does the associated environment. As in the case of galactic cosmic rays, it is the energetic charged particles, accelerated near the sun during some solar flare events, that cause single event phenomena and total dose damage. Our understanding of solar activity is too rudimentary for us to be able to predict far in advance the exact onset time of a solar flare. Individual flare occurrences appear to be quite random, except that their frequency follows the 11-year sunspot cycle mentioned above.

Most solar flares produce proton fluxes which do not contribute significantly to the single event rate. Generally, the flux of the heavier ions in those flares also is not very significant. However, as the example in Fig. 8 shows, flares rich in heavy ions do occur sometimes, and the flux of medium energy heavy ions from such a flare can exceed the galactic background by more than one order of magnitude. Finally, a "monster" flare like the one in August, 1972 can cause general havoc in spacecraft systems. It is indeed fortunate that these events are rare and of relatively short duration (a few hours to a day or so). A summary of recent solar flare environment data of interest in single event effects work has been published by Chenette and Dietrich⁹.

In regions around the Earth, only the inner Van Allen belt is of concern, and even then only for devices with relatively low degree of immunity against single event effects. The trapped proton flux in the inner belt is many orders of magnitude higher than the flux of galactic cosmic rays. However, as was pointed out above, protons can cause single event effects in currently available devices only indirectly, by way of nuclear reactions in or near the device sensitive regions. Since the probability of these reactions taking place is extremely small, only a few of the devices currently used in space are vulnerable to proton induced single effects. More will be said on this subject later.

EXPERIENCE IN ORBIT

Early observations of SEU on various spacecraft with payloads containing MSI and LSI devices have already been shown in Figure 2. Here the data all seem to cluster around an upset rate of approximately 1 upset per day for a 100,000-bit memory and the rate does not appear to depend strongly on the device technologies used in the various spacecraft.

More recently, Blake and Mandel¹⁰ have published upset rates in CMOS/bulk RAMs on board a spacecraft in a low altitude, polar orbit. The observed rate of approximately 3×10^{-7} per bit per day is considerably lower than the values appearing in Figure 3. At the other end of the scale, upset rates in the neighborhood of 3×10^{-3} per bit per day have been observed in low power bipolar RAMs on board the LEASAT vehicle¹¹.

Upsets have also been observed in devices flown by the NASA Goddard Space Flight Center on the Space Shuttle as part of the Cosmic Ray Upset Experiment (CRUX). The payload flew in an orbit with 57 degrees inclination. It contained complements of VLSI, NMOS dynamic and static RAMs, as well CMOS non-volatile PROMs. No upsets were observed in the PROMs, while the RAM SEU rates fell in the range of 10^{-7} - 10^{-6} upsets per bit per day. Clearly, there appears to be a large range of vulnerability to SEU among the various device technologies.

SUMMARY OF GROUND-TEST AND MODELING ACTIVITY

In view of the fact that the severity of single event effects in space can range from inconsequential to catastrophic,

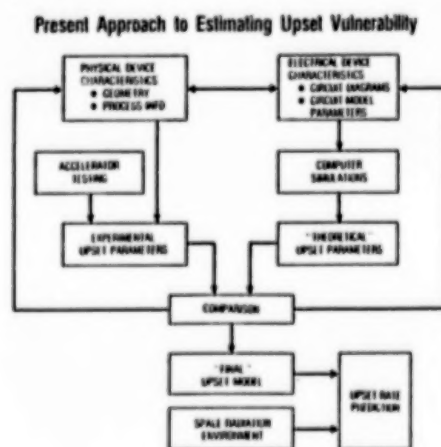


Fig. 9. Flowchart of Modeling Effort.

it is not surprising that during the past decade considerable effort has been expended in testing, modeling and hardening devices against single event effects. The ultimate objectives of these efforts are to acquire the capability of predicting the single event effect rates in orbit for commercially available devices, to harden existing payload designs wherever feasible, and to develop new device technologies resistant to single event effects. Attempts to attain these objectives have concentrated on device modeling, circuit analysis, ground testing of devices and test structures, and acquisition of on-orbit data. This work is briefly summarized below. Figure 9 is an idealized flow-chart of the activities which result in a prediction of single event rate in space.

The parameters absolutely necessary for predicting the single event rate are the minimum charge(s) needed to induce a single event such as an upset, the geometry of the sensitive region(s) and the charge-collection efficiency at the relevant circuit node(s). Because of the fast and microscopic nature of the single event process, circuit parameters like the critical charge or the current-pulse shape cannot be simulated and measured with conventional electronic test equipment.

Instead, theoretical computer models of field configuration and current flow originating from the ion track are developed and used to determine the extent of the sensitive region and minimum charge density along the ion track needed to initiate a particular type of single event.

Ground tests are then performed to validate the model predictions of minimum charge density and probability of upset (SEU cross-section) in the ion beam. Figure 10 summarizes in schematic form the test activities and type of data ob-

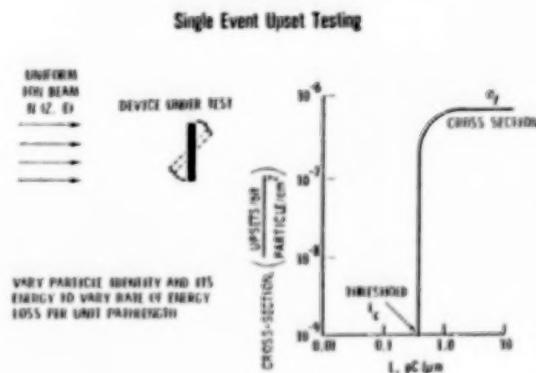


Fig. 10. Summary of Test Procedures.

tained. The devices under test are placed in a uniform beam of protons or heavy ions and exercised in appropriate fashion while being irradiated. The number of bit errors or other upsets, as well as the beam fluence, are recorded and the cross-section computed using the expression

$$\sigma_L = N \sec(\theta) / F,$$

where σ_L , N , θ and F are, respectively, the upset cross-section in cm^2 , number of errors, beam angle of incidence with respect to the chip-surface normal and the total beam fluence in particles/ cm^2 . This process is repeated at various angles of beam incidence and with particles having the range of LETs needed to determine the threshold value of LET. More often than not, the parts have to be de-lidded in order to allow the ions to penetrate into the sensitive region of the device.

After one or more iterations of theoretical simulation and ground testing, heavy ion upset rates are predicted for specific environments using computer programs like J. C. Pickell's Cosmic Ray Induced Error (CRIER)¹² or J. Adams' Cosmic Ray Upset Model (CRUM)¹³ codes. In these calculations, LET spectra for orbits of interest are first generated in the presence of shielding appropriate for the payload under consideration. The dimensions of the sensitive regions and critical charges for upset, generated in the modeling and test efforts are then provided to the programs which generate random path-length distributions and determine which particles within the calculated LET spectrum deposit enough charge to induce the single event effect.

Petersen et al.¹⁴ have developed a simple and useful expression for estimating the upset rate of microcircuit memories in the so-called "10 percent worst case" galactic cosmic ray environment of Adams⁸. The upset rate R , measured in upsets per cell per day, is computed from the expression

$$R = 5 \times 10^{-10} \sigma_L / L_c^2,$$

where σ_L is the upset cross-section expressed in square microns and L_c is the critical LET expressed in pC/micron. This useful "Figure of Merit" is valid in regions of space where the galactic cosmic ray environment is not significantly affected by the Earth's magnetic field. In regions where trapped radiation is dominant, upsets due to galactic cosmic rays will be in general less, and the contribution from trapped protons has to be computed.

We have seen that proton upsets are induced indirectly via nuclear reactions and so the techniques outlined above for calculating heavy ion upset rates in space do not apply in the case of protons. A semi-empirical method for estimating proton induced upsets in spaceborne memories has been developed by Bendel and Petersen¹⁵. Upon examining trends in proton test data obtained on a large variety of devices and reconciling these trends with nuclear reaction data at the low and high proton-energy extremes, they came up with a rather simple and elegant equation for the proton-upset probability or cross-section which depends on just two variables, viz. E , the proton energy and the parameter A which is equivalent to the apparent threshold at low energy. Their result is shown in Figure 11, plotted as a function of proton energy for various fixed

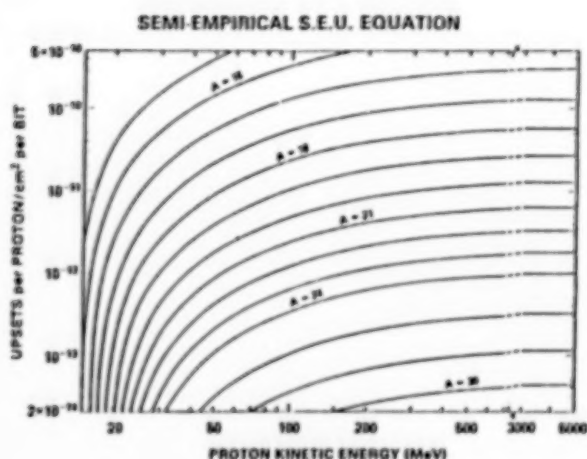


Fig. 11. Bendel and Petersen Model.

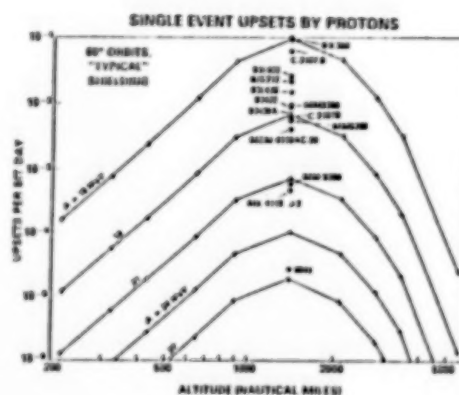


Fig. 12. Predicted Proton SEU Rates.¹⁵

values of the parameter A. Note that in this model, the measurement of the upset cross-section at a single proton energy significantly above threshold is enough to determine the device upset cross-section at all energies and hence the upset rate in any given proton space environment. Figure 12 shows the upset rates predicted by Bendel and Petersen for some devices flying in a 60 degree inclination orbit, at 1400 nm altitude. In Figure 13, the proton SEU rate in a part with A=25 MeV is

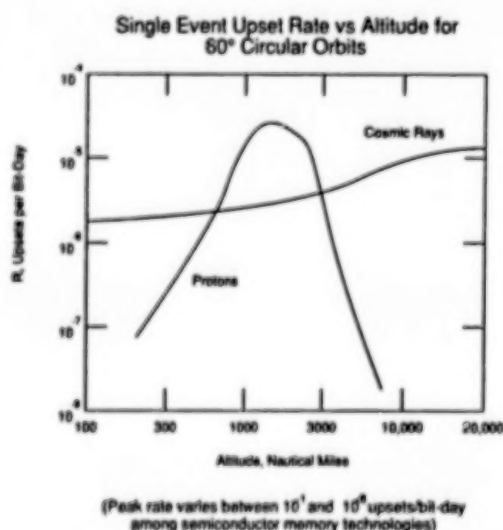


Fig. 13. Galactic and Solar Cosmic Ray SEU Rates Compared.

compared with the upset rate induced by galactic cosmic rays. In general, we would expect the trapped proton contribution to upset rate to dominate in low inclination orbits within the inner Van Allen belt, while in highly inclined orbits the rate should be comparable to the galactic cosmic ray contribution.

Validation of the model predictions is, of course, obtained from observations of single event rates in space. Unfortunately, while some data showing that the predictions are "in the right ballpark" exist, there are not nearly enough of such data, particularly of those acquired under carefully controlled conditions, so that their validity and correlation with an actual environment can be established.

In concluding this talk, I would like to give you an idea of the range of vulnerability of existing device technologies, as determined in the studies outlined above. Figures 14 and 15 show the predicted heavy ion upset rates for some representative device types in bipolar and MOS technologies, respectively. The comparisons listed in Figs. 14 and 15 are based on the Petersen et al. "Figure of Merit"¹⁴ and do not reflect the proton induced SEU rates in the inner Van Allen radiation belt. However, devices showing upset rates of less than 10^{-6} per bit-day can be expected in general to be quite hard against proton-induced SEU. I base this statement on the empirical observation that devices with threshold LETs above

26

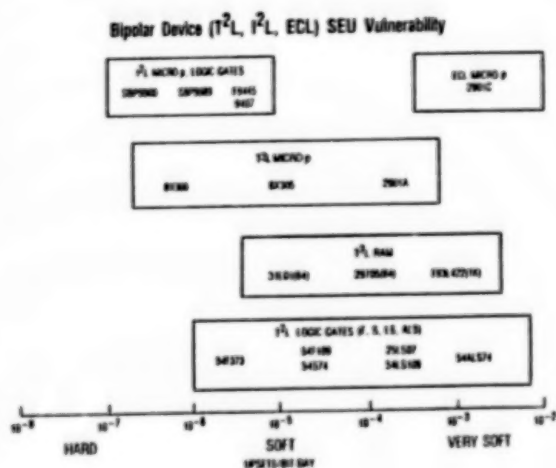


Fig. 14. SEU Rates for Bipolar Devices.

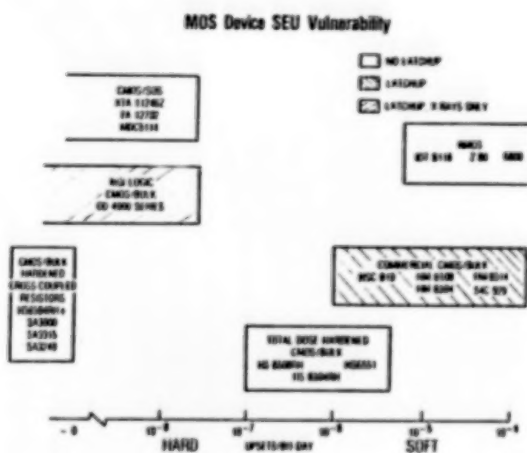


Fig. 15. SEU Rates for MOS Devices

REFERENCES

1. J. T. Wallmark and S. M. Marcus, "Minimum size and maximum packing density of nonredundant semiconductor devices", *Proc. IRE* March, 286-298 (1962).
2. D. Binder, E. C. Smith and A. B. Holman, "Satellite Anomalies from Galactic Cosmic Rays", *IEEE Trans Nucl. Sci.*, **NS-22**, 2675-2680 (1975).
3. J. C. Pickel and J. T. Blandford, "Cosmic Ray Induced Errors in MOS Memory Cells", *IEEE Trans Nucl. Sci.*, **NS-25**, 1166-1171 (1978).
4. W. A. Kolasinski, J. B. Blake, J. K. Anthony, W. E. Price and E. C. Smith, "Simulation of Cosmic Ray Induced Soft Errors and Latchup in Integrated Circuit Computer Memories", *IEEE Trans Nucl. Sci.* **NS-26**, 5087-5091 (1979).
5. C. S. Guenzer, E. A. Wolicki and R. G. Allas, "Single Event Upset of Dynamic RAMs by Neutrons and Protons", *IEEE Trans Nucl. Sci.*, **NS-26**, 5048-5052 (1979).
6. R. C. Wyatt, P. J. McNulty, P. Toumbas, P. L. Rothwell and R. C. Filz, "Soft Errors Induced by Energetic Protons", *IEEE Trans. Nucl. Sci.* **NS-26**, 4905-4910 (1979).
7. T. K. Sanderson, D. Mapper and J. H. Stephen, "Effects of space radiation on advanced semiconductor devices", *Interim Report for the European Space Agency*, **G 2532**, December, 1982.
8. J. H. Adams, R. Silberger and C. H. Tsao, "Cosmic Ray Effects on Microelectronics. Part I: The near-earth particle environment", *NRL Memorandum Report* **4506**, 1981.
9. D. L. Chenette and W. F. Dietrich, "The solar flare heavy ion environment for single-event upsets: a summary of observations over the last solar cycle, 1973-1983", *IEEE Trans. Nucl. Sci.* **NS-31**, 1217-1222 (1984).
10. J. B. Blake and R. Mandel, "On-orbit observations of single event upset in Harris HM-6508 1K RAMs", *IEEE Trans. Nucl. Sci.*, **NS-33**, 1616-1619 (1986).
11. M. Shoga, P. Adams, D. L. Chenette, R. Koga, and E. C. Smith, "Verification of single event upset rate estimation methods with on-orbit observations", *IEEE Trans. Nucl. Sci.*, **NS-34**, 1256-1259 (1987).
12. J. C. Pickel and James T. Blandford Jr., "Cosmic-ray induced errors in MOS devices", *IEEE Trans. Nucl. Sci.* **NS-26**, 1006-1015 (1980).
13. James H. Adams, Jr., "Cosmic ray effects on Microelectronics, Part IV", *NRL Memorandum Report* **5901**, December, 1986.
14. E. L. Petersen, J. B. Langworthy and S. E. Diehl, "Suggested Single Event Upset Figure of Merit", *IEEE Trans. Nucl. Sci.* **NS-30**, 4533-4539 (1983).
15. W. L. Bendel and E. L. Petersen, "Proton Upsets in Orbit", *IEEE Trans. Nucl. Sci.*, **NS-30**, 4481-4485 (1983).

SESSION 7: SOLAR RADIATION

Chairman: Wayne S. Slemp
NASA Langley Research Center

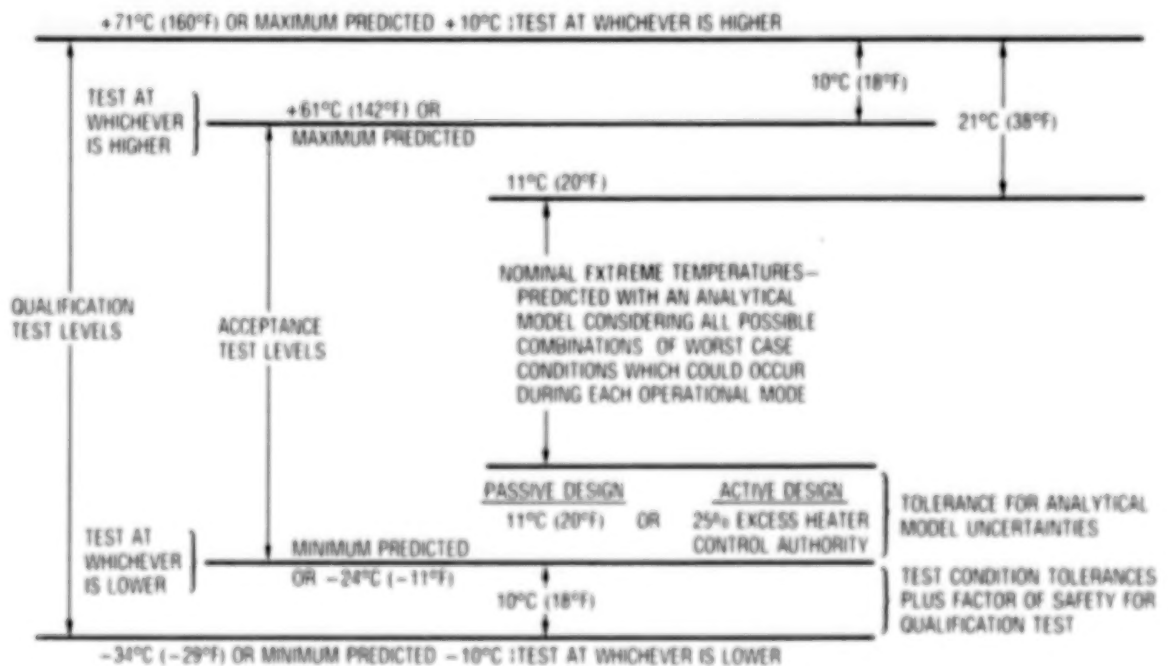
SPACE VEHICLE THERMAL TESTING: PRINCIPLES, PRACTICES,
AND EFFECTIVENESS

Donald F. Gluck
Thermal Control Department
The Aerospace Corporation
El Segundo, California

MIL-STD-1540B TEST REQUIREMENTS FOR COMPONENTS

Component qualification and acceptance temperatures are derived from worst case thermal analyses and analytic uncertainty margin subject to certain specified temperature extremes. Nominal extreme temperatures are predicted by applying an analytical model (e.g., SINDA computer program TMM) to each operational mode which considers worst case combinations of equipment operation, space vehicle attitude, solar radiation, eclipse conditions, degradation of thermal surfaces, et cetera. This must be done component by component, as a worst combination of conditions for one component may not prove to be worst for another. To these results an uncertainty margin is added. This margin, which can be quite large at the beginning of a program (e.g., 20 to 40°C), is reduced as the design and analytic process progresses. Following successful correlation of the thermal analysis with thermal balance test data, this uncertainty margin can be reduced to as little as $\pm 11^\circ\text{C}$. If a component is heater controlled, 25% excess heater control authority is required in lieu of an 11°C temperature margin. These temperatures set component acceptance test levels, subject to the requirement that the mounting plate or case temperature be at least as cold as -24°C and at least as hot as 61°C . These specified extremes are required in order to (a) provide adequate environmental stress screening, (b) demonstrate component survival capability, and (c) assure that temperature-insensitive and high-quality parts and materials are used in component design. Component qualification tests are conducted at temperatures 10°C colder (even if heaters are used for temperature control) and 10°C hotter than the acceptance test temperatures.

For some temperature-sensitive components such as batteries, propellant valves, and inertial reference units, the specified extremes are waived.



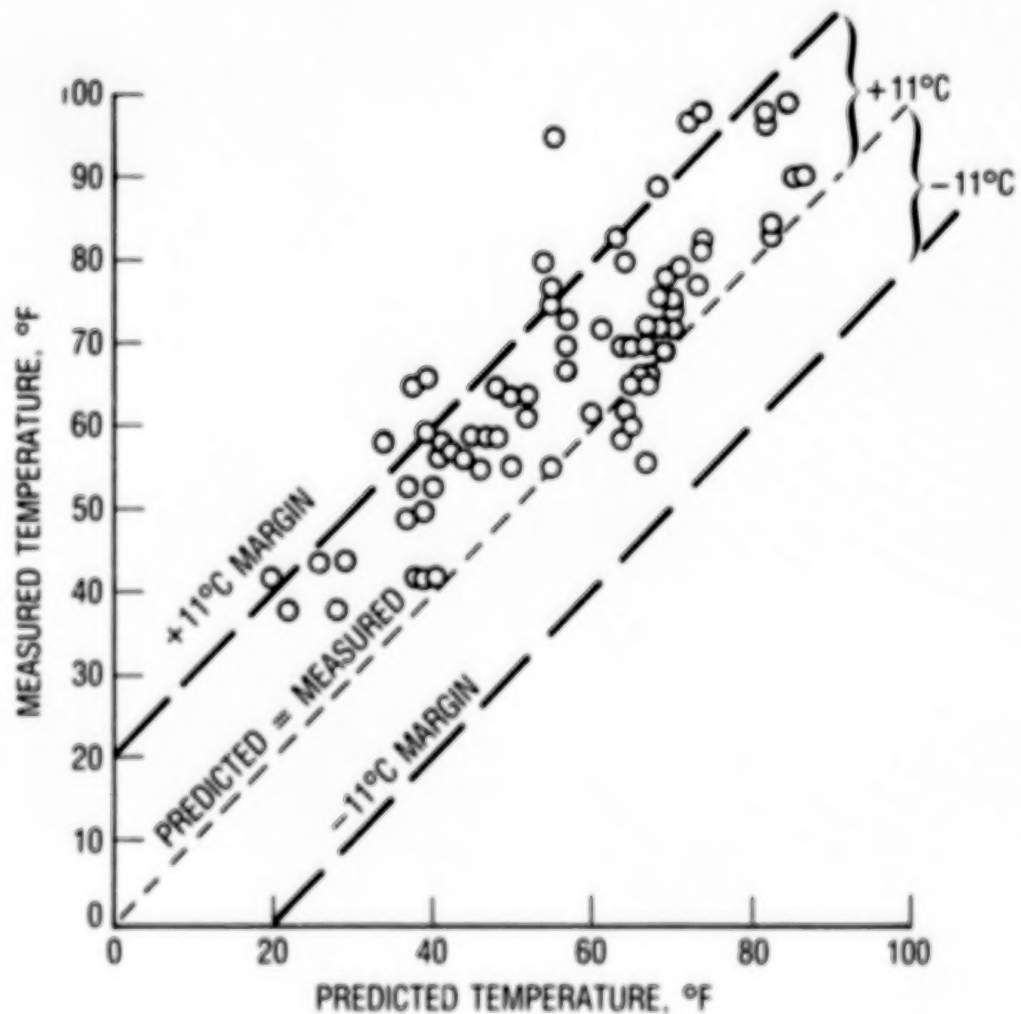
REPRESENTATIVE SPACE VEHICLE THERMAL CONTROL REQUIREMENTS

Temperature requirements are shown for equipment operation within specification and for survival and turn-on (need not operate within specification, but must not experience any degradation when returned to operational range). Temperature excursions for most equipment are seen to be 20 to 50°C above and below room temperature. Components without active electronics which are mounted outboard, such as solar arrays and antennas, are usually designed to withstand wider temperature excursions, particularly at the cold end. Batteries are tightly controlled at cold temperatures to increase life. Payload components such as extremely accurate clocks for precise navigation are controlled over a relatively narrow temperature range.

<u>COMPONENT/SUBSYSTEM</u>	<u>OPERATING TEMPERATURE RANGE (°C)</u>	<u>SURVIVAL/TURN-ON TEMPERATURE RANGE (°C)</u>
DATA HANDLING AND TT&C SUBSYSTEMS	-28.9/60	-28.9/60
ELECTRIC POWER AND DISTRIBUTION SUBSYSTEM	-28.9/60	-28.9/60
EPDS REGULATOR	-28.9/60	-28.9/60
STABILIZATION AND CONTROL COMPONENTS	-28.9/60	-28.9/60
COMPUTER	-28.9/43.3	-28.9/60
DIPOLE RING ARRAY ANTENNA	-150/100	-150/100
CONE ANTENNA	-150/110	-150/110
BICONE ANTENNA	-150/110	-150/110
SOLAR ARRAY	-141/61	-141/61
SOLAR ARRAY DAMPERS	-45.5/55.5	TBD/55.5
PAYLOAD ELECTRONICS	-12.2/43.3	-28/60
PAYLOAD ELECTRONICS	-6.7/43.3	-28.9/48.9 (SURVIVAL)
BATTERIES	0 → 5 (TRICKLE CHARGE) 21.1 (DEEP DISCHARGE)	-6.7/48.9 (TURN-ON) 0/30
PROPULSION SUBSYSTEM	-3.9/26.7	TBD/40
THRUSTERS	-3.9/26.7	TBD/40
RUBIDIUM CLOCK	20/45	-19/45
CESIUM CLOCK	20/45	-19/45

FLTSATCOM-F1 PREDICTED TEMPERATURES VERSUS MEASURED TEMPERATURES,
EQUINOX DIURNAL EXTREMES

The Aerospace Corporation's Thermal Control Department personnel, B. J. Smith and A. L. Bavetta, compared thermal balance test correlated model predictions with on-orbit measurements for the space vehicle FLTSATCOM-F1. Equinox data showed that measured temperatures were skewed towards being higher than predicted. Of 74 temperature measurements, 65 were within $\pm 11^{\circ}\text{C}$ of prediction, with a maximum deviation of 22°C . While the skewing was not necessarily experienced on other space vehicles, the pattern and spread were typical.



STP P78-1 SATELLITE (NO THERMAL BALANCE TEST)
COMPARISON OF ON-ORBIT TEMPERATURE MEASUREMENT WITH
CONTRACTOR ANALYTIC PREDICTIONS

Air Force Space Test Program Satellite P78-1 was launched without a thermal balance test. A comparison has been made of 12th day on-orbit measurements with contractor predictions. The temperature of 10 of 17 components within the wheel (rotating portion of the space vehicle) and 5 of 8 components within the sail (sun-fixed portion of the space vehicle) were within 11°C of the predicted values. The temperature of seven wheel components and three sail components exceeded prediction by more than 11°C, with the largest deviation being 24°C. Agreement between prediction and measurement was substantially poorer than for a typical satellite which had received a thermal balance test.

WHEEL EQUIPMENT, °C

	BATTERIES			ELECTRIC CHARGE CNTR.	POWER SHUNT REQ.	19V REG.	TAPE RECORDERS			TELEMETRY DISTRIBUTION UNIT	TRANS- MITTERS		COMMAND & DATA PROCESSOR	SPIN ASSEMBLY	AZIM. DRIVE ASSEMBLY	REFRIGERATOR PAA ELECTRONICS	
	1	2	3				A	B	C		1	2				GAMMA 3	GAMMA 4
ON-ORBIT TEMPERATURE MEASUREMENT 12th DAY AFTER LAUNCH	17	18	17	18	15	18	20	27	15	16	17	25	31	27	18	7.5	10
CONTRACTOR PREDICTION, NORMAL RESOLUTION	11	11	10	13	6	7	15	15	8	8	0	8	7	10	11	-9	-6

SAIL EQUIPMENT, °C

	REMOTE COMMAND AND DATA PROCESSOR		AMPLIFIER		AUXILIARY CONTROL ELECTRONICS	TRUNNION	NUTATION DAMPER	SOLAR ARRAY
	1	2	SERVO	POWER				
ON-ORBIT TEMPERATURE MEASUREMENT 12th DAY AFTER LAUNCH	21	16	28	24	30	24	25	63
CONTRACTOR PREDICTION, NORMAL RESOLUTION	14	21	15	19	7	16	2	55

THE BASIS OF MIL-STD-1540's TEMPERATURE UNCERTAINTY MARGIN

The table is supported by The Aerospace Corporation's data base. An uncertainty margin of 11°C is used in MIL-STD-1540 for analytic predictions correlated to thermal balance test results. Note that the intent of the standard is to provide 95% confidence that acceptance test temperatures will not be exceeded during mission life.

STANDARD DEVIATION	PERCENT OF CONFIDENCE	TEMPERATURE UNCERTAINTY (°C)	
		UNVERIFIED ANALYTICAL PREDICTIONS	PREDICTIONS VERIFIED BY TESTING
1.0	68%	8.3	5.6
1.4	85%	12.2	7.8
2.0	95%	16.7	11.0
3.0	99%	25.0	16.7

MIL-STD-1540 COMPONENT TEST BASELINE

MIL-STD-1540 defines a component as "a functional unit that is viewed as an entity for purposes of analysis, manufacturing, maintenance, or record-keeping. Examples are hydraulic actuators, valves, batteries, electrical harnesses, and individual electronic boxes such as transmitters, receivers, or multiplexers." Components are made up of modules and assemblies which, in turn, are made up of piece parts. Test and screens are conducted at these lower levels of assembly. However, the lowest level of assembly addressed in MIL-STD-1540 is the component level.

These tables are abstracted from tables in this Standard. Thermal vacuum, thermal cycling, and burn-in are component thermal tests and screens. MIL-STD-1540 requires thermal cycling rather than elevated temperature burn-in. Functional tests, while not considered here as thermal tests, are required at temperature extremes during thermal cycling and thermal vacuum tests.

COMPONENT QUALIFICATION TESTS

TEST	REFERENCE PARAGRAPH	SUGGESTED SEQUENCE	ELECTRONIC OR ELECTRICAL EQUIPMENT	ANTENNAS	MOVING MECHANICAL ASSEMBLY	SOLAR PANEL	BATTERIES	VALVES	FLUID OR PROPULSION EQUIPMENT	PRESSURE VESSELS	THRUSTERS	THERMAL EQUIPMENT	OPTICAL EQUIPMENT
FUNCTIONAL	6.4.1	1 ⁽¹⁾	R	R	R	R	R	R	R	R	R	R	R
THERMAL VACUUM	6.4.2	9	R	R	R	R	R	R	R	O	R	R	R
THERMAL CYCLING	6.4.3	8	R	O	O	O	O	O	O	—	—	—	—

COMPONENT ACCEPTANCE TESTS

TEST	REFERENCE PARAGRAPH	SUGGESTED SEQUENCE	ELECTRONIC OR ELECTRICAL EQUIPMENT	ANTENNAS	MOVING MECHANICAL ASSEMBLY	SOLAR PANEL	BATTERIES	VALVES	FLUID OR PROPULSION EQUIPMENT	PRESSURE VESSELS	THRUSTERS	THERMAL EQUIPMENT	OPTICAL EQUIPMENT
FUNCTIONAL	7.3.1	1 ⁽¹⁾	R	R	R	R	R	R	R	R	R	R	R
THERMAL VACUUM	7.3.2	7	R ⁽²⁾	O	R	O	R	R	R	O	R	R	R
THERMAL CYCLING	7.3.3	6	R	O	O	O	O	O	O	—	—	—	—
BURN-IN	7.3.9	8	R	—	O	—	—	R	—	—	R	—	—

LEGEND R = REQUIRED
O = OPTIONAL TEST
— = NO REQUIREMENT

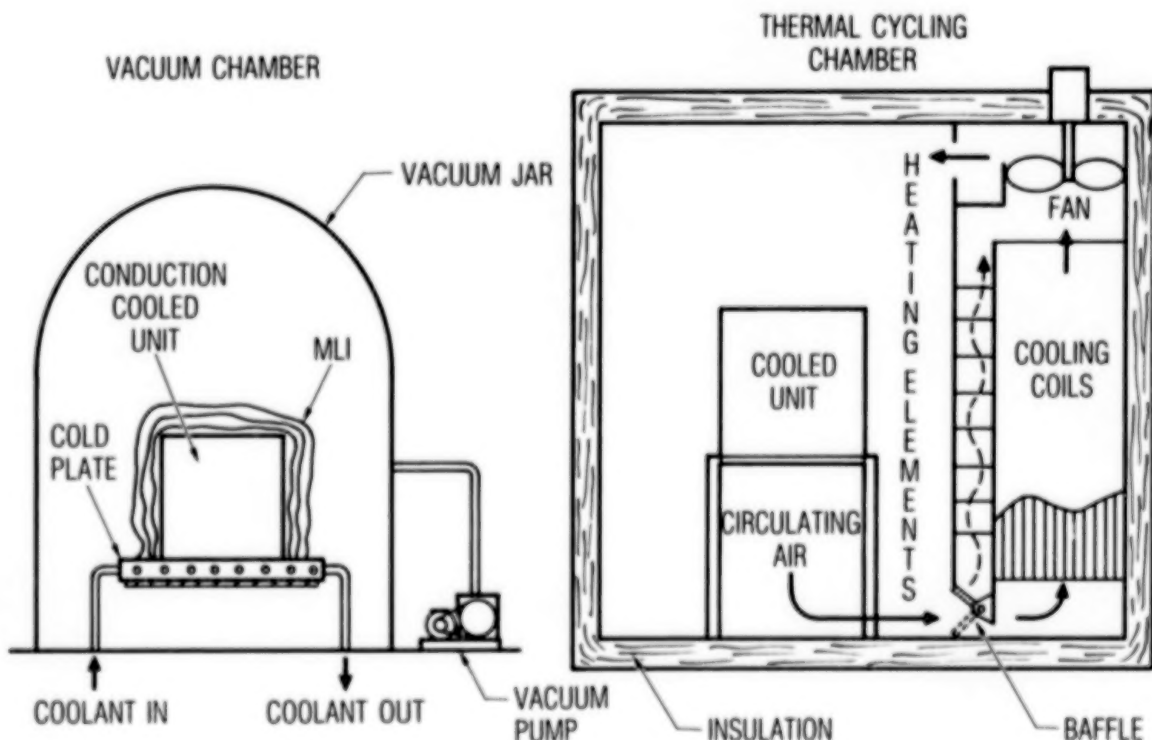
Notes: (1) Functional tests shall be conducted prior to and following environmental test
(2) Required only on unsealed units and on high power, RF equipment

COMPONENT THERMAL ENVIRONMENTS

A wide variety of test chambers are available for thermal cycling tests. Nitrogen or humidity-controlled air is used to prevent water vapor condensation. Heating, cooling, and a rapid air or gas flow are required. A rapid rate of temperature change at the base plate or case of the component of interest is often difficult to achieve. This may be the major technical challenge faced in thermal cycling testing.

Thermal vacuum tests are divided into two categories: (1) those where conduction to a mounting plate is the dominant mode of cooling, and (2) those where radiation to the surroundings dominates or where cooling is by both conduction and radiation. The former has proved to be the more likely occurrence. Conduction cooling is usually accomplished by torquing the component down onto a monolithic, thermally-controlled plate. This is not truly representative of actual component installation, which may, for example, have delron inserts in an aluminum honeycomb with face sheets. However, this is usually acceptable for component testing and buy-off, provided the differences between test mounting and flight mounting are accounted for by analysis and verified by testing at the subsystem or the system level.

Many components are cooled primarily by radiation or by both conduction and radiation. Such components include control moment gyroscopes, horizon sensors, and inertial reference units. Here, control of the heat loss paths should be such that radiation and conduction occur in the same proportion as calculated for the flight environment. This is necessary so that module and piece part temperatures and component temperature gradients duplicate those which occur in actual usage. This can be achieved, for example, by the use of heated baffles and shields and the control of mounting plate temperatures.



OBJECTIVES OF COMPONENTS THERMAL CYCLING, THERMAL VACUUM, AND BURN-IN TESTS

The specified tests (thermal cycling, thermal vacuum, and burn-in) can be construed as having three functions: environmental stress screening (ESS), demonstration of survival and turn-on capability, and performance verification. ESS, by subjecting hardware to physical stresses, forces flaws which are not ordinarily apparent into observable failures. Flaws are latent defects in design, workmanship, parts, processes, or materials which could cause premature component failure. The defective elements are repaired or removed prior to usage. The intent of the survival and turn-on function is to demonstrate that the equipment can be soaked, started, and operated at cold and hot survival temperature limits without experiencing permanent damage or performance degradation when returned to the operational temperature range. Survival/ turn-on temperature limits derive from ascent, safemode and threat mission phases, and factory and launch site checkout. Finally, the tests verify that the component electronic and mechanical performance is within specification.

0 ENVIRONMENT STRESS SCREENING

- FINDS FAULTS IN COMPONENT DESIGN. WORKMANSHIP, PARTS, MATERIALS, AND PROCESSES

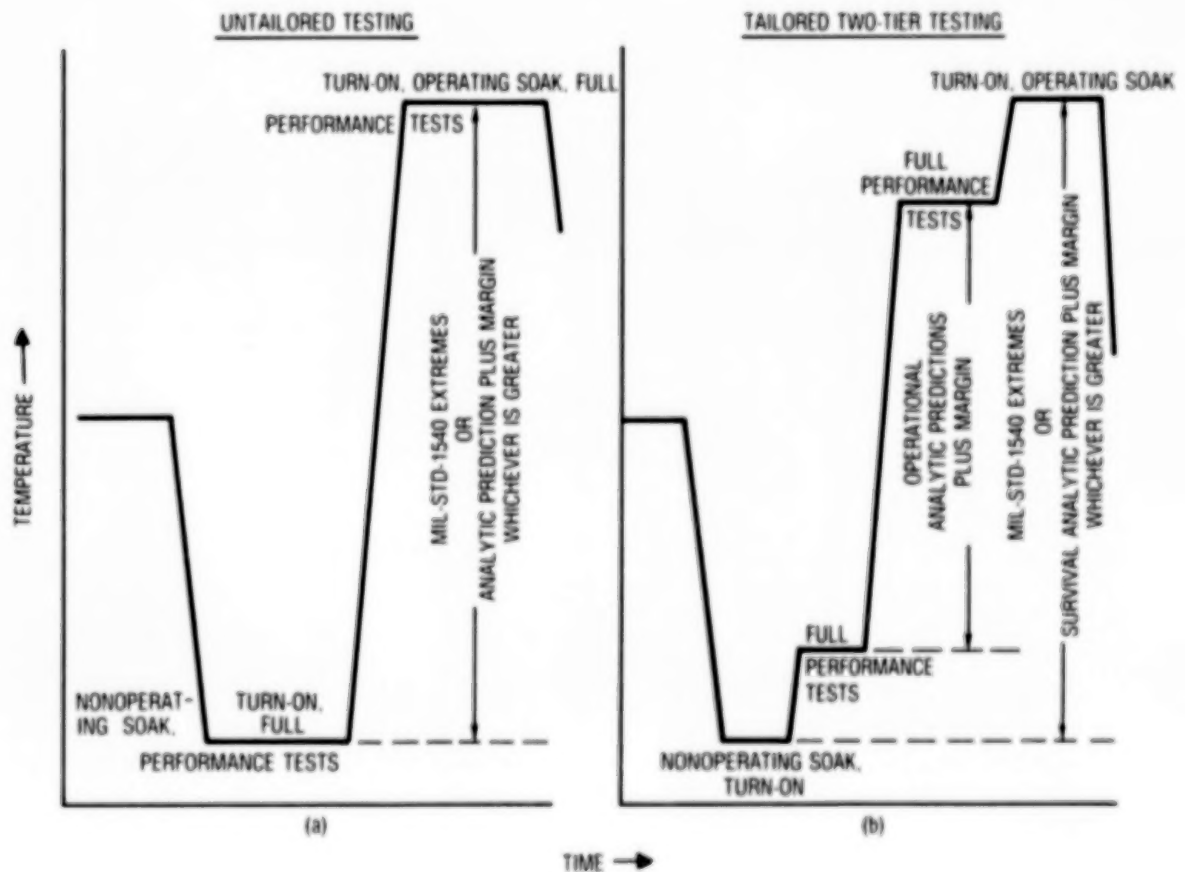
0 VERIFICATION OF SURVIVAL AND TURN-ON CAPABILITY

- DEMONSTRATION THAT COMPONENT CAN BE TURNED ON AND OPERATED OVER SURVIVAL TEMPERATURES WITHOUT EXPERIENCING PERMANENT DAMAGE OR PERFORMANCE DEGRADATION WHEN RETURNED TO OPERATIONAL TEMPERATURE RANGE

0 VERIFICATION THAT COMPONENT PERFORMANCE IS WITHIN SPECIFICATION OVER ITS OPERATIONAL TEMPERATURE RANGE

TEMPERATURE TIMELINES

Test temperature limits are the same for performance, screening, and survival/turn-on, if MIL-STD-1540 is applied without tailoring. In this case, component thermal tests are conducted at cold and hot limits determined from analytic predictions plus analytic uncertainty margin or at specified extremes whichever is greater. Some suppliers have requested a waiver for units originally built and qualified before the Standard was issued and for a limited number of new units with special temperature sensitivity; they have proposed, in lieu of the Standard, that tailored two-tier testing be conducted as in Figure b. For such testing, performance is verified over the narrower regime of operational analytic predictions plus margin, while screening is accomplished and survival/turn-on are demonstrated over the wider range of MIL-STD-1540 specified extremes or survival temperature analytic prediction. Unfortunately, this waiver request has propagated, so that it is now being requested for many units regardless of heritage, temperature sensitivity, and the like. Additionally, the outer tier tests and temperature levels have been weakened.



COMPARISON OF MIL-STD-1540 ACCEPTANCE TEST REQUIREMENTS
WITH RECOMMENDATIONS

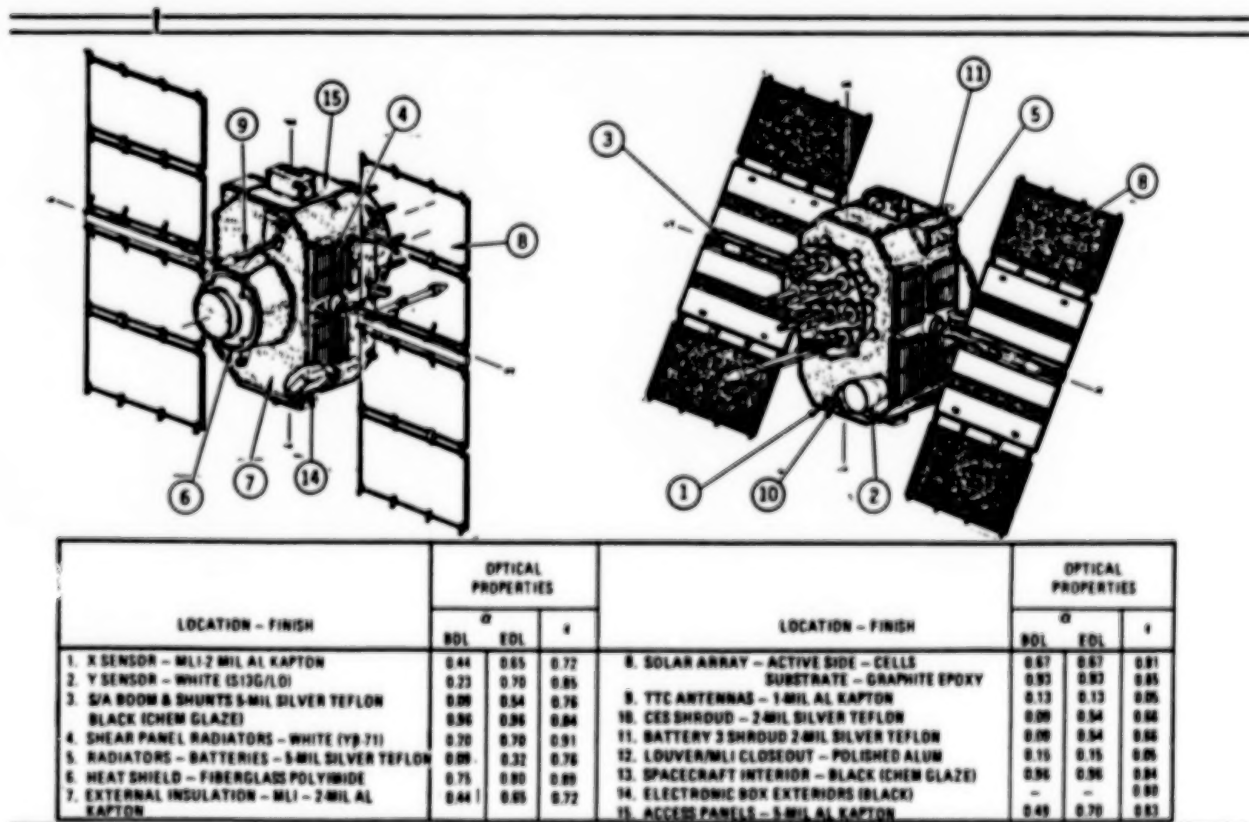
Key Parameter	Recommendations		MIL-STD-1540B Requirements	Conclusions
	IEE Guidelines (Ref. 1)	MPC Study (Ref. 2)		
No. of thermal cycles	12 cycles	<p>Recom- mended No. of Cycles</p> <p>Part Count</p> <p>100 1 500 3 2000 6 4000 10</p>	<p>Thermal cycling -8 cycles Thermal vacuum -1 cycle</p> <p>For TC and TC conduct full functional test at high and low temperature extreme, first and last cycles</p> <p>Burn-in -18 cycles (includes thermal cycling and thermal vacuum)</p>	<p>MIL-STD requirements consistent with industry practice</p> <p>No. of cycles not excessive, may be insufficient</p>
Temp. extremes and range	-40 to +70°C	-54 to +55°C	-24 to +61°C	<p>MIL-STD requirements within design and performance capability and within experience base of suppliers</p> <p>Makes sense for space vehicles because of unattended long-life requirement</p>
Temp. transition rate of change	5°C/minute of surrounding media	-	At least 1°C/minute measured at baseplate of unit	<p>MIL-STD requirements more work is needed on subject</p> <p>Rate of change probably too low; should be at least as great as maximum predicted rate</p>
Operation/non-operation profile	Power ON	-	<p>Power ON during transition Cycles through operational modes</p> <p>Monitor perceptive parameters</p> <p>Cold start/hot start</p>	MIL-STD-1540 requirements are sound and well founded
Dwell	-	-	One hour minimum dwell at high and low temp. extreme, long enough to obtain internal temp. equilibrium	MIL-STD-1540 requirements seem reasonable

THERMAL CONTROL SURFACES AND FINISHES

Surfaces and finishes are the most basic thermal control hardware. Some are illustrated for a typical space vehicle. Solar absorptance, α , tends to increase with mission life because of contamination and attack by ultra-violet radiation and charged particles. The composite Kapton-H/aluminum film is widely used as the external surface of structure and multilayered insulation because it has good handling and bonding characteristics and experiences relatively minor mechanical damage due to the natural environment. Teflon/silver film has lower values of α/ϵ than the Kapton film, but it is seeing less use as a flexible second surface mirrors because of mechanical degradation in the natural environment. This satellite did not use the more durable fused silica/silver rigid second surface mirrors commonly called OSRs. White paint such as S13S/LO, composed of zinc oxide pigment and RTV-602 (organic) binder, degrade more rapidly than the newer YB-71 white paint, which is composed of zinc orthotitanate pigment and PS7 potassium silicate (inorganic) binder. The YB-71 paint, sometimes called "ZOT," also appears to have good survival characteristics in some threat environments.

High emissivity white and black paints are widely used for interior surfaces. Polished aluminum, with its low emissivity, is usually employed in applications where there is no direct solar incidence and where low thermal coupling to space and to spacecraft surfaces is desired.

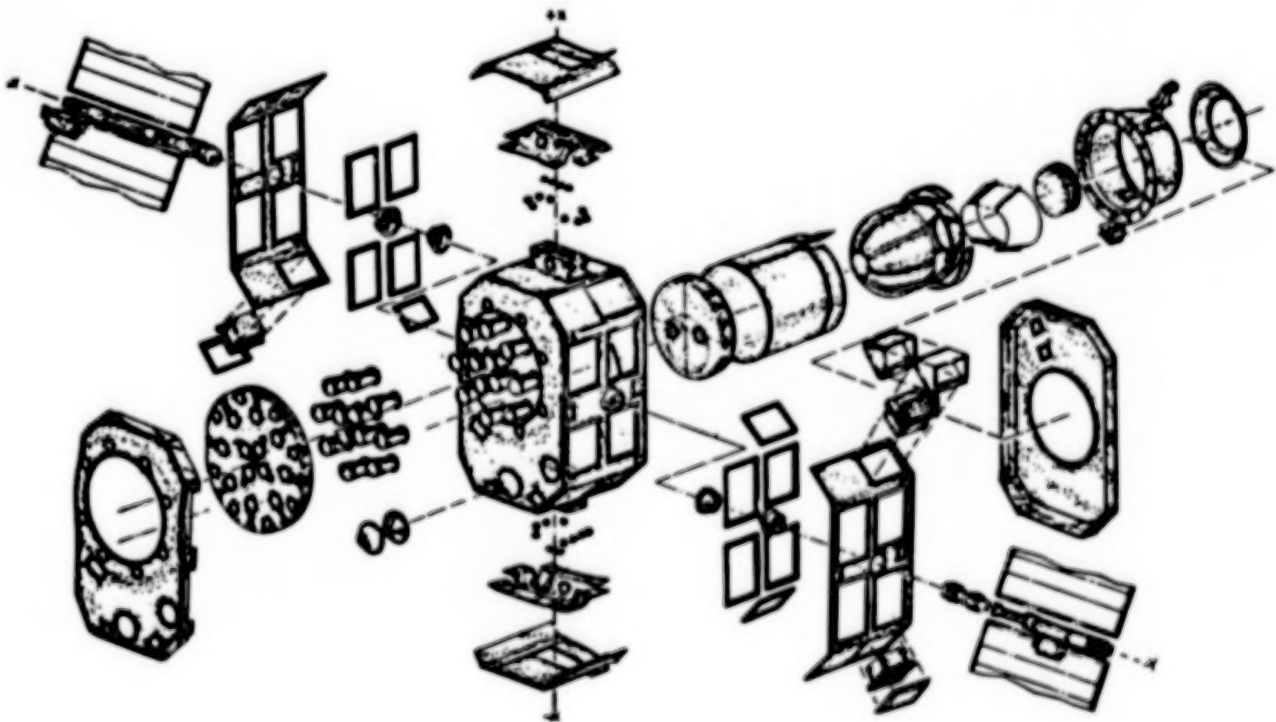
TCS COATINGS



INSULATION BLANKETS

The exploded insulation illustration shows the wide variety of multilayered insulation blankets used on space vehicles. These blankets use a layered approach to reduce conduction and radiation heat transfer to low values. Typically, alternate layers of aluminized Mylar or Kapton and a highly porous spacer material control radiation and conduction, respectively.

Blanket construction and installation can cause performance degradation. Heat shorts can be introduced by blanket compression over curved surfaces (especially those with compound curvature or small radii of curvature); penetration of support posts; blanket electrical grounding, venting and outgassing provisions; and stitching, pinning, and binding. Such problems are usually more severe with smaller blankets and those with cutouts, where the ratio of edge length to surface is large. A well-instrumented, properly controlled thermal balance test, using a qualification space vehicle or subsystem which is a true facsimile of the flight article, is necessary to determine blanket effective emissivity.

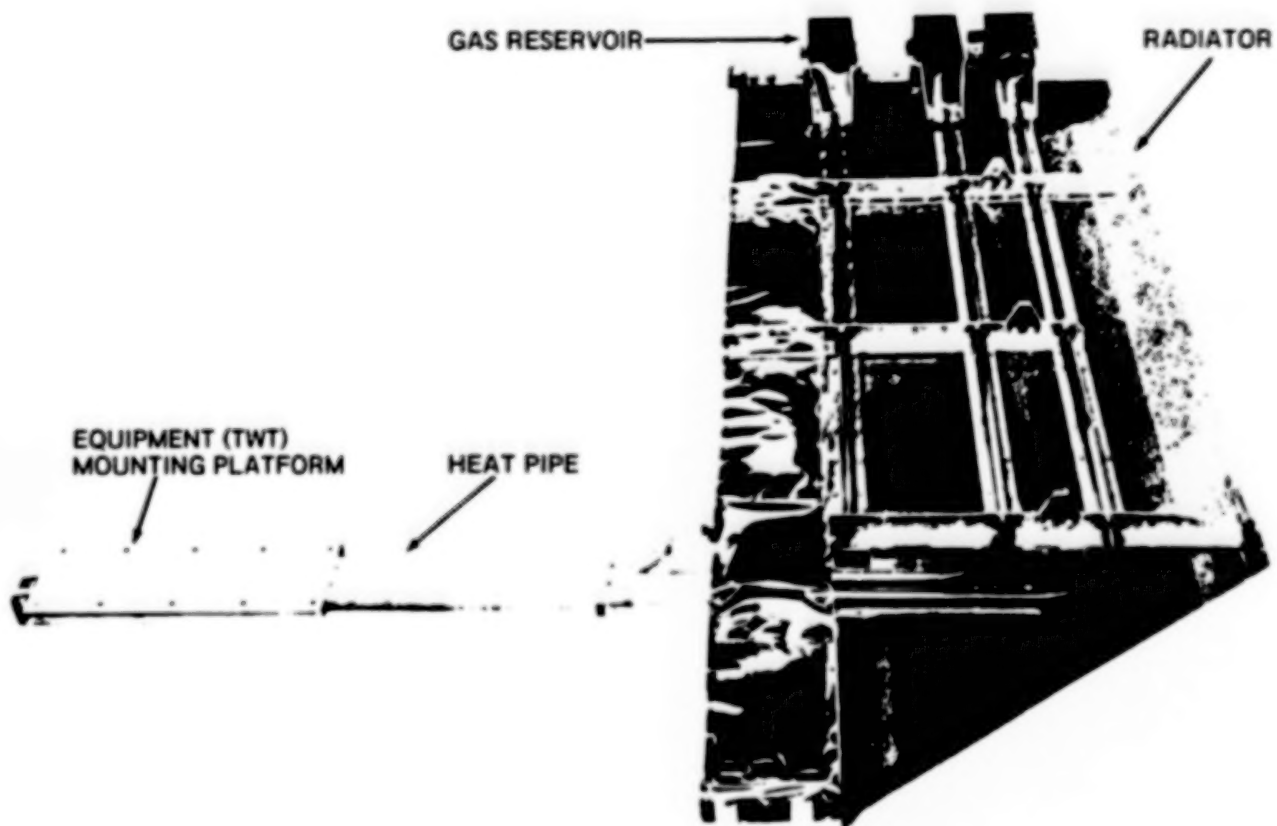


HEAT PIPE ASSEMBLIES

Heat pipes (tubes containing internal wicks and liquid and vapor phase working fluid) are coming into extensive use on space vehicles. Newer vehicles may use more than 100 heat pipes of five to 15 different configurations and types. Evaporation in the region of equipment heat dissipation causes menisci contraction to small radii of curvature. The evaporated vapor condenses in the cold radiator portion of the heat pipe. The differential pressure caused by evaporator menisci pumps the condensed liquid within the wicking grooves to the evaporator end of the heat pipe. A countercurrent convection loop is thereby set up in the pipe which transfers heat at substantially higher rates than a solid aluminum tube of the same diameter. More complex designs offering greater control precision and reduced cold case heater power usage are possible (e.g., the variable conductance heat pipe assembly illustrated here). It employs inert gas within gas reservoirs to block portions of the condenser during mission phases with reduced equipment heat dissipation or environmental loading. For higher heat load applications, capillary pumped loops are receiving consideration. Operation and control of such loops entails yet a higher level of complexity.

Heat pipe performance, as it depends on relatively small capillary forces, is sensitive to body (gravitational) forces. Consequently, a heat pipe which will work excellently in the near zero gravity space environment, could be rendered inoperative by evaporator height exceeding condenser height by a fraction of an inch during ground tests. The effect on vehicle design and ground testing is profound. Precise tolerance control of the design and the test set up may be required to assure that a heat pipe meets leveling requirements. Because of design requirements and allowable test configurations, some heat pipes cannot possibly be tested in the horizontal configuration during space vehicle tests. The thermal performance of such heat pipe assemblies must be verified at the subsystem level; here, it is often possible to rotate the assembly so that the heat pipes of interest are horizontal. A space test may prove to be the ideal way to verify the performance of new capillary pumped loop designs.

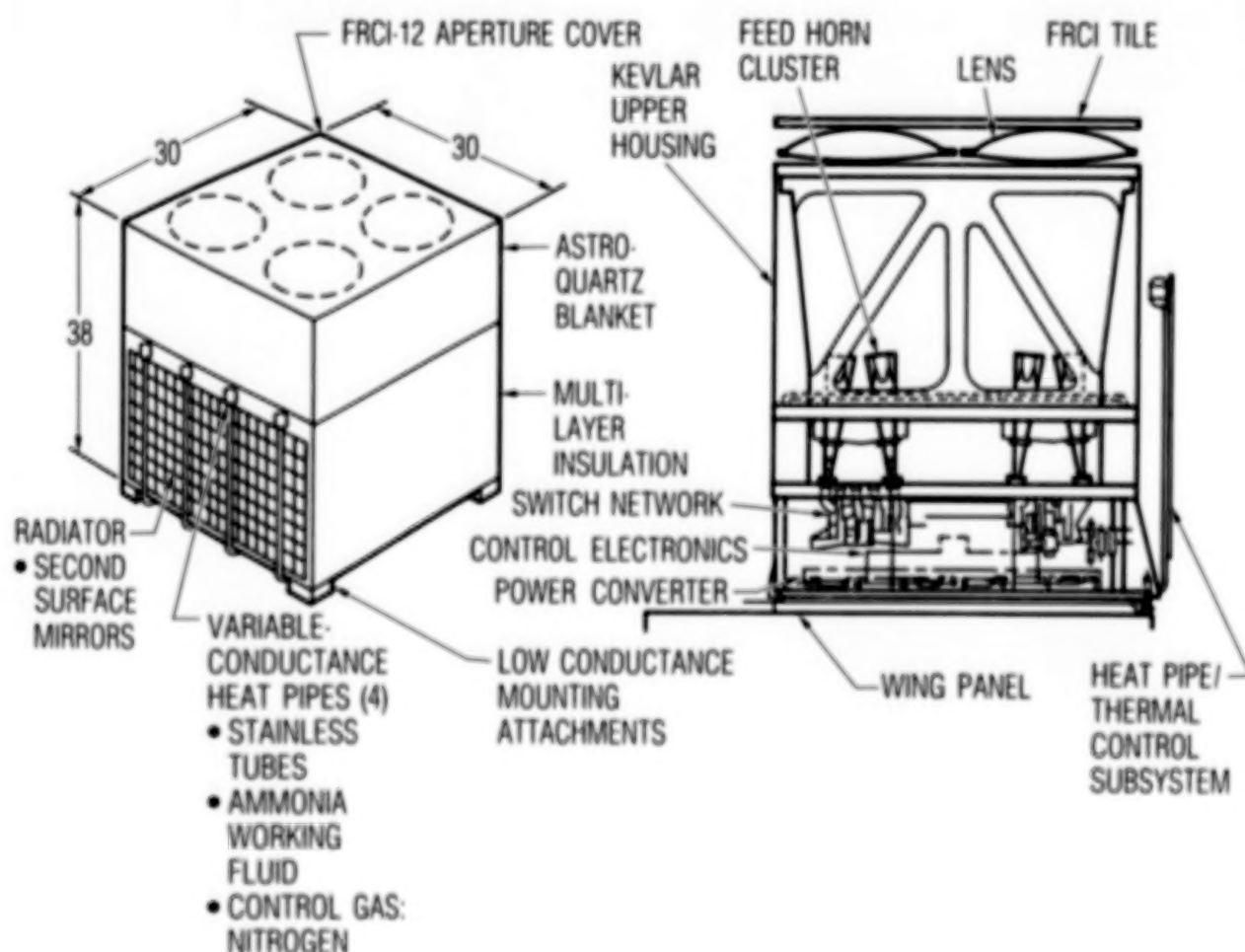
SATELLITE VARIABLE CONDUCTANCE
HEAT PIPE ASSEMBLY



SUBSYSTEM AND ASSEMBLY THERMAL VACUUM TESTS

As spacecraft size and complexity has grown, and buildup time has lengthened, the need has developed for intermediate tests between component and space vehicle testing. Such tests may be conducted on all or part of a subsystem. For example, the thermal design of the depicted antenna assembly is sufficiently complex to warrant an assembly level thermal vacuum test. Design features include multilayered insulation, a second surface mirror radiator, conduction coupling to active electronics, variable conductance heat pipes, and heaters and controllers. The test will verify the ability of the thermal design to hold components within allowable temperatures under specified hot and cold conditions.

Subsystem and assembly tests allow use of smaller test facilities than required for the space vehicle tests, and make it easier to tailor the thermal environment to the specific requirements of the components under test. Usually, configuration and leveling requirements can be more readily met in a subsystem, rather than in a space vehicle test. Results are obtained in a more timely manner, facilitating necessary remedial action.



SPACE VEHICLE THERMAL TESTS

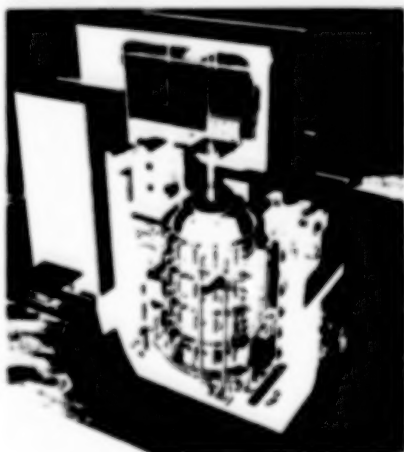
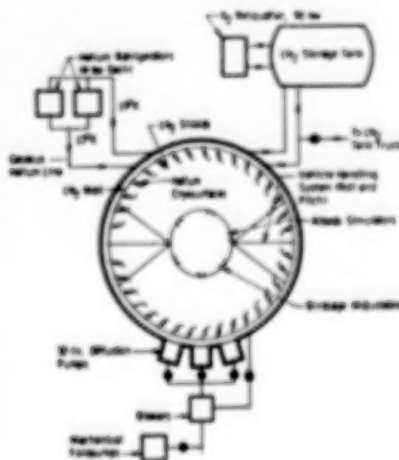
Space Vehicle (SV) qualification thermal tests are more demanding than the SV acceptance tests in that there is a wider temperature range, more thermal cycles, and the inclusion of a thermal balance test. The qualification tests are formal contractual demonstrations that the design, manufacturing, and assembly of hardware have resulted in conformation to specified requirements. The acceptance tests are required formal tests which demonstrate the acceptability of an item for delivery. They are intended to demonstrate performance to specified requirements and to act as environmental screens to detect deficiencies of workmanship, material, and quality. Acceptance test temperature levels should encompass all specified flight environments.

The thermal vacuum test consists primarily of system level functional performance tests (e.g., payload performance, electrical, mechanical, and thermal) between and at temperature extremes. Emphasis is on component and subsystem interaction and interfaces; integrity of mounting, cabling, and connectors; and on end-to-end system performance. An optional thermal cycling test functions as a high level environmental screen. The thermal balance test, conducted as part of the thermal vacuum test for the qualification vehicle, is a dedicated thermal test to correlate the thermal analytic models and demonstrate the design and functional capability of thermal control hardware.

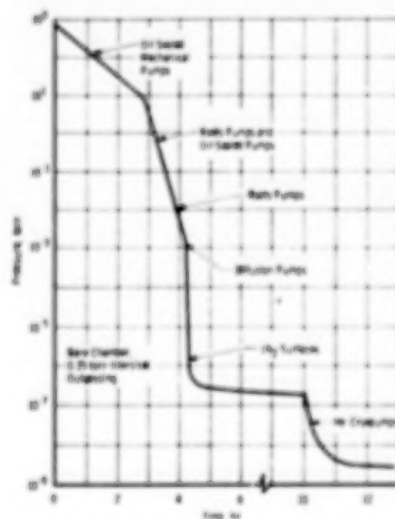
A variety of components, often tested to different temperature extremes during component qualification and acceptance, must be accommodated during SV thermal vacuum testing. The approach taken is to drive as many components as possible (but at least one component per vehicle equipment zone) to their qualification or acceptance temperature extremes, with the constraint that no component should exceed its component level test temperature extremes. This requires pretest analysis, use of test equipment and instrumentation, and local heating or cooling within the chamber. Safeguards are necessary to avoid damage during handling and testing.

ARNOLD ENGINEERING DEVELOPMENT CENTER

The AEDC Mark I Chamber, in Manchester, Tennessee, is described in order to illustrate a large thermal vacuum facility. The 42-ft diameter, 82-ft high chamber is housed in a 10-story building. It features a 20-ft diameter top hatch for vehicle entry and an 8-ft bottom hatch for personnel access. The cool-down and pump-down systems are shown in the schematic. They feature an 8 kW gaseous helium refrigeration system and a 90 kW nitrogen reliquification system. Diffusion pump capability is 2×10^5 l/sec at 10^{-7} torr and cryopump nitrogen capability is 15×10^6 l/sec.

**Mark I Facility Arrangement**

Mark I Schematic



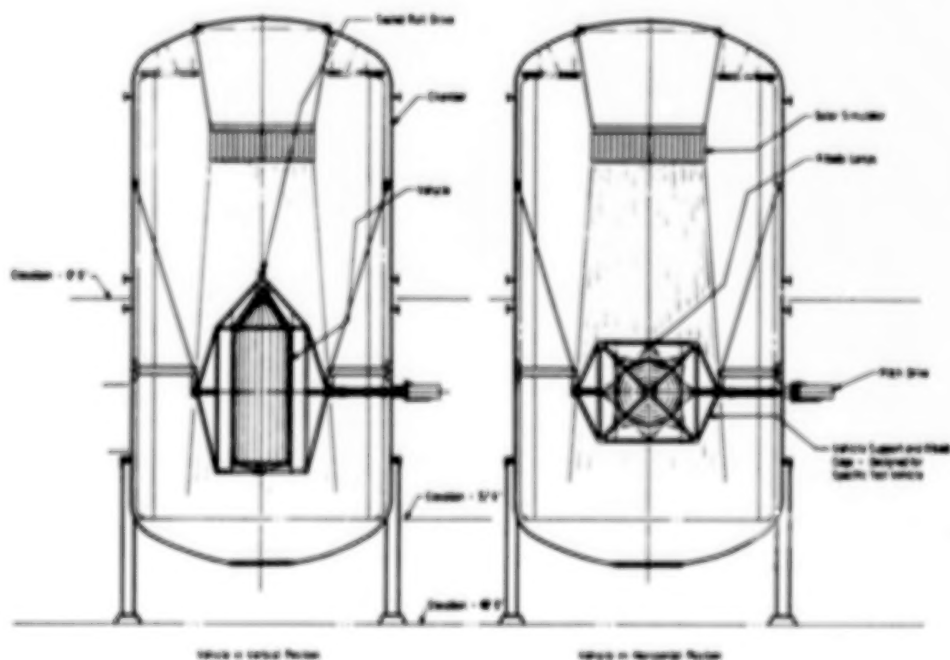
Mark 1 Pumpdown Curve

MARK I CHAMBER: THERMAL ENVIRONMENTS AND VEHICLE HANDLING

The vehicle handling system accommodates moderate size, symmetric shape test articles to 50,000 lb. A pitch drive and slip-ring assembly is used for power transfer. The handling system is capable of simultaneous real time motion about two axes. However, wire bundles and test instrumentation leads may make this impractical. The Block II GPS-NAVSTAR, recently tested in this chamber, utilized motion about one axis to simulate the time-varying solar vector for the beta-equals-zero orbit.

Solar simulation is accomplished using an array of modules, each containing a 1-kW quartz-iodine lamp and a water-cooled collimator tube. As the created spectrum approximates a 3000°K blackbody, with the sun more nearly like a 5800°K blackbody, augmenting xenon short-arc lamps can be used to improve spectral matching. The Mark I system is capable of continuously variable radiation for 0 to 110% of the solar constant with $\pm 3\%$ uniformity. Solar simulation is the preferred method of spacecraft heating, as this technique allows the natural blockage and cavity effects to occur, while imposing direct and reflected solar-like radiant heating. This method also creates infrared sources, which can approximate actual self heating by virtue of reradiation of absorbed solar energy. Because of cost and complexity, spacecraft heating is often done by methods that do not simulate the spectral content and directionality of the sun, but do attempt to impose the proper intensity and distribution of heating.

The cold environment of space is well-simulated by a liquid nitrogen-cooled high emissivity internal wall. Because of the fourth power dependence of radiant energy interchange, a wall at 77°K constitutes only a minor radiant energy source for a room temperature spacecraft.



SPACE VEHICLE (SV) THERMAL BALANCE TEST

This test formally qualifies the Thermal Control Subsystem (TCS). It is used to correlate the analytic thermal models; to verify the design and performance of TCS hardware such as insulation blankets, louvers, heat pipes, and heaters/thermostats; and to demonstrate that the TCS maintains all payloads and equipment within allowable temperature limits for all mission phases under worst case environments. This test should be conducted for one-of-a-kind spacecraft; the lead vehicle of a series of spacecraft; and a block change in a series of vehicles, upper stages, and sortie pallets designed to fly with the Shuttle.

The thermal balance test is conducted in a cryogenically cooled thermal vacuum chamber. The tests should simulate worst case combinations of equipment usage (primary and redundant), bus voltage, and solar angles and intensities. During these largely steady state tests all important internal heat flow paths and external radiative surfaces should be exercised. Some tests typically involve simulation of non-operational or transient mission phases: transfer orbit cooldown, eclipse, safemode entry or exit. Large appendages such as solar arrays, booms, and antennas are sometimes not part of the tested configuration. Both stowed and deployed vehicle configurations may be tested, requiring vacuum break. Environmental heating is usually simulated by infrared lamps, heated (radiating) plates, and/or test heaters affixed to external surfaces. Solar simulation is less frequently used.

The contractor should compare pretest temperature predictions with corresponding test data. The Aerospace Corporation has proposed, as a guideline, that those differences that fall outside a $\pm 3^{\circ}\text{C}$ band require either a good explanation or a model adjustment, depending on the size of the deviation. In practice, deviations as large as $\pm 6^{\circ}\text{C}$ are often accepted, with narrower limits for temperature-sensitive or mission-critical components.

SPACE VEHICLE (SV) THERMAL BALANCE TEST (Continued)

A variety of test-related factors contribute to a fairly large residual analytic uncertainty after completion of the thermal balance test. These include imperfect spectral matching, inadvertent test heat losses, end-of-life properties not simulated, test set radiation blockage, and measurement and calibration error.

Model correlation to test data may not be effective if an incorrect heat transfer mechanism is employed. Some design changes that were made because of thermal balance test results are not test verified until the acceptance test of the first flight vehicle and, sometimes, unfortunately there is no test validation.

Overall, the thermal balance test has proved successful in correcting major thermal modeling errors, in reducing the standard deviation between prediction and flight measurements, and in providing physical insight into heat transfer mechanisms.

The thermal balance test and portions of the thermal vacuum test serve to verify the design and performance of thermal control hardware. Primary and redundant heaters and thermostats are exercised and the circuitry is proven, location and response time is verified, and 25% excess heater control authority is demonstrated for the cold case. Radiator surface emissive power and insulation blanket effective emissivity are verified. Performance of louvers and heat pipes (if horizontal) is characterized. The ability of the TCS to maintain SV components within their specified temperature extremes under worst hot and cold case conditions is demonstrated.

THERMAL CONTROL REQUIREMENTS TO SUPPORT FACTORY AND LAUNCH SITE CHECKOUT AND FUNCTIONAL TESTING

Checkout and functional tests are required at various stages during the buildup of a space vehicle. Such tests often are not part of the formal developmental, qualification, and acceptance process. For example, these tests: (1) allow checkout at intermediate stages during the buildup process, (2) can verify that a subsystem has not been damaged or degraded during shipment, and (3) allow continuity, checkout, and limited functional tests during and after assembly at the launch site. Thermal control (i.e., gas or liquid cooling) often is required to ensure that components do not overheat during these tests. Compounding the difficulty of this requirement is the fact that the subsystem or space vehicle configuration and surrounding environment can encumber the cooling process. The cold radiation sink for which the space vehicle is designed is lacking during these tests, and natural convection cooling is not very efficient. Moreover, the subsystem or space vehicle may be oriented so that heat pipes are inoperative and may be enveloped with contamination covers, shrouds or the like, so that there is limited accessibility to fluid cooling.

It is important to identify, early in a program, factory and launch site cooling requirements for checkout and functional tests. This is especially important for sensitive components such as batteries. Space vehicle design accommodations and auxiliary ground equipment which may be required to allow adequate cooling should be specified. This may include ducting and fans, piping and pumps, and leveling hardware and instrumentation.

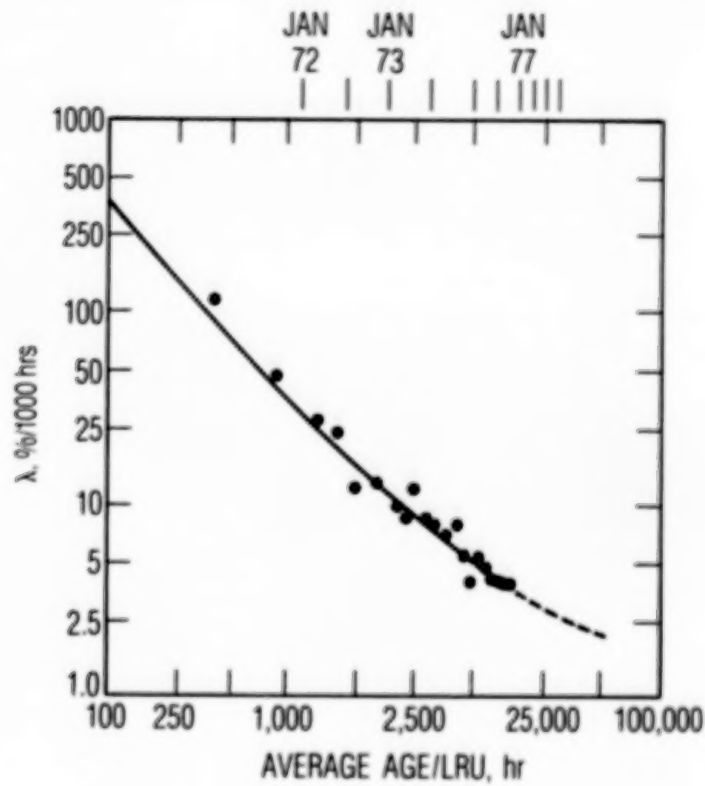
UNIFIED FAILURE THEORY - DEMISE OF THE BATHTUB CURVE

Bezatz and Montague (Ref. 3) have used laboratory and field failure data for the Honeywell Digital Air Data Computer to develop the failure rate curve below. The data base encompassed 6.5 years of revenue service and 11×10^9 part hours. The authors point out that the decreasing failure rate with time is consistent with their experience with semi-conductor devices. Herbert and Myron Hecht (Ref. 4) report a similar trend for spacecraft. Their data base was obtained from over 300 satellites, comprising 96 programs, launched between the early 1960s through January 1984. Primary data sources were The Aerospace Corporation's Orbital Data Analysis Program (ODAP) and the On-Orbit Spacecraft Reliability (OOSR) data compiled by the Planning Research Corporation for NASA. This and other data were the basis for Wong's paper, "Unified Field (Failure) Theory - Demise of the Bathtub Curve" (Ref. 5). Wong points out that the same failure pattern is seen in the laboratory, manufacturing screening, in the field, and that failure rate for electronic equipment trends downward (although the path may have some bumps) for all times of practical interest.

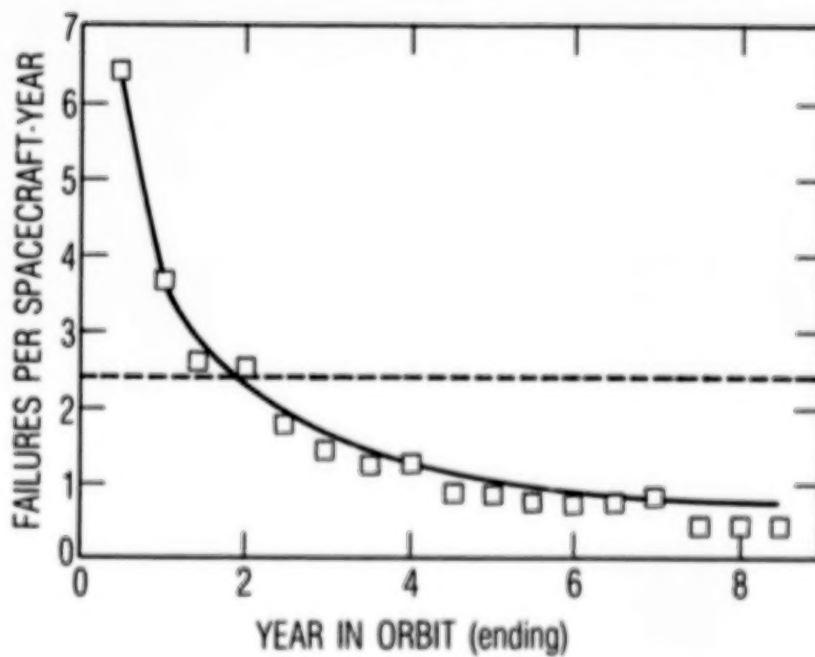
The implications for spacecraft testing and reliability, as we see it, are as follows:

1. No amount of testing will prevent infant mortality failures.
2. Testing can reduce the initial failure rate of this downward trending curve.
3. Provided that failures are detected and repaired, electronic equipment cannot be worn out by testing.
- 4a. Accelerated testing at high stress levels (even beyond flight levels) may be very beneficial for long term reliability.
- 4b. Ambient temperature burn-in with little monitoring is ineffective in screening defective equipment.
5. Quality standards and testing requirements fall off very slowly as mission duration decreases.

Honeywell Digital Air Computer Failure Rate Curve

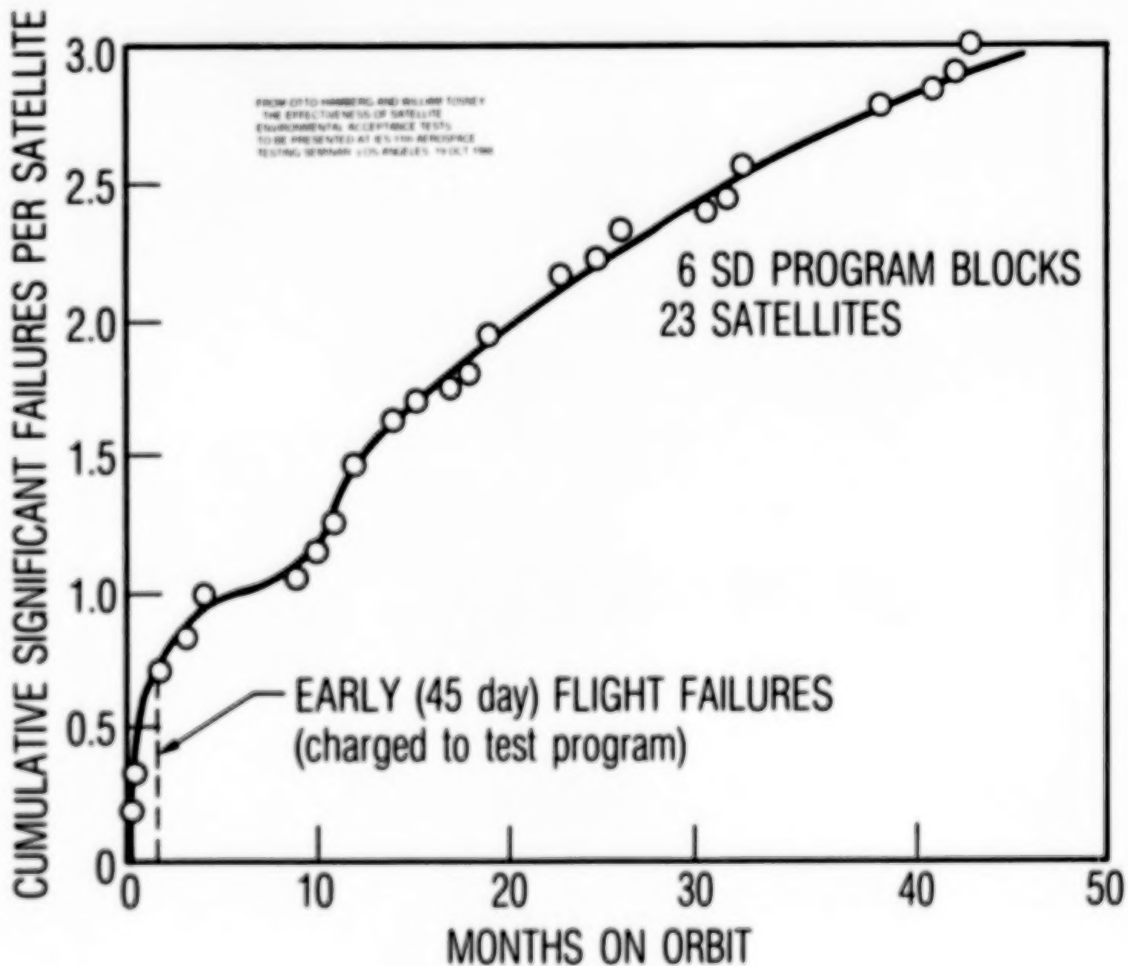


Hecht Study-Satellite Failure History



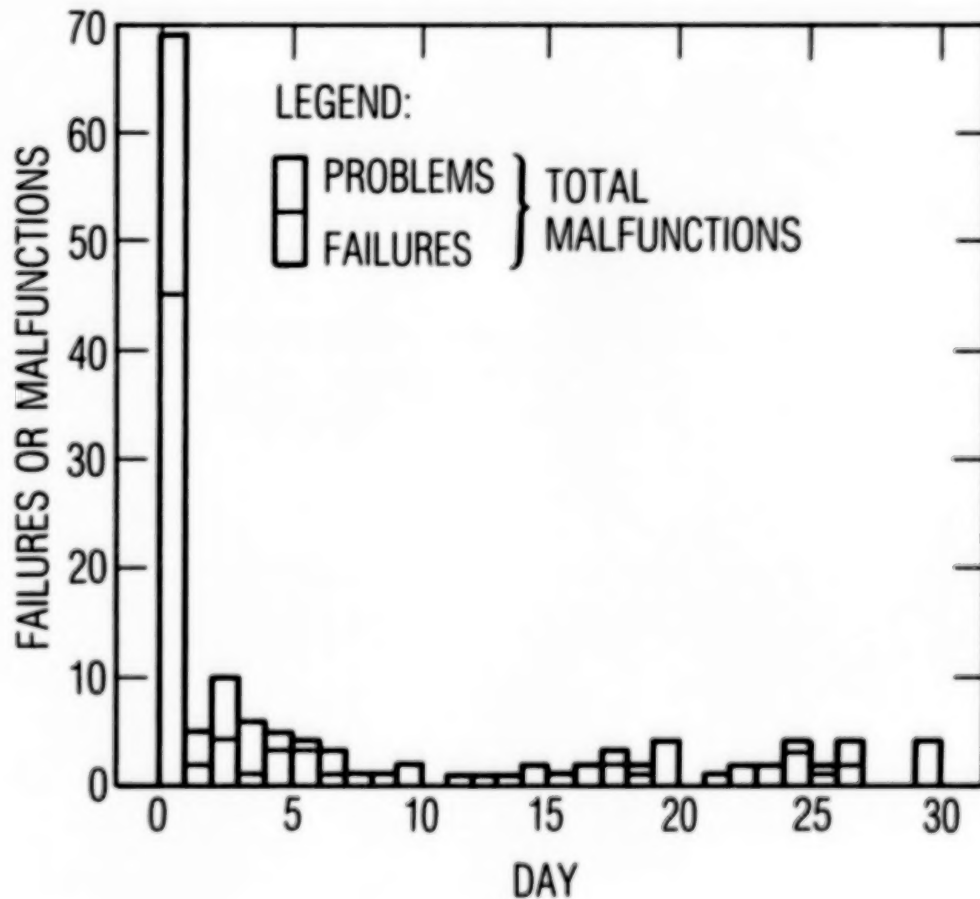
AEROSPACE ON-ORBIT FAILURE DATA

The flight failure history of six Air Force program blocks and 23 satellites is shown (Ref. 6). Only the initial four satellites from each program block were included to minimize the effect of program maturity, and only mission degrading (changes satellite reliability) failures are included. The data were obtained from The Aerospace Corporation's ODAP. It can be noted that the initial high failure rate has moderated somewhat by 45 days. This timeframe coincides with satellite launch, ascent, and the in-orbit operational performance tests. This high failure rate period is considered to be related to the imperfection of the ground test program. The infant mortality period appears to extend out to approximately 12 months of operational flight time. The failure rate after 12 months shows a slowly decreasing rate which is in agreement with the work of the Hechts (Ref. 4).



NASA/GODDARD EARLY ON-ORBIT FAILURE DATA

The work of Timmins (Ref. 7) on NASA/Goddard programs shows that early failures are dominated by first day failures. No corresponding day-by-day failure data has been assembled by The Aerospace Corporation. However, a cursory review by Tosney shows a similar trend, with first day of usage failures quite high.



DEFINITION OF TEST EFFECTIVENESS

The premise underlying the definition of test effectiveness (Ref. 8) is that failures found in environmental tests would have occurred early in flight (first 45 days); these early failures are charged to the test program. Aerospace's ODAP data base was used with only significant test and early flight failures considered. Such failures potentially reduce mission life. Generic failures were counted only once and induced failures not counted. This first order method attempts to account for test sequence as illustrated below.

● QUANTITATIVE MEASURE TO EVALUATE/COMPARE TESTS

$$\frac{\text{TEST FAILURES}}{\text{TEST PLUS FLIGHT FAILURES}}$$

● EXAMPLE PROGRAM A

FAILURES PER SATELLITE (average of satellite group)

TESTS			FLIGHT
ACOUSTIC	THERMAL CYCLING	THERMAL VACUUM	45 day
0.9	1.4	1.6	0.6

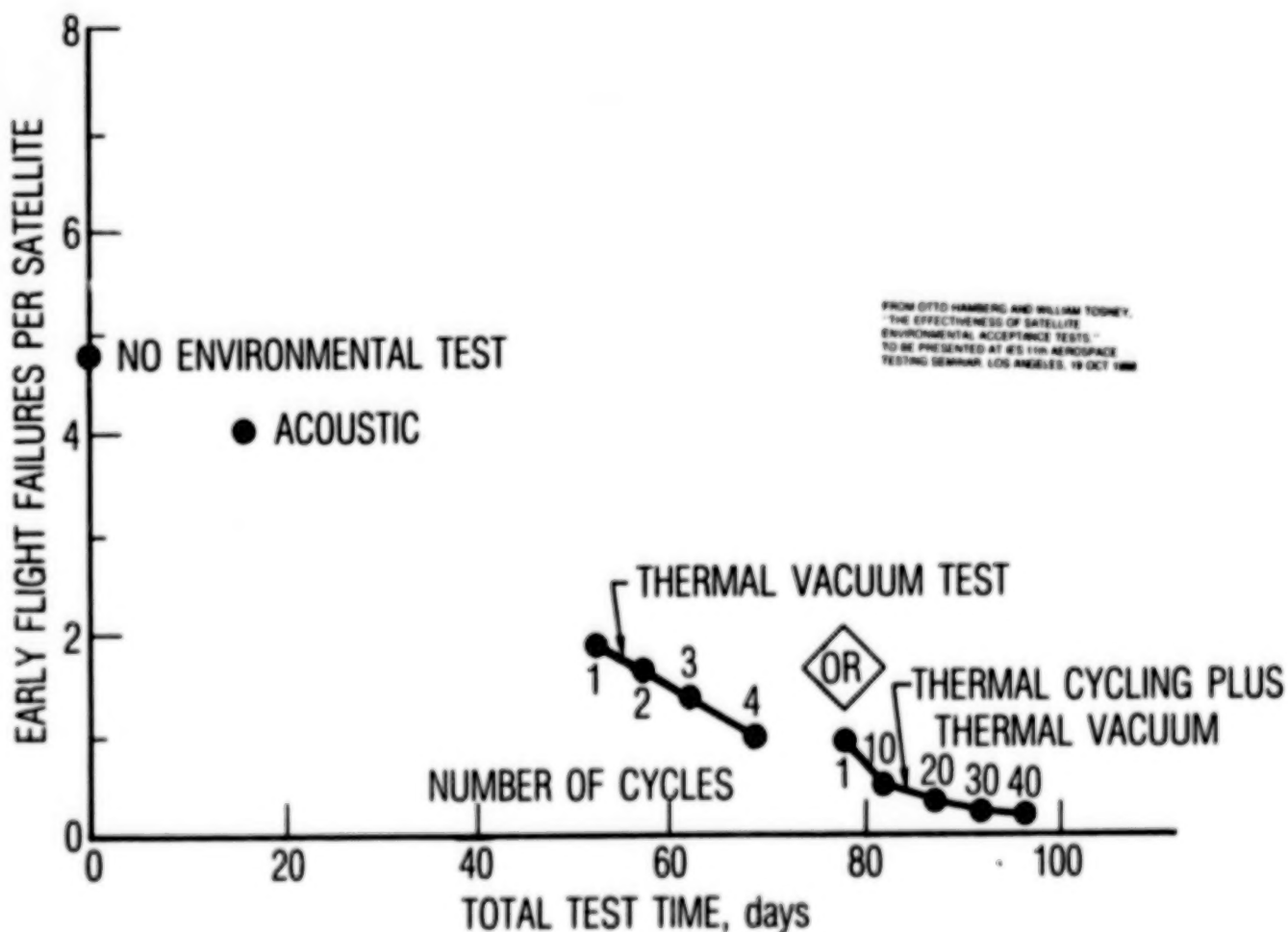
● TEST EFFECTIVENESS

PERCENT

- ACOUSTIC	$= (0.9 \times 100) / (0.9 + 1.4 + 1.6 + 0.6)$	$= 20$
- THERMAL CYCLING	$= (1.4 \times 100) / (1.4 + 1.6 + 0.6)$	$= 39$
- THERMAL VACUUM	$= (1.6 \times 100) / (1.4 + 0.6)$	$= 73$
- COMBINED	$= (0.9 + 1.4 + 1.6 \times 100) / (0.9 + 1.4 + 1.6 + 0.6)$	$= 87$

ENVIRONMENTAL TEST VALUE

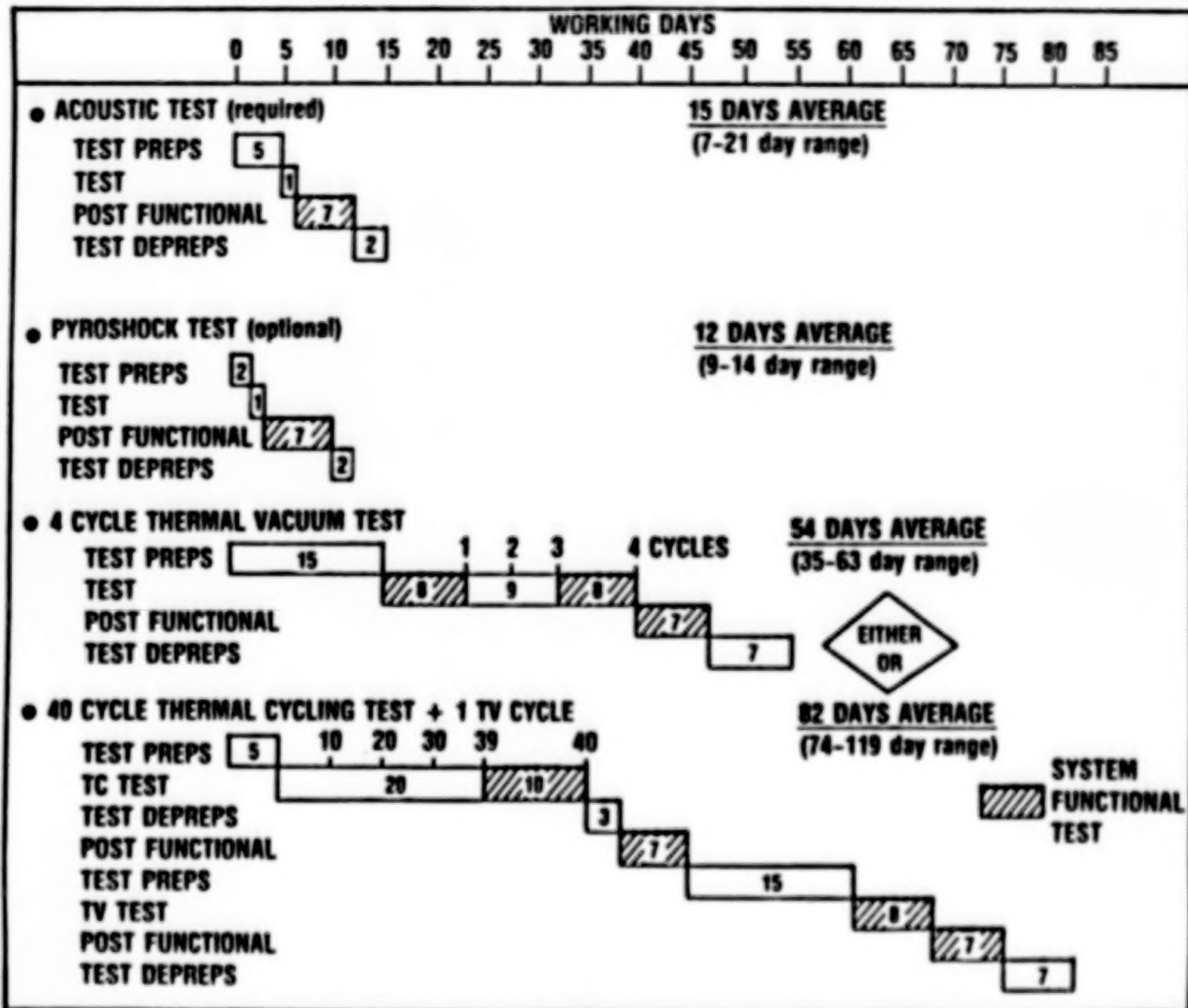
The data bank (Ref. 8) developed by Laube has been used by Hamberg and Tosney (Ref. 6) to generalize about the effectiveness of space vehicle environmental acceptance tests in eliminating first-45-day mission degrading failures. On the average, in the absence of any environmental tests, 4.5 early failures per satellite are anticipated. The acoustic test while only moderately successful at eliminating early failures (0.63 per satellite) is a relatively short test, 15 days. The four cycle thermal vacuum test or the optional 40 cycle thermal cycling test plus one cycle thermal vacuum test, while markedly more successful at eliminating early failures, are time consuming. As a rule of thumb environmental testing avoids about 0.05 early flight failures per day of test.



Generalized Failure Data

56

Typical Timelines



REFERENCES

1. Mandel, C. E., "Environmental Stress Screening Guidelines for Assemblies," Institute of Environmental Sciences, September 1984.
2. Burrows, R. W., "Special Long-Life Assurance Studies," Long-Life Assurance Study for Manned Spacecraft Long-Life Hardware, Martin Marietta Report No. MCR-72-169, Vol. IV, September 1972.
3. Bezat, A. G. and L. L. Montague, "The Effect of Endless Burn-in on Reliability Growth Projections," Proceedings 1979 Annual Reliability and Maintainability Symposium.
4. Hecht, Herbert and Myron Hecht, "Reliability Prediction for Spacecraft," RADC-TR-85-229, December 1985.
5. Wong, Kam, "Unified Field (Failure) Theory -- Demise of the Bathtub Curve," 1981 Proceedings Annual Reliability and Maintainability Symposium.
6. Hamberg, Otto and William Tosney, "The Effectiveness of Satellite Environmental Acceptance Tests," IES 11th Aerospace Testing Seminar, Los Angeles, 19 October 1988.
7. Timmins, A. R., and R. E. Heuser, "A Study of First-Day Space Malfunctions," NASA TN D-6474, September 1971.
8. Laube, R. B., "Test Data Bank," The Aerospace Corporation, TOR-0084(4902-06)-1, October 1983.

BIBLIOGRAPHY

Gluck, D. F., "Thermal Testing of Space Vehicle Electronic Components," The Aerospace Corporation, TOR-0084A(5404-10)-2, 31 May 1985.

MIL-HDBK-340 (USAF), Military Handbook, "Application Guidelines for MIL-STD-1540B; Test Requirements for Space Vehicles," 1 July 1985.

Gluck, D. F., "Space Vehicle Thermal Testing: Environments, Related Design and Analysis, Requirements, and Practice," The Aerospace Corporation, TOR-0086A(2902-08)-1, 27 September 1987.

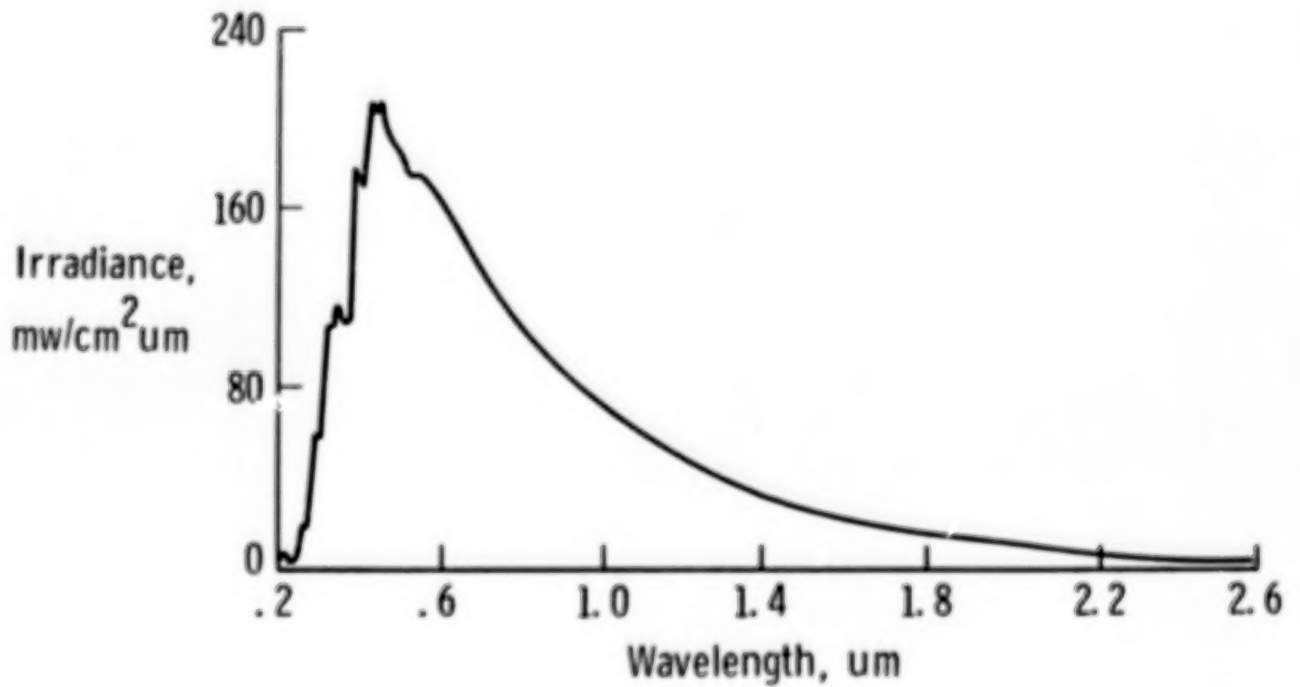
MIL-STD-1540B (USAF), Military Standard, "Test Requirements for Space Vehicles," 10 October 1982.

ULTRAVIOLET RADIATION EFFECTS

Wayne S. Slomp
Materials Division
NASA Langley Research Center
Hampton, Virginia 23665-5225

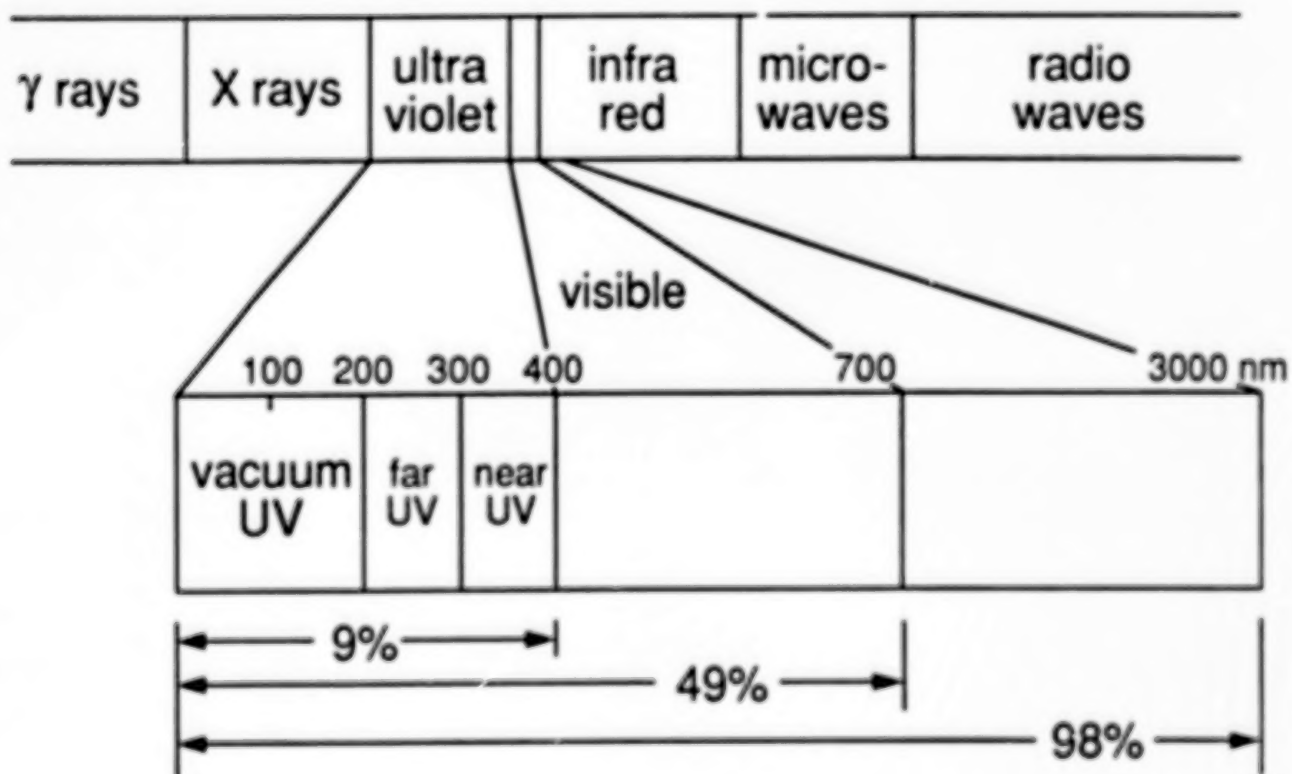
SOLAR SPECTRUM

The irradiance of the solar spectrum for air mass 0 is presented in the figure for the wavelength range of 0.2 micrometers to 2.6 micrometers.



THE ELECTROMAGNETIC SPECTRUM

The electromagnetic spectrum from gamma rays to radio waves is represented in the figure. The ultraviolet, visible, and near-infrared radiation found in the space solar spectrum is only a small part of this electromagnetic spectrum. The UV spectrum is divided into three parts--the vacuum or extreme UV below 200 nm, the far UV from 200 nm to 300 nm, and the near UV from 300 nm to 400 nm. Nine percent of the solar energy is found in the UV.



ULTRAVIOLET ABSORPTION AND PHOTOCHEMICAL EFFECTS

The chemical changes resulting from exposure of a polymer to ultraviolet light are illustrated in the figure. The first law states that only those radiations that are absorbed by a material can produce a chemical change. If a material does not absorb the particular wavelength of UV incident upon the material, then UV cannot cause a chemical change in the material. The second law states that each molecule taking part in a reaction absorbs one quantum ($h\lambda$) of energy. If moles are substituted in the Stark-Einstein law, the Bohr law is obtained. Since this equation is divided by wavelength, the smaller the UV wavelength, the greater the UV energy.

- 1) Only those radiations that are absorbed by a material can produce a chemical change (Grotthuss-Draper)
- 2) Energy absorbed by a reacting molecule is given by $h\lambda$ (Plank's const. x freq. of absorbed light) (Stark and Einstein)
- 3) Change molecules to moles (Bohr Law)

Equation: $E = Nh = N h c / \lambda$

N - Avagadro's No.

$E = 2.86 \times 10^5 / \lambda$ k cal/mole

C - Velocity of light

λ - Wavelength, angstroms

Examples:

$\lambda = 4000\text{A}$ the Einstein is 71 k cal/mole

$\lambda = 2537\text{A}$ the Einstein is 113 k cal/mole

TYPICAL VALUES OF BOND ENERGIES

The typical values of bond energies are shown in this table. This illustrates that several chemical bonds can be broken by the 113 k cal/mole energy of the 2537Å wavelength of UV radiation. Since the solar radiation in space extends to wavelengths as low as 1000Å, most polymer bonds can be broken with UV radiation.

CHEMICAL BOND ENERGY

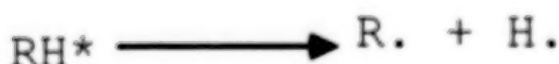
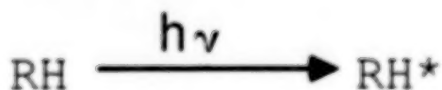
<u>Bond</u>	<u>Bond Energy Term E (K cal./mole, 25°)</u>
C-C	82.6
C=C	145.8
C≡C	199.6
C-N	72.8
C=N	147
C≡N	212.6
C-O	85.5
C=O aldehydes	176
C=O ketones	179
C-S	65
N-N	39
N=N	100
Si-O silicones	106? ^b

^aAll values are deduced from aliphatic compounds and are taken from T.L. Cottrell, "The Strengths of Chemical Bonds," Butterworths Scientific Publications, London, 1958, pp. 270-275.

^b? = doubtful value

ULTRAVIOLET RADIATION EFFECTS

Most organic molecules lie in a singlet ground state (RH). Absorption of a photon raises the molecule to an excited singlet or triplet state (RH*). If the molecule has sufficient energy in the excited state, bond dissociation may take place (R. + H.). This decomposition process must compete with other deexcitation processes. The excited molecule may revert to the ground state by emission of heat or energy (hv) in the form of fluorescence or phosphorescence. The later processes allow the excited molecule to return to the ground state without producing a chemical change. Reversion to the ground state may also occur by the transfer of electronic energy from one group to another group in the vicinity of the excited molecule. An example of this occurs in polymethylphenylsiloxane where the phenyl group absorbs the UV energy then transfers this to the methyl group where degradation occurs.

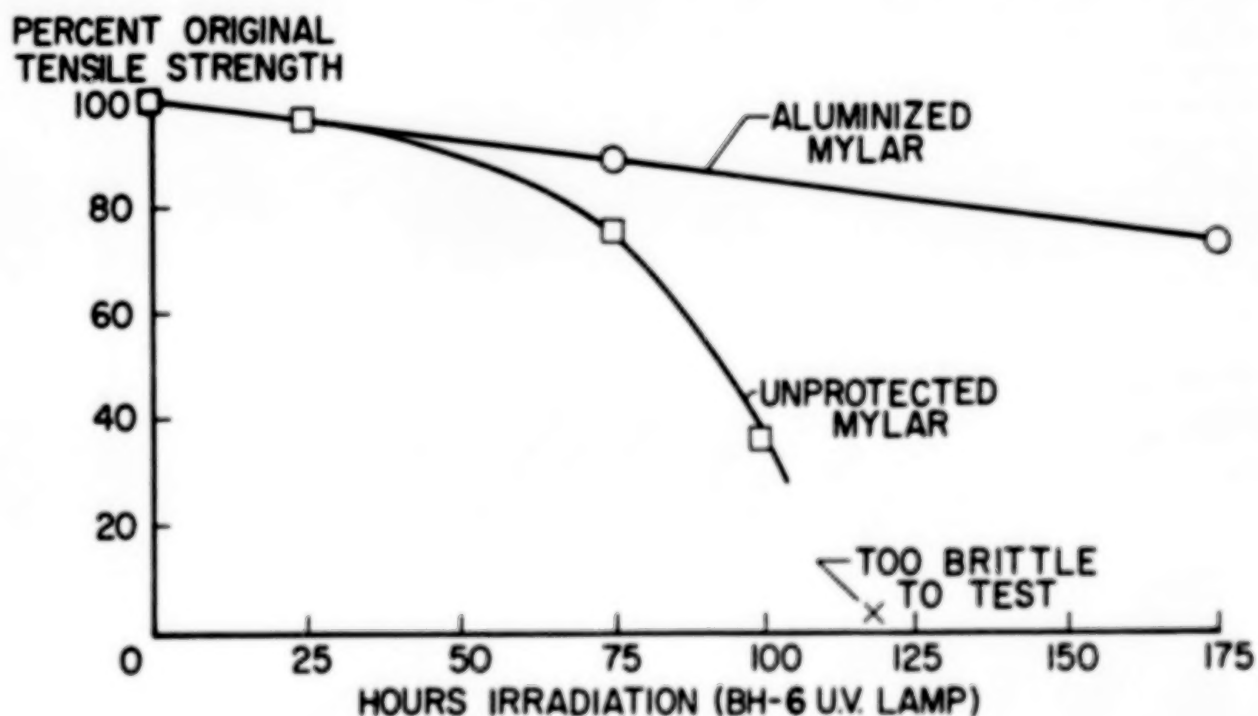


OTHER POSSIBLE REACTIONS



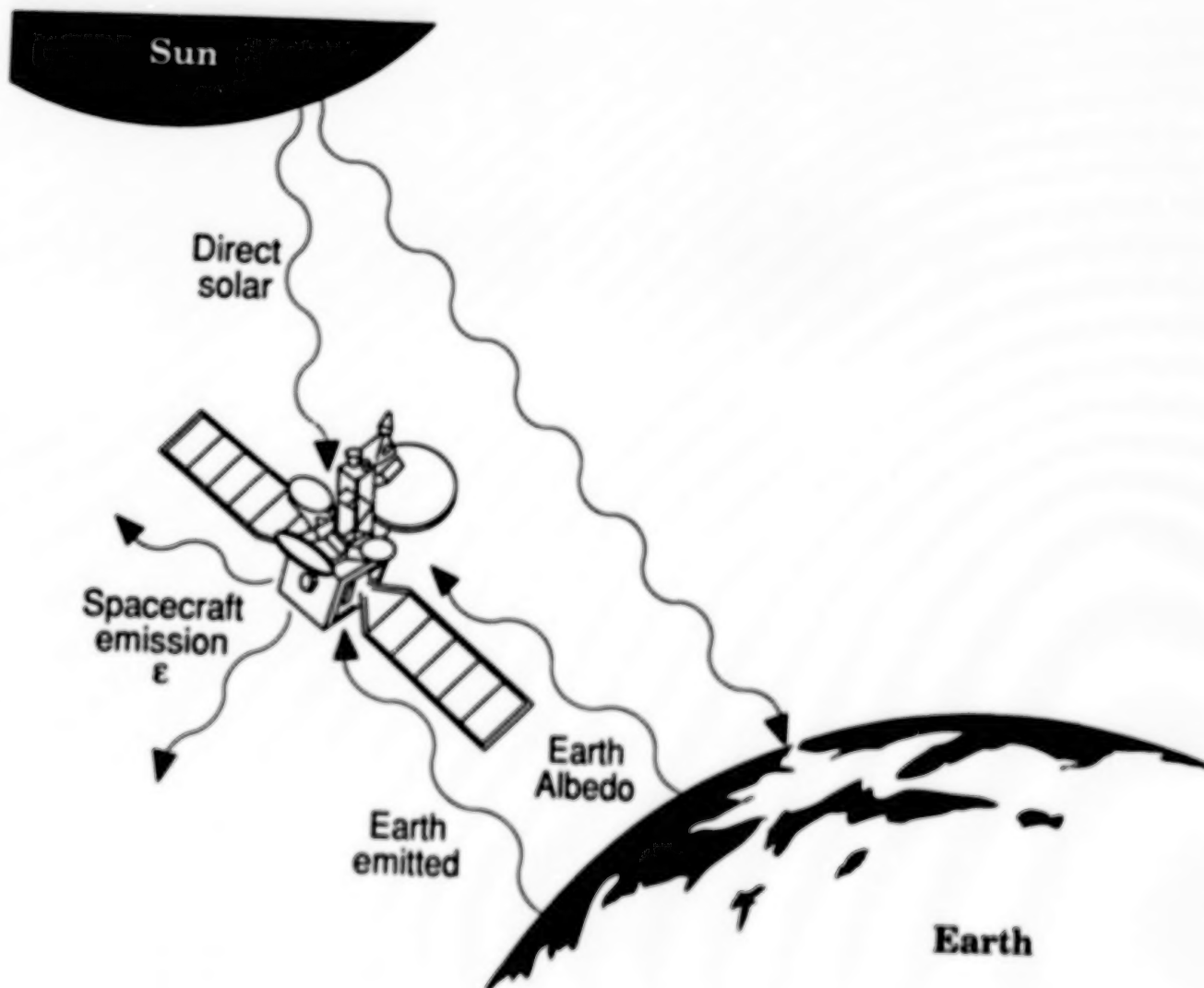
EFFECT OF ULTRAVIOLET RADIATION ON THE TENSILE STRENGTH OF MYLAR

This figure illustrates that UV radiation can degrade the mechanical properties of polymeric materials although the major research emphasis has been on changes in optical properties of polymer films.



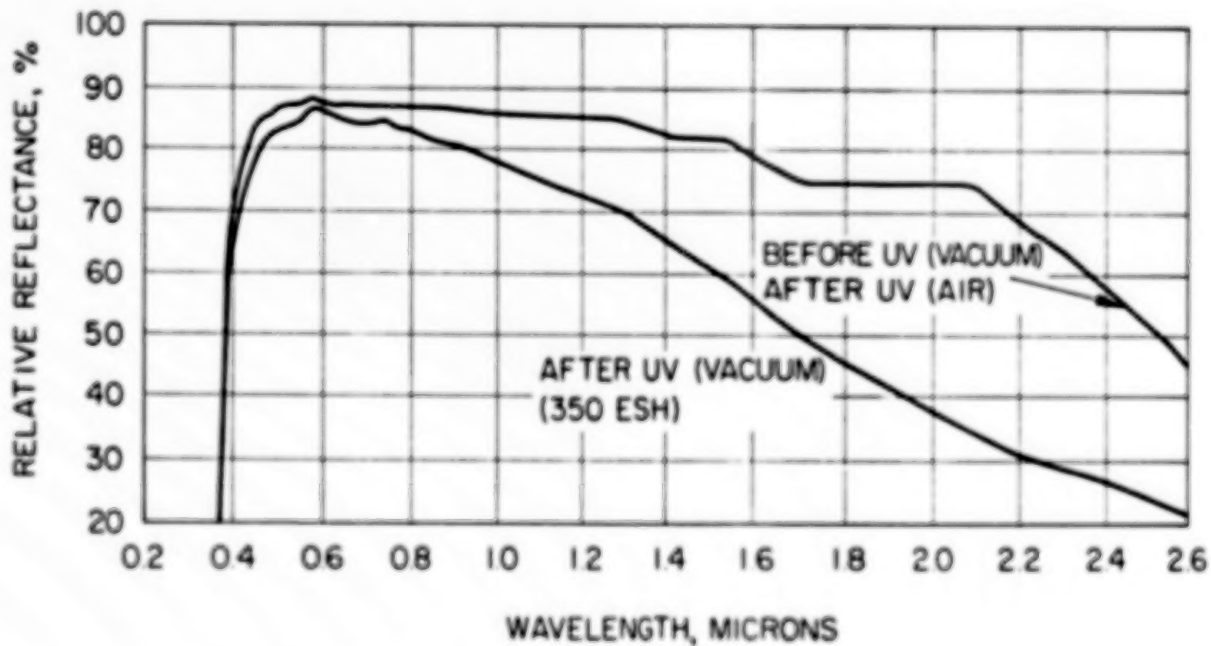
LEO SPACECRAFT THERMAL CONTROL ENVIRONMENT

The thermal control environment for a low Earth orbital satellite consists of the direct solar radiation, the Earth albedo (sunlight reflected from clouds, terrain, and water), and the emitted radiation from the Earth. The absorptance of the spacecraft with its view factor to each of these heat sources is balanced against the emission of heat from the spacecraft.



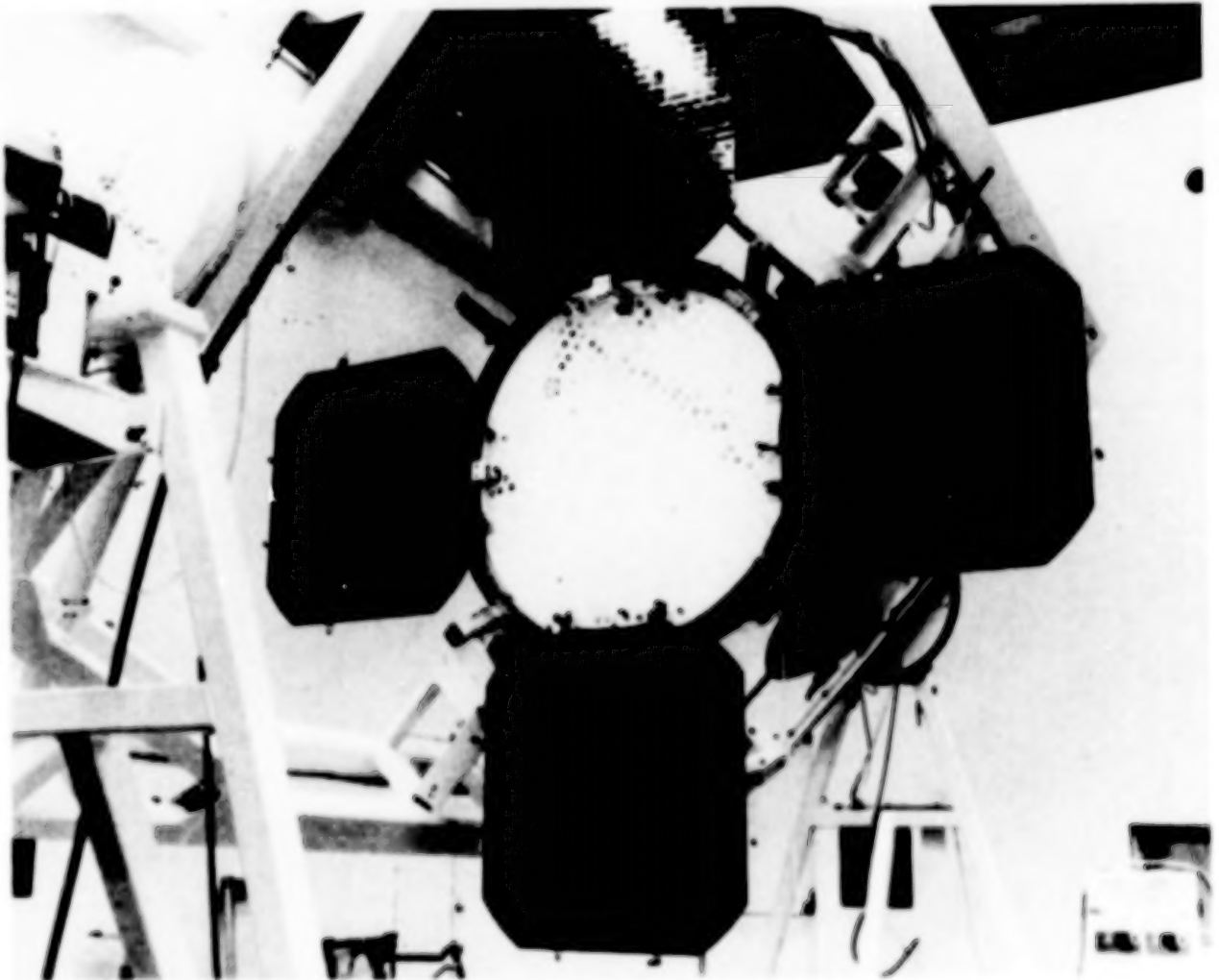
STRUCTURAL REFLECTANCE OF ZINC OXIDE-SILICONE

This figure illustrates the change in spectral reflectance due to UV exposure in vacuum for a zinc-oxide, pigmented silicone paint S-13. The figure also illustrates that upon introduction of air (oxygen) into the vacuum system, bleaching occurs which eliminates the UV degradation to this coating. This bleaching of white paints has led to the need for in situ testing of spacecraft coatings.



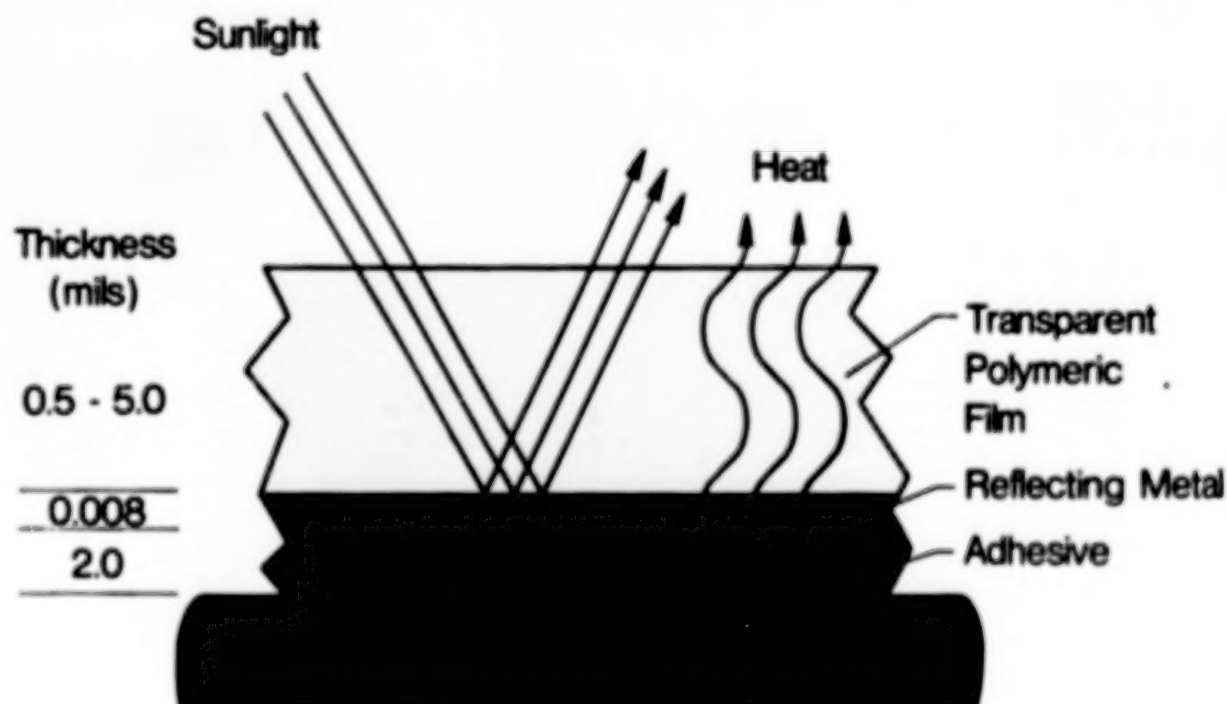
LUNAR ORBITER IV

The radiator on the Lunar Orbiter spacecraft was coated with the S-13 paint before in situ testing was found to be required. Lunar Orbiters I and II experienced very dramatic temperature increases due to UV and solar wind plasma degradation of the coating. To offset the increase in solar absorptance of the white paint, about 20 percent of the radiator area on Lunar Orbiters IV and V were coated with quartz optical solar reflectors.



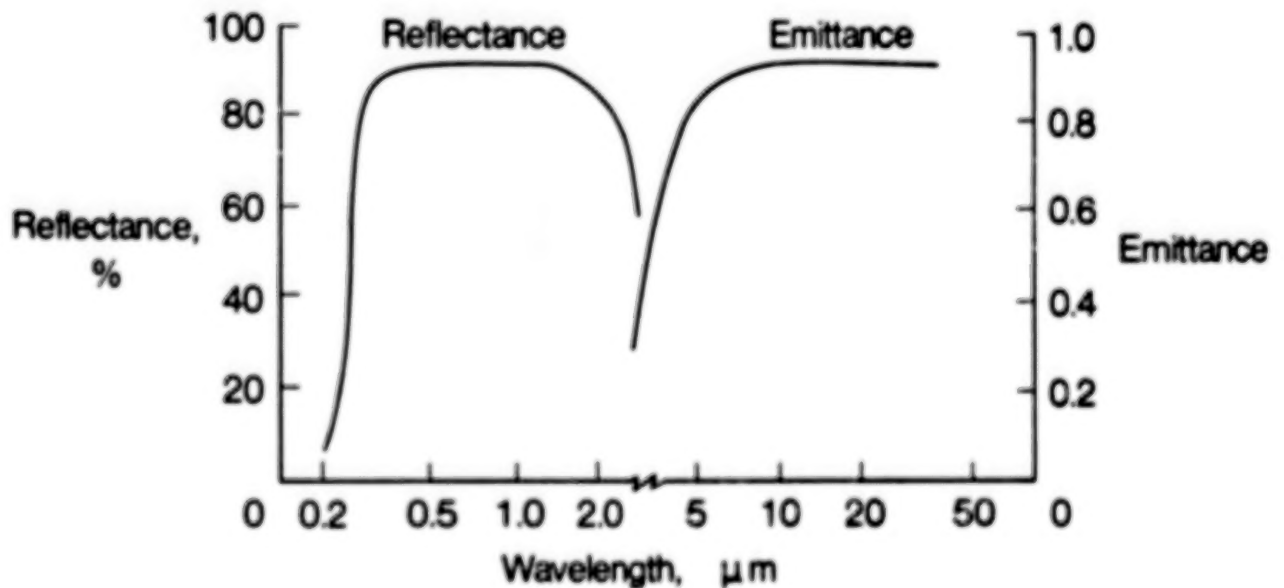
FLEXIBLE SECOND-SURFACE MIRROR (SSM) THERMAL CONTROL COATING

This figure is a schematic of a flexible second-surface mirror coating. The coating consists of a polymeric film that is transparent in the solar wavelength region and is coated on the back side with a reflecting, opaque metal like aluminum or silver. An adhesive is placed behind the metal to hold the coating to the spacecraft. Typically, the larger the thickness of the polymeric film, the stronger the absorption bands are in the infrared, out of the solar wavelength region, and therefore, the higher the emittance of the coating. An example of an SSM coating is silvered - perfluorinated ethylene propylene copolymer (FEP) Teflon.



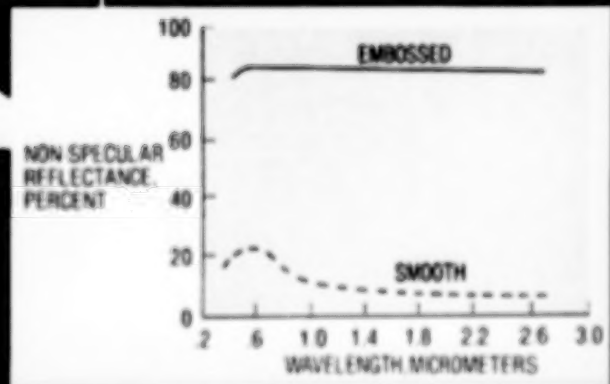
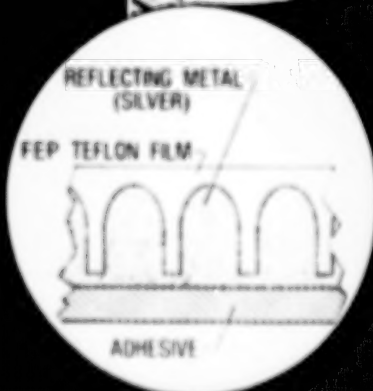
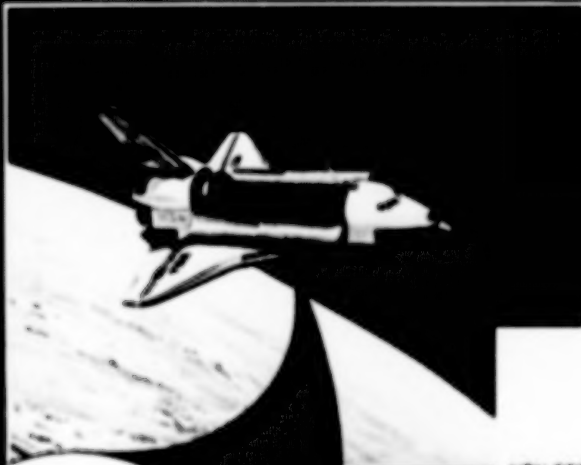
CHARACTERISTICS OF THERMAL CONTROL COATINGS

The figure helps to explain the radiation characteristics of the SSM coating in the previous figure. The reflectance of this coating and the transparency of the polymeric film must occur from 0.2 to 3.0 micrometers, the region of maximum solar energy. But the coating is radiating heat away from a spacecraft which has a maximum temperature of about 100°C; therefore, this energy is found in the infrared from 10 to 50 micrometers. The characteristic absorption bands of polymers provide this infrared emittance.



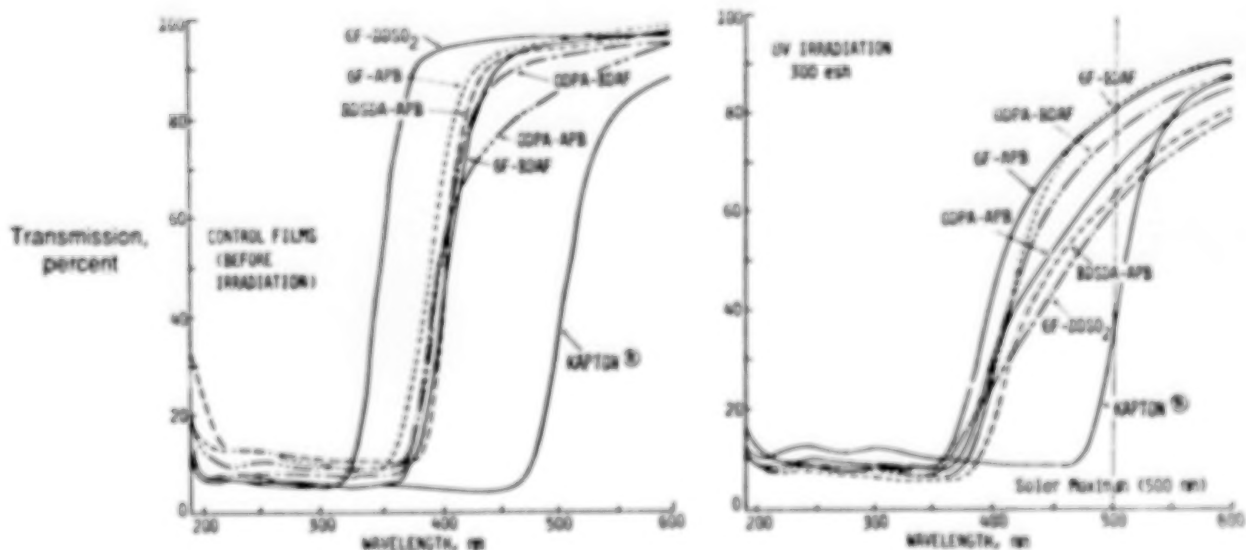
NON-SPECULAR SILVERED TEFLON

The non-specular reflecting silvered Teflon SSM coating used on the Orbiter's radiators was developed at NASA Langley. The FEP Teflon is embossed with a special roller to provide light scattering on the metal coating side leaving the outside smooth to prevent trapping contamination in the Teflon surface. The process reduces the specular reflectance to about 15 percent but maintains the 0.09 solar absorptance of the smooth silvered Teflon SSM.



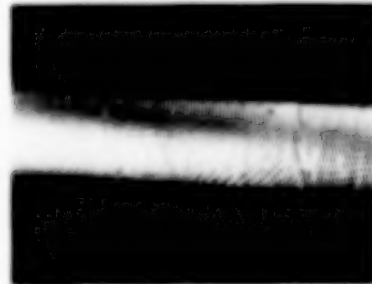
EFFECT OF UV RADIATION ON TRANSMISSION OF TRANSPARENT POLYIMIDE FILMS

This figure illustrates some current studies being conducted at NASA Langley on highly transparent polyimide films. These films are stable to about 300°C and are soluble in the imide form, which means they are sprayable. Some of these experimental films have exhibited high stability to simulated solar UV and high energy electron radiation.



ALUMINUM FOIL COATING FOR COMPOSITE TUBES

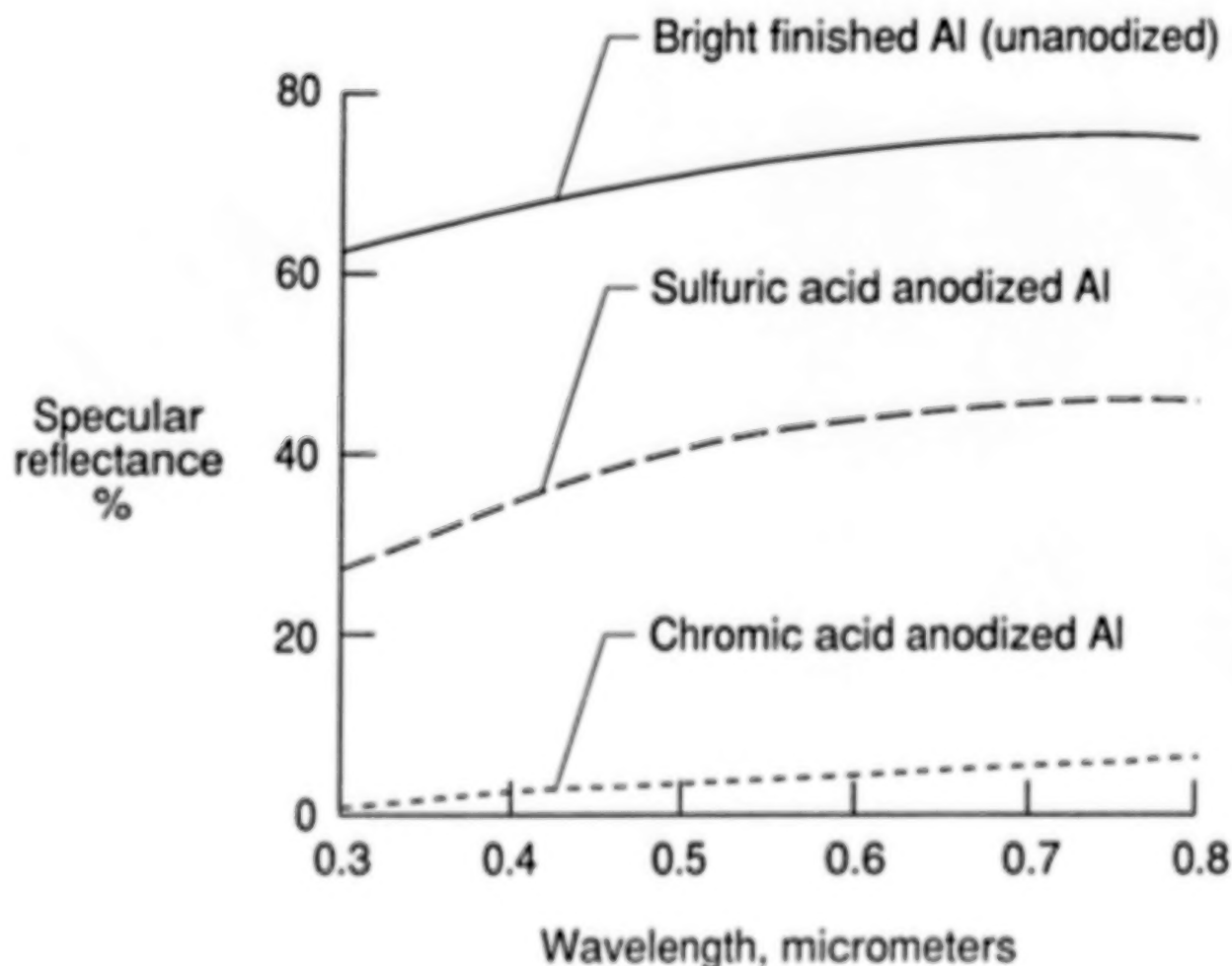
A concept for thermal control and atomic oxygen protection for the composite tubes used as structural elements in the Space Station Freedom has been developed at NASA Langley and demonstrated under contract with Boeing Aerospace Company. Aluminum foil 0.008 cm thick is anodized or sputter coated with SiO_x to achieve the desired radiation properties of 0.3 solar absorptance and 0.65 emittance. This aluminum foil is then adhesively bonded to the exterior of the graphite/epoxy tube. Process specifications have been developed for achieving the radiation properties with chromic acid anodizing.



- Can be anodized or sputter coated to achieve desired optical properties
- Application techniques can provide a non-specular reflecting coating
- Provides atomic oxygen protection for composite tubes
- Resistant to abrasion and UV degradation
- Demonstrated on 2 inch dia. X 8 feet long P75/934 graphite/epoxy composite tubes

SPECULAR REFLECTANCE OF CHEMICALLY TREATED ALUMINUM

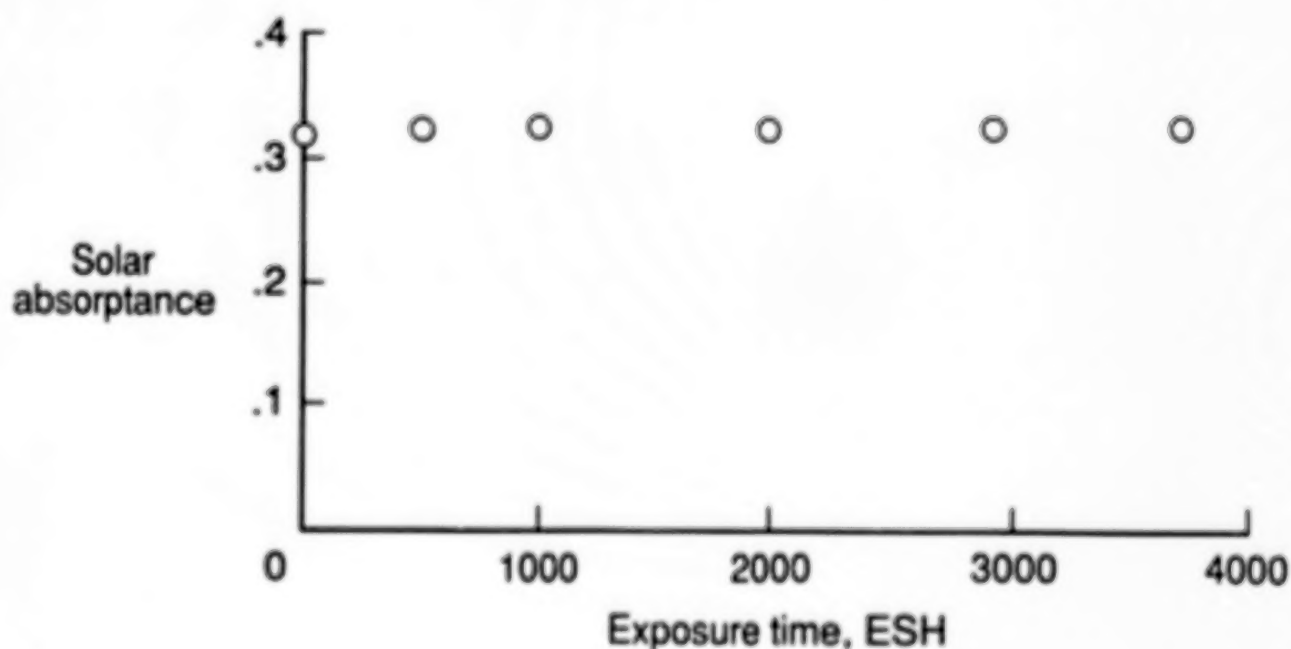
It is highly desirable to have a low solar absorptance coating on the composite structural members which would not be a specular reflector. With the large number of structural members in the Space Station Freedom, sunlight reflected from these members can interfere with optical experiments on the Freedom. This figure shows that the chromic acid anodizing process provides less than 5 percent specular reflectance at 0.5 micrometers, the peak solar wavelength, where the sulfuric acid process has nearly 40 percent specular reflectance.



EFFECTS OF UV ON SOLAR ABSORPTANCE OF
SEALED CHROMIC-ACID ANODIZED 1145 AL 3 MIL FOIL

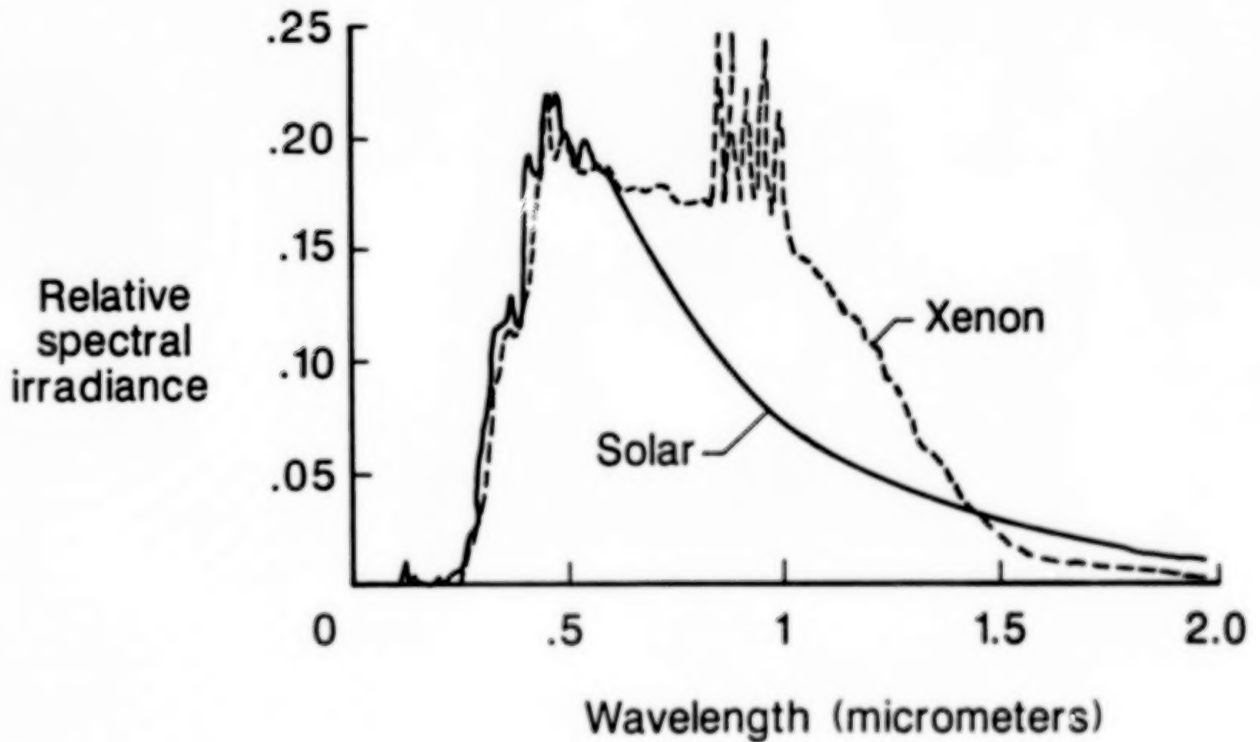
The chromic acid anodized aluminum foil used to coat the composite tubes for the Space Station Freedom has been exposed to simulated solar ultraviolet radiation at NASA Langley. These results show that the coating is very stable to UV radiation having only a 0.02 increase in solar absorptance in 4,000 equivalent solar hours (2,000 hours x 2 solar constants).

2x ESH, air mass zero



SOLAR IRRADIANCE SIMULATION WITH XENON

This figure compares the spectral irradiance of a xenon short-arc lamp with a quartz envelope to the solar irradiance at air mass zero. The figure clearly shows that xenon has a good UV solar match from approximately 0.2 to 0.7 micrometers but is much more intense in the infrared region. This IR radiation leads to over heating of test specimens when accelerated exposure is attempted. Experimental results indicate that acceleration factors of only 3X are possible without substantially overheating the test specimens.



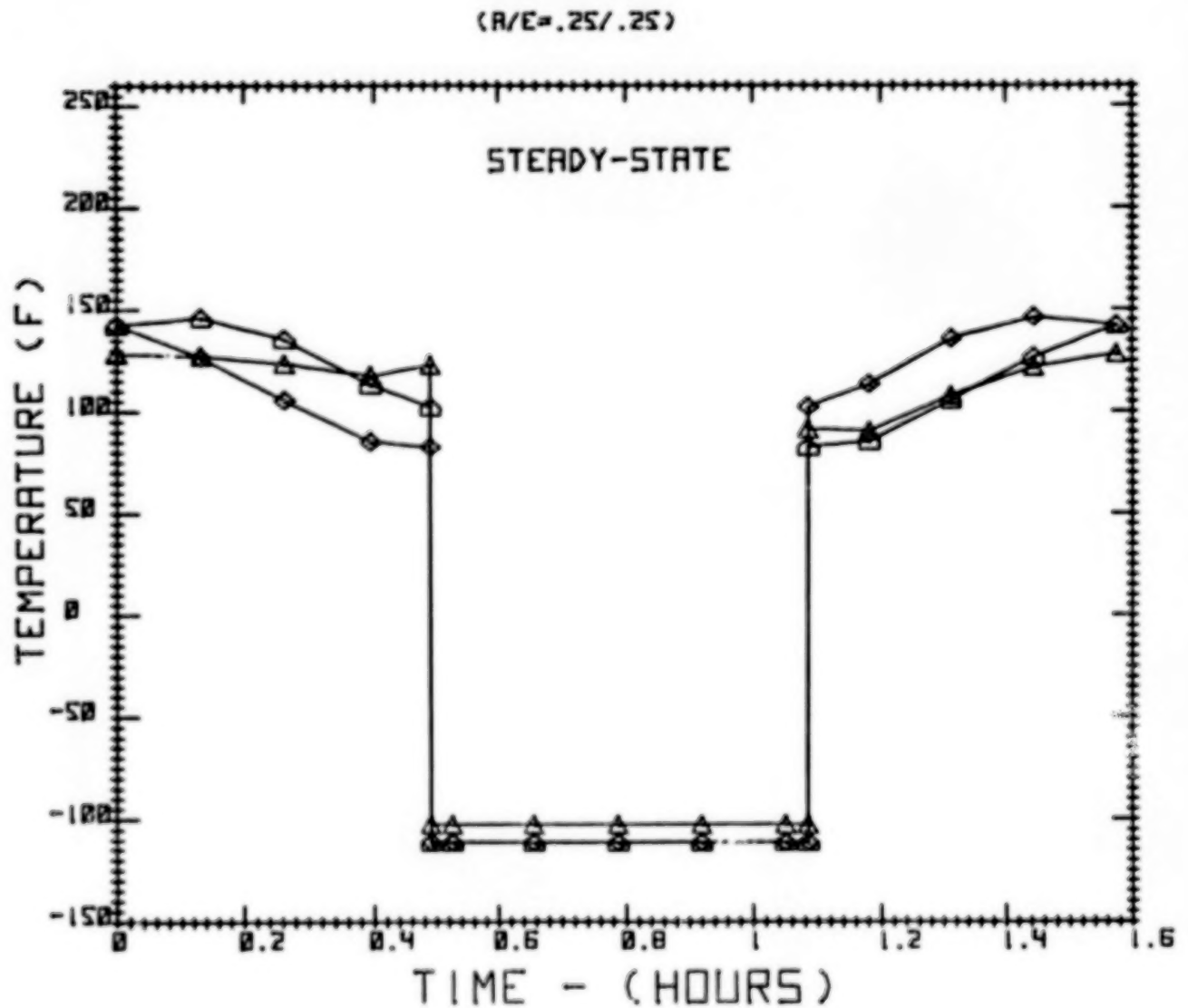
PROBLEMS ASSOCIATED WITH SOLAR SIMULATION

When most investigators expose materials to simulated solar UV, the irradiance of the UV beam is measured and referred to as a percentage of the solar irradiance at air mass 0. Since many spacecraft rotate, then this must be taken into account in calculating one solar constant. Also the shape factor for the spacecraft surface and the orbital parameters must be considered. Many spacecraft will have only 25 percent of their time in orbit in the sun. This would be a 4 to 1 acceleration factor even if the laboratory exposures were conducted at one solar constant.

- One solar constant assumes nonrotating spacecraft in constant sunlight, but most rotate
- Shape factor of 1 where, in reality, shape factor is near 0.5
- Near Earth orbit is approximately 90 min. with about 30 min. in solar occult
- Reality is 25% to 40% of time in sunlight for spacecraft surfaces

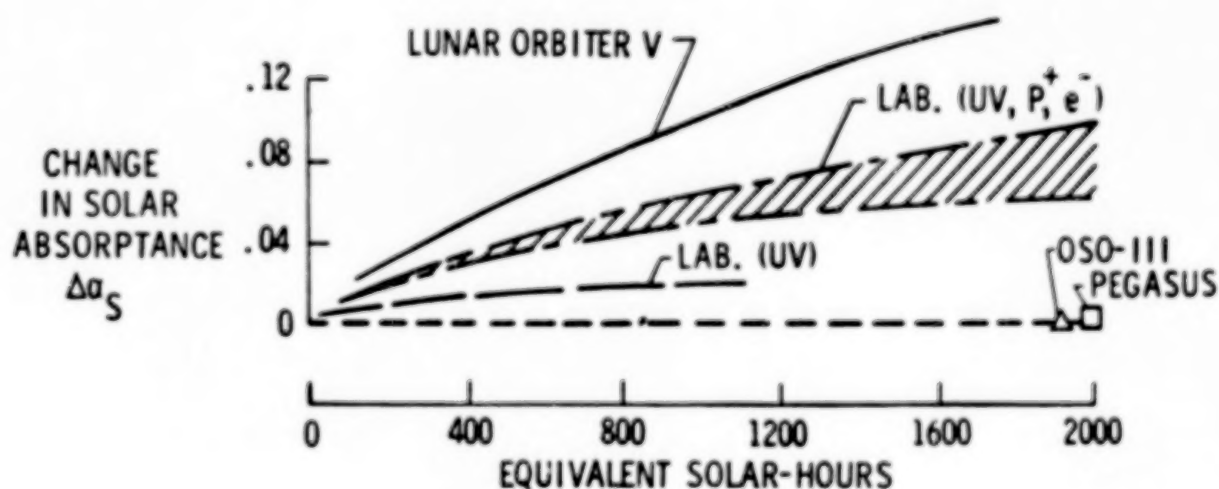
TRUSS TUBE TEMPERATURES

This is a steady state calculation for a composite tube with an α/ϵ of .25/.25 in the proposed Space Station Freedom orbit. This projects the thermal cycle range and shows the typical occult for these conditions.



COMPARISON OF FLIGHT AND LABORATORY DATA ON ZINC OXIDE-POTASSIUM SILICATE COATING Z-93

This figure was prepared a number of years ago from flight and laboratory data conducted using short arc xenon UV source and a 3 kev solar wind proton source with thermal electrons for charge neutralization. The combined UV and solar wind plasma experienced on Lunar Orbiter V was under simulated in the laboratory. The UV degradation experience by OSD-III and Pegasus was over simulated in the laboratory test. No changes in procedures or equipment which have been made since these tests were conducted would alter these results.



SUMMARY

Solar ultraviolet testing has not been developed which will provide highly accelerated (20 to 50X) exposures that correlate to flight test data. Additional studies are required to develop an exposure methodology which will assure that accelerated testing can be used for qualification of materials and coatings for long-duration space flight.

- **Solar UV radiation is present in all orbital environments**
- **Solar UV does not change in flux with orbital altitude**
- **UV radiation can degrade most coatings and polymeric films**
- **Laboratory UV simulation methodology is needed for accelerated testing to 20 UV solar constants**
- **Simulation of extreme UV (below 200 nm) is needed to evaluate requirements for EUV in solar simulation**

EFFECTS OF THERMAL CYCLING ON COMPOSITE MATERIALS FOR
SPACE STRUCTURES

Stephen S. Tompkins
Materials Division
NASA Langley Research Center
Hampton, Virginia 23665-5225

THERMAL CYCLING OF COMPOSITE MATERIALS IN ORBIT

Thermal cycling, which can result from the spacecraft orbiting the Earth, is one of several space service environmental parameters that can affect composite structural materials, ref. 1. As the spacecraft passes in and out of the Earth's shadow, the temperature of the structure rises and falls. The minimum and maximum temperatures reached and the induced effects on the material are directly related to the properties of the material and the thermal control coating. The materials may also experience thermal cycling as a result of structural members casting shadows on other parts of the structure.



OBJECTIVE

The objective of this paper is to briefly describe the effects of thermal cycling on the thermal and mechanical properties of composite materials that are candidates for space structures. The outline for this paper is shown below. The results from a thermal analysis of the orbiting Space Station Freedom will be used to define a typical thermal environment and the parameters that cause changes in the thermal history. The interactions of this environment with composite materials will be shown and described. The effects of this interaction on the integrity as well as the properties of Gr/thermoset, Gr/thermoplastic, Gr/metal and Gr/glass composite materials are discussed. Emphasis will be placed on the effects of the interaction that are critical to precision spacecraft. Finally, ground test methodology will be briefly discussed.

EFFECTS OF THERMAL CYCLING ON COMPOSITE MATERIALS FOR SPACE STRUCTURES

OUTLINE

- Thermal environment
- Material/environment interaction
- Effects on materials:
 - Gr/thermoset
 - Gr/thermoplastic
 - Metal - matrices
 - Glass - matrices
- Ground test methodology

SPACE STATION FREEDOM TRUSS STRUCTURE THERMAL ANALYSIS

The expected thermal history of the Space Station Freedom truss structure will be used to illustrate a typical thermal input to a spacecraft. The temperature history of a single 2-inch diameter, P75 graphite/epoxy tube orbiting the earth at 270 nautical miles was analyzed with the TRASYS orbital mechanics model and the SINDA thermal analyzer assuming no shadowing by other structural members. The tube temperature history is shown below.

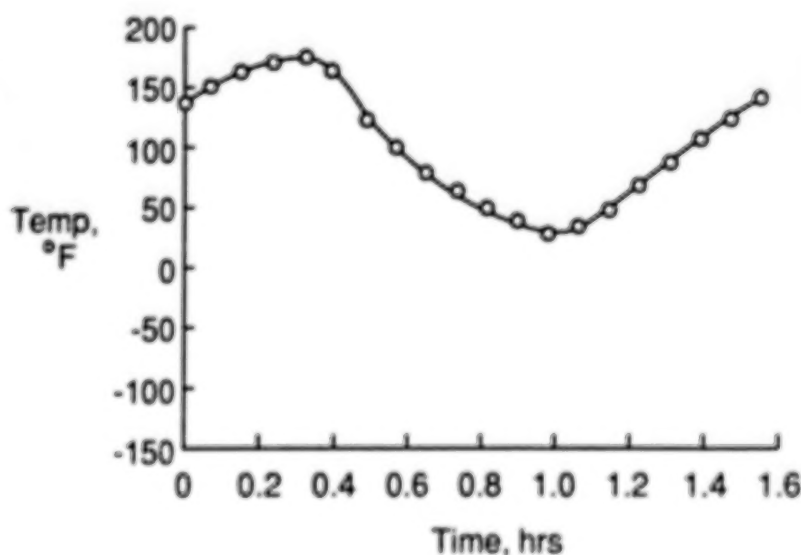
For a tube with a solar absorptance-to-emittance ratio, α_s/ϵ , of 0.3/0.2, the temperature varies between about 175°F to about 25°F over a period of about 90 minutes. The period of the thermal cycle depends upon the altitude of the orbit and the amplitude of the cycle depends upon the α_s/ϵ ratio.

Typical tube temperature cycling range

Solar absorptance/emittance = .3/.2

Thermal analysis

- Single tube (9 ft long, 2 in. ID)
- P75 graphite/epoxy
- Orbital parameters
 - Beta = 0 deg.
 - Altitude = 270 N. miles
- TRASYS and SINDA models

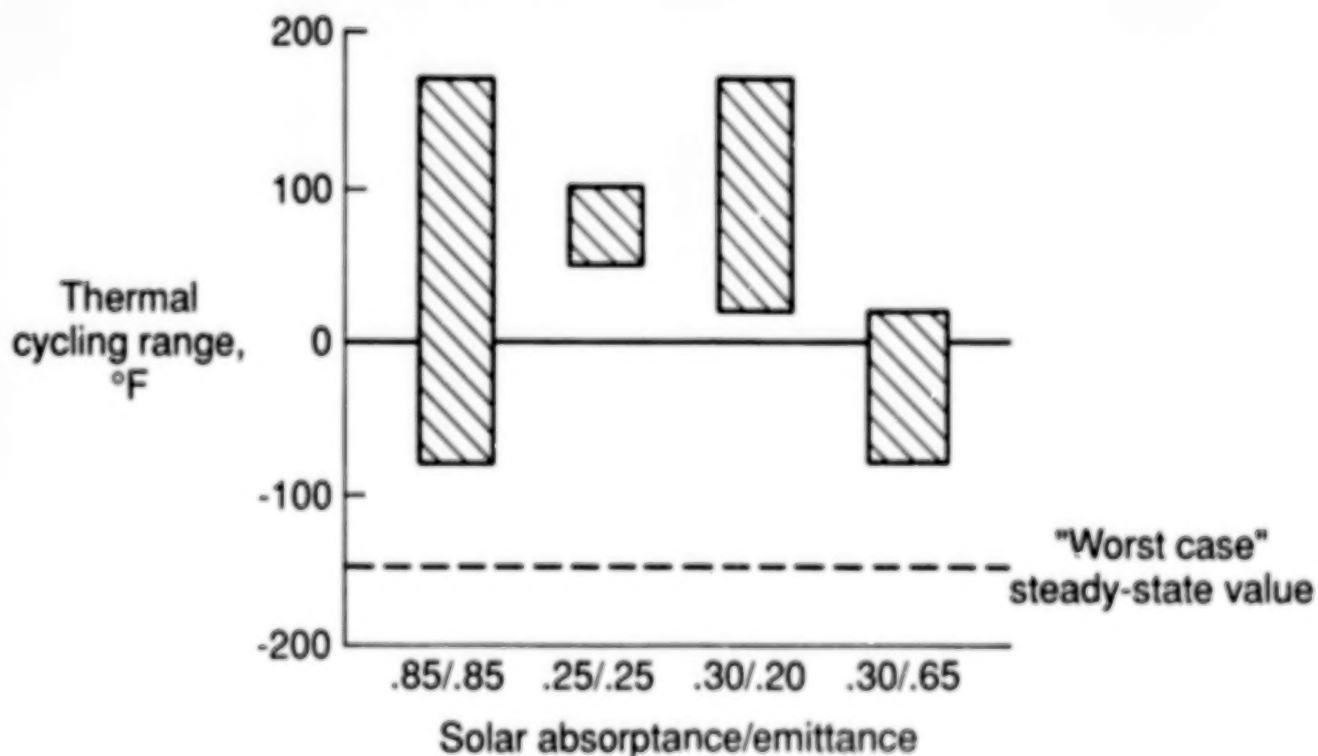


EFFECTS OF SOLAR ABSORPTANCE/EMITTANCE ON TEMPERATURE RANGE

The effects of material surface solar absorptance/emittance ratio, α_s/ϵ on the amplitude of the thermal cycle is shown in the figure below. These results are from a transient analysis of a 2-inch diameter, P75S Gr/Ep composite tube orbiting the Earth. The data shows that the temperature range is very sensitive to α_s/ϵ . For a bare Gr/Ep tube, $\alpha_s/\epsilon = 0.85/0.85$, the temperature range is from about 175°F to about -80°F. The ideal range would be small and centered around room temperature. However, degradation of the thermal control coating could change the α_s/ϵ ratio and significantly change the range. For example, degradation from 0.25/0.25 to 0.30/0.20, causes the temperature range to change from 50°F to 100°F to about 20°F to 175°F. For Space Station Freedom the steady-state cold temperature is estimated to be -150°F; however, some spacecraft could reach as low as -250°F.

SPACE STATION TRUSS STRUCTURE THERMAL CYCLING RANGE

Single 2 in. i.d., P75 Gr/Ep tube



COMPOSITE CONSTITUENT AND LAMINA PROPERTIES

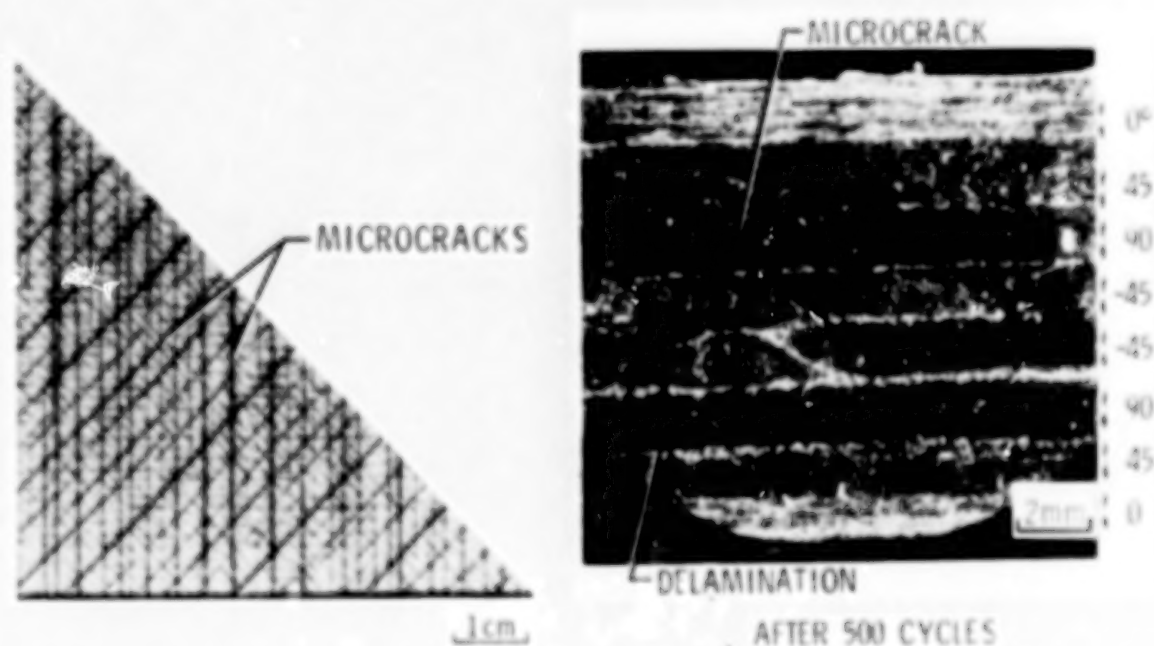
Composite materials are made by combining fibers and matrix materials to form a simple lamina. Laminae are then stacked in various ways to form laminates with the desired properties. Typical room temperature thermal and mechanical properties of continuous graphite fibers, matrix and laminate considered for space structures are shown below. Both high strength and modulus fibers are candidates. The orthotropic character of the fibers becomes evident when the axial and radial properties are compared. Note that the axial coefficients of thermal expansion (CTE), A_1 , are small and negative. The matrix materials have low strength and low modulus and, except for the glass, have large, positive CTE. When combined, the fibers and matrices form highly orthotropic unidirectional lamina. The large differences in the CTE of the fiber and matrix as well as the differences in the directional CTEs of the lamina can result in very high stresses induced by thermal cycling in the laminates as well as the lamina.

Material	Modulus		Strength		CTE	
	E1 Msi	E2 Msi	Xt ksi	Yt ksi	A1 ppm/F	A2 ppm/F
Fibers						
T300	33.8	3.35	350	--	-0.30	5.6
HMS	55.0	0.90	250	--	-0.55	3.80
P75	79.8	1.38	300	--	-0.75	3.80
P100	115.5	1.05	325	--	-0.78	3.80
Matrix						
934	0.67	--	8.5	--	24.4	--
PMR 15	0.5	--	8	--	20.0	--
2024 Al	10.6	--	60	--	12.9	--
Glass	9.1	--	--	--	1.8	--
Lamina						
T300/934	18.9	1.4	223	9.37	-0.01	16.13
P75/934	42.0	0.83	102	3.51	-0.58	19.18
HMS/Glass	24.	1.1	86.3	2.6	-0.23	2.1
P100/2024	47.8	3.6	92.2	8.89	0.800	14.51

TYPICAL THERMAL INDUCED MICRODAMAGE

The primary effect of thermal cycling on composites is the induced thermal stresses and the resulting damage. Typical microdamage induced by thermal cycling of continuous graphite reinforced polymers is shown in the figure below. The micrograph shows microcracks and delaminations formed in a $[0/45/90/-45]_s$ laminate of C6000/PMR-15 after 500 cycles between -156°C and 316°C , as viewed along a polished edge of the specimen. The thermal cycling in orbit can be considered low amplitude thermal fatigue with the net material effects (microdamage) changing with time. The microcracks began as intraply cracks and grew to interply cracks as the number of cycles increased. Delaminations appeared as the number of cycles increased. An X-ray of the top of the specimen is also shown below. The dark lines are the cracks, enhanced with a dye, that run parallel to the fibers in each lamina over the entire width and length of the specimen. Although this composite material is very brittle, has a high cure temperature (resulting in high residual stresses), and the temperature range is large, similar cracks have been observed in composites with lower cure temperatures even after cycling between a smaller temperature range, -100°C to 66°C .

TYPICAL X-RAY OF C6000/PMR-15 LAMINATE [0/45/90/-45] AFTER 500 CYCLES BETWEEN -156°C AND 316°C

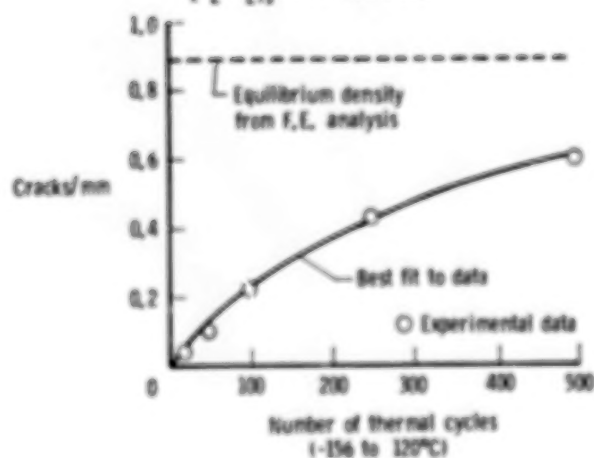


THERMAL CYCLING EFFECTS ON GRAPHITE/EPOXY COMPOSITES

The increase in the crack density (cracks/length of specimen) as thermal fatigue progresses, is shown below. As the number of cycles increases, the crack density asymptotically approaches an equilibrium value. For the T300/5208 $[0_2/90_2]_3$ graphite/epoxy laminate shown here, the equilibrium density may not be reached for several thousand cycles. The coefficient of thermal expansion, CTE, is one of the laminate properties that can be greatly affected by microcracking. For this laminate, the CTE was reduced by about 40% after 500 thermal cycles. Additional reduction may be expected since the laminate had not reached its equilibrium crack density for this temperature range.

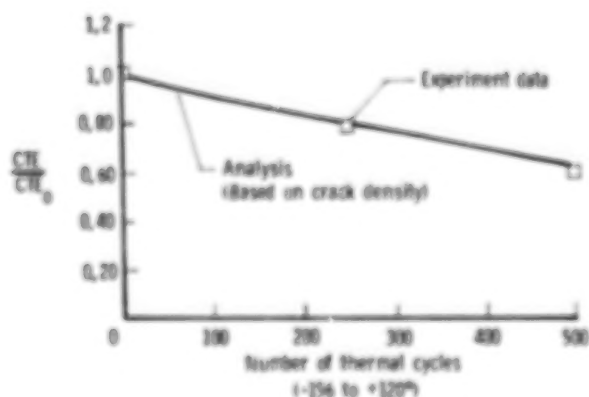
EFFECT OF THERMAL CYCLING ON MICROCRACK DENSITY

$[0_2/90_2]_3$ T300/5208 Gr/Ep



EFFECT OF THERMAL CYCLING ON THE COEFFICIENT OF THERMAL EXPANSION

$[0_2/90_2]_3$ T300/5208 Gr/Ep

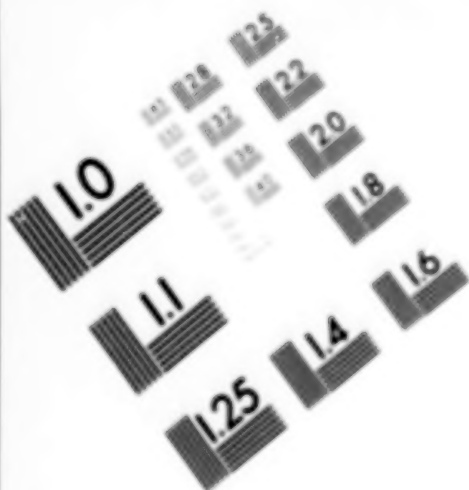




AIM

Association for Information and Image Management

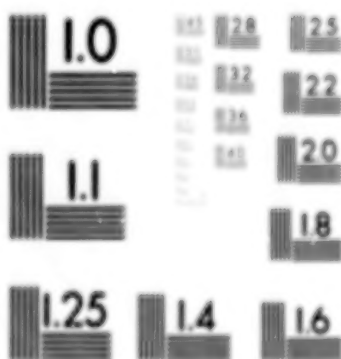
1100 Wayne Avenue, Suite 1100
Silver Spring, Maryland 20910
301/587-8202



Centimeter



Inches



MANUFACTURED TO AIM STANDARDS
BY APPLIED IMAGE, INC.

